ISSN 1980-9743
ISSN-e 2675-5475

Soils and Rocks

Soils and Rocks
Volume 43, N. 4
2020

SOILS and ROCKS

An International Journal of Geotechnical and Geoenvironmental Engineering

Editor Renato Pinto da Cunha - University of Brasília, Brazil

Co-editor José Couto Marques - University of Porto, Portugal

Soils and Rocks publishes papers in English in the broad fields of Geotechnical Engineering, Engineering Geology, and Geoenvironmental Engineering. The Journal is published quarterly in March, June, September and December. The first issue was released in 1978, under the name *Solos e Rochas*, being originally published by the Graduate School of Engineering of the Federal University of Rio de Janeiro. In 1980, the Brazilian Association for Soil Mechanics and Geotechnical Engineering took over the editorial and publishing responsibilities of *Solos e Rochas*, increasing its reach. In 2007, the journal was renamed Soils and Rocks and acquired the status of an international journal, being published jointly by the Brazilian Association for Soil Mechanics and Geotechnical Engineering, by the Portuguese Geotechnical Society, and until 2010 by the Brazilian Association for Engineering Geology and the Environment.

Soils and Rocks

1978,	1 (1, 2)
1979,	1 (3), 2 (1,2)
1980-1983,	3-6 (1, 2, 3)
1984,	7 (single number)
1985-1987,	8-10 (1, 2, 3)
1988-1990,	11-13 (single number)
1991-1992,	14-15 (1, 2)
1993,	16 (1, 2, 3, 4)
1994-2010,	17-33 (1, 2, 3)
2011,	34 (1, 2, 3, 4)
2012-2019,	35-42 (1, 2, 3)
2020,	**43 (1, 2, 3, 4)**

ISSN 1980-9743
ISSN-e 2675-5475 CDU 624.131.1

ISSN 1980-9743
ISSN-e 2675-5475

SOILS and ROCKS
An International Journal of Geotechnical and Geoenvironmental Engineering

Publication of
ABMS - Brazilian Association for Soil Mechanics and Geotechnical Engineering
SPG - Portuguese Geotechnical Society
Volume 43, N. 4, October-December 2020

Table of Contents

LECTURE
Lessons learned from dam construction in Patagonia Argentina
Oscar A. Vardé *503*

ARTICLES
Evaluation of the accuracy of the cubic law for flow through fractures using Lattice Boltzmann method
Ali Ghassem, Javad Abbaszadeh, Ali Pak 521

The influence of the fluid dielectric constant on the shear strength of a unsaturated soil
M.S.S. Almeida, S.L. Machado, H.M.C. Andrade 535

Mass movements in the Northeast region of Brazil: a systematic review
Bruna Silveira Lira, Maria Natália de Melo Sousa, Olavo Francisco dos Santos Junior, Carina Silvani, Edilza Rakel Nóbrega, Gustavo Clementino Santos 549

Experimental study on particle size effect on mechanical behaviour of dense calcareous sand
Du-min Kuang, Zhi-lin Long, Jie Wang, Xu-tong Zhou, Piao-yi Yu 567

A predictive model for the peak shear strength of infilled soft rock joints developed with a multilayer perceptron
Ana Raquel Sena Leite, Silvrano Adonias Dantas Neto 575

Behavioral evaluation of earth dams built with materials above optimum moisture content in high rainfall areas
Julián Buriticá García, André Pacheco de Assis, Juan P. Villacreses 591

Application of kernel k-means and kernel x-means clustering to obtain soil classes from cone penetration test data
L.O. Carvalho, D.B. Ribeiro 607

Geostatistical data analysis of the Standard Penetration Test (SPT) conducted in Maringá-Brazil and correlations with geomorphology
Augusto Montor de Freitas Luiz, Nelcí Helena Maia Gutierrez 619

Advances on dosages for cement stabilized rammed Guabirotuba silt depending on climate conditions
Jair de Jesús Arrieta Baldovino, Ronaldo Luis dos Santos Izzo, Juliana Lundgren Rose 631

Constitutive modeling of residual soils based on irreversible strains decomposition
Alessandro Cirone, Eurípedes Vargas Jr., Tácio de Campos 647

TECHNICAL NOTES
Determination of liquid limit by the Fall Cone method
C.W. Clemente, V.P. Faro, M.P.H. Moncada 661

The effect of grain size of ground glass particles on the strength of green stabilized sand
Hugo Carlos Scheuermann Filho, Rafael Luís Sacco, Nilo Cesar Consoli 669

Mechanical and environmental performance of polymer stabilized iron ore tailings
Andressa de Araujo Carneiro, Michéle Dal Toé Casagrande 679

CASE STUDY
Compression and shear strengths of sandy limestone and the role of the porosity: a case study
Yousr Koobaa, Houda Guiras, Mehrez Jamei 693

Victor de Mello Lecture

The Victor de Mello Lecture was established in 2008 by the Brazilian Association for Soil Mechanics and Geotechnical Engineering (ABMS), the Brazilian Association for Engineering Geology and the Environment (ABGE) and the Portuguese Geotechnical Society (SPG) to celebrate the life and professional contributions of Prof. Victor de Mello. Prof. de Mello was a consultant and academic for over 5 decades and made important contributions to the advance of geotechnical engineering. Every second year a worldwide acknowledged geotechnical expert is invited to deliver this special lecture, on occasion of the main conferences of ABMS and SPG.

This 7th Victor de Mello Lecture is presented by one of the most prominent geotechnical engineers of South America and an old friend of Victor de Mello since 1963. Prof. Oscar A. Vardé is an internationally renowned professor, researcher and consultant. He wrote in the introduction to the de Mello Volume, published in Victor's tribute by his disciples in 1989 at the same time of the International Conference for Soil Mechanics and Foundation Engineering, in Rio de Janeiro in 1989. At this Conference Dr. Vardé presented a Special Lecture "Embankment Dams and Dam Foundations" written in collaboration with Victor de Mello, Peter Anagnosti and Norbert Morgenstern. Victor and Vardé participated as Consultants and Experts in numerous large hydroelectric projects in Argentina, Potrerillos, Yaceretá among others, as well as in other South American countries. For Prof. Vardé, Victor had an enormous influence on his professional and personal life that was not only based on his abilities and his teachings, but on his very essence, becoming a mentor, colleague and very close personal friend, an hermano.

Prof. Oscar A. Vardé, Civil Engineer, University of Buenos Aires, Engineering Faculty, Suma Cum Laude, 1959. Post-graduate studies in Canada and U.S.A. Honorary President of the Argentine National Academy of Engineering. Vice-President of ISSMGE, 1985-1989, and of ISRM, 1991-1995. Ex-President of the Geotechnical Argentine Society. Ex-Associate Professor of Soil Mechanics and Foundation Engineering, Universidad Católica Argentina, and Universidad Nacional de Buenos Aires. Arthur Casagrande Award, Panamerican Conference on Soil Mechanics and Foundation Engineering, Chile 1991; Raúl J. Marsal Prize, 1993; Academia Nacional de Ciencias Exactas, Físicas y Naturales; Konex Award in Science and Technology, as one of the five more distinguished engineers in Civil Engineering and Mechanics of Materials in Argentina, in the decade 1993-2003, among others recognitions. Author of 140 papers published in argentine and international technical events and Co-Editor of 5 books. Lecturer, general reporter and panelist in national and international congresses, seminars and conferences. Member as Consultant on International Boards, on Dams, Tunnels and Foundations.

Soils and Rocks
v. 43, n. 4

Soils and Rocks
An International Journal of Geotechnical and Geoenvironmental Engineering
www.soilsandrocks.com
ISSN 1980-9743
ISSN-e 2675-5475

Lessons learned from dam construction in Patagonia Argentina

Oscar A. Vardé[1,#]

Lecture

Keywords
Drainage galleries
Grouting
Karstic formations
Microgravimetry
Monitoring
Patagonia
Weak rocks

Abstract
Three case histories of large dams built in North Patagonia which experienced unforeseen problems during construction, or after several years of operation are described. The necessary remedial and corrective works involved the development of important programs, being economic and programmatic impacts of great magnitude. The lessons learned from these experiences were very useful to the practice of design and construction of dams in the region. At the sites of three projects: Casa de Piedra, Alicura and El Chocon weak rock foundation are founded. In Casa de Piedra, located in a regional environments with clear evidence of limestone and gypsum formations, the use of microgravimetry was appropriate for the detection of cavities or discontinuities that traditional survey research may not detect. In Alicura where major structures were located on the left abutment, it was important to increase knowledge in the sector through early specific exploratory interventions, such as trenches, deep wells and exploration galleries. The importance of a good drainage system and percolation controls during operation through galleries and drains was fundamental. The case of El Chocon, where the situation becomes critical after ten years of normal operation, again shows the need for control and monitoring of the project throughout the useful life of the dam. The instrumentation system and the permanent control carried out by the Owner, Hidronor, made it possible to detect unfavorable conditions and plan an adequate corrective action in time.

1. Introduction

1.1 Victor de Mello. In Memoriam

It is really a privilege and an honor to have the opportunity to present this 7th Lecture in memory of Victor de Mello at the X Luso-Brazilian Congress.

Victor brilliant personal qualities has been described by the De Mello previous lecturers: “Friend, Engineer and Philosopher”, John Burland; “De Mello Foundation Engineering Legacy”, Harry Poulos; “My mentor and my role model”, M. Jamiolkowski; “Giant of Geotechnics”, Jim Mitchel; “A visionary”, Giroud; “Victor devoted his life to the betterment of people not only of Brazil, but also the world at large”, N. Morgenstern. I agree with all of them.

I had the honorable opportunity to write in the introduction to De Mello Volume, published in his tribute by his disciples and the unconditional support of his wife Maria Luiza, in 1989, my vision of Victor’s transcendent influence in the world of Geotechnical Engineering and especially in our region: “Victor de Mello in Latinoamerica” (Figure 1).

Some paragraphs included in that writing synthesize our relationship and I think it is appropriate to repeat:

“I made acquaintance with Victor de Mello during de 2nd Panamerican Conference on Soil Mechanics and Foundation Engineering, held in Brazil, in 1963”. I was 27 years old.

“I was deeply impressed by the clarity of his concepts and the acuity of his judgment.”

“His salient personality results in that in all areas in which he exercises activity, he achieves an outstandingly high level, as a consequence of the unusual compounding of natural gifts that are rarely encountered, developed to such a high degree in a single person: he has the indefatigable capacity of work of a Portuguese; the stoicism, and patience and interior peace of an Hindu; the preoccupation with perfectionism of a Swiss; the method and systematism of a Britisher; the pragmatism of an American; and the eloquence and enthusiasm of a Brazilian”.

[#]Corresponding author. E-mail address: oavarde@gmail.com.
[1]President in Argentinian National Academy of Engineering, Buenos Aires, Argentina.

Invited Lecture. No discussions.
DOI: https://doi.org/10.28927/SR.434503

Figure 1. De Mello Volume - Victor signing my copy.

Figure 2. V Pan American Soil Mechanics and Foundation Engineering Congress, Buenos Aires, 1975.

The publication of the De Mello Volume was in fact coincident with the First International Society for Soil Mechanics and Foundation Engineering held in South America, in Rio de Janeiro in 1989. At this Conference I had the privilege to present a Special Lecture "Embankment Dams and Dam Foundations" written in collaboration with Victor De Mello, Peter Anagnosti and Norbert Morgenstern. It was really a great and a grateful experience.

In Argentina Victor participated in the most important events since our first conference on Soil Mechanics in 1968. His invaluable support for our country was continuous. In 1975 as Vice President of the ISMSFE for South America (Figure 2), he contributed as author and final evaluator of the Pan American Soil Mechanics and Foundation Engineering Congress, in Buenos Aires, and then in any meeting and technical event in which we ask for his participation.

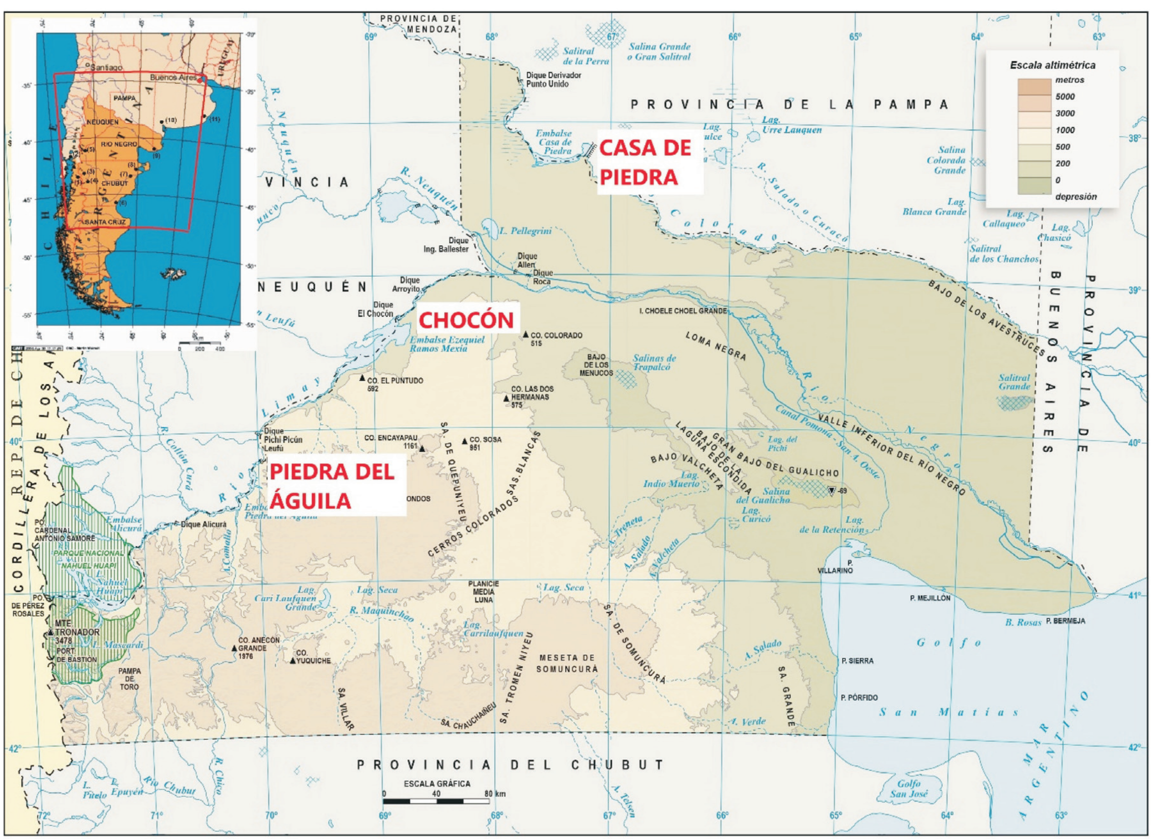

Figure 3. Location of dams: Casa de Piedra, El Chocón, Alicura.

In 1990 Victor made an unforgettable presentation of my Casagrande Conference in the Pan American Soil Mechanics and Foundation Engineering Congress held in Viña del Mar, Chile, in 1991 with its characteristic ingenuity and generosity that I keep on my mind as an unforgettable memory (Vardé, 1991).

His professional support was no less important. He participated as a Consultant and Expert in numerous large hydroelectrical projects in Argentina: Paraná Medio and Yacyretá as a Board Member; Potrerillos as a member of the Board with Giovanni Lombardi and myself; Casa de Piedra and Rio Hondo as an Independent Consultant, among others. In all of them he gave his experience and knowledge generously as was his characteristic.

I cannot fail to mention the role of Maria Luiza, who devoted her effort and life to Victor during long years of his brilliant career, and Maria, who gave peace and support to Victor in his last years.

Victor, an unrepeatable human being, had an enormous influence on my professional and personal life that was not only based on his abilities and his teachings, but on his very essence.

For me it was a before and after meeting him, becoming more than a mentor, colleague and friend but "brother" as he called a small number of people in the world.

For all that my eternal recognition and admiration to his memory.

1.2 This paper

Three case histories of large dams built in North Patagonia which experienced unforeseen problems during construction, or after several years of operation are described.

The necessary remedial and corrective works involved the development of importance programs, being economic and programmatic impacts of great magnitude.

The lessons learned from these experiences were very useful to the practice of design and construction of dams in the region.

2. Location

The three projects described in this paper: Casa de Piedra, Alicura and El Chocón were built, as mentioned before, in the region of Northern Patagonia Argentina (Figure 3).

The Patagonia, located in the southern end of South America, is bounded by the Colorado River on its north. On this river is located Casa de Piedra Dam.

El Chocón and Alicura Dams are across the Río Limay, in a subregion called Comahue, which is one of the richest in Argentina in natural resources. Particularly the third largest world reserve of natural shale gas, after China and U.S.A, is located in the Comahue region.

At the sites of the three dams weak rock formations are founded in which studies and specific investigations were carried by local and international geotechnical engineers in the last 50 years, related to the construction of large hydroelectrical projects (Deere & Vardé, 1986; Vardé, 1987; Vardé, 1988; Vardé et al., 1989; among others).

3. Case histories

3.1 Casa de Piedra dam

The Casa de Piedra dam, located on the Colorado River is owned by a multidistrict administration: "Ente Casa de Piedra", with representatives from the governments of the Provinces of La Pampa, Rio Negro, Buenos Aires, and from the National Interior Ministry of Argentina.

The dam was designed by a Consulting Group including Sir Alexander Gibbs and Partners from England, TAMS from U.S.A. and IATASA from Argentina. The Contractor was Impregilo, from Italy (Vardé, 1990).

The earth dam has a total length of 11 km, a maximum height of 54 m in the 200 m river Gorge, and an average height of 20 m founded on both banks on the river Terraces. Seven kilometers are on the left bank (partial view in Figure 4).

Foundations are mostly marine deposits of upper Cretaceous and Lower Tertiary, including marls, claystone, fossiliferous and coquina, and limestones (Figure 5).

Unfavorable geological features were detected during work dam foundations, consisting of caverns (Figure 6) and dissolution channels through massive gypsum below a zone of the left bank, with a length of 800 m, between stations 700-1500 m, (Vardé, 1986; Vardé et al., 1990; Etcheon & Speziale, 1989). The impact in the project construction and the total costs were very significant. The investigation of the problem was initiated because of a fortuitous event. The presence of a saline paleo layer prevented the setting of the concrete from a cut-off in that sector. The noticeable presence of gypsum, the loss of injection water in the boreholes and the fall of tools detected

Figure 4. Casa de Piedra - detail: spillway and powerhouse.

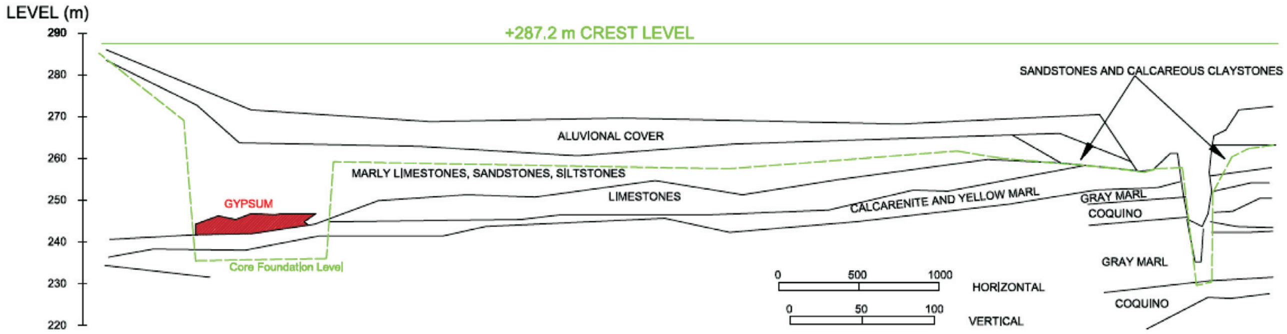

Figure 5. Longitudinal profile, showing location of the gypsum stratum.

Figure 6. Karst cavern.

the cavities. It was possible to define the extent of the anomaly and also rule out the existence of karst formations outside the delimited area.

It was necessary to carry out a very thorough investigation program specifically addressing these issues and introducing important changes in the design, which included geological, geomorphological and special geophysical methods using microgravimetric techniques.

A large open pit, 80.000 m^3 was excavated to check the effect of grouting test and pumping tests to determine the feasibility of dewatering a local ancient aquifer.

The program allowed to determine the extension of the karstic gypsum bed, 20 m deep 5 m thick, which lies over the pervious calcarenite and underneath the red claystones. The test excavation had a defining impact on the scheduling of subsequent tasks. Pumping tests were carried out and blasting test allowed the selection of the excavation method.

The microgravity survey has been a major help to assess the occurrence and location of karstic cavities. The technique was successfully used for cavities detection in important structures like the Great Pyramid of Cheops.

The investigation in Casa de Piedra was carried out by the Compagnie de Prospection Geophysique Francaise under de supervision of Geoconseil of France (Mariotti et al., 1990). A total of 619 gravimetric stations were installed, using a gravimeter of high precision, 0.5 cgal. The detection of negative anomalies, between -2 to -8 cgal in the zone of stations 700-1500 were in very good agreement with the location of cavities and gypsum dissolution phenomena, as was lately verified during the excavations for dam construction.

Several alternatives were considered for the foundation treatment of the affected zone, and a big excavation of about 2.000.000 m^3 was adopted to remove all the potential karstic materials in the core, filters and part of the shell foundation. The treatment through injections and the partial removal by sectors was evaluated. Finally, due to the associated uncertainties, the total excavation of the area affected by karsting was decided.

It caused one year delay in the dam construction program.

The central excavation was complemented by two symmetrical trenches, normal to dam axis, 86 m long, founded in the gray marls and filled with core material, to avoid potential short seepage paths through the more pervious materials (Figure 7). In situ permeability tests and numerical modeling were made to check critical hydraulic gradients and piping potential.

There have been many records of dams affected by the dissolution of salts, causing the formation of caverns, and increasing the permeability in foundations by enlarging rock discontinuities, dramatically increasing the flow rate. In the case of karstic foundations, like Casa de Piedra, where karsts were revealed during construction, although a very extensive conventional investigation (boreholes, geological mapping) was carried out without detecting the abnormality, adequate techniques and early works were required.

Proper and specific investigation techniques such as inspection adits and special geophysical methods, like gravimetry, are mandatory in order to achieve a successfully project of foundations on karstic formations.

3.2 Alicura dam

The Alicura Hydroelectrical Project has been constructed on Limay River, 100 km NE of San Carlos de Bariloche city, Argentina. The project includes a 130 m high

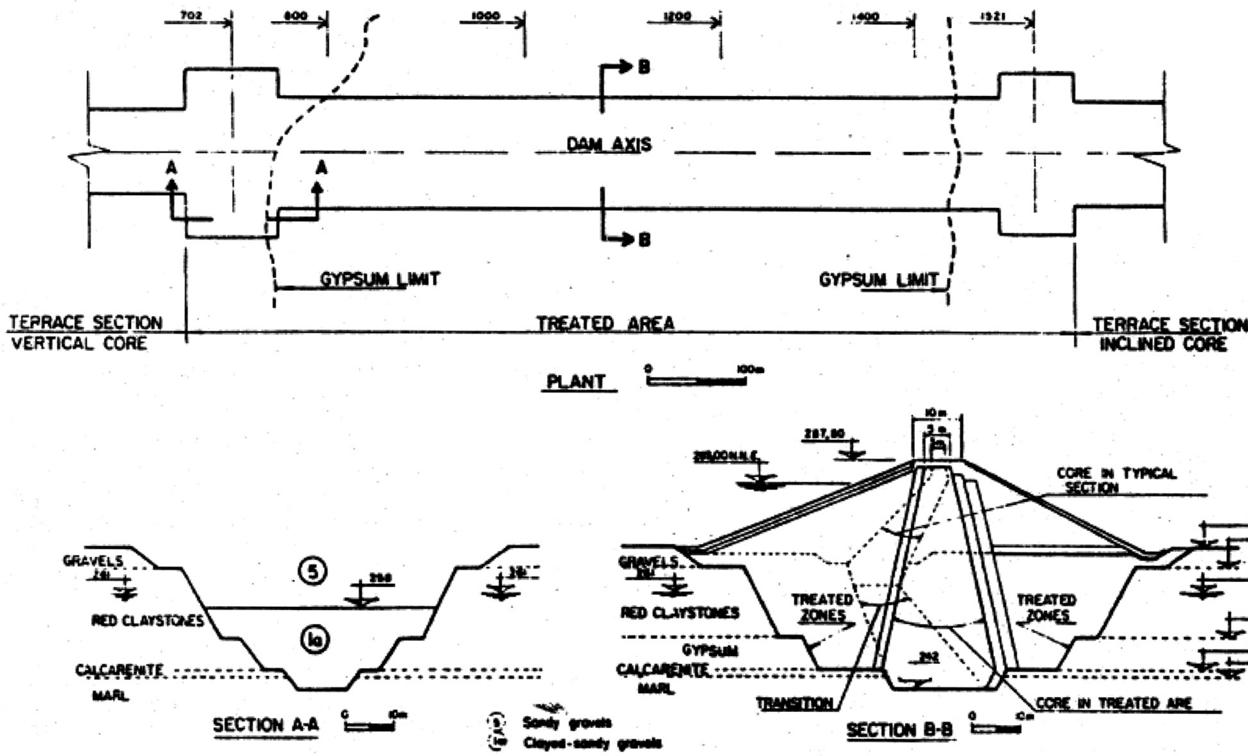

Figure 7. Casa de Piedra - Adopted Solution S700-S1500.

earth fill dam with the principal appurtenant structures located on the left bank, taking advantage of topographical features (Figure 8).

The total volume of the dam is 13 millions of cubic meters, with a central core of morainic material founded on rock, while the shells rest directly on 10-15 m of alluvium. The owner was Hidronor S.A. a state-owned public utility who also operated El Chocón Dam. The design and supervision of construction was made by Consorcio Consultores Alicura, a joint venture of local consulting firms of Argentina, Electrowatt from Switzerland, and Sweco from Sweden. The Contractor was Impregilo from Italy. The Hidronor Board of International Experts were Don U. Deere (USA), Giovanni Lombardi (Switzerland), Jack Hilf (USA), Flavio Lyra (Brazil), and Bolton Seed (USA), who reviewed the design, construction and performance.

Figure 8. Alicura. Aerial view.

The bedrock of the project area consists of a succession of psammitic (sandstone) and pelitic (mostly mudstone and siltstone, some claystone) rocks of Liassic (Lower Jurassic) age. Planar sedimentary structures do not persist over any considerable distance and individual sandstone or pelitic layers cannot be correlated between drillholes and outcrops, affected by neotechtonics movements (Vardé et al., 1986). The bedding interfaces are the dominant structural element in the bedrock, being in general horizontal with some very gentle folding. A major fault, denominated fault 1, running roughly NNE to SSW and dipping steeply SE intersects the penstock trench and spillway chute downslope of the corresponding intake structures (Figure 9 and Figure 10).

At the downhill side of the fault, in the penstock, as well as in the spillway area, the bedding of the rock abruptly changes to a dip of 20 to 38° SE to E, i.e. parallel to the slope (Figure 11). The existence of the zone of inclined bedding on the left bank was not known at the initial design stage, when the investigation was based mainly on geological mapping of outcrops and 8.000 meters of rotary drilling borings size NX. The inclined bedding was subsequently encountered in trench excavations in the area of penstocks

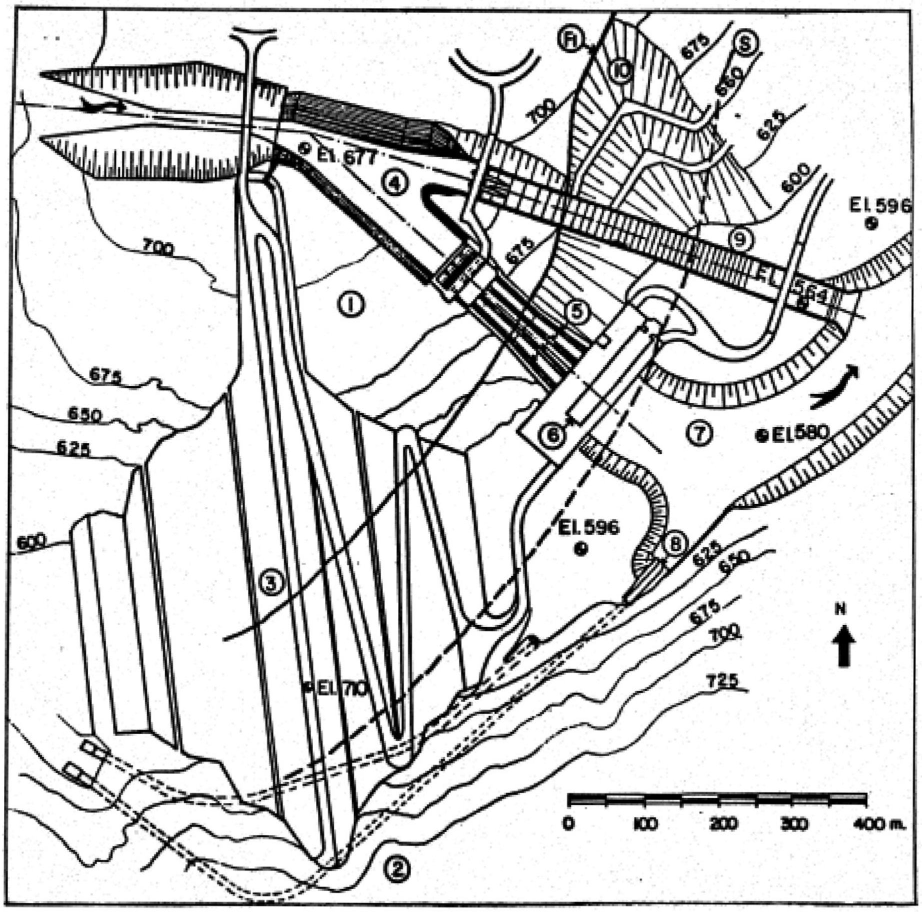

1. Left abutment
2. Right abutment
3. Dam
4. Approach channel
5. Penstocks
6. Powerhouse
7. Tailrace channel
8. Bottom outlet
9. Spillway
10. Stabilization excavation
F1: Fault 1 S: syncline

Figure 9. General layout - Fault alignments.

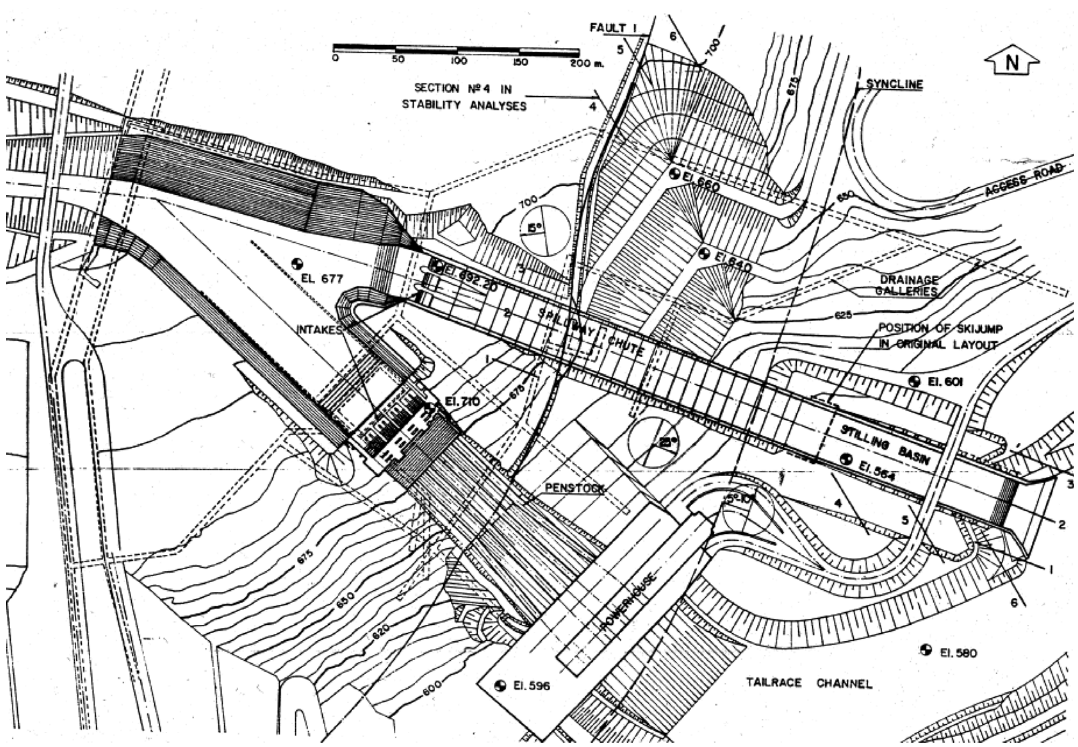

Figure 10. Detail of the left bank.

and considerable efforts were directed towards exploring this feature in detail.

An exploratory gallery at El 590 and a vertical shaft were also excavated. It should be noted that these investigations and the survey of the real conditions of the massif were defined during the excavations in the first stage of construction. At the design stage they were not detected despite having carried out more than 4000 m of exploratory boreholes and an exploration gallery with load plate tests.

The gallery crossed fault identified as 1, which proved to consist of a zone of plastic mylonitized rock, 2 m thick. Fault 1 appears quite impervious, forming a barrier that cut off seepage from the uphill side. The trenches carried out in the area of the penstocks and along the spillway provided useful information together with investigation borings and laboratory testing of samples. Drill holes, shafts and trenches in the valley floor indicated a return to flat dips probably due to the presence of additional faults.

A large number of pelitic interlayers are intensely sheared, predominantly along the upper contact with the sandstones. The shearing produced slickensides parallel to the bedding planes. There were also thin 5 cm thick clay and silt bands of totally crushed material. This clay/silt mylonite is quite frequently squeezed out. In the lower parts of the pelite beds randomly oriented "mirror" faces can be observed.

Moreover, horizontal layers of weak pelites were observed upstream of fault 1 in some investigation drillings. The most important one at El 655 to 660 below the penstock and spillway intakes became visible during the penstock trench excavation. It was deemed necessary to improve the safety by constructing shear keys under these structures, which were formed by excavating galleries and filling them with concrete.

The geotechnical properties of the sandstones are variable:

- Unconfined compressive strength from 30 to 40 MPa.
- Compression wave velocity of 2800 m/s.
- Friction angle (ϕ') from 35 to 55°; cohesion (*c*') from 200 to 250 kPa.

The competent pelites gave test values somewhat lower than the sandstones, but most of the efforts were concentrated on assessing the rock properties on the weaker pelites due to their crucial importance in the stability.

Weak pelites exists along the sliding planes. It can be classified as a clay to medium plasticity, with plasticity indices of 5 to 20 and liquid limit between 20 to 40. The most plastic samples contained about 40 % of clay (minor to 2 microns). The samples taken in the field had a natural water content at or below the plastic limit and were practically fully saturated. The dry density was between 1.8 to 1.9 g/cm^3 and the specific density ranged from 2.44 to 2.68 g/cm^3.

Since it was very difficult to extract good undisturbed samples, the drained strength parameters were determined by direct shear and triaxial tests mainly on remolded samples, which were reconsolidated to a density similar to the undisturbed ones. The results are summarized in Table 1.

The residual friction angles are plotted against the corresponding range of plasticity indices in Figure 12, where the empirical boundary curves proposed by Deere and Seycek, respectively are indicated.

It can be observed that the values obtained by direct shear tests are lower than those by triaxial tests and rather close to the lower boundary. The direct shear test in this case is the most appropriate procedure due to the possibility of orienting the samples and allows greater deformations of the specimens, including repeated and reverse cutting stages to reach the residual condition.

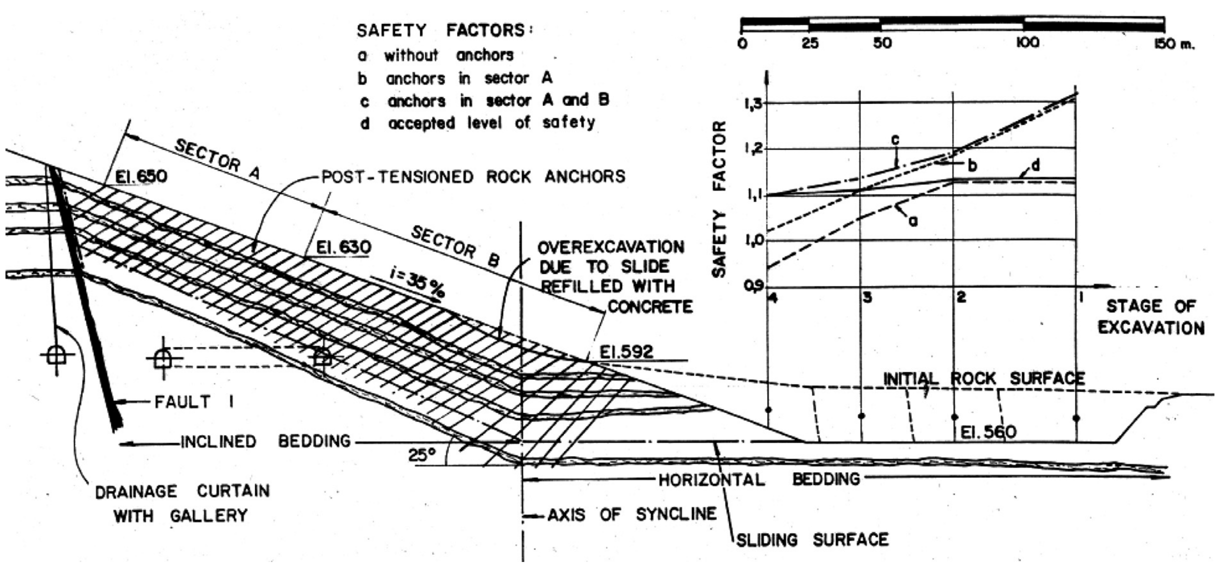

Figure 11. Cross section left bank, Stilling basin, spillway - stability analysis.

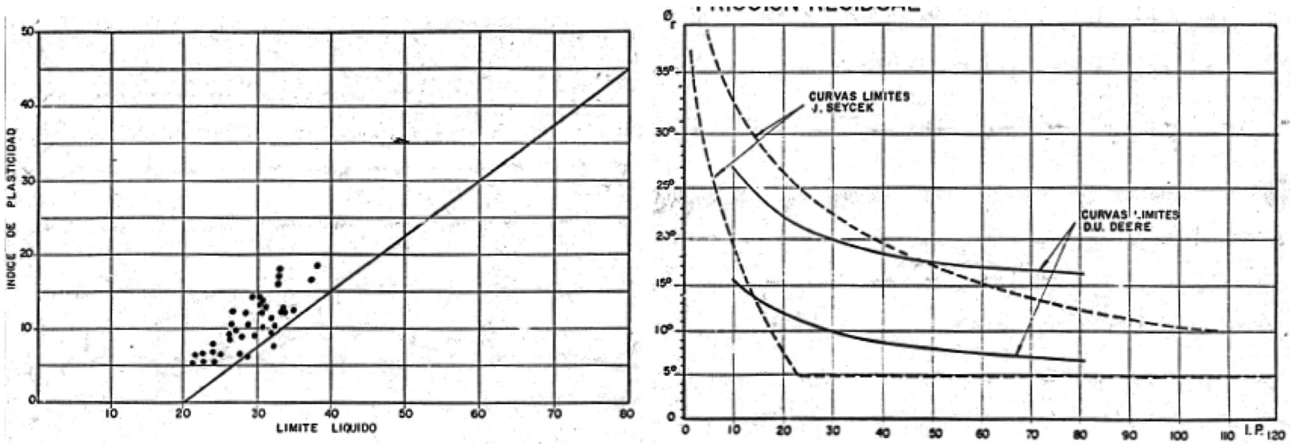

Figure 12. Plasticity chart showing results from sheared pelite; Deere and Seycek curves relating plasticity index and the residual friction angle.

Table 1. Summary of results from shear strength tests.

Type of test	Peak shear strength		Residual shear strength	
	c' (kPa)	ϕ' (°)	*c*' (kPa)	ϕ' (°)
Direct shear tests	0-30	22-31	0-10	17-21
Triaxial tests	0-30	22-30	0-10	21-24

Routine testing in the field laboratory of the Atterberg limits was then used to check that the plasticity indices fell in the known range. The geological and geotechnical characteristics of the left bank required a thorough design work in order to guarantee the stability of the slopes and its structures in the penstock area and the spillway chute and energy dissipator. The intake for the penstock and spillway structures required also an extensive stability analyses to guarantee that sliding would not occur on the weak horizontal pelite layers.

The stability of the left bank had to be improved by an extensive drainage system, shear keys and post-tensioned rock anchors (Andersson et al., 1985). These included 5.500 m of drainage galleries with 35.000 m of drain holes to form 150.000 m^2 of drainage curtain, a 1360 m long grouting gallery and 65.000 m^3 of grout curtain (Figure 13).

The purpose of the excavated galleries was to allow the execution, supervision and control of the screens of per-

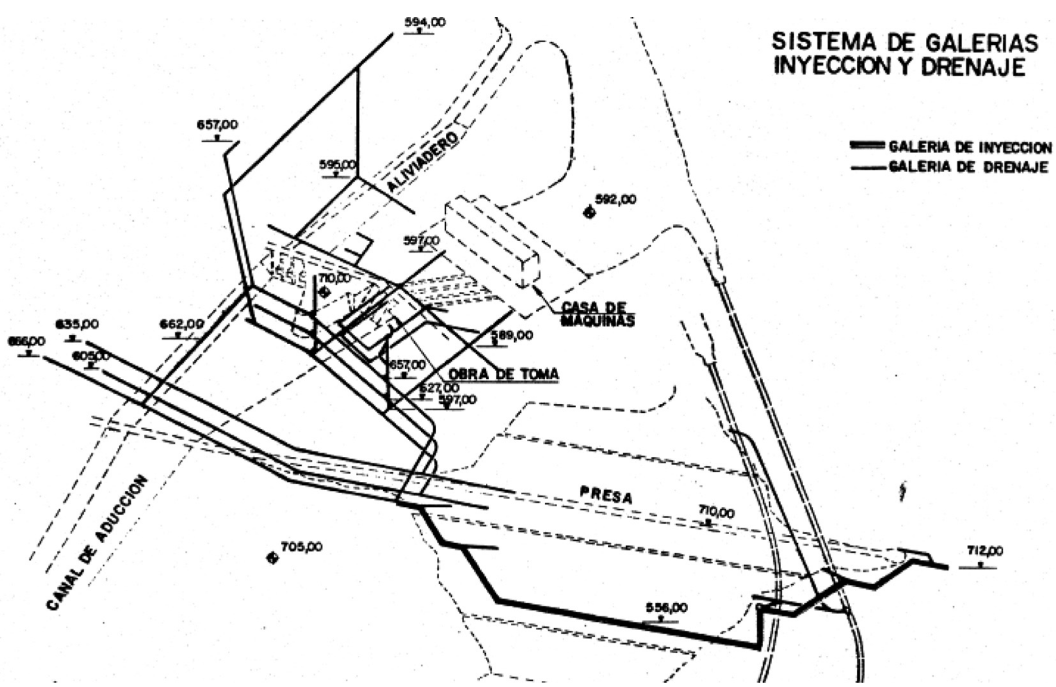

Figure 13. Drainage system on the left abutment.

forated vertical drains drilled by rotopercution equipment and spaced between 6 and 3 m.

On the left bank, three interceptors fronts of the water coming from the reservoir have been located by means of different galleries located at different levels, 605, 635 and 666. The first two are in the same vertical plane and are connected to each other by means of drains. The last one, at level 666 is 20 m upstream and continues towards the river valley to become an injection gallery below the earth dam, at level 556. Three parallel galleries conformed a second drainage curtain. They were connected to each other with vertical drains and to the previous ones. Those of the upper and lower levels extended parallel to the spillway to the surface of the hillside as a lateral drainage curtain. Two other superimposed galleries in the form of "U", also connected by vertical drains, were located at heights 635 and 655 in the area of foundation of the intake structure and in correspondence with the sheared pelite layers. The drainage galleries section was rectangular, 2 m wide and 3 m high; the walls and roof were protected with sprayed concrete and have a concrete floor slab with a draining gutter (Figure 14).

The drainage system is accessed from galleries on both sides of the Power House and also through two shafts 115 m deep, located near the intake and connecting the three levels of galleries in that sector. The effective drainage of the left bank was essential for the stability of the slope and the structures due to the inclined bedding and the fact that excavations would partly undercut the slope.

After a slide of around 120.000 m^3 occurred at a fairly early stage of construction in the area of the ski jump, revealing more unfavorable geotechnical conditions that had been considered in the original design, it was decided to substitute the spillway ski jump by a concrete stilling basin as the plunge pool could undercut the slope. Stabilizing measures were required including the removal of about one million of cubic meters of soil and rock to the left of the spillway chute to unload the slope, and the installation of about 600 anchors, 30-50 m long and post-tensioned to 1,000 kN. The Tensacciai system, similar to Freyssinet system was used. About 1 % of the anchors were provided with load cells in order to monitor the anchor forces. Additionally, horizontal extensometers were installed to detect any movement in the slope (Pujol & Andersson, 1985).

Figure 14. Drainage gallery.

The stability analyses were performed using a two-dimensional model composed of an active block and a passive one. The active block was delimited by the subvertical plane of fault 1 and by an inclined plane corresponding to a possible weak layer of pelite (Figure 11). The shear strength parameters assigned to the continuous plastic layers were $c' = 0$ and $\phi' = 17°$. Furthermore, a reduction of one third of the uplift water pressure and a minimum anchor pressure of 24 kPa with an active depth of 25 m were used.

The important conclusion obtained during the construction of the Alicura Project is that the adequate characterization of rock massifs affected by relatively small fault structures, but with shear planes between the strata, can only be achieved through a research plan that includes trench excavations, deep shafts and galleries. Conventional investigations through boreholes including special procedures do not adequately reveal the unfavorable features of thin sheared layers between more competent rocks, as in this case.

In the case of Alicura, where concrete structures are located on a terrace due to topographic advantages, guaranteeing the stability of the slopes is a critical factor for the execution of the works. Its economic impact can also be very important.

Consequently, the special work program must be carried out from the early stages of the studies.

In thin sheared strata, where in-situ tests have no application, it is important to define the continuity of weak planes and their shear strength properties through systematic sampling and characterization tests. It is of vital importance the implementation of an efficient drainage system. The installation of drains from different gallery levels allows control of the system operation.

3.3 El Chocón dam

El Chocón Hydroelectrical 1200 MW installed capacity, is located across the Limay river. A general view of the earth dam, the spillway and Power House is shown in Figure 15. Figure 16 presents the plan of El Chocón Dam.

The original design was made by a consortium formed by Italconsult, Sofrelec and Harza Engineering Co., between 1962 and 1965. The operation was assigned to Hidronor S.A. in 1968. The revision of the design and the construction supervision were carried out by Sir Alexander Gibb & Partners. The contractor was a joint venture formed by Impregilo, from Italy, and Sollazo, a local firm.

The first impounding of the reservoir took place in 1972. The earth dam is one of the largest in Argentina, 92 m maximum height, 13 millions m^3 volume and 2.245 m crest length. The plan layout was based on the topography. The

Figure 15. El Chocón dam - general view.

spillway is located on the right bank, about 100 m from the right abutment.

The dam cross section was designed using a thin sloping clay core between sandy gravel shells to reduce the differential settlements between the clay core and the gravel shells and also reducing the risks of horizontal cracking due to arching of the core between the shells. The top 14 m of the core were vertical (Figure 17).

The core material, obtained from a borrow area located in the reservoir area consisted of interbedded layers of clayed sands and silty sands, with a mean plasticity index of 23 %. Subsequent investigations on core material samples obtained between 1989 and 1990, from the right abutment by drilling into the core at different levels, have shown that the clay has dispersive characteristics. It is worth mentioning that at the time of design and construction stages of the works (1960 decade and early 1970 decade) the dispersive properties of the soils were not well known in civil engineering.

Various seepage control features were provided in both abutments and in the foundation of the dam. A cut off zone was excavated 5 m deep into rock in the river valley and a single line grout curtain was provided under the core centerline. The design grouting pattern consisted of holes on 10 m spacing, dipping upstream 35° along the dam axis to intersect the main joints. The depth of primary holes in the river valley was generally 25 m below the core-rock foundation rock contact. Grouting and drainage galleries were provided at the left abutment behind the Power Station to reduce seepage through the rock and to ensure that the phreatic surface exit point was kept below the toe of the cliff.

The geology at the site are predominantly horizontally bedded sandstone of late Cretaceous age. The Upper sandstone is formed by alternating layers of lithic sandstones with lenses of wacky siltstones and claystones generally 3 to 5 cm in thickness. Discontinuous thin gypsum levels of secondary origin were detected at the top and the base of the units. The sandstone forms the abutments as well as the left dam foundation.

Gypsum infillings in the foundation rock discontinuities were found in the river valley bottom and in both banks. These joint infillings are rather thin, ranging from several millimeters to 1 or 2 cm. Considerable evidence of

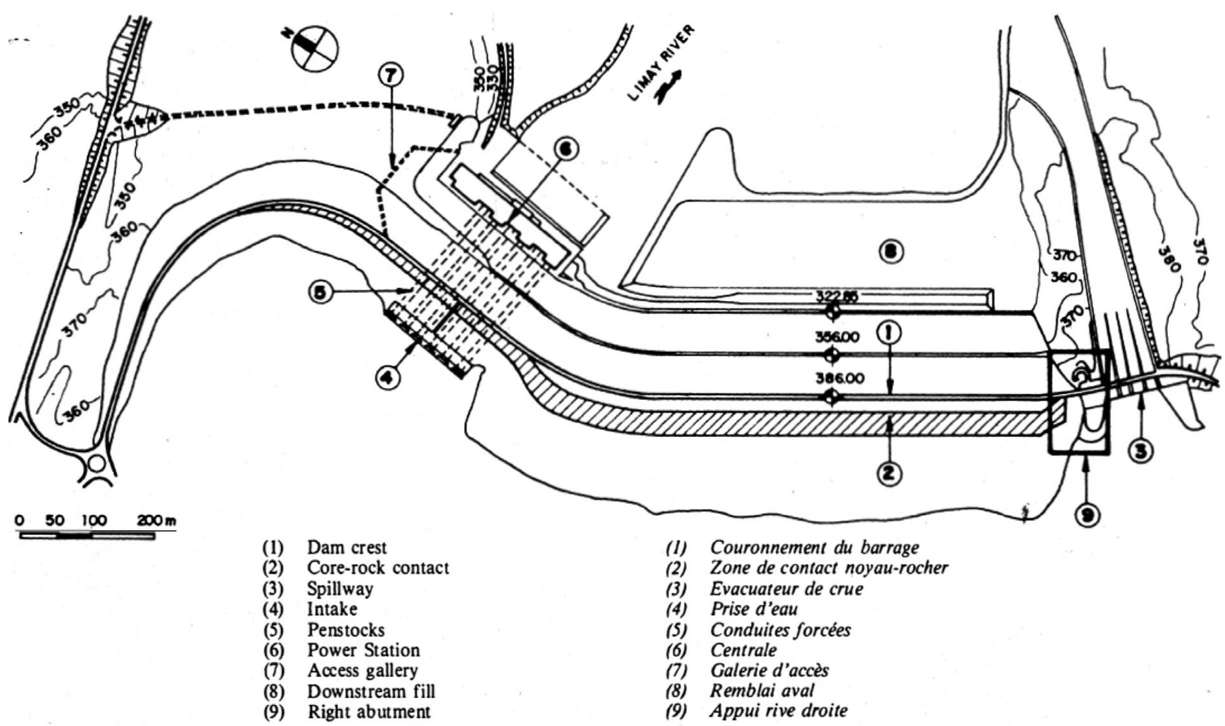

Figure 16. El Chocón dam - plan.

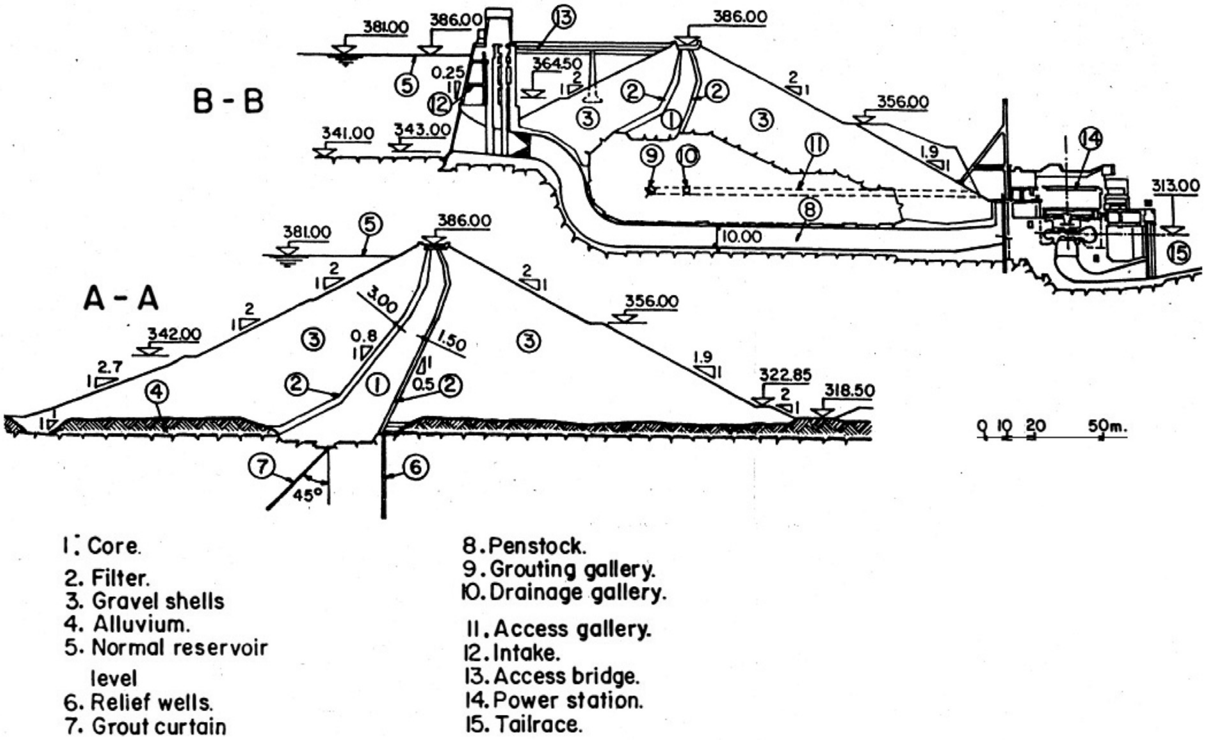

Figure 17. El Chocón dam - cross sections.

gypsum infillings was present on both banks, mainly as horizontal layers.

The instrumentation has generally performed satisfactorily. The piezometer levels in the core and the dam foundations had been considered reasonable during the first ten years after impounding. The performance of the dam and its foundation did not cause any particular concern in the period from 1972 to 1982.

In November 1982 the attention was focused on the development of high piezometric levels recorded in the core contact with the right abutment. An extensive program of studies and investigations was initiated by Hidronor to determine the causes of this behavior. A review of the pertinent data related to design, construction, geologic and geotechnical aspects were done and seepage and piezometric levels were monitored. Chemical analyses carried out on water samples from different drains showed that the measured seepage water of about 100 L/min contained an average of 2 g of soluble solids per liter. A boring program was performed to identify some of the existing fissures and joints and the amount of water seeping through them to know the percolation pattern through the dam foundation.

A first evaluation of the dam was made in August 1983. The conditions of the dam contact were of particular concern. The presence of high concentrations of soluble salts in the water effluents of drains and downstream of the dam, implied that an appreciable quantity of solids was removed during ten years of operation. It could be also indicative of progressive opening of joints in the rock foundations due of gypsum. Increasing flow could also result in some erosion of non-soluble fillings.

Field surveys had detected the presence of valley stress relief related joints, particularly on the right cliff between the dam and spillway area. A grouting program was considered necessary at both the right and left banks to reduce the potential of clay core piping through open rock joints (Aisiks et al., 1991a; Vardé, 1991).

A shaft in the rock, 107 m deep and three galleries at elevations of 346, 308 and 282 m were constructed to permit remedial grouting and drainage treatment of the rock abutment in the zone adjacent to the rock-core contact. The core is founded at the right bank in a cut off trench. A horizontal section of the abutment core-rock contact at El. 357 m is shown in Figure 18.

The core against the rock, face AB, and downstream, face BC, bears directly against the rock, without any protective filter. The layout of the shaft galleries in relation with the core is shown in Figure 19. Figure 20 shows the drillholes for right abutment treatment in detail.

The first few holes drilled towards the contact face AB revealed worse conditions that had been anticipated. A number of rack joints near the contact were found to be open and full of water at hydraulic pressures near reservoir level. The core when contacted was found in some cases to be either in a near fluid state or with very low consistency. The samples were recovered using special procedures.

All drilling and grouting done afterwards using a double gate system (SAS, Figures 21 and 22), and a pressure

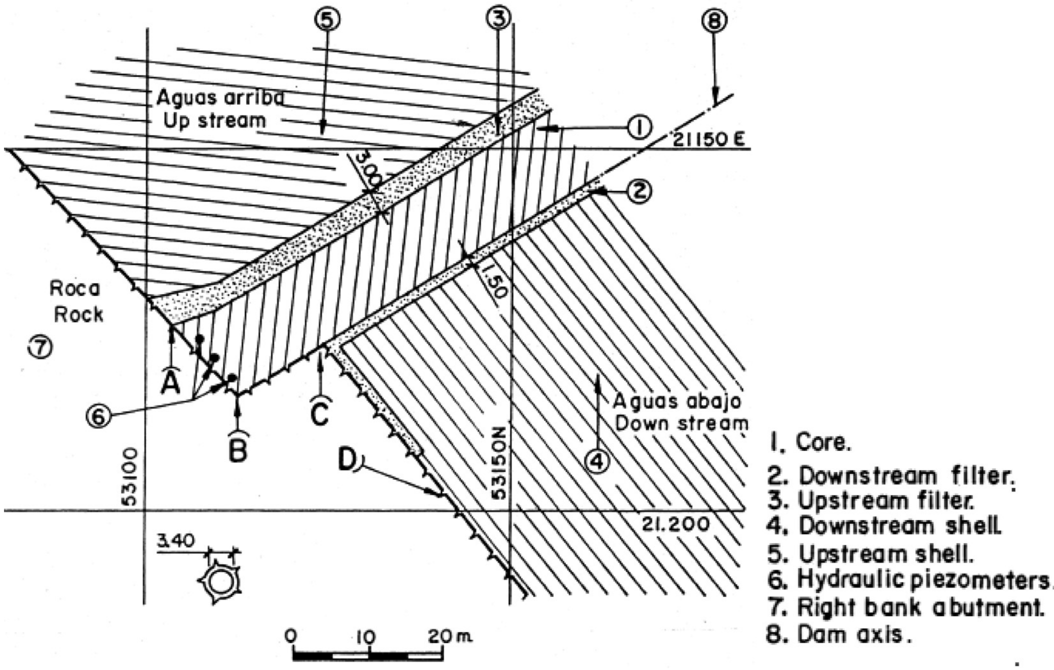

Figure 18. Horizontal cross section al elevation 357.

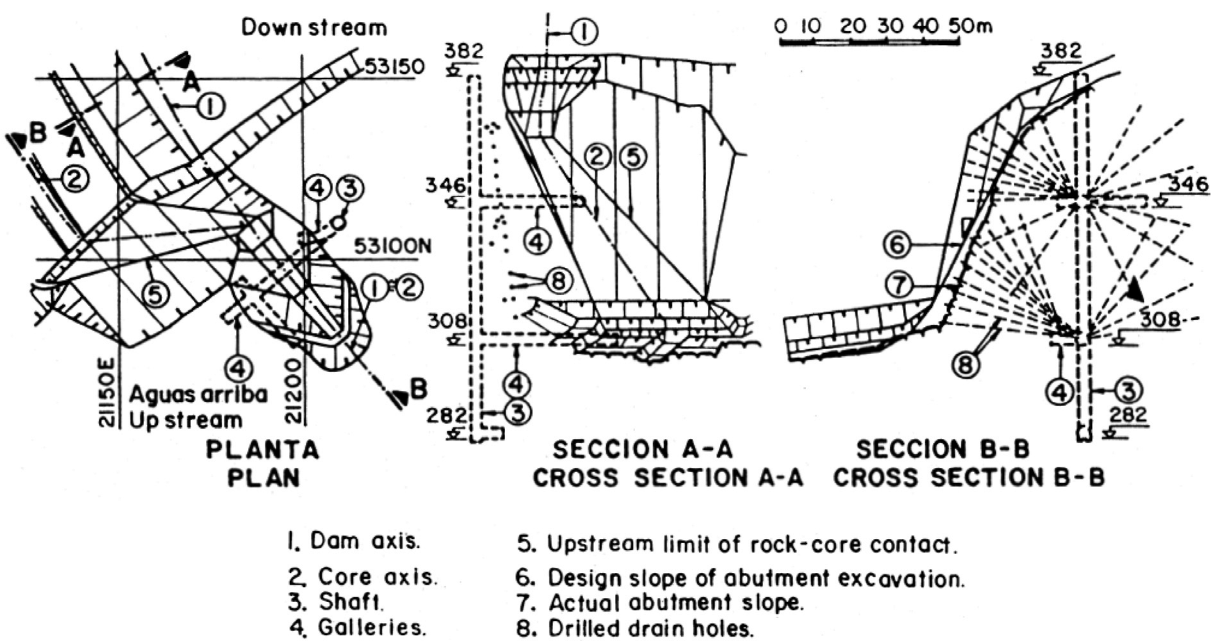

Figure 19. Layout of right abutment shaft and galleries.

regulation device (PRD), mounted at each borehole mouth. This system permits maintaining the pressure inside the hole equal or larger than the reservoir pressure to eliminate the danger of piping through the drillholes. More details of the special techniques used to treat the abutment of El Chocon can be found in Aisiks et al. (1991b).

It was concluded from the observation of the rock cores of drill holes that the rock near the contact was highly fractured due probable to stress relief and to blasting effects. Hydraulic piezometers located in the core adjacent to the steep abutment rock, 1 to 4 horizontal-vertical provided a way to assess the state of stress in the core. These tests show that with a reservoir level at El 369 m there was zero effective stress at the rock-contact above El 357 m. These data confirm that a crack existed within the core close to the steep abutment, cause by differential settlement and arch-

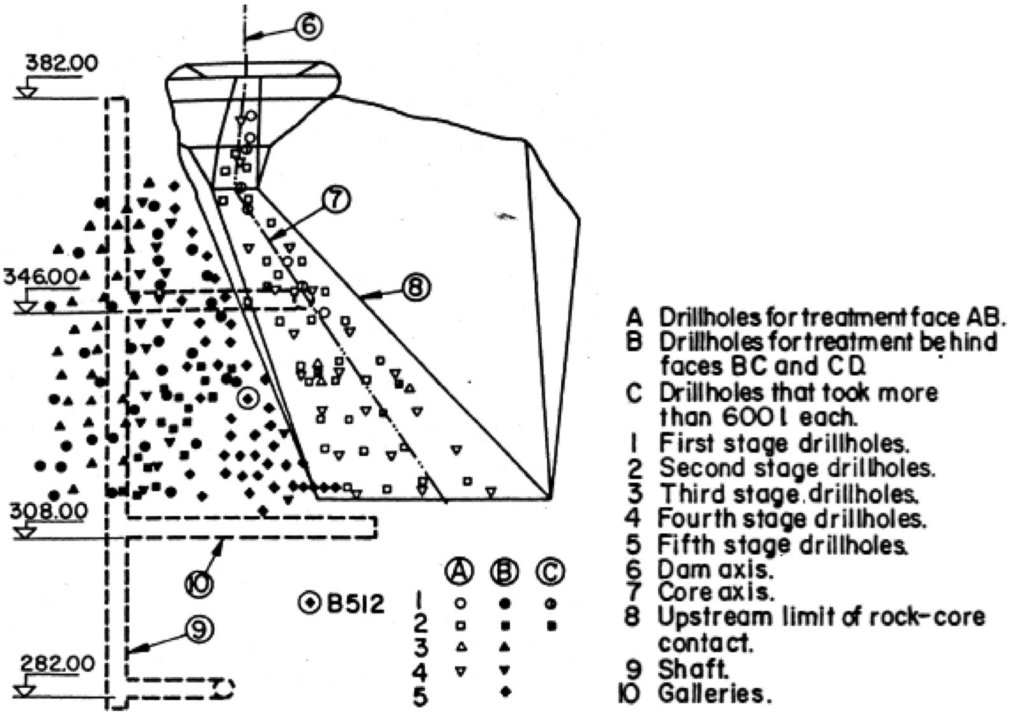

Figure 20. Drillholes for right abutment treatment.

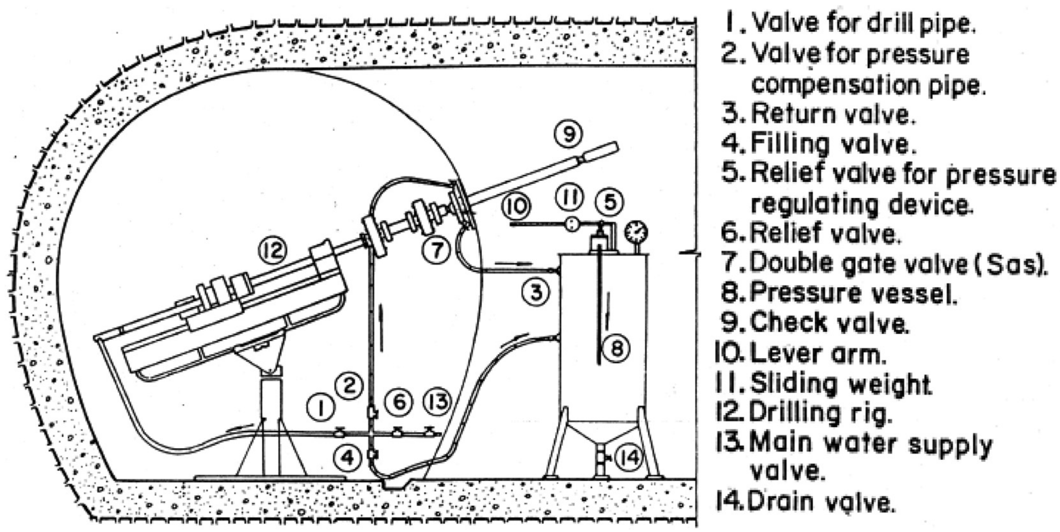

Figure 21. Gallery working station.

ing between the core and the rock face. An additional drainage system of the rock mass downstream of the BC rock-core contact face was installed. A second stage of grouting operations of the core-rock contact using a pressure controlled system. Grout takes up to 10,000 l per hole were recorded at El 340 m. Core samples containing hardened grout were recovered during the grouting program provided evidence of core cracking. Exploratory holes confirmed using impression packers showed open joints up to 2 cm wide.

The fissures, subvertical and parallel to the river valley, are attributed to stress relief in the recent geological past due to valley erosion and possibly widened by blasting during construction. This condition, considered critical to the dam soundness and its safety and remedial grouting and the drilling a new drainage system was programmed in several stages.

Stable mixes were used in conjunction with consistent volume-pressure relationships. A water-cement 0.67/1.00 ratio by weight was generally used (Deere, 1982)

Figure 22. Double gate valve (#7 in Figure 21).

with a relative cohesion 0.4 to 0.3 mm as defined by Lombardi (1969), to avoid the risk of hydraulic fracturing of the core. The volume of grouting resulted in about 53 m^3 at face AB, in 4 stages, and about 60,000 m^3 at face CD, in 5 stages. Total volume injected was more than 100 m^3, sealing the rock mass open joint system and the cracks existing in the core.

In the left bank the treatment behind the Power Station was performed from the original grouting gallery and extensions excavated at both extremes during 1984 and 1985. The amount of grout absorption was high in some areas, with more than 200 kg of grout per meter. The treatment was also extended to the left of Power Station. A total amount of 460 tons of cement was injected through a drilled length of 6700 m. Stable mixes were used with a 1:1 water cement ratio by weigh with 1 % of hydrated bentonite.

The potential problem of internal erosion of the core in contact with the rock in the foundation trench at the bottom of the valley led to the expansion of treatment work in successive stages. Between 1992 and 1994, the treated areas in both abutments extended to the valley.

On the right bank, a gallery of 100 m in length with an internal diameter of 3 m, lined with concrete, was excavated. Three rows of injection holes and a drainage curtain, located downstream, were made from the gallery to reinforce the existing system.

On the left bank a 622 m long gallery was built that descends from El 325 m to El 273, 25 m below the deepest foundation of the dam.

In February 1995, with the dam under the system of private concession it was decided to complete the treatment of foundations of the dam by building a section of central gallery joining both abutments. The gallery is 700 m long with a diameter of 3.4 m (Vardé, 1995).

The decision was based on having detected, through boreholes carried out from the galleries with double gate system and a pressure regulation device as mentioned hereinabove, areas of the core with a low degree of consistency, practically in the liquid limit. The excavation was conducted without the use of explosives by means of pilot advance drilling with a maximum unlined excavation length of 30 m. The injection curtain has three lines complemented by one line of drainage.

The serious conditions observed at El Chocón Dam are the result of the combination of various natural, design and construction features. The most important natural features are:

1) The flat-lying sedimentary weak sandstones and claystones beds having stress-relief joints in the bluffs and floor on the river valley;
2) The presence of subvertical and horizontal joints filled with salts, particularly gypsum;
3) The relative clean and neutral reservoir water with high dissolution capacity.

The significant design features comprise:

1) A layout leaving a rock nose between the spillway and the earth dam;
2) A steep right abutment face designed with a 2V:1H that was finally excavated to 4V:1H;
3) A core trench shape in the valley floor and the abutments that was difficult to blast in a weak rock;
4) A dispersive clay material used in the core;
5) Absence of a filter on the right abutment face B-C;
6) An inclined core with a relatively thin section and several changes in a slope, including a vertical upper section that tended to increase local arching effects.

The construction features worth mentioning are:

1) Reactivation and widening of right abutment joint and fissures due to blasting effects;
2) Grout mixes depending on takes but generally unstable and very lean;
3) The single-line grout curtain not guided throughout the foundation by geological evidence uncovered during excavation. The vertical primary grout holes could not seal the subvertical joints and were probable ineffective in sealing these potential water passages.

The experience and lessons acquired at El Chocón dam can be summarized as below:

- Drainage and grouting gallery: The construction of a drainage and grouting gallery under the foundation is generally very important for dams built on weak rocks with relatively low permeability and joints that, in some cases, are filled with soluble salts. Such a gallery allows monitoring the performance of grouting and drainage works during and after the first reservoir filling. In the case of El Chocón Dam, the availability of a bottom gallery under the entire dam, across the valley bottom and both abutments, would have provided a very efficient way to monitor the foundation behavior during operation. It would have also provided access to perform the remedial work needed;

- Grouting program and grout mixes: The remedial grouting program was guided by knowledge of the joint system gained through borehole investigations as well as gallery construction. It was very successful in sealing all the rock as evidenced by a small amount of grout takes in the core-rock contact zone in the final stage of grouting. Such grouting program has stopped an accelerated ageing process of El Chocón Dam and improved its safety;
- Instrumentation: The adequate instrumentation available and the efficient monitoring and analysis of foundation behavior performed at El Chocón Dam detected a condition of premature ageing and led to adequate action correcting a situation that had reduced the degree of safety of the structure and brought it back to acceptable levels.

4. Conclusions

The historical cases cited in this lecture clearly show that the project, construction and operation of large dams require high levels of competence in all the stages of the projects. The "unique work" character of a large dam is also evidenced in the sense that each project has individual characteristics that differs from other similar dams.

In the region of North Patagonia where there are weak rocks formations, the situations that could arise are even more demanding.

In Casa de Piedra, located in regional environments with clear evidence of limestone and gypsum formations, the investigation should pay attention to the evidence of water leaks or anomalies that imply the presence of soluble rocks and cavities. The use of microgravimetry is appropriate for the detection of cavities or discontinuities that traditional survey research may not detect.

In Alicura where important works are located on the left abutment, it was important to increase knowledge in the sector through early interventions in the work such as trenches, deep wells, exploration galleries. Due to their magnitude, these investigations require the presence of the Contractor due to the need for equipment and are intended to investigate geological features of little importance due to their size, but significant due to their influence on the safety of the works. The importance of a good drainage system and percolation controls during operation through galleries and drains is fundamental. The forecasts of investigations of this nature must be raised from the design for an adequate programming.

The case of El Chocón, where the situation becomes critical after ten years of normal operation, again shows the need for control and monitoring of the works throughout the useful life of the dam. The instrumentation system used and the permanent control carried out by the Owner, Hidronor, made it possible to detect unfavorable conditions and plan an adequate corrective action in time.

Proper management of large dams in all stages allows controlling contingencies and occurrences of unforeseen events, avoiding the risk of failure in some catastrophic cases.

Acknowledgments

I appreciate the assistance of Engineer Rodolfo Guidobono who reviewed and edited this Lecture. My deep recognition to the distinguished engineers who contributed to the professional and human development of my activity during 60 years, and who are no longer among us, very especially to Victor. My gratitude to Luiz Guilherme de Mello and his family.

References

Aisiks, E., Giuliani, F., Tipping E., & Vardé, O. (1991a). Remedial works at El Chocón Dam. *Pro. 17th International Congress on Large Dams*, *Vienne*. ICOLD, 1211-1230.

Aisiks, E., Pallares J., Tipping, E., & Vardé, O. (1991b). Special techniques for corrective treament of right abutment at El Chocón Dam. *Proc. 17th International Congress on Large Dams*, *Vienne*. ICOLD, Q65 R 65.

Andersson, C., Jansson, S., & Vardé , O. (1985). Grouting and drainage system at the Alicura Hydroelectric project, Argentina. *Proc. 15th International Congress on Large Dams*, *Lausanne*. ICOLD, 701-719.

Deere, D. (1982). Cement-bentonite grouting for dams. *Proc. Conference on Grouting in Geotechnical Engineering, New Orleans*. ASCE, 279-300.

Deere, D., & Vardé, O. (1986). Engineering geological problems related to foundations and excavations in weak rocks. *Proc. 5th International Congress International Association of Engineering Geology*, *Buenos Aires*. IAEG/AAGI, 1-16.

Etcheon, A., & Speziale, J.F. (1989). Difficult foundations characterize the Casa de Piedra Dam. *International Water Power and Dam Construction*, 41(12).

Lombardi, G. (1985). The role of cohesion in cement grouting of rock. *Transactions 15th ICOLD Congress*, Lausanne, Switzerland.

Mariotti, G., Rondot, E., & Speziale, J.F. (1990). Le barrage de Casa de Piedra. Mise en evidence de condition de foundations dangereuses au cour de la construction. Adaptation du project. *Colloque International des Grands Ouvrages*, *Paris*. SGF, 77-85 (in French).

Pujol, A., & Andersson, C. (1985). Instrumentation of the Dam and left bank at the Alicura project. *Proc. 15th Congress on Large Dams*, *Laussane*. ICOLD, 387-416.

Vardé, O. (1986). Geotechnical investigation. Casa de Piedra dam. *Proc. 5th International Congress of Engineering Geology*, *Buenos Aires*. Balkema

Vardé, O. (1987). La mecánica de rocas débiles en la Argentina. *Proc. Conferencia en la Academia Nacional de Ciencias Exactas, Fisicas y Naturales*, *Buenos Aires*. National Academy of Sciences, 6-7 (In Spanish).

Vardé, O. (1988). La mecánica de Rocas Débiles. Tipo 2. Debilidad estructural. *Proc. I Simposio Argentino de Mecánica de Rocas*, *La Plata*. (in Spanish).

Vardé, O., Anagnosti P., de Mello, V.F., & Morgenstern, N. (1989). Embankment dams and dam foundations. *Proc. 7th Int. Conference on Soil Mechanics and Foundation Engineering*, *Rio de Janeiro*. Vol. 4, Balkema, 2177.

Vardé, O., Capdevila, E., & Reissian, E. (1990). Presa Casa de Piedra. Su comportamiento durante la primera etapa del llenado del embalse. *Proc. XI Congreso Argentino de Mecánica de Suelos e Ingeniería de Fundaciones*, *Mendoza*. SAIG (in Spanish).

Vardé, O. (1991). Presa El Chocón. Tareas de reparación. *Proc. IX Panamerican Conference on Soil Mechanics and Foundation Engineering*, *Viña del Mar*. Sochige (in Spanish).

Vardé, O. (1995). Presa El Chocón. Aspectos geológicos-geotécnicos vinculados al tratamiento de las fundaciones. *Actas de la Asociación Argentina de Geología Aplicada a la Ingeniería*, 9, 12-42 (in Spanish).

Articles

Soils and Rocks
An International Journal of Geotechnical and Geoenvironmental Engineering
www.soilsandrocks.com
ISSN 1980-9743
ISSN-e 2675-5475

Evaluation of the accuracy of the cubic law for flow through fractures using Lattice Boltzmann method

Ali Ghassemi[1,#], Javad Abbaszadeh[1], Ali Pak[2]

Article

Keywords
Cubic law
Fracture
Hydraulic aperture
Lattice Boltzmann method

Abstract

In this study, a particle-based approach is employed to simulate the fluid flow through single fractures considering detailed geometrical characteristics of the fracture walls at meso-scale. For this purpose, Lattice Boltzmann Method (LBM) which is an efficient computational fluid dynamic method for simulation of fluid flow in media with grossly irregular geometries is employed. The developed numerical model is validated against some benchmark problems with available theoretical solutions including fluid flow through planar channel with non-parallel walls and non-planar channel with parallel walls. The results indicate the capability of the developed numerical model for simulation of flow through irregular boundary conditions of natural fractures. The effect of the variability of fracture aperture, tortuosity of fracture centerline and roughness of fracture walls on the volumetric flow rate is investigated. Moreover, appropriate definition of hydraulic aperture as the key parameter of the well-known cubic equation for estimation of volumetric flow rate in natural fractures is evaluated by numerical simulation of randomly generated fractures with various geometrical conditions.

1. Introduction

The understanding of fluid flow behavior and accurate estimation of flow rate in fractured media is essential for many engineering applications. Groundwater flow and solute transport in rock mass are typically controlled by fractures as the preferential flow pathways. The estimation of fluid flow through fractured reservoirs for prediction of oil or natural gas production is of great importance in petroleum industry. Moreover, fluid flow behavior in fractured rocks should be appropriately identified in engineering problems such as geothermal energy extraction, liquid waste disposal/injection and grouting activities (Singh et al., 2015).

Laboratory and field measurement are usually considered as reliable sources for obtaining the rate of fluid flow through fractured media. However, most experimental techniques fail to directly observe the details of the flow behaviors in real fractures which are locally influenced by the complex geometry of the fractures (Wang et al., 2016). Alternatively, analytical relationships and numerical modeling can be used for investigation of flow behavior. Because of the inherent flexibility of numerical modeling in incorporating various conditions, these tools can be used besides the laboratory and field tests for fluid flow measurement.

Generally, study of fluid flow in a medium containing a network of natural fractures requires understanding the controlling mechanisms of fluid flow through a single fracture. For precise description of fluid flow through a single fracture, the Navier-Stokes equations of hydrodynamics should be solved. However, fluid flow in a natural fracture, which is normally bounded by two irregular walls with rough surfaces, is complex even under a laminar flow regime. Therefore, fluid flow through fractures is typically conceptualized by using the assumption of laminar flow between parallel plates.

The parallel-plate solution for the Navier-Stokes equations leads to the commonly used “cubic law” (Lomize, 1951; Louis, 1969; Kranzz et al., 1979; Tsang & Witherspoon; 1983; Klimczak et al., 2010, Wang et al., 2015). The cubic law (CL) states that the volume rate of fluid flow across a section in such a fracture is proportional to the applied pressure gradient and the cube of the separation distance. The important implication of the cubic law is that fluid flow may be fully characterized by the separation

[#]Corresponding author. E-mail address: a_ghassemi@qiau.ac.ir; ali.ghassemi.geo@gmail.com.
[1]Islamic Azad University, Qazvin, Iran.
[2]Sharif University of Technology, Tehran, Iran.

Submitted on September 8, 2018; Final Acceptance on July 29, 2020; Discussion open until March 31, 2021.
DOI: https://doi.org/10.28927/SR.434521

distance, called "aperture," although the velocity varies across that distance (Ge, 1997).

The equivalent aperture that gives the same fluid flow rate by cubic law, called the hydraulic aperture, is normally smaller than the actual opening displacement of the fracture or mechanical aperture (Klimczak et al., 2010). This is mainly due to several important features that are not supported by the simple CL including throats along the path of flow, tortuosity of flow through natural channels and surface roughness of fracture walls (Neuzil & Tracy, 1981; Walsh, 1981; Tsang, 1984; Walsh & Brace, 1984; Tsang & Tsang, 1987; Brown et al., 1995; Nicholl et al., 1999; Klimczak et al., 2010). All of these factors lead to an increase in the energy dissipation over that predicted by the CL, resulting in lower observed flow rates than the ideal.

Several different modifications of the CL have been proposed to account for the abovementioned effects on the flow behavior averaged over a single fracture. These modifications usually have been considered either by applying a correction factor to incorporate other involving factors into conventional cubic law (*e.g.* Lomize, 1951; Louis, 1969; Patir & Cheng, 1978; Witherspoon et al., 1980; Walsh, 1981; Walsh & Brace, 1984; Zimmerman et al., 1991; Gutfraind & Hansen, 1995) or by utilizing alternative definitions of mean aperture (*e.g.* Neuzil & Tracy, 1981; Tsang & Witherspoon, 1981; Brown, 1987; Hakami & Barton, 1990; Tsang & Tsang, 1990; Unger & Mase, 1993; Renshaw, 1995; Nicholl et al., 1999; Méheust & Schmittbuhl, 2001, Baghbanan & Jing, 2007, Akhavan et al., 2012).

In this study, 2D meso-scale modeling of fluid flow through a single fracture using Lattice Boltzmann Method (LBM) has been considered. Unlike the traditional computational fluid dynamics (CFD) methods that directly solve the Navier-Stokes equations, LBM actually simulates macroscopic flows by means of a particulate approach. The particle-like nature of LBM permits a transparent treatment of grossly irregular geometries of fracture walls in terms of elementary mechanical events, such as mirror and bounce-back reflections without comprising great computational costs.

In this work, the applied numerical method has been validated by simulation of the fluid flow through channels with simple geometries. The effects of variable fracture aperture, fracture tortuosity, and roughness of fracture surfaces on the rate of fluid flow through a single fracture has been investigated using the developed numerical tool. Moreover, different definitions of hydraulic aperture have been evaluated by numerical simulation of randomly generated fractures with various geometrical conditions.

2. Cubic law

Solving the Navier-Stokes equations under a set of boundary conditions will provide details on pressure and flow velocity distributions in discrete fractures. In general, the explicit treatment of fracture surfaces as boundary conditions complicates the approach and does not lead to simple solutions. However, according to Zimmerman et al. (1991), under certain geometric and kinematic constraints, the Navier-Stokes equations can be locally reduced to the much simpler Reynolds (Equation 1).

$$\nabla \cdot [d^3(x, y)\nabla p] = 0 \tag{1}$$

where (x, y) are orthogonal coordinates in the plane of the fracture, d is local aperture of the fracture, and p is fluid pressure. One of the requirements for the Reynolds equation to be valid is the viscous forces dominate the inertial forces (very small Reynolds number). Equation 1 is a linear partial equation that describes the pressure field in the fracture plane. The volumetric flow rate per unit width perpendicular to the direction of flow is then related to the pressure, as presented in Equation 2 (Zimmerman et al., 1991).

$$Q = \frac{d^3(x, y)}{12\mu}\nabla p \tag{2}$$

where Q is the volumetric flow rate, and $\mu$is the dynamic viscosity of the fluid.

For an ideal laminar flow through two smooth parallel plates, Equation 2 is simplified to the well-known cubic law (CL), which has the form described by Equation 3 (Bear et al., 1993).

$$Q = \frac{d^3}{12\mu}\frac{\Delta p}{\Delta L} \tag{3}$$

where $\Delta p/\Delta L$ is the magnitude of the pressure gradient.

Due to the approximate planar nature of fractures, flow behavior in discrete fractures has often been assumed to be similar to flow through two smooth, parallel plates. The major factor causing deviation of predicted fracture flow behavior from the ideal parallel plate theory is the nature of non-parallel and non-smooth geometry of fracture surfaces. Important questions on the validity of the cubic law and the Reynolds equation for complicated fracture geometries have been studied by many researchers (Witherspoon et al., 1980; Tsang & Witherspoon, 1983; Walsh, 1981; Brown, 1987; Zimmerman et al., 1991; Bear et al., 1993; Oron & Berkowitz, 1998; Brush & Thomson, 2003). The general conclusion from these efforts is that the cubic law is valid provided that an appropriate mean aperture (hydraulic aperture) is used and modification factors for tortuosity and surface roughness is applied. Many types of mean apertures have been proposed, and for some cases, some averaging procedures work better than others (Ge, 1997). Some of the proposed hydraulic apertures will be discussed in this paper.

It should also be noted that laminar flow is assumed in derivation of cubic law and therefore, the inertial effects of flow is ignored where cubic law is used. For flows with high Reynolds numbers (Re), large fluid velocity gradient across the aperture will occur. This results in a broader distribution of the immobile regions along the rough fracture wall (Dou & Zhou, 2014). The immobile region is enlarged with the increase of *Re* and roughness, and its impact cantnot be captured using conventional cubic law. To characterize the nonlinear flow through fractures, the complete form of Navier-Stokes equations including the acceleration and inertial terms should be adopted as the governing equation (Wang et al., 2016).

Surface roughness is one of the most important factors affecting the hydro-mechanical behaviour of rock fractures. Pioneer study by Lomize (1951) was one of the comprehensive efforts to indicate the accuracy of the cubic law for laminar flow under low hydraulic gradient by considering a correction factor for surface roughness. Later, the equation was confirmed by some other researchers (*e.g.* Snow, 1965). Based on extensive experimental studies, Louis (1969) proposed a similar reduction factor to be applied to the cube law (Equation 4).

$$Q = \frac{d^3}{12\mu}\frac{\Delta p}{\Delta L}\frac{1}{F}; \quad F = (1 + 8.8R_r^{1.5}) \tag{4}$$

where R_r is relative roughness factor.

In this approach, the friction factor depends only on the relative roughness and therefore, ignores the frequency (or wavelength) of the asperities (Zambrano et al., 2019). The roughness correction factor can be also calculated based on the joint roughness coefficient (JRC) as proposed by Barton et al. (1985). JRC has been widely used in geotechnical and rock engineering applications and several researchers used this coefficient to study the fluid flow through rock fractures (Zhang & Nemcik, 2013; Crandall et al., 2010; Niya & Selvadurai, 2019). However, the JRC is estimated subjectively based on visual inspection of the roughness profiles and the results always vary based on the experience level of the investigator (Su et al., 2020). Moreover, the accuracy of JRC for relatively wide apertures decreases due to its moderate resolution, which is about 1 mm (Zambrano et al., 2019).

Tortuosity is another important factor that influences the connectivity of fluid flow paths because of fracture contact area (Tsang 1984). Walsh & Brace (1984) investigated the effects of tortuosity and presented an equation for flow through the fractures (Equation 5).

$$Q = \frac{d^3}{12\mu}\frac{\Delta p}{L}\frac{1}{\tau^2} \tag{5}$$

In Equation 5, the parameter τ is the curvature coefficient of tortuosity that equals to the ratio of the actual length to the apparent length of the flow path. The same tortuosity modification factor was used by Nazridoust et al. (2006).

On the other hand, some researches focused on finding modification coefficient based on distribution function characteristics of the aperture (Tsang & Tsang, 1990; Renshaw, 1995; Zimmerman & Bodvarsson, 1996). For example, Equation 6 presented by Zimmerman & Bodvarsson (1996) allows the estimation of the volumetric flow rate through rough fractures.

$$\frac{Q}{B} = \frac{d^3}{12\mu}\frac{\Delta p}{L}C_r C_t \tag{6}$$

where C_r and C_t are roughness and tortuosity correction factor, respectively that can be calculated based on arithmetic average and standard deviation of aperture variation.

Various definitions of mean aperture (d), including the arithmetic mean (AM), geometric mean (GM), harmonic mean (HM), volume averaged mean (VAM), and effective aperture (EA) have been proposed to be applied into the conventional cubic law in order to account for important features that are not supported by the simple cubic law (Akhavan et al., 2012). Most studies show that for natural fractures, the cubic law calculates the amount of the flow more than its actual quantity, especially if the arithmetic mean value of aperture is used in the cubic law (Konzuk & Kueper, 2004). In some studies, geometric average has been suggested as a better representative of the hydraulic aperture (Jensen, 1991; Renshaw, 1995; Konzuk & Kueper, 2004; Baghbanan & Jing, 2007). Some other researchers believe that the flow is controlled by the least aperture width along the flow path (*e.g.* Pyrak-Nolte et al., 1988).

Nazridoust et al. (2006) proposed an effective fracture aperture (H_{eff}) based the average aperture (H_{avg}), and the standard deviation of the fracture apertures (σ). For a normal distribution of the apertures, H_{eff} given by Equation 7 is an estimate of smaller apertures (the probability of a randomly selected aperture in the fracture that is larger than H is 84.14 %).

$$H_{eff} = H_{avg} - \sigma \tag{7}$$

By extending a technique originally suggested by Dietrich et al. (2005), Akhavan et al. (2012) indicate that effective aperture as defined by the following equation is the appropriate representative of hydraulic aperture to be applied in cubic law:

$$d_{eff} = \sqrt[3]{\frac{1}{n}\sum_{j=1}^{n} d_j^3} \tag{8}$$

The equation can be derived simply by discretization of a fracture into a series of local parallel channels with different apertures (d_j), and n is the number of fracture elements.

As an alternative approach to conventional CL, Equation 1 can be used to consider the local variation of aperture explicitly. The Local Cubic Law (LCL) has been extensively applied in investigations of fluid flow through fractures (Zimmerman et al., 1991; Mourzenko et al., 1995; Nicholl et al., 1999; Wang et al., 2015). Under LCL, local flow magnitude is proportional to the cube of the local aperture. The local aperture can be measured using different methods (Mourzenko et al., 1995; Ge 1997; Oron & Berkowitz 1998; Wang et al., 2015). Ge (1997) provided analytical solutions for fluid flow through two-dimensional non-parallel and parallel fractures by considering the normal-to-local-centerline aperture. Wang et al. (2015) modified the LCL to take into account the local tortuosity and roughness, and low inertial effects where local Re ≤ 1. The proposed LCL is more accurate than previous modifications of the LCL. However, the governing equation is a nonlinear differential equation that should be solved numerically.

The focus of this study is to investigate the use of hydraulic aperture in conventional cubic law. For this purpose, several hydraulic aperture definitions have been numerically investigated using the developed meso-scale model. The numerical model has been validated against analytical solutions proposed by Ge (1997) using local cubic law approach for two problems including fluid flow through single fracture with regular geometries.

3. Lattice Boltzmann method

During the last two decades, particle-based methods such as Lattice Boltzmann Method (LBM) have been developed as a robust numerical approach in computational fluid dynamics (CFD). In this method, macroscopic flow is simulated by means of a particulate approach. It can be considered as a special finite-difference form of the continuum Boltzmann equation, but historically it is a pre-averaged improvement to its predecessor, the lattice-gas method (Sangani & Acrivos, 1982; Chen & Doolen, 1998; Succi, 2001).

The fundamental idea of the LBM is to construct simplified kinetic models that incorporate the essential physics of microscopic or mesoscopic processes, so that the macroscopic averaged properties obey the desired macroscopic equations (Pan et al., 2001). Unlike most of the other particle methods, LBM is a mesh-based method. In LBM, the spatial space is discretized in a way that it is consistent with the kinetic equation (Pan et al., 2001). The LBM simulates the flow phenomenon by tracking fluid particles that move and collide in space under the rules that the collision does not result in mass and momentum changes.

In LBM, space is divided into regular lattices normally with the same spacing h in both directions and at each lattice site a particle distribution function $f_i(x, t)$ is defined which is equal to the probable amount of fluid particles at site x moving in the direction of i at time t. During each discrete time step of the simulation (Δt), fluid particles move to the nearest lattice site along their direction of motion with different velocities of $\vec{e}_i$, where they "collide" with other bundles of fluid particles that arrive at the same site. The outcome of the collision is determined by solving the kinetic (Boltzmann) equation for the new particle distribution function at that site and the particle distribution function is updated. The magnitude of speed in different directions which is called lattice speed is defined as $C = h/\Delta t$.

Propagation and collision of fluid particles in LBM can be mathematically summarized by the below two-step scheme (Eqs. 9 and 10):

Propagation step:

$$f_i(x + \vec{e}_i \Delta t, t + \Delta t) = f_i^{updated}(x, t) \tag{9}$$

and collision step:

$$f_i^{updated}(x, t) = \Omega_i(f(x, t)) \tag{10}$$

The collision rule Ω should be chosen to leave the sum of the $f_i(x, t)$ unchanged (no fluid particles are lost.) The rule is also selected to conserve the total momentum at each lattice site. The collision process is mimicked by a distribution function rather than solving for collisions of every fluid particle. Lattice-Boltzmann models can be constructed using Fermi-Dirac or Maxwellian distributions as the collision process (Engler, 2003). However, solving these distribution functions is complicated and computationally expensive.

The single relaxation time operator, also known as Bhatnagar-Gross-Krook (BGK) operator after Bhatnagar et al. (1954), is an uncomplicated approach which simply approximates the collision by assuming that the momentum of the interacting fluid particles will be redistributed at some constant rate toward an equilibrium particle distribution function f_i^{eq} . BGK allows one to solve the equilibrium distribution such that the microscopic equations are satisfied and the N-S equations are recovered. In BGK lattice Boltzmann method, the collision rule is given by:

$$\Omega_i(x, t) = f_i(x, t) - \frac{\Delta t}{\lambda}(f_i(x, t)) - f_i^{eq}(x, t) \tag{11}$$

where f_i^{eq} is the local equilibrium density distribution for the fluid and λ is relaxation parameter.

The two-dimensional model implemented in this study uses a square, nine-velocity lattice typically referred to as D2Q9 model. For this model, f_i^{eq} is given by Eqs. 12 and 13, presented by Qian et al. (1992).

$$f_0^{eq} = w_0 \rho \left(1 - \frac{3}{2C^2} \vec{V} \cdot \vec{V}\right) \tag{12}$$

$$f_i^{eq} = w_i \rho \left[1 + \frac{3}{C^2}(\vec{e}_i \cdot \vec{V}) + \frac{9}{2C^2}(\vec{e}_i \cdot \vec{V})^2 - \frac{3}{2C^2}(\vec{V} \cdot \vec{V})\right], \quad i = 1, 2, \ldots, 8 \tag{13}$$

where ρ and V are macroscopic fluid density and velocity and w_i are the fixed weighting values $w_0 = \frac{4}{9}$, $w_{1,2,3,4} = \frac{1}{9}$ and $w_{5,6,7,8} = \frac{1}{36}$.

The macroscopic parameters are regained by:

$$\rho = \sum_{i=0}^{i=8} f_i \quad (14)$$

$$\rho \cdot \vec{V} = \sum_{i=0}^{i=8} f_i \cdot \vec{e}_i \quad (15)$$

$$P = C_s^2 \rho \quad (16)$$

where P is pressure and C_s is termed fluid's speed of sound which is related to the lattice speed by $C_s = C/\sqrt{3}$. The dimensionless relaxation parameter $\tau = \lambda/\Delta t$ is related to the kinematic viscosity of the fluid ν by Equation 17.

$$\nu = \frac{1}{3}\left(\tau - \frac{1}{2}\right)\frac{h^2}{\Delta t} \quad (17)$$

A constraint to the parameter selection is that the lattice speed C must be sufficiently larger than the maximum fluid velocity (V_{max}) in the simulation to ensure a sufficient solution accuracy. This is calculated by the 'computational' Mach number, defined by $Ma = V_{max}/C$. Theoretically it is required that $Ma << 1$. In practice, Ma should be, at least, smaller than 0.1 (Feng et al., 2007). This becomes very important in modeling fluid flow through packing of solid particles, when fluid particles may have high velocities in small communication between channels (Succi, 2001).

In classical fluid dynamics, the interface between the solid boundaries and the flowing fluid is assumed to be a non-slip boundary. Simulating slip and non-slip boundaries in the LBM is an area where progress is still being made (Qian et al., 1992; Noble et al., 1995). Among the existing methods, the simplest is called 'bounce-back' method. In this approach, to ensure that the fluid particles have zero average velocity at the boundaries (both perpendicular and parallel to the walls): any flux of fluid particles that hits a boundary simply reverses its velocity so that the average velocity at the boundary is automatically zero. This type of boundary is utilized in this study. For this purpose, fracture walls should be characterized by the lattice nodes. The discrete nature of the lattice will result in a stepwise representation of the curve boundaries, so for acquiring the required accuracy and smoothness, sufficiently small lattice spacing is used.

4. Model validation

4.1 Planar channel with non-parallel walls

Equation 3 is valid for a smooth, straight, and parallel plate fracture. However, natural fractures rarely have such characteristics. Here, to validate the LB model in simulation of fractures with irregular walls, fluid flow through a planar channel but with zigzag walls, as illustrated in Figure 1a, was modeled. Higher ratios of zigzag height to channel width (h/d_m) show channels with variable width along the length of the channel. On the other hand, lower h/d_m. ratios represent channels with rough wall surfaces. Ge (1997) provided an analytical solution for this problem using a general governing equation based on the principle of mass conservation and the assumption that CL is locally established. In this solution, the fracture walls should be described by an explicit function $f(x)$. For the fracture illustrated in Figure 1a, the top surface of the fracture can be described mathematically using Fourier series (Equation 18).

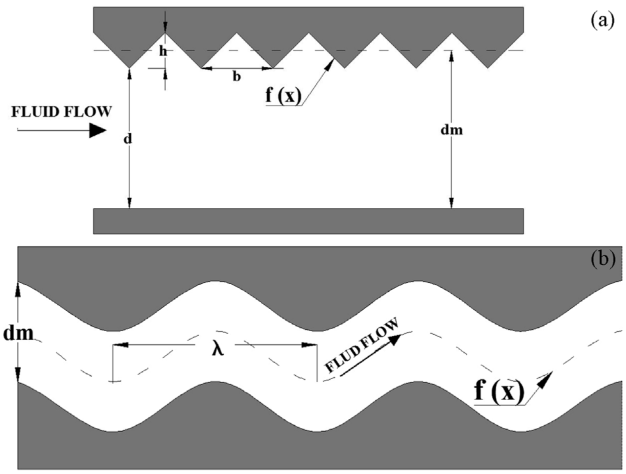

Figure 1. a) planar channel with non-parallel walls, b) non-planar channel with parallel walls.

$$f(x) = \frac{a_0}{2} + \sum_{n=1}^{\infty}\left(a_n \cos\frac{2n\pi}{b}x\right) \quad (18)$$

where a_0 and a_n are Fourier coefficients and can be found from the following equation.

$$a_n = \frac{h}{(n\pi)^2}(2\cos n\pi - \cos 2n\pi - 1)$$
$$\text{and} \quad a_0 = \frac{2}{b}\int_0^b f(x)dx \quad (19)$$

where b and h are geometrical characteristic of the top fracture wall as defined in Figure 1a.

All parameters are shown on Figure 1a. Based on Ge (1997)'s solution, true aperture at a given x in the direction of the flow can be defined as follows:

$$m(x) = C(x)d_a = C(x)f(x) \quad (20)$$

$$C(x) = \frac{2\cos(\alpha(x))}{\cos(\frac{(\alpha(x)}{2})(1+\cos((\alpha(x)))} \quad (21)$$

$$\alpha(x) = \tan^{-1}(f'(x)) \quad (22)$$

where $\alpha(x)$ is the slope of the top surface, d_a is apparent aperture (distance between top and bottom surfaces for a given x), $m(x)$ is true aperture for a given x and f' is derivative of f. Zimmerman et al. (1991) show that the Reynolds equation can lead to the following expression for the hydraulic aperture:

$$d_h^3 = \frac{1}{x_2 - x_1}\left[\int_{x_1}^{x_2} \frac{dx}{m(x)^3}\right]^{-1} \tag{23}$$

The above equation gives the appropriate hydraulic aperture for estimating flow rate by the cubic law. In this study, LBM was applied for simulation of the flow in the same problem. For this purpose, a domain including a 300 × 40 lattices with spacing h = 0.0002 cm and dimensionless relaxation parameter τ = 0.65 was considered. Pressure boundaries were applied at both downstream and upstream sides of the channel and no-slip boundary condition was assumed at the left and right of the domain to model the rigid walls.

The results of numerical simulations as well as flow rates obtained by CL by application of hydraulic aperture (d_h) are presented in Figure 2a. The numerical results are in good agreement with the analytical solution for different sizes of surface zigzags. Both results show that the volumetric flow rates increase with the decreases of h/d_m. Also, as shown in Figure 2b, where the size of zigzags on top wall is the same for all analyses, both analytical solution and LB results imply that flow rates do not follow the CL in which the flow rate is a function of the cube of the average channel

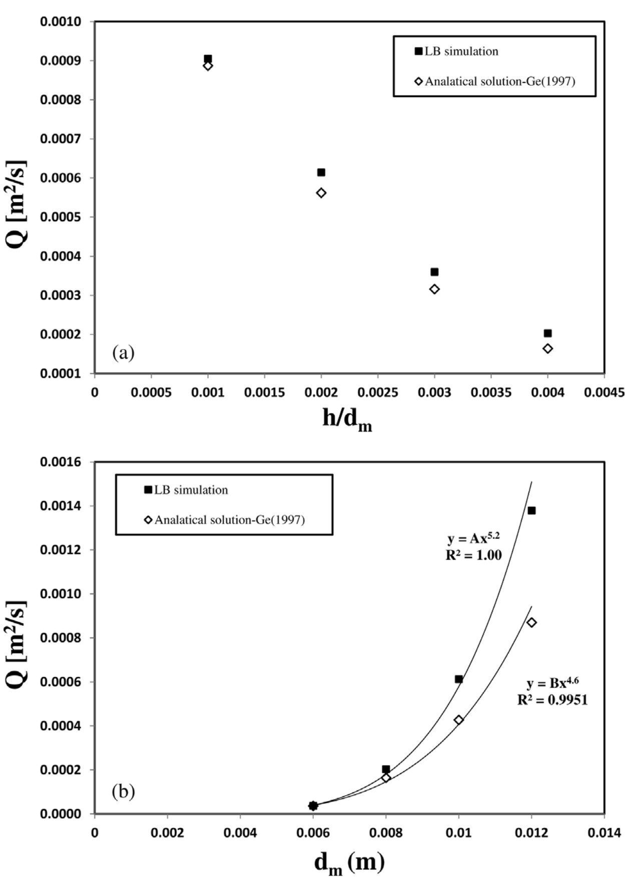

Figure 2. Comparison between flow rate obtained by numerical results and Ge's (1997) solution: a) different sizes of surface zigzags, b) different mean aperture.

width d_m. This deviation confirms the inaccuracy of using average aperture for estimation of flow rate by conventional CL equation.

4.2. Non-planar channel with parallel walls

Another benchmark problem considered to validate the developed LB model is simulation of flow through channels with non-planar walls as shown in Figure 1b. The mathematical equation for centerline of this channel is given by a sinusoidal function as follows:

$$f(x) = \delta \sin \frac{2\pi x}{\lambda} \tag{24}$$

where δ and λ are amplitude and wavelength of the channel centerline, respectively.

Because the Reynolds equation does not account for tortuosity, the viscous force due to tortuosity is totally ignored. Consequently, this oversight can cause errors in fracture permeability estimation and in the accuracy of the cubic law. In an effort to examine the cubic law under a two-dimensional fracture condition, Brown (1987) used tortuosity factor to correct the calculated flow rate. For this problem, the tortuosity can as shown in Equation 25.

$$\tau(x) = \left[1 + \left(\frac{2\pi\delta}{\lambda}\right)^2 \cos^2 \frac{2\pi x}{\lambda}\right]^{1/2} \tag{25}$$

Based on Equation 25, Ge (1997) obtained the following expression for hydraulic aperture for estimation of volumetric flow rate by the cubic law (Equation 26).

$$d_h^3 = \frac{1}{\lambda}\left[\int_0^{\lambda} \frac{dx}{m(x)^3}\right]^{-1} \tag{26}$$

Here, analyses with different characteristics of channel centerline equation are considered. As shown in Figure 3a, the results show that the increase of the wavelength, while the amplitude of the centerline curve remains constant, increases the flow rate. The rate of increase is considerable for lower values of wave lengths. The sensitivity of tortuosity factor to the variation of wavelength can be obtained with Equation 25. In Figure 3a, comparison is also made between LB results and analytical solution proposed by Ge (1997) that shows relatively good agreement especially for lower values of wavelengths.

Figure 3b presents the variation of flow rate with amplitude of channel centerline for a case with constant wavelength. As the amplitude of the channel centerline increases, the ratio of the length of the actual path of flow to the shortest path length in the direction of the flow (tortuosity factor) increases that in turn decreases the rate of the flow.

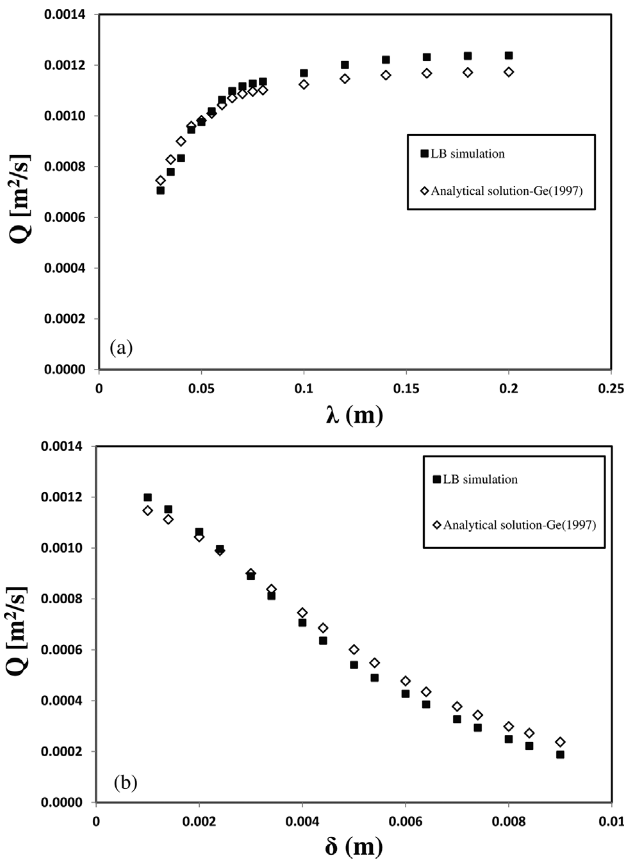

Figure 3. Comparison between flow rate obtained by numerical results and Ge's (1997) solution: a) different wavelengths, b) different amplitudes.

5. Simulation of flow through natural fractures

5.1 Fracture tortuosity

One of the main differences between natural fractures and straight channels is tortuosity. Common definition of tortuosity is the ratio of the length of the fracture centerline to the shortest path length in the direction of the flow. Therefore, tortuosity is equal to unity for straight channels and has larger values for natural fractures. Also, other definitions have also been proposed for tortuosity factor such as those by Zhang & Nagy (2004) and Ghassemi & Pak (2011). However, application of such definitions is mostly limited to researches. Herein, the traditional definition of tortuosity is applied for evaluation of fracture tortuosity.

The results of numerical analyses conducted by changing amplitude and wavelength of a sinusoidal fracture while other parameters were constant are shown in Figure 4. As shown in the figure, for all simulations volumetric flow rate is inversely proportional with tortuosity factor. It should be noted that the tortuosity of flow in natural 3D fractures is affected by the complexity of the velocity field induced by factors such as small and/or large scale roughness, out-of-plane tortuous flow paths and the change of flow direction (Cook, 1992, Oron & Berkowitz, 1998; Wang et al., 2015). These factors are not fully captured by the simple conventional definition of tortuosity. For example, conventional definition of tortuosity only accounts for the curvature of the fracture centerline, but it is insensitive to the form of curvature which governs the change of flow path direction. As shown in Figure 5, the curve of the largest half-circle has the same length as the curve composed of a series of smaller half-circles. However, the results of numerical simulation of flow through channels with equal length but different number of half-circles indicate that the maximum effect of number of half-circles on the flow rate is less than 5 %.

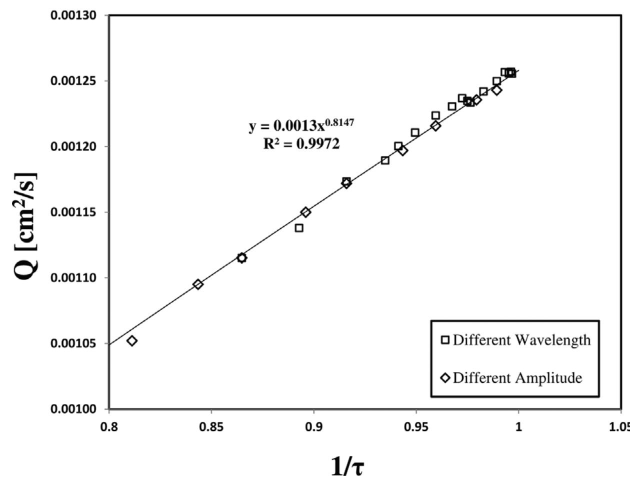

Figure 4. Variation of flow rate with tortuosity factor.

5.2 Throats and surface roughness

Even through a fracture with straight centerline where tortuosity factor is unity, abrupt constrictions of channel walls as well as surface roughness can significantly affect the rate of flow. Herein, a series of analyses in channels with different height (h), length (b) and number of throats was considered (see Figure 6). Furthermore, surface roughness was also investigated by modeling a channel including

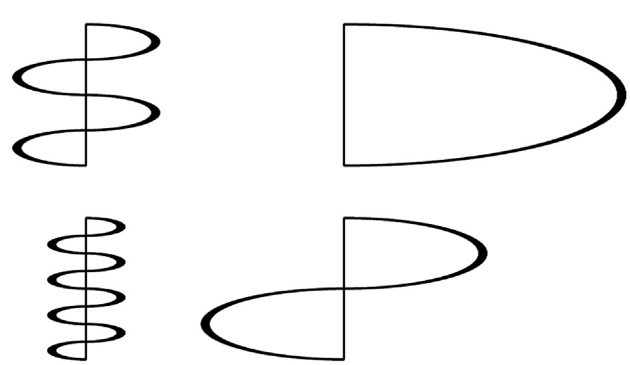

Figure 5. Curves with the same length but different number of half-circles.

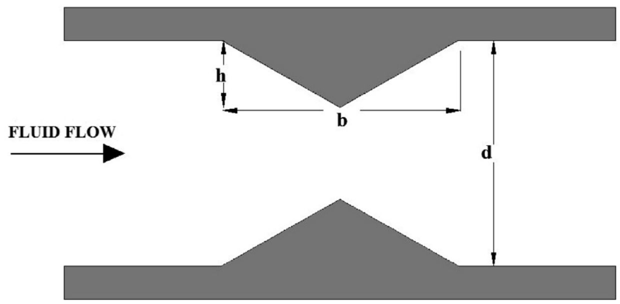

Figure 6. Throat in a channel with straight centerline.

regular subsequent constrictions with low values of h/d_m. As mentioned in Section 2, a couple of relationships for hydraulic aperture have been proposed to be applied in the well-known cubic law for more accurate estimation of flow rate through single fracture. Some of these definitions were examined by the results of LB numerical simulations as shown in Figure 7.

Figures 7a and 7b indicate the variation of the volumetric flow rate over arithmetic and geometrical mean of the channel width along the centerline of the fracture. As can be seen in these figures, although applying geometrical mean of fracture width decrease the scatter of the results, for both methods distinct linear trends are observed for each group of analyses. It should be noted that the appropriateness of meaning method can be related to the form of fracture centerline. For example, use of the geometric mean for isotropically correlated apertures with a lognormal distribution will result in obtaining reasonably flow rates using cubic law (Konzuk & Kueper, 2004).

Similar pattern was obtained by using the correction factor (Cr) proposed by Zimmerman & Bodvarsson (1996) as shown in Figure 7c. However, a relatively well-fitted linear trend can be found in Figure 8a where for all numerical simulations, the results are presented in the form of effective width as defined by Akhavan et al. (2012).

Among the results presented in this figure, some data were extracted from analyses of flow through channels without any variation in width but with rough walls (by considering several constrictions with low values of h/d_m). From Figure 8a, it can be found that the slope of linear trend for these set of data (shown with non-filled symbols) is fairly different from other results shown in the figure. In this study, in order to enhance the convergence of the results to the linear trend, some of different reduction factors proposed in the literature to be applied to the cube law to account for the effects of wall roughness were examined. The outcome implies that modification factor, as defined in Equation 6, gives the best correlation for the conducted analyses. Comparison of Figures 8a and 8b confirms that higher R-squared value can be reached if reduction factor proposed by Louis (1969) is applied to the cube of effective width.

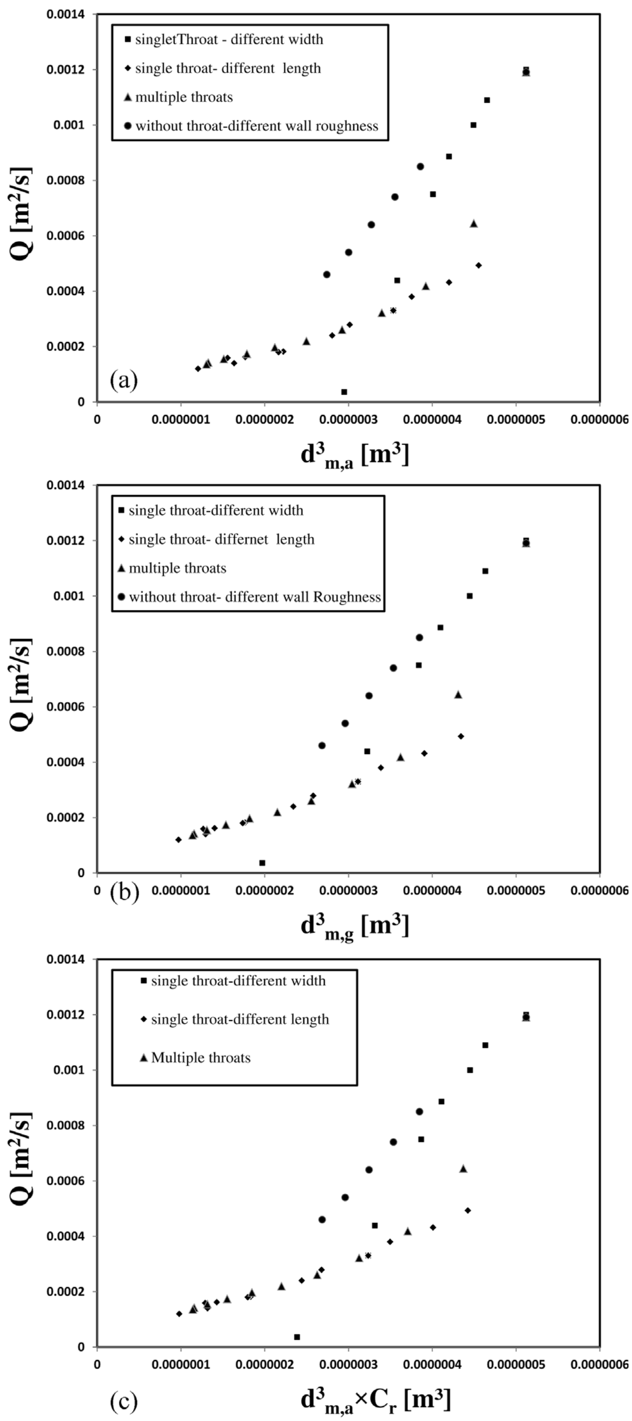

Figure 7. Variation of the volumetric flow rate over mean channel width a) arithmetic average, b) geometrical average, c) modified arithmetic average.

5.3 Randomly generated fractures

Single fractures in geo-materials such as rock mass or concrete always contain tortuous flow paths with variable aperture and rough wall surfaces. In previous parts of this paper, different important geometrical parameters influencing flow through channels such as tortuosity factor, average width and wall roughness were investigated by the developed LB numerical model independently. Herein, attempt is made to study the effects of these parameters on flow through fractures with more realistic geometrical characteristics.

There are various methods to construct a synthetic fracture with rough wall surfaces such as the successive random addition method, the randomization of the Weierstrass function based on Mandelbrot, and the Fourier transformation (Dou & Zhou, 2014). In this study, a random generation process similar the approach used by Yang (2014) was applied to provide fractures with irregular geometries to be used in the fluid flow analyses. In this procedure, the shape of the centerline is defined as a backbone for the fracture. Also, it is assumed that the fracture walls have a zigzag shape and the total numbers of zigzags are defined.

A certain number of random numbers are generated and they are assigned as slopes for those zigzag lines. A scale factor is used to adjust the slopes, if necessary. Another set of random numbers were generated (between 0.5 and 1) for fracture widths. These random numbers are multiplied with appropriate width factor to get the desired fracture width at a given point on the zigzag line. Hence numbers of zigzag lines, width factor and scale factor are the parameters that can be controlled in the process of generation of the fracture. The mentioned procedure was applied to a MATLAB code to generate fractures with random wall geometries which are the boundary conditions for the fluid flow analyses by LB model. A representative illustration of some of the generated fractures by the mentioned procedure is shown in Figure 9.

Several flow simulations through generated fractures with different geometrical properties are conducted to examine the validity of cubic law for estimation of the flow rate using different definition of hydraulic aperture. For comparison, the results of flow rate for these analyses are presented in terms of arithmetic mean, geometrical mean and effective width in Figures 10a, b and c, respectively. These figures indicate that application of the effective width in the cubic law can significantly improve the R-squared value of the obtained data. Therefore, the effective width can be evaluated as an appropriate hydraulic aperture of the fractures for estimation of flow rate using global cubic law.

6. Conclusion

In this study, Lattice Boltzmann Method (LBM) was employed for simulation of fluid flow through channels with grossly irregular wall geometries representing the condition of natural fractures in the geo-materials such as rock and concrete. The developed numerical model was validated against analytical solutions proposed by Ge (1997) using local cubic law approach for two fluid flow

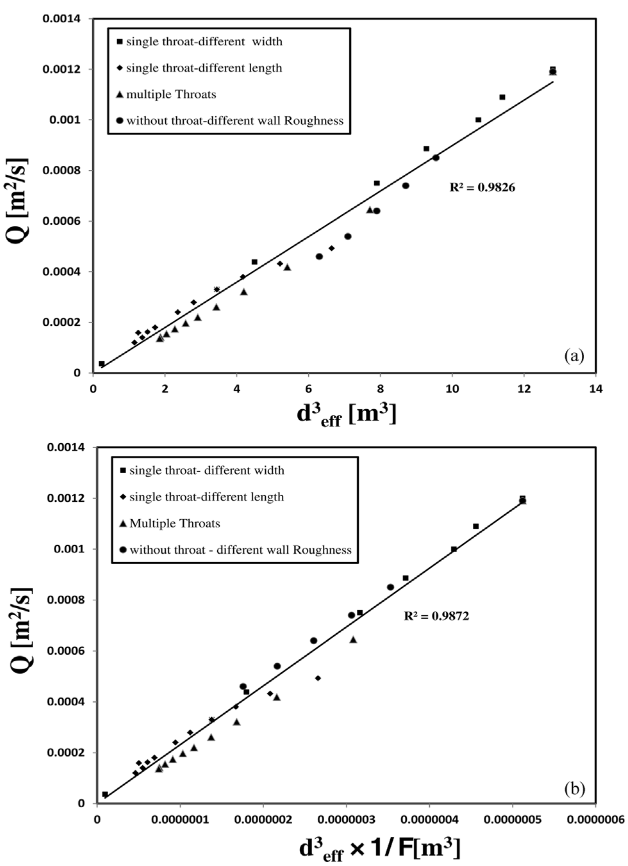

Figure 8. Variation of the volumetric flow rate over a) effective width as defined by Akhavan et al. (2012), b) modified effective width using the reduction factor by Louis (1969).

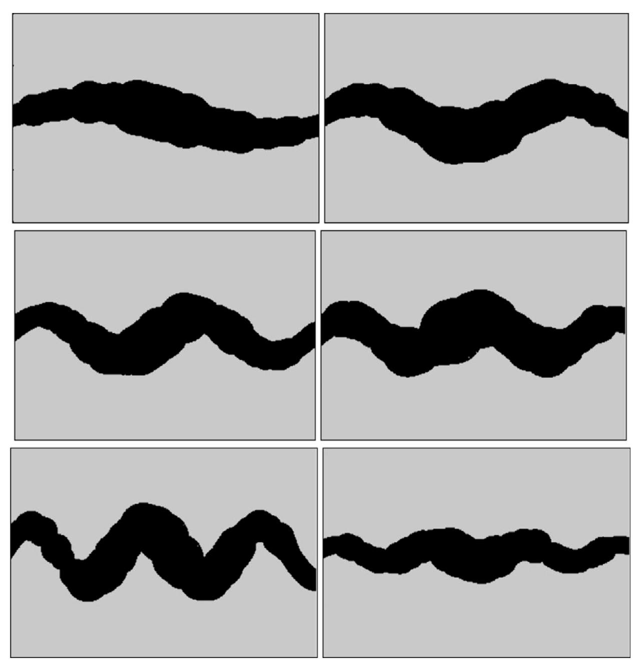

Figure 9. A representative illustration of some of the randomly generated fractures.

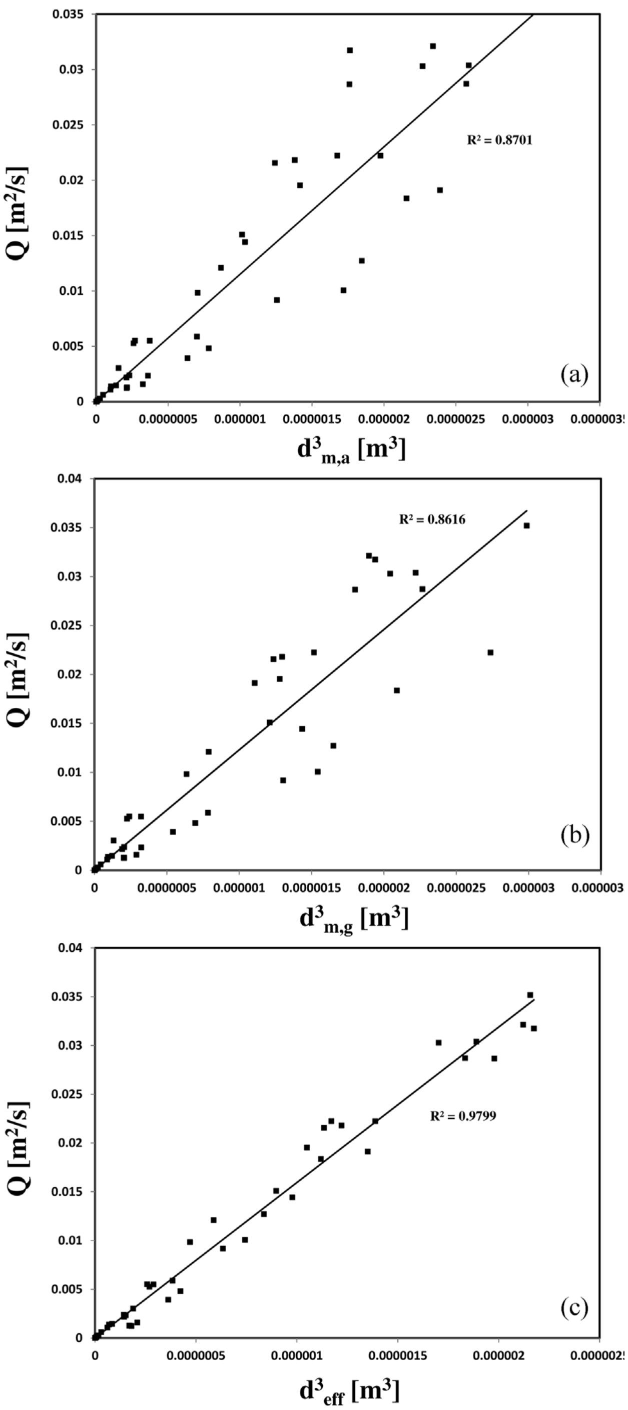

Figure 10. Variation of the volumetric flow rate over a) arithmetic average of width, b) geometrical average of width, c) effective width for randomly generated channels.

problems through single fracture with regular geometries. In general, the obtained results indicate that in spite of the fact that certain physical features of real fractures cannot be fully represented by the applied 2D model; the LBM is a promising numerical method that can be used for estimation of fluid flow through natural fractures.

The focus of the study was evaluation of different definition of hydraulic aperture for implication in the conventional cubic law implying that the volume rate of fluid flow across a section in a fracture is proportional to the cube of the hydraulic aperture.

Based on the obtained results, the following conclusions can be drawn:

1) Volumetric flow rate is inversely proportional with tortuosity factor. Furthermore, the numerical results indicate that flow rate is sensitive not only to the length of centerline curve, but depends on its curvature variation. However, the error of mere consideration of distance ratio in the conventional definition of tortuosity factor is not significant.
2) Even through a fracture with straight centerline (where tortuosity factor is unity), abrupt constrictions of fracture can considerably affect the rate of flow. Numerical results indicate that applying effective width instead of arithmetic or geometrical average of channel width can significantly improve the linear trend expected by the cubic law.
3) The numerical results imply that stronger correlation between the flow rate and the cube of effective width can be reached if reduction factor proposed by Louis (1969) is applied to the cube of effective width for channels with rough surfaces.
4) Flow simulations through randomly generated fractures with different geometrical properties imply that application of the effective width can be evaluated as a more appropriate average parameter representing the hydraulic aperture of the fractures for estimation of flow rate by the conventional cubic law.

More investigations are required for overcoming the limitations of the developed numerical tool such as simulation of non-Darcy flow and implication of 3D formulation in the model. The future work of this research program is the study of the fluid flow in natural fracture profiles using three-dimensional model.

References

Akhavan, A., Shafaatian, S.M.H., & Rajabipour, F. (2012). Quantifying the effects of crack width, tortuosity, and roughness on water permeability of cracked mortars. *Cement and Concrete Research*, 42(2), 313-320. https://doi.org/10.1016/j.cemconres.2011.10.002

Baghbanan, A., & Jing, L. (2007). Hydraulic properties of fractured rock masses with correlated fracture length and aperture. *International Journal of Rock Mechanics and Mining Sciences*, 44(5), 704-719. https://doi.org/10.1016/j.ijrmms.2006.11.001

Barton, N., Bandis, S., & Bakhtar, K. (1985). Strength, deformation and conductivity coupling of rock joints. *International Journal of Rock Mechanics and Mining Sciences & Geomechanics Abstracts*, 22(3), 121-140. https://doi.org/10.1016/0148-9062(85)93227-9

Bear, J., Tsang, C.F., & Marsily, G.D. (1993). *Flow and contaminant transport in fractured rocks*. Academic Press.

Bhatnagar, P.L., Gross, E.P., & Krook, M. (1954). A model for collision processes in gases. I. Small amplitude processes in charged and neutral one-component systems. *Physical Review*, 94(3), 511. https://doi.org/10.1103/PhysRev.94.511

Brown, S.R. (1987). Fluid flow through rock joints: the effect of surface roughness. *Journal of Geophysical Research: Solid Earth*, 92(B2), 1337-1347.

Brown, S.R., Stockman, H.W., & Reeves, S.J. (1995). Applicability of the Reynolds equation for modeling fluid flow between rough surfaces. *Geophysical Research Letters*, 22(18), 2537-2540. https://doi.org/10.1029/JB092iB02p01337

Brush, D.J., & Thomson, N.R. (2003). Fluid flow in synthetic rough-walled fractures: Navier-Stokes, Stokes, and local cubic law simulations. *Water Resources Research*, 39(4), 5-1-5-4. https://doi.org/10.1029/2002WR001346

Chen, S., & Doolen, G.D. (1998). Lattice Boltzmann method for fluid flows. *Annual Review of Fluid Mechanics*, 30(1), 329-364. https://doi.org/10.1146/annurev.fluid.30.1.329

Cook, N.G. (1992). Natural joints in rock: mechanical, hydraulic and seismic behaviour and properties under normal stress. *International Journal of Rock Mechanics and Mining Sciences & Geomechanics Abstracts*, 29(3), 198-223. https://doi.org/10.1016/0148-9062(92)93656-5

Crandall, D., Bromhal, G., & Karpyn, Z.T. (2010). Numerical simulations examining the relationship between wall-roughness and fluid flow in rock fractures. *International Journal of Rock Mechanics and Mining Sciences*, 47(5), 784-796. https://doi.org/10.1016/j.ijrmms.2010.03.015

Dietrich, P., Helmig, R., Hötzl, H., Sauter, M., Köngeter, J., & Teutsch, G. (2005). *Flow and transport in fractured porous media*. Springer Science & Business Media.

Dou, Z., & Zhou, Z.F. (2014). Lattice Boltzmann simulation of solute transport in a single rough fracture. *Water Science and Engineering*, 7(3), 277-287. https://doi.org/10.3882/j.issn.1674-2370.2014.03.004

Engler, S.T. (2003). Benchmarking the 2D lattice Boltzmann BGK model. Short communication. *Amsterdam Center for Computacional Science*, Amsterdam.

Feng, Y., Han, K., & Owen, D. (2007). Coupled lattice Boltzmann method and discrete element modelling of particle transport in turbulent fluid flows: Computational issues. *International Journal for Numerical Methods in Engineering*, 72(9), 1111-1134. https://doi.org/10.1002/nme.2114

Ge, S. (1997). A governing equation for fluid flow in rough fractures. *Water Resources Research*, 33(1), 53-61. https://doi.org/10.1029/96WR02588

Ghassemi, A., & Pak, A. (2011). Pore scale study of permeability and tortuosity for flow through particulate media using Lattice Boltzmann method. *International Journal for Numerical and Analytical Methods in Geomechanics*, 35(8), 886-901. https://doi.org/10.1002/nag.932

Gutfraind, R., & Hansen, A. (1995). Study of fracture permeability using lattice gas automata. *Transport in Porous Media*, 18(2), 131-149. https://doi.org/10.1007/BF01064675

Jensen, J.L. (1991). Use of the geometric average for effective permeability estimation. *Mathematical Geology*, 23(6), 833-840. https://doi.org/10.1007/BF02068778

Klimczak, C., Schultz, R.A., Parashar, R., & Reeves, D.M. (2010). Cubic law with aperture-length correlation: implications for network scale fluid flow. *Hydrogeology Journal*, 18(4), 851-862. https://doi.org/10.1007/s10040-009-0572-6

Konzuk, J.S., & Kueper, B.H. (2004). Evaluation of cubic law based models describing single phase flow through a rough-walled fracture. *Water Resources Research*, 40(2), 973-991. https://doi.org/10.1029/2003WR002356

Kranzz, R., Frankel, A., Engelder, T., & Scholz, C. (1979). The permeability of whole and jointed Barre granite. *International Journal of Rock Mechanics and Mining Sciences and Geomechanics*, 16(4), 225-234. https://doi.org/10.1016/0148-9062(79)91197-5

Lomize G.M. (1951). Flow in Fractured Rocks. *Gosenergoizdat*, Moscow, 127, 97.

Louis C. (1969). *A study of groundwater flow in jointed rock and its influence on the stability of rock masses* [Unpublished doctoral thesis]. University of Karlsruhe English translation, Imperial College Rock Mechanics. Research Report n2 10 London Sept. 1969 (90 p.) Univ. Microfilm.

Méheust, Y., & Schmittbuhl, J. (2001). Geometrical heterogeneities and permeability anisotropy of rough fractures. *Journal of Geophysical Research: Solid Earth*, 106(B2), 2089-2102. https://doi.org/10.1029/2000JB900306

Mourzenko, V.V., Thovert, J.F., & Adler, P.M. (1995). Permeability of a single fracture; validity of the Reynolds equation. *Journal de Physique II*, 5(3), 465-482. https://doi.org/10.1051/jp2:1995133

Nazridoust, K., & Ahmadi, G. (2006). Airflow and pollutant transport in street canyons. *Journal of Wind Engineering and Industrial Aerodynamics*, 94(6), 491-522. https://doi.org/10.1016/j.jweia.2006.01.012

Neuzil, C., & Tracy, J.V. (1981). Flow through fractures. *Water Resources Research*, 17(1), 191-199. https://doi.org/10.1029/WR017i001p00191

Nicholl, M., Rajaram, H., Glass, R., & Detwiler, R. (1999). Saturated flow in a single fracture: Evaluation of the Reynolds equation in measured aperture fields. *Water Resources Research*, 35(11), 3361-3373. https://doi.org/10.1029/1999WR900241

Niya, S.R., & Selvadurai, A.P.S. (2019). Correlation of joint roughness coefficient and permeability of a fracture. *International Journal of Rock Mechanics and Mining Sciences*, 113, 150-162. https://doi.org/10.1016/j.ijrmms.2018.12.008

Noble, D.R., Georgiadis, J.G., & Buckius, R.O. (1995). Direct assessment of lattice Boltzmann hydrodynamics and boundary conditions for recirculating flows. *Journal of Statistical Physics*, 81(1-2), 17-33. https://doi.org/10.1007/BF02179965

Oron, A.P., & Berkowitz, B. (1998). Flow in rock fractures: The local cubic law assumption reexamined. *Water Resources Research*, 34(11), 2811-2825. https://doi.org/10.1029/98WR02285

Pan, C., Hilpert, M., & Miller, C.T. (2001). Pore-scale modeling of saturated permeabilities in random sphere packings. *Physical Review E*, 64(6), 066702. https://doi.org/10.1103/PhysRevE.64.066702

Patir, N. & Cheng, H.S. (1978). An average flow model for determining effects of three-dimensional roughness on partial hydrodynamic lubrication. *Journal of Lubrication Technology*, 100(1), 12-17. https://doi.org/10.1115/1.3453103

Pyrak-Nolte, L.J., Cook, N.G., & Nolte, D.D. (1988). Fluid percolation through single fractures. *Geophysical Research Letters*, 15(11), 1247-1250. https://doi.org/10.1029/GL015i011p01247

Qian, Y., D'humières, D., & Lallemand, P. (1992). Lattice BGK models for Navier-Stokes equation. *EPL (Europhysics Letters)*, 17(6), 479. https://doi.org/10.1209/0295-5075/17/6/001

Renshaw, C.E. (1995). On the relationship between mechanical and hydraulic apertures in rough-walled fractures. *Journal of Geophysical Research: Solid Earth*, 100(B12), 24629-24636. https://doi.org/10.1029/95JB02159

Sangani, A., & Acrivos, A. (1982). Slow flow through a periodic array of spheres. *International Journal of Multiphase Flow*, 8(4), 343-360. https://doi.org/10.1016/0301-9322(82)90047-7

Singh, K.K., Singh, D.N., & Ranjith, P.G. (2015). Laboratory simulation of flow through single fractured granite. *Rock Mechanics and Rock Engineering*, 48(3), 987-1000. https://doi.org/10.1007/s00603-014-0630-9

Snow D.T. (1965). *A parallel plate model of fractured permeable media* [Unpublished doctoral thesis] University of California at Berkeley.

Su, X., Zhou, L., Li, H., Lu, Y., Song, X., & Shen, Z. (2020). Effect of mesoscopic structure on hydro-mechanical properties of fractures. *Environmental Earth Sciences*, 79(6), 1-23. https://doi.org/10.1007/s12665-020-8871-2

Succi, S. (2001). *The lattice Boltzmann equation: for fluid dynamics and beyond*. Oxford University Press.

Tsang, Y.W., & Tsang, C.F. (1987). Channel model of flow through fractured media. *Water Resources Research*, 23(3), 467-479. https://doi.org/10.1029/WR023i003p00467

Tsang, Y.W., & Tsang, C.F. (1990). Hydrological characterization of variable-aperture fractures. *Proc. International Symposium on Rock Joints, Loen*, 423-430.

Tsang, Y.W., & Witherspoon, P.A. (1983). The dependence of fracture mechanical and fluid flow properties on fracture roughness and sample size. *Journal of Geophysical Research: Solid Earth*, 88(B3), 2359-2366. https://doi.org/10.1029/JB088iB03p02359

Tsang, Y.W. (1984). The effect of tortuosity on fluid flow through a single fracture. *Water Resources Research*, 20(9), 1209-1215. https://doi.org/10.1029/WR020i009p01209

Unger, A.J.A., & Mase, C.W. (1993). Numerical study of the hydromechanical behavior of two rough fracture surfaces in contact. *Water Resources Research*, 29(7), 2101-2114. https://doi.org/10.1029/93WR00516

Walsh, J. (1981). Effect of pore pressure and confining pressure on fracture permeability. *International Journal of Rock Mechanics and Mining Sciences and Geomechanics*, 18(5), 429-435. https://doi.org/10.1016/0148-9062(81)90006-1

Walsh, J.B., & Brace, W. (1984). The effect of pressure on porosity and the transport properties of rock. *Journal of Geophysical Research: Solid Earth*, 89(B11), 9425-9431. https://doi.org/10.1029/JB089iB11p09425

Wang, L., Cardenas, M.B., Slottke, D.T., Ketcham, R.A., & Sharp Jr, J.M. (2015). Modification of the Local Cubic Law of fracture flow for weak inertia, tortuosity, and roughness. *Water Resources Research*, 51(4), 2064-2080. https://doi.org/10.1002/2014WR015815

Wang, M., Chen, Y.F., Ma, G.W., Zhou, J.Q., & Zhou, C.B. (2016). Influence of surface roughness on nonlinear flow behaviors in 3D self-affine rough fractures: Lattice Boltzmann simulations. *Advances in Water Resources*, 96, 373-388. https://doi.org/10.1016/j.advwatres.2016.08.006

Witherspoon, P.A., Wang, J.S., Iwai, K., & Gale, J.E. (1980). Validity of cubic law for fluid flow in a deformable rock fracture. *Water Resources Research*, 16(6), 1016-1024. https://doi.org/10.1029/WR016i006p01016

Yang, P. (2014). *Numerical simulations of electrically induced chloride ion transport and moisture permeability through cracked concrete* [Master's thesis, Arizona State University]. Arizona State University's repository. https://repository.asu.edu/items/25116

Zambrano, M., Pitts, A.D., Salama, A., Volatili, T., Giorgioni, M., & Tondi, E. (2019). Analysis of fracture roughness control on permeability using SfM and fluid flow simulations: Implications for carbonate reservoir characterization. *Geofluids*, 4132386. https://doi.org/10.1155/2019/4132386

Zhang, T., & Nagy, G. (2004). Surface tortuosity and its application to analyzing cracks in concrete. *Proc. 17th International Conference on Pattern Recognition*, *Cambridge*. Vol. 2, IEEE, 851-854. https://doi.org/10.1109/ICPR.2004.1334392

Zhang, Z., & Nemcik, J. (2013). Fluid flow regimes and nonlinear flow characteristics in deformable rock fractures. *Journal of Hydrology*, 477, 139-151. https://doi.org/10.1016/j.jhydrol.2012.11.024

Zimmerman, R.W., & Bodvarsson, G.S. (1996). Hydraulic conductivity of rock fractures. *Transport in Porous Media*, 23(1), 1-30. https://doi.org/10.1007/BF00145263

Zimmerman, R.W., Kumar, S., & Bodvarsson, G.S. (1991). Lubrication theory analysis of the permeability of rough-walled fractures. *International Journal of Rock Mechanics and Mining Sciences and Geomechanics*, 28(4), 325-331. https://doi.org/10.1016/0148-9062(91)90597-F

Soils and Rocks

An International Journal of Geotechnical and Geoenvironmental Engineering

www.soilsandrocks.com

ISSN 1980-9743
ISSN-e 2675-5475

The influence of the fluid dielectric constant on the shear strength of a unsaturated soil

M.S.S. Almeida[1,#], S.L. Machado[2], H.M.C. Andrade[2]

Article

Keywords
Dielectric constant
Napl
Shear strength
Unsaturated soils

Abstract

Results of triaxial tests performed in saturated and unsaturated compacted soil specimens with different interstitial fluids are presented. Tests were carried out in order to study the influence of the fluid relative dielectric constant, ε_r, on the soil shear strength of a granite-gneiss clayey residual soil from Salvador, Bahia, Brazil. It is shown that the soil shear strength is affected not only by the interstitial fluid saturation degree (or suction) but it is also a nonlinear function of the interstitial fluid value of ε_r. The shear strength of the saturated samples decreased with ε_r, following the order (air $\varepsilon_r = 1$, diesel $\varepsilon_r = 2.13$, ethanol $\varepsilon_r = 24.3$ and water $\varepsilon_r = 80$), whereas fluids with higher dielectric constants presented a more pronounced increase in shear strength under drying (replacement of the interstitial liquid with air). An empirical model is proposed to predict soil shear strength as a function of (ε_{rw} - ε_f), the difference between the relative dielectric constant of the water and the interstitial fluid. Good adherence between experimental and fitted results was obtained.

1. Introduction

According to Garcia et al. (2004), leaks of organic and inorganic products that occur in fuel tanks and pipes are the most common cause of contaminant releases to the environment. Besides the possible contamination, the presence of these substances can affect the soil stress-strain behavior depending on the soil-fluid interaction, which differs according to the physical-chemical properties of the fluids involved. It can be said, however, that studies concerning the mechanical behavior of soil when saturated by different interstitial fluids, such as hydrocarbons, are still scarce. Almost all the papers published since the 1980s (Brown & Anderson, 1983; Brown & Thomas, 1984; Brown & Thomas, 1986; Fernandez & Quigley, 1985; Schramm et al., 1986; Budhu et al., 1991; Li et al., 1996; Oliveira, 2001) focus on the hydraulic behavior of the soil when percolated by different fluids.

The fluid polarity can be evaluated by its dielectric constant. The value of ε_r can be calculated by the ratio between the charge storage capacity of a capacitor filled with the medium of interest with that of the same capacitor with vacuum between the plates. According to Halliday et al. (2007), ε_r is related to the ability of the fluid molecules to polarize, orienting their poles under an electric field. For three phase media such as the soil, the value of ε_r can be estimated through semi-empiric formulas such as the CRIM (Complex Refractive Index Method, comprised by Equation 1), which relates the dielectric constant of a unsaturated porous medium with its porosity, n, and the water degree of saturation, Sr. Although this equation was originally proposed for water, its use can be extended for a unsaturated porous medium partially filled with other interstitial fluids.

$$\sqrt{\varepsilon_r} = n \cdot Sr\sqrt{\varepsilon_{rw}} + (1-n)\sqrt{\varepsilon_{rs}} + n(1-Sr)\sqrt{\varepsilon_{rair}} \qquad (1)$$

where ε_r, ε_{rw}, ε_{rs} e ε_{rair} are, respectively, the relative dielectric constant of the soil as a whole, water, solid particles and air. Table 1 shows ε_r typical values for different materials (Davis & Annan, 1989). Most minerals have ε_r values between 4 and 5. These values are near to the minimum values presented in Table 1 for silt, sand, and clay.

Anandarajah & Zhao (2000) evaluated the shear strength of a clay when saturated by fluids of different dielectric constants. The samples were saturated and tested in a triaxial equipment. The fluids used in the tests were formaldehyde ($\varepsilon_r = 111$), water ($\varepsilon_r = 80$), ethanol ($\varepsilon_r = 24.3$), acetic acid ($\varepsilon_r = 6.16$), triethylamine ($\varepsilon_r = 2.42$) and heptane

[#]Corresponding author. E-mail address: mario_almeida10@yahoo.com.br.
[1]Universidade Federal do Recôncavo da Bahia, Cruz das Almas, BA, Brazil.
[2]Universidade Federal da Bahia, Salvador, BA, Brazil.

Submitted on December 14, 2018; Final Acceptance on June 10, 2020; Discussion open until March 31, 2021.
DOI: https://doi.org/10.28927/SR.434535

Table 1. Typical values of the relative dielectric constants for different materials.

Material	Relative dielectric constant (ε_r)
Air	1
Water	80
Diesel	2.13
Ethanol	24.3
Solid particles	4-5
Dry sand	3-5
Silt	5-30
Clay	5-40

Source: Adapted from Davis & Annan (1989).

(ε_r = 1.91). Figure 1 presents the results obtained by the cited authors. As can be noted, the soil shear strength varies non-linearly with ε_r.

Di Maio et al. (2004) studied the shear strength of two clays from Italy (Bisaccia clay and bentonite Ponza) when saturated with water, NaCl solutions and cyclohexane. According to these authors, the minimum values of shear strength for both clays occurred when the specimens were saturated with water. The use of interstitial fluids with ε_r values lower than water increased soil shear strength. Calvello et al. (2005) found similar results when performing direct shear and unconfined compression tests in soil samples saturated with distillate water, salt solutions in different concentrations and organic fluids with different dielectric constants.

The influence of the interstitial fluid polarity on the soil shear strength values is explained, at least partially, by the double layer theory. The most widely accepted conceptual model to represent the interactions between the fluid and the clay surface is the diffuse double layer system. This model is an evolution of the Helmholtz-Smoluchowski theory proposed by Helmholtz (1879-1914; see Helmholtz, 1879) and improved by the work of Gouy-Chapman (1910-1913). The diffuse double layer system consists of the clay particles, adsorbed cations, and water molecules in one layer, while the other layer is a diffuse swarm of counterions. Although this model does not take into account the effect of the potential energy in the oriented molecules of water that surround the clay particles, it is useful to explain some basic phenomena in a clay-water-electrolyte system (Fang, 1997).

Equation 2 can be used to predict the double layer thickness, t, based on the Gouy-Chapman theory (Gouy, 1910). It can be seen from Equation 2 that an increase in the electrolyte concentration or a decrease in the fluid dielectric constant reduces the double layer thickness, bringing the particles closer to each other and increasing soil particle interaction forces.

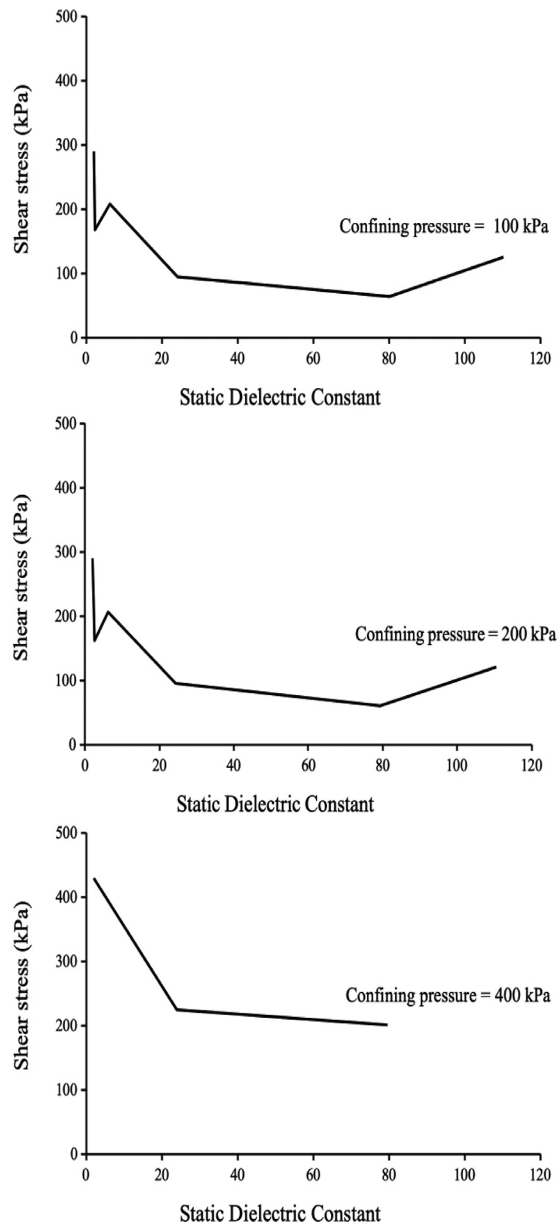

Figure 1. Shear strength variation with ε_r. Source: Adapted from Anandarajah & Zhao (2000).

$$t = \sqrt{\frac{\varepsilon . k_b T}{8\pi n_e e^2 v^2}} \tag{2}$$

In Equation 2, ε is the dielectric constant, K_b is the Boltzmann constant, T is the temperature, n_e is the electrolyte concentration, e is the elementary charge and ν is the ionic valence. In this paper, an investigation is performed about how the shear strength of a residual soil of granite-gneiss is affected when its voids are filled, in different proportions, with fluids of dielectric constants smaller than water.

2. Testing materials and methods

2.1 Materials - soil

The soil used in this study was a granite-gneiss residual soil, RGG, which is predominant in the city of Salvador, BA, Brazil. The geotechnical characterization tests were executed according to the following standards: NBR 7181 (ABNT, 1984); NBR 6489 (ABNT, 1984); NBR 7180 (ABNT, 1984); NBR 6508 (ABNT, 1984) and NBR 7182 (ABNT, 1986). Table 2 presents the main RGG geotechnical characteristics (void ratio, *e*, and porosity, *n*, correspond to optimum compaction conditions, normal Proctor energy).

Complementary tests were also performed on RGG specimens in order to determine specific surface area, SS, pore volume, PV, chemical composition and liquid retention curves, SLRC, besides optical microscopy analysis. SS and PV were determined using the physisorption of N_2 technique, B.E.T. method (Brunnauer et al., 1938) and a Micromeritics ASAP 2020 Porosimetry System. Samples were heated at 300 °C for 12 h in vacuum (≈267 Pa) for the removal of water or any other physisorbed substances prior to the tests.

The effects of soil texture on the values of the SS values were analyzed by preparing the samples in four different conditions: a) material passing through the sieve #10 and retained on the sieve #16; b) material passing through the sieve #80; c) material passing through the sieve #200; and d) clay fraction obtained in a sedimentation procedure. Specimen mass for each test was about 0.20 g. Table 3 presents the obtained results. More results are available in Almeida (2016). The SS values of the clay fraction, according to Hillel (1980), indicate the presence of the minerals kaolinite and ilite.

Optical microscopy was performed according to procedures proposed by Kaya & Fang (2005). A 10 mL beaker was filled with a solution containing 10 % of the soil and 90 % of the given fluid (water, ethanol, or diesel) in weight and then stirred for one minute in order to improve soil-fluid interactions. After that, a drop of the solution was poured onto a glass streak plate and then taken to the optical microscope (Olympus brand, BX41 model, 100x resolution and attached photographic camera Olympus brand, Evolt E330 model). Figure 2 presents the results of the optical microscopy analyses. In this figure it is possible to visualize the effect of each fluid in terms of soil flocculation/dispersion (tests were performed in duplicate). Samples with high polarity interstitial fluid (water) tended to present a disperse structure, whereas samples immersed in diesel presented a flocculated structure. Ethanol (intermediate ε_r) presented an intermediate behavior.

Table 3. RGG specific surface and pore volume in different texture conditions.

Material	SS (m^2/g)	PV (cm^3/g)
Passing through the sieve #10 and retained on the sieve #16	44.2	0.197
Passing through the sieve #80	50.8	0.240
Passing through the sieve #200	72.0	0.342
Clay	83.7	0.420

RGG elementary composition was determined using the X-ray fluorescence technique (EDX) and an EDX-720 Shimadzu spectrometer. RGG powder samples were analyzed in 5mm polypropylene holders, tightly covered with a 5 μm polypropylene film. The X-rays fluorescence spectra were collected in a vacuumed environment. Tests were performed in a single batch of sixteen samples retrieved from a

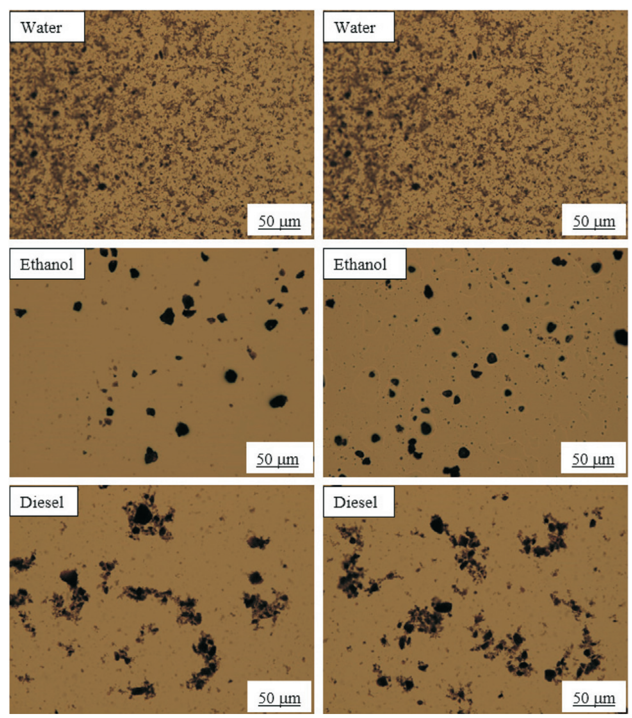

Figure 2. Optical microscopy images of RGG samples immersed in different fluids.

Table 2. Results from the geotechnical characterization of the residual granite-gneiss soil.

Grain size composition (%)			Atteberg limits (%)			Compaction normal Proctor energy		γ_s (kN/ m^3)	*e*	*n*
Sand	Silt	Clay	W_L	W_P	I_P	γ_{dmax} (kN/m^3)	w_{ot} (%)	27.04	1.03	0.51
26	18	56	78	42	36	13.34	31.80			

compacted specimen (four samples at the top, four at the bottom and eight samples at the middle portion of the specimen). Table 4 summarizes the obtained results from EDX tests. It can be observed that silicon, aluminum, and iron are the main oxides found in the RGG specimens, comprising 98.86 % ± 0.09 of all detected oxides. TiO_2, BaO, SO_3, MnO and ZrO_2 are the main remaining oxides in the samples (1.14 % ± 0.13). The SiO_2/Al_2O_3 ratio was about 1.15, indicating the predominance of the kaolinite mineral group (1:1 structure).

2.2 Materials - fluids

Water, diesel, and ethanol were the interstitial fluids used in this study. Their density, viscosity and superficial tension were determined in the laboratory. A Krüs Easydyne Tensiometer, k20 model, was used for superficial tension determination. Temperature was controlled using a Brookfield bath, TC-550 model. Fluids were tested at 15, 20, 25, 30, 35 and 40 °C. Once the temperature of equilibrium was reached, the densities of the fluids were determined using a standard volume of known density which was immersed in the fluid sample. After that, fluid superficial tension was determined using the ring method (ASTM D 971, 2012). A Brookfield viscometer, DV2T model, was used for the viscosity tests, which were performed at the same temperatures cited above (ASTM D 4016, 2014). Table 5 summarizes the obtained results for density, viscosity, and superficial tension of the fluids at 20 °C. More results are available in Almeida (2016).

2.3 Materials - soil-fluid interactions

Soil liquid retention curves, were determined in order to evaluate soil/fluid interactions. Compacted soil specimens (normal Proctor energy) at the optimum water content were used. The following techniques were used for suction control/measurement: direct suction measurement with tensiometers (water), adapted pressure plate (water, diesel), Richard's pressure chamber (water, diesel and ethanol) and filter paper (water). Tests were performed according to ASTM D 6836 (ASTM, 2008) and ASTM C 5298 (ASTM, 1994) when applicable. Figure 3 summarizes the results.

Experimental results were fitted by Equation 3, proposed by Fredlund & Xing (1994). For the sake of comparison, some results obtained for ethanol are also shown in Figure 3(b). As can be observed, the obtained results are close to those obtained for diesel. However, no suction-controlled tests were performed using ethanol.

The main water wetting branch was obtained by completely drying the sample from the optimum water content prior to the test. In the case of the main drying water branch, samples were first saturated from the optimum water content. The tests performed with diesel and ethanol, however, required that samples were first dried, then saturated with the fluid of interest, and finally left to dry by suction imposition. Because completely drying the samples induces non recoverable reduction in their void ratios, the experimental results are not completely comparable. Table 6 presents the main fitting parameters of the experimental results by Equation 3.

$$\theta = \theta_{sat}\left[1-\frac{\ln\left(1+\frac{\psi}{\psi_r}\right)}{\ln\left(1+\frac{10^6}{\psi_r}\right)}\right]\left[\frac{1}{\ln\left(e+\left(\frac{\psi}{a}\right)^n\right)}\right]^m \tag{3}$$

Table 4. Soil chemical composition by EDX.

Values	Chemical substances			
	SiO_2 (%)	Al_2O_3 (%)	Fe_2O_3 (%)	Others (%)
Average	46.83	40.65	11.38	1.14
SD	0.85	0.74	0.45	0.13
COV (%)	1.82	1.82	3.98	11.52

Table 5. Fluid properties at 20 °C.

Fluid	Superficial tension (mN/m)	Viscosity (cP)	Density (g/cm^3)
Diesel	25.98	3.08	0.829
Ethanol	24.45	1.67	0.845
Water	70.75	0.87	0.998

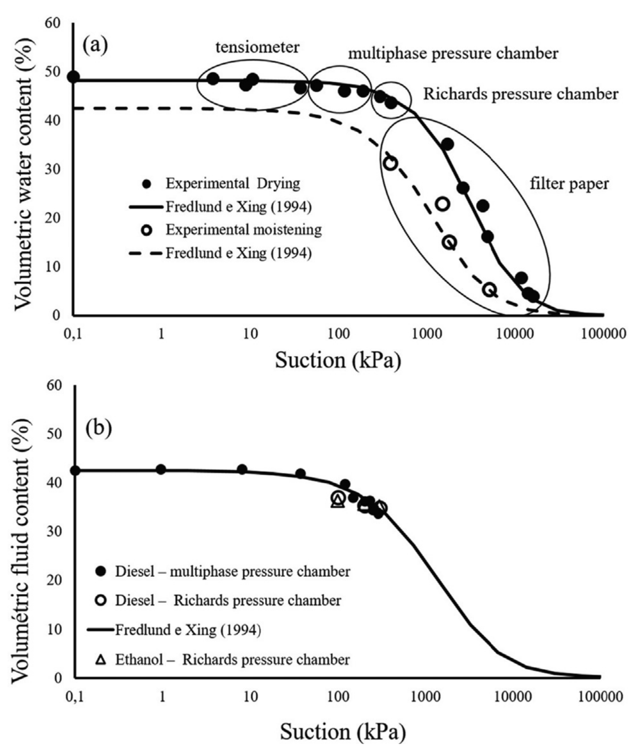

Figure 3. Retention curves for different fluids. Experimental data fitting using the Fredlund & Xing (1994) equation.

Table 6. Fitting parameters of experimental results by Equation 3.

Procedure	θ_{sat} (%)	θ_r (%)	ψ_r (kPa)	a	m	n	R^2
Main drying water	48.21	4.01	25 000	4929	3.98	1.20	0.99
Main wetting water	42.52	2.50	20 000	1818	3.80	1.05	0.90
Main drying diesel	42.51	2.50	20 000	2000	3.50	0.95	0.98

where θ is the volumetric content, θ_{sat} is the saturated volumetric content, ψ is the suction, ψ_r is the suction corresponding to residual volumetric content, e is the base of the natural logarithm, and a, n and m are fitting parameters.

3. Methods

3.1 Triaxial tests

Triaxial tests were performed on compacted samples (50 mm × 100 mm, nominal dimensions) in the same conditions as for SLRC tests. All tests were of the Consolidated Isotropically Drained type and performed in triplicate, by using different interstitial fluids (water, ethanol, diesel and dried soil, or air saturated). Tests were performed on saturated samples, with suction control or at a "constant" fluid content.

As all specimens were compacted at optimum water content in order to allow the use of different interstitial fluids, they were dried at atmospheric conditions (conditioned temperature room) for five days and then oven-dried at 70 °C for two days. Specimens were compacted in one single compaction batch. All the specimens were randomly chosen to be tested after compaction and drying procedures. Tests performed with saturated samples employed upward flow and back pressure saturation techniques ($B \geq 0.90$, where B is the Skempton's parameter). Specimens to be tested with suction control were first immersed after drying in the fluid of interest, water, ethanol or diesel, for at least 2 days and then taken to a Richard's chamber to impose the desired suction for at least 15 days. Finally, the specimens were transferred to a triaxial chamber (use of a porous stone with an high air entry value, HAEV, of 1,500 kPa in the chamber base) and the desired top, base and confining pressures were applied, adopting a net confining pressure of about $\sigma - u_a = 20$ kPa. Two more days were allowed for suction stabilization before triaxial tests began. Suction-controlled tests were performed (use of axis translation technique) employing suction values of 100 kPa, 200 kPa and 300 kPa. Air (top) and water (base) pressures were kept constant during all the tests.

In the case of the tests performed keeping a constant fluid content, the specimens were taken directly to the triaxial chamber after drying. The confining pressures adopted in the triaxial tests were 50 kPa, 100 kPa, 200 kPa and 400 kPa for tests with saturated/constant fluid content samples, and 50 kPa, 100 kPa, and 200 kPa for suction-controlled tests. Volume change readings of saturated specimens were performed employing the water pressure lines (top and base) and a volume change gauge. In the suction-controlled tests the fluid drainage of the specimens was performed by the triaxial chamber base and the volume change gauge was connected to the confining pressure line (externally made volume change measurements with chamber compressibility correction). The same procedure was used for the "constant" fluid content tests. In this case however, the top and base lines were open to the atmosphere to avoid excess pore water pressure generation. A PVC film with a small hole was used in the fluid exits to prevent evaporation. No fluid was observed being expelled from the specimens during the tests.

Axial Force and displacement measurements were performed externally to the triaxial chamber. Shearing rates were adopted taking into consideration the consolidation rate and the HAEV porous stone impedance in suction-controlled tests. All tests were performed by keeping the confining stress during the shearing phase constant. Tables 7 to 9 summarize the initial and final physical indexes

Table 7. Average physical indexes. Saturated samples.

Fluid	Confining stress (kPa)	Compaction				Saturated samples			
		γ_d (kN/m^3)	w (%)	CD (%)	n	After molding		After test	
					w (%)	n	w (%)	n	
Water	50	14.46	30.69	108.37	0.46	1.16	0.39	27.99	0.43
	100	14.31	30.43	107.27	0.47	1.24	0.39	27.17	0.42
	200	14.66	29.94	109.92	0.46	2.36	0.39	26.36	0.42
	400	14.64	30.29	109.77	0.46	1.72	0.39	26.45	0.42

Table 7 (cont.)

Fluid	Confining stress (kPa)	Compaction				Saturated samples			
		γ_d (kN/m^3)	*w* (%)	CD (%)	*n*	After molding		After test	
					w (%)	*n*	*w* (%)	*n*	
Ethanol	50	14.07	32.83	105.47	0.48	3.10	0.40	22.12	0.42
	100	14.04	32.66	104.94	0.48	2.73	0.41	22.50	0.42
	200	14.01	32.51	105.05	0.48	2.71	0.39	22.14	0.42
	400	14.09	32.18	105.62	0.48	3.87	0.41	22.24	0.42
Diesel	50	13.96	33.22	104.62	0.48	2.24	0.41	20.60	0.40
	100	13.98	33.52	104.82	0.48	4.27	0.41	20.18	0.40
	200	14.23	33.36	106.67	0.47	4.23	0.41	19.18	0.39
	400	14.12	33.20	105.82	0.48	4.01	0.42	20.17	0.40
Air	50	14.01	33.65	105.00	0.48	3.13	0.41	3.13	0.41
	100	14.00	32.66	104.97	0.48	2.38	0.41	2.38	0.41
	200	14.04	33.05	105.27	0.48	2.47	0.41	2.47	0.41
	400	14.08	32.33	105.57	0.48	1.91	0.40	1.91	0.40

Obs: CD is the compaction degree of the sample.

Table 8. Average physical indexes. Suction controlled samples.

Fluid	Suction (kPa)	Confining stress (kPa)	Compaction				After suction equalization		
			γ_d (kN/m^3)	*w* (%)	CD (%)	*n*	*w* (%)	*n*	*Sr* (%)
Water	100	50	14.43	30.68	108.17	0.47	29.80	0.46	94.58
		100	14.42	30.27	108.10	0.47	31.53	0.46	98.63
		200	14.32	30.26	107.37	0.47	30.62	0.47	95.30
Diesel	100	50	14.41	28.92	108.05	0.47	19.04	0.40	90.87
		100	14.50	29.37	108.67	0.46	19.30	0.40	92.57
		200	14.55	29.46	109.07	0.46	18.82	0.41	89.58
Water	200	50	14.51	29.31	108.77	0.46	29.33	0.45	95.84
		100	14.60	26.68	109.42	0.46	30.29	0.46	96.42
		200	14.35	30.74	107.57	0.47	29.57	0.46	95.42
Ethanol	200	50	14.53	30.63	108.90	0.46	18.96	0.41	86.25
		100	14.60	30.08	109.47	0.46	18.34	0.40	89.33
		200	14.60	30.42	109.42	0.46	18.96	0.40	89.10
Diesel	200	50	14.47	29.30	108.50	0.46	17.99	0.40	90.39
		100	14.50	29.41	108.67	0.46	17.79	0.40	87.17
		200	14.47	29.52	108.45	0.47	17.95	0.40	87.46
Water	300	50	14.21	31.06	106.52	0.47	28.92	0.47	90.69
		100	14.31	30.68	107.30	0.47	28.27	0.47	90.94
		200	14.25	30.85	106.82	0.47	29.56	0.47	90.66
Ethanol	300	50	14.32	31.27	107.37	0.47	18.59	0.40	88.57
		100	14.31	30.95	107.27	0.47	19.13	0.42	85.17

Table 8 (cont.)

Fluid	Suction (kPa)	Confining stress (kPa)	Compaction				After suction equalization		
			γ_d (kN/m^3)	*w* (%)	CD (%)	*n*	*w* (%)	*n*	*Sr* (%)
		200	14.38	30.27	107.77	0.47	18.39	0.41	82.52
Diesel	300	50	14.39	29.43	107.87	0.47	17.84	0.40	86.20
		100	14.31	29.95	107.27	0.47	17.38	0.40	83.96
		200	14.38	29.44	107.80	0.47	17.22	0.41	83.87

Obs: CD is the compaction degree of the sample.

Table 9. Average physical indexes. Constant water content.

Sr average (%)	Confining stress (kPa)	Compaction			Constant content samples after molding		
		γ_d (kN/m^3)	*w* (%)	CD (%)	*w* (%)	*n*	*Sr* (%)
14	50	14.42	30.69	108.10	3.49	0.40	14.16
	100	14.28	31.67	107.05	3.43	0.40	13.91
	200	14.76	30.80	110.64	3.49	0.40	14.16
	400	14.58	30.59	109.30	3.16	0.40	12.82
28	50	14.19	30.82	106.37	6.77	0.39	28.63
	100	14.30	31.59	107.20	6.58	0.39	27.83
	200	14.58	30.11	109.30	6.34	0.39	26.81
	400	14.52	31.07	108.85	6.52	0.39	27.58
42	50	14.58	28.86	109.30	9.32	0.38	41.12
	100	14.19	31.60	106.37	10.05	0.39	42.50
	200	14.08	30.76	105.55	10.21	0.39	43.18
	400	14.49	30.74	108.62	9.60	0.39	40.60
54	50	14.65	29.03	109.82	12.59	0.38	55.54
	100	14.43	30.66	108.17	12.96	0.39	54.81
	200	14.30	31.43	107.20	13.14	0.40	53.30
	400	14.53	31.08	108.92	12.74	0.39	53.88
66	50	14.52	30.55	108.85	15.86	0.41	61.71
	100	14.52	30.44	108.85	15.95	0.39	67.46
	200	14.29	31.13	107.12	16.50	0.39	69.78
	400	14.60	29.65	109.45	15.60	0.39	65.98
81	50	14.53	30.01	108.92	19.01	0.39	80.40
	100	14.67	29.84	109.97	18.64	0.39	78.83
	200	14.21	31.50	106.52	19.88	0.39	84.08
	400	14.41	30.93	108.02	19.39	0.39	82.01
87	50	14.55	29.92	109.07	22.16	0.41	86.23
	100	14.51	30.61	108.77	22.33	0.41	86.89
	200	14.40	31.11	107.95	22.76	0.41	88.56
94	50	14.50	30.46	108.70	25.53	0.42	95.33
	100	14.43	30.70	107.17	25.78	0.43	92.41
	200	14.33	31.38	107.42	26.18	0.43	93.84
	400	14.47	30.51	108.47	25.68	0.42	95.89

of the samples used in the triaxial tests. When applicable, tests followed the ASTM C 5298 (ASTM, 1994) standard.

4. Results and discussion

Figures 4 and 5 present typical stress/strain curves for the diesel and water saturated samples and suction controlled tests (ψ = 300 kPa) whereas Table 10 summarizes the obtained shear strength parameters for all the performed suction-controlled tests. The standard deviation of the experimental results around the fitted shear strength envelope, S_y and the coefficient of determination, R^2 are also shown. As can be observed, saturated diesel samples presented an over-consolidated behavior, reaching failure at low axial strains (2-4 %). Regarding the suction-controlled tests, this tendency is even more evident, with samples presenting brittle or fragile behavior.

Results presented in Table 10 were used to plot the graphs presented in Figures 6 and 7. Besides the expected shear strength envelope, the limits for the 95 % confidence interval (expected value ±1.96 S_y) are also presented in the figures. For the sake of comparison, Y axis scale was maintained the same for all the obtained results.

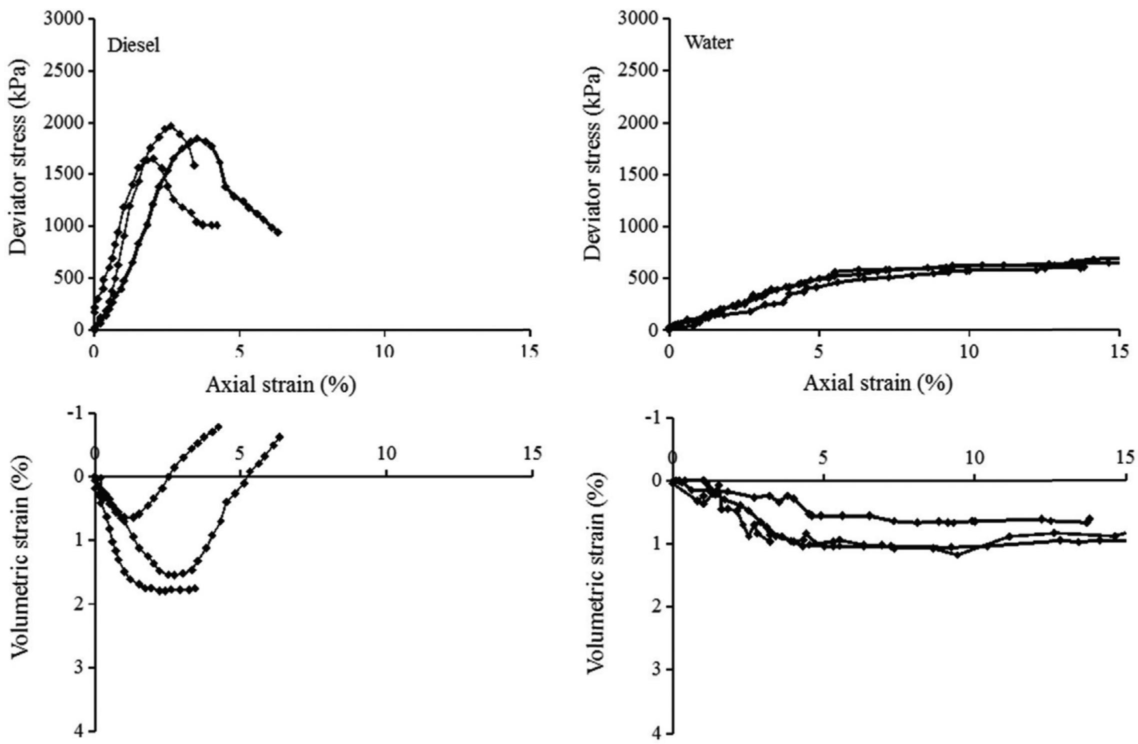

Figure 4. Stress/strain curves for saturated samples. σ_3 = 100 kPa.

Table 10. Shear strength parameters obtained in the tests.

Conditions	Fluid	ε_r	Suction (kPa)	c' (kPa)	ϕ' (graus)	S_y (kPa)	R^2
Saturated	Water	80.00	0	111.60	32.70	12.52	0.99
	Alcohol	24.3	0	137.40	39.60	21.67	0.99
	Diesel	2.13	0	344.30	39.00	51.54	0.95
	Air	1.00	0	466.20	48.50	34.53	0.99
Unsaturated	Water	74.65	100	133.10	14.10	8.61	0.85
		74.27	200	198.00	11.10	6.89	0.85
		67.41	300	286.60	8.90	6.81	0.83
	Diesel	2.01	100	159.70	54.20	36.81	0.98
		1.98	200	238.10	49.60	32.08	0.97
		1.93	300	169.50	53.80	46.23	0.96

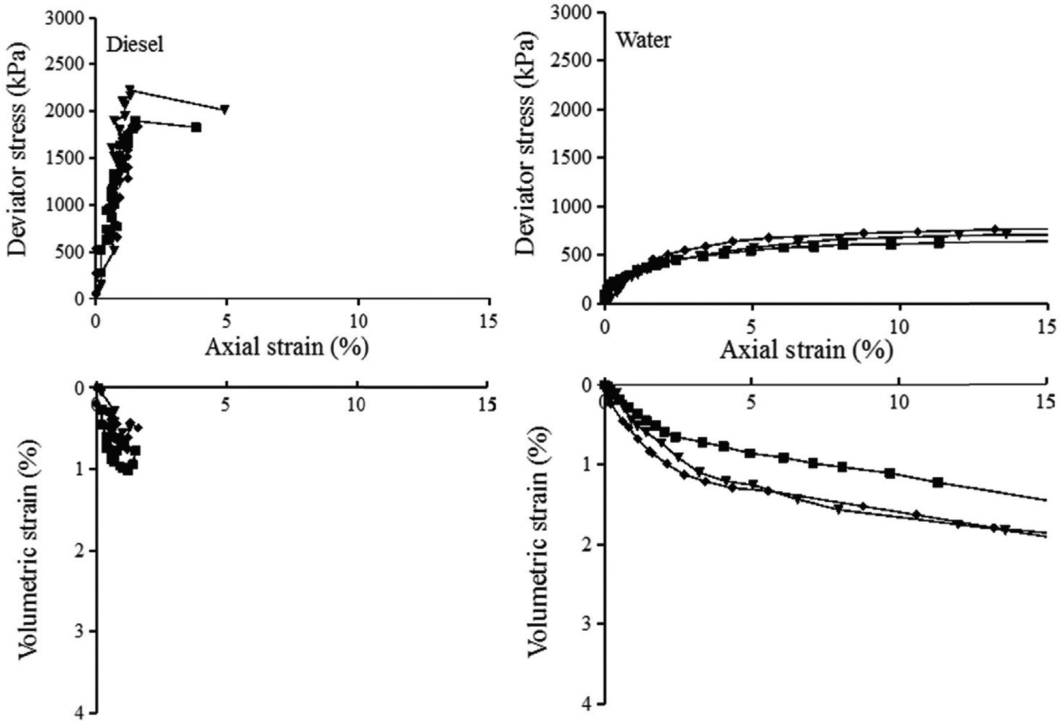

Figure 5. Stress/strain curves for suction controlled tests. ψ = 300 kPa and σ_3 = 100 kPa.

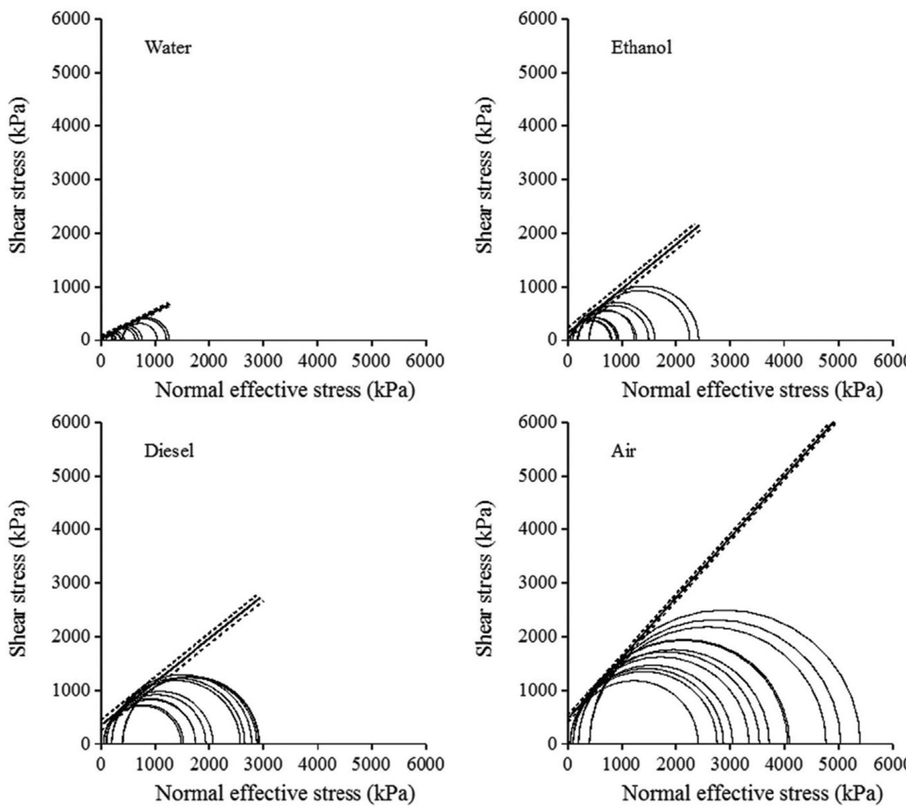

Figure 6. Shear strength envelopes for saturated samples.

It can be observed in Table 10 that in all the tests the shear strength decreases as the fluid polarity increases (air → diesel → alcohol and water, see Table 10). Figure 8 presents the shear strength values (deviator stress at failure,

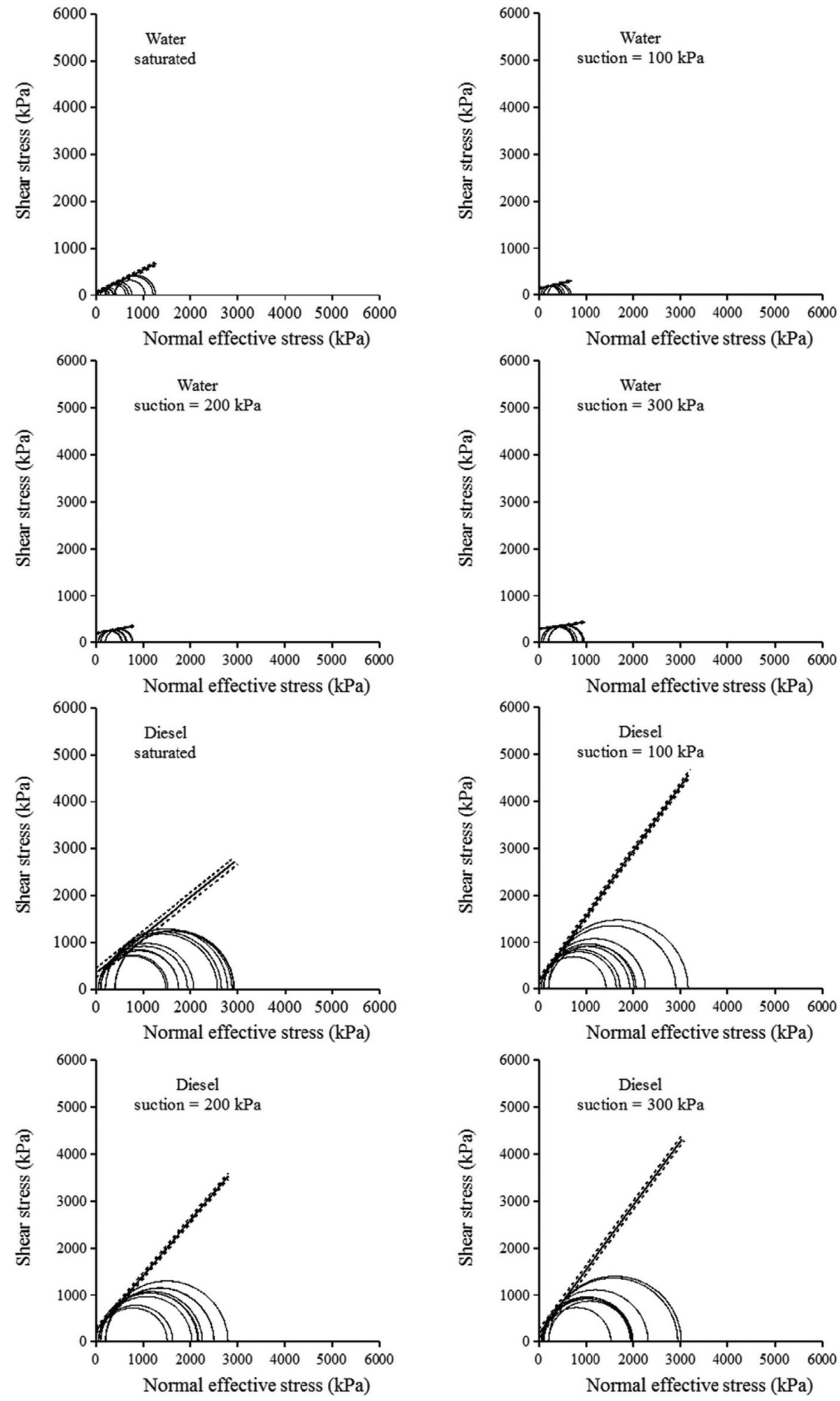

Figure 7. Shear strength envelopes for suction controlled tests.

q_{ff}) of the soil considering a confining stress of 200 kPa as a function of the fluid dielectric constant. For the case of unsaturated samples, the fluid dielectric constant was estimated through Equation 4.

$$\sqrt{\varepsilon_{rf}} = Sr\sqrt{\varepsilon_{rliq.}} + (1 - Sr)\sqrt{\varepsilon_{rair}} \tag{4}$$

where ε_{rf} - Relative dielectric constant of the interstitial fluid; S_r - Liquid degree of saturation; ε_{rliq} - Relative dielec-

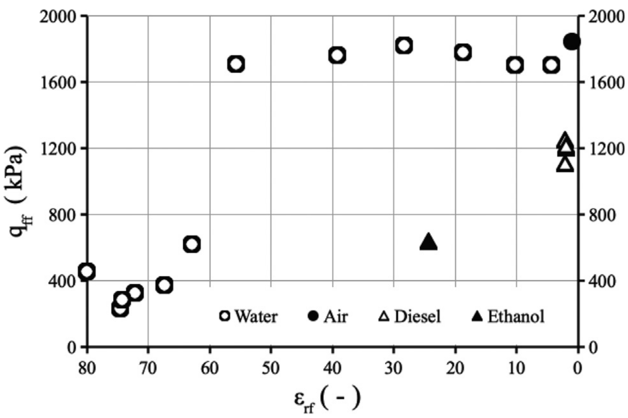

Figure 8. Shear strength values of the soil as a function of the fluid dielectric constant.

tric constant of the soil interstitial liquid (see Table 1); ε_{rair} - Relative dielectric constant of the air (~1).

It is evident that despite data scattering, q_{ff} decreases with an increase in ε_{rf}. Tables 11 to 13 summarize the obtained results for all the performed tests. As tests were performed in triplicate, the presented results are average values. Figure 9 presents the obtained results in terms of the ratio q_{ff}/q_{fw} vs. (ε_{rw} - ε_{rf}). The parameters q_{ff} and the q_{fw} correspond to the values of q at failure for tests performed with a fluid of interest (air, ethanol or diesel) and the fluid of reference (water). The paramters ε_{rliq} and ε_{rf} are the relative dielectric constants of the interstitial liquid and interstitial fluid (liquid + air) respectively. They are equal in saturated tests but differ in unsaturated ones. The parameter ε_{rw} is the

Table 11. Results and values adopted for the parameters of interest. Saturated samples.

Fluid	Sr (%)	σ'_3 (kPa)	q_{ff} (kPa)	q_{fw} (kPa)	q_{ff}/q_{fw}	ε_{rliq}	ε_{rf}	ε_{rw} - ε_{rf}	T_{sf} (10^{-3} N/m)
Air	0	50	1280.93	252.78	5.07	1.00	1.00	79.00	70.75
	0	100	1579.76	334.99	4.72	1.00	1.00	79.00	70.75
	0	200	1842.70	453.06	4.07	1.00	1.00	79.00	70.75
	0	400	2206.13	665.36	3.32	1.00	1.00	79.00	70.75
Diesel	100	50	734.27	252.78	2.90	2.13	2.13	77.87	25.98
	100	100	877.25	334.99	2.62	2.13	2.13	77.87	25.98
	100	200	1108.69	453.06	2.45	2.13	2.13	77.87	25.98
	100	400	1210.01	665.36	1.82	2.13	2.13	77.87	25.98
Ethanol	100	50	389.54	252.78	1.54	24.30	24.30	55.70	24.45
	100	100	470.73	334.99	1.41	24.30	24.30	55.70	24.45
	100	200	635.95	453.06	1.40	24.30	24.30	55.70	24.45
	100	400	971.00	665.36	1.46	24.30	24.30	55.70	24.45
Water	100	50	252.78	252.78	1.00	80.00	80.00	0.00	70.75
	100	100	334.99	334.99	1.00	80.00	80.00	0.00	70.75
	100	200	453.06	453.06	1.00	80.00	80.00	0.00	70.75
	100	400	665.36	665.36	1.00	80.00	80.00	0.00	70.75

Table 12. Results and values adopted for the parameters of interest. Suction controlled tests.

Fluid	Sr (%)	σ'_3 (kPa)	q_{ff} (kPa)	q_{fw} (kPa)	q_{ff}/q_{fw}	ε_{rliq}	ε_{f}	ε_{rw} - ε_{rf}	T_{sf} (10^{-3} N/m)
Water	96.17	50	192.74	107.25	1.80	80.00	74.65	5.35	70.75
	96.17	100	201.95	144.92	1.39	80.00	74.65	5.35	70.75
	96.17	200	232.42	247.44	0.98	80.00	74.65	5.35	70.75
	95.89	50	248.36	107.25	2.32	80.00	74.27	5.73	70.75
	95.89	100	269.99	144.92	1.86	80.00	74.27	5.73	70.75
	95.89	200	285.66	247.44	1.15	80.00	74.27	5.73	70.75
	90.76	50	344.36	107.25	3.21	80.00	67.41	12.59	70.75
	90.76	100	354.48	144.92	2.34	80.00	67.41	12.59	70.75

Table 12 (cont.)

Fluid	Sr (%)	σ'_3 (kPa)	q_{ff} (kPa)	q_{fw} (kPa)	q_{ff}/q_{fw}	ε_{rliq}	ε_f	ε_{rw} - ε_{rf}	T_{sf} (10^{-3} N/m)
	90.76	200	370.78	247.44	1.50	80.00	67.41	12.59	70.75
Diesel	91.01	50	776.18	252.78	3.07	2.13	2.01	77.99	25.98
	91.01	100	984.79	334.99	2.94	2.13	2.01	77.99	25.98
	91.01	200	1251.81	453.06	2.76	2.13	2.01	77.99	25.98
	88.34	50	852.85	252.78	3.38	2.13	1.98	78.02	25.98
	88.34	100	1028.67	334.99	3.07	2.13	1.98	78.02	25.98
	88.34	200	1200.92	453.06	2.65	2.13	1.98	78.02	25.98
	84.68	50	882.54	252.78	3.49	2.13	1.93	78.07	25.98
	84.68	100	992.82	334.99	2.96	2.13	1.93	78.07	25.98
	84.68	200	1214.31	453.06	2.84	2.13	1.93	78.07	25.98

Table 13. Results and values adopted for the parameters of concern. Constant moisture content tests.

Fluid	Sr (%)	σ'_3 (kPa)	q_{ff} (kPa)	q_{fw} (kPa)	q_{ff}/q_{fw}	ε_{rliq}	ε_{rf}	ε_{rw} - ε_{rf}	T_{sf} (10^{-3} N/m)
Water	13.76	50	1160.45	252.78	4.59	80.00	4.38	75.62	70.75
	13.76	100	1348.66	334.99	4.03	80.00	4.38	75.62	70.75
	13.76	200	1701.44	453.06	3.76	80.00	4.38	75.62	70.75
	13.76	400	2071.42	665.36	3.11	80.00	4.38	75.62	70.75
	27.71	50	1148.97	252.78	4.55	80.00	10.25	69.75	70.75
	27.71	100	1430.24	334.99	4.27	80.00	10.25	69.75	70.75
	27.71	200	1700.85	453.06	3.75	80.00	10.25	69.75	70.75
	27.71	400	1872.42	665.36	2.81	80.00	10.25	69.75	70.75
	41.85	50	1303.61	252.78	5.16	80.00	18.70	61.30	70.75
	41.85	100	1561.52	334.99	4.66	80.00	18.70	61.30	70.75
	41.85	200	1779.64	453.06	3.93	80.00	18.70	61.30	70.75
	41.85	400	1850.89	665.36	2.78	80.00	18.70	61.30	70.75
	54.38	100	1596.87	334.99	4.77	80.00	28.30	51.70	70.75
	54.38	200	1822.47	453.06	4.02	80.00	28.30	51.70	70.75
	54.38	400	1842.35	665.36	2.77	80.00	28.30	51.70	70.75
	66.23	100	1699.06	334.99	5.07	80.00	39.21	40.79	70.75
	66.23	200	1760.00	453.06	3.88	80.00	39.21	40.79	70.75
	66.23	400	1996.85	665.36	3.00	80.00	39.21	40.79	70.75
	81.33	100	1682.78	334.99	5.02	80.00	55.67	24.33	70.75
	81.33	200	1708.47	453.06	3.77	80.00	55.67	24.33	70.75
	81.33	400	1735.06	665.36	2.61	80.00	55.67	24.33	70.75
	87.23	50	466.07	107.25	4.35	80.00	62.88	17.12	70.75
	87.23	100	493.51	144.92	3.41	80.00	62.88	17.12	70.75
	87.23	200	618.72	247.44	2.50	80.00	62.88	17.12	70.75
	87.23	400	629.94	382.02	1.65	80.00	62.88	17.12	70.75
	94.37	50	293.37	107.25	2.74	80.00	72.20	7.80	70.75
	94.37	100	349.78	144.92	2.41	80.00	72.20	7.80	70.75
	94.37	200	324.96	247.44	1.31	80.00	72.20	7.80	70.75
	94.37	400	379.31	382.02	0.99	80.00	72.20	7.80	70.75

relative dielectric constant of water and T_{sf} is the superficial tension at the liquid/air interface.

An attempt to build an empirical model for the experimental results presented in Tables 11 to 13 was performed. Several parameters were tested as dependent and independent variables using linear and nonlinear functions to reach the higher R^2 value. Better fitted results were obtained using the ratio q_{ff}/q_{fw} as dependent variable. $(\varepsilon_{rw} - \varepsilon_{rf}).(\sigma_{atm}/\sigma'_3).(T_{sf}/T_{sw})$ and $(\varepsilon_{rw} - \varepsilon_{rf}).(\sigma_{atm}/\sigma'_3)$ were used as independent variables. The ratio (T_{sf}/T_{sw}) was introduced in the modeling because the superficial tension interferes in the capillary suction and therefore in the suction values, mainly at low suction levels.

Equation 5 presents the model used for the prediction of the ratio q_f/q_w as a function of the variables cited above.

$$\frac{q_{ff}}{q_{fw}} = \left\{ \frac{(\varepsilon_{rw} - \varepsilon_{rf})\left(\frac{\sigma_{atm}}{\sigma'_3}\right)\left(\frac{T_{sf}}{T_{sw}}\right) + a}{a + b(\varepsilon_{rw} - \varepsilon_{rf})\left(\frac{\sigma_{atm}}{\sigma'_3}\right)} \right\} \tag{5}$$

where q_{ff} is the deviator stress for samples moistened with the fluid of concern (kPa), q_{fw} is the deviator stress for samples saturated with water (kPa), ε_{rw} is the water relative dielectric constant (~80), ε_{rf} is the relative dielectric constant of the interstitial fluid calculated using Equation 4, σ_{atm} is the atmospheric pressure (~100 kPa), σ'_3 is the effective or net confining stress, T_{sf} is the superficial tension of the fluid of concern (see Table 1), T_{sw} is the water superficial tension, *a* and *b* are fitting constants.

Figure 10 presents the fitting of the experimental results presented in Figure 9 with the use of Equation 5. The best fitting parameters were $a = 3.7$ and $b = 0.16$, with a value of $R^2 = 0.88$. Experimental results could also be fitted using the suction values instead of $(\varepsilon_{rw} - \varepsilon_{rf})$. However, the SLRC for the case of ethanol presented several experimental challenges (mainly due to its high vapor pressure) which could not be overcome until now.

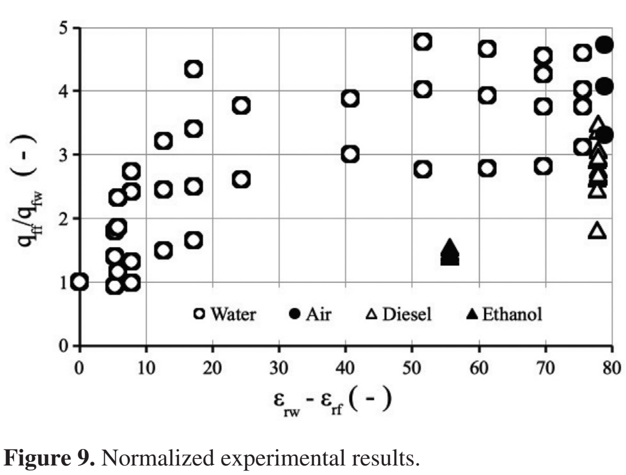

Figure 9. Normalized experimental results.

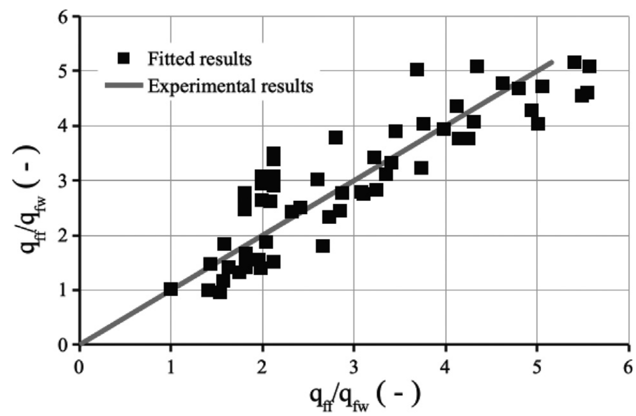

Figure 10. Fitting of experimental results using Equation 5.

5. Conclusions

This paper presents the results of several triaxial tests performed on saturated and unsaturated compacted soil samples filled with different interstitial fluids. A nonlinear relationship was obtained between the shear strength of the soil and the relative dielectric constant of the interstitial fluid, ε_{rf}, so that the higher the ε_{rf}, the lower the shear strength of the soil. The explanation for such behavior is due to the fact that the polarity of the fluid affects the electric fields around the clay particles, the thickness of the double layer and thus the electrical interactions between the particles, which are increased.

An empirical model to predict soil shear strength was proposed, based on the dielectric constant of the interstitial fluid, which presented a good adherence between experimental and fitted results. The use of this model could be an option in more complex scenarios involving multi-phase problems where suction determination/estimation may not be as prompt as the dielectric constant of the interstitial fluid.

References

Almeida, M.S.S. (2016). *Estudo da resistência ao cisalhamento de um solo não saturado quando percolado por fluidos de diferentes constantes dielétricas* [Doctoral thesis, Federal University of Bahia]. Federal University of Bahia's repository (in Portuguese). http://repositorio.ufba.br/ri/handle/ri/28861

Anandarajah, A., & Zhao, D. (2000). Triaxial Behavior of Kaolinite in Different Pore Fluids. *Journal of Geotechnical and Geoenvironmental Engineering*, 126(2), 148-156. https://doi.org/10.1061/(ASCE)1090-0241(2000)126:2(148)

ASTM D971-12. (2012). Standard Test Method for Interfacial Tension of Oil against Water by the Ring Method. *ASTM International, West Conshohocken, PA.*

ASTM D4016-14. (2014). Standard Test Method for Viscosity and Gel Time of Chemical Grouts by Rotational Viscometer (Laboratory Method). *ASTM International, West Conshohocken, PA*. https://doi.org/10.1520/D4016-14

ASTM D5298. (1994). Standard Test Method for Measurement of Soil Potential (Suction) Using Filter Paper. *ASTM International, West Conshohocken, PA.*

ASTM D6438-02. (2008). Standard Test Methods for Determination of the Soil Water Chararcteristic Curve for Desorption Using a Hanging Column, Pressure Extractor, Chilled Mirror Hygrometer, and/or Centrifuge. *ASTM International, West Conshohocken, PA*.

Brown, K.W., & Anderson, D.C. (1983). *Effect of organic solvents on the permeability of clay soils*. US Environmental Protection Agency, Municipal Environmental Research Laboratory.

Brown, K.W., & Thomas, J.C. (1984). Conductivity of three commercially available clays to petroleum products and organic solvents. *Journal of Hazardous Wastes*, 1(4), 545-553. https://doi.org/10.1089/hzw.1984.1.545

Brown, K.W., Thomas, J.C., & Green, J.W. (1986). Field cell verifications of effects of concentrated organic solvents on the conductivity of compacted soils. *Journal of Hazardous Wastes*, 3(1), 1-19. https://doi.org/10.1089/hwm.1986.3.1

Brunnauer, S., Emmett, P.H., & Teller, E. (1938). Adsorption of Gases in Multimolecular Layers. *Journal of the American Chemical Society*, 60(2), 309-319. https://doi.org/10.1021/ja01269a023

Budhu, M., Giese Jr., R.F., Campbell G., & Baumgrass, L. (1991). The permeability of soils with organic fluids. *Canadian Geotechnical Journal*, 28(1), 140-147. https://doi.org/10.1139/t91-015

Calvello, M., Lasco, M., Vassalo, R., & Di Maio, C. (2005). Compressibility and residual shear strength of smectitic clays: influence of pore aqueoussolutions and organic solvents. *Italian Geotechnical Journal*, 1(2005), 34-46.

Davis J.L., & Annan A.P. (1989). Ground penetrating radar for high resolution mapping of soil and rock stratigraphy. *Geophysical Prospecting*, 37(5), 531-551. https://doi.org/10.1111/j.1365-2478.1989.tb02221.x

Di Maio, C., Santoli, L., & Schiavone, P. (2004). Volume change behavior of clays: the influence of mineral composition, pore fluid composition and stress state. *Mechanics of Materials*, 36(5-6), 435-451. https://doi.org/10.1016/S0167-6636(03)00070-X

Fang, H.Y. (1997). *Introduction to Environmental Geotechnology*. CRC Press.

Fernandez, F., & Quigley, R. (1985). Hydraulic conductivity of natural clays permeated with simple liquid hydrocarbons. *Canadian Geotechnical Journal*, 22(2), 205-214. https://doi.org/10.1139/t85-028

Fredlund, D.G., & Xing, A. (1994). Equations for the soil-water characteristic curve. *Canadian Geotechnical Journal*, 31(4), 521-532. https://doi.org/10.1139/t94-061

Garcia, J.R., Rodrigues, R.A., & Lollo, J.A. (2004). A influência de diferentes fluidos de inundação no colapso estrutural de um solo arenoso laterítico. *Civil Engineering Journal*, 21, 49-58 (in Portuguese).

Gouy, G. (1910). Sur la constitution de la charge electrique a la surface d'un electrolyte. *Anniue Physique*, 4(9), 457-468 (in French). https://doi.org/10.1051/jphystap:019100090045700

Halliday, D., Resnick, R., & Walker, J. (2007). *Fundamentos de Física: Eletromagnetismo*. LTC (in Portuguese).

Hillel, D. (1980). *Fundamentals of Soil Physics*. Academic Press.

Helmholtz, H.V. (1879). Studien über electrische Grenzschichten. *Annalen der Physik*, 243(7), 337-382 (in German). https://doi.org/10.1002/andp.18792430702

Li, J., Smith, J.A., & Winquist, A. (1996). Permeability of earthen liners containing organobentonite to water and two organic liquids. *American Chemical Society*, 30(10), 3089-3093. https://doi.org/10.1021/es960172p

Kaya, A., & Fang, H. (2005). Experimental evidence of reduction in attractive and repulsive forces between clay particles permeated with organic liquids. *Canadian Geotechnical Journal*, 42(2), 632-640. https://doi.org/10.1139/t04-099

Oliveira, J.C.S. (2001). *Contaminação de sedimentos argilosos por combustíveis automotivos: problemas de avaliação da permeabilidade* [Unpublished doctoral thesis]. Federal University of Bahia (in Portuguese).

Schramm, M., Warrick, A.W., & Fuller, W.H. (1986). Permeability of soils to four organic liquids and water. *Hazardous Waste and Hazardous Materials*, 3(1), 21-27. https://doi.org/10.1089/hwm.1986.3.21

Soils and Rocks
An International Journal of Geotechnical and Geoenvironmental Engineering
www.soilsandrocks.com
ISSN 1980-9743
ISSN-e 2675-5475

Mass movements in the Northeast region of Brazil: a systematic review

Bruna Silveira Lira[1,#], Maria Natália de Melo Sousa[1], Olavo Francisco dos Santos Junior[2], Carina Silvani[1], Edilza Rakel Nóbrega[1], Gustavo Clementino Santos[2]

Article

Keywords
Engineering geology
Erosion
Geomorphology
Landslide
Slope instability

Abstract
Mass movements are one of the main causes of loss of people and environmental assets. Several factors contribute to mass movements, such as terrain morphology, rainfall regime, soil properties, land use and occupation. Studies showed that in the Northeast region of Brazil, between the years of 1991 and 2012, 38 events related to mass movements were recorded, resulting in 55,963,164 people affected by these events. Based on this information, the aim of this study was to build a systematic review of mass movement and erosion events that occurred in the northeast region of Brazil and were reported in Brazilian academic sources. The research was based on the articles published by the Soils and Rocks Journal and the proceedings of the Brazilian academic events: Brazilian Congress of Soil Mechanics and Geotechnical Engineering, the Brazilian Conference on Slope Stability and the Brazilian Congress of Engineering and Environmental Geology. A survey of all the articles involving the subject matter was conducted between the years of 1954 and 2019 using the key words Landslides, Mass Movements, Geomorphology and Engineering Geology. From the data found, it was possible to identify the main geotechnical characteristics of mass movement occurrences in the region and their causes.

1. Introduction

Slope instabilities, such as erosion, mass transport and mass movements are forms of land degradation and are considered global problems. These processes are the main causes of risk for exposed elements that include people, properties, environmental assets, economic activities, cultural heritage. (Ferlisi & De Chiara, 2016; Guerra et al., 2017).

Slope instabilities along with their spatial/temporal distribution and related consequences differ within a given country and, more in general, from country to country. The slope failures characteristics depend on the specific features of *i*) factors either predisposing to or triggering slope instabilities, *ii*) intensity parameters of hazard scenarios, *iii*) elements at risk (*e.g.* in terms of population density) (Ferlisi & De Chiara, 2016).

According to Li & Mo (2019) the database "Landslide and Other Mass Movements on Slopes" by the International Association of Engineering Geology (IAEG) indicates approximately 14 % of injuries and deaths in natural catastrophes are caused by slope failures. Studies by the Centre for Research on the Epidemiology of Disasters (CRED) revealed that slope failures caused more than 2.5 million people to become homeless during the first decade of the 21st century. Clague & Roberts (2012) stated that more than 1000 people lose their lives in slope failures worldwide annually.

In Brazil, risk areas associated with slope instabilities are common and the Northeast region of the country fits into this context. According to Santos Junior (2005) the whole coast of the Northeast region of Brazil presents conditions for the development of mass movements. This could be due to the precipitation index of the region and the anthropic action on the physical environment. Landslides are one of the most significant threats to the development of Brazil's Northeast region.

[#]Corresponding author. E-mail address: brunaslira@gmail.com.
[1]Departamento de Engenharia Civil, Universidade Federal de Campina Grande, Campina Grande, PB, Brazil.
[2]Departamento de Engenharia Civil, Universidade Federal do Rio Grande do Norte, Natal, RN, Brazil.

Submitted on December 28, 2019; Final Acceptance on July 29, 2020; Discussion open until March 31, 2021.
DOI: https://doi.org/10.28927/SR.434549

Over the past 20 years the number of disasters has been increased, due to the increase of the population living in risk areas and the intensification of geodynamic, hydro-meteorological and climate events in the region (Assis Dias et al., 2018).

Information gathered on mass movements in Brazil showed that 38 records of disasters related to landslides were recorded in the period from 1991 to 2012 in the Northeast region of Brazil, which resulted in 55,963,164 people affected (CEPED, 2012). Studies made by Santos et al. (2018) using the Integrated Disaster Information System organized by the Brazilian Ministry of National Integration through the National Secretariat for Civil Defense and Protection (SEDEC) and the University Center for Disaster Studies and Research (CEPED) of the Federal University of Santa Catarina database identified 40 total erosion events and 96 mass movement events for the northeast region between the years of 1980 and 2017 (Table 1). Table 1 also shows the number of cases for all States that comprise the Northeast region of Brazil.

Comprehending the parts of the mass movement process as intimately interconnected could result in significant reduction in the societal and economic losses that the Northeast region of Brazil experiences as a result of slope instability. Thus, the present work aims to survey cases of mass movements that occurred in Northeast region of Brazil that were reported in the academic publications of the Soils and Rocks Journal and the proceedings of three Brazilian academic events, COBRAMSEG (Brazilian Conference on Soil Mechanics and Geotechnical Engineering), COBRAE (Brazilian Conference on Slope Stability) and CBGE (Brazilian Congress on Engineering and Environmental Geology) which constitute the main forum for discussion on the slope stability theme in the Brazilian geotechnical community and determine the factors that contributed to the generation of mass movements on slopes.

Table 1. Erosion and mass movement case records by State of the Northeast region of Brazil from 1980 to 2017.

State	Erosion cases	Mass movement cases
Alagoas	5	0
Bahia	12	25
Ceará	3	1
Maranhão	0	4
Paraíba	3	2
Pernambuco	17	60
Piauí	0	1
Rio Grande do Norte	0	1
Sergipe	0	2

Source: Adapted from Santos et al. (2018).

2. Types and causes of mass movements on slopes

The term mass movement describes a wide variety of processes that result in the downward and outward movement of slope-forming materials. The different types of mass movements can be differentiated by the type of material involved and the mode of movement, making a classification of each type of mass movement necessary in order to better understand the processes that occur during the mass movement. Each classification is associated with the characteristics of the mass and the factors that condition the movements. A classification system based on these parameters was proposed by Varnes (1978) and updated in 2014 by Hungr et al. (2014). This classification system is, to this day, the most widely used (Table 2). According to this system, the types of movements are classified as: Fall, Topple, Slide, Spread, Flow and Slope Deformation. The materials involved in the movements are divided into rocks or soils. The soils movement include boulders, debris, gravel, silt and clay. The words in italics are placeholders, use only one.

Despite not being considered in the Varnes (1978) classification system updated by Hungr et al. (2014), erosions represent a process that develops from a set of dynamic phenomena and processes, which alter the conditions of stability and can lead to risk situations for the population and infrastructure (Gerscovich, 2016). With erosion and mass movements being two forms of land degradation, erosion is considered by many authors as a cause for slope instabilities (Selby, 1993; Nadal-Romero et al., 2014; Gerscovich, 2016; Guerra et al., 2017).

The causes that determine the generation of the mass movements in a slope depend on the phenomenon that contributes to an increase in shear stress on the soil and/or a reduction in shear strength of the soil. According to Giani (1992), the main causes that contribute to a reduction in shear strength depend on soil texture, rock origin and its structural defects. Studies by Suzen & Kaya (2011) recorded 18 different factors used in data-driven landslide hazard or susceptibility assessment procedures in a review of 145 articles between 1986 and 2007. The factors were categorized into four major groups: geological, topographical, geotechnical and environmental. However, according to Budimir et al. (2015), in any given situation, some of these factors may be important whilst others are irrelevant.

The diversity of causative factors influences the different types of mass movement. Within the aforementioned factors, Cruden & Varnes (1996) categorizes the causes or factors that influence mass movements, the main causes of mass movements are divided into the cause groups: geological, morphological, physical and human. The description of these groups is in Table 3.

The origin of landslides might relate to a complex suite of causes and triggers that involve climatic factors, in-

Table 2. Varnes (1978) classification system updated by Hungr et al. (2014).

Type of movement	Rock	Soil
Fall	*Rock / Ice* falls*	*Boulder/debris/silt* fall*
Topple	Rock block topple*	*Gravel/sand/silt* topple*
	Rock flexural topple	-
Slide	Rock rotational slide	*Clay/silt* rotational slide
	Rock planar slide*	*Clay/silt* planar slide
	Rock wedge slide*	*Gravel/sand/debris* slide*
	Rock compound slide	*Clay/silt* compound slide
	Rock irregular slide*	-
Spread	Rock slope spread	*Sand/silt* liquefaction spread*
		Sensitive clay spread*
Flow	Rock/ice avalanche*	*Sand/silt/debris* dry flow
		Sand/silt/debris flowslide*
		Sensitive clay flowslide*
		Debris flow*
		Mud flow*
		Debris flood
		Debris avalanche*
		Earthflow
		Peat flow
Slope deformation	Mountain slope deformation	Soil slope deformation
	Rock slope deformation	Soil creep
		Solifluction

trinsic changes within the rock mass, seismic activity and anthropogenic effects (McColl, 2015). The processes that generate landslides are complex and understanding them depends on the determination of many variables, such as the physical characteristics of the environment, climate, changes in land/soil use, urban growth and vulnerability (Smyth & Royle, 2000).

Table 3. Mass movements groups and descriptions.

Groups	Description
Geologic causes	Weakened materials;
	Sensitive materials;
	Saturated materials;
	Cut material;
	Unstructured or cracked material;
	Adverse oriented discontinuous mass (stratification, schistosity, etc);
	Adverse oriented discontinuous structure (failure, contact, etc.);
	Contrast in permeability;
	Contrast in stiffness (rigid, dense material over plastic material).
Morphological causes	Volcanic or tectonic elevation;
	Glacial expansion;
	Fluvial erosion of the slope;
	Erosion due to crumbling of the slope;
	Underground erosion (cracks, piping);
	Loading on top or bottom of the slope;
	Vegetation removal (fire, drought)
Physical causes	Intense rainfall;
	Rapid melting of snow;
	Extended exceptional precipitation;
	Rapid lowering (by floods and high tides);
	Earthquakes;
	Volcanic eruptions;
	Defrosting;
	Saturation by freezing and thawing;
	Saturation by dilation and contraction.
Human causes	Digging at the top or bottom of the slope;
	Loading on top or bottom of the slope;
	Lowering of reservoirs;
	Deforestation;
	Irrigation;
	Mining;
	Artificial tremor;
	Water leakage from public services.

3. Study area

The Northeast of Brazil is a region comprising 9 States: Maranhão (MA), Piauí (PI), Ceará (CE), Rio Grande do Norte (RN), Paraíba (PB), Pernambuco (PB), Alagoas (AL), Sergipe (SE) and Bahia (BA) (Figure 1). The Northeast Region represents 18 % of Brazilian territory and its area is approximately 1,558,196 km^2. It has a population of 53.6 million people, 28 % of the total population of the country.

Figure 2 presents the simplified geological map of the studied region. The geology can be subdivided into four large units: sedimentary materials from the Cenozoic, the clastic/carbonate sedimentary rocks from the Mesozoic, the clastic and sporadically calcareous rocks from the Paleozoic and the Precambrian Crystalline Rocks.

In the coastal region, sedimentary materials are deposited in marginal basins in the Cenozoic, with emphasis on the Barreiras Formation. The Barreiras Formation consists of a sequence of sediments that covers the entire northeastern coast. They are usually poorly consolidated and formed by layers of silty sand, clayey sand and silty clay (Santos Junior, 2005). The presence of conglomeratic layers is common, as well as lateritic horizons. Dune fields cover the Barreiras Formation in some parts of Rio Grande do Norte, Ceará, Piauí and Maranhão. In the coast of Pernambuco there are outcrops of the Maria Farinha Formation, which is formed by an alternation of clayey limestones and stratified calciferous clays, yellow to gray in color (Gusmão Filho et al., 1982).

The Mesozoic geological units are associated with flat and elevated reliefs due to tectonic processes (Chapadas). According to Costa et al. (2020), this is the case for Chapada do Araripe, which has elevations up to 900 m and steep edges. In some cases, this form of relief occurs associated with the edges of sedimentary basins, such as Chapada

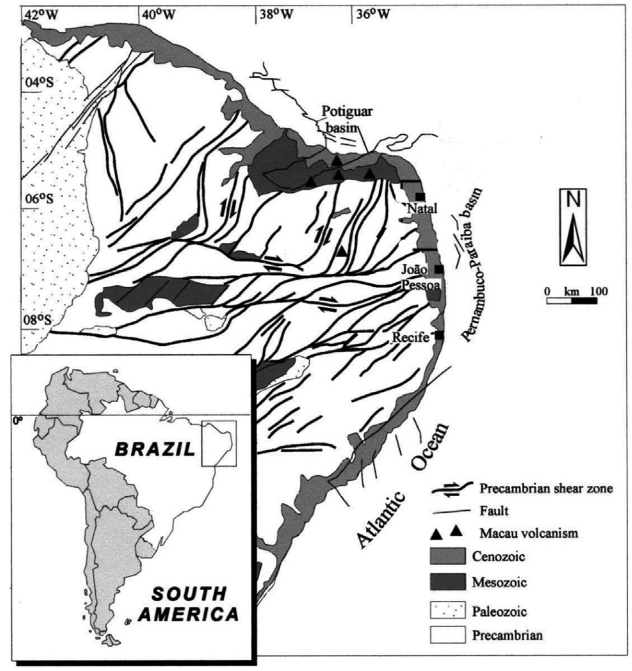

Figure 2. Northeastern geology (Adapted from Bezerra et al., 2001).

do Apodi. Which has levels between 100 and 140 m and cuestiform edges (in the form of a cuesta), adjacent to the Potiguar Basin.

Paleozoic basins in northern Brazil contain thick sequences of sedimentary rocks (Caputo, 1984), more commonly the presence of clastic sedimentary rocks formed by

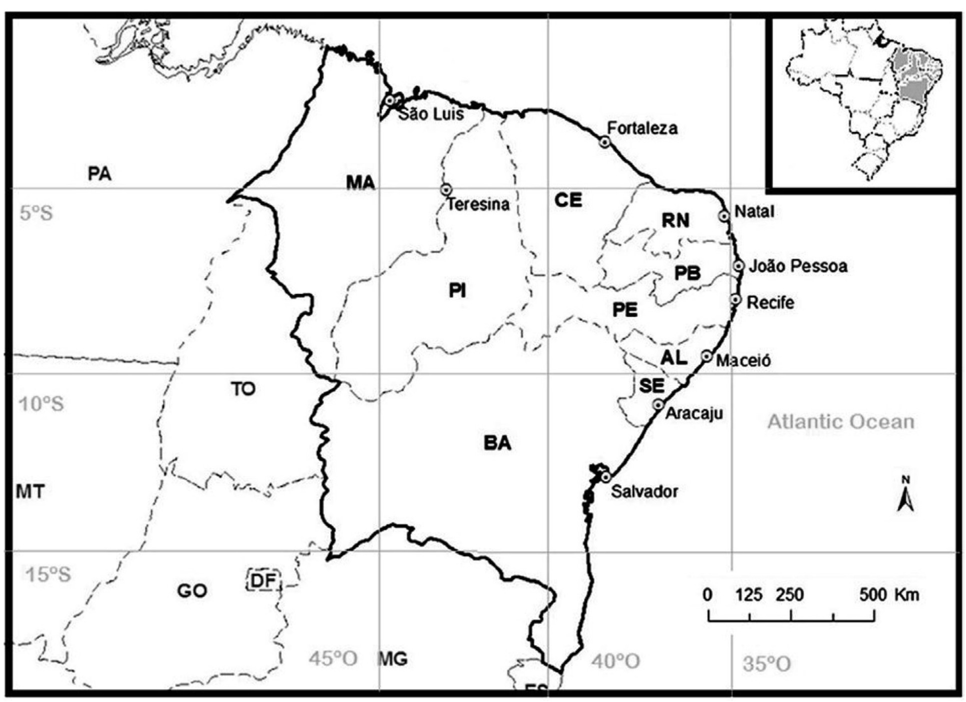

Figure 1. Northeast region of Brazil (Lopo et al., 2014).

the deposition of fragments of magmatic and metamorphic rocks. The Parnaiba basin, whose evolutive processes are chiefly of the Paleozoic age, shows thick cratonic sedimentary sequences that are neatly superimposed on the crystalline basement structures (Almeida et al., 1981).

The Precambrian rocks are of magmatic and metamorphic origin and form the crystalline basement. They emerge in the interior of the studied region. Residual soils are formed by the weathering acting on the crystalline rocks. They are present more expressively in regions where the climate is wet and rainy. This occurs at approximately 100 km from the coast. Deep profiles of residual soil have been reported by Campos (2013) in Salvador and by Coutinho et al. (2019) in Pernambuco.

In geomorphological terms, there is a correspondence between the geology and the relief of the region, which is strongly conditioned by structural aspects. Costa et al. (2020) studied the relief of the septentrional part of the Brazilian Northeast and proposed the existence of the following morphological units associated with the Precambrian rocks located further inland: the Crystalline Massifs (MC), the Sertaneja Surface - SS (subdivided into 1 and 2), the Small Plateaus (PP) and the Pre-coastal Surface (SPL). Figure 3 shows a schematic representation of these relief forms.

The crystalline massifs are the highest areas with altimetric levels ranging from 500 to 900 m. The Sertaneja Surface has levels ranging from 50 to 250 m (Sertaneja Surface 1) and 250 to 400 m (Sertaneja Surface 2). The small Plateaus are flat and elevated reliefs, with levels between 600 and 700 m, which occur in a dispersed manner, mainly in the States of Ceará, Rio Grande do Norte and Paraíba. In some situations, these Plateaus present sedimentary materials and result from the relief inversion by uplift. The Precoastal Surfaces are similar to the Sertaneja Surface with a lower level and constitute the transition with the Coastal Tablelands (Costa et al., 2020).

Closer to the coast are the Coastal Tablelands, supported by the sediments of the Barreiras Formation (Costa et al., 2020). Coastal Tablelands are tabular reliefs formed by sediments that were eroded on the continent, transported and deposited close to the coast. In some sections of Ceará, Rio Grande do Norte, Paraíba and Bahia, the Tablelands extend to the coastline, forming cliffs at the edge of the Tableland. This unity of relief is presented in the form of hills in Paraíba, Pernambuco and Alagoas. According to Costa et al. (2020) these hills result from the dissection caused by the drainage network under more humid conditions. Figure 4 shows a schematic cross section, representative of the conditions in force between the municipalities of João Pessoa in Paraíba and Recife in Pernambuco.

On the coast of the States of Rio Grande do Norte, Ceará, Piauí and Maranhão there are expressive dune fields that result from the accumulation of sandy sediments (fine to medium sands) transported by the action of the wind from the sandy beaches. Also present are the reliefs associated with the Coastal Plains and the Fluvial Plains.

4. Methods

This research aimed to develop a systematic review, using as database the literature available in Brazilian academic sources on the subject of mass movements in the Northeast region of Brazil. This type of review aims to investigate and summarize evidence related to a specific theme by applying detailed search methods, critical analysis and synthesis of the information found.

The first step of the research was the elaboration of the main question for the investigation. Therefore, the purpose of this research was to find the cases of mass movements that occurred in the Northeast region of Brazil that were reported in national academic publications and proceedings.

A manual systematic literature search was conducted following the structure of Figure 5. All papers were searched in the Soils and Rocks Journal and three national

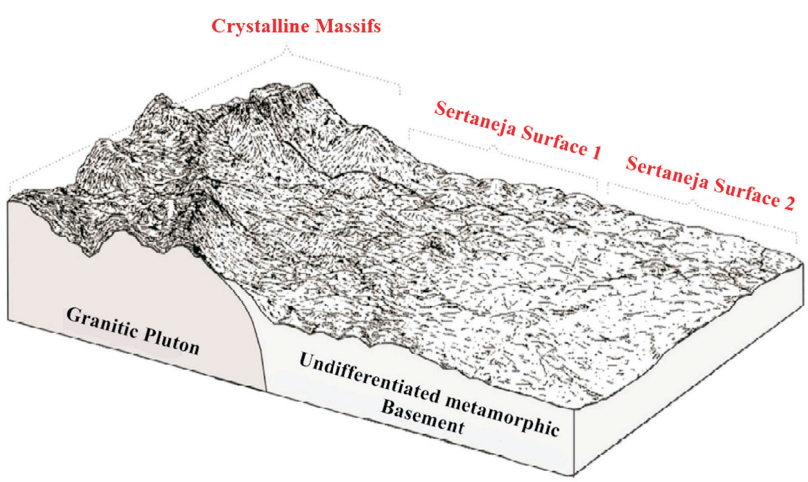

Figure 3. Northeastern geomorphology: Crystalline massifs and Sertaneja surface (Adapted from Costa et al., 2020).

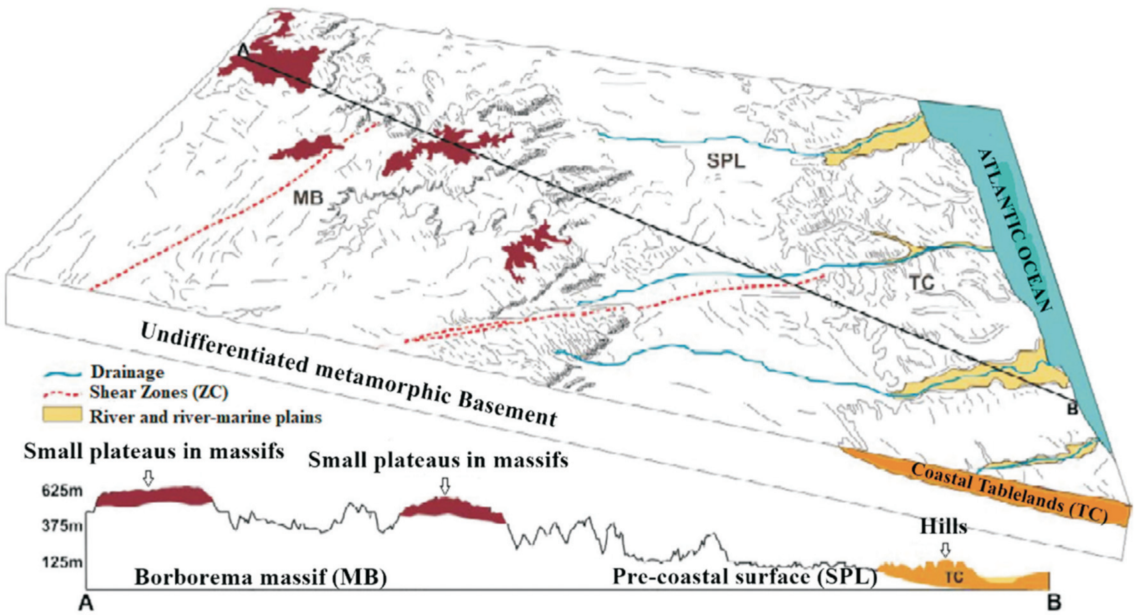

Figure 4. Cross section A-B showing some aspects of Northeastern geomorphology (Adapted from Costa et al., 2020).

academic events, the COBRAMSEG - *Congresso Brasileiro de Mecânica dos Solos e Engenharia Geotécnica* (Brazilian Conference on Soil Mechanics and Geotechnical Engineering), the COBRAE - *Conferência Brasileira sobre Estabilidade de Encostas* (Brazilian Conference on Slope Stability) and CBGE - *Congresso Brasileiro de Geologia de Engenharia e Ambiental* (Brazilian Conference on Engineering and Environmental Geology).

A total of 7348 articles were analyzed. The key words searched were Landslides, Mass Movements, Geomorphology and Engineering Geology restricted to the Brazilian Northeast region within the years of the academic publications and proceedings, between 1954 and 2019. The aim was to determine the number of mass movements that happened in the Brazilian Northeast region and their main causes.

For each step in the systematic search, papers were selected based on a reading of the paper abstract, title and a diagonal reading to determine if the paper was applicable to the study. Of the selected papers, only papers conforming to the aforementioned conditions were accepted into the database. The conformity of the paper to the conditions was determined by a more thorough reading of the papers. Of the 7348 articles searched, 97 articles presented data related to the Brazilian Northeast region. The articles selected were reviewed one by one.

The next criterion for filtering the articles was the presence of the following information within the articles' content: the type of movement, the material involved, the causes, the location and preferably the date of occurrence. Of the 97 articles reviewed, 47 articles were selected based on these criteria. A summary of each article was developed followed by a table with the database obtained for analyses of the data.

5. Results

5.1 Search results by number of events

The studied literature resulted in 47 articles that described mass movement events that occurred in the Northeast region of Brazil. The first and the latest events described in the selected articles occurred in 1944 and 2014, respectively. Of the 47 articles studied, 65 cases of mass movements were accounted. Selected articles are presented in the appendix. The map in Figure 6 shows the occurrence of these mass movements across the States in the Northeast region.

It is observed in the map of Figure 6 that, in general, mass movements present a higher concentration in the State of Pernambuco, showing a higher commitment from the local academic community to study the events that occurred in the State. It was noted from the study of the articles that there is a bigger incentive in the research of mass movements, from the academic point of view, in the States that presented the largest number of mass movement records. Interest in the subject in these States can be attributed to the need for knowledge, since there are a significant number of events occurring in these locations.

According to Santos et al. (2018) the mass movements that occurred in the State of Pernambuco are due to the combination of two factors: physical-natural conditions (geology, relief and climate) and the largest urban concentration in the State associated with disordered occupation. A greater number of occurrences can also be noted in places near the coast, this context is due to the outcropping of the

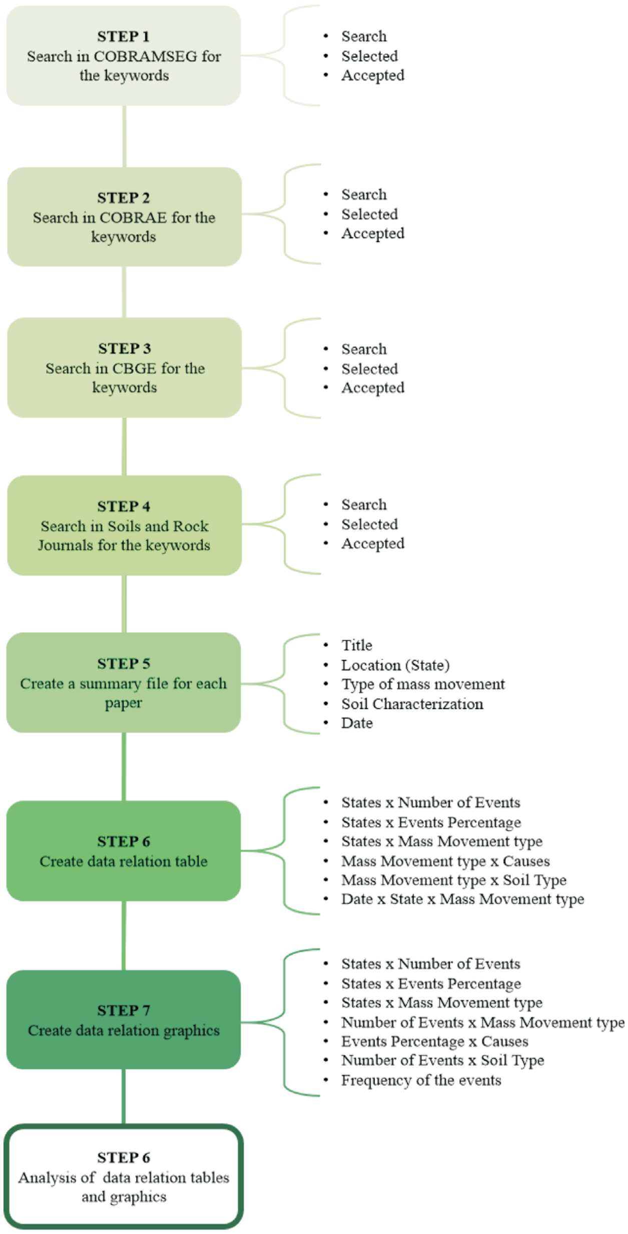

Figure 5. Flowchart for the current research.

crystalline basement that underlines the geological formations of the area in the eastern portion of the country, represented by metamorphic and granitic Precambrian rocks of the Atlantic shield (CEPED, 2012).

The percentages of mass movement records by State that occurred in the Northeast region of Brazil are shown in the graph in Figure 7. The States of Pernambuco and Rio Grande do Norte stand out with the highest number of events, corresponding respectively to 32 % and 31 % of the total mass movements records, followed by the States of Bahia, Alagoas, Ceará and Maranhão with 25 %, 6 %, 5 % and 1 %, respectively. The States of Paraíba, Piauí and Sergipe were the least affected, with 0 % of the mass movements that reached the Northeast within the study period.

According to the data in Table 4, which presents the number of records of mass movements by State, it is verified that the three most affected States were Pernambuco, Rio Grande do Norte and Bahia. The State of Pernambuco presented the largest number of mass movements, with 21 cases described, followed by Rio Grande do Norte and Bahia, which totaled 20 and 16 occurrences, respectively.

Studies conducted by the University Center for Disaster Studies and Research (CEPED, 2012) showed that the States of Pernambuco and Bahia presented the largest percentages of reported mass movements between the years of 1991 and 2012, with 68 % and 21 % respectively, data that agrees with the results obtained by Santos et al. (2018), as shown in Table 1. The University Center for Disaster Studies and Research study also revealed that the States of Rio Grande do Norte and Alagoas did not present reported mass movements between the years of 1991 and 2012, indicating that the events that occurred within these States did not have federal recognition or were not reported by the government.

Torres & Pfaltzgraff (2014) point out that most of the landslides that occur in the urban areas of Pernambuco are the result of the inadequate geometry of the slopes; landfilling without compaction; inadequate vegetation planting; alteration of natural drainages and improper disposal of wastewater.

Through the study it was possible to determine the types of mass movements that occurred in the Brazilian Northeast, the data is presented in Figure 8.

It can be seen from the graph in Figure 8 that the types of mass movements that occur most in the Northeast of Brazil are flow, erosion and slides. With 19 occurrences of flows, 18 occurrences of erosion and 17 occurrences of slides being identified.

The erosion process is defined as the removal of soil particles from the upper parts of the relief by the action of rainwater and wind, resulting in the transport and deposi-

Table 4. Records of the number of mass movement occurrences in the Northeast.

State	Occurrences	Percentage of events (%)
Alagoas	4	6
Bahia	16	25
Ceará	3	5
Maranhão	1	1
Paraíba	0	0
Pernambuco	21	32
Piauí	0	0
Rio Grande do Norte	20	31
Sergipe	0	0

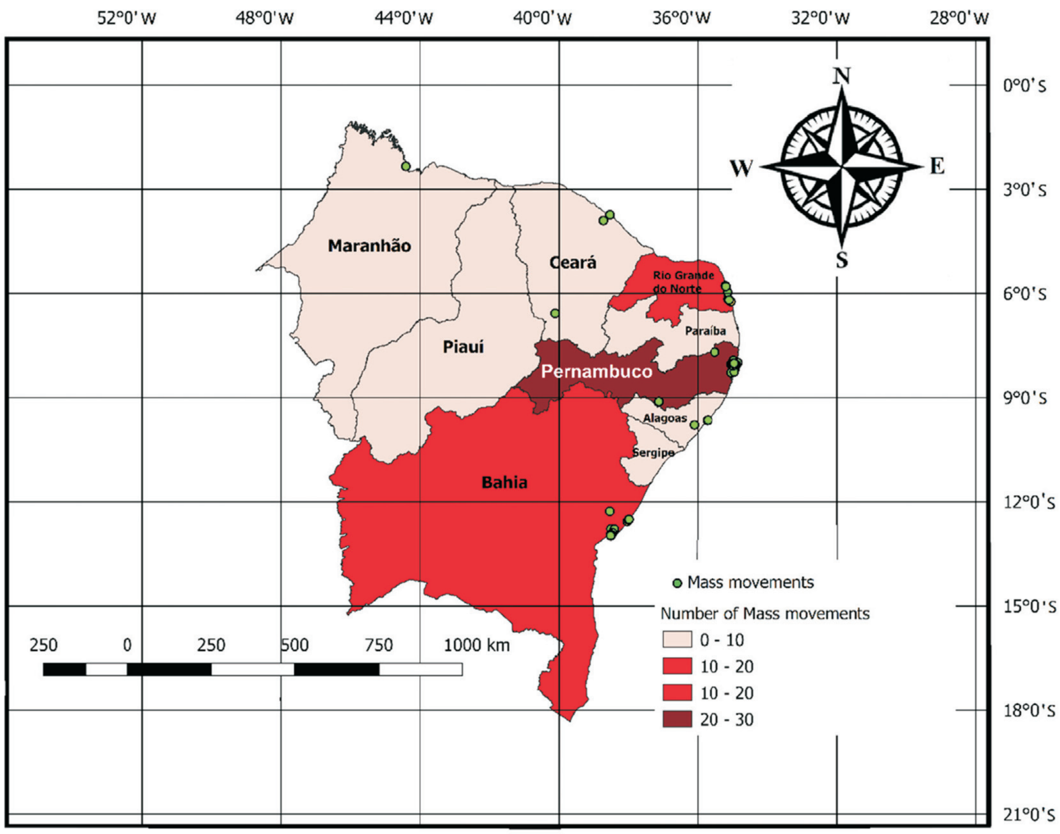

Figure 6. Occurrence of mass movements in the Brazilian Northeastern States.

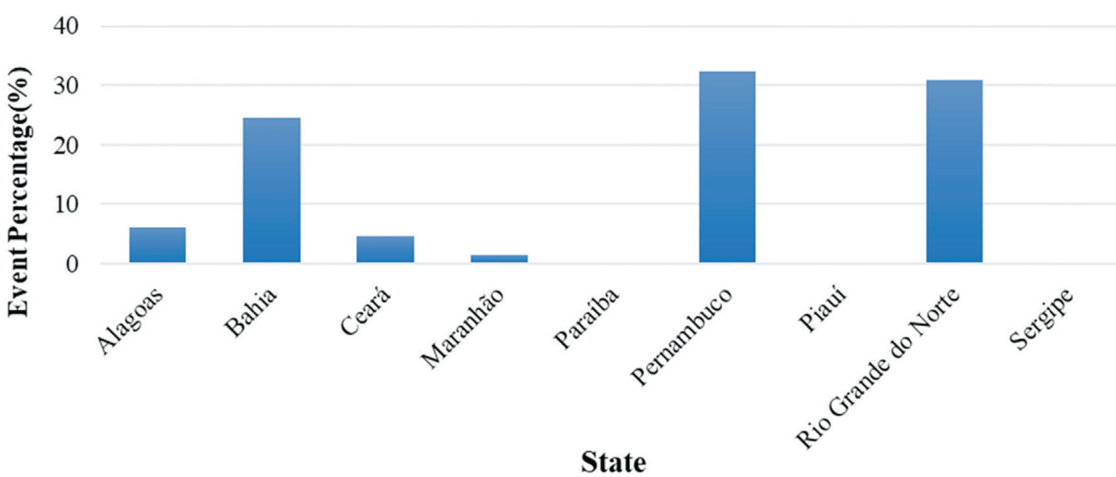

Figure 7. Percentage of mass movements by State.

tion of these particles in the lower portions of the relief or to the bottom of lakes, rivers and oceans (Lepsch, 2002). According to Souza (2014) slides are one of the most important processes related to mass movements in Brazil, due to the geological, geomorphological and climatic characteristics of the country, associated with the intense urbanization and low income power of the population, there is a high frequency of occurrence and a large extension of areas with potential for landslides.

According to Santos et al. (2018), the occurrence of risk areas associated with such phenomena in the Northeast region of Brazil is common, especially in the cities located in coastal regions, where hills and/or tabular reliefs usually predominate with an increase in the urbanization process. Changes in temperature and precipitation have a range of impacts, including the effect in frequency and magnitude of mass movements (Stoffel & Huggel, 2012). The climactic characteristics of the Brazilian Northeast region that are

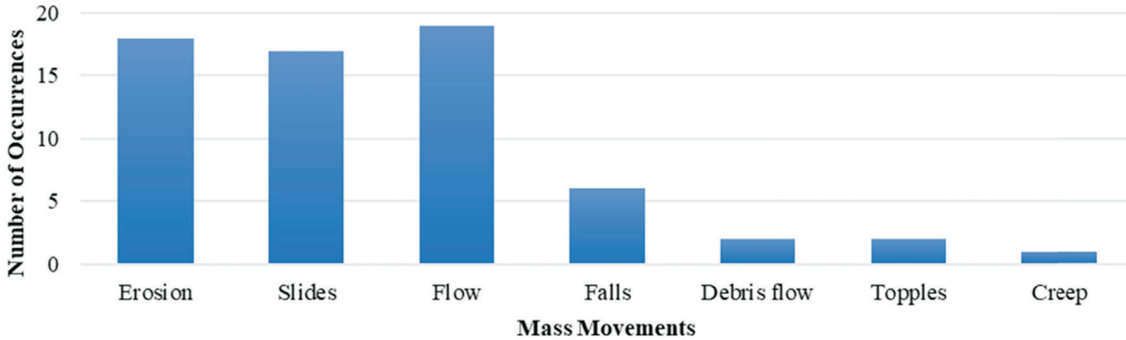

Figure 8. Number of occurrences in the Northeast region of Brazil by mass movement type.

represented by the droughts that periodically affect the location followed by heavy rain seasons, may increase the possibility of mass movements (Handwerger et al., 2019).

Relating the types of mass movements identified by the number of occurrences in each State (Figure 9). It is observed that Pernambuco, Rio Grande do Norte and Bahia are also the States that present the most cases of the three most frequent types of mass movements in the Northeast of Brazil. In addition to the mass movements of higher incidence in the Northeast identified in the graph of Figure 6, Rio Grande do Norte also presents fall and topple events. Of the cases studied in the Brazilian Northeast region, it is clear that these types of movements occur more frequently and in number in cliffs of the Barreiras Formation, which are very present in the State of Rio Grande do Norte. The United States Geological Survey (USGS, 2004) states that falls and topples occur mainly on steep cliffs or slopes, characteristic of the cliffs found on the coast of the State of Rio Grande do Norte.

5.2 Search results by cause

Regarding the causes that culminated in the occurrence of recorded mass movements, five main types of causes in the Northeast region of Brazil were identified. Figure 10 relates these causes to the number of events.

Figure 10 shows that the occurrence of mass movements in the Northeast region of Brazil is associated with a set of factors composed by high precipitation index and anthropic action on the physical environment. The percentage of events that occur due to these causes is much higher than the others. Precipitation and anthropic action are responsible for 41 % and 34 % of the events, respectively. In about 6 % of the occurrences identified in the literature, the determinant causes that led to mass movements were not listed, thus being recorded as not identified in the graph of Figure 10.

The effects of prolonged rainfall on slope stability in soils have been studied by several authors (Sweeney & Robertson, 1979; Chipp et al., 1982; Pitts, 1983; Brand et al., 1984; Tan et al., 1987). Most mass movements occur in places where the soil is in unsaturated conditions and its safety margin against sliding depends on the capillary stresses responsible for the increase of soil strength (Silva, 2006). According to Olivares & Damiano (2007), water infiltration causes a decrease in suction and, consequently, a decrease in soil shear strength that leads to mass movement. The Brazilian Northeast region, being located in the intertropical zone of the Earth, has a high local temperature and badly distributed rainfall throughout the year (Freitas, 2019). This situation, where heavy rain seasons followed

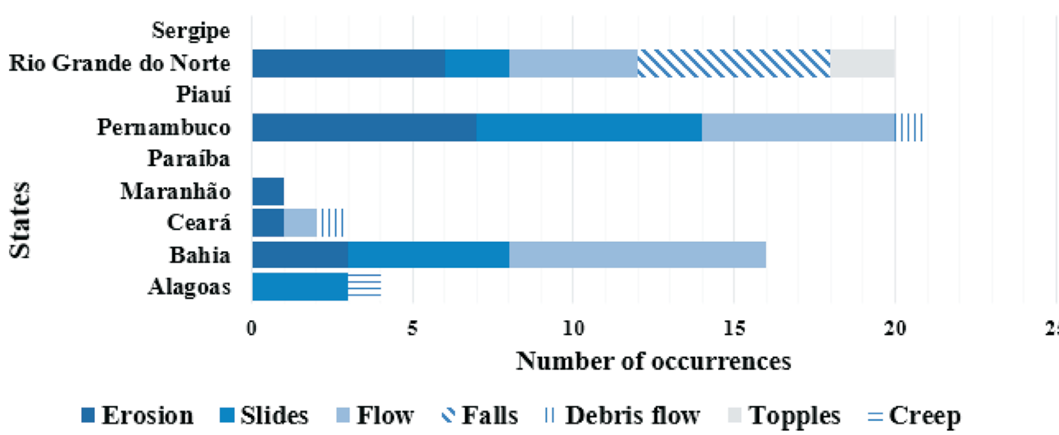

Figure 9. Types of mass movements in the Brazilian Northeast region by State.

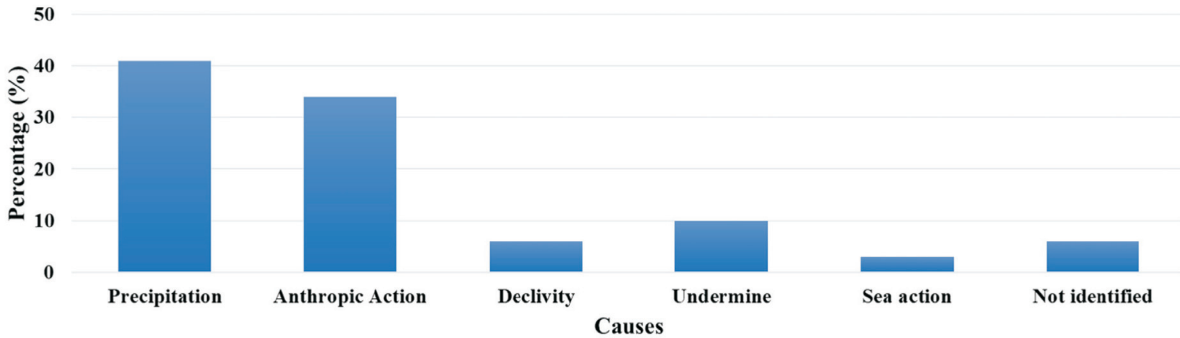

Figure 10. Influence of causes on mass movements in the Brazilian Northeast region.

by severe droughts occur, increases the possibility of natural disaster incidence (Tominaga et al., 2009).

Regarding anthropic actions, it is understood that they are actions derived from human decisions, some examples of these actions would be the civil engineering constructions in inadequate locations, inefficient drainage systems and waste disposal in places with deficiency of stability. It has been observed in the literature that in most of the described cases, the occupations disrespect the capacity of land use, adopting inadequate practices for housing installation, actions that result in mass movements.

5.3 Search results by geological formation

In the Northeast region of Brazil there is an extensive variety of geological formations. From the coast to the interior of the region, the soils are very distinct from each other, both in formation and origin as well as in structure. In the research conducted, the geological formation of each mass movement occurrence was listed in Figure 11, where it relates the geological formation with the number of mass movement occurrences.

It was observed that many of the mass movement events occurred in areas that contained more than one type of material, especially in areas that contained soils from the Barreiras Formation associated with other types of soils from different geological formations, such as Granite and/or gneiss Residual Soils.

Regarding the number of occurrences, the Barreiras Formation soil presented the largest number of events, with 47 occurrences. Most of the Brazilian Northeast is covered by unconsolidated sediments of the Barreiras Formation, whose typical relief form are flat top plateaus (Figure 12). Especially in the metropolitan region of the city of Recife in the State of Pernambuco, the slopes of these plateaus are exposed to landslides during the rainy season (Torres & Pfaltzgraff, 2014). Its thickness varies according to its relationship with the irregular surface of the crystalline basement, on which it rests in erosive disconformity, deepening towards the coast (Brandão, 1995).

The Barreiras Formation has layers of coarse sand, interspersed with layers of fine sand and/or clays, very friable and erodible that favor the installation of erosive processes on the slopes. According to Coutinho & Severo (2009), the clay/sand alternation creates peculiar situations regarding the stability of the slopes in the Barreiras formation. If the slope has clay as its top layer, it will hold the relief, reducing the erosion of the underlying layer; however, if the top

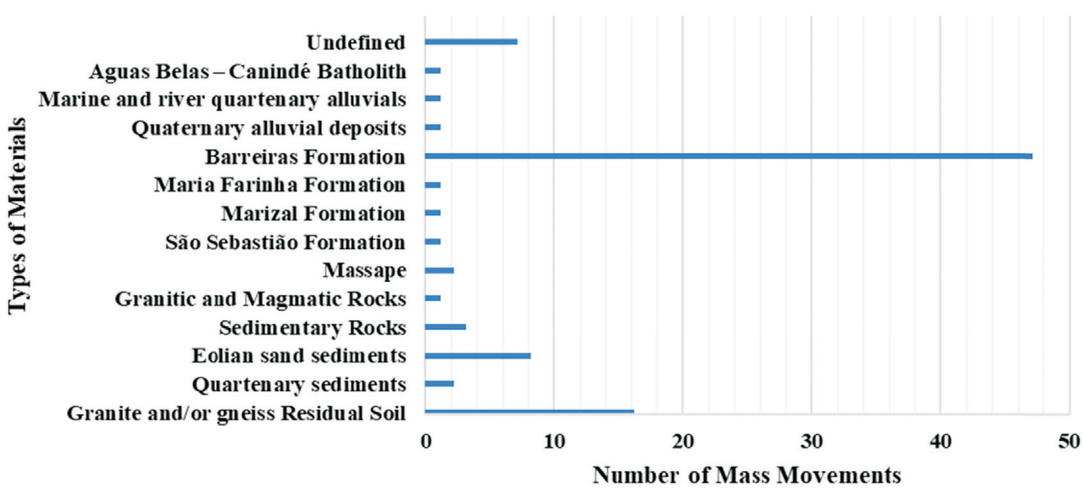

Figure 11. Influence of geological formation on mass movements in Brazilian Northeast region.

Figure 12. Flat top plateaus in Rio Grande do Norte (Muehe, 2006).

layer is sand, high surface infiltration will favor saturation, appearance of erosion processes and possible landslides.

The second material with the largest number of events was residual soils from granite and/or gneiss rocks, with a record of 16 occurrences of mass movements. In general, residual soils present peculiarities in their properties and behavior, due to their performance in geological and/or pedological processes, typical of humid tropical regions. As such, they are most likely unsaturated soils and of relatively high permeability, which means that their engineering properties are easily affected by precipitation (Calle, 2000).

Menezes & Campos (1992) stated that residual soils, in their natural condition present a saturation degree of 80 % or less, when rain occurs, there is an increase in the degree of saturation that causes a reduction in the suction of the soil, consequently there is a decrease in shear strength, which can cause rupture.

5.4 Search results by number of events by year of occurrence

In order to analyze the relevance of the studies on mass movement occurrences in the Northeast region of Brazil, a graph with the number of events by year of occurrence was constructed. The intention of the graph was not to verify how often these events occur, but rather how much, over the years, these events were studied. Figure 13 shows the graph with the number of events that occurred over the years

Figure 13 shows that even though the first article published in this research was from 1954, the first reported event occurred in 1944. The years between 2015 and 2019 did not present recorded events, with the last reported event dated in the articles occurring in 2014. Between the years of 1944 and 1989 there was a record of 10 events, that is, in 45 years only 10 occurrences of mass movement were reported in academic studies. In contrast, from 1991 to 2019 that is, in 23 years, 25 events were recorded in academic events. The higher number of events recorded in recent years can be attributed to the greater need for knowledge on the subject, since there is a significant number of events occurring in the region. The increasing urbanization in the last 20 years brings with it the disordered growth of cities in areas unfit for occupation due to unfavorable geological and geomorphological features. Anthropic interventions in these lands increase the dangers of their instability, requiring solutions to reduce the risk arising from mass movements, solutions that can only be obtained through the study and knowledge of the phenomena that occur on site.

It is also observed from Figure 13 that 30 recorded events have not been dated. The undated events could indicate a lack of precision, accuracy and/or availability regarding the temporal occurrence of the mass movements in the researched articles. The determination of the year in which the events occurred represents an important step towards understanding the causes, frequency and hazards connected to the mass movements. The knowledge about the temporal occurrence of mass movements in a given area may also help to decipher the recent and future responses of slope instabilities to climate change (Pánek, 2015).

6. Conclusions

This research aimed to find the cases of mass movements that occurred in the Northeast region of Brazil that

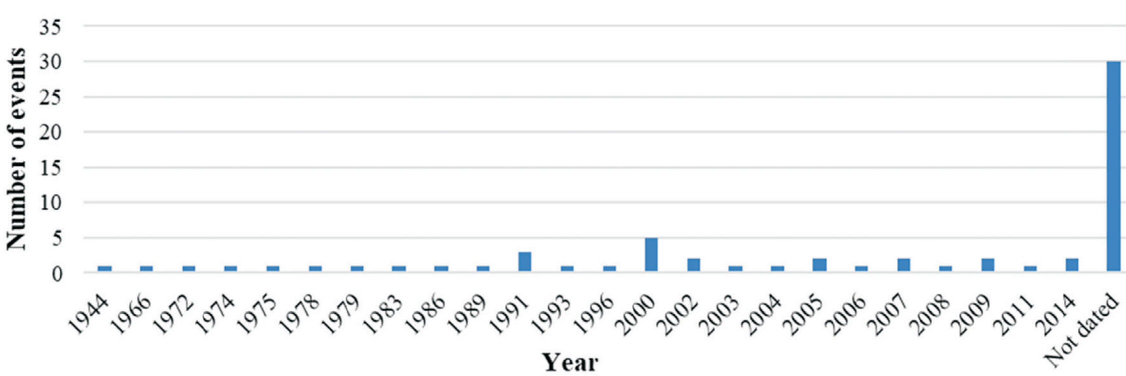

Figure 13. Number of events by year of occurrence.

were reported in national academic publications and proceedings. The data base was comprised of literature available in the Soils and Rocks Journal and three national academic events, the COBRAMSEG (Brazilian Conference on Soil Mechanics and Geotechnical Engineering), the COBRAE (Brazilian Conference on Slope Stability) and CBGE (Brazilian Conference on Engineering and Environmental Geology). The key words searched were Landslides, Mass Movements, Geomorphology and Engineering Geology restricted to the Brazilian Northeast region within the years of the academic publications and proceedings.

With the data and analysis performed, it could be concluded that studies on mass movements in the Northeast of Brazil are still little addressed in academic research. In a period of 65 years of publications, where 7348 articles were analyzed, only 47 of them dealt with research that presented cases of mass movements in the Brazilian Northeast. In several articles studied, the mass movement event was not the object of research but served as a subsidy for the author's study. Out of 65 cases identified, the majority of the events occurred in the States of Pernambuco, Rio Grande do Norte and Bahia. It was also identified that the types of mass movements that occur most frequently in the region are flows, erosion and slides, respectively. The cases of mass movements in the three States with the highest percentage of records were mostly located in the littoral and coastal regions of the States, with depressions such as hills and cliffs.

Regarding the causes of mass movements, precipitation and anthropic actions were presented as the main causes of the events. The effect of rainfall changes the structural organization of the soil, which loses strength, resulting in mass movements. Rainfall in conjunction with anthropic actions, with respect to actions arising from human decisions, were decisive in the occurrence of several of the recorded events. In the analysis of the cases, it was clear that human decisions were a major impact factor in the occurrence of mass movements, especially in those cases reported in settlement sites.

The geological formation that presented the most cases of mass movements was the Barreiras Formation, which is consistent with the locations of occurrence since it is a typical formation of the Brazilian Northeastern coast. The second geological formation with the largest number of cases was the residual soil derived from granite and/or gneiss rocks, also typical of the Northeast region of Brazil. Both geological formations are strongly affected by the actions of rainfall, and with the region being tropical and humid, it can be understood why the events of mass movements occurred in these types of geological formations.

From the research carried out, there was an increase in the number of researches on cases of mass movements in the region. It was noticed that the need for more information and knowledge about the soils, slopes and situation of the locations has become more relevant to the academic community, since it is clear there is a pattern in the disposition of the causes of the events. Several cases have not only involved material losses, but also lives, and the interest in preventing these types of losses also encourages research on the subject.

Systematic reviews are believed to be quite useful for integrating information from various studies with a common theme, in this case, mass movements in the Brazilian Northeast. Therefore, from this systematic review it was possible to identify the main geotechnical characteristics of mass movement occurrences in the region, as well as their causes. It was also identified that this theme is starting to be of more interest to the academic community, as the number of researches involving the theme has been increasing. It is expected that the data presented here will serve as evidence, helping to carry out further research related not only to the subject of mass movements in the Brazilian Northeast, but also to the study of the soils and geological formations and settlements of the region, serving as subsidy for future investigations.

References

Almeida, F.F.M., Hasui, Y., de Brito Neves, B.B., & Fuck, R.A. (1981). Brazilian structural provinces: an introduction. *Earth-Science Reviews*, 17(1):1-29. https://doi.org/10.1016/0012-8252(81)90003-9

Assis Dias, M.C., Saito, S.M., Alvalá, R.C.S., Stenner, C., Pinho, G., Nobre, C.A., & Lima, C.O. (2018). Estimation of exposed population to landslides and floods risk areas in Brazil, on an intra-urban scale. *International Journal of Disaster Risk Reduction*, 31(1):449-459. https://doi.org/10.1016/j.ijdrr.2018.06.002

Bezerra, F.H., Amaro, V.E., Vita-Finze, C., & Saady, A. (2001). Pliocene-Quaternary fault control of sedimentation and coastal plain morphology in NE Brazil. *Journal of South American Earth Sciences*, 14(1):61-75. https://doi.org/10.1016/S0895-9811(01)00009-8

Brand, E.W., Premchitt, J., & Phillipson, H.B. (1984). Relationship between rainfall and landslides in Hong Kong. *Proc. 4th International Symposium on Landslides*, *Toronto*, Vol. 1, CGS, 377-384.

Brandão, R.L. (1995). *Mapa Geológico da RMF - Texto Explicativo*. CPRM (in Portuguese).

Budimir, M.E.A., Atkinson, P.M., & Lewis, H.G. (2015). A systematic review of landslide probability mapping using logistic regression. *Landslides*, 12(1):419-436. https://doi.org/10.1007/s10346-014-0550-5

Calle, J.A.C. (2000). *Slope back analysis in unsatured soils* [Master's dissertation, University of São Paulo]. University of São Paulo's repository (in Portuguese). https://doi.org/10.11606/D.18.2000.tde-10062008-082455

Campos, L.E.P. (2013). Ações e desastres na Bahia. *Proc. VI Conferência Brasileira de Encostas, Angra dos Reis*. Vol. 1, ABMS & CBMR, 153-159 (in Portuguese).

Caputo, M.V. (1984). *Stratigraphy, tectonics, paleoclimatology and paleogeography of Northern basins of Brazil* [Unpublished doctoral dissertation]. University of California at Santa Barbara.

CEPED. (2012). *Atlas Brasileiro de Desastres Naturais: 1991-2010*. CEPED UFSC.

Chipp P.N., Henkel D.J., Clare D.G., & Pope, R.G. (1982). Field measurement of suction in colluvium covered slopes in Hong Kong. *Pro. 7th Southeast Asian Geotechnical Conference*, *Hong Kong*. Vol. 1, SAGS, 49-62.

Clague, J.J., & Roberts, N. (2012). Landslide hazard and risk. In *Landslides: Types, Mechanisms and Modeling* (pp. 1-9). Cambridge University Press.

Costa, L.R.F., Maia, R.P., Barreto, L.L., & Sales, V.C.C. (2020). Geomorphology of the Northern Brazilian Northeast: a classification proposal. *Revista Brasileira de Geomorfologia*, 21(1):185-208 (in Portuguese). http://dx.doi.org/10.20502/rbg.v21i1.1447

Coutinho, R.Q., & Severo, R.N.F. (2009). Investigação geotécnica para projeto de estabilidade de encostas. *Proc. 5a Conferência Brasileira de Encostas*, São Paulo. Vol. 1, ABMS, 19-74 (in Portuguese).

Coutinho, R.Q., Silva, M.M., Dos Santos, A.N., & Lacerda, W.A. (2019). Geotechnical characterization and failure mechanism of landslide in granite residual soil. *Journal of Geotechnical and Geoenvironmental Engineering*, 145(8):05019004. https://doi.org/10.1061/(ASCE)GT.1943-5606.0002052

Cruden, D.M., & Varnes, D. (1996). *Landslides: Investigation and Mitigation - Special Report 247*. US National Research Council.

Ferlisi, S., & De Chiara, G. (2016). Risk analysis for rainfall-induced slope instabilities in coarse-grained soils: Practice and perspectives in Italy. In *Landslides and Engineered Slopes. Experience, Theory and Practice* (pp. 137-154). CRC Press.

Freitas, E. (2019). *Clima e Vegetação do Nordeste*. Brasil Escola (in Portuguese). Retrieved in November 22, 2019, from https://brasilescola.uol.com.br/brasil/o-clima-vegetacao-nordeste.htm

Gerscovich, D.M.S. (2016). *Estabilidade de Taludes*. Oficina de Textos (in Portuguese).

Giani, G.P. (1992). *Rock Slope Stability Analysis*. Balkema.

Guerra, A.J.T., Fullen, M.A., Jorge, M.C.O., Bezerra, J.F.R., & Shokr, M.S. (2017). Slope processes, mass movement and soil erosion: A Review. *Pedosphere*, 27(1):27-41. https://doi.org/10.1016/S1002-0160(17)60294-7

Gusmão Filho, J.A., Silva, J.M.J., Figueiredo, L.C., Costa, W.D., & Amorim J.R.W.M. (1982). Caracterização Geológico-Geotécnica dos Morros de Olinda. *Proc. VII Congresso Brasileiro de Mecânica dos Solos e Engenharia de Fundações*, *Olinda*. Vol. 1, ABMS, 75-102 (in Portuguese).

Handwerger, A.L., Huang, M., Fielding, E.J., Booth, A.M., & Bürgmann, R. (2019). A shift from drought to extreme rainfall drives a stable landslide to catastrophic failure. *Scientific Reports*, 9(1):1569. https://doi.org/10.1038/s41598-018-38300-0

Hungr, O., Leroueil, S., & Picarelli, L. (2014). The Varnes classification of landslide types, an update. *Landslides*, 11(2):167-194. https://doi.org/10.1007/s10346-013-0436-y

Lepsch, I.F. (2002). *Formação e Conservação dos Solos*. Oficina de Textos (in Portuguese).

Li, Y., Mo, P. (2019). A unified landslide classification system for loess slopes: A critical review. *Geomorphology*, 340(1):67-83. https://doi.org/10.1016/j.geomorph.2019.04.020

Lopo, A.B., Spyrides, M.H.C., Lucio, P.S., & Sigró, J. (2014). Ozone and aerosol influence on ultraviolet radiation on the east coast of the Brazilian Northeast. *Atmospheric and Climate Sciences*, 4(1):92-99. http://doi.org/10.4236/acs.2014.41012

McColl, S.T. (2015). *Landslide Causes and Triggers* (pp. 17-42). Elsevier.

Menezes, M.S.S., & Campos, L.E.P. (1992). Estabilização de taludes em solos residuais tropicais. *Proc. 1a Conferência Brasileira Sobre Estabilidade de Encostas*, *Rio de Janeiro*, Vol. 1, ABMS, 101-109 (in Portuguese).

Muehe, D. (2006). *Erosão e Progradação do Litoral Brasileiro*. Brazilian Ministry of Environment (in Portuguese).

Nadal-Romero, E., Petrlick, K., Verachtert, E., Bochet, E., & Poesen, J. (2014). Effects of slope angle and aspect on plant cover and species richness in a humid Mediterranean badland. *Earth Surface Processes and Landforms*, 39(13):1705-1716. https://doi.org/10.1002/esp.3549

Olivares, L., & Damiano, E. (2007). Post failure mechanics of landslides: laboratory investigation of flowslide in pyroclastic soils. *Journal of Geotechnical and Geoenvironmental Engineering*, 133(1):51-62. https://doi.org/10.1061/(ASCE)1090-0241(2007)133:1(51)

Pánek, T. (2015). Recent progress in landslide dating: A global overview. *Progress in Physical Geography*, 39(2):168-198. https://doi.org/10.1177 %2F0309133314550671

Pitts, J. (1983). The form and causes of slope failures in an area of West Singapore Island. *Singapore Journal of Tropical Geography*, 4(2):162-168. https://doi.org/10.1111/j.1467-9493.1983.tb00140.x

Santos, C.L., Listo, F.L.R., Silva, O.G., & Reis, R.B. (2018). Análise metodológica de estudos referentes a eventos de movimentos de massa e erosão ocorridos na região Nordeste do Brasil. *Caderno de Geografia*, 28(55):959-979 (in Portuguese). https://doi.org/10.5752/P.2318-2962.2018v28n55p959-979

Santos Junior, O.F. (2005). Estabilidade de encostas e erosão. In *Geotecnia no Nordeste* (pp. 181-203). Editora Universitária, (in Portuguese).

Selby, M.J. (1993). *Hillslope Materials and Processes*. Oxford University Press.

Silva, E.M. (2006). *Slope stability analysis in soils of alteration of metamorfic rocks of Quadrilátero Ferrífero* [Master's dissertation, Federal University of Viçosa]. Federal University of Viçosa's repository (in Portuguese). https://locus.custom.ufv.br//handle/123456789/3742

Smyth, C.G., & Royle, S.A. (2000). Urban landslides hazards: incidence and causative factors in Niterói, Rio de Janeiro. *Applied Geography*, 20(2):95-118. https://doi.org/10.1016/S0143-6228(00)00004-7

Souza, A.P.L. (2014). *Estudos geotécnicos e de estabilidade de taludes da encosta do Alto do Padre Cícero no município de Camaragibe - PE* [Master's dissertation, Federal University of Pernambuco]. Federal University of Pernambuco's repository (in Portuguese). https://repositorio.ufpe.br/handle/123456789/14984

Stoffel, M., & Huggel, C. (2012). Effects of climate change on mass movements in mountain environments. *Progress in Physical Geography*, 36(3), 421-439. https://doi.org/10.1177 %2F0309133312441010

Suzen, M.L., & Kaya, B.S. (2011). Evaluation of environmental parameters in logistic regression models for landslide susceptibility mapping. *International Journal of Digital Earth*, 5(4), 338-355. https://doi.org/10.1080/17538947.2011.586443

Sweeney, D.J., & Robertson, P.K. (1979). A fundamental approach to slope stability problems in Hong Kong. *Hong Kong Engineer*, 10(7):35-44.

Tan, S.B., Lim, T.L., Tan, S.L., & Yang, K.S. (1987). Landslide problems and their control in Singapore. *Proc. 9th Southeast Asian Geotechnical Conference, Bangkok*. SEAGS, pp. 1-25.

Tominaga, L.K., Santoro, J., & Amaral, R. (2009). *Desastres Naturais: Conhecer Para Prevenir*. Instituto Geológico (in Portuguese).

Torres, F.S.M., & Pfaltzgraff, P.A.S. (2014). *Geodiversidade do Estado de Pernambuco*. CPRM.

USGS. (2004). Landslide Types and Processes. *USGS - United States Geological Survey*, *Reston*, *VA*.

Varnes, D.J. (1978). Slope movement types and processes. *Transportation Research Board Special Report*, 176(1):11-33.

Appendix - Selected articles

1.	Uma aplicação das micro-ancoragens na estabilização de taludes naturais	VIII Cobramseg	1986	Nunes, A.J.C.; Craizer, W.; Dias, P.H.V.
2.	Mecanismos dos movimentos dos morros de Olinda	VIII Cobramseg	1986	Gusmão Filho, J.A.; Jucá, J.F.T.; Silva, J.M.J.
3.	Ocorrência de voçorocas em plataformas genéticas arenosas em Alcântara - MA	VIII Cobramseg	1986	Vertamatti, E.; Araújo, F.A.R.
4.	A erosão urbana e seus impactos ambientais nos morros da cidade do Recife	IX Cobramseg	1990	Melo, L.V.
5.	Mapeamento de áreas de risco de movimentos de massa em encostas formadas por dunas na cidade de Natal	XI Cobramseg	1998	Santos, L.A.O.; Amaral, R.F.
6.	Análise de estabilidade e proposta de estabilização de uma ruptura ocorrida em encosta com ocupação desordenada no bairro do Ibura, Recife - PB	XIII Cobramseg	2006	Coutinho, R.Q.; Santana, R.G.; Gusmão, A.D.
7.	Análise de soluções de engenharia para contenção em encostas ocupadas na região metropolitana do Recife - PE	XIII Cobramseg	2006	Santana, R.G.; Coutinho, R.Q.
8.	Avaliação da erodibilidade em uma encosta ocupada pertencente à Formação Barreiras	XV Cobramseg	2010	Meira, F.F.D.A.; Coutinho, R.Q.; Cantalice, J.M.B.
9.	Caracterização geológico geotécnica dos materiais presentes nas encostas na região metropolitana do Recife	XV Cobramseg	2010	Bandeira, A.P.N.; Coutinho, R.Q.; Alheiros, M.M.
10.	Chuvas críticas associadas aos escorregamentos de encostas na região metropolitana do Recife	XV Cobramseg	2010	Bandeira, A.P.N.; Coutinho, R.Q.; Alheiros, M.M.
11.	Análise da estabilidade de um movimento de massa ocorrido em Pernambuco	XV Cobramseg	2010	Silva, M.M.; Coutinho, R.Q.; Lacerda, W.A.
12.	Estudos sobre escorregamentos de encostas da formação barreiras de Maceió - AL	XVI Cobramseg	2012	Marques, J.A.F.; Marques, A.G.; Marques, R.F.
13.	Análise da estabilidade de taludes de solos naturais da região metropolitana de Salvador	I COBRAE	1992	Guimarães, R.B.
14.	Condicionamento geológico de uma ruptura de encosta na falha de Salvador	I COBRAE	1992	Santos, L.A.O.; Lima, I.A.; Silva, J.C.B.J.; Leal, G.R.N.
15.	Soil nailing - chumbamento de solos - experiência de uma equipe na aplicação do método	I COBRAE	1992	Zirlis, A.C.; Pitta, C.A.
16.	Tentativa de correlação entre precipitação e deslizamentos na cidade de salvador	I COBRAE	1992	Elbachá, A.T.; Campos, L.E.P.; Bahia, R.F.C.
17.	Escorregamento em morros urbanos do Recife: o caso do boleiro	II COBRAE	1997	Gusmão Filho, J.A.; Ferreira, S.R.M.; Amorim Jr., W.M.
18.	Geotechnical characterization and slope stability evaluation of a slope in residual soil in Pernambuco, Brazil	II COBRAE	1997	Coutinho, R.Q.; Costa, F.Q.; Sousa Neto, J.B.
19.	Situações de risco e medidas de prevenção de acidentes em encostas ocupadas na cidade de Maceió (AL), Brasil	II COBRAE	1997	Anjos, C.A.M.; Cerri, L.E.S.; Gandolfi, N.
20.	Estudo das encostas ocupadas do recife	II COBRAE	1997	Gusmão Filho, J.A.; Alheiros, M.M.; Gusmão, A.D.
21.	Erosão e assoreamento de lagunas no litoral leste do Rio Grande no Norte	III COBRAE	2001	Santos Jr, O.F.; Scudelari, A.C.; Medeiros, A.G.B.; Amaral, R.F.
22.	Inventário e análise das corridas de detritos no Brasil	III COBRAE	2001	Gramani, M.F.; Kanji, M.S.

23.	Mecanismos de ruptura de taludes em sedimentos terciários da Formação Barreiras no Litoral do Rio Grande do Norte	III COBRAE	2001	Santos Jr, O.F.; Pereira, D.A.; Nóbrega, P.G.B.; Amaral, R.F.
24.	Monitoramento de um processo de creep em um talude de massapê	III COBRAE	2001	Machado, S.L.; Presa, E.P.
25.	Análise da estabilidade nas falésias entre Tibau do Sul e Pipa RN	IV COBRAE	2005	Santos Jr, O.F.; Severo, R.N.F.; Freitas Neto, O.; França, F.A.N.
26.	Aplicação de geoprocessamento na avaliação de movimento de massa em Salvador BA	IV COBRAE	2005	Campos, L.E.P.; Miranda, S.B.; Jesus, A.C.; Burgos, P.C.
27.	Avaliação da erodibilidade como parâmetro no estudo de sulcos e ravinas numa encosta no Cabo de Santo Agostinho PE	IV COBRAE	2005	Lafayette, K.P.V.; Coutinho, R.Q.; Queiroz, J.R.S.
28.	Avaliação da susceptibilidade ao risco de uma área piloto de Salvador	IV COBRAE	2005	Jesus, A.C.; Dias, L.S.O.; Miranda, S.B.; Campos, L.E.P.
29.	Avaliação espacial da perda de solo por erosão da bacia experimental de Aiuaba CE através do uso de SIG	IV COBRAE	2005	Cavalcante, S.P.P.; Araújo, J.C.
30.	Caracterização geológica geotécnica de um deslizamento numa encosta em Camaragibe PE	IV COBRAE	2005	Silva, M.M.; Coutinho, R.Q.; Lacerda, W.A.; Alheiros, M.M.
31.	Estabilização de uma área utilizando a contribuição da sucção - o caso de Barro Branco	IV COBRAE	2005	Campos, L.E.P.; Fonseca, E.C.; Burgos, P.C
32.	Quantificação da evolução de erosões em encostas - Cabo de Santo Agostinho PE	IV COBRAE	2005	Silva, E.P.; Coutinho, R.Q.; Lima Filho, M.
33.	Análise e tratamento de erosão na base de uma fundação da linha de transmissão Recife ii-Joairim	V COBRAE	2009	Quental, J.C.; Ferreira, S.R.M.
34.	Avaliação da segurança de um talude não saturado em obra do metrô de Fortaleza CE	V COBRAE	2009	Silva Filho, F.C.; Dantas Neto, S.A.
35.	Avaliação de processos erosivos de falésias em Pirangi do Norte - Parnamirim - RN	V COBRAE	2009	Santos Jr, O.F.; Costa, Y.D.J.; Chaves, L.F.; Costa, C.M.L.
36.	Estudo de um movimento de massa ocorrido numa encosta em Camaragibe PE	V COBRAE	2009	Silva, M.M.; Coutinho R.Q.; Lacerda, W.A.
37.	Proposta para recuperação de uma área degradada no recôncavo baiano	V COBRAE	2009	Araruna Jr., J.T.; Amaral, C.P.; Pires, P.J.M.; Moncada, M.P.H.; Domingues, D.L.P.; Campos, L.E.P.; Burgos, P.C.
38.	Investigação geotécnica para projeto de estabilidade de encostas	V COBRAE	2009	Coutinho, R.Q.; Severo, R.N.F.
39.	Desastres e ações na Bahia	VI COBRAE	2013	Campos, L.E.D.
40.	Escorregamento no maciço do Julião - Salvador	II CBGE	1978	Presa, E.P.; Silva, J.C.F.
41.	Estudo da erosão da encosta do Horto Dois Irmãos - PE	IX CBGE	1999	Coutinho, R.Q.; Oliveira, J.T.R.; Lima Filho, M.F.; Coelho, F.A.B.; Dos Santos, L.M.
42.	Estudo da dinâmica das falésias do município de Tibau do Sul - RN	XI CBGE	2005	De Freitas Neto, O.; Costa, F.A. De A.; Severo, R.N.F.; Santos Jr, O F.; Scudelari, A.C.
43.	Estudo preliminar sobre a adequabilidade das contenções de encostas ao longo da BA 099, litoral norte da Bahia	XIII CBGE	2011	Bastos, E.S.; Lima, C.C.U.; Carneiro, C.S.; Abreu, J.S.
44.	Fatores que ocasionam os movimentos de massa nas encostas entre Guarajuba e Massarandupió, litoral norte do estado da Bahia.	XIII CBGE	2011	Abreu, J.S.; Lima, C.C.U.; Carneiro, C.S.; Bastos, E.S.

45.	Análise de risco remanescente do movimento de massa Ocorrido na comunidade do Jacó - Natal/RN	XV CBGE	2015	Santos, F.G.; Beltrão, B.A.
46.	O desastre na comunidade Mãe Luíza - Natal - RN: fatores de desestabilização relacionados à ocupação antrópica desordenada	XV CBGE	2015	Beltrão, B.A.; Melo, R.C.; Elldorf, B.; Santos, F.G.
47.	Análise das Condicionantes Geológicas da Corrida de Massa ocorrida na Serra das Antas, Águas Belas-PE	XV CBGE	2015	Melo, R.C.; Elldorf, B.; Dias, G.P.

Soils and Rocks
An International Journal of Geotechnical and Geoenvironmental Engineering
www.soilsandrocks.com
ISSN 1980-9743
ISSN-e 2675-5475

Experimental study on particle size effect on mechanical behaviour of dense calcareous sand

Du-min Kuang[1], Zhi-lin Long[1,#], Jie Wang[1], Xu-tong Zhou[1], Piao-yi Yu[1]

Article

Keywords
Calcareous sand
Particle size
Triaxial test

Abstract
To investigate the effect of particle size on mechanical properties of calcareous sand, a series of consolidated drained triaxial tests were performed on calcareous sand with different particle sizes. At a low effective confining pressure of 50 kPa, the shear peak strength increases with the increasing particle size. However, under a relatively large effective confining pressure (≥ 200 kPa), the shear peak strength decreases with the increasing particle size. Moreover, the apparent cohesion increases, and the corresponding friction angle decreases with the increase of particle size. The softening and dilatancy coefficient were proposed to evaluate the softening and dilatancy behaviour quantitatively. Calcareous sands with larger particle size show the greater strain hardening and volumetric contraction behaviour, which is more susceptible to the effective confining pressure.

1. Introduction

Calcareous sand, which is primarily composed of remains of coral and snail, is largely located in tropical or subtropical areas around the world, such as South China Sea, Red Sea, the Hormuz Island and the Persian Gulf (Coop et al., 2004; Morsy et al., 2019; Shahnazari et al., 2016; Suescun-Florez & Iskander, 2017; Wang and Jiao, 2011). In ocean geotechnical engineering, calcareous sands are commonly used as the backfill material for road embankments or airport runways (Wang et al., 2011; Xiao et al., 2019). As an essential part of construction material, the physical and mechanical properties of calcareous sand have attracted increasing research attention. The character of calcareous sands is quite different from that of terrigenous sands, exhibiting the irregular particle shape, the high Calcium carbonate content, and the large internal voids (Liu et al., 2019; Mcdowell & Bolton, 2000). As a result of these special physical properties, calcareous sands exhibit typical characteristics such as costly saturation (Lade et al., 2009), large strains to failure (Wei et al., 2018), high compressibility (Yang et al., 2017), and a dilative behaviour at low relative densities (Hyodo et al., 1998; Wang & Zhu, 2018). For granular materials, it is widely acceptable that the particle size effect can affect the mechanical properties significantly. A large number of studies for particle size effect of granular materials have been reported. Generally, the shear strength of particle assemblies increases with the increase in elementary particle size (Dadkhah et al., 2010; Wen et al., 2018; Varadarajan et al., 2003). Although there have been a few works that have addressed the mechanical properties of calcareous sand including shearing characteristics (Desrosiers et al., 2002; Salehzadeh et al., 2006; Pham et al., 2017; Zhang et al., 2018), compression characteristics (Yang et al., 2017) and hydraulic characteristics (Wang et al., 2019; Xiao et al., 2018), most of them have not focus on the particle size effect of calcareous sand. In practical engineering, the particle sizes of calcareous sands are in the range of some millimetre to some dozen-millimetres. For a comprehensive understanding of the engineering characteristics of calcareous sands, it is significant to analyse the effect of particle size on mechanical properties of calcareous sands.

In this study, a series of consolidated drained triaxial tests for calcareous sand with different particle sizes were performed. Based on the experimental results, the effect of particle size on strain-stress responses and volumetric responses were obtained. Moreover, the apparent cohesion and friction angle based on the Mohr-Coulomb failure criterion for different particle sizes were further analysed. Furthermore, the empirical softening index and dilatancy index were proposed to evaluate the effect of particle size on strain softening and dilatancy quantitatively.

[#]Corresponding author. E-mail address: longzl@xtu.edu.cn.
[1]College of Civil Engineering and Mechanics, Xiangtan University, Xiangtan, PR China.

Submitted on December 19, 2019; Final Acceptance on June 10, 2020; Discussion open until March 31, 2021.
DOI: https://doi.org/10.28927/SR.434567

2. Materials and methodology

The calcareous sand used in this study was obtained from Nansha islands in south of China. The calcareous sand particles own irregular and angular appearance which contains numerous cavities. Six groups of calcareous sand with particle sizes of 5-2 mm (G1), 2-1 mm (G2), 1-0.5 mm (G3), 0.5-0.25 mm (G4), 0.25-0.075 mm (G5), and 0.075-0 mm (G6) were adopted by sieving, as shown in Figure 1. Following the standards JTG E40-2007 (RIOH, 2007), the specific gravities (G_s) and the maximum (ρ_{max}) and minimum (ρ_{min}) dry densities of six particle size groups of calcareous sand are tabulated in Table 1.

The mode SLB-1 stress strain controller triaxial shear permeation test apparaus used in this study. The maximum axial pressure of this apparatus is 600 kN. The measuring capcacity of confining pressure, back pressure, and pore pressure are all 3 MPa with a resolution of 1 kPa.

In the following traxial tests, the conventional samples with 39.1 mm in diametr and 80 mm in height were assembled by the same relative density of 70 % for different particle size groups. The saturation process was conducted by the method of water head staturation combined withg back pressure saturation suggested by Yang et al. (2018). The samples are considered to be fully saturated when the Skempton's parameter *B* is greater than 0.95. Following this step, the samples were isotropically consolidated under different effective confining pressures of 50, 200, 400, and 800 kPa. Finally, all samples were sheared at a specific axial loading rate of 0.1 mm/min. It should be noted that all the tests were performed under drained conditions.

3. Results and discussions

3.1 Effect of particle size on stress-strain responses

Figure 2 shows the stress-strain responses of calcareous sand samples with different particle sizes under various effective confining pressures. At a low effective confining pressure (σ_3 = 50 kPa), the calcareous sand samples for different particle sizes exhibit slight strain softening behaviour, which is consistent with the shear behaviour of dense quartz sand. However, as the effective confining pressure increases (≥ 200 kPa), the samples with particle size ranging from 5 (G1 sand) to 0.25 mm (G4 sand) exhibit strain hardening behaviour. Similar results have also been reported by Hyodo et al. (1998). They suggested that the strain softening can be suppressed by the particle breakage induced by the high stress level, leading to a strain harden-

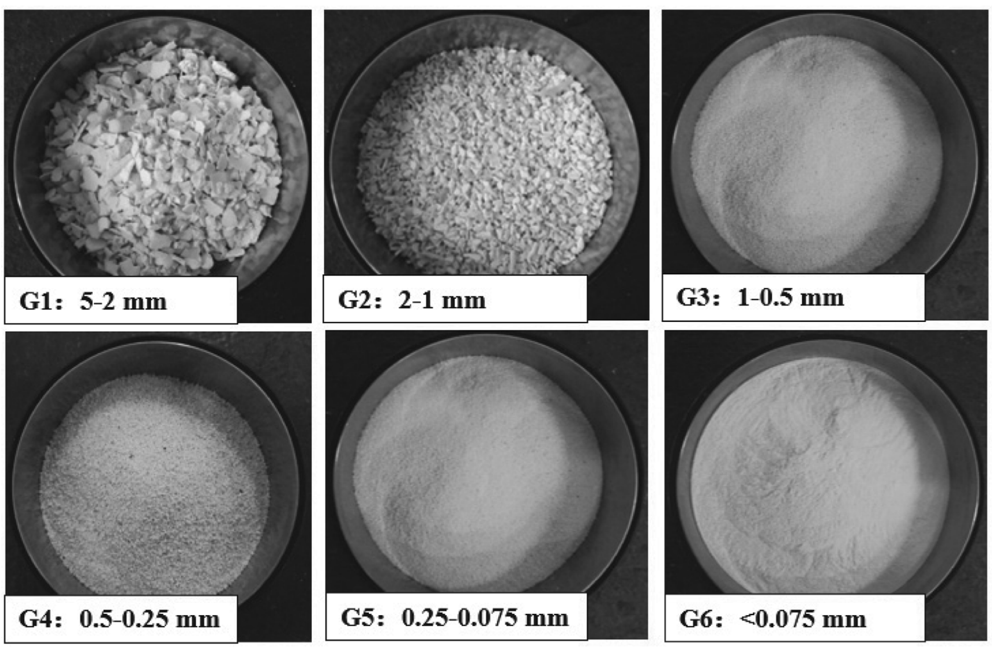

Figure 1. Original calcareous sand particles with different size groups.

Table 1. Basic physical properties of calcareous sand.

Size groups	G1	G2	G3	G4	G5	G6
G_s	2.790	2.791	2.792	2.795	2.801	2.811
ρ_{max} (g/cm^3)	1.131	1.000	1.047	0.999	1.303	1.442
ρ_{min} (g/cm^3)	0.678	0.683	0.743	0.747	0.925	1.045

ing behaviour in stress-strain response and a contraction behaviour in volumetric strain. Furthermore, for the samples with particle size ranging from 0.25 to 0.075 mm (G5 sand), a strain hardening behaviour is triggered by an effective confining pressure of 800 kPa, which is more than 200 kPa for the samples with particle size ranged from 5 (G1 sand) to 0.25 mm (G4 sand). This indicates that the effective confining pressure corresponding to a strain softening-hardening transition increases with the increase in particle size, which is further supported by the fact that the samples with particle size smaller than 0.075 mm (G6 sand) still demonstrate a strain softening behaviour under the effective confining pressures of 800 kPa. Similar results can also be found in Wang et al. (2018). This phenomenon is caused by the difference in particle breakage, dependent on the particle size, and is explained as follows. The sample with larger particles having lower particle crushing strength can be crushed easily under a low effective confining pressure, which increases the deviatoric stress and leads to a strain hardening behaviour. For the samples with smal-

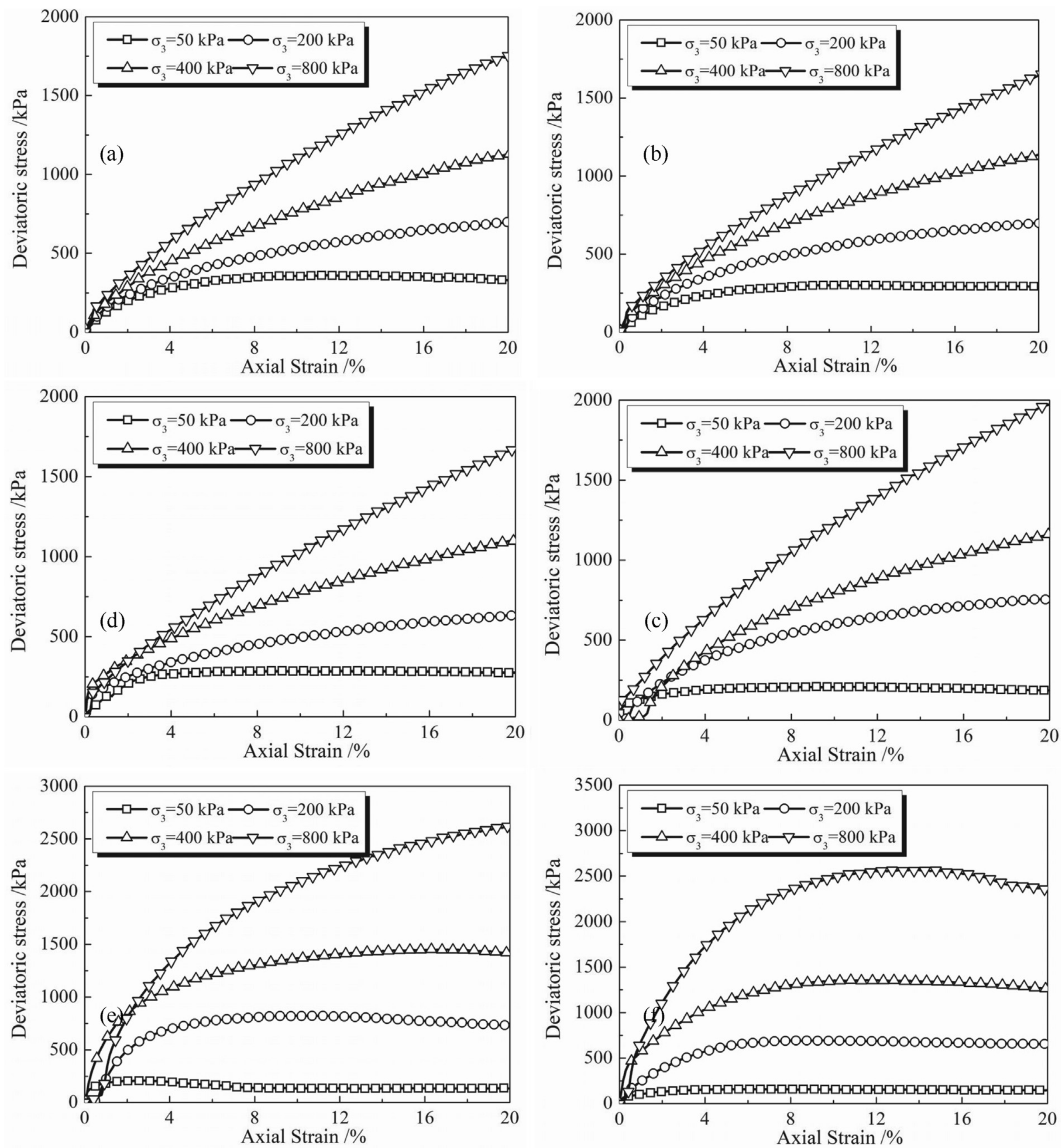

Figure 2. Stress-strain responses for different particle sizes: (a) G1: 5-2 mm, (b) G2: 2-1 mm; (c) G3: 1-0.5 mm, (d) G4: 0.5-0.25 mm, (e) G5: 0.25-0.075 mm, (f) G6: < 0.075 mm.

ler particles, the effective confining pressure corresponding to a strain softening-hardening transition increases owing to the contributions of higher particle crushing strength.

The relationships between the shear peak strength and particle size under various effective confining pressures are shown in Figure 3. It is apparent from Figure 3 that the shear peak strength of calcareous sand under different effective confining pressures depends on the particle size. The shear peak strength decreases with the decreasing particle size under the effective confining pressure of 50 kPa. However, under relatively large effective confining pressure ($\sigma_3 \geq 200$ kPa), the shear peak strength increases with the decreasing particle size. In addition, the shear peak strength of samples with small particles is more susceptible to the effective confining pressure upon increasing particle crushing strength compared to samples with large particles, so that there is a significant increase in the peak shear strength for effective confining pressures higher than 400 kPa for groups G5 and G6.

3.2 Effect of particle size on volumetric responses

Figure 4 presents the volumetric responses of calcareous sand samples with different particle sizes under various effective confining pressures. In Figure 4, the volumetric strain is positive for contraction. Experimental observations show that the dense calcareous sand samples are more likely to exhibit volumetric contraction behaviour under high effective confining pressure. Furthermore, a higher effective confining pressure produces a larger volumetric contraction. There is a higher probability for the calcareous sand particles to break under higher effective confining pressure, which reduces the volumetric dilatancy. However, at a low effective confining pressure ($\sigma_3 = 50$ kPa), the samples with particle size ranged from 5 (G1 sand) to 1 mm (G2 sand) demonstrate slight volumetric contraction at a relatively large axial strain, which is considered to be produced by the particle breakage induced by the increasing deviatoric stress during shearing.

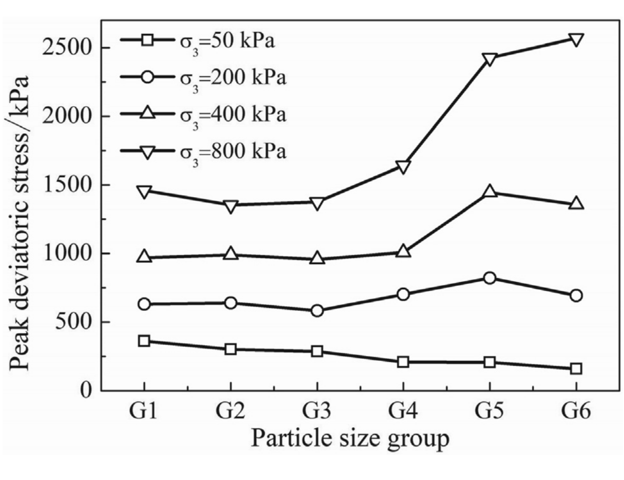

Figure 3. Relationships between shear peak strength and particle size.

3.3 Effect of particle size on apparent cohesion and friction angle

Traditionally, shear strength of granular materials is represented by the Mohr-Coulomb failure criterion, which can be expressed as follows:

$$\tau = c + \sigma_n \tan \phi \tag{1}$$

where τ is the shear strength of the sample; c is the apparent cohesion; σ_n is the normal stress on shear plane; ϕ is the friction angle.

According to the Mohr-Coulomb failure criterion, both the apparent cohesion and the friction angle for all samples with different particle sizes were obtained. Figure 5 illustrates the relationships between the Mohr-Coulomb strength index and particle size. Obviously, both the apparent cohesion and the friction angle are strongly dependent on the particle size, which is in accordance with the experimental results reported by Wang et al. (2018), shown in Figure 5. Generally, the quartz sand is considered to be non-cohesive, exhibiting a friction angle of about 30°. However, the calcareous sand samples have a high apparent cohesion which decreases with the decreasing particle size. As calcareous sands consist of corals, shells, and alga, the particle shapes are columnar, dendritic, honeycomb, or sheet (Shahnazari et al., 2016; Wang et al., 2018). Therefore, grain interlocking between coarse particles behaves as apparent cohesion in shearing. Besides, as stated by Wang et al. (2018), the large calcareous sand particle is more irregular and angular in shape than the smaller calcareous sand particle, leading to a higher apparent cohesion. For the samples with particle size less than 0.075 mm (G6 sand), the apparent cohesion is almost zero, indicating that the shear strength is more likely to be supplied by the friction component rather than the cohesion component. Besides, it is also can be seen that the friction angle increases with the decreasing particle size.

3.4 Effect of particle size on strain softening and dilatancy

In order to further analyse the softening behaviour of calcareous sand with different particle sizes, the empirical softening index is proposed, which can be calculated as follows:

$$\beta = \frac{q_p - q_r}{q_p} \tag{2}$$

where q_p is the shear peak strength, q_r is the reference strength, which is taken as the deviatoric stress corresponding to an axial strain of 20 %, as shown in Figure 6. For the strain-stress responses exhibiting a strain hardening behaviour, q_p and q_r are taken as the deviatoric stress corresponding to an axial strain of 15 % and 20 %, respectively. Based on definition of the empirical softening index, the samples

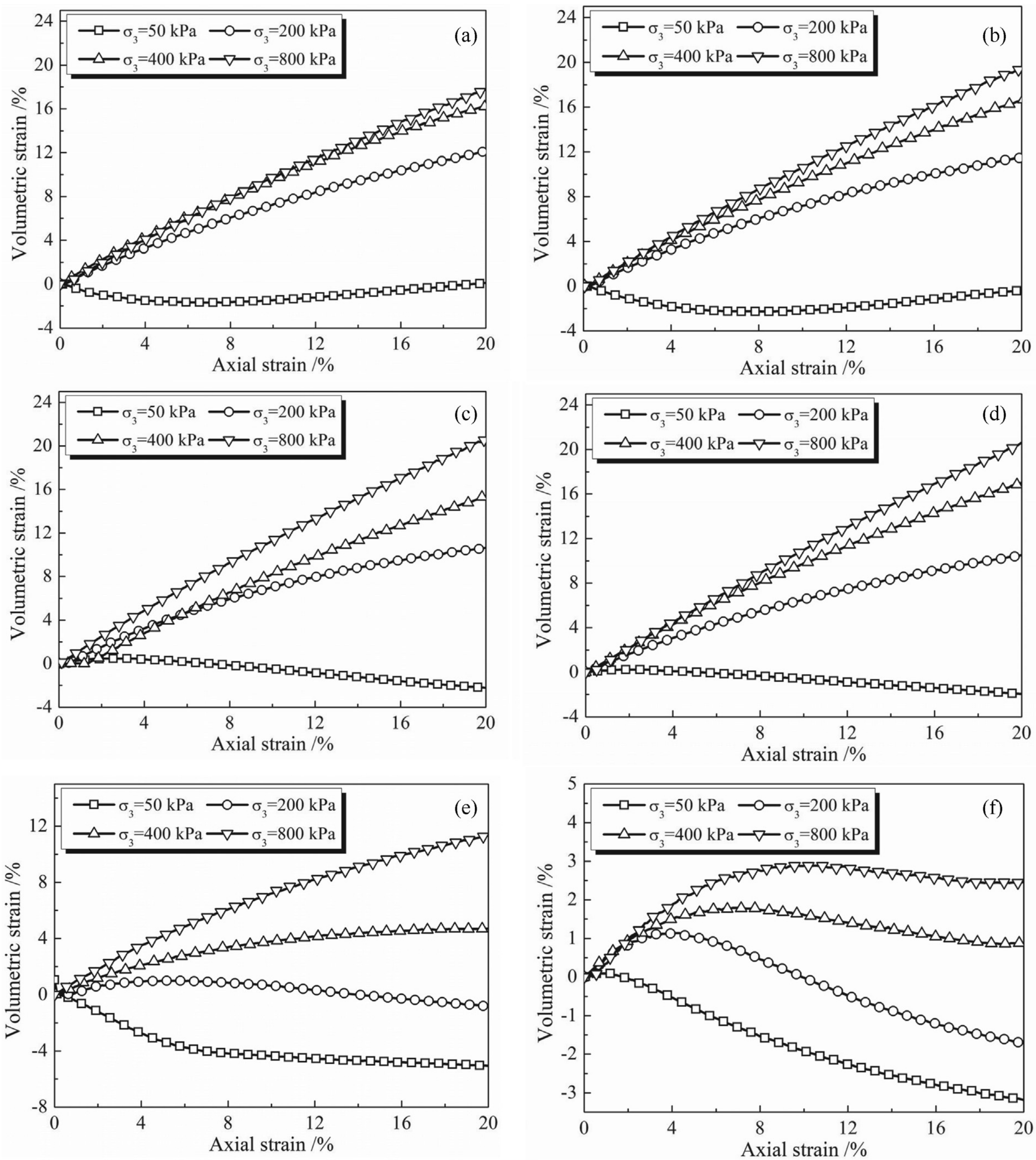

Figure 4. Volumetric responses for different particle sizes: (a) G1: 5-2 mm, (b) G2:2-1 mm, (c) G3: 1-0.5 mm, (d) G4: 0.5-0.25 mm, (e) G5: 0.25-0.075 mm, (f) G6: < 0.075 mm.

exbibit a strain softening behaviour with $\beta > 0$, whereas the samples exbibit a strain hardening behaviour with $\beta \leq 0$.

The relationships between the empirical softening index and confining pressure for different particle sizes are illustrated in Figure 7 on a semi-logarithmic scale. Significant linear relationships were obtained between the empirical softening index and the effective confining pressure for different particle sizes, which could be expressed as $\beta = k_\beta \log(\sigma_3) + b_\beta$. For the samples with particle size ranged from 5 (G1 sand) to 0.075 mm (G5 sand), the empirical softening index decreases with the increasing effective confining pressure, implying that the strain softening behaviour is more obvious under a lower effective confining pressure. In addition, it is also can be found that the strain softening behaviour is slightly influenced by the effective confining pressure for the samples with particle size less than 0.075 mm (G6 sand).

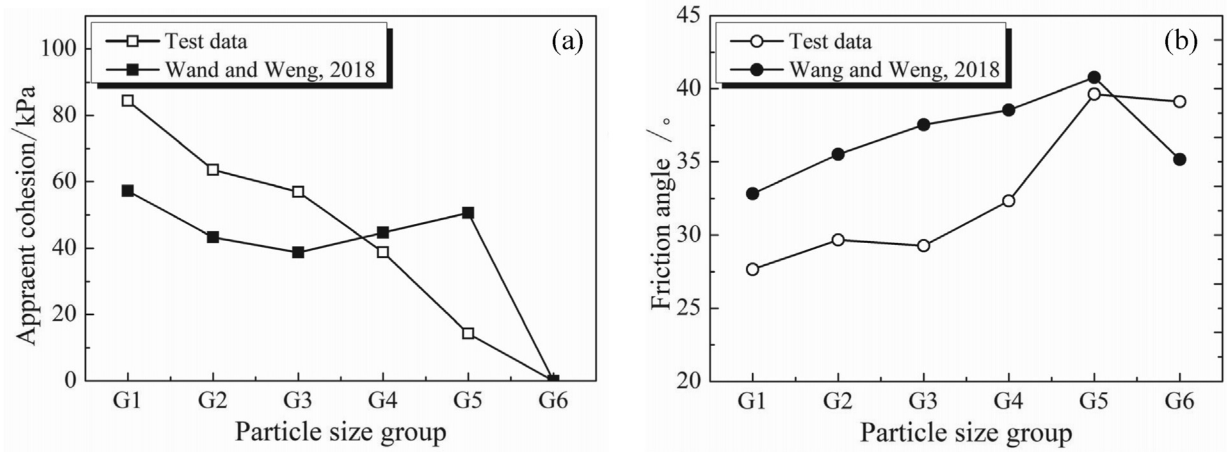

Figure 5. Relationships between Mohr-Coulomb strength index and particle size: (a) apparent cohesion, (b) friction angle.

An empirical dilatancy index is also proposed to evaluate the dilatancy behaviour quantificationally. The empirical dilatancy index is defined as:

$$\xi = \frac{\varepsilon_{vc} - \varepsilon_{vp}}{\varepsilon_{qc} - \varepsilon_{qp}} \tag{3}$$

where ε_{vc} is the volumetric strain at $d\varepsilon_v^p \,/\, d\varepsilon_q^p = 0$, with $d\varepsilon_v^p$ being the increment of volumetric plastic strain and $d\varepsilon_q^p$ being the increment of axial plastic strain. ε_{vp} is the volumetric strain corresponding to the shear peak strength. ε_{qc} and ε_{qp} are the axial strain corresponding to ε_{vc} and ε_{vp}, respectively. Based on the definition, the samples exhibit a volumetric contraction behaviour continuously with $\xi \geq 0$, whereas the samples exhibit a volumetric dilatancy behaviour with $\xi < 0$. The corresponding values of four parameters (*e.g.*, ε_{vc}, ε_{vp}, ε_{qc}, and ε_{qp}) mentioned above for different types of volumetric responses are shown in Figure 8. Note that both the ε_{vc} and ε_{qc} are assumed to be zero for the type D volumetric response.

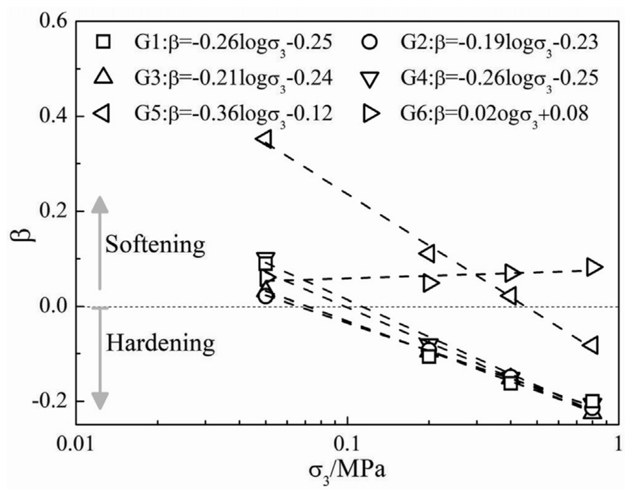

Figure 7. Relationships between empirical softening index and effective confining pressure for different particle sizes.

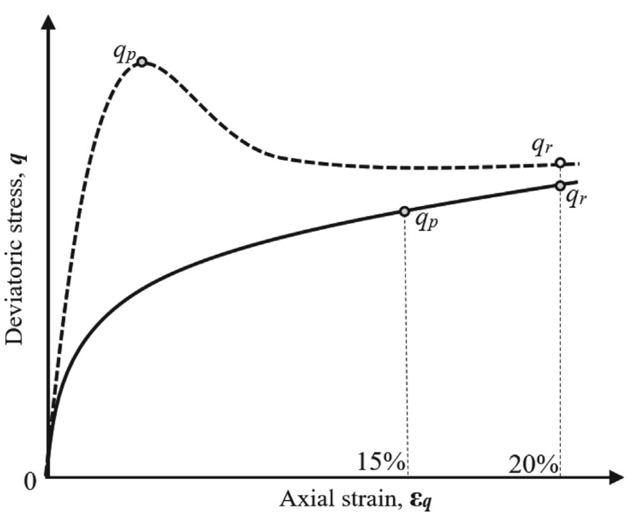

Figure 6. Representation of the empirical softening index.

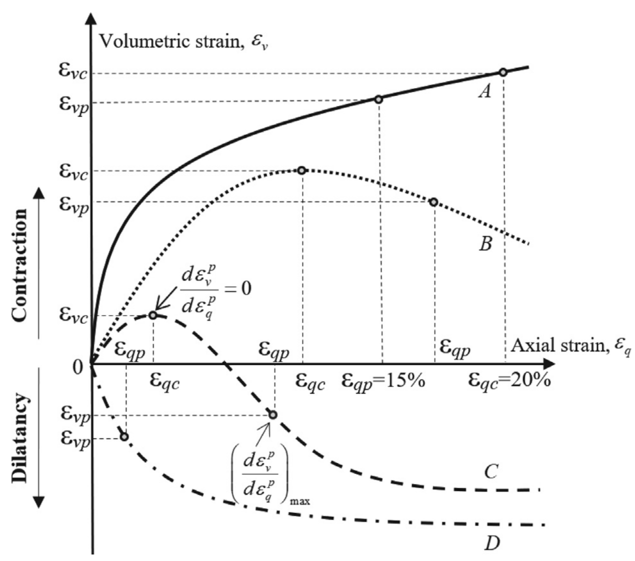

Figure 8. Representation of the empirical dilatancy index.

Figure 9 shows the relationships between the empirical dilatancy index and the effective confining pressure for different particle sizes. As shown in Figure 9, the empirical dilatancy indexes are linearly related to the effective confining pressures in semi-logarithmic scale, which can be described by $\xi = k_{\xi}\log(\sigma_3) + b_{\xi}$. It is found that the empirical dilatancy index for different particle sizes increases with the increasing effective confining pressure, indicating that the volumetric dilatancy behaviour is suppressed by the increasing effective confining pressures. For calcareous sand, the particle breakage has a significant influence on the volumetric behaviour (Bandini & Coop, 2011; Shahnazari et al., 2014; Shahnazari et al., 2015). It seems that both a higher effective confining pressure and a larger particle size can lead to a larger extent of particle breakage, which reduces the volumetric dilatancy (Wang et al., 2018; Shahnazari et al., 2015). It can be concluded that the volumetric behaviour of calcareous sand sample is the result of synergy of particle breakage and dilatancy (Wang et al., 2018). In addition, for G6 sand, the samples exhibit a volumetric dilatancy behaviour under various effective confining pressures.

4. Conclusions

To investigate the effect of particle size on mechanical properties of calcareous sand, a series of consolidated drained triaxial tests were performed on calcareous sand with different particle sizes. The test results indeed reveal the effect of particle size on the shear behaviour of dense calcareous sands. The following main conclusions are drawn from the present study:

(1) The shear peak strength, the apparent cohesion, and the friction angle are all dependent on the particle size. At a low effective confining pressure of 50 kPa, the shear peak strength increases with the increasing particle size. However, under a relatively large effective confining pressure (≥ 200 kPa), the shear peak strength decreases with the increasing particle size. Moreover, the apparent cohesion increases, and the corresponding friction angle decreases with the increase of particle size.

(2) The high effective confining pressure may lead to strain hardening behaviour for dense calcareous sand samples, corresponding to contraction in volumetric strain. The softening and dilatancy indexes were proposed to evaluate the softening and dilatancy behaviour quantitatively. Calcareous sands with larger particle size showed the greater strain hardening and volumetric contraction behaviour, which is more susceptible to the effective confining pressure.

(3) In order to further investigate the particle size effect of shear behaviour of dense calcareous sands, a comprehensive analysis should be combined with the microstructure of calcareous sands. In addition, it is also worthwhile to explore the engineering characteristics of calcareous sands with different gradations under complex stress conditions.

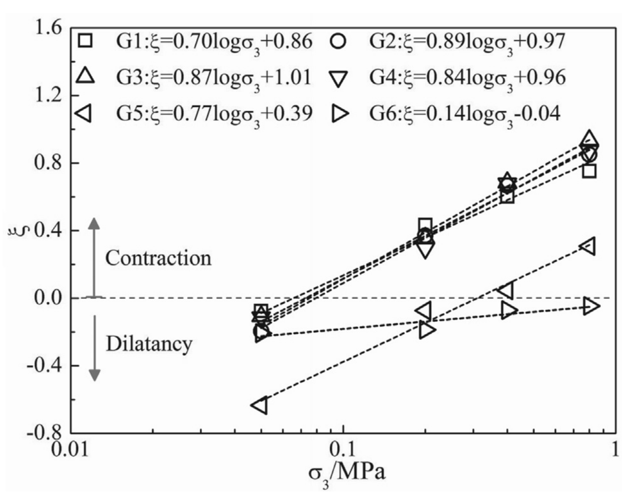

Figure 9. Relationships between empirical dilatancy index and effective confining pressure for different particle sizes.

Acknowledgments

This research was supported by the National Natural Science Foundation of China (Grant Nos. 51971188 and 51071134), the Science and Technology Major Project of Hunan Province (Grant No. 2019GK1012), Huxiang High-Level Talent Gathering Program of Hunan Province-Innovative team (Grant No. 2019RS1059) and the Degree and Postgraduate Education Reform Project of Hunan Province (Grant No. CX20190493). All these supports are acknowledged.

References

Bandini, V., & Coop, M.R. (2011). The influence of particle breakage on the location of the critical state line of sands. *Soils and Foundations*, 51(4), 591-600. https://doi.org/10.3208/sandf.51.591

Coop, M.R., Sorensen, K.K., Bodas Freitas, T.M., & Georgoutsos, G. (2004). Particle breakage during shearing of a carbonate sand. *Geotechnique*, 54(3), 157-163. https://doi.org/10.1680/geot.2004.54.3.157

Dadkhah, R., Ghafoori, M., Ajalloeian, R., & Gholam, R.L. (2010). The effect of scale direct shear test on the strength parameters of clayey sand in Isfahan City, Iran. *Journal of Applied Sciences*, 10(18), 2027-2033.

Desrosiers, R., & Silva, A.J. (2002). Strength behavior of marine sands and elevated confining stresses. *Marine Georesources and Geotechnology*, 20(1), 1-19. https://doi.org/10.1080/106411902753556834

Hyodo, M., Hyde, A.F.L., & Aramaki, N. (1998). Liquefaction of crushable soils. *Glotechnique*, 48(2), 527-543. https://doi.org/10.1680/geot.1998.48.4.527

Liu, L., Liu, H.L., Stuedlein, A.W., Evans, M.T., & Yang, X. (2019). Strength, stiffness, and microstructure characteristics of biocemented calcareous sand. *Canadian Geotechnical Journal*, 56(10), 1502-1513. https://doi.org/10.1139/cgj-2018-0007

Lade, P.V., Liggio, C.D., & Nam, J. (2009). Strain rate, creep, and stress drop-creep experiments on crushed coral sand. *Journal of Geotechnical and Geoenvironmental Engineering*, 135(7), 941-53. https://doi.org/10.1061/(ASCE)GT.1943-5606.000006

Morsy, A.M., Salem, M., & Elmamlouk, H.H. (2019). Evaluation of dynamic properties of calcareous sands in Egypt at small and medium shear strain ranges. *Soil Dynamics and Earthquake Engineering*, 116, 692-708. https://doi.org/10.1016/j.soildyn.2018.09.030

Mcdowell, G.R., & Bolton, M.D. (2000). Effect of particle size distribution on pile tip resistance in calcareous sand in the geotechnical centrifuge. *Granular Matter*, 2(4), 179-187. https://doi.org/10.1007/PL00010913

RIOH JTG E40-2007. (2007). Test methods of soils for highway engineering. *RIOH - Research Institute of Highway Ministry of Transport*, Beijing, China.

Shahnazari, H., Jafarian, Y., Tutunchian, M.A., & Rezvani, R. (2016). Undrained cyclic and monotonic behavior of hormuz calcareous sand using hollow cylinder simple shear tests. *International Journal of Civil Engineering*, 14(4), 209-219. https://doi.org/10.1007/s40999-016-0021-6

Shahnazari, H., Rezvani, R., & Tutunchian, M.A. (2015). An experimental study on the phase transformation point of crushable and noncrushable soil. *Marine Georesources and Geotechnology*, 35(2), 176-85. https://doi.org/10.1080/1064119X.2015.1126773

Shahnazari, H., Salehzadeh, H., Rezvani, R., & Dehnavi, Y. (2014). The effect of shape and stiffness of originally different marine soil grains on their contractive and dilative behavior. *KSCE Journal of Civil Engineering*, 18(4), 975-83. https://doi.org/10.1007/s12205-014-0286-8

Suescun-Florez, E., & Iskander, M. (2017). Effect of fast constant loading rates on the global behavior of sand in triaxial compression. *Geotechnical Testing Journal*, 40(1), 52-71. https://doi.org/10.1520/GTJ20150253

Salehzadeh, H., Procter, D., & Merrifield, C.M. (2006). Medium dense non-cemented carbonate sand under reversed cyclic loading. *International Journal of Civil Engineering*, 4(1), 54-63.

Wang, X.Z., Jiao, Y.Y., Wang, R., Hu, M.J., Meng, Q.S., & Tan, F.Y. (2011). Engineering characteristics of the calcareous sand in Nansha Islands, South China Sea. *Engineering Geology*, 120(4), 40-47. https://doi.org/10.1016/j.enggeo.2011.03.011

Wang, X., Zhu, C.Q., Wang, X.Z., & Qin, Y. (2018). Study of dilatancy behaviors of calcareous soils in a triaxial test. *Marine Georesources and Geotechnology*, 37(9), 1507-1070. https://doi.org/10.1080/1064119X.2018.1526236

Wei, H.Z., Zhao, T., Meng, Q.S., Wang, X.Z., & He, J.Q. (2018). Experimental evaluation of the shear behavior of fiber-reinforced calcareous sands. *International Journal of Geomechanics*, 18(12), 04018175. https://doi.org/10.1061/(ASCE)GM.1943-5622.0001307

Wen, R., Tan, C., Wu, Y., & Wang, C. (2018). Grain size effect on the mechanical behavior of cohesionless coarse-grained soils with the discrete element method. *Advances in Civil Engineering*, 2018, 4608930-1-6. https://doi.org/10.1155/2018/4608930

Wang, Y., Zhou, L., & Yang, Q. (2019). Hydro-mechanical analysis of calcareous sand with a new shape-dependent fluid-particle drag model integrated into CFD-DEM coupling program. *Powder Technology*, 344, 108-120. https://doi.org/10.1016/j.powtec.2018.12.008

Wang, X.Z., Weng, Y.L., Wang, X., & Chen, W.J. (2018). Interlocking mechanism of calcareous soil. *Rock and Soil Mechanics*, 39(9), 3113-3120 (In Chinese).

Giang, P.H.H., Van Impe, P.O., Van Impe, W.F., Menge, P., Cnudde, V., & Haegeman, W. (2017). Effects of particle characteristics on shear strength of calcareous sand. *Acta Geotechnica Slovenica*, 14(2), 77-89.

Varadarajan, A., Sharma, K.G., Venkatachalam, K., & Gupta, A.K. (2003). Testing and modeling two rockfill materials. *Journal of Geotechnical and Geoenvironmental Engineering*, 129(3), 206-218. https://doi.org/10.1061/(ASCE)1090-0241(2003)129:3(206)

Xiao, Y., Yuan, Z., Chu, J., Liu, H., Huang, J., Luo, S.N., & Lin, J. (2019) Particle breakage and energy dissipation of carbonate sands under quasi-static and dynamic compression. *Acta Geotechnica*, 14(6), 1741-1755. https://doi.org/10.1007/s11440-019-00790-1

Xiao, P., Liu, H.L., Xiao, Y., Stuedlein, A.W., & Evans, T.M. (2018). Liquefaction resistance of bio-cemented calcareous sand. *Soil Dynamics and Earthquake Engineering*, 107, 9-19. https://doi.org/10.1016/j.soildyn.2018.01.008

Yang, S., Zhu, Y.H., Liu, H.L., Li, A., & Ge, H.Y. (2018). Macro-meso effects of gradation and particle morphology on the compressibility characteristics of calcareous sand. *Bulletin of Engineering Geology & the Environment*, 77, 1047-1055. https://doi.org/10.1007/s10064-017-1157-6

Zhang, X., Hu, W., Scaringi, G., Baudet, B.A., & Han, W. (2018). Particle shape factors and fractal dimension after large shear strains in carbonate sand. *Gotechnique Letters*, 8(1), 73-79. https://doi.org/10.1680/jgele.17.00150

Soils and Rocks
An International Journal of Geotechnical and Geoenvironmental Engineering
www.soilsandrocks.com
ISSN 1980-9743
ISSN-e 2675-5475

A predictive model for the peak shear strength of infilled soft rock joints developed with a multilayer perceptron

Ana Raquel Sena Leite[1,#], Silvrano Adonias Dantas Neto[1]

Article

Keywords
Artificial neural networks
Peak shear strength
Soft rock discontinuities

Abstract
Several analytical methodologies help estimate the shear strength of rock discontinuities whose main limitations are the difficulty to obtain all necessary parameters to satisfactorily represent the boundary conditions and influence of infill materials. The objective of this study is to present a predictive model of peak shear strength for soft rock discontinuities developed making use of an artificial neural network known as multilayer perceptron. The model's input variables are: normal stiffness; initial normal stress acting on the discontinuity; joint roughness coefficient (JRC); ratio *t/a* (fill thickness/asperity height); uniaxial compressive strength and the basic friction angle of the intact rock; and finally the internal friction angle of infill material. To do so, results from 115 direct shear tests, with different soft rock discontinuities conditions were used. The herein proposed ANN predictive model, with an architecture 7-20-1, have shown coefficient of correlation in training and validation of 99.8 % and 99 %, respectively. The results from the model satisfactorily fit the experimental data and were also able to represent the influence of the input variables on the peak shear strength of soft rock discontinuities for different infill and boundary conditions.

1. Introduction

The peak shear strength is the leading mechanical property of interest when adopting limit equilibrium theories for design and analyze a project whose failure mechanisms are governed by the discontinuities existing in a rock mass. Consequently, it is of the utmost importance to determine it in order to develop rational designs in Rock Mechanics.

Several analytical formulations help estimate the shear strength of rock discontinuities, and it is worth mentioning traditional methods such Patton (1966), Barton (1973), Barton & Choubey (1977), Barton & Bandis (1982, 1990). In such methodologies, the shear strength of rock discontinuities is determined indirectly considering the discontinuities roughness, uniaxial compressive strength of the intact rock or wall strength, and the initial normal stress. These simplified models having been validated by direct shear tests performed under constant normal load conditions (CNL), for certain load conditions. However, parameters such as the presence of infill material and also normal stiffness caused by the surrounding rock mass or rock bolts, which significantly influence the shear strength of the discontinuities are not considered (Ladanyi & Archambault, 1977; Papaliangas et al., 1993; Haque, 1999; Haque & Indraratna, 2000; Indraratna et al., 1999, 2005, 2010, 2012, 2013, 2014, 2015; Oliveira et al., 2009; Naghadehi, 2015; Karakus et al., 2016; Mehrishal et al., 2016; Shrivastava & Rao, 2017). On the other hand, the use of analytical models for rationally considering the effect of the infill and the normal stiffness of the rock discontinuities is hampered by the number of parameters required. These parameters obtained by direct shear tests are not always able to represent the discontinuity's boundary conditions satisfactorily and comprehensively (Ladanyi & Archambault, 1977; Papaliangas et al., 1993; Indraratna et al., 1999; Oliveira et al., 2009).

Nowadays, one of the increasingly used modelling techniques in geotechnical engineering to manage complex, multivariate and nonlinear phenomena are the artificial neural networks (ANN), especially those known as multilayer perceptrons (MLP). Many geotechnical applications have confirmed the efficiency of this tool in model-

#Corresponding author. E-mail address: ana.leite@ifce.edu.br.
1Departamento de Engenharia Hidráulica e Ambiental, Universidade Federal do Ceará, Fortaleza, CE, Brazil.

Submitted on January 9, 2020; Final Acceptance on July 29, 2020; Discussion open until March 31, 2021.
DOI: https://doi.org/10.28927/SR.434575

ling physical phenomena in geotechnics, such as, definition of longitudinal pavement defects (Farias et al., 2003), prediction of physical properties of asphalt materials for paving (Dantas Neto et al., 2004), development of models for estimating settlements in deep pile foundations (Amancio et al., 2014; Dantas Neto et al., 2014); predictive shear behavior in unfilled rock discontinuities (Dantas Neto et al., 2017).

Artificial neural networks are parallel processors massively distributed consisting of single processing units, which have a natural propensity to store experimental knowledge and make it available for use. From a mathematical viewpoint, an artificial neural network can be understood as a set of nodes, or neurons, organized in successive layers, analogous to the human brain. It has been proved useful in developing predictive models of complex, multivariate and nonlinear phenomena, as in the case of the shear strength of rock discontinuities. Among the benefits of making the use of artificial neural networks is the fact that, once their parameters are acquired, the predictive model can be easily implemented in any calculation spreadsheets, thereby facilitating their practical use in engineering.

This study proposes a predictive model for the peak shear strength of soft rock discontinuities by using a multilayer perceptron, a practical method that can be used in engineering daily basis without, in a first moment, the need of large-scale laboratory results, or even the use of hard-to-get parameters. The proposed predictive model presents as input variables the following: normal stiffness (k_n); the initial normal stress (σ_{no}) acting on the discontinuity; roughness of the discontinuity represented by the value of the joint roughness coefficient (JRC) proposed by Barton (1973); influence of the infill represented by the *t/a* ratio (thickness of the infill/asperity height); the characteristics of intact rock represented by uniaxial compressive strength (σ_c) and by the basic friction angle (ϕ_b); and at last the shear strength of the infill, if any, represented by its internal friction angle (ϕ').

2. Shear behavior of rock discontinuities

Peak shear strength of rock discontinuities is one of the critical mechanical properties used in Rock Mechanics design, mainly in situations that make use of limit equilibrium theories to analyze rock masses whose failure mechanisms are governed by such geological structures. There are several analytical methodologies to estimate the peak shear strength of rock discontinuities, the majority of them validated using results from large-scale direct shear tests performed under constant normal load conditions (CNL) and applicable only for cases of unfilled discontinuities.

Patton (1966), based on a series of large-scale direct shear tests under CNL conditions, proposed one of the first analytical models in Rock Mechanics to estimate the peak shear strength of unfilled rock discontinuities with regular roughness profiles. This author states that the failure envelope of unfilled rock discontinuities presents a bilinear behavior represented by the curve B shown in Figure 1. It is observed that: for low levels of normal stress, the peak shear strength (τ_p) is given by sliding between the asperities, as a function of the applied normal stress (σ_n) and friction angle of the discontinuity, which is given by a combination of the basic friction angle (ϕ_r) of the rock and the roughness conditions of the discontinuity, represented by the angle of initial roughness inclination (i_o), as shown in Equation 1; while for high levels of normal load, the shearing occurs producing damage on the asperities, creating a cohesion intercept in the failure envelope given by Equation 2 after the sliding along a flat surface, with a friction angle equal to the basic or residual friction angle (ϕ_r).

Therefore, for low levels of normal stress, the shear strength of the discontinuities is given by the necessary friction to overcome the roughness caused by asperities and the rock-rock shear characterized by the basic friction angle. In contrast, for high load levels, the shear strength is the result og the effort required to produce the failure or degradation of the actual rough edges. Although it is quite a simple model, Patton's (1966) concept was the basis for numerous analytical methodologies, such as, the proposals by Indraratna et al. (2005, 2008a, b, 2013, 2014), Oliveira et al. (2009), Premadasa & Indraratna (2015), Shrivastava & Rao (2017).

$$\tau_p = \sigma_n \tan(\phi_b + i_o) \quad (1)$$

$$\tau_p = c_j + \sigma_n \tan \phi_b \quad (2)$$

Barton & Choubey (1977) proposed a predictive analytical model for the peak shear strength in unfilled discontinuities considering simultaneously the sliding between the asperities and their shearing represented in the bilinear envelope proposed by Patton (1966). In this, the peak shear strength can be estimated from the roughness of the discontinuity represented by the joint roughness coefficient (JRC), the joint compressive strength (JCS), obtained directly from the discontinuity wall using the Schmidt ham-

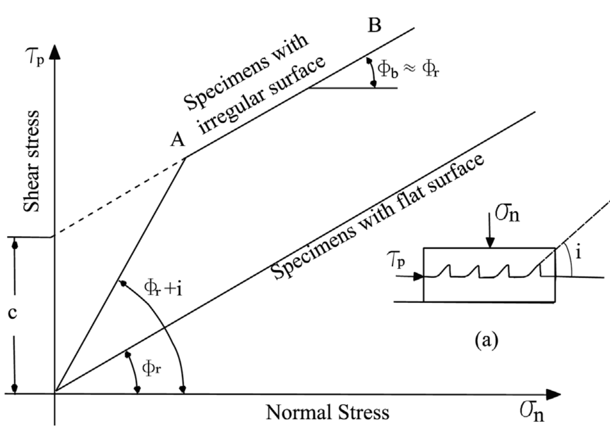

Figure 1. Shear strength envelope proposed by Patton (1966).

mer, and the residual friction angle (ϕ_r), as shown in Equation 3.

$$\tau_p = \sigma_n \tan\left[\mathrm{JRC}\log\left(\frac{\mathrm{JCS}}{\sigma_n}\right)+\phi_r\right] \quad (3)$$

The residual friction angle presented in Equation 3 is estimated as a function of the basic friction angle of the rock (ϕ_b) and of the results of the Schmidt hammer tests as demonstrated in Equation 4.

$$\phi_r = (\phi_b - 20°) + 20\frac{r}{R} \quad (4)$$

where R is the result from the sclerometer test in dry unweathered discontinuities, r is the result from the sclerometer test in wet weathered discontinuities.

Singh & Basu (2018) used results from 196 direct shear tests under CNL conditions to evaluate different analytical models for predicting the peak shear strength in unfilled rock discontinuities. This assessment was made using parameters such as the mean error and the root mean square error between the test results and the predictions from some existing models, obtaining the exposed in Table 1. According to these authors, although the models of Barton (1973) and Barton & Choubey (1977) are some of the most commonly used in Rock Mechanics, the models by Zhang et al., 2016, Yang et al. (2016) and Lee et al. (2014) provided results that are closer to the tests data than those obtained by applying the Barton (1973) and Barton & Choubey (1977) models.

The models by Xia et al. (2014), Zhang et al. (2016), and Yang et al. (2016) use the roughness characteristics of the discontinuities obtained by scanning the rock surface for the peak shear strength estimation, thus considering their three-dimensional morphology. However, having been considered an efficient representation when compared with other models by Singh & Basu (2018), obtaining the necessary parameters is somewhat difficult, considering the methodologies of classification and collecting data originally used in Rock Mechanics.

Studies by Horn & Deere (1962), Goodman (1969), Zeigler et al. (1972), Richard (1975), Ladanyi & Archambault (1977), Papaliangas et al. (1993), Haque (1999), Haque & Indraratna (2000), Indraratna et al. (1999, 2005, 2008a, b, 2010, 2012, 2013, 2014, 2015), Naghadehi (2015), Karakus et al. (2016), Mehrishal et al. (2016) and Shrivastava & Rao (2017), based on large-scale direct shear test results, demonstrate that other parameters not considered in the classical models presented on Equations 1 and 3 are also important when determining the shear strength of the rock discontinuities. Among which mention should be made of the following: the condition of normal stiffness of the discontinuity due the boundary conditions of the surrounding rock mass; type and strength characteristics of the infill material in the rock discontinuities; and the ratio between the infill thickness (t) and average height of the asperities (a), referred to as the t/a ratio.

Papaliangas et al. (1990) studied the shear strength of discontinuities filled with fine particles by carrying out direct shear tests on artificially shaped sandstone rock discontinuities with different JRC values (Figure 2). The authors' results showed a drop in the peak shear strength of

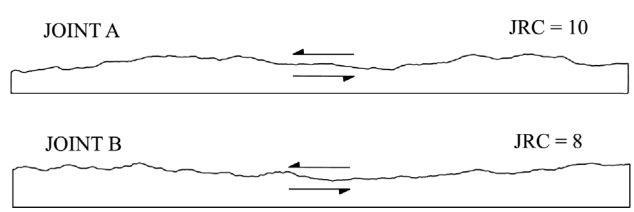

Figure 2. Discontinuity profiles tested by Papaliangas et al. (1990).

Table 1. Comparison between analytical methods for predicting the peak shear strength in rock discontinuities (Singh & Basu, 2018).

Shear strength criteria	Granite		Quartzite		Sandstone	
	Avg. error (%)	RMSE	Avg. error (%)	RMSE	Avg. error (%)	RMSE
Barton (1973)	12.17	0.102	26.68	0.198	20.57	0.185
Aydan et al. (1996)	21.06	0.188	20.12	0.175	31.93	0.304
Tatone & Grasselli (2009)	67.22	0.567	39.23	0.352	55.57	0.41
Gahzvinian et al. (2012)	55.07	0.448	30.82	0.262	44.19	0.307
Lee et al. (2014)	16.8	0.118	15.7	0.132	13.82	0.129
Tang et al. (2014)	27.45	0.224	13.87	0.102	12.16	0.096
Xia et al. (2014)	17.8	0.152	15.05	0.109	10.09	0.087
Jang & Jang (2015)	102.43	0.774	81.72	0.649	192.68	1.444
Kumar & Verma (2016)	22.05	0.241	19.54	0.136	18.57	0.181
Yang et al. (2016)	10.48	0.092	18.37	0.132	11.63	0.11
Zhang et al. (2016)	11.07	0.085	21.85	0.155	14.14	0.12

the rock discontinuities with the increase of the *t/a* ratio up to a critical value between 1.25 and 1.5. From this critical value of *t/a*, the shear strength of the rock discontinuity tends to remain constant, its strength becomes controlled only by the infill material.

Based on large-scale direct shear test results performed on infilled rock discontinuities under CNL, Papaliangas et al. (1993) proposed a model to estimate the friction coefficient (μ) of the discontinuity that considers the effect of the infill as seen in Equation 5 and Figure 3. In this equation, c and m are experimental constants, where *c* represents the critical *t/a* ratio and *m* the rate of shear strength reduction with the increase of infilling thickness. The authors recommend the following values: *c* = 1 for clayey infills and *c* = 1.5 for granular materials.

$$\mu = \mu_{\min} + (\mu_{\max} - \mu_{\min})^{\left[1 - \frac{1}{c}\left(\frac{t}{a}\right)\right]^m} \tag{5}$$

Indraratna et al. (1999), in their experimental study, found that the influence of infill on the peak shear strength of saw-tooth soft rock discontinuities tested under CNL (constant normal load) and CNS (constant normal stiffness) conditions were similar. Those authors noted that there was a sharp drop in dilation during the shearing when the infill began to influence the failure mechanism of the rock discontinuities and proposed an hyperbolic equation to determine the drop in shear strength of the infilled discontinuities with the rise of the *t/a* ratio as shown in Equation 6.

$$\tau_{p,\,infilled} = \tau_{p,\,unfilled} - \sigma_{no} \frac{\frac{t}{a}}{\alpha\left(\frac{t}{a}\right) + \beta} \tag{6}$$

where $\tau_{p,infilled}$ is the peak shear strength of infilled discontinuity, $\tau_{p,unfilled}$ is the peak shear strength of unfilled discontinuity, σ_{no} is the initial normal stress acting on the rock discontinuity, α and β are empirical parameters.

Haque (1999) also proposed that the peak shear strength could be expressed by a Fourier series, as shown in Equation 7, with parameters regarding also the boundary conditions acting on the discontinuity, expressed by the initial normal stress (σ_{no}), normal stiffness (k_n), *t/a* ratio, basic

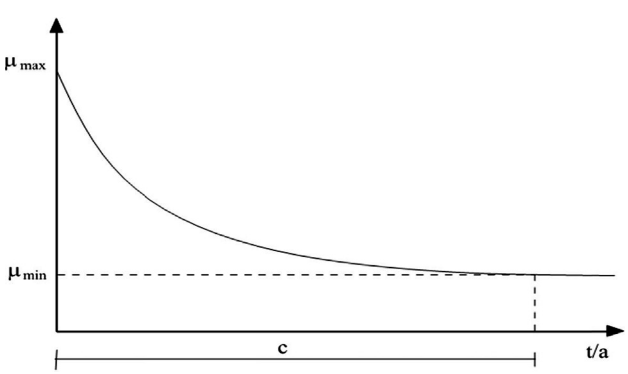

Figure 3. Variation of friction coefficient μ with the *t/a* ratio (Papaliangas et al., 1993).

friction angle (ϕ_b), and initial asperity angle (i_o). In Equation 7, h_p and i_{hp} are the horizontal displacement and dilation angle corresponding to the peak shear stress. The a_0, a_1 and T are the Fourier series parameters obtained by interpolating the experimental data from large-scale direct shear tests.

$$\tau_{p,\,infilled} = \left[\sigma_{no} + \frac{k_n}{A}\left(\frac{a_0}{2} + a_1 \cos\frac{2\pi h_p}{T}\right)\right] \times \left[\frac{\tan\phi_b - \tan i_o}{1 - \tan\phi_b - \tan i_{hp}}\right] - \sigma_{no}\frac{\frac{t}{a}}{\alpha\left(\frac{t}{a}\right) + \beta} \tag{7}$$

Oliveira et al. (2009) developed the model shown in Equation 8 to predict the peak shear strength from direct shear tests under CNS conditions in saw-tooth rock discontinuities. In such a proposal, the authors considered the cohesion (c_{fill}) and friction angle (ϕ_{fill}) of infill material, and the $(t/a)_{cr}$ ratio in the estimation of peak shear strength, the dilatation angle at peak shear stress for clean joint ($i_{\tau p(clean)}$) and when compared to that one proposed by Haque (1999) and shown in Equation 7.

$$\tau_{p,\,infilled} = c'_{fill} + \sigma_n \left[\frac{\tan\phi_b + \tan i_0}{1 - \tan\phi_b - \tan i_{\tau p(clean)}}\right] \times \left(1 - \frac{\frac{t}{a}}{\left(\frac{t}{a}\right)_{cr}}\right)^{\alpha} + \tan\phi_{fill}\left(\frac{2}{1 + \frac{\left(\frac{t}{a}\right)_{cr}}{\frac{t}{a}}}\right)^{\beta} \tag{8}$$

Shrivastava & Rao (2017) proposed a model to obtain the peak shear strength of infilled rock discontinuities after direct shear testing on saw-tooth rock discontinuities under CNL and CNS conditions, for different values of the *t/a* ratio, whose infill material was formed by fine sand and mica powder, and different roughness conditions. The model proposed by these authors uses the basic friction angle (ϕ_b) and the uniaxial compressive strength (σ_c) of the intact rock, the initial normal stress (σ_{no}) acting on the discontinuity, and the roughness of the discontinuity represented by the angle of its asperities (*i*), as shown in Equation 9. According to the authors, the parameter *a* can be close to the unit value (*a* = 1), and the value of *b* ranges from zero to 0.36, while constants *x* and *y* are obtained according to the conditions presented in Table 2.

$$\tau_p = (a\sigma_n + b)\tan\left[\phi_b + x\ln\left(\frac{a\sigma_n + b}{\sigma_c} + y\right)i\right] \tag{9}$$

Studies seeking to include the effect of infill material conditions (overconsolidation, unsaturation, water flow) in its shear strength were also implemented (Indraratna et al., 2008a, b, 2013, 2014; Premadasa & Indraratna, 2015). Such studies have shown that the evaluation of the influence of the various parameters on the peak shear strength of

Table 2. Coefficients *x* and *y* for different *t*/*a* values for be used in Equation 9.

i	*t*/*a*	*x*	*y*	R^2
30°-30°	0	-0.3	-0.356	0.95
	1	-0.26	-0.494	0.96
	1.4	-0.33	-0.821	0.99
	2	-0.13	-0.906	0.75
15°-15°	1	-0.51	-1.14	0.88
0°-0°	*t* = 5 mm	-0.07	0.73	0.99

the discontinuities has contributed to propose analytical models that satisfactorily represent this property for the widest variety of rock discontinuities and boundary conditions. However, the use of such analytical methodologies is still somewhat laborious, bearing in mind the need in specific cases to perform detailed laboratory tests to obtain the parameters required.

In order simplify the predictive process of the shearing behavior of discontinuities, eliminating many existing problems in the use of the current analytical proposals, it is worth mentioning some predictive models developed with artificial neural networks (ANN), fuzzy logic and neuro-fuzzy techniques, for instance the proposals by Dantas Neto et al. (2017), Matos (2018), and Matos et al. (2019a, b). Such models do not intend to replace other models or tests, but they present themselves as tools that can be used for estimating dilation and shear stress data of rock discontinuities enabling fast applications compatible with the day-to-day demands in engineering. Despite the good results presented by these models, they did not consider the infill materials which was the motivation for the present study.

3. Artificial neural networks

3.1 Basic concepts

Nowadays Artificial Neural Networks (ANN) are the computer models most commonly used in different areas of knowledge (Schmidhuber, 2015). ANN are based on the functioning of the human brain and its capacity to perceive and learn complex, nonlinear and multivariate phenomena (Dantas Neto et al., 2017; Chen et al., 2018; Schmidhuber, 2015).

Among the different kinds of existing artificial neural networks with well-proven applications in engineering, it is worth mentioning the multilayer perceptron (Dantas Neto et al., 2014, 2017; Schmidhuber, 2015; Haykin, 2008). The multilayer perceptron (MLP), illustrated in Figure 4, is a neural feedforward network comprising three types of layers: the input layer, consisting of nodes designed to receive stimulus from outside the system, that is, the values of the variables governing the modelled phenomenon; one or more hidden layers of neurons, responsible for increasing the capacity of the artificial neural network in extracting the most complex behavior or the environment in which it intends to establish a predictive model; and the output layer, comprising neurons whose signals are responses to the stimulus presented to the neural network.

Figure 5 shows the structure of each constituent artificial neuron of a multilayer perceptron, whose response in mathematical terms is obtained by successively applying Equation 10 to 12 (Haykin, 2008).

$$u_k = \sum w_{km} x_m = \{w\}^T \{x\} \tag{10}$$

$$v_k = u_k + b_k = \{w\}^T \{x\} + b_k \tag{11}$$

$$y_k = f(v_k) = f(\{w\}^T \{x\} + b_k) \tag{12}$$

where x_m are input variables, w_{km} are synaptic weights, v_k is the induced local field, u_k is the output of linear combiner, b_k is the bias, v_k is the induced local function, *yk* is the neuron output result, d_k are the expected result, *ek* is the output neuron error.

One of the most relevant properties of a neural network is its skill to learn from the environment in which it is inserted and to improve its performance through an ongoing training process. Training an artificial neural network consists of altering all synaptic weights (w_{kj}) and existing

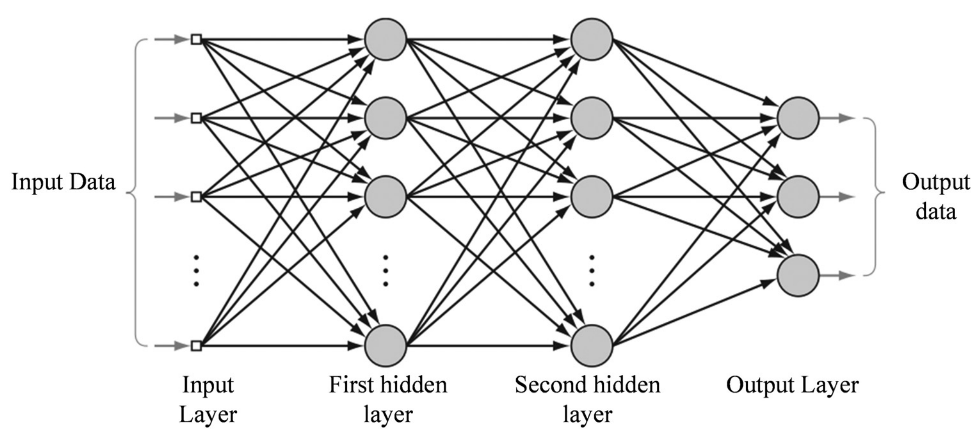

Figure 4. Diagram of a multilayer perceptron (Haykin, 2008).

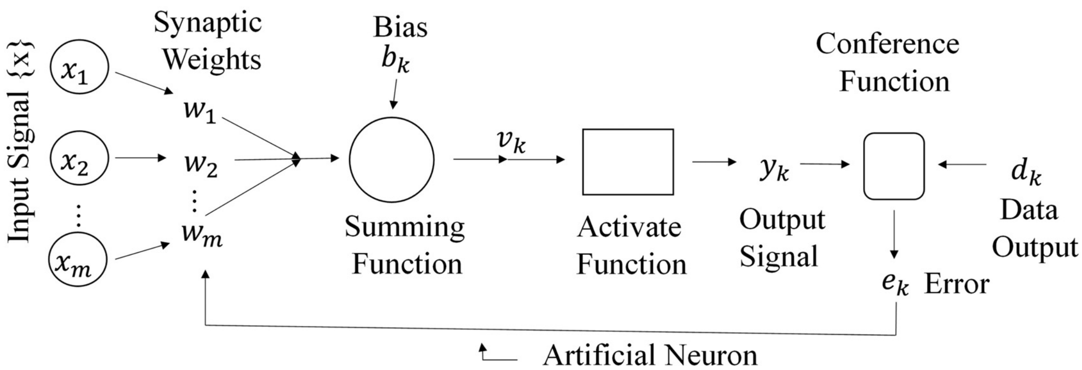

Figure 5. Diagram of an artificial neuron.

bias (b_k), from the known experience of the phenomenon studied, commonly available in a set of known in-out experimental data.

The performance of a neural network can be assessed by comparing the values obtaining for each neuron existing in the output layer with its corresponding one available in the training set, based on an average cost function defined as:

$$E_{med}(n) = \frac{1}{2L}\sum_{i=1}^{L}\sum_{kec} e_k^2 = \frac{1}{2L}\sum_{i=1}^{L}\sum_{kec}[d_k(i) - y_k(i)]^2 \tag{13}$$

where c is the set of all neurons from the output layer in the example I of the training set, $d_k(i)$ is the desired (known) output for the neuron k, in example i, $y_k(i)$ is the response calculated by neuron k, for the stimuli known in example i, $e_k(i)$ is the error signal of neuron k, in example i, n is the discrete period (period), corresponding to each alteration in the set of synaptic weights in the training set.

The training process of a neural network consists of successive adjustments of its synaptic weight to minimize the value of the average cost function throughout the available training set. For one neuron belonging to the output layer $y_k(n)$, the vector of the synaptic weights linking to the neurons of the previous layer $\{y_j(i)\}$ is adjusted by interactively minimizing the average cost function passing throughout the training set. This rule for altering the synaptic weights, known as Delta Rule, is described by the following expression:

$$\begin{aligned} w_{kj}(n+1) &= w_{kj}(n) - \eta\nabla E_{med}(n) \\ &= w_{kj}(n) + \frac{\eta}{L}\sum_{i=1}\delta_k(i)y_k(i) \end{aligned} \tag{14}$$

where $w_{kj}(n+1)$ is the vector of synaptic weights between neurons k and j in the iteration (period) n+1, $w_{kj}(n)$ is the vector of synaptic weights between neurons k and j in the iteration n, $\nabla E_{med}(n)$ is the gradient of the average cost function, η is the learning rate, $y_j(i)$ is the vector of neuron input $y_k(n)$ in the nth example available in the training set, $\delta_k(i)$ is the local gradient of neuron $y_k(n)$, defined as:

$$\delta_k(i) = e_k(i)f'(v_k(i)) \tag{15}$$

where $e_k(i)$ is the error signal of neuron $y_k(i)$ in the nth example of the training set, $v_k(i)$ is the induced local field of neuron $y_k(i)$ in the nth example of the training set.

For a neuron in the hidden layer, the direct calculation of the local gradient, according to Equation 15 is not possible, since the signal produced therein cannot be compared to a known value and, therefore, no error signal can be generated. In this case, the local gradient of the neuron in the hidden layer is determined by back-propagation of the error signal produced in the neurons in the output layer $y_k(i)$. This procedure is known as error backpropagation algorithm and was developed by Rumelhart et al. (1986), based on which the local gradient of a neuron belonging to a hidden layer immediately before the output layer is defined as:

$$\delta_j(i) = -\frac{1}{L}f'(v_j(i))\sum_i\sum_{k\in C}\delta_k(i)w_{kj}(n) \tag{16}$$

Bearing in mind the heavy dependence of the backpropagation algorithm convergence on the value of the learning rate adopted, Rumelhart et al. (1986) also proposed to introduce a parameter α, known as constant of momentum, in Equation 14 in order to improve the stability of the algorithm convergence resulting in the expression presented by Equation 17.

$$w_{kj}(n+1) = w_{kj}(n) + \frac{\eta}{L}\sum_{i=1}\delta_k(i)y_k(i) + \alpha(\Delta w_{kj}(n-1)) \tag{17}$$

3.2 Applications of the artificial neural networks in Rock Mechanics

In Rock Mechanics many studies were performed using neural networks as a powerful and valuable tool for developing predictive models. The majority of them contemplate the prediction of intact rock properties such as the uniaxial compressive strength (Grima et al., 2000; Moshrefii et al., 2018), Young's modulus (Sonmez et al., 2016; Yilmaz & Yusek, 2008; Dehghan et al., 2010), and even tensile strength (Singh et al., 2001). Concerning the development of predictive models for rock discontinuities using MLP, it is worth mentioning the studies by Dantas Neto et al. (2017) and Leite et al. (2019).

Dantas Neto et al. (2017) proposed a model of six input variables (normal stiffness, initial normal stress, JRC, uniaxial compressive strength of intact rock, basic friction angle and shear displacement), a hidden layer with 20 neurons, with the shear stress and dilation as the network outputs. This model was based on 44 direct shear tests obtained from the studies by Benmokrane & Ballivy (1989), Skinas et al. (1990), Papaliangas et al. (1993), Haque & Indraratna (2000), and Indraratna et al. (2010) and provided coefficients of correlation of 0.99 in both the training and testing phases. Although the results from the model satisfactorily fit the test results used in its development and can also satisfactorily express the influence of the input variables in the shear strength and dilation, this model is also to unfilled discontinuities.

Dantas Neto et al. (2018) provided an ANN predictive model of the shear strength of the unfilled discontinuities only for soft rock, considering as input variables normal stiffness (k_n), initial normal stress (σ_{no}), height (a) and initial inclination (i_o) of joint asperities and shear displacement (h) imposed on the discontinuity. The correlation coefficients were also high, approximately 0.99, both in the training and testing phases. This model's main limitations lie in the fact that the impact of the infill on the shear strength is not considered.

Leite et al. (2019) proposed a predictive model similar to the model suggested by Dantas Neto et al. (2017) but including the influence of the infill on the shear behavior of the rock discontinuities. This neuronal model has an A:8-20-10-5-2 architecture, with eight (8) input neurons and three (3) hidden neuron layers, providing as output the shear stress and dilation of the rock discontinuity as a function of shear displacement imposed on the discontinuity. Correlation coefficients of 0.99 were obtained in both the training and validation phases of the model, which showed proper adjustments to the test data used in developing the model. This work was still preliminary with no further applicable information provided about the ANN model used and required a horizontal displacement data for its application.

4. Development of model

4.1 Data collection and definition of input variables

The present predictive model was developed based on the results of 115 direct shear tests performed by Haque & Indraratna (2000), Haque (1999), Indraratna et al. (2010), Oliveira et al. (2009), and Shrivastava & Rao (2017) on soft rock discontinuities with different characteristics and boundary conditions. The parameters used are listed below in Table 3. From the tests, 58 % were performed on infilled discontinuities and 67 % carried out under CNS conditions.

Based on the literature review, it is undeniable that the peak shear strength of the rock discontinuities is governed by its boundary conditions, roughness characteristics, intact rock properties and by the condition and shear strength characteristics of infill materials. Consequently, the following parameters were adopted as input variables for the predictive ANN model for the peak shear strength of soft rock discontinuities:

- x_1 = normal stiffness of the discontinuity (k_n), in kPa/mm;
- x_2 = t/a ratio;

Table 3. Joint parameters used in the ANN development.

Reference	Data	Joint type	Filling material	Limit	Normal stiffness (kPa/mm)	t/a	σ_{n0} (MPa)	JRC	σ_c (MPa)	ϕ_b (°)	ϕ_{fill} (°)	τ_p (MPa)
Indraratna & Haque (2000) and Haque (1999)	62	Saw-toothed	Bentonite	Min	0	0	0.16	2	12	32	0	0.14
				Max	453	1.8	2.69	13	20	37.5	35.5	3.34
Papaliangas et al. (1993)	11	Natural	Granular material	Min	0	0	0.05	12	3.5	30	0	0.02
				Max	0	1.1	0.1	12	3.5	30	30	0.1
Oliveira (2009) and Indraratna et al. (2010)	5	Saw-toothed	Clayey sand	Min	453	0	0.8	8	21.5	35.5	0	0.38
				Max	453	2	0.8	8	21.5	35.5	27.5	1.63
Shrivastava & Rao (2017)	37	Saw-toothed	Fine sand and mica dust	Min	0	0	0.05	7	11.75	30	0	0.08
				Max	90.7	2	2.04	15	11.75	30	28.8	2.6

- x_3 = initial normal stress (σ_{no}) acting on the discontinuity, in MPa;
- x_4 = JRC;
- x_5 = uniaxial compressive strength of intact rock (σ_c), in MPa;
- x_6 = basic friction angle (ϕ_b), in degrees;
- x_7 = internal friction angle of the discontinuity infill material (ϕ_{fill}), in degrees.

Although in the different studies that used experimental data to develop the model, the uniaxial compressive strength had been obtained from uniaxial compressive tests, in this study it is recommended that the σ_c value to be used for representing the uniaxial compressive strength of the intact rock be obtained from the Schmidt hammer. As a result, it shall take into account the change in intact rock properties, due to weathering action, in the determination of the rock discontinuities peak shear strength.

The expression in Equation 18 broadly represents the predictive model of the peak shear strength of soft rock discontinuities depending on their governing variables. The relationship between input and output variables of the neuronal model are defined by the neural network architecture, activation functions of its neurons and the values obtained for the synaptic weights and bias.

$$\tau_p = f\left(k_n, \frac{t}{a}, \sigma_{no}, \mathrm{JRC}, \sigma_c, \phi_b, \phi_{fill}\right) \tag{18}$$

4.2 Training, testing and validation of the neuronal model

In order to set up the predictive neuronal model of the peak shear strength of soft rock discontinuities, eight (8) different architectures (7-30-1; 7-20-1; 7-15-1; 7-10-1; 7-30-15-1; 7-20-10-1; 7-30-15-5-1; 7-20-10-5-1) were used and submitted to the training, testing and validation phases

Training each ANN model represented by specific architecture consists of altering the synaptic weights using the backpropagation algorithm of Rumelhart et al. (1986) and the experimental data available in the training set formed by 80 %, randomly selected, of the 115 results of the aforementioned direct shear tests. During the training phase, the performance of each neuronal model studied was assessed from the variation in the number of iterations vs. the coefficient of correlation between the value of the output supplied by the neuronal model and the existing target-value in the training set for each used input-output example. In this study, the alterations in the synaptic weights occurred up to a maximum of 1,000,000 iterations.

Test phase used the remaining 20 % of input-output examples in the available experimental data set that were left unused in the neuronal model training phase to assess the performance of the models when predicting data to which they were not submitted during the training phase. In addition to assessing the models' performance, monitoring the correlation values with the number of iterations in the test phase, also helps identify the optimal stopping point aiming to prevent any overfitting process that tends to impair the generalization capacity of the neuronal models (Haykin, 2008).

Validation phase consisted of assessing the neuronal models for the different architectures previously described by comparing the models' results with the test results. This enabled the identification of which models have enough capacity to properly interpolate the test results and satisfactorily express the influence of the different input variables in the peak shear strength of soft rock discontinuities.

The feedforward multilayer perceptron with back-propagation software QNET2000 was used in the training, testing and validation phases of the studied neuronal models. The sigmoid function given in Equation 19 was adopted to activate all neurons in the neuronal models studied because it is one of the most commonly used activation functions with satisfactory results in developing multilayer perceptron neuronal models (Runxuan, 2006; Dantas Neto et al., 2017, and Moshrefii et al., 2018).

$$f(x) = \frac{1}{1 + e^{-x}} \tag{19}$$

To calculate the error signals between the values available in the training set and those calculated by the studied neuronal models using the sigmoid function for activating the neurons in the output layer, it was necessary to normalize the input and output data available in the training and testing sets. This study involves normalizing these data in the 0.15 to 0.85 interval according to the Equation 20. Table 4 provides the variation intervals for the input and output variable values existing in the experimental set used for training and testing the studied neuronal models.

$$\frac{x_{nor} - 0.15}{0.85 - 0.15} = \frac{x - x_{\min}}{x_{\max} - x_{\min}} \tag{20}$$

Table 4. Maximum and minimum values used for ANN training and validation.

k_n (kN/mm)	t/a	σ_{no} (MPa)	JRC	σ_c (MPa)	ϕ_b (°)	ϕ_{fill} (°)	τ_p (kPa)
0	0	0.05	2	3.5	30	21	20.8
453	2	2.69	15	21.5	37.5	35.5	3343

where x_{nor} is the normalized variable value, x_{min} is the minimum variable value in the training set, x_{max} is the maximum variable value in the training set.

In order to optimize the training process and, when altering the synaptic weights, avoid affecting any minimal points of the cost function, a variation range was used for the learning rate (η) of 0.001 and 0.1, and adopted the 0.8 value for the constant of momentum (α).

The criteria to define the best performing neuronal model to predict the peak shear strength of the soft rock discontinuities took into account the following aspects in order of priority: highest correlation value between the values available in the experimental set adopted and those calculated by the neural network in the test phase; the model's capacity to interpolate test data; and the model's capacity to represent the influence of input variables on the peak shear strength of soft rock discontinuities; and, in case of similarity for the above criteria, the model formed by the architecture with the smallest number of synaptic weights will be adopted.

5. Results and discussions

5.1 Training, testing and defining the model

Within the eight architectures studied in the search for a predictive neuronal model for the peak shear strength of soft rock discontinuities, the one with architecture 7-20-1 had the best performance since it provided in both the training and testing phases a correlation between the experimental data and results calculated by the neuronal model equal to 0.99 after 337,000 iterations. Figure 6 illustrates the architecture of the proposed neuronal model whose synaptic weights between the different neuron layers and their biases are addressed in Tables 5 to 7.

5.2 Validation of ANN model

As mentioned earlier, validation of the proposed neuronal model after the training and testing phases consists of comparing the results with their application and test data for different soft rock discontinuities.

Figure 7 shows comparisons of the failure envelopes from direct shear test results carried out under CNL conditions presented by Shrivastava & Hao (2017), the results from the proposed ANN model and those ones estimated

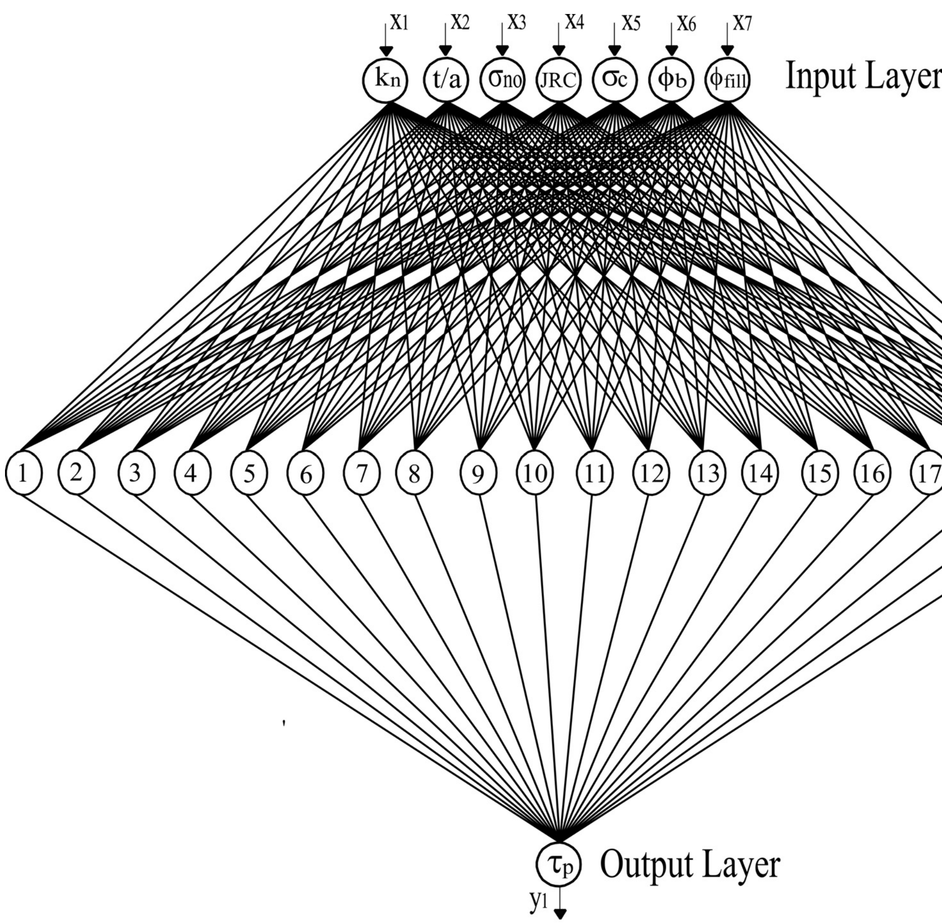

Figure 6. ANN model architecture 7-20-1.

Table 5. Synaptic weights (*wki*) and bias (*bk*) of neurons in hidden layer.

Input	Hidden layer									
	1	2	3	4	5	6	7	8	9	10
x_1	0.1416	-0.8811	0.193	-0.1562	0.0562	-2.3061	-1.9421	3.0309	1.375	0.526
x_2	-0.2145	-0.0837	-0.5042	0.3932	-0.2649	2.3582	-3.7504	-0.8594	0.4828	-0.365
x_3	0.0063	0.16	0.8752	-1.1484	-0.1157	12.786	0.5292	-1.5711	-2.5849	0.1757
x_4	-0.2017	0.7687	-0.3094	0.6241	-0.4964	0.7973	5.2511	-1.2502	0.829	-0.2095
x_5	0.1704	-0.0202	-0.4904	-0.1536	-0.2423	1.6387	-0.2118	0.0581	0.3203	0.0923
x_6	0.2337	-1.1127	0.6014	-0.1615	-0.5537	1.2615	-2.7554	3.2622	0.4041	0.301
x_7	-0.2355	-0.5445	0.6088	-0.0838	-0.5975	3.0077	2.8265	-0.5001	-2.133	0.0831
Bias	0.289	0.4365	0.0379	-0.1559	-0.0911	-1.5388	-0.4761	0.4959	0.7315	0.2195

Table 6. Synaptic weights (*wki*) and bias (*bk*) of neurons in hidden layer (cont.).

Input	Hidden layer									
	11	12	13	14	15	16	17	18	19	20
x_1	-3.2523	-4.881	-0.5783	0.5272	1.5663	0.0281	-0.3282	-0.3803	-3.2965	-2.6106
x_2	-2.3051	-3.6737	5.3678	-0.7055	-1.1681	0.0205	0.2985	0.3775	1.3031	3.7516
x_3	-4.9798	-6.6378	-4.9182	0.899	-0.5241	-0.1658	-0.4961	-0.4149	2.2127	0.3535
x_4	0.9742	0.773	-3.1227	-0.5871	-15.764	0.1729	0.0643	0.7375	4.4023	2.8022
x_5	0.217	-1.6545	3.8664	-0.9088	-1.2279	0.0344	0.3095	0.0699	0.0123	1.0277
x_6	0.9007	2.5998	-0.7639	0.7168	2.54	0.0568	-0.6372	-0.7115	-1.2114	-1.3662
x_7	0.1656	3.262	-0.443	1.2052	-0.427	-0.0958	-0.3801	-0.7264	2.7936	-2.4229
Bias	1.6647	1.2909	4.5642	0.1562	-0.2943	0.1202	0.0439	0.1577	-0.1563	-0.0681

Table 7. Synaptic weights (*wk*i) and bias (*bk*) of neurons in output layer.

Output	Hidden layer										
	1	2	3	4	5	6	7	8	9	10	
t	-0.0815	-1.8272	1.0229	-1.3309	-0.6106	5.8633	2.8745	3.363	-3.4452	0.3857	
Output	Hidden layer										
	11	12	13	14	15	16	17	18	19	20	Bias
t	4.1295	-4.2364	-4.5397	1.6681	-7.9778	-0.4047	-1.1373	-1.6871	-4.4917	3.0341	-1.0859

based on the analytical model by Barton and Choubey (1977) for a soft rock discontinuity with σ_c = 11.75 MPa, JRC = 15, ϕ_b = 30° and infill material with ϕ_{fill} = 28.8°. The results show that the neuronal model is able to interpolate the experimental data, and to represent the nonlinear behavior of the failure envelopes as the influence of normal stress and the presence of the infill in the peak shear strength of soft rock discontinuities. Moreover, it more realistically reproduces the shear behavior of the unfilled discontinuity (*t*/*a* = 0) than the analytical model of Barton & Choubey (1977).

Figure 8 shows the variations in the peak shear strength with the *t*/*a* ratio for the soft rock discontinuities studied by Haque and Indraratna (2000) under CNS conditions with k_n = 453 kPa/mm, JRC = 4 and 8, σ_c = 12 MPa and ϕ_b = 37.5°, and those obtained by the proposed neuronal model with architecture 7-20-1 for a initial normal stress (σ_{no}) equal to 0.56 MPa, with the infill material of ϕ_{fill} = 35.5°. The results show that the neuronal model once again satisfactorily fit the experimental data and it is also able to express the increase in peak shear strength with the rise in roughness of the discontinuity to low *t*/*a* ratio values, and the drop in peak shear strength with the increase in the *t/a* ratio. Similar results were achieved with the neuronal model for soft rock discontinuities and with very low uniaxial compressive strength values (σ_c = 3.5 MPa), JRC = 12, σ_{no} = 0.1 MPa, ϕ_b = 30° and ϕ_{fill} = 30° like those studied by Papaliangas et al. (1993) under CNL conditions, as shown in Figure 9.

Table 8 shows the contribution in percentages of each input variable in the proposed neuronal model's response with architecture 7-20-1 provided by software QNET2000. The results show that within the input variables considered, the initial normal stress, roughness and *t/a* ratio, that is, the infill, contribute the most in the prediction of the value of the peak shear strength of soft rock discontinuities. Since none of the input variables had a much smaller contribution than the others, the general

Table 8. Contribution of input variables to the model's response.

k_n	t/a	σ_{n0}	JRC	σ_c	ϕ_b	ϕ_{fill}
6 %	13 %	33 %	20 %	9 %	9 %	10 %

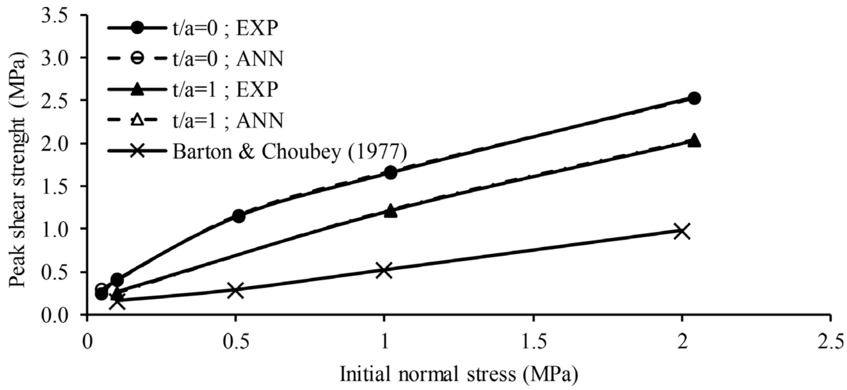

Figure 7. Failure envelopes for soft rock discontinuities from Shrivastava & Hao (2017).

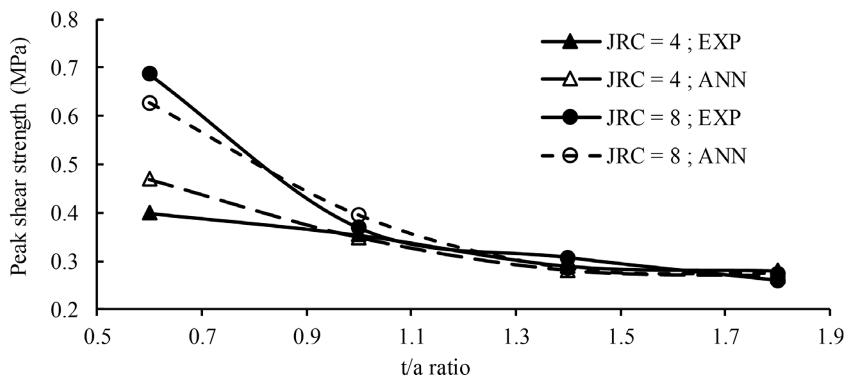

Figure 8. Variation in shear peak strength with the *t/a* ratio for soft rock discontinuities from Haque & Indraratna (2000).

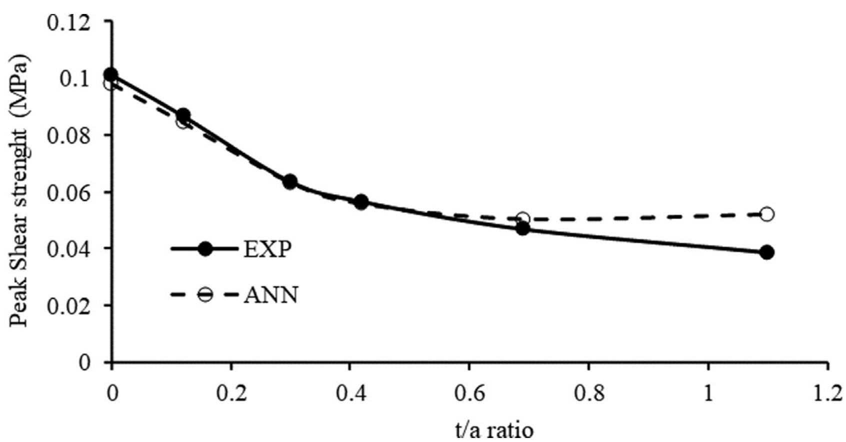

Figure 9. Variation of the shear peak strenght with the *t/a* ratio for very soft rock discontinuities from Papaliangas et al. (1993).

conclusion is that every variable considered in developing the model is relevant regarding the prediction of the peak shear strength of the soft rock discontinuities studied.

5.3 Routine for the use of neuronal model

When developing a neuronal model, the knowledge regarding the phenomenon studied is stored in the values of the synaptic weights and bias obtained after completing the training and testing processes and having made the due validations on the model's behavior. Therefore, knowing about these parameters helps implement the neuronal model in any calculation spreadsheet without requiring specific software, thereby facilitating the use of the predictive model in practical problems in the Rock Mechanics field.

First, after defining the boundary conditions, roughness, intact rock properties and characteristics of the infill material, the input parameters of the rock discontinuity must be normalized using the expression in Equation 20 and the information provided in Table 4. Once the normalized values of the input parameters are in hand, each hidden layer neuron is calculated using the data presented in Tables 5 and 6, and Equations 10-12, adopting the expression in Equations 19 to calculate the output signal of each hidden layer neuron.

Having calculated all hidden layer neurons, their feedforward values calculate the output layer neuron, using the same aforementioned calculation sequence and the synaptic weights and bias in Tables 7 and 8. After using the sigmoid function to calculate the model's response, the peak shear strength of the rock discontinuity in the units system in Table 4 is obtained by transforming the normalized value for the neuron in the output layer also using Equation 20.

The ANN model can be easily used for the representation of constitutive models in numerical analysis. This can be performed using the input variables and the values presented for the synaptic weights and biases in some code to predict the shear behavior of the infilled rock joints.

6. Conclusions

The proposed neuronal model was obtained from 115 large-scale direct shear test results, and the use of 80 % of data available for training and 20 % for validation was efficient, since the proposed neuronal model not only satisfactorily interpolated the test data but was also able to represent the impact of the input variables on the shear strength of soft rock discontinuities, such as, for example, the increase in the peak shear strength with rise in normal stiffness, initial normal stress, roughness and its drop with the increase in the *t/a* ratio. It is worth mentioning, within the input variables used to develop the proposed neuronal model, the initial normal stress (σ_{no}) and ratio (*t/a*) as those that most contribute to the model's response.

It is found from the results that the neuronal model that performed best had an architecture 7-20-1, that is, was made up of 7 input variables (normal stiffness, *t/a* ratio, JRC, uniaxial compressive strength of intact rock in the discontinuity, basic friction angle, and internal friction angle of infill material), 20 neurons in a single hidden layer, the answer being the peak shear strength of soft rock discontinuities. For this model, a correlation was obtained between the calculated and test results of 0.99 after 337,000 iterations in both the training and testing phases.

Since one of the critical characteristics of the artificial neural networks is their capacity to generalize, the proposed neuronal model has diverse application, despite being developed using input data within certain value ranges. Once limitations can be considered only that their application should be restricted to soft rock discontinuities, and should infill material be present, it is of a granular nature, since in the proposed neuronal model the cohesion mechanism was not considered to represent the shear strength of the fill material.

Lastly, it is found that the use of multilayer perceptrons for modelling complex, nonlinear and multivariate phenomena, as in the present case of the shear behavior in soft rock discontinuities it is a valuable tool. Results obtained from the ANN model can be considered satisfactory, even when compared to the use of well-established analytical models. One of its many benefits is the fact that once the training and testing processes are over, and the model duly validated, knowing the architecture of the network, synaptic weights, bias and activation functions of all neurons, it is easy to implement the model in calculation spreadsheets without requiring major computer resources or complex laboratory parameters which availability is still limited.

It is worth emphasizing that the use of artificial neural networks as tools to predict engineering phenomena would not replace any necessary test procedures to determine geotechnical properties of the materials involved in some problem. This tool appears only as an initial additional means to achieve a satisfactory response to a certain problem in order to optimize all the experimental work required.

Acknowledgments

The authors thank Funcap (Fundação Cearense de Apoio ao Desenvolvimento Científico e Tecnológico) and Capes/Proex for their financial support to the Post-Graduate Civil Engineering Program of the Federal University of Ceará.

References

Amancio, L.B., Dantas Neto, A.S., & Anjos, G.J.M. (2014). Modelo de previsão de recalques em estacas hélice contínua utilizando redes neurais artificiais. *Proc. XVII Congresso Brasileiro de Mecânica dos Solos e Engenharia Geotécnica*, *Goiânia*. ABMS, 1-9.

Aydan, Ö., Shimizu, Y., & Kawamoto, T. (1996). The anisotropy of surface morphology characteristics of rock discontinuities. *Rock Mechanics and Rock Engi-*

neering, 29(1), 47-59. https://doi.org/10.1007/BF01019939

Barton, N.R. (1973). A review of a new shear-strength criterion for rock joints. *Engineering Geology*, 7(4), 287-332. https://doi.org/10.1016/0013-7952(73)90013-6

Barton, N.R., & Bandis, S. (1982). Effect of block size on the shear behavior of jointed rock. *Proc. 23rd US Sympium on Rock Mechanics, Berkeley*. ARMA, 739-760.

Barton, N.R., & Bandis, S. (1990). Review of predictive capabilities of JRC-JCS model in engineering practice. *Proc. International Symposium on Rock Joints, Loen*. Balkema, 603-610.

Barton, N.R., & Choubey, V. (1977). The shear strength of rock joints in theory and practice. *Rock Mechanics*, 10(1), 1-54. https://doi.org/10.1007/BF01261801

Benmokrane, B., & Ballivy, G. (1989). Laboratory study of shear behaviour of rock joints under constant normal stiffness conditions. In *Rock Mechanics as a Guide of Efficient Utilization of Natural Resources* (pp. 899-906). Balkema.

Chen, T.C.T., Liu, C.L., & Lin, H.D. (2018). Advanced artificial neural networks. *Algorithms*, 11(7), 102. https://doi.org/10.3390/a11070102

Dantas Neto, S.A., Farias M.M., & Pais, J.C. (2004). Modelagem da viscosidade absoluta dos asfaltos-borracha usando redes neurais artificiais. *Proc. XVIII Congresso da Associação Nacional de Pesquisa e Ensino em Transportes, Florianópolis*. Vol. 8, ANPET, 28-39 (in Portuguese).

Dantas Neto, S.A., Silveira V.S., Amâncio, L.B., & Anjos, G.M. (2014). Pile settlement modeling with multilayer perceptrons. *Electronic Journal of Geotechnical Engineering*, 19, 4517-4528.

Dantas Neto, S.A., Indraratna, B., Oliveira D.A.F., & Assis, P. (2017). Modelling the shear behaviour of clean rock discontinuities using artificial neural networks. *Rock Mechanics and Rock Engineering*, 50(7), 1817-1831. https://doi.org/10.1007/s00603-017-1197-z

Dehghan, S., Sattari, G., Chelgani, C.S., & Aliabadi, M.A. (2010). Prediction of uniaxial compressive strength and modulus of elasticity for travertine samples using regression and artificial neural networks. *Mining Science and Technology*, 20(1), 41-46. https://doi.org/10.1016/S1674-5264(09)60158-7

Farias M.M., Dantas Neto, S.A., & Sousa, R.O. (2003). Prediction of longitudinal roughness using neural network. *Proc. 3rd International Symposium on Maintenance and Rehabilitation of Pavements and Technological Control, Guimarães*. University of Minho, 87-97.

Ghazvinian, A.H., Azinfar, M.J., & Vaneghi, R.G. (2012). Importance of tensile strength on the shear behavior of discontinuities. *Rock Mechanics and Rock Engineering*, 45(3), 349-359. https://doi.org/10.1007/s00603-011-0207-9

Grima M.A., Bruines, P.A., & Verhoef, P.N.W. (2000). Modeling tunnel boring machine performance by neuro-fuzzy methods. *Tunnelling and Underground Space Technology*, 15(3), 259-269. https://doi.org/10.1016/S0886-7798(00)00055-9

Goodman, R.E. (1969). The deformability of joints: Determination of the in-situ modulus of deformation of rock. *Determination Committee D-18 session, Denver*. ASTM, 174-196.

Haque, A. (1999). *Shear behaviour of soft rock joints under constant normal stiffness* [Doctoral dissertation, University of Wollong]. University of Wollong's repository. https://ro.uow.edu.au/theses/1266/

Haque, A., & Indraratna, B. (2000). Experimental and numerical modeling of shear behaviour of rock joints. *Proc. International Conference on Geotechnical & Geological Engineering, Melbourne*. Vol. 1, Lancaster, 1-6.

Haykin, S. (2008). *Neural Networks and Learning Machines*. Pearson.

Horn, H.M., & Deere D.U. (1962). Frictional characteristics of minerals. *Géotechnique*, 12(4), 319-335. https://doi.org/10.1680/geot.1962.12.4.319

Indraratna, B., Haque, A., & Aziz, N. (1999) Shear behaviour of idealized infilled joints under constant normal stiffness. *Géotechnique*, 49(3), 331-355. https://doi.org/10.1680/geot.1999.49.3.331

Indraratna, B., Welideniya, H.S., & Brown, E.T. (2005). A shear strength model for idealized infilled joints under constant normal stiffness. *Géotechnique*, 55(3), 215-226. https://doi.org/10.1680/geot.2005.55.3.215

Indraratna, B., Jayanathan, M., & Brown, E.T. (2008a). Shear strength model for overconsolidated clay-infilled idealised rock joints. *Géotechnique*, 58(1), 55-65. https://doi.org/10.1680/geot.2008.58.1.55

Indraratna, B., Oliveira D.A.F., & Jayanathan, M. (2008b). Revised shear strength model for infilled rock joints considering overconsolidation effect. *Proc. 1st Southern Hemisphere International Rock Mechanics Symposium, Perth*. ACG, 16-19.

Indraratna, B., Oliveira, D.A.F., & Brown, E.T. (2010). A shear-displacement criterion for soil-infilled rock discontinuities. *Géotechnique*, 60(8), 623-633. https://doi.org/10.1680/geot.8.P.094

Indraratna, B., Fasce, A.M., Oliveira, D.A.F., & Premadasa, W. (2012). Shear behaviour of rock joints under cyclic loading. *Proc. 11th Australia - New Zealand Conference on Geomechanics: Ground Engineering in a Changing World, Melbourne*. AGS & NZGS, 1256-1261.

Indraratna, B., Premadasa, W., & Brown, E.T. (2013). Shear behaviour of rock joints with unsaturated infill. *Géotechnique*, 63(15), 1356-1360. https://doi.org/10.1680/geot.12.P.065

Indraratna, B., Premadasa, W., Brown, E.T., Gens, A., & Heitor, A. (2014). Shear strength of rock joints influenced by compacted infill. *International Journal of Rock Mechanics and Mining Sciences*, 70, 296-307. https://doi.org/10.1016/j.ijrmms.2014.04.019

Indraratna, B., Kumara, C., Zhu, S-P., & Sloan, S. (2015). Mathematical modeling and experimental verification of fluid flow through deformable rough rock joints. *International Journal of Geomechanics*, 15(4), 04014065. https://doi.org/10.1061/(ASCE)GM.1943-5622.0000413

Jang, H.S., & Jang, B.A. (2015). New method for shear strength determination of unfilled, unweathered rock joint. *Rock Mechanics and Rock Engineering*, 48(4), 1515-1534. https://doi.org/10.1007/s00603-014-0660-3

Karakus, M., Liu, Y., Zhang, G., & Tang, H. (2016). A new shear strength model incorporating influence of infill materials for rock joints. *Geomechanics and Geophysics for Geo-Energy and Geo-Resources*, 2(3), 183-193. https://doi.org/10.1007/s40948-016-0032-4

Kumar, R., & Verma, A.K. (2016). Anisotropic shear behavior of rock joint replicas. *International Journal of Rock Mechanics and Mining Sciences*, 90, 62-73. https://doi.org/10.1016/j.ijrmms.2016.10.005

Ladanyi, B., & Archambault, G. (1977). Shear strength and deformability of filled indented joints. In: Proc. *International Symposium on Geotechnics of Structurally Complex Formations.* Vol. 1, AGI, 317-326.

Lee, Y-K., Park, J-W., & Song, J-J. (2014). Model for the shear behavior of rock joints under CNL and CNS Conditions. *International Journal of Rock Mechanics and Mining Sciences*, 70, 252-263. https://doi.org/10.1016/j.ijrmms.2014.05.005

Leite, A.R.S., Dantas Neto, S.A., Polemis Júnior, K., & Oliveira, C.M.O. (2019). Study on the shear behaviour of rock joints using different models of artificial neural networks. *Proc. International Congress on Rock Mechanics and Rock Engineering*, *Foz do Iguaçu*. Vol. 6. CRC Press, 2707-2714.

Matos, Y.M.P. (2018). *Development of models of prediction of the shear behavior in discontinuities without filling of rock masses using fuzzy and neuro-fuzzy techniques* [Master's dissertation, Federal University of Ceará]. Federal University of Ceará's repository. http://www.repositorio.ufc.br/handle/riufc/30223

Matos, Y.M.P., Dantas Neto, S.A., & Barreto, G.A. (2019a). A Takagi-Sugeno fuzzy model for predicting the clean rock joints shear strength. *REM - International Engineering Journal*, 72(2), 193-198. https://doi.org/10.1590/0370-44672018720083

Matos, Y.M.P., Dantas Neto, S.A., & Barreto, G.A. (2019b). Predicting the shear strength of unfilled rock joints with the first-order Takagi-Sugeno fuzzy approach. *Soils and Rocks*, 42(1), 21-29. https://doi.org/10.28927/SR.421021

Mehrishal, S., Sharifzadeh, M., Shahriar, K., & Song, J.J. (2016). An experimental study on normal stress and shear rate dependency of basic friction coefficient in dry and wet limestone joints. *Rock Mechanics and Rock Engineering*, 49(12), 4607-4629. https://doi.org/10.1007/s00603-016-1073-2

Moshrefii, S., Shahriar, K., Ramezanzadeh, A., & Goshtasbi, K. (2018). Prediction of ultimate strength of shale using artificial neural network. *Journal of Mining and Environment*, 9(1), 91-105. https://doi.org/10.22044/jme.2017.5790.1390

Naghadehi, M.Z. (2015). Laboratory study of the shear behaviour of natural rough rock joints infilled by different soils. *Periodica Polytechnica Civil Engineering*, 59(3), 413-421. https://doi.org/10.3311/PPci.7928

Oliveira, D.A.F., Indraratna, B., & Nemcik, J. (2009). Critical review on shear strength models for soil-infilled joints. *Geomechanics and Geoengineering*, 4(3), 237-244. https://doi.org/10.1080/17486020903128564

Papaliangas, T., Lumsden, A.C., Hencher, S.R., & Manolopoulou, S. (1990). Shear strength of modelled filled rock joints. *Proc. International Symposium on Rock Joints*, *Loen*. Balkema, 275-282.

Papaliangas, T., Hencher, S.R., Lumsden, A.C., & Manolopoulou, S. (1993). The effect of frictional fill thickness on the shear strength of rock discontinuities. *International Journal of Rock Mechanics and Mining Sciences and Geomatics*, 30(2), 81-91. https://doi.org/10.1016/0148-9062(93)90702-F

Patton, F.D. (1966). Multiple modes of shear failure in rocks. *Proc. 1st Congress of the International Society for Rock Mechanics*, *Lisbon*. Vol. 1, LNEC, 509-513.

Premadasa, W., & Indraratna. (2015). Shear behaviour of infilled rock joints related to partially saturated infill conditions. *Proc. International Conference on Geotechnical Engineering, Colombo*. SLGS, 1-4.

Richard, L.R. (1975). *The shear strength of joints in weathered rock* [Doctoral dissertation, University of London]. University of London's repository. http://hdl.handle.net/10044/1/22541

Rumelhart, D.E., Hinton, G.E., & Williams, R.J. (1986). Learning representations by back-propagating errors. *Nature*, 323, 533-536. https://doi.org/10.1038/323533a0

Runxuan, Z. (2006). *Efficient sequential and batch learning artificial neural network methods for classification problems* [Doctoral dissertation, Nanyang Technological University]. Nanyang Technological University's repository. https://doi.org/10.32657/10356/3468

Schmidhuber, J. (2015). Deep learning in neural networks: An overview. *Neural Networks*, 61, 85-117. https://doi.org/10.1016/j.neunet.2014.09.003

Shrivastava, A.K., & Rao, K.S. (2017). Physical modeling of shear behavior of infilled rock joints under CNL and CNS boundary conditions. *Rock Mechanics and Rock Engineering*, 51(1), 101-118. https://doi.org/10.1007/s00603-017-1318-8

Singh, V.K., Singh, D., & Singha, T.N. (2001). Prediction of strength properties of some schistose rocks from petrographic properties using artificial neural networks. *International Journal of Rock Mechanics and Mining Sciences*, 38(2), 269-284. https://doi.org/10.1016/S1365-1609(00)00078-2

Singh, H.K., & Basu, A.A. (2018). Comparison between the shear behavior of `real' natural rock discontinuities and their replicas. *Rock Mechanics and Rock Engineering*, 51(1), 329-340. https://doi.org/10.1007/s00603-017-1334-8

Skinas, C.A., Bandis, S.C., & Demiris, C.A. (1990). Experimental Investigations and Modelling of Rock Joint Behaviour Under Constant Stiffness. *Proc. International Symposium on Rock Joints*. Balkema, 301-307.

Sonmez, H., Ercanoglu, M., Kalender, A., Dagdelenler, G., & Tunusluogly, R. (2016). Predicting uniaxial compressive strength and deformation modulus of volcanic bimrocks considering engineering dimension. *International Journal of Rock Mechanics and Mining Sciences*, 86, 91-103. https://doi.org/10.1016/j.ijrmms.2016.03.022

Tang, Z.C., Liu, Q.S., & Huang, J.H. (2014). New criterion for rock joints based on three- dimensional roughness parameters. *Journal of Central South University*, 21(12), 4653-4659. https://doi.org/10.1007/s11771-014-2473-7

Tatone, B.S., & Grasselli, G. (2009). A method to evaluate the three-dimensional roughness of fracture surfaces in brittle geomaterials. *Review of Scientific Instruments*, 80(12), 1-10. https://doi.org/10.1063/1.3266964

Xia, C.C., Tang, Z.C., Xiao, W.M., & Song, Y.L. (2014). New peak shear strength criterion of rock joints based on quantified surface description. *Rock Mechanics and Rock Engineering*, 47(2), 387-400. https://doi.org/10.1007/s00603-013-0395-6

Yang, J., Rong, G., Cheng, L., Hou, D., & Wang, X. (2016). Experimental study of peak shear strength of rock joints. *Chinese Journal of Rock Mechanics and Engineering*, 34(5), 884-894. https://doi.org./10.13722/j.cnki.jrme.2014.1096-en

Yilmaz, I., & Yuksek, A.G. (2008). An example of artificial neural network (ANN) application for indirect estimation of rock parameters. *Rock Mechanics and Rock Engineering*, 41(5), 781-795. https://doi.org/10.1007/s00603-007-0138-7

Zeigler, T.W. (1972). In situ tests for the determination of rock mass shear strength - Technical Report S-72-12. *US Army Engineer Waterways Experiment Station, Vicksburg, MS*.

Zhang, X., Jiang, Q., Chen, N., Wei, W., & Feng, X. (2016). Laboratory investigation on shear behavior of rock joints and a new peak shear strength criterion. *Rock Mechanics and Rock Engineering*, 49(9), 3495-3512. https://doi.org/10.1007/s00603-016-1012-2

Soils and Rocks
An International Journal of Geotechnical and Geoenvironmental Engineering
www.soilsandrocks.com
ISSN 1980-9743
ISSN-e 2675-5475

Behavioral evaluation of earth dams built with materials above optimum moisture content in high rainfall areas

Julián Buriticá García[1,#], André Pacheco de Assis[1], Juan P. Villacreses[2]

Article

Keywords
Earth dams
Flow
Slope stability
Stress-strain
Wet compaction
Wet core

Abstract
South Americas topographic characteristics and available materials have led engineers to select earth or rockfill material for dams construction. However, there are tropical regions with high annual rainfall where the soil compaction above the optimum moisture must be studied in detail. This research presents the results of tests performed on compacted soil samples, with water contents of +2 % and +5 % above the optimum moisture. Such samples were classified as low plasticity sandy silt by the USCS and as sandy lateritic clay by MCT methods. The investigation analyses a seepage, slope stability, and stress-strain numerical analysis conducted on typical hypothetical homogeneous and heterogeneous dams. In general terms, the heterogeneous sections showed adequate behavior for all the modeled soils. However, the slopes of the homogeneous sections exhibited low safety factors during the rapid drawdown of the reservoir water level. The material compacted above the optimum water content presented a superior performance to dissipate pore water pressure along the time than the other soils. Concluding that the use of soil above the optimum can be convenient and economical for dam construction, in the case where no other material is available, and a fast pore water relief is sought.

1. Introduction

A series of accidents during the construction and operation of earthen dams has drawn the scientific community's attention. As an example, the tailings dam failure of the Brumandino dam located in Brazil brought social, economic, and environmental consequences. In detail, hundreds of people died as a consequence of dam failure. Additionally to this social consequence, the Paraopeba river was polluted. High levels of mercury were detected in the water coming from the dam upstream, where iron mines were located (Thompson et al., 2020). Therefore, the need for research about the mechanical performance of these structures is always pertinent. Special attention must be taken in the constitutive materials used in the design or the construction of earthen dams. A particular case of analysis is soil water content's influence on the mechanical performance of the structures.

The soil's mechanical properties used to construct dams are directly dependent on the soil water content at the moment of compaction. Properties such as permeability, compressibility, and ultimate strength are affected by the soil water content. These properties are used to compute the mechanical performance of the structure. As an example, the Young modulus of soils compacted above the optimum water content is lower than in those samples compacted at the optimum water content. It implies that the soil generates low resistance and elevated pore water pressure during the construction phase. Despite these well-known disadvantages of using soils with water content above the optimum, there is no other option than to use these high water content soils in some regions of South and Central America. Techniques of constructions like silt stabilization, air drying, or mixing with dryer granular materials produce delays and increase the construction cost that most of the cases make them inapplicable (Jalili & Jahanandish, 2009). Therefore, professional practitioners need to understand the implications that have the use of soil above the water content in the design, construction, and performance of dams.

On the contrary to what it should be expected, there is a lack of information regarding the design or mechanical

[#]Corresponding author. E-mail address: julianburitica@gmail.com.
[1]Universidade de Brasília, Campus Darcy Ribeiro, Brasília, DF, Brazil.
[2]University of San Francisco de Quito, Campus Cumbayá, Quito, Ecuador.

Submitted on March 5, 2020; Final Acceptance on August 26, 2020; Discussion open until March 31, 2021.
DOI: https://doi.org/10.28927/SR.434591

assessment of dams constructed with water contents above the optimum. In the literature, there are construction descriptions of dams built using soil 2 % to 10 % above the optimum water content (Bernell, 1982; Kerkes, 1988; Morpurgo, 1976; Villegas et al., 1976a, 1976b). To mention one example, Villegas et al. (1976a) describe the experience acquired during the construction of Santa Rita Dam. This region has an average annual precipitation of 6210 mm of water. Consequently, conditioning the soil to its optimum water content was almost impossible, and the contractors decided to use soil above the optimum water content in the construction process. The construction process was done using rigorous control compaction procedures and a long period of construction process between each layer of soil. This project's economic success achieved by using a non-standard material is an example that non-traditional techniques and materials could be used to reduce the building cost. Additionally to this economical benefits, using soil above the optimum water content reduces the time of settlements, and it is reported that around 88 % of the total settlement could be achieved during the construction process (Rashidi & Haeri, 2017). This research seeks to contribute to the understanding of dams' mechanical performance that were built using soil with water content above the optimum.

This research compares the performance of two types of dams built with soil above the optimum water content (i.e. homogenous and heterogeneous dams). A numerical model was developed to assess the pore water pressure during a rapid drawdown of the earthen dams. Moreover, a slope stability analysis was performed using the results of pore water pressure. The mechanical parameters used in the model were experimentally obtained from soil compacted with different water contents. For this research, compaction, microscopy, permeability, consolidation, and triaxial tests were performed on samples compacted at the optimum, 2 %, and 5 % above the optimum water content. The results found in this research showed that this un-standard material could be used with caution in dam projects. Especially when the designer seeks pore water pressure relief.

2. Experimental programme

Laboratory tests were performed by Garcia (2013) on compacted silty sand soil from the Federal District - Brazil. The paper presents the parameters and analysis of the physical, mechanical, and microstructural properties of the material. These results were used in the numerical models of homogeneous and heterogeneous dams with an impermeable core. The purpose is to understand the influence of compaction water continent in dams. Two hypothetical cross-sections were analyzed, and seepage, slope stability, and stress-strain were computed with these parameters.

2.1 Experimental protocol

The soil utilized was collected from the University of Brasilias Geotechnics experimental foundations campus. The samples were extracted by manual digging of a well with an approximate diameter of 1 m and depth of 1,5 m. The extracted samples were disturbed, and different compacted samples were fabricated using this soil. The selected soil is a good representation of the soils of the Federal District of Brazil. These soils are covered by a soil mantle according to Mendonca et al. (1994) cited by Araki (1997). These soils are a result of the chemical weathering associated with lixiviation and lateralization from the quaternary tertiary period.

Conventional tests were performed on the compacted soil specimens. The specimens were constructed with different moisture contents and the standard compaction energy. The tests had the objective of measuring the physical, mechanical, and hydraulic characteristics of the studied samples. These results were used in the numerical simulation to study the effect of soil moisture content on dam behavior. In this research, the conducted tests were natural moisture content, solids specific weight, natural unit weight, grain size analysis, liquid limit, plastic limit, compaction test, scanning electron microscopy, variable head permeability tests, consolidation tests, and CID triaxial tests. The following sections present the results of the material characterization. All tests were performed following the Brazilian Association of Technical Standards (ABNT) procedures.

2.1.1 Physical characterization tests

Table 1 presents the test results obtained of natural moisture, natural unit weight, specific gravity, grain size analysis with and without deflocculates, Atterberg limits, SUCS, and MCT classification.

The results show a considerable alteration when the procedures are performed using dispersant, which presumes that the material presents clay and sand aggregations. The soil matrix is predominantly sandy and silty.

In earth dam projects, the soil aggregation directly influences the infrastructure performance. The most aggregated soils have a greater quantity of macropores, which is directly related to permeability, isotropy, and low resistance. However, the orientation of the particles during the compaction process gives to the sample the following characteristics: less aggregated soils are susceptible to exhibit anisotropic hydraulic and mechanical behaviors.

The classifications exhibited in Table 1 show that USCS classifies the studied soil as ML (low plasticity silt). This classification is not coherent with the material tactile-visual analysis, nor with the grain size analysis. The significant presence of clay and the predominance of sand and silt gives this soil, particular characteristics. On-site, the Federal District soil behaves similarly to clay, which is the reason it is known as the porous clays of Brasilia.

The MCT classification (Cozzolino & Nogami, 1993), catalogs the soil as a LA'-LG' since the soil is located in the interface of both types of soil (i.e., the soil is classified as sandy lateritic and lateritic clay). This classification is coherent with the tactile-visual analysis and with the soil behavior.

2.1.2 Compaction testing

In the compaction curve in Figure 1, the values of optimum moisture content and maximum dry density for the tested soil were 23 % and 15,5 kN/m^3. This point has an approximate saturation degree between 80 % and 90 %.

The shape of the compaction curve shows the influence of the sand and silt fraction. The curve presents a closed format with high dry unit weight.

Table 1. Results from physical characterization tests and soil classification.

Grain size distribution	Distilled water + dispersant	Gravel (%)	0
		Sand (%)	58.9
		Silt (%)	24.4
		Clay (%)	16.7
	Distilled water	Gravel (%)	0
		Sand (%)	74.8
		Silt (%)	24
		Clay (%)	1.2
		Natural unit weight - γ (kN/m^3)	17.5
		Solids specific weight - γ_s (kN/m^3)	26.9
		Natural moisture content - *w* (%)	27
		Liquid limit - w_l (%)	35
		Plastic limit - w_p (%)	23
		Plasticity index - *IP* (%)	12
		SUCS Classification	ML
		MCT Classification	LA’-LG’

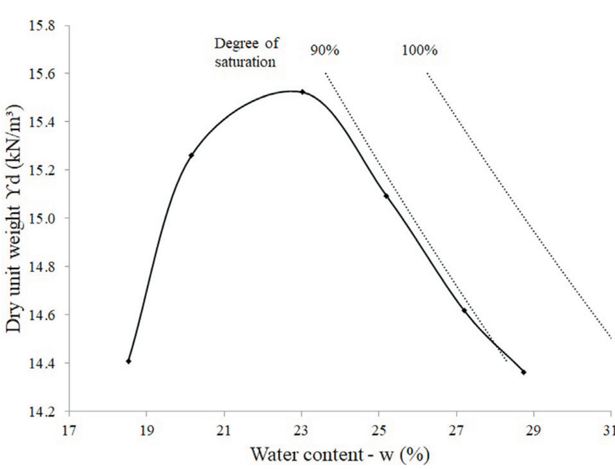

Figure 1. Compaction curve for the UnB experimental site soil.

The samples for consolidation, permeability, and triaxial tests were fabricated using the results of the compaction test. The defined moistures of 23 %, 25 %, and 28 % correspond to the optimum moisture content, optimum moisture content + 2 %, and optimum moisture content + 5 %.

2.1.3 Scanning electron microscopy analysis

The study of the compacted soil microstructure was carried out qualitatively. SEM images were obtained during the compaction process over a range of moisture continents.

Figures 2, 3 and 4, present the images of the surfaces observed during the braking and dehydration of the samples, which were obtained by the SEM for the three test

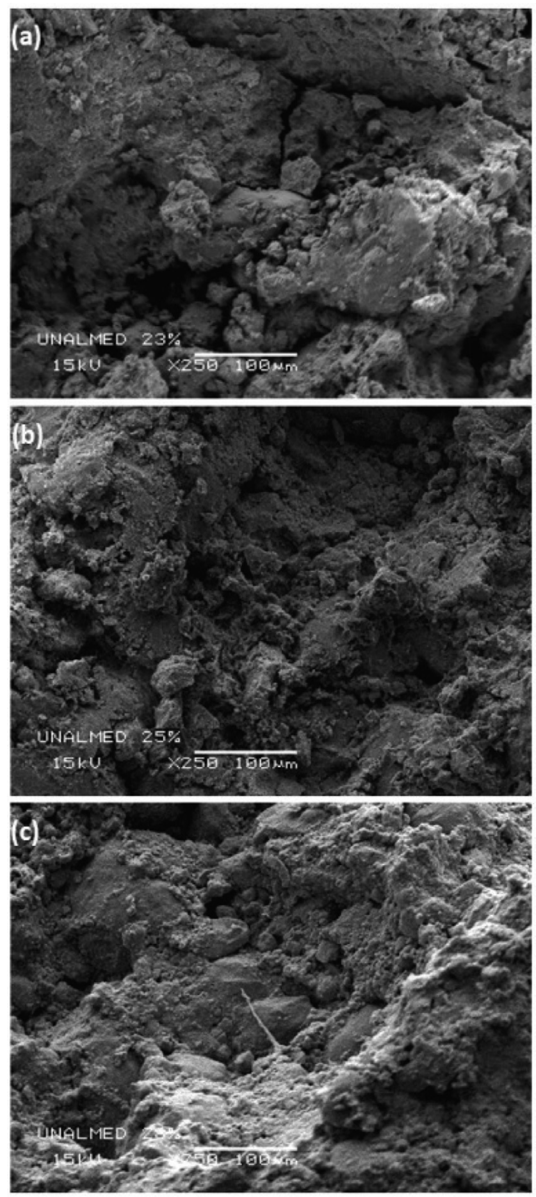

Figure 2. Images obtained by SEM for x250 magnification: (a) Image of compacted soil with 23 % moisture content; (b) Image of compacted soil with 25 % moisture content; (c) Image of compacted soil with 28 % moisture content.

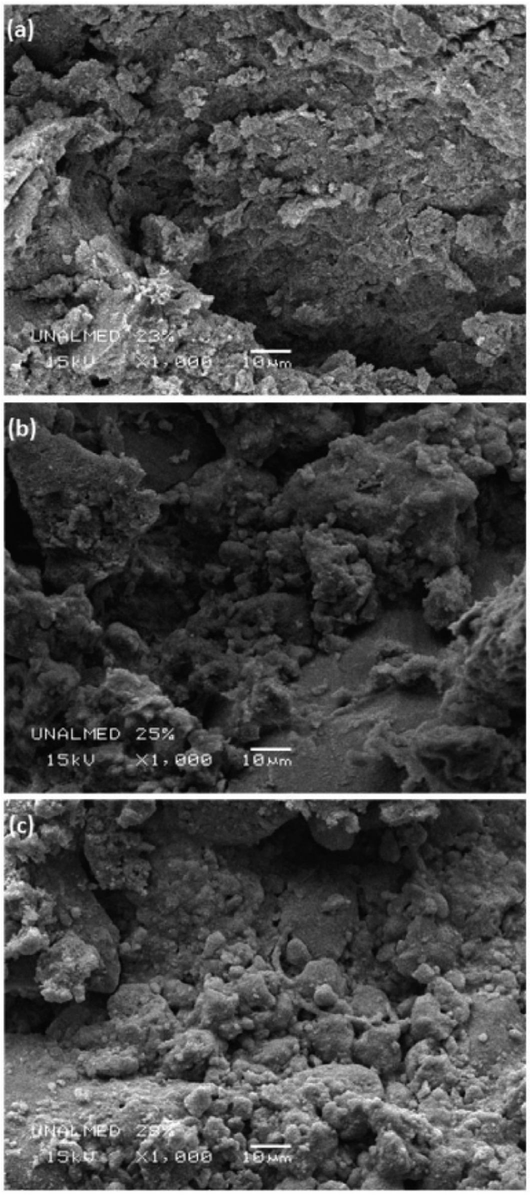

Figure 3. Images obtained by SEM for x1000 magnification: (a) Image of compacted soil with 23 % moisture content; (b) Image of compacted soil with 25 % moisture content; (c) Image of compacted soil with 28 % moisture content.

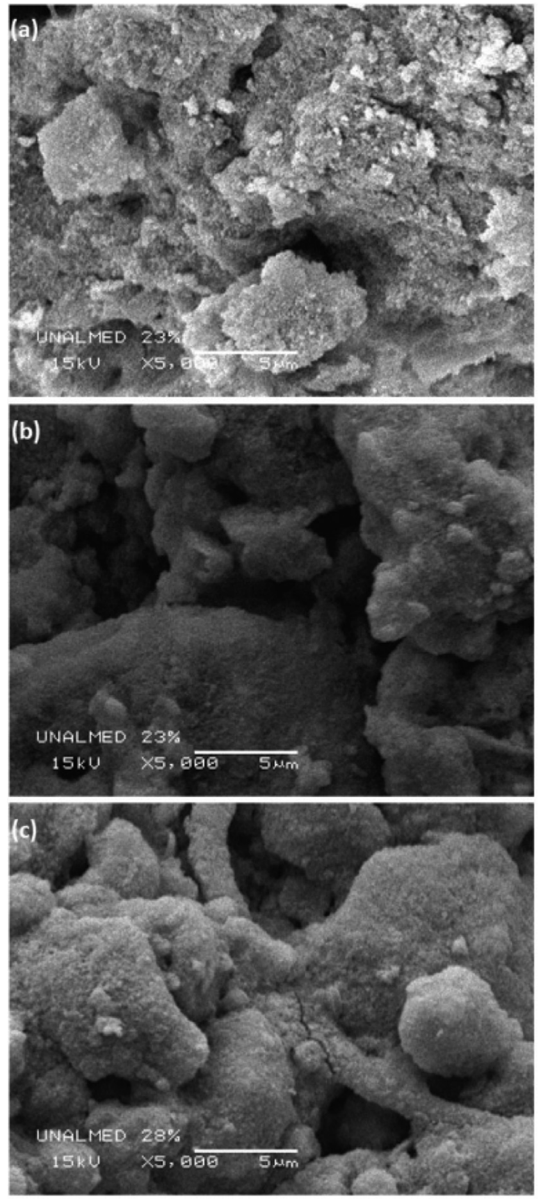

Figure 4. Images obtained by SEM for x5000 magnification: (a) Image of compacted soil with 23 % moisture content; (b) Image of compacted soil with 25 % moisture content; (c) Image of compacted soil with 28 % moisture content.

moisture contents with 250, 1000, and 5000 magnifications. On these images, it is possible to observe that the compacted soils exhibit a highly porous structure.

In Samples with optimum moisture content, the aggregates form a denser and more massive soil structure. The high-density value is achieved due to the low aggregate strength, which deforms and breakdown easily reducing the pores. On the other hand, the samples above the optimum moisture content, particularly samples with 28 % moisture content, the clay matrix wraps the silt grains and closes the micropores.

The most representative shapes exhibit soft vertexes and dimensions that vary between 5 and 20 µm (Figures 3b and 4b) but can reach 30 to 40 µm. On Figures 2a, 3a and 4a are not possible to identify the individual grains, as it happens in compacted samples above optimum moisture content.

In Samples with moisture contents above optimum, it is possible to visualize the cavities generated by the grains during the breakdown process. Additionally, in these figures, it is possible to observe a few micropores with cavities superior to 5 µm.

In the SEM images for 5000x magnification (Figure 4.a, 4.b, and 4.c), it is possible to observe the following features: rectangular aggregations of sand, silt and clay with grain to grain contact, rough superficial texture, and the presence of micropores with openings with diameters smaller than 1 μm. These measured characteristics are bidimensional, which means they are not realistic. However, it still provides a clear idea of the size of the pores and the aggregate shape.

In this type of soil, the phenomenon of aggregation of particles is more important than the colloidal phenomenon suggested by Lambe (1958). In the case of samples with moisture contents above optimum, the soil is not homogeneous and particles are not oriented. As an example, the SEM results show that these soils behave similarly to the soils presented by Cetin et al. (2007) and Mitchell (1993). In these researches, compacted soils bellow optimum moisture content show an aleatory orientation, and the orientation changes as the moisture content increases until it reaches the optimum moisture content. However, the study reveals that that beyond the optimum moisture content, the degree of preferential orientation decreases, opposite to the generally accepted point of view in classic soil mechanics and the previously stated studies.

2.1.4 Variable head permeability test

Table 2 presents the measurements of the variable head permeability test. The tests were carried out on the compacted soil samples, and permeability was measured in the vertical direction. The numerical model assumed isotropy of this parameter.

It is possible to observe that the soil permeability decrease as water content increase. This fact is a consequence of the larger micropores presented in samples with water content above the optimum.

Table 2. Permeability coefficients for different compaction moisture contents.

Moisture content (%)	*K* (m/s)
22.7	1.05E-09
24.7	6.45E-09
27.8	1.34E-08

2.1.5 Oedometric tests

The saturated consolidation tests were performed with the following stresses: 25, 50, 100, 200, 400, 800, and 1600 kPa. Figure 5 presents the normalized compressibility curve of each of the three studied samples. These graphs represent the variation of the void ratio when increasing the pressure over the test soils.

Figure 5 shows that the compressibility increase as moisture increases. As an example, samples with a moisture content of 28 % presents the highest compressibility. The compressibility of samples with 23 % and 24 % of water content is equal. This fact is evidenced in the virgin side of the compressibility curve of these two samples. It is important to point out that even though the test specimens were elaborated with compacted material at different moisture contents, generating different initial void ratios, the final void ratios were similar. This fact can be seen in Figure 5.

2.1.6 CID triaxial tests

The triaxial tests were performed under drained controlled strain and isotropically consolidated (CID triaxial tests). The soils were compacted at different moisture contents by following conventional stress paths (axial load), with effective confining stresses of 50, 100, 200, and

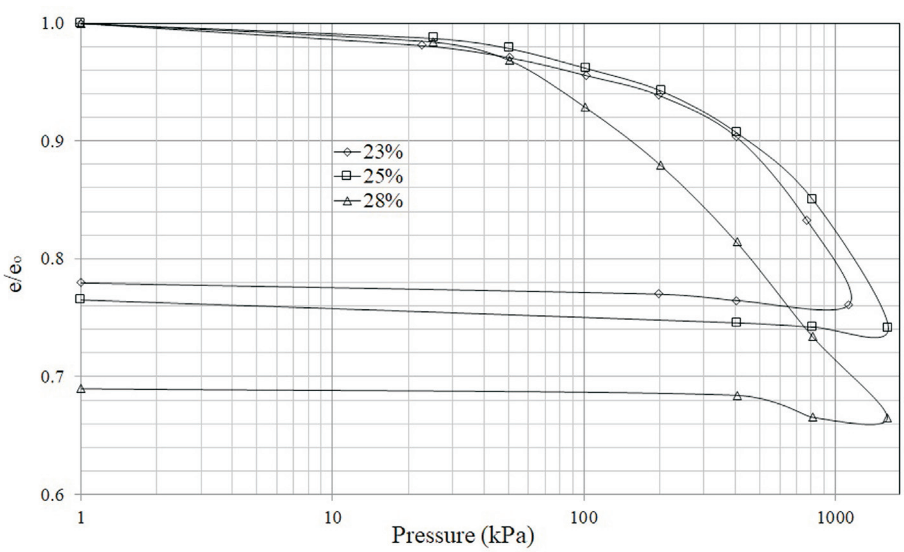

Figure 5. Normalized compressibility curve for the three compaction moisture contents.

400 kPa. Furthermore, back pressure was applied through the drainage tubes at the base and head of the sample to saturate the sample.

The tests performed using samples at optimum moisture content had a degree of saturation ranging between 77 % and 79 %, while for tests performed with samples of +2 % above the optimum had an initial saturation degree of 84 %. On the other hand, samples with a water content of +5 % above the optimum had an initial saturation degree of 85 %. For all the samples, the final degree of saturation was above 98 %.

Figures 6, 7, and 8 show deviatoric stress vs. the axial strain graphs for the samples that were compacted at optimum moisture content, optimum moisture content +2 %, and optimum moisture content +5 %.

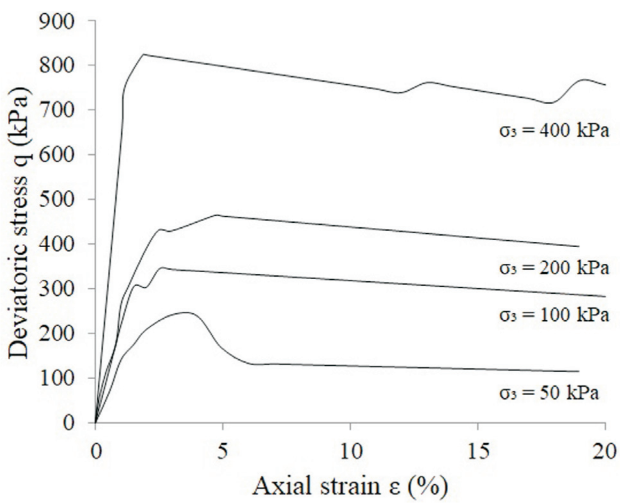

Figure 6. CID triaxial tests result for soil sample compacted at optimum moisture content.

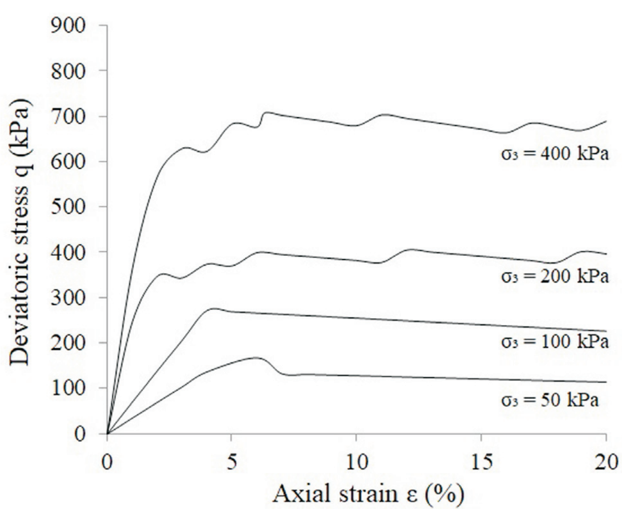

Figure 7. CID triaxial tests result for soil sample compacted at optimum moisture content +2 %.

From Figures 6 to 8, it is possible to observe that for all the samples the soil stiffness increase as the effective confining stress increases. Additionally, it is possible to notice a prominent decrease in the soil maximum peak stress and stiffness as the compaction moisture content increases. The maximum deviatoric stress for the soil compacted at 28 % of the moisture content was approximately 50 % of that for the soil compacted with 23 % of moisture content (i.e., optimum moisture content). Meanwhile, the failure strain for all of the test soils ranged between 4 % and 6 %.

A linear failure envelope was established for each type of tested soil (Figure 9) from the maximum values of effective stress paths in the *p-q* plane. The straight line was obtained by the linear regression for the maximum value of *q*, for the four test confining stresses at the different moisture contents analyzed during the investigation.

In Figure 9, it is possible to observe that the envelopes for 23 % and 25 % moisture contents are parallel, which means that the friction angle will be very similar in both cases. However, the interception with the y-axis has a lower value in the case of the soil compacted with 25 % of mois-

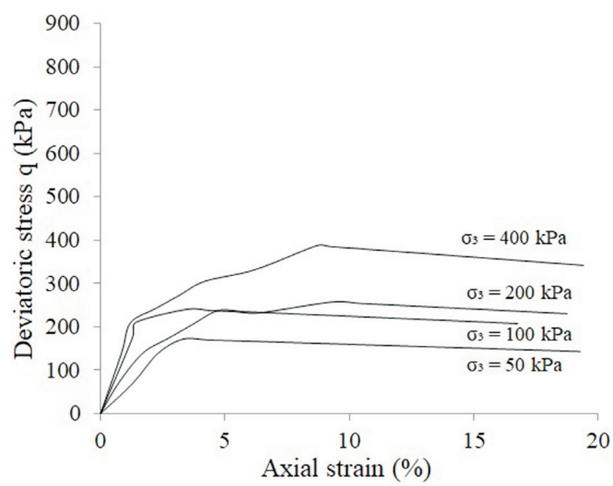

Figure 8. CID triaxial tests result for soil sample compacted at optimum moisture content +5 %.

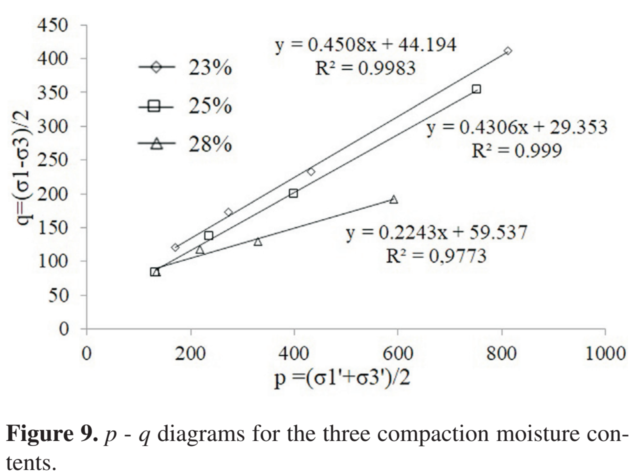

Figure 9. *p* - *q* diagrams for the three compaction moisture contents.

ture content, which means that the cohesion drops with the increase of 2 % of moisture content.

In the case of the soil compacted with 28 % of moisture content, the curve has a lower slope which means that the friction angle decreases considerably. It also presents an increase in the cohesion that can be a result of the structure that the soil forms when it is compacted with moisture contents that considerably surpass the optimum moisture content. This behavior is attributed to the structures formed by the clay and silt aggregations, as observed in the electron microscope scanning images (Figures 3c and 4c).

In general terms, the results were expected, and the strength parameters are better for soils compacted at optimum moisture content. On the contrary, the mechanical parameters were decreased in samples with water content above the optimum.

2.2 Geotechnical parameters of the tested soil

From the experimental setup, strength, consolidation, and permeability parameters of the core material for heterogeneous dams and the filling material for homogeneous dams were obtained.

The constitutive model utilized throughout the analysis was the nonlinear hyperbolic model, which was initially attributed to Kondner (1963) and later modified by Duncan & Chang (1970). The model simulates the non-linearity stress-strain behavior of soils, the stress-strain curve is hyperbolic and the soil stiffness modulus varies with the confining stress.

Tables 3 and 4 present a summary of the selected model's geotechnical parameters for the different compacted samples. Additionally, the parameters for foundation soils, backstraps, transition material, and typical filter materials are presented. These parameters can be found in the literature for projects with similar weather conditions.

From the triaxial modulus results presented in Table 4, it was possible to find a relationship between the Young modulus and the confining stress for each tested soil type. The experimental data were fitted based on the nonlinear hyperbolic model proposed by Duncan & Chang (1970). The equation is presented below:

$$Ei = KP_a\left(\frac{\sigma_3}{P_a}\right)^n \quad (1)$$

where K and n are the parameters of the equation to be fitted, P_a is the atmospheric pressure, assumed as 101.3 kPa

Figure 10 presents the modulus for soils compacted with the three moisture contents used during the investigation. The correlation coefficient of each curve presented in the figure has a value of 1. Table 5 shows the calculated values for the K and n constants of the hyperbolic model.

From the values of K and n, it is possible to establish a relationship with the compaction moisture content for this soil (Figures 11 and 12) and the mentioned parameters. The results were validated with aditional trials.

2.3 Dam behavior analysis using numerical simulations from GeoStudio software

Numerical simulations of seepage flow used SEEP/W software. The slope stability sued SLOPE/W software. Finally, stress-strain was computed using SIGMA/W. The commercial package of this software is named GeoStudio package by Slope International Ltda.

Table 3. Geotechnical parameters of the dam's constituent materials.

Material	E (MPa)	γ (kN/m^3)	ν	f (°)	c (kPa)	k (m/s)	K_o	R_u
Foundation soil	60	18	0.35	28	30	1.00E-11	0.5	0.2
Gravel shell	60	20	0.35	38	10	1.00E-04	0.5	0
Transition filter	100	20	0.35	32	0	1.00E-03	0.5	0.05
Filter	100	20	0.35	30	0	1.00E-03	0.5	0.05
Embankment soil	23 %	19.1	0.4	27	48	1.00E-09	0.55	0.25
	25 %	18.9	0.4	26	30	5.00E-09	0.56	0.3
	28 %	18.5	0.4	14	50	1.00E-08	0.7	0.5

Table 4. Deformability modulus for the three types of soils for various confinement pressure.

Moisture content	E (MPa)			
	σ_c' = 50 kPa	σ_c' = 100 kPa	σ_c' = 200 kPa	σ_c' = 400 kPa
Optimum moisture content	14.2	22.4	27.4	62.5
Optimum moisture content + 2 %	4.7	8.5	25	37.3
Optimum moisture content + 5 %	3.5	5.9	12.9	19.4

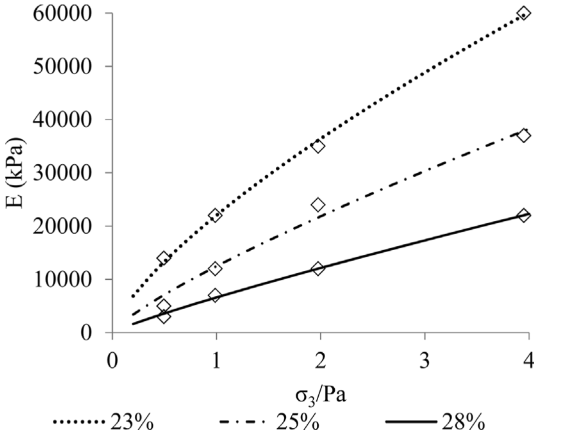

Figure 10. The relation between the deformability modulus and the confinement pressure.

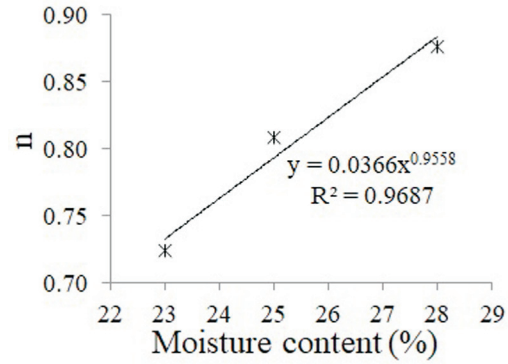

Figure 11. The relation between n and the compaction moisture content.

Table 5. Parameters K and n for the three compaction moisture contents.

w (%)	K	n	R^2
23	22036.4	0.72	0.99
25	12468.3	0.81	0.98
28	6612.1	0.88	0.99

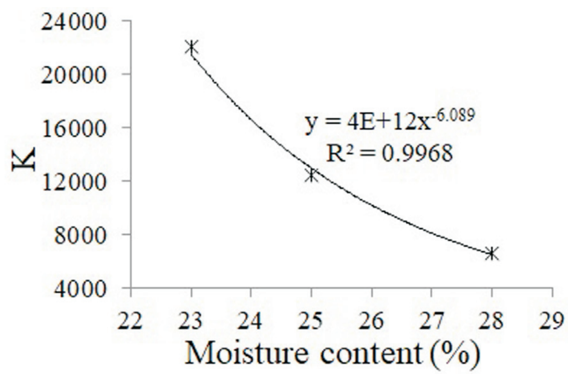

Figure 12. The relation between K and the compaction moisture content.

2.3.1 Typical cross-sections adopted for analysis

This research studied two typical cross-sections for dams. One is a homogeneous dam with a vertical filter, and the other a heterogeneous dam (Figures 13 and 14). Computations are presented in meters.

2.3.2 Seepage flow analysis

In dam design, the control of flow through backfill, body dam, and foundations constitutes an essential analysis for the safety of the project (Cruz, 1996). The water seepage, forming *piping*, is one of the most common causes of earth dam failures.

2.3.3 Steady-state operation regime

In the steady-state operation regime, the water level is maximum (level 157 m). The flow values are low due to the low permeability coefficients for compacted soil. These values of flow are represented by a unit length of the dam.

Figure 15 shows the flow Q (m^3/s) values for both cross-sections analyzed using soil with different moisture contents. The lowest flow corresponds to dams compacted with silt clay material with 23 % moisture content. This material exhibits the lowest value of the permeability coefficient.

2.3.4 Rapid drawdown

Rapid drawdown analysis was performed, adopting a drainage time of 15 days (1.296.000 s). The hydraulic head at the beginning was 157 m (maximum reservoir level) and 100 m in the end (dam's foundation).

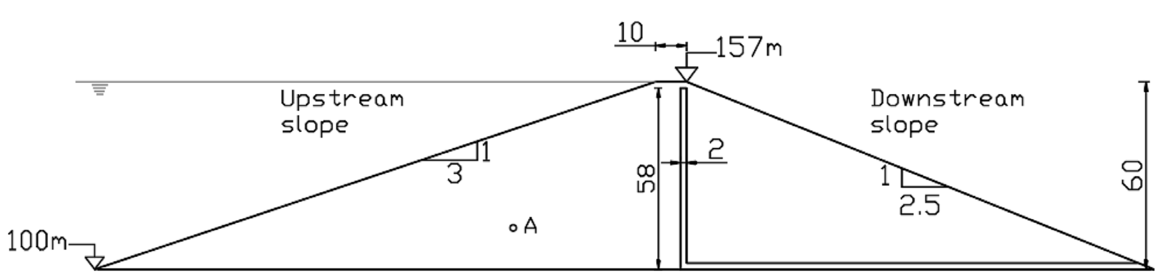

Figure 13. Typical cross-section 1 (homogeneous dam).

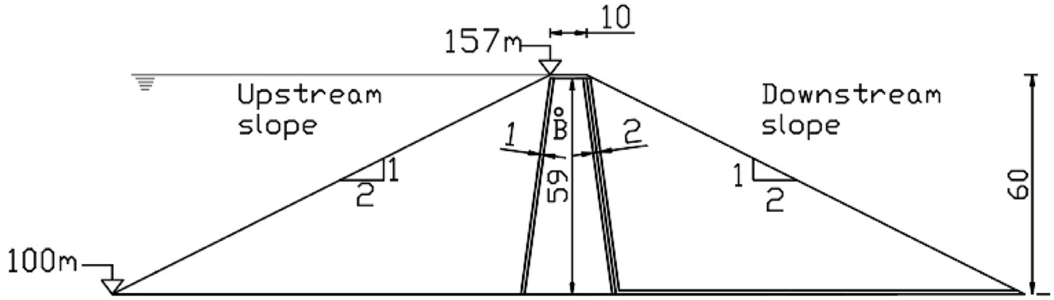

Figure 14. Typical cross-section 2 (heterogeneous dam).

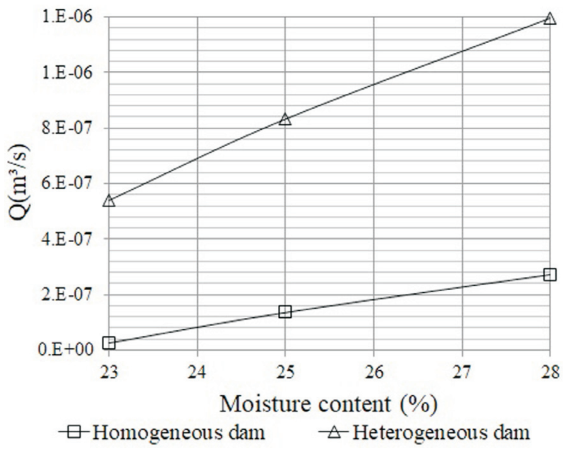

Figure 15. Flow for different compaction moisture contents.

Pore pressures were calculated in tow different points for each dam, a point in the backstrap upstream from the homogeneous dam (point A, Figure 13) and a point in the core of the heterogeneous dam (point B, Figure 14).

Figures 16 and 17 show the pore pressure distribution for those points for the three different water contents. The rapid drawdown process has a higher effect over soils compacted at optimum moisture content since after being compacted the soil structure formed a less permeable structure. This causes a slower pore pressure dissipation.

None of the three types of soils present a good behavior under rapid drawdown. The pore pressure dissipation is slow. This slow rate of dissipation of pressure generates instability in the slopes of the dam. During the 15 days of drainage, the pore pressure decreases slightly (the phreatic line remains stagnant), generating instability problems. In the soils with 25 % and 28 % compaction moisture contents, the soils exhibit a good rate of pore pressure dissipation 50 days after the rapid drawdown initiation.

In the case of the heterogeneous dam, the slow pore pressure dissipation will not have a great influence over the dam backfill stability because these are constructed with gravel, which has a high permeability coefficient, thus a high capacity to dissipate pore pressures. This fact is shown in Figure 17.

2.4 Slope stability analysis

The slope stability analyses were performed for the final stages of construction, operation, and rapid drawdown of the reservoir. For the operation regime, the pore water pressure was imported from the SEEP / W program and the slope stability analyzes were carried out in the SLOPE / W program using the Morgenstern & Price (1965) method. For the rapid drawdown of the reservoir, the coupled pore pressure - stress analysis was performed using the SEEP/W and SIGMA/W programs, determinis-

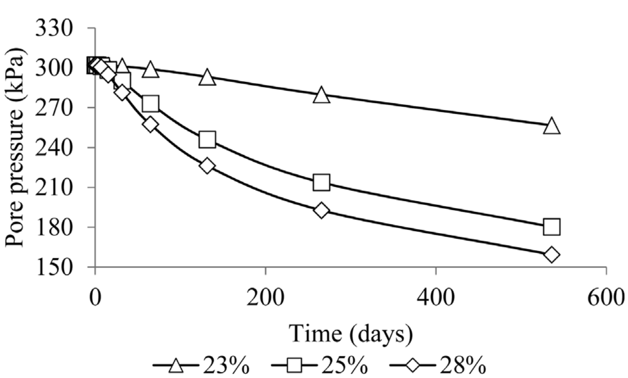

Figure 16. Pore pressures in point A for the three compaction moisture contents, homogeneous dam.

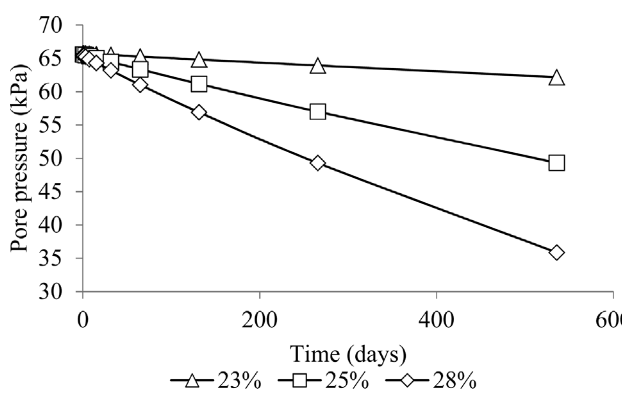

Figure 17. Pore pressures in point B for the three compaction moisture contents, heterogeneous dam.

tic safety factors were obtained using the Morgenster & Price (1965) method.

According to USACE (1970), the minimum suggested value for the factor of safety in the slope stability analysis is 1.3 during the end of the construction phase, 1.5 during the steady-state operation regime and 1.1 during the rapid drawdown of the reservoir.

2.4.1 End of construction

The safety factor evaluation during the final construction stage is performed for the slopes located upstream and downstream of the dam. Table 6 shows the safety factors for the homogeneous and heterogeneous dams, where it is possible to observe that all safety factors are greater than the minimum suggested values.

For the final construction stage, the constructive pore pressure coefficient Ru was used at the dam - foundation soil interface to consider the most critical situation. For both types of dams, the obtained safety factors under the conditions of material compacted at 23 % and 25 % moisture contents are similar.

2.4.2 Steady-state operation regime

It is important to point out that the seepage nets and pore pressures were imported from the seepage analysis performed in Seep/W, which was presented previously. The analysis was only performed for the downstream slope because the water level in the upstream slope acts as a stabilizer agent. The minimum safety factors for the homogeneous and heterogeneous dams in the three moisture contents are presented in Table 7.

Table 6. Safety factors for homogeneous and heterogeneous dams during the final construction stage.

Moisture content	Upstream slope safety factor		Downstream slope safety factor	
	Homogeneous dam	Heterogeneous dam	Homogeneous dam	Heterogeneous dam
23 %	2.2	2.0	2.2	1.9
25 %	2.2	2.0	1.9	2.0
28 %	1.6	1.9	1.6	2.0

Table 7. Safety factors for the homogeneous and heterogeneous dams during the operation phase.

Moisture content	Safety factors for upstream slope (homogeneous dam)	Safety factor for downstream slope (heterogeneous dam)
23 %	1.9	1.7
25 %	1.8	1.7
28 %	1.4	1.6

As shown in Table 7, the safety factors during the construction phase are lower than the values obtained during the final construction stage, due to the formation of the flow network.

In the case of the homogeneous dam, the soil that shows the lowest safety factor is the soil compacted at optimum moisture content +5 %, which means that it would not be acceptable. As a result, it would be necessary to flat the slope geometry or modify the construction material.

On the other hand, in the case of the homogeneous dam, the lowest safety factors are greater than 1.5. Therefore, the homogeneous dam does not present stability problems during this phase due to the core compaction moisture content, as in almost 100 % of the cases the failure surface occurs in the gravel backfill.

In both analyzed cross-sections, the lowest safety factors for optimum moisture content and optimum +2 % moisture content soils are very similar, which agrees with the literature's result, where a range of +/- 2 % of the specified compaction moisture content is accepted worldwide.

2.4.3 Rapid drawdown

The coupled stress - pore pressure analyzes were performed by using Sigma/W and Slope/W software. The flow network and initial pore pressures were imported from the seepage analysis performed in Seep/w.

During the reservoir drawdown, the load imposed by the water over the upstream slope is eliminated, leaving the backfill saturated. The excess of pore pressure can lead to failure, which is the reason it is generally the most critical condition to be analyzed.

The downstream slope did not exhibit variations in the safety factor in relation to the operation condition. Therefore, the only simulations performed were on the critical upstream slope.

Figures 18 and 19 show the time results of minimum safety factors for the homogeneous and heterogeneous dams with the three compaction moisture contents. The total drainage time was 15 days, but the safety factors are pre-

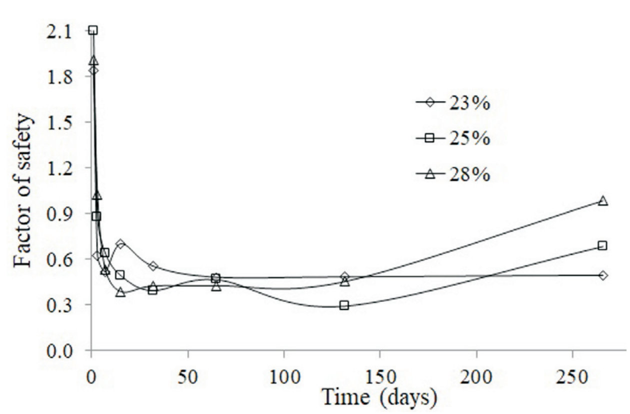

Figure 18. Time variation of the safety factors for the homogeneous dam.

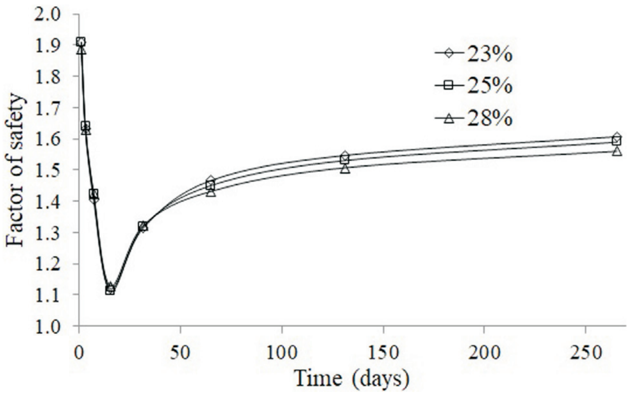

Figure 19. Time variation of the safety factors for the heterogeneous dam.

sented every 266 days, due to the slow pore pressure dissipation by the silt clay material.

In the case of the homogeneous dam, the most critical value occurs approximately at day 15, where the reservoirs drainage is completed. The slow dissipation of pore pressure caused the safety factor to become greater than 1.1 on day 300 after starting the drainage. Opposite to the homogeneous dam, the safety factor for the heterogeneous dam are greater than 1.1 overtime, this result shows an adequate and favorable factor of safety for this type of dam in this critical condition.

Comparing the results for the three soils with different moisture content, it is possible to observe (Figure 18) that for the homogenous dam the soil compacted above optimum moisture content (25 % and 28 % moisture content) showed lower safety factors. However, these soils compacted above optimum moisture content have greater permeability coefficients, thus the dissipation of pore pressure occurs faster over time which improves rapidly the stability. Figures 20 and 21 show the geometry of the potential failure surface in the critical condition that corresponds to the period between the seventh day and the end of the rapid drawdown for the homogeneous and heterogeneous dam.

In all types of stability analysis, the heterogeneous dam showed satisfactory performance. On the other hand, the homogeneous dam showed a critical performance in the rapid drawdown stage. In this case, the factor of safety can increase by building flatter slopes as demonstrated by Garcia et al. (2019). The upper limit of 5 % above the optimum moisture content must be respected to obtain the expected factors of safety.

2.5 Strain-stress analysis

The following analyzes were performed using SIGMA/W software. The results analyzed were expressed in total stresses and strains. According to Silveira (2006), 70 % to 90 % of settlements occur during the construction phase. These results were obtained during the construction of instrumented dams, where settlements were monitored.

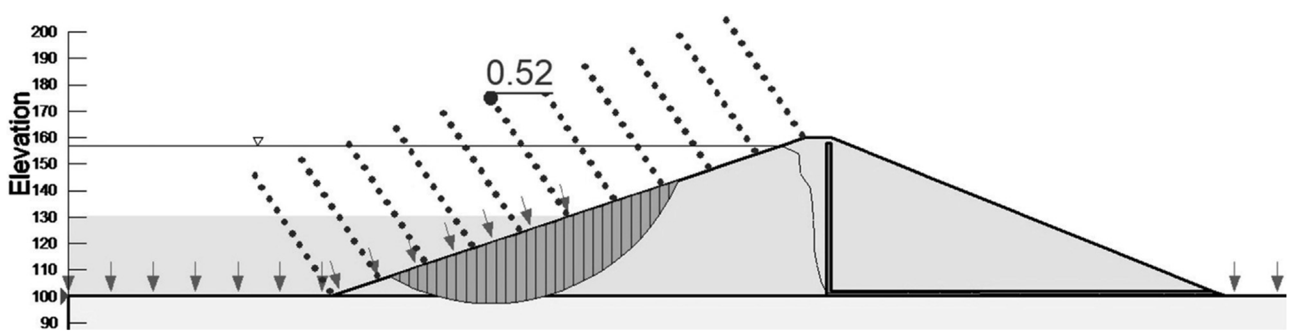

Figure 20. Minimum safety factor for the homogeneous dam (7-15 days - end of the rapid drawdown).

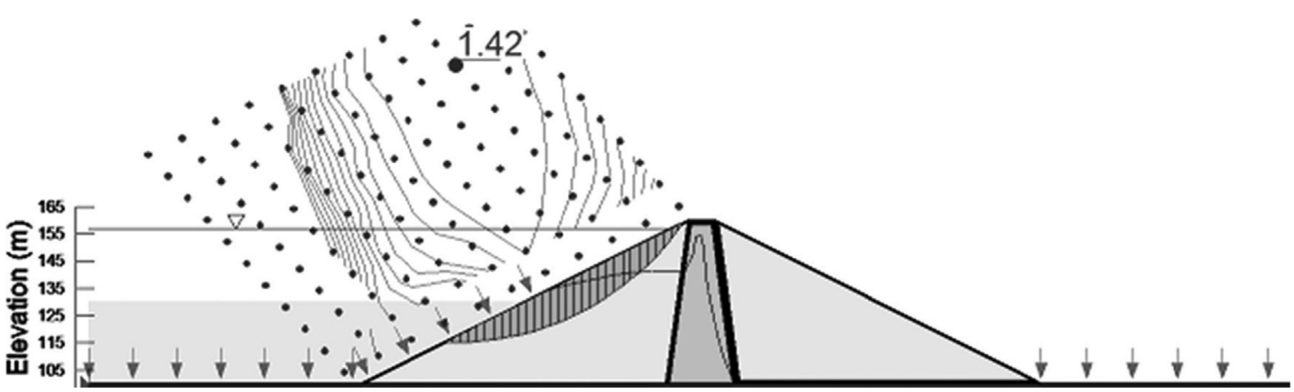

Figure 21. Minimum safety factor for the heterogeneous (7-15 days - end of the rapid drawdown).

2.5.1 End of construction

The maximum stress at the base was approximately 800 kPa for both of the analyzed cross-sections. In the case of the homogeneous dam, in Figure 22 it is possible to observe the phenomenon of concentrated stresses in the filter zone for the dam built +5 % above the optimum. This occurs as a consequence of the stiffness differences between the sand and the filling material. The plastic points did not present evident concentrations, which means that clear signs of failure-zone formations were not observed (Figure 23). On the other hand, in the case of the heterogeneous dam, it is possible to observe the stress arching phenomenon in the transition zone (Figure 24). The plastic points present a slight concentration in the base of the core and the superficial part of the gravel backstraps (Figure 25).

2.5.2 Construction by stages

The numerical simulation was performed in six stages, each step represents a construction of a layer of a thickness of 10 m. For the homogeneous dam, the settlements were computed for the three soils. These settlements were found to be similar. The maximum settlement for the soil compacted at optimum moisture content was 2.26 m, while for the soil compacted with +5 % above optimum moisture content was 2.4 m.

Figures 26 and 27 show the distribution of maximum vertical and horizontal displacements along the dam's central axis in the last compaction stage. It is possible to observe that the maximum settlement is located between the 10 and 30 m from the top o the dam. The maximum horizontal displacements in the homogeneous dam do not exceed 90 cm, which is an acceptable value for large homogeneous earth dams.

These analyses were performed for the heterogeneous dam as well. The maximum settlement for the soil compacted at optimum moisture content was 2.26 m, and 2.31 m for the soil compacted at optimum moisture +5 % content. The settlements for the heterogeneous dam were lower than those computed for homogeneous dams.

Figures 28 and 29 show the distribution of maximum vertical and horizontal displacements along the central axis of the heterogeneous dam for the sixth stage of construction. The maximum horizontal displacements were around 70 cm.

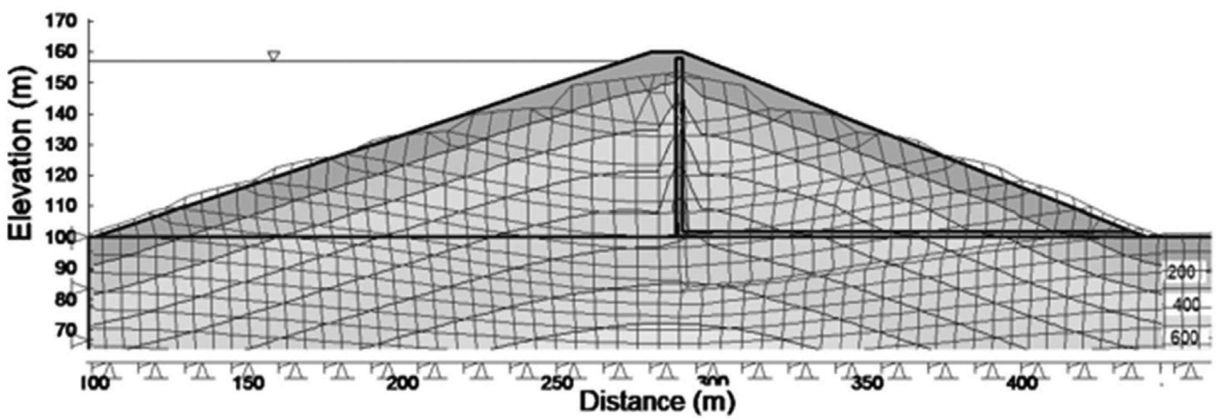

Figure 22. Total stress for the homogeneous dam.

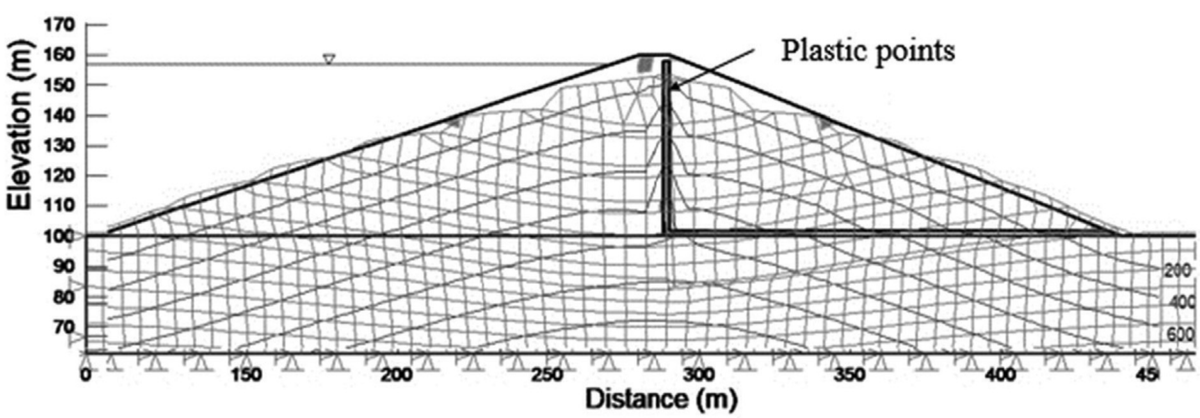

Figure 23. Plastic points for the homogeneous dam.

3. Conclusions

This research analyses the influence of water content in compacted soil for dam construction. The study begins with the characterization of the construction materials. Then a numerical model uses these results to model two geometries of dams. The research found that earthen dams could be constructed using soil above the optimum water content under strict conditions of this research. These results could be an aid in the construction of dams in tropical regions. The conclusion was divided into material characterization and numerical model results. The conclusions are summarised as follows:

3.1 Experimental campaign

The macro and micro-structures of the samples constructed with different water contents presented a diverse configuration. Soils compacted above the optimum present a random particle orientation, where the aggregation is more notorious in samples with height water content.

The variable head permeability tests show that the soil samples compacted at optimum moisture content presented the lowest hydraulic conductivity value. Additionally, an increment of hydraulic conductivity was observed

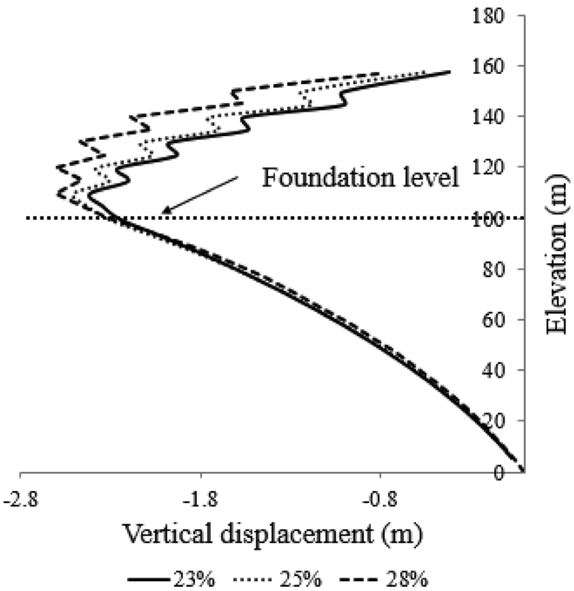

Figure 26. Maximum vertical settlement in the central axis (elevation) for the homogeneous dam.

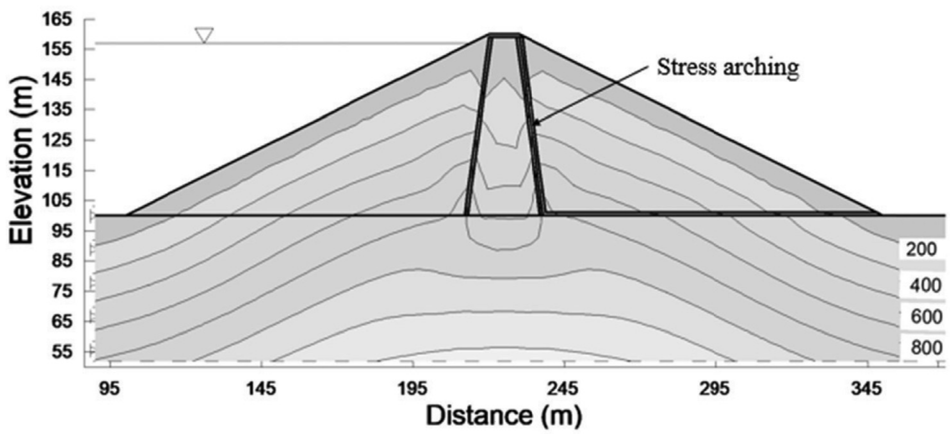

Figure 24. Total stress for the heterogeneous dam.

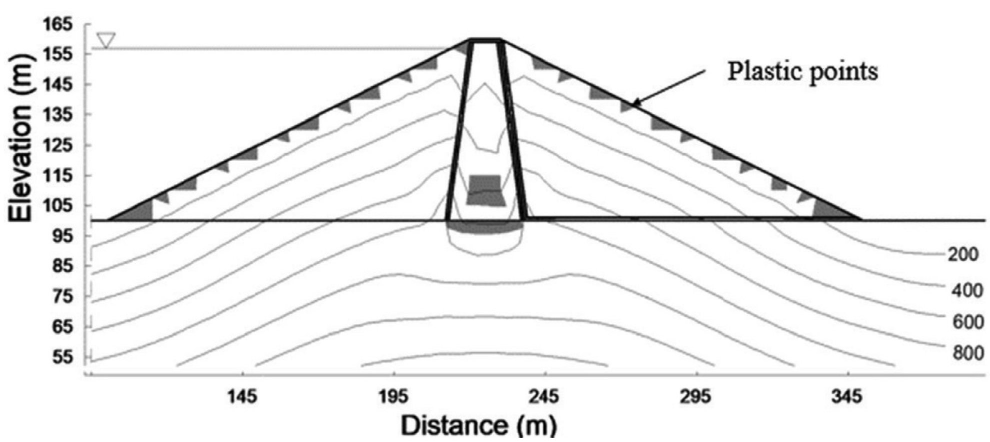

Figure 25. Plastic points for the heterogeneous dam.

for samples constructed with 2 % to 5 % water content above the optimum.

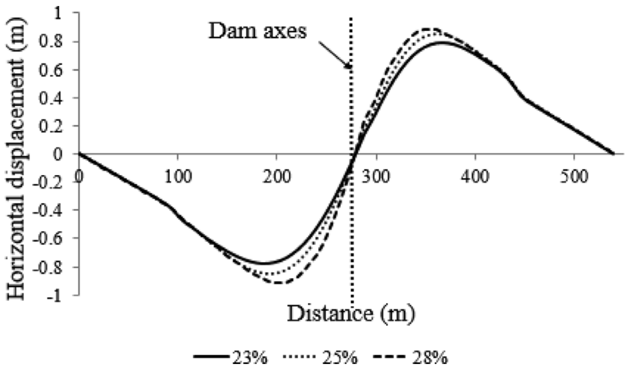

Figure 27. Maximum horizontal displacement along the homogeneous dam base.

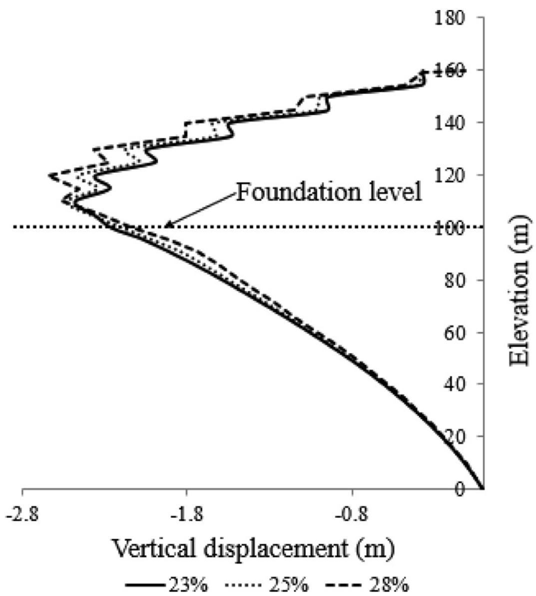

Figure 28. Maximum vertical settling in the central axis for the heterogeneous dam.

From the consolidation, it is possible to conclude that the samples compacted at optimum moisture content present the minimum compressibility, and they have similar behavior to the soil compacted 2 % above optimum. On the other hand, the soil compacted +5 % above the optimum moisture content have the maximum compressibility.

The soil compacted at optimum moisture content exhibited the best strength parameters from the consolidated drained triaxial tests. The soil compacted 2 % above optimum moisture content showed a decrease in the cohesion and friction angle, while the soil compacted at optimum moisture +5 % content showed a significant reduction in the friction angle but an increase of cohesion.

3.2 Numerical simulations

The two studied cross-sections will not tend to have problems related to flow across the dam, due to the material low permeability coefficients. Also, observing the gradients, it is possible to conclude that both cross-sections will not tend to suffer from *piping*.

According to the stability analysis for the homogeneous dam during the end of construction and operation phases, it can be observed that the safety factor decreases as the compaction moisture content increases, for the end of construction stage, the safety factors were always higher than the recommended minimum values. Additionally, it is possible to observe that the safety factors during the operation phase are inferior to those obtained at the end of construction. This fact can be attributed to seepage developed in the operational phase.

In the case of the homogeneous dam, the lowest safety factor corresponds to the soil compacted at optimum moisture +5 % content. The minimum factor of safety was 1.4 for the upstream slope, very close to the recommended minimum value. Thus soils with water content above the optimum could be used with small changes in geometry or

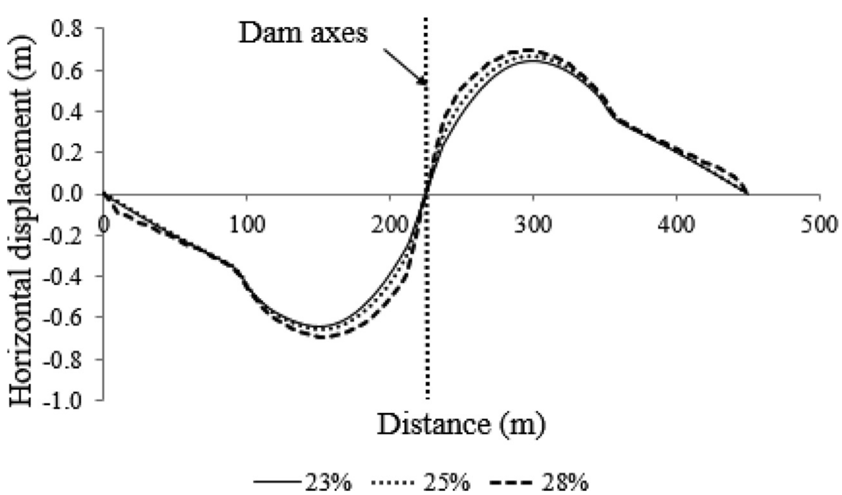

Figure 29. Maximum horizontal deformations along the heterogeneous dam.

compaction energy when considering the steady-state operation regime.

For the rapid drawdown analysis, the homogeneous dam showed lower safety factors than heterogenous dams. In the case of homogeneous dams, water pore pressures were relived in a longer period which leads to an inferior factor of safety.

On the other hand, the heterogeneous dam shows satisfactory safety factors. Also, it is possible to observe that for both analyzed cross-sections, the material compacted with higher moisture content has a superior long-term stability behavior than the other materials. This can be attributed to the rapid dissipation of pore water pressure. During the construction stage, the maximum vertical displacement is located between the base and the first 30 m of the dam height.

In general, it is possible to conclude that the behavior of the compacted fine material above the optimum moisture content for the heterogeneous dam presents an acceptable mechanical performance during the seepage, slope stability, and stress-strain analyses. The simulations exhibited favorable safety factors. The deformations were below the permitted limits, showing the acceptable mechanical performance of the tested soils. Therefore, using soil above the optimum water content is technically acceptable and can represent significant savings for projects built in tropical regions with high rainfall, difficult access, and difficulty accessing certain materials.

Using compacted local fine soils with water content above the optimum may be the only and the best option from the economic point of view in these high precipitation regions. The technical requirements necessary to guarantee the stability and functionality could be achived using this soil.

It is important to take into account that the moisture content control during the compaction process must be rigorous so that it does not exceed the upper limit and the best characteristics of the materials are achieved. Additional studies must be carried out for different types of materials. The permeability, deformability, and strength depend on factors such as mineralogy, particle shape, and structure of the material.

This research shows the importance of the topic, and leave guidelines to professional practitioners about the considerations taken when non-standard materials are used.

Acknowledgments

The authors would like to thank the following institutions for their support in the research activities described in this paper: Foundation for Research Support of the Federal District (FAP-DF), Brazilian Research Council (CAPES), the National Council for Scientific and Technological Development (CNPq) and the University of Brasilia. The authors would like to thank Enrique Moreno a student from Universidad San Francisco de Quito for his cooperation during the edition of this document.

References

Araki, M.S. (1997). *Aspectos relativos às propriedades dos solos porosos colapsíveis do Distrito Federal* [Unpublished master's dissertation]. University of Brasília (in Portuguese).

Bernell, C.E. (1982). Experiences of wet compacted dams in Sweden. *Proc. 14th International Congress on Large Dams*, *Rio de Janeiro*. Vol. 4, ICOLD, 421-431.

Cetin, H., Fener, M., Soylemez, M., & Gunaydin, O. (2007). Soil structure changes during compaction of a cohesive soil. *Engineering Geology*, 92(1-2), 38-48. https://doi.org/10.1016/j.enggeo.2007.03.005

Cozzolino, V.M.N., & Nogami, J.S. (1993). Classificação geotécnica MCT para solos tropicais. *Solos e Rochas*, 16(2), 77-91.

Cruz, P.T. (1996). *100 Barragens Brasileiras: Casos Históricos, Materiais de Construção, Projeto*. Oficina de Textos.

Duncan, J.M., & Chang, C.Y. (1970). Nonlinear analysis of stress and strain in soils. *Journal of Soil Mechanics and Foundation Division*, 96(5), 1629-1653.

Garcia, J.A.B. (2013). *Behavior analysis of dams built with clay cores compacted in the wet side* [Master's dissertation, University of Brasília]. University of Brasília's repository (in Portuguese). https://repositorio.unb.br/handle/10482/15402

Garcia, J.A.B., Pinto, V.Q.R., & Assis, A.P. (2019). Effect of moisture content compaction in the definition of Earth Dams. *Proc. 20th International Conference on Geotechnical Modelling, Measurements and Analysis*. Vol. 13, n. 6.

Jalili, J., & Jahanandish, M. (2009). Investigation of construction method of a wet core earth dam in the north of Iran. *Iranian Journal of Science & Technology - Transactions of Engineering*, 33(4), 347-353. https://doi.org/10.22099/IJSTC.2009.712

Kerkes, D.J. (1988).Wet core construction (WCC) technology for embankment dams. *Proc. 16th International Congress on Large Dams*, *San Francisco*. Vol. 3, ICOLD, 1237-1254.

Kondner, R.L. (1963). Hyperbolic stress-strain response: Cohesive soils. *Journal of the Soil Mechanics and Foundations Division*, 89(1), 115-143.

Lambe, T.W. (1958). The engineering behavior of compacted clay. *Journal of the Soil Mechanics and Foundations Division*, 84(2), 1-35.

Mitchell, J.K. (1993). *Fundamentals of Soil Behavior*. John Wiley & Sons.

Morgenstern, N.R., & Price, V.E. (1965). The analysis of the stability of general slip surfaces. *Géotechnique*, 15(3), 79-93. https://doi.org/10.1680/geot.1968.18.3.393

Morpurgo, S. (1976). Influence of climate conditions on Chivor dam construction. *Proc. 12th International*

Congress on Large Dams, *Mexico City*. Vol. 3, ICOLD, 1209-1221.

Rashidi, M., & Haeri, M. (2017). Evaluation of behaviors of earth and rockfill dams during construction and initial impounding using instrumentation data and numerical modelling. *Journal of Rock Mechanics and Geotechnical Engineering*, 9(4), 709-725. https://doi.org/10.1016/j.jrmge.2016.12.003

Silveira, J.F.A. (2006). *Instrumentação e Segurança de Barragens de Terra e Enrocamento*. Oficina de Textos.

Thompson, F., Oliveira, B.C., Cordeiro, M.C., Masi, B.P., Rangel, T.P., Paz, P., & Soares, M. (2020). Severe impacts of the Brumadinho dam failure (Minas Gerais, Brazil) on the water quality of the Paraopeba River. *Science of The Total Environment*, 705, 135914. https://doi.org/10.1016/j.scitotenv.2019.135914

USACE (1970). Engineering and Design: Stability of Earth and Rock-Fill Dams, Engineering Manual 1110-2-1902. *Corps of Engineers, Washington, D.C*.

Villegas, E.; Mejia, O., & Sanchez, G. (1976a). Construction of an earth dam built of silt in Colombia under extremely rainy weather. *Proc. 12th International Congress on Large Dams*, *Mexico City*. Vol. 3, ICOLD, 931-947.

Villegas, E.; Mejia, O., & Sanchez, G. (1976b). Experience on earth dams built of silt in Colombia. *Proc. 12th International Congress on Large Dams*, *Mexico City*. Vol. 1, ICOLD, 581-597.

Soils and Rocks
An International Journal of Geotechnical and Geoenvironmental Engineering
www.soilsandrocks.com
ISSN 1980-9743
ISSN-e 2675-5475

Application of kernel k-means and kernel x-means clustering to obtain soil classes from cone penetration test data

L.O. Carvalho[1], D.B. Ribeiro[1]

Article

Keywords
Artificial neural network
Cone penetration test
Clustering
Soil classification

Abstract

Most methods available in the literature for soil classification from cone penetration test (CPT) data define soil classes using laboratory tests. One disadvantage of this approach is that field soil conditions are difficult to replicate in a lab. The alternative adopted in this work is trying to define soil classes only by the similarity of the CPT measurements, using clustering. This study is the first, to the best knowledge of the authors, to cluster soil classes in a four-dimensional input feature space using measurements directly taken from the CPT experiment. Nine soil classes are produced from a general dataset containing 179 CPT soundings and, in a complementary study, four more specialized classes are obtained from 5 CPT soundings. Artificial neural networks (ANN) are used to produce simple models capable of reproducing both class groups, which are compared with classical soil classifications from the literature and with standard penetration test (SPT) samples. Results show that both general and specialized class groups can be reproduced by ANN although accuracy is better for the latter, reaching a 97.04 % accuracy with a standard deviation of 1.24 %. Furthermore, it is shown that accuracies above 80 % are obtained even if incomplete data is used. This shows that the here proposed soil classes can become an interesting alternative in engineering practice.

1. Introduction

The more commonly used soil classification standard is the Unified Soil Classification System, which is based on granulometry and plasticity. Nevertheless, it has disadvantages like the difficulty of extracting undisturbed samples and the time delay required to get the results. On the other hand, the cone penetration test (CPT) allows an accurate measurement of soil parameters, which can be instantaneously used to classify soil layers along a vertical axis. One important issue concerning this classification is its connection to soil behavior in detriment of soil granulometry. In this context, although pioneer work proposing soil classification from CPT data focused only soil granulometry (Begemann, 1965), following studies stated that soil behavior should guide class definitions for being related to the soil load-bearing capacity (Douglas & Olsen, 1981). In later investigations, pore pressure information was included to define soil classes and propose normalizations for the cone resistance and lateral friction to account for the overburden pressure and better separate classes, which produced the well known Robertson charts (Robertson, 1990). A new friction ratio-based chart was later proposed, changing the circular curves of Robertson (1990) by hyperbolic ones (Schneider et al., 2012). Robertson (2016) modified these charts, defining a fully behavioral classification, including also the dilative and contractive behaviors for each of the three soil types.

Most work that use machine learning techniques for classifying soil from CPT data apply clustering to propose new soil classes (Hegazy & Mayne, 2002; Facciorusso & Uzielli, 2004; Bhattacharya & Solomtine, 2006; Liao & Mayne, 2007; Das & Basudhar, 2009; Rogiers et al., 2017; Wang et al., 2019). One limitation of these work is the reduced number of input features included, most times only two. Another limitation is that most work explore only hierarchical clustering techniques (Hegazy & Mayne, 2002; Facciorusso & Uzielli, 2004; Bhattacharya & Solomtine, 2006; Liao & Mayne, 2007). Nevertheless, a recent study stated that including depth as an input can improve cluster-

[#]Corresponding author. E-mail address: dimas@ita.br.
[1]Departamento de Geotecnia, Divisão de Engenharia Civil, Instituto Tecnológico de Aeronáutica, São José dos Campos, SP, Brazil.

Submitted on April 29, 2020; Final Acceptance on July 15, 2020; Discussion open until March 31, 2021.
DOI: https://doi.org/10.28927/SR.434607

ing results and that the x-means algorithm can lead to good results (Rogiers et al., 2017). In spite of these conclusions, to the best knowledge of the authors, no work from the literature investigated clustering techniques including all measured CPT parameters. Furthermore, the traditional x-means algorithm implemented with the original k-means can only be used for linearly separable classes.

The kernel k-means algorithm is an iterative clustering technique based on the minimization of the variance inside clusters. It allows objects changing from one cluster to another to reduce the overall variance. The kernel x-means algorithm works running kernel k-means several times, splitting the clusters into new ones in each round. In this context, the objective of this work is to use kernels k-means and kernels x-means to produce soil classification methods using four input features: depth, cone resistance, lateral friction and pore pressure. First, kernel k-means is applied to a dataset composed by 179 CPT soundings, of which 5 have paired SPT soundings, generating 9 soil classes. These classes are compared to SPT samples and to Robertson classification methods (Robertson, 1991, 2016) obtained with a student version of the CPeT-IT v2.0.2.5 software. An alternative specialized approach is also presented using the kernel x-means algorithm, which was found to be effective in previous work (Rogiers et al., 2017). It is shown that both proposed soil classification methods can be replicated by an ANN model, even if the pore pressure is not included as an input. This enables reproducing the obtained methods in simple spreadsheets.

2. Classification methods for comparison

The two soil classification methods here used for comparison were developed by Robertson. Only a brief view of their theory is presented here, once they are also used and described in previous work from the authors (Carvalho & Ribeiro, 2019).

2.1 Influenced by soil granulometry (ISG)

This method was proposed by Robertson (1991) and its classes descriptions allude to granulometry:

1. Sensitive, fine grained
2. Organic soils - peats
3. Clays - clay to silty clay
4. Silt mixtures - clayey silt to silty clay
5. Sand mixtures - silty sand to sandy silt
6. Sands - clean sand to silty sand
7. Gravelly sand to sand
8. Very stiff sand to clayey sand
9. Very stiff, fine grained

The normalized parameters used for classification are:

$$F_r = \frac{f_s}{q_t - \sigma_{v0}} \tag{1}$$

$$B_q = \frac{u_2 - u_0}{q_t - \sigma_{v0}} \tag{2}$$

$$Q_{tn} = \left(\frac{q_t - \sigma_{v0}}{p_a}\right)\left(\frac{p_a}{\sigma'_{v0}}\right)^n \tag{3}$$

where q_t is the total cone resistance, which is a correction of the raw cone resistance q_c. f_s is the lateral friction, u_2 is the pore pressure measured behind the cone tip, u_0 is the hydrostatic pore pressure, σ_{v0} is the total overburden stress and σ_{v0}' is the effective overburden stress. n is given by

$$n = 0.381 I_c + 0.05\left(\frac{\sigma'_{v0}}{p_a}\right) - 0.15 \tag{4}$$

where p_a = 0.1 MPa is a reference pressure and I_c is defined as (Robertson, 2009):

$$I_c = [(3.47 - \log Q_{tn})^2 + (\log F_r + 1.22)^2]^{0.5} \tag{5}$$

The charts of the ISG method are shown in Figure 1 and Figure 2.

2.2 Focused on soil behavior (FSB)

This method presented by Robertson (2016) is considered fully behavioral and proposes the following classes:

1. CCS: Clay-like - Contractive - Sensitive
2. CC: Clay-like - Contractive
3. CD: Clay-like - Dilative
4. TC: Transitional - Contractive
5. TD: Transitional - Dilative
6. SC: Sand-like - Contractive
7. SD: Sand-like - Dilative

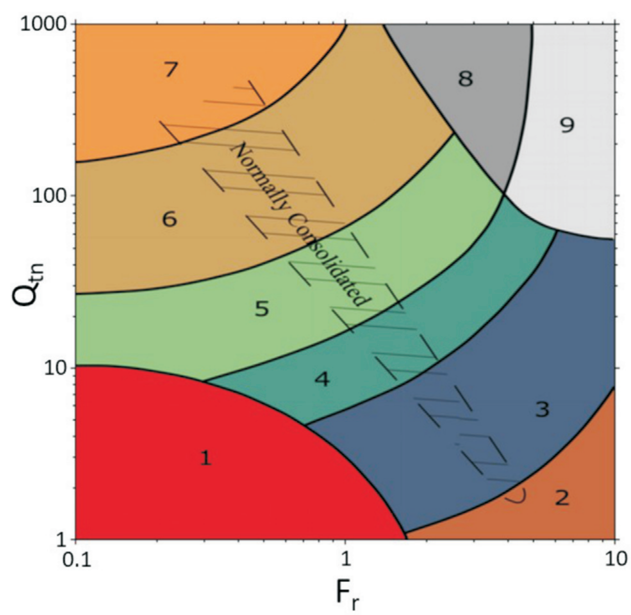

Figure 1. $Q_{tn} \times F_r$ chart from Robertson (1991).

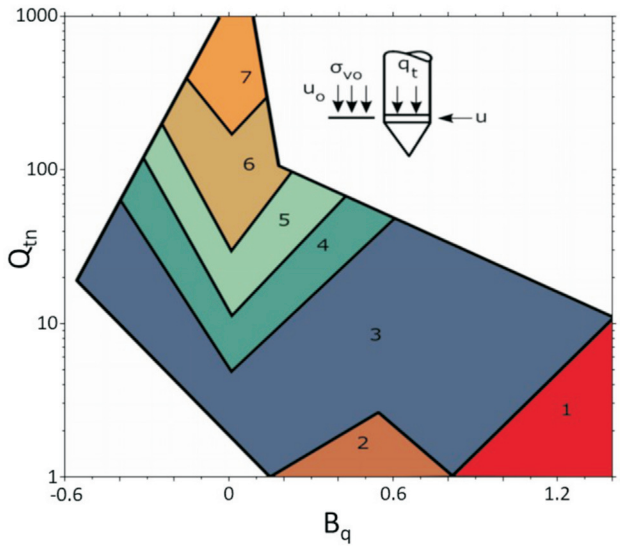

Figure 2. $Q_{tn} \times B_q$ chart from Robertson (1991).

It uses the charts presented in Figure 3 and Figure 4 (Schneider et al., 2008, 2012), where U_2 is given by:

$$U_2 = \frac{u_2 - u_0}{\sigma'_{v0}} \tag{6}$$

3. Machine learning tools

3.1 Kernel k-means

The kernel k-means algorithm is a modification of the k-means algorithm, which groups the instances by partition, with a fixed number k of clusters. It is an iterative clustering technique based on the optimization of a clustering criterion, the mean squared error. For each iteration, differently from the hierarchical clustering, the objects can change from one cluster to another to reduce the error. The error is a measure of the variance inside the clusters, which has to be minimized. The mean squared error E is then given by the sum of the variances inside clusters for the k clusters as follows:

$$E = \sum_{j=1}^{k} \sum_{\mathbf{x}_i \in C_j} d(\mathbf{x}_i, \mathbf{x}^{(j)})^2 \tag{7}$$

where $d(\mathbf{x}_i, \mathbf{x}^{(j)})$ is the distance between the object $\mathbf{x}_i$ and the cluster centroid $\mathbf{x}^{(j)}$.

The algorithm does the following steps:

1. The first k centroids are randomly chosen
2. Each object is included in the group whose centroid is closer
3. A new centroid is then defined for each group in order to minimize the mean squared error
4. Steps (2) and (3) are repeated until conversion is observed, within a predefined error margin.

The most used similarity measure is the Euclidean distance, which requires data normalization in order to avoid distortions due to data scale. The main advantage of k-means is its linear complexity, but its main disadvantages include the possibility of converging to local optimum and

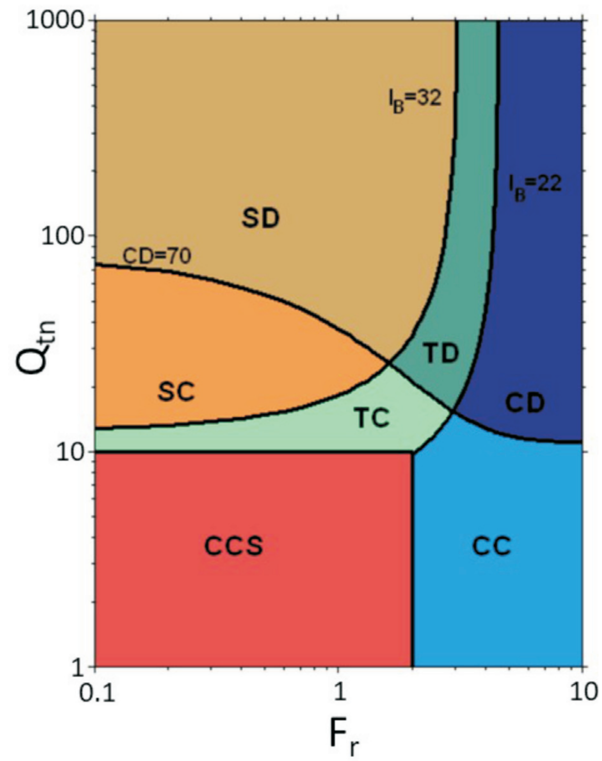

Figure 3. $Q_{tn} \times F_r$ chart from Robertson (2016).

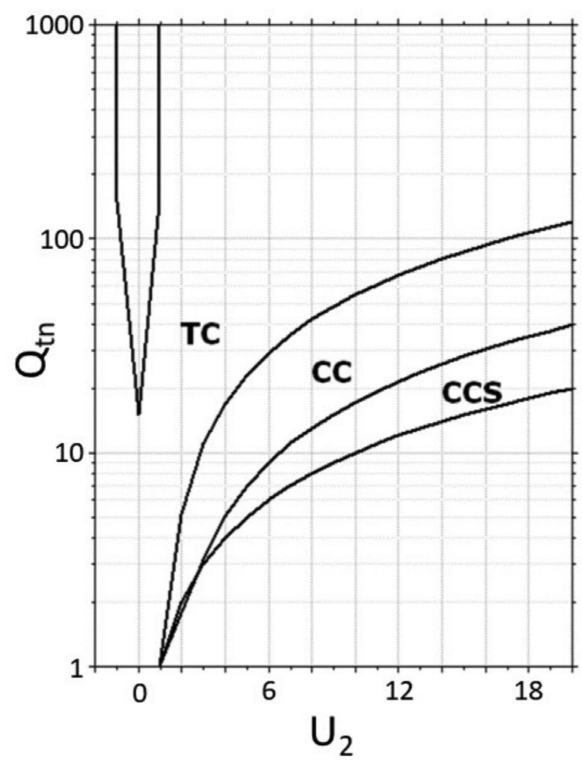

Figure 4. $Q_{tn} \times U_2$ chart from Robertson (2016).

being applicable only to linearly separable classes. Other weaknesses that can compromise analysis are its sensitivity to initialization, the possibility of generating imbalanced clusters and the need of previously fixing *k*. One simple alternative to search for the best *k* and avoid local minimums is running the algorithm several times, varying *k* and the initialization. This procedure is adopted in this work.

One way to deal with classes that are not linearly separable is using a function to map the data from the original feature space into a higher dimensionality feature space wherein the objects are linearly separable. Nevertheless, non-linear transformation and high dimensionality are required to guarantee linear separability. Most work that make use of this approach do not define the function directly, but only a kernel function, which is sufficient to obtain the Euclidean distance. The Gaussian kernel adopted in this work is exp $(-\sigma\|\mathbf{x}_i - \mathbf{x}_j\|^2)$, where $\mathbf{x}_i$ and $\mathbf{x}_j$ are points within input feature space and σ is the only calibration parameter required, which can be estimated from the data as the median of $\|\mathbf{x}_i - \mathbf{x}_j\|^2$.

3.2 Artificial neural networks

Artificial neural networks (ANN) are based on the brain functioning, with a structure constituted by processing units called neurons, which are connected by weighted signals called synapses. The first artificial neuron model, called Perceptron, was proposed by McCulloch & Pitts (1943). Its practical applicability was formalized with the work of Rosenblatt (1957).

In a Perceptron neuron, an object **x** receives *n* signals (inputs), which are weighted by a vector **w**. After these weighted inputs are gathered, an excitatory threshold or bias θ is discounted, producing a net signal *u*. This net signal is then subjected to an activation function g to produce an output signal $y = g(u) = g(\mathbf{w}.\mathbf{x} - \theta)$. This process is illustrated in Fig. 5. In this work, the sigmoid function is used for activation, which is presented below.

$$g(u) = \frac{1}{1+e^{-\lambda u}} \tag{8}$$

where λ is a parameter to be calibrated. Data normalization is required, rescaling each input feature to the range [0,1]. One limitation of this model is that it can only be used for linearly separable classes. Non-linear cases require using multi-layer neural networks, which can be trained with the back-propagation algorithm (Rumelhart et al., 1986). Figure 6 represents the structure of this model, wherein each neuron is a Perceptron. According to the universal approximation theorem (Hornik et al., 1989), an ANN with one hidden layer is sufficient to replicate any continuous function. Thus, two hidden layers are enough to replicate even discontinuous functions.

Once there are infinite possibilities for an ANN model, restrictions must be defined to limit the number of calibration tests. The sigmoid function was fixed based on previous experience of the authors, the number of neurons for each layer was limited to double the number of classes and the number of layers was limited to 2. These decisions about architecture were based on the universal approximation theorem. Readers interested in further discussions about this issue are referred to Carvalho et al. (2019).

4. Methodology

4.1 Used datasets

Two datasets are used in this work, one named Full dataset and the other named Specific dataset. The objective is to demonstrate that more homogeneous datasets lead to ANN models with better accuracy. The Full dataset is composed by measurements taken within 179 CPT soundings, which are briefly described below:

- 38 taken in several countries and provided by Professor Peter Robertson. See Carvalho & Ribeiro (2019);
- 73 were taken in the USA and made available online by Professor Paul Mayne. See Carvalho & Ribeiro (2019);
- 1 was taken in Vancouver, Canada and provided by Professor Renato da Cunha. See Cunha (1994);
- 5 were taken in Brazil paired with SPT soundings and provided by Professor Heraldo Giacheti. See reference Ide (2009).
- 62 were taken in Brazil and provided by the São Paulo Metropolitan Trains Company, São Paulo, Brazil.

The 179 CPT soundings produced 130966 examples for the machine learning techniques, each example consisting on a CPT measurement taken at a specific depth. Figures 7a and 7b show histograms for the objects distribution

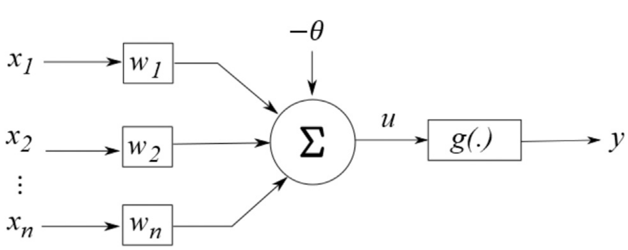

Figure 5. Perceptron neuron.

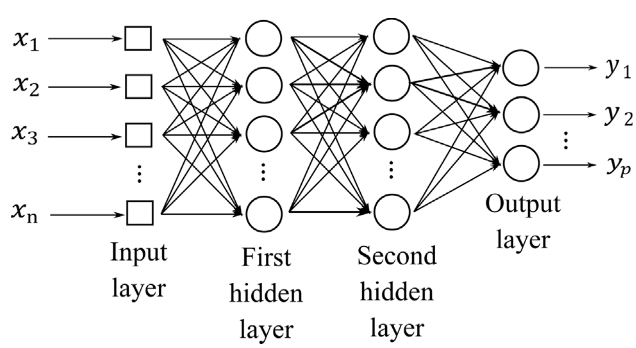

Figure 6. Multilayer neural network.

of the Full dataset among the ISG and FSB classes, respectively. Even though there is an imbalance, the minority classes for the ISG and FSB methods have 381 and 5136 objects, respectively. Preliminary tests have shown that this is enough to represent these minority classes among the majority ones.

The Specific dataset is a subset of the Full dataset and is composed by the measurements taken within the 5 CPT soundings provided by Professor Heraldo Giacheti. The paired SPT soundings provided 2847 soil samples, which are here divided into three classes, sands (60,2 % of samples), silts (16,1 % of samples) and clays (23,7 % of samples).

One of the objectives of this work is comparing these three SPT classes to the ones of the ISG method, of the FSB method and also to the ones here obtained by clustering.

4.2 Clustering analysis

Two separated studies are performed, one using the Full dataset and the other using the Specific dataset. Both of them are divided into two phases: clustering analysis and ANN modeling. First, the objects are grouped by the kernel k-means algorithm. For this step, the four measured CPT parameters are used to compose the original feature space: depth z (m), raw cone resistance q_c (MPa), lateral friction f_s (kPa) and pore pressure measured behind the cone tip u_2 (kPa). Using these inputs instead of normalizations such as Q_t, B_q and F_r avoids reducing information within the dataset. Thus, a previous work from the authors suggests that dismissing this type of normalizations makes sense for soil classification (Carvalho & Ribeiro, 2019). For both approaches the Gaussian kernel, which is calibrated by the median of the distance between points, is used to map the objects into a higher dimension feature space (see Section 3.1).

For the Full dataset, the procedure adopted to define the number of classes was manually varying this number and adopting the one with the lowest total variance inside clusters. This procedure lead to 9 classes, as described in Section 5.1. For the Specific dataset, the kernel x-means algorithm was employed. One basic version of this algorithm consists in running the kernel k-means several times from $k = 2$ and splitting the clusters into two new clusters in each round while a parameter called Bayesian Information Criterion is improved (Pelleg & Moore, 2000). Once this parameter gets any worse, the algorithm stops. The result for this case was 4 classes, as presented in Section 5.2.

After obtaining the clusters, they are compared to ISG classes, to FSB classes and to the three SPT classes defined in Section 4.1.

4.3 ANN modeling

In this work, ANN models are created to replicate soil classification systems obtained by clustering. The 10-fold cross-validation procedure (Stone, 1974) is employed to evaluate the predictive performance of the ANN models, as illustrated in Fig. 8. This procedure was adopted to avoid overfitting and to calculate a standard deviation of the accuracies obtained within the 10 iterations, which is an important information to be presented together with the mean accuracy.

The procedure starts dividing the dataset in 10 folds of the same size. At each step, one of the 10 folds is randomly selected and separated from the other 9. These 9 folds are then used for training, while the one kept apart is used for testing, obtaining an accuracy. Selection is made without reposition, allowing all folds to be tested after 10 steps. The mean and standard deviation of the obtained accuracies represent the predictive performance of the ANN model.

Notice that all soil samples received a class within the clustering procedure described in Section 4.2, making possible to check all predictions given by the ANN algorithm. Recall R_i is defined as the number of right predictions for one class i divided by its number of examples n_i:

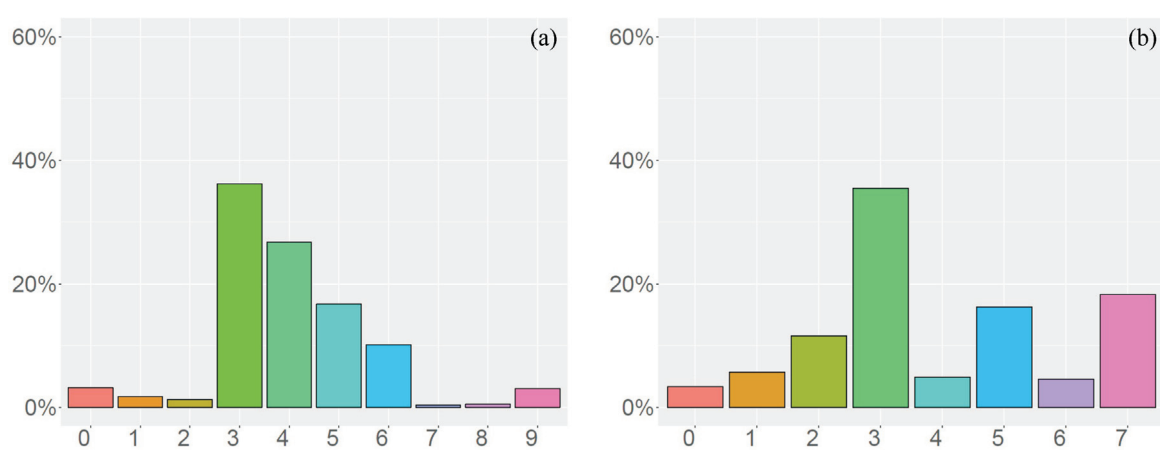

Figure 7. Histograms for the Full dataset: (a) distribution for ISG classes and (b) distribution for FSB classes.

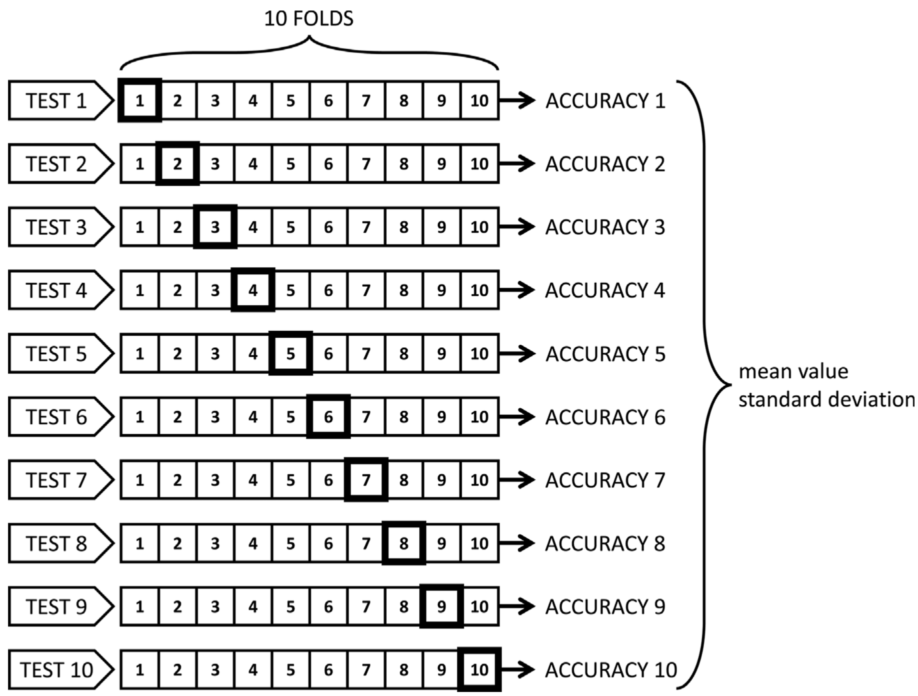

Figure 8. 10-fold cross validation.

$$R_i = \frac{1}{n_i}\sum_{j=1}^{n_i} I_{ij} \tag{9}$$

where $I_{ij} = 1$ if the model made a right prediction and $I_{ij} = 0$ otherwise. In this work, the mean recall is used as performance measure and, from this point of the text, referred simply as accuracy A for a sake of clarity. For c classes, it is obtained as

$$A = \frac{1}{c}\sum_{i=1}^{c} R_i \tag{10}$$

Preprocessing procedures are used within the 10-fold cross validation procedure to improve the predictive performance of the ANN algorithms. Once these procedures are described in previous work from the authors (Carvalho et al., 2019), they are here omitted for conciseness.

5. Results and discussion

5.1 Clustering analysis with the full dataset

To produce the results presented within this section, the kernel k-means algorithm was applied. k was varied from 7 to 10, using the Full dataset and all CPT original measurements: z (m), q_c (MPa), f_s (kPa) and u_2 (kPa). The model with $k = 9$ was the one with the lowest total internal cluster variance, therefore it is the only one here presented. The 9 clusters, each one representing a soil class, have centers which coordinates are presented in Table 1.

In Tables 2 and 3 the clustering results are compared to ISG and FSB classes, respectively. Lines represent clustering classes and columns represent chart-based methods.

Table 1. Clusters centers.

Class	z (m)	q_c (MPa)	f_s (kPa)	u_2 (kPa)
1	44.16	32.33	662.38	1864.94
2	38.10	21.35	262.94	2296.68
3	53.57	35.98	369.36	2391.77
4	67.26	63.86	787.28	2835.83
5	57.50	53.01	573.79	2490.12
6	54.30	51.00	835.36	1964.86
7	44.93	35.75	612.18	4017.64
8	68.29	24.19	278.07	4931.17
9	23.91	20.88	165.71	2036.20

Each value is a percentage of soil samples that were assigned to a clustering class (line) and also to a specific ISG or FSB class (column). ISG class 0 is omitted from Table 2 due to its low representative among the used examples.

Observing Tables 2 and 3, the following interpretations were produced for the 9 cluster classes:

- Classes 1 and 2: They present similar distributions among ISG classes, with a predominance of clay behavior (ISG classes 3 and 4). This predominance is also observed within FSB classes (1, 2 and 3), although the cluster classes appear to become different.
- Class 3: ISG classes 5 and 6, which represent sand behavior, compose 65 % of this cluster class. Similar per-

Table 2. Comparing cluster classes to ISG classes (%).

	Sensitive	Organic	Clays	Clayey silt	Sand mixtures	Sands	Gravelly sand	Stiff to clayey sand	Stiff fine grained
1		2	3	4	5	6	7	8	9
1	0	1	46	34	14	2	0	0	3
2	3	3	48	24	17	4	0	0	0
3	0	1	19	15	24	41	0	0	0
4	0	0	0	1	4	94	1	0	0
5	0	0	0	1	12	86	1	0	0
6	0	0	15	23	19	38	0	1	3
7	0	0	28	19	18	15	1	7	13
8	8	1	67	19	5	0	0	0	0
9	5	6	22	21	30	14	0	0	1

Table 3. Comparing cluster classes to FSB classes (%).

		CCS	CC	CD	TC	TD	SC	SD
	0	1	2	3	4	5	6	7
1	1	1	7	55	1	23	0	12
2	12	11	26	14	9	9	8	10
3	2	4	17	1	10	4	18	44
4	1	0	0	0	0	2	0	97
5	0	0	0	0	0	1	2	96
6	1	0	1	27	0	21	0	50
7	8	4	18	25	6	15	0	24
8	19	37	26	2	11	4	1	1
9	29	10	5	11	10	4	18	13

centage is obtained if FSB classes 6 and 7 are added, which also represent sand behavior.

- Classes 4 and 5: These classes clearly represent sand behavior, with high percentages assigned to ISG class 6 and FSB class 7. Their similarity suggests merging them together.
- Classes 6 and 7: Once the behavior of these classes is well distributed among ISG and FSB classes, they are here considered transitional. In other words, behavior that cannot be clearly distinguished between sand and clay.
- Class 8: This class is strongly identified with clay behavior, with 86 % of ISG classes 3 and 4 and 65 % of FSB classes 1, 2 and 3.
- Class 9: Its behavior is also distributed among ISG and FSB classes, being here considered transitional.

Table 4 was produced to compare ISG classes (columns) with the sample observations obtained via SPT sampling (lines). Numbers represent percentages, similarly to the previous tables, and some ISG classes are omitted for being underrepresented with samples. As defined in Section 3, SPT classes represent sand, silt and clay. Moving from ISG classes 3 to 6, one can observe an increase of sand and decrease of clay, which is coherent with their names given in Section 2.1. An analogous analysis is proposed with Table 5, comparing FSB classes (columns) to SPT (lines). The correspondence to the FSB class names given in Section 2.2 is not clear, except for FSB classes 3 and 7. This suggests that FSB is less sensitive to soil granulometry than ISG.

The clustering results were also compared to the SPT sample observations, resulting Table 6. Cluster classes 3 and 8 contain relevant parts of sand and clay, being here identified as transitional. Class 4 is the only one with predominance of clay and the other can be identified with sand. These observations do not match the ones provided by the comparisons to the ISG and FSB methods, showing that

Table 4. Comparison between SPT observations and ISG classes (%).

	Clays	Clayey silt	Sand mixtures	Sands
	3	4	5	6
Sand	45	59	62	69
Silt	25	13	17	12
Clay	30	28	21	19

Table 5. Comparison between SPT observations and FSB classes (%).

	CC	CD	TC	TD	SC	SD
	2	3	4	5	6	7
Sand	39	46	66	61	53	68
Silt	5	29	13	11	23	13
Clay	56	25	20	28	25	19

Table 6. Comparison between the k-means clustering and the SPT observations (%).

	Sand	Silt	Clay
1	53	20	27
2	62	22	17
3	47	14	39
4	39	0	61
5	79	0	21
6	69	0	31
7	40	52	8
8	63	0	37
9	90	10	0

soil granulometry alone is not enough to explain its mechanical behavior.

To better illustrate the cluster classes obtained, a case study is presented in Fig. 9. A 29.3 m sounding from the USA was used, being classified using the ISG classes (Fig. 9a), the FSB classes (Fig. 9b) and the cluster classes presented in this section (Fig. 9c). The name of the classes is the same adopted in Tables 2 and 3 and colors are used independently for each classification method.

The last step of this analysis is applying ANN to produce a model capable of reproducing the obtained classification method. This procedure resulted a model with an accuracy of 89.35 % with a standard deviation of 0.40 %, corresponding to an architecture with only one hidden layer with 18 neurons.

Another ANN model was trained using only z, q_c and f_s as input features. The objective is verifying if CPT equipment without a pore pressure filter can provide enough information to approximate the method. The resultant model presented an accuracy of 84.47 % with a standard deviation of 0.30 %, corresponding to an architecture with two hidden layers, the first with 16 neurons and the second with 18 neurons.

The weight matrices and bias vectors produced for the ANN models of this section are here omitted for conciseness. Readers interested in this information are advised to contact the authors.

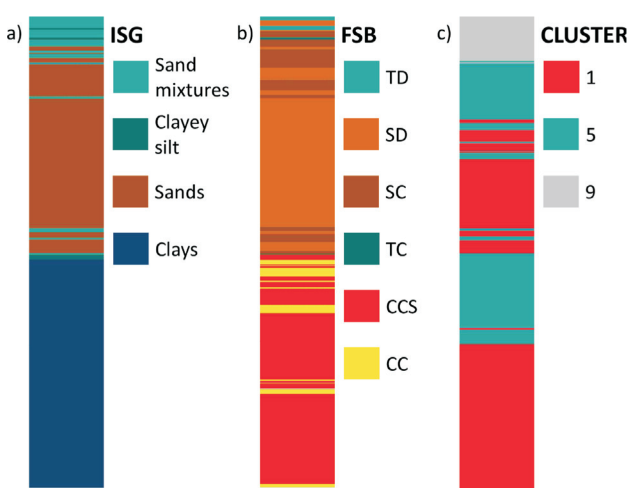

Figure 9. Comparing cluster classes to ISG and FSB classes: (a) distribution for ISG classes, (b) distribution for FSB classes and (c) distribution for cluster classes.

5.2 Specialized approach

Using CPT data from only 5 soundings, all from the same site, tends to improve classification accuracy. Nonetheless, the obtained model becomes limited to the soil types measured within these 5 soundings. For that reason, these clusters are here considered more specialized than those obtained in the previous section. This strategy is here investigated using the kernel x-means algorithm instead of varying manually the number of classes, which enables maintaining the minimum total internal cluster variance as a performance measure. This allows comparing different results given by this algorithm in cases wherein a high variation of the number of classes k is observed.

Only 5 CPT soundings are used to obtain the specialized classification method by clustering, all taken from the same location and paired with SPT soundings. With the kernel x-means algorithm, 4 classes were found to be the best for the considered dataset, with their centers presented in Table 7.

Crossing results with the ISG and FSB classification methods and to SPT soundings, Tables 8, 9 and 10 are obtained, respectively. As in the previous section, values represent percentages of soil assigned to a cluster class (line) and also to a reference method class (column).

Table 7. Specialized clusters centers.

Class	z (m)	q_c (MPa)	f_s (kPa)	u_2 (kPa)
1	11.61	18.77	304.56	828.22
2	12.24	29.70	394.80	842.16
3	10.23	15.94	270.72	605.18
4	6.83	15.54	214.32	423.96

Table 8. Comparison between the specialized x-means clustering and the ISG classes (%).

	Organic	Clays	Clayey silt	Sand mixtures	Sands
	2	3	4	5	6
1	0	25	27	40	8
2	0	0	6	26	68
3	3	32	16	37	12
4	0	12	19	27	43

Table 9. Comparison between the specialized x-means clustering and the FSB classes (%).

	CCS	CC	CD	TC	TD	SC	SD
	1	2	3	4	5	6	7
1	0	4	26	3	22	8	36
2	0	0	2	0	10	0	89
3	2	10	27	8	8	16	29
4	0	1	15	6	10	7	60

Table 10. Contribution of each soil granulometrical type for each behavior (%).

	Sand	Silt	Clay
1	52	12	36
2	73	0	27
3	56	17	28
4	63	37	0

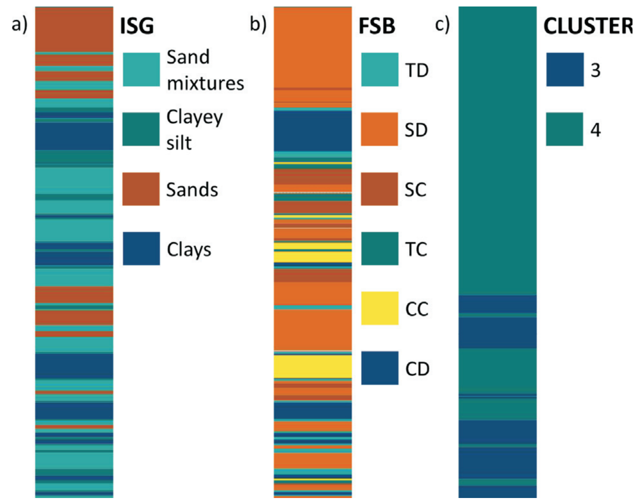

Figure 10. Specialized cluster classes compared to ISG and FSB classes: (a) distribution for ISG classes, (b) distribution for FSB classes and (c) distribution for specialized cluster classes.

For this case, some agreement can be observed for the soil type of the cluster classes when compared to ISG, FSB and SPT. Cluster class 1 shows a subtle predominance of sand over clay when compared to the ISG, which is also observed for FSB and SPT. The predominance of sand is clearer for cluster class 2, specially comparing to FSB. Cluster class 3 seems to confuse the ISG and FSB methods, although it can be identified as sand considering SPT alone. Finally, cluster class 4 can be also identified as sand, although such correlation is weaker than the one observed for cluster class 2.

Comparing these results with the ones of the previous section, one can conclude that specializing classification improves agreement with SPT sampling. This can be considered an advantage, for uniting the model capability of predicting soil behavior to a correspondence with SPT visual-tactile observations.

A case study is also presented for the specialized cluster classes, which can be observed in Fig. 10. This sounding is 12.3 m long and is one of the 5 used to produce the specialized cluster classes used in this section. Class names are the same used in Tables 8 and 9.

In the end, an ANN model was produced in order to reproduce the obtained specialized classification method. The obtained model presented very good predictive performance, with an accuracy of 97.04 % and a standard deviation of 1.24 %. This result can be considered significantly better than the one obtained for the general approach, suggesting that limited extrapolations with the specialized approach are feasible. The weight matrices and their respective bias vectors for this last ANN model are:

$$\mathbf{W}_1^T = \begin{bmatrix} 10.85171 & -4.92947 & -0.90277 & 5.630497 \\ -6.626574 & -11.7869 & -11.2992 & -4.61007 \\ -23.57666 & -3.75753 & -5.7113 & -17.3486 \\ 24.05597 & 15.3592 & 6.625066 & 24.37708 \\ -6.341736 & -32.29 & -18.1987 & -1.49596 \end{bmatrix}, \quad \Theta_1 = \begin{bmatrix} -5.71002 \\ 19.23977 \\ 25.96866 \\ -42.46379 \\ 35.97992 \end{bmatrix} \tag{11}$$

$$\mathbf{W}_2 = \begin{bmatrix} -7.511974 & 6.628167 & -2.40889 & -9.79977 \\ -7.438816 & -2.86605 & 7.8636 & 6.841357 \\ -10.67961 & -6.61815 & -23.5403 & 15.40886 \\ 15.99294 & 4.706883 & -15.8327 & -7.36243 \\ 19.26499 & -16.8685 & -5.45426 & 1.734535 \end{bmatrix}, \quad \Theta_2 = \begin{bmatrix} -14.7905 \\ -5.20106 \\ 10.22392 \\ -7.19002 \end{bmatrix} \tag{12}$$

One can notice that these matrices correspond to an architecture with only one hidden layer containing five neurons. In this case it was also evaluated if suppressing pore pressure information prejudices predictive performance. The resultant ANN model, that makes use of only z, q_c and f_s, presented an accuracy of 90.37 % with a standard deviation of 2.48 %. This accuracy can be considered good within geotechnical engineering problems, with the advantage of enabling the use of alternative CPT equipment. This ANN model uses the following weight matrices and bias vectors:

$$\mathbf{W}_1^T = \begin{bmatrix} 26.01 & 7.43 & 0.63 \\ -27.72 & 0.3 & 2.88 \\ -11.63 & -17.05 & 2.1 \\ 10.45 & 12.12 & 13.9 \\ 0.37 & 0.52 & -24.2 \\ 19.4 & -24.54 & -12.07 \end{bmatrix}, \quad \Theta_1 = \begin{bmatrix} -22.3225 \\ 19.83825 \\ 15.85711 \\ -23.10527 \\ 10.44827 \\ 0.0736 \end{bmatrix} \tag{13}$$

$$\mathbf{W}_2 = \begin{bmatrix} -1{,}74 & -16.37 & -14.24 & -0.92 & 0.15 \\ -3.11 & 5.96 & 15.79 & -1.36 & -5.08 \\ 6.34 & 2.68 & 6.87 & 2.68 & -16.13 \\ -3.42 & -13.38 & -4.87 & -11.16 & 11.62 \\ 4.09 & 7.71 & 7.26 & -2.25 & -356 \\ 9.62 & -5.48 & -8.32 & 8.63 & -17.26 \end{bmatrix}, \quad \Theta_2 = \begin{bmatrix} 0.77985 \\ -5.41468 \\ 11.45654 \\ -0.42104 \\ -9.51452 \end{bmatrix} \tag{14}$$

$$\mathbf{W}_3 = \begin{bmatrix} 3.14 & -6.33 & -3.29 & 0.44 \\ -6.64 & -4.56 & -6.56 & 8.56 \\ -6.35 & -2.3 & 6.44 & 2.5 \\ -4.74 & -2.06 & 4.74 & -0.92 \\ -11.77 & 9.8 & -2.39 & -6.47 \end{bmatrix}, \quad \Theta_3 = \begin{bmatrix} 4.40147 \\ -3.49722 \\ -4.38422 \\ -6.43941 \end{bmatrix} \tag{15}$$

These matrices correspond to an ANN architecture with two hidden layers, the first with 6 neurons and the second with 5 neurons.

6. Conclusions and recommendations

This work explores the kernel k-means and kernel x-means clustering algorithms to group CPT data into different soil classes. Using a kernel function to modify the k-means algorithm enables evaluating classes that are not linearly separable. Next, ANN are used to create mathematical models which can be easily reproduced. Two different approaches are studied, one is general and the other more specialized. The general approach uses 179 soundings from different sources to develop an ANN model that can be better extrapolated to any new CPT data. On the other hand, the specialized approach requires running the kernel x-means to generate specialized classes for each site investigation, as well as producing a new ANN model. The specialized model is expected to be more accurate for sites with soils similar to those for which it was trained, but it is also expected to be more limited for extrapolation. This approach is applied to 5 soundings for which the CPT soundings were paired with SPT soundings. Results confirm that the specialized model produces more well-defined classes and a more accurate ANN model. The mean accuracy (*MA*) and standard deviation (*SD*) obtained for all ANN models are summarized in Table 11.

Table 11. Mean accuracy and standard deviation obtained for all ANN models.

	Inputs	*MA* (%)	*SD* (%)
Full dataset	$z\ q_c\ f_s\ u_2$	89.35	0.40
	$z\ q_c\ f_s$	84.47	0.30
Specific dataset	$z\ q_c\ f_s\ u_2$	97.04	1.24
	$z\ q_c\ f_s$	90.37	2.48

These values can be considered reasonable when compared to other studies from the literature that used ANN to predict soil classes from CPT data, as Bhattacharya & Solomatine (2006) that achieved 83 % and Kurup & Griffin (2006) that achieved 86 %. Thus, Elkateb et al. (2003) cite a case study that shows that pure engineering judgment can lead to 70 % of poor to bad soil predictions.

One advantage of the here proposed methodology is that the ANN models can be reproduced with spreadsheets by simply combining the calibrated weights with the used activation functions. What makes it different from other methods from the literature is the possibility of approximating the soil classes without pore pressure information, becoming an important alternative for geotechnical engineers in cases that high accuracies are not required. Thus, to the best knowledge of the authors, this is the first study that produces ANN models from tropical soil CPT data, being recommended for projects within tropical countries. Nonetheless, this model can be considered limited to the types of soil for which the ANN models were trained, which is critical particularly for the specialized approach.

Acknowledgments

To Peter K. Robertson, Paul W. Mayne, Company of São Paulo Metropolitan, Renato P. da Cunha and Heraldo L. Giacheti for making available the dataset used in this work.

References

Begemann, H.K.S. (1965). The friction jacket cone as an aid in determining the soil profile. *Proc. 6th International Conference on Soil Mechanics and Foundation Engineering*, Montreal, Vol. 1, Univ. of Toronto Press, 17-20.

Bhattacharya, B., & Solomatine, D.P. (2006). Machine learning in soil classification. *Neural Networks*, 19(2), 186-195. https://doi.org/10.1016/j.neunet.2006.01.005

Carvalho, L.O., & Ribeiro, D.B. (2019). Soil classification system from cone penetration test data applying distance-based machine learning algorithms. *Soils and Rocks*, 42(2), 167-178. https://doi.org/10.28927/SR.422167

Carvalho, L.O., Ribeiro, D.B., & Monteiro, F.A.C. (2019). Comparing artificial neural networks with support vector machines for soil classification. *Proc. XL Ibero-Latin-American Congress on Computional Methods in Engineering*, Natal, ABMEC, 11-14.

Cunha, R.P. (1994). *Interpretation of selfboring pressuremeter tests in sand* [Doctoral dissertation, The University of British Columbia] University of British Columbia's repository. https://doi.org/10.14288/1.0050418

Das, S.K., & Basudhar, P.K. (2009). Utilization of self-organizing map and fuzzy clustering for site characterization using piezocone data. *Computers and Geotechnics*, 36(1-2), 241-248. https://doi.org/10.1016/j.compgeo.2008.02.005

Douglas, B.J. (1981). Soil classification using electric cone penetrometer. *Proc. Symp. on Cone Penetration Testing and Experience, Geotechnical Engineering Division, New York*, ASCE, 209-227.

Elkateb, T., Chalaturnyk, R., & Robertson, P.K. (2003). An overview of soil heterogeneity: quantification and implications on geotechnical field problems. *Canadian Geotechnical Journal*, 40(1), 1-15. https://doi.org/10.1139/t02-090

Facciorusso, J., & Uzielli, M. (2004). Stratigraphic profiling by cluster analysis and fuzzy soil classification from mechanical cone penetration tests. *Proc. ISC-2 on Geotechnical and Geophysical Site Characterization, Porto*. Vol. 1, Millpress, 905-912.

Hegazy, Y.A., & Mayne, P.W. (2002). Objective site characterization using clustering of piezocone data. *Journal of Geotechnical and Geoenvironmental Engineering*, 128(12), 986-996. https://doi.org/10.1061/(ASCE)1090-0241(2002)128:12(986)

Hornik, K., Stinchombe, M., & and White, H. (1989). Multilayer feedforward networks are universal approximators. *Neural Networks*, 2(5), 359-366. https://doi.org/10.1016/0893-6080(89)90020-8

Ide, D.M. (2009). *Geotechnical site characterization and study of an erosion process caused by urban setting* [Master's dissertation, University of São Paulo] University of São Paulo's repository. https://doi.org/10.11606/D.18.2009.tde-22032010-094227

Kurup, P.U., & Griffin, E.P. (2006). Prediction of soil composition from CPT data using general regression neural network. *Journal of Computing in Civil Engineering*, 20(4), 281-289. https://doi.org/10.1061/(ASCE)0887-3801(2006)20:4(281)

Liao, T., & Mayne, P.W. (2007). Stratigraphic delineation by three-dimensional clustering of piezocone data. *Georisk*, 1(2), 102-119. https://doi.org/10.1080/17499510701345175

McCulloch, W., & Pitts, W. (1943). A logical calculus of ideas immanent in nervous activity. *Bulletin of Mathematical Biophysics*, 5(4), 115-133. https://doi.org/10.1007/BF02478259

Pelleg, D., & Moore, A. (2000). X-means: Extending k-means with efficient estimation of the number of clusters. *Proc. 17th Int. Conf. Mach. Learning*, *Stanford.* Stanford University, 727-734.

Robertson, P.K. (1990). Soil classification using the cone penetration test. *Canadian Geotechnical Journal*, 27(1), 151-158. https://doi.org/10.1139/t90-014

Robertson, P.K. (1991). Soil classification using the cone penetration test: Reply. *Canadian Geotechnical Journal*, 28(1), 176-178. https://doi.org/10.1139/t91-024

Robertson, P.K. (2009). Interpretation of cone penetration tests - a unified approach. *Canadian Geotechnical Journal*, 46(11), 1337-1355. https://doi.org/10.1139/T09-065

Robertson, P.K. (2016). Cone penetration test (CPT)-based soil behaviour type (SBT) classification system - An update. *Canadian Geotechnical Journal*, 53(12), 1910-1927. https://doi.org/10.1139/cgj-2016-0044

Rogiers, B., Mallants, D., Batelaan, O., Gedeon, M., Huysmans, M., & Dassargues, A. (2017). Model-based classification of CPT data and automated lithostratigraphic mapping for high-resolution characterization of a heterogeneous sedimentary aquifer. *Plos One*, 12(5), e0176656. https://doi.org/10.1371/journal.pone.0176656

Rosenblatt, F. (1957). The Perceptron: A Perceiving and Recognizing Automation. Technical Report. *Cornell Aeronautical Laboratory, Buffalo*, NY.

Rumelhart, D.E., Hinton, G.E., & Williams, R.J. (1986). Learning representations by back-propagation errors.

Nature, 323(9), 340-347. https://doi.org/10.1038/323533a0

Schneider, J.A., Hotstream, J.N., Mayne, P.W., & Randolph, M.F. (2012). Comparing CPTU Q-F and Q-$\Delta u_2/\sigma'_{v0}$ soil classification charts. *Geotechnique Letters*, 2(4), 209-215. https://doi.org/10.1680/geolett.12.00044

Schneider, J.A., Randolph, M.F., Mayne, P.W., & Ramsey, N.R. (2008). Analysis of factors influencing soil classification using normalized piezocone tip resistance and pore pressure parameters. *Journal of Geotechnical and Geoenvironmental Engineering*, 134(11), 1569-1586. https://doi.org/10.1061/(ASCE)1090-0241(2008)134:11(1569)

Stone, M. (1974). Cross-validatory choice and assessment of statistical predictions. *Journal of the Royal Statistical Society: Series B (Methodological)*, 36(2), 111-133. https://doi.org/10.1111/j.2517-6161.1974.tb00994.x

Wang, X., Wang, H., Liang, R.Y., & Liu, Y. (2019). A semi-supervised clustering-based approach for stratification identification using borehole and cone penetration test data. *Engineering Geology*, 248, 102-116. https://doi.org/10.1016/j.enggeo.2018.11.014

Internet resources

Prof. Paul Mayne website, http://geosystems.ce.gatech.edu/Faculty/Mayne/Research/index.html, accessed at 02/03/2020.

List of symbols

A: mean recall
B_q: normalized excess pore pressure
c: number of classes
$d(\mathbf{x}_i, \mathbf{x}^{(j)})$: distance between $\mathbf{x}_i$ and $\mathbf{x}^{(j)}$
E: mean squared error
F_r: normalized friction ratio
f_s: lateral friction
I_c: classification index
I_{ij}: equals 1 if prediction j of class i is correct, equals 0 otherwise
k: number of clusters
n: exponent of σ_{v0}'
n_i: number of examples of class i
p_a: reference pressure
q_c: cone resistance
q_t: total cone resistance
Q_{t1}: normalized cone resistance
Q_{tn}: updated normalized cone resistance
R_i: recall of class i
u_0: equilibrium pore pressure
u_2: pore pressure measured behind the cone tip
U_2: updated normalized excess pore pressure
$\mathbf{w}$: Gaussian weighting
$\mathbf{x}_i$, $\mathbf{x}_j$: points representing objects
$\mathbf{x}^{(j)}$: cluster centroid
y, g, u, w, x, θ, λ: parameters of the Perceptron neuron
z: depth
σ: calibration parameter
σ_{v0}: total overburden pressure
σ_{v0}': effective overburden pressure

Soils and Rocks
An International Journal of Geotechnical and Geoenvironmental Engineering
www.soilsandrocks.com
ISSN 1980-9743
ISSN-e 2675-5475

Geostatistical data analysis of the Standard Penetration Test (SPT) conducted in Maringá-Brazil and correlations with geomorphology

Augusto Montor de Freitas Luiz[1,#], Nelcí Helena Maia Gutierrez[2]

Article

Keywords
Geomorphology
Geostatistical analysis
Geotechnical mapping
Impenetrable layer
SPT

Abstract

The Standard Penetration Test (SPT), widely used in Brazil, provides reference data to geotechnical projects. The data obtained are punctual and often dispersed due to its execution, that is, there is no concern in gathering and analyzing such information jointly for a specific region. In addition to the wide dispersion of these data, due to their anisotropic nature, classical statistics may not be the best approach for data with spatial variability. In this way, the application of methods that use spatial analysis, especially Geostatistics, become essential in the mapping of geotechnical variables. Therefore, this study proposes to gather, organize, and analyze data originated from SPT conducted in the municipality of Maringá, Brazil, applying the ordinary kriging geostatistical technique to identify correlations with the Geomorphology of the studied region. To achieve the proposed objectives, we selected 109 boreholes distributed in the municipality of Maringá, between the years of 2011 to 2015, and treated them using the ArcGis geostatistical analysis software. It was noticed a relationship between the thickness of the subsoil layers considering the position and slope form, reflecting on the depth to bedrock and, consequently, on the resistance of the layers associated with N-value of the SPT.

1. Introduction

The success of geotechnical works fundamentally depends on extensive knowledge of the characteristics and properties of the constituent materials of the subsoil. When laboratory tests are impractical to perform, the field tests allow a satisfactory definition of the substrate stratigraphy and, in some cases, a more realistic estimate of the geotechnical properties of the materials involved, indispensable in the preparation of geotechnical projects.

The data obtained in subsoil prospecting for a specific region, when available, are usually found in a dispersed manner, that is, there is no concern to gather and present them to the general community, which often lacks the knowledge regarding the soils on which they support their buildings.

According to Zhang et al. (2019), one of the most popular in-situ testing procedures in Geotechnics, the Standard Penetration Test (SPT), was developed to provide values in order to collaborate with soil classification concerning its consistency and compactness through its resistance to vertical penetration.

The SPT has been recently considered as an instrument for acquiring primary data to elaborate maps or geotechnical charts that can aid in urban zoning, using the Geographic Information System (GIS). Auvinet et al. (2009) highlight the numerous geotechnical surveys performed in urban area of Mexico City and emphasize its use to obtain a better knowledge of the subsoil and improve the accuracy of geotechnical zoning maps for regulatory purposes of construction. El May et al. (2010) analyzed boreholes data to obtain the water table depth, as well as geotechnical and liquefaction potential layers. Sharma & Rhaman (2016) analyzed boreholes of 30 m depth, performed in 200 locations in Guwahati City and prepared contour maps of standard penetration test N-value at different depth and average contour map of N value. Razmyar & Eslamini (2018) used different geotechnical field tests, such as standard penetration test and cone penetrometer test (CPT), to estimate geotechnical parameters and presented them through zoning maps.

[#]Corresponding author. E-mail address: augustom@utfpr.edu.br.
[1]Coordenação de Engenharia Civil, Universidade Tecnológica Federal do Paraná, Apucarana, PR, Brazil.
[2]Departamento de Engenharia Civil, Universidade Estadual de Maringá, Maringá, PR, Brazil.

Submitted on April 10, 2020; Final Acceptance on June 16, 2020; Discussion open until March 31, 2021.
DOI: https://doi.org/10.28927/SR.434619

Considering the availability of data obtained from standard penetration tests and the features, properties, and behavioral characteristics of a silty clay founded in the study site, this paper illustrates the direct application of geostatistical methods for the municipality of Maringá, Brazil and presents them using the Geographic Information System (GIS), emphasizing the evolution of soils layers, the depth to the bedrock, and the N-value at different depths.

2. Standard Penetration Test (SPT)

The first reports on soil sampling through the dynamic driving process occurred at approximately 1902 (Fletcher, 1965). According to Belincanta (1998), before this, the geological investigation was performed by digging wells of considerable diameter or by drilling with water circulation, it is worth noting that during the water circulation there was no concern in determining mechanical properties of soils. The sample removal process in a borehole was gradually enhanced after the emergence of the percussion drilling method, reflecting of the on quality of the soil samples. Even so, there was no consensus about the proportions of SPT apparatus, such as sampler dimensions, hammer weight, drop height and the count the number of blows.

In the following years, several authors (Terzaghi & Peck, 1948; Hvorslev, 1949; Mello, 1971) pointed out the importance of using standardized proceedings and standardized measurements on SPT, in order to ensure the reliability of this test to estimate soil parameters.

The SPT standardized in Brazil consists of driving a standard sampler until reaching 45 cm of soil penetration, using a 65 kg hammer falling from a height of 75 cm, noting the number of blows for each segment of 15 cm. The parameter obtained in this test is denominated N-value, which corresponds to the number of blows required to drive the last 30 cm of the standard soil sampler (ABNT NBR 6484, 2001).

The SPT also allows the removal of deformed samples from the subsoil during the sampling driving meter-by-meter, allowing direct contact with the soil through the tactile and visual analysis of the samples, thus consolidating an expedient method of subsoil reconnaissance.

The semi-empirical methods used to predict the load capacity of the soils requires parameters obtained through correlations with the N-value and the expeditious characterization of the subsoil. Despite not being the only ones, these methodologies are widespread in Brazil justifying the relevance of this test as a tool to design a foundation project.

3. Characterization of the study area

The municipality of Maringá is in the northern portion of the state of Paraná (Figure 1), approximately 430 km from its capital, Curitiba, and 650 km from the municipality of São Paulo. It has an average altitude of 596 m above sea level and is spread over an area of approximately 473 km^2.

The study area is in the Serra Geral Group that was formed by successive volcanic spills that occurred over the years. These volcanic events were responsible for the formation of the basaltic rock on which the Paraná Basin is based on and which generally vary in thickness, position within the slope, degree of weathering among other factors according to the number of spills (Besser et al., 2018).

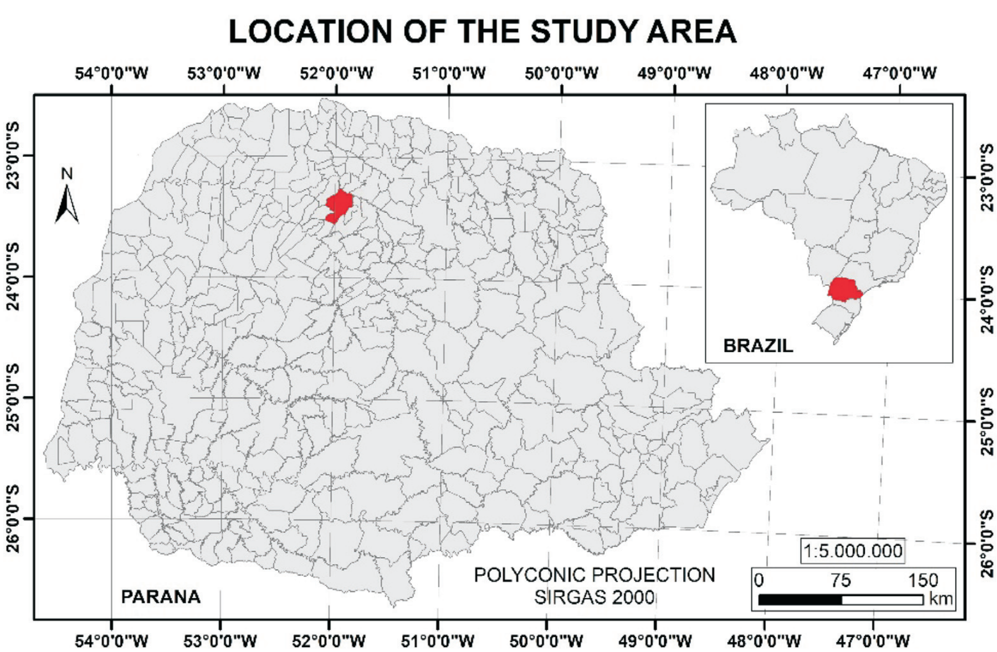

Figure 1. Location of the municipality of Maringá.

These eruptions have occurred horizontally, which determines the current configuration of soft corrugated hills with deep soils and high nutrient contents (França Junior et al., 2010).

According to Nakashima & Nóbrega (2003), Red Latosol of clayey texture predominates in the top regions (high and middle slope). Towards the valley regions (low slope) the Red Nitosol begin to emerge.

Santos et al. (2018) defines the Latosols as a highly weathered soils that presents clays with the predominance of iron, aluminum, and silicon oxides, among other minerals, in their composition. The Red Latosols are a type of Latosol in which the amount of iron oxides is predominant, justifying its marked red coloration. According to the mapping presented by Bhering et al. (2007), these soils occur mainly in regions of flat and slightly undulating relief, as occurs in most of the central region of Maringá.

Figure 2 shows part of the survey conducted by Bhering et al. (2007) on the recognition of the soils of the state of Paraná, highlighting the region of the municipality of Maringá. The Nitosols are predominantly located in the proximity of the drainage network, following its outline. The Latosols occur in the intermediate portions, coinciding with medium to high slope regions.

A study conducted on the Maringá subsoil by Gutierrez & Belincanta (2004) found the existence of two well-individualized sets in terms of color, characteristics, and behavior: a) An upper set composed of porous silty clay of a reddish-brown color, with variable thickness, reaching up to 12 m in the regions of a high and medium slope. This set corresponds to an evolved material (mature soil) - the dystroferric Red Latosol; b) a lower set consisting of silty clay and clay-sandy silt of predominantly purple and yellowish-gray colors, with the presence of black or yellow diaclases. This set corresponds to the layer of altered soil from basalt rock - the saprolite.

Two geopedological profiles typical of the north-south and east-west regions of Maringá were presented by Gutierrez et al. (2015) demonstrating how materials from the alteration of basaltic rock are associated to the soil types (Latosols and Nitosols).

Along the top of the interfluvial region (Figure 3), where most of the urban area is installed, the data obtained from the SPT indicate the occurrence of a young soil that can reach up to 30 m of thickness or more. The surface layer consists of a mature soil with a clayey texture (up to 12 m depth) with a clay-silty or silt-clayey saprolite below.

In the low slope or higher positions where the breaks in the slope are accentuated, the young soil suffers a significant reduction in its thickness and the Latosol gives place to the typical Eutrophic Red Nitosol or Latosolic Eutrophic Red Nitosol, also clayey but less thick than the first.

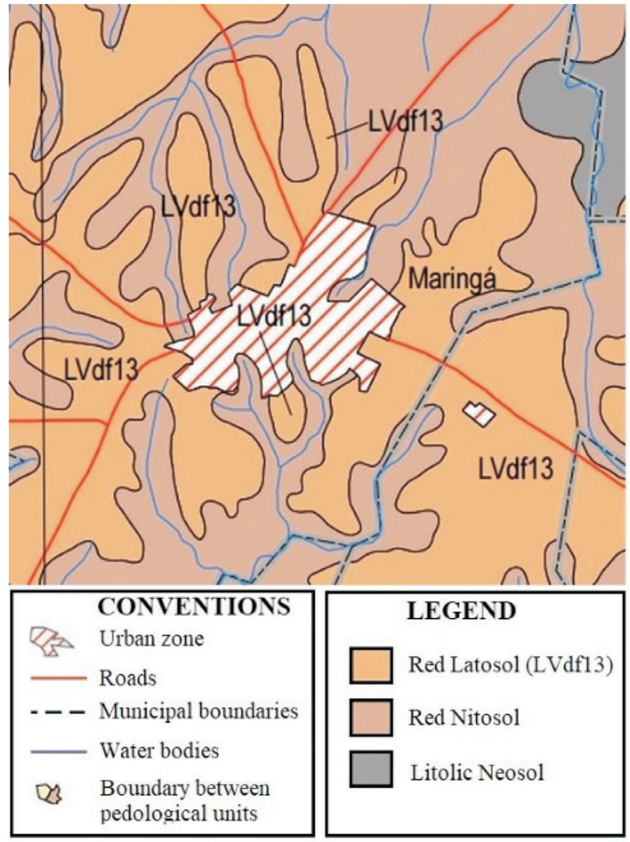

Figure 2. Reconnaissance of the soils of the region of Maringá, highlighting the Latosols and Nitosols (adapted from Bhering et al., 2007).

4. Geostatistics in geotechnics

Even though a soil originated from the same rock commonly presents different mechanical and hydraulic behavior, some characteristics are preserved because these soils present the same origin. Thus, the study of Geotechnics is combined with statistics to understand how these relations develop and identify similar behaviors or properties for the soil of a specific region.

Within this concept, the geotechnical mapping allows to visualize similarities and differences in the considered properties, on a regional scale, also pondering the spatial variability of the data through a more refined statistical tool: geostatistics.

In Mining Engineering, the use of software for modeling the spatial distribution of the ores is already widespread (Olea, 1999; Yunsel, 2012). The mineral exploration projects are based on the concept that the concentration of a given ore, in an unexplored region, can be estimated in function of a few points where this data is known. It is necessary to apply statistical methods that consider the variability of this parameter (concentration) both on the surface and at depth for such estimates to be made valid. In this scenario, geostatistics aims to solve problems of this nature.

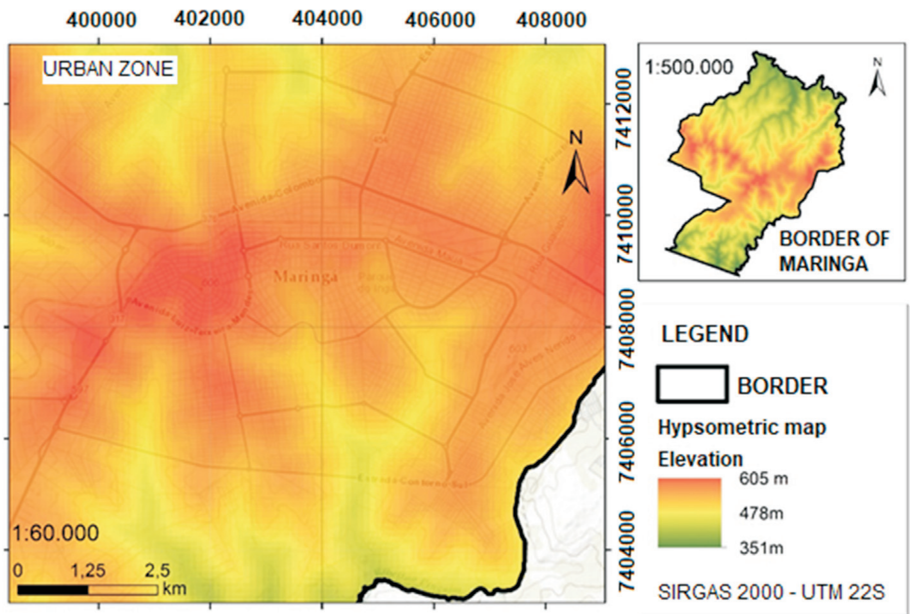

Figure 3. Hypsometric map of the municipality of Maringá, Brazil.

The main objective of geostatistics is to provide an estimator based on a few sample points that allow the reconnection of the complete spatial distribution of the concentrations of metals, for example, inside the studied body of ore (Folle, 2009). Geostatistics is considered a special topic of applied statistics that deals with problems related to regionalized variables. These variables present two distinct aspects: a random factor characterized by irregularities and unpredictable variation from one point to the other in space, and a structural factor characterized by the relationships between these points in space and their genesis (origin), as described by Matheron (1963).

When studying the behavior of generalized variables, there are two fundamental tools for the geostatistical methods: semivariogram and kriging. The semivariogram function γ (h) shows the measure of the spatial dependence degree between samples along with specific support (vector h) and, to build them, the squared differences of the obtained values are used, assuming stationarity in the increments (Landim, 2006). Kriging consists of a punctual value estimation process of variables distributed in space and time while considered as interdependent by the semivariogram considering the sample distance and the grouping.

In recent years, some authors have sought to associate geostatistics, already consolidated in other areas, with the field of Geotechnics (Thallak & Samui, 2007; Samui & Thallak, 2010; Boezio et al., 2013, Maroufpoor et al., 2017). These studies are based mainly on the systematized organization of data, obtained in geotechnical tests, for mapping such as the water level in wells, simulation of the behavior of the subsoil in terms of the plots of the constituent materials, rock genesis, N-value estimation, and a variety of other spatial variability data.

5. Materials and methods

The methodology applied in this study consists of collecting data to elaborate a database structured on the GIS platform for the posterior verification of the applicability of geostatistical techniques and later model employing ordinary kriging.

The surveys that comprise the databank were conducted by civil construction companies and by the Soil Mechanics Laboratory of the State University of Maringá (Paraná-Brazil). Aiming to save time and processing resources, it is worth noting that only single borehole was selected to represent the terrain. When there was more than one borehole available on the terrain, the selection criteria was based on its spatial location: it was selected the borehole nearest the front of the terrain, where its spatial coordinates were determined. Thus, the databank presents 109 boreholes distributed in the municipality of Maringá, made from 2011 to 2015. Most points are concentrated in the central region of the municipality, in the neighborhoods that present a more significant development of civil construction in recent years, as can be observed in Figure 4.

The SPT data selected to comprise the database were performed according to the Brazilian Standard (ABNT NBR 6484, 2001) presenting the boreholes location plan, reference level, borehole elevation, N-value, division of the soil layers meter by meter, and the groundwater level. The structure of the tables used as collection storage instruments was elaborated in function of the information contained in the survey bulletins.

The geostatistical modeling by ordinary kriging, including the exploratory data analysis, spatial correla-

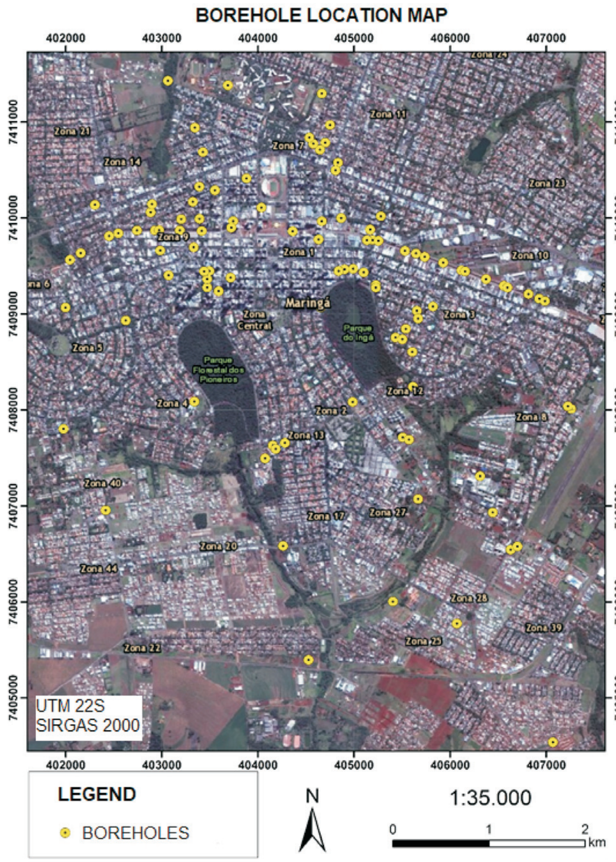

Figure 4. Location of the boreholes in Maringá.

tion structure analysis/modeling, and surface statistical interpolation was conducted using the ArcGIS 10.3 software.

6. Results

The declivity map was elaborated to verify the possible relationships between these data with the topography (top, high, intermediate, and low slope areas), as well as the form of these slopes, especially the pedological types: Latosol and Nitosol. Furthermore, it was elaborated geotechnical maps based on the impenetrable layer depth and the N-value at different depths.

6.1 Declivity map

In the northern section of the urban site (domain of the Pirapó River basin, affluent of the Paranapanema River), the slopes are generally long, convex-rectilinear, with slight declivities but that increase in the inferior third, while the southern section (Ivai River basin) has shorter slopes, convex and convex-rectilinear, with increased declivities, as presented in Figure 5.

The central region of the municipality has relief declivities ranging from flat to slightly corrugated (up to 8 %), apart from the regions near the bodies of water, where it ranges from moderately corrugated to corrugated (up to 20 %). We verified that this characteristic could be correlated to the soils pedology and N-value of the SPT.

6.2 Evolution of soil layers

Despite presenting specific intrinsic variability to natural materials, it was verified a pattern in the behavior and properties of soils originating from the same parent rock due to geomorphology and pedology.

As demonstrated in Figure 6, until the depth of 8 m, most soil samples were classified as mature soil. The same does not occur at 12 m depth, in which more altered soils

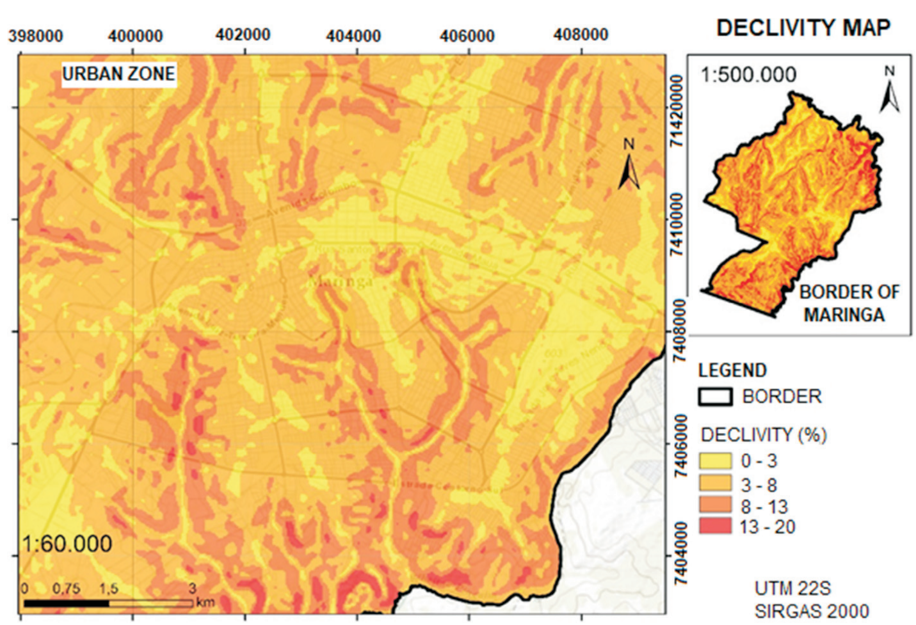

Figure 5. Declivity map of Maringá.

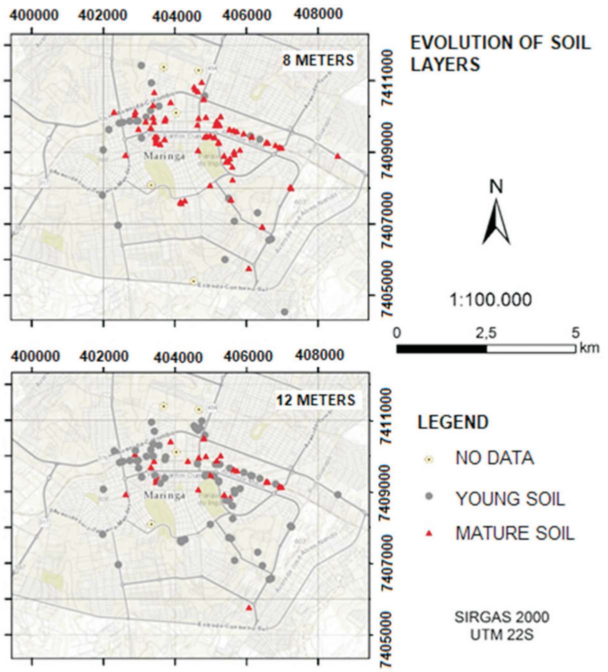

Figure 6. Evolution of soils at the depths of 8 and 12 m.

(with traces of parent rock) predominate indicating that, between the depths of 8 and 12 m there is a transition zone.

In particular, a few surveys presented very thick profiles, superior to 15 m, of mature soil in the central region of Maringá. The soil evolution can indicate the proximity to the bedrock since the unweathered rock is subjacent to the young soil (saprolite) and can be more or less thick due to the weathering that occurs in the region.

6.3 Impenetrable layer depth

The depth of the impenetrable to the SPT, which can be measured as corresponding to the quota of the bedrock (N-value higher than 60 blows/30 cm), has significant variations in the interval of the studied region. Figures 8 and 9 illustrate this phenomenon for a northern and southern section of the region, respectively, thus divided to obtain better results during the kriging stage. The boreholes are distributed over an area of approximately 10 km^2 and 11,5 km^2 in the northern and southern section, respectively.

Note that in the central region of the northern section (Figure 7), the bedrock is located at greater depths. This is a top region characterized by altimetric quotas superior to 560 m and a flat relief. On east side of the northern section

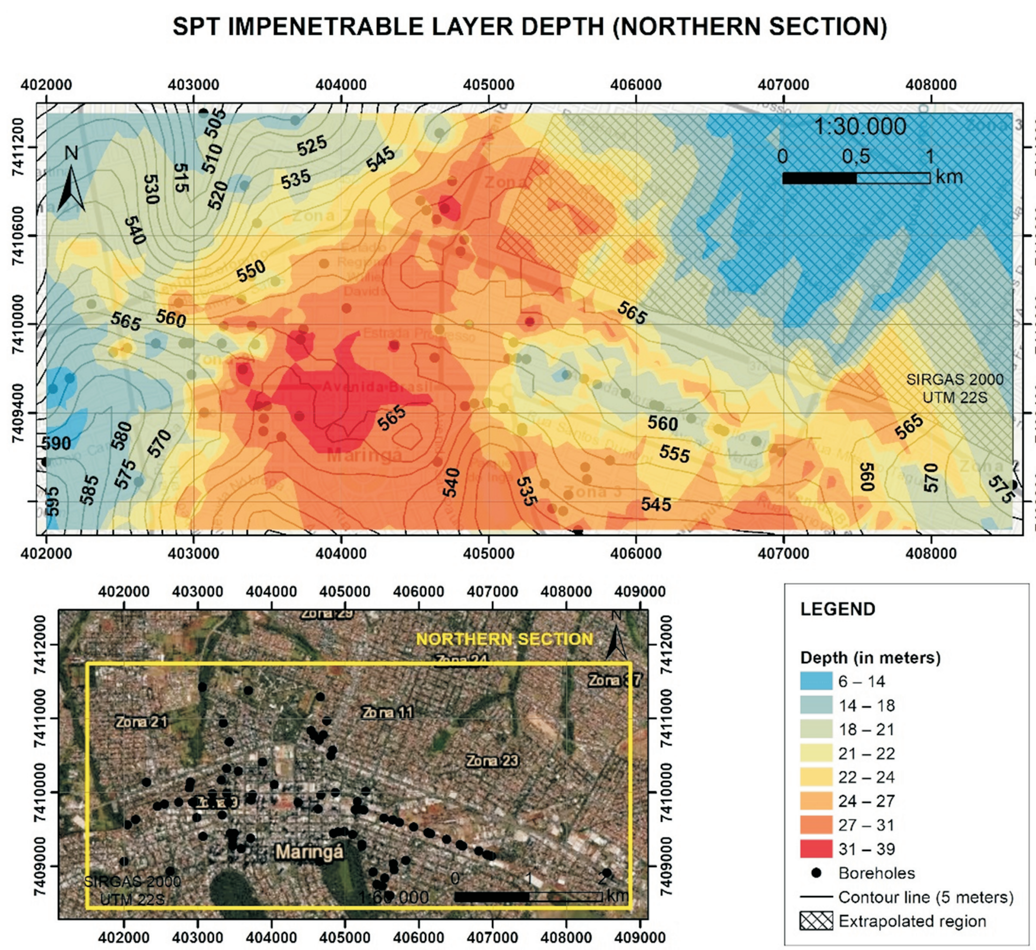

Figure 7. Impenetrable layer depth for a microregion north of Maringá.

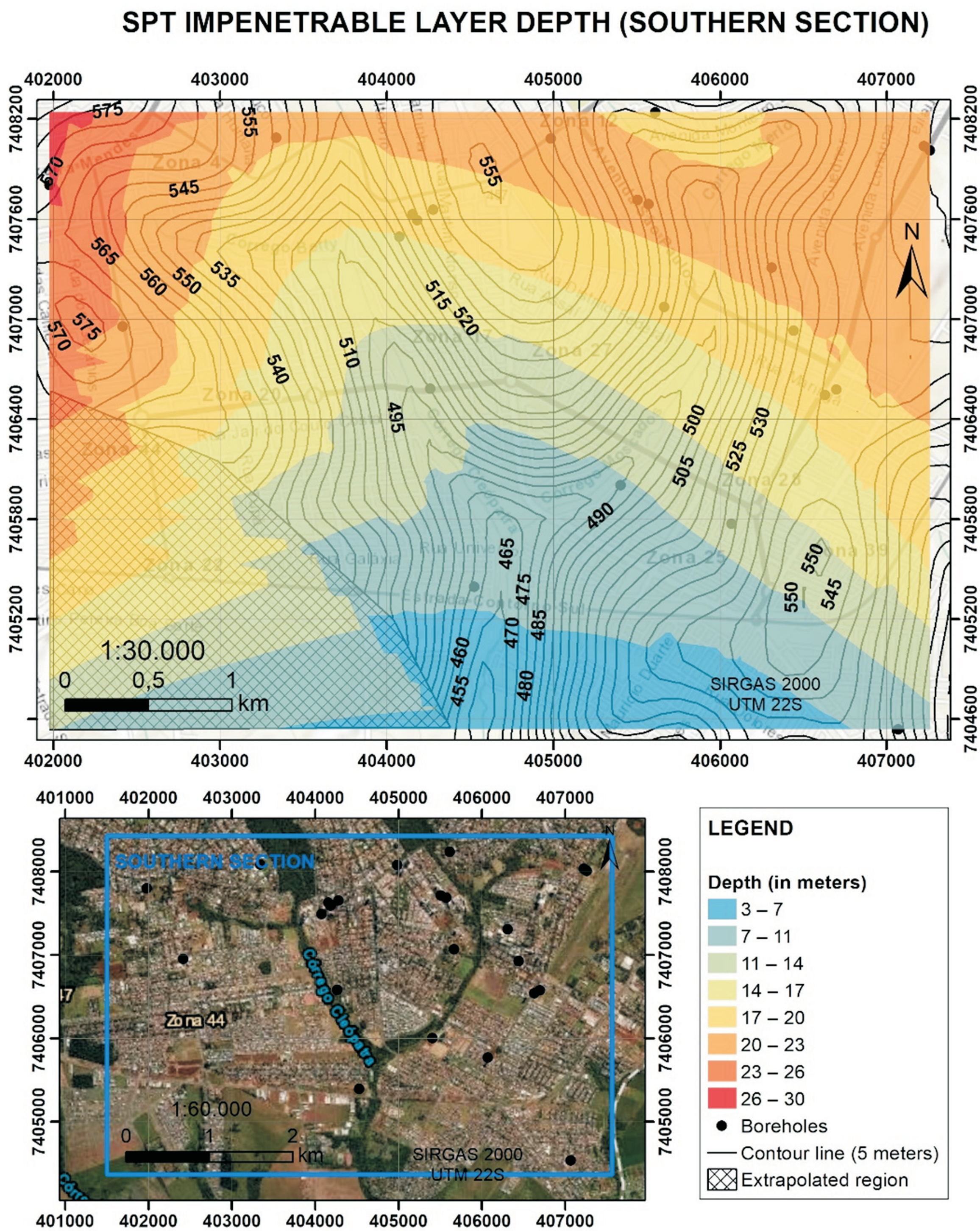

Figure 8. SPT impenetrable layer depth for a microregion south of Maringá.

there is an inversion in this behavior, although it is a peak region (high slope), presents declivities ranging from moderately corrugated to corrugated, justifying the presence of thinner layers until reacting the bedrock. Such occurs in other points of the northern and southern sections of the municipality.

Besides, even in a top region (high slope), the thickness of the soil layers varies due to the form of the relief. When comparing the top regions of the northern section to the declivity of the region, we can observe the tendency for more pronounced high slope terrains to present thinner soil profiles while top regions with flatter relief present thicker soil profiles until reaching the parent rock.

The center-south region presented in Figure 8 has a moderate to low slope with rugged relief. It is also in the regions of more pronounced slopes that we can find the Red Nitosols, while the Red Latosols occur in the central region (Figure 2). The disposition of both soil groups can be associated with soil resistance, correlated to N-value.

6.4 N-value

The N-value, obtained for the more superficial depths, hardly surpasses the value of 20 blows/30 cm for the analyzed region. Most of the index values range from 2 to 10 blows/30 cm, as demonstrated in Figure 9. Note that, around the coordinates of 4,040,000 m and 7,410,000 m, which coincides with the flatter region of the study area and with the predominance of Red Latosols, the N-value presented the lowest values for the depth of 4 m.

From 8 m depth, some of the surveys presented N-value superior to 60 blows/30 cm, which corresponds to the soil layers with high load capacity. This region is characterized by a moderately corrugated relief and the presence of Red Nitosols and corresponds to locations with intermediate to low slope in the southern portion, presented in Figure 10. At this depth, in the central region of the municipality (around coordinated 4,040,000 m and 7,410,000 m), the N-value hardly surpasses the value of 10 blows/30 cm, demonstrating a more linear growth in the regions where the soil profiles are thicker when compared to the thinner layers.

At the depth of 25 m, only the surveys located in the central portion of Maringá had not reached the SPT impenetrable layer. Figure 11 shows the tendency of the N-value to be higher in steep regions (top left and bottom right). In the central portion, where the relief is flatter, the N-value does not exceed 42 blows/30 cm.

7. Discussion

It was identified well-defined regions in the studied area in which the soil layers are thinner and other regions where they are thicker due to its position and form of the slope. There is a tendency of regions of intermediate to high slopes with flat relief present thicker soil profiles and, consequently, greater depths until reaching the impenetrable to the SPT. The increase of the N-value with the depth is slighter in these thicker profiles in which Red Latosols predominate, allowing the association of such behavior with the type of soil in the studied area.

In regions of intermediate to low slopes, or even in regions of high slopes but with pronounced declivities, the soil profiles are thinner, revealing lower depths until the SPT impenetrable layer (superficial rocks). In these low slope regions in which the Red Nitosol predominates, we verified that the increase in the N-value is more significant,

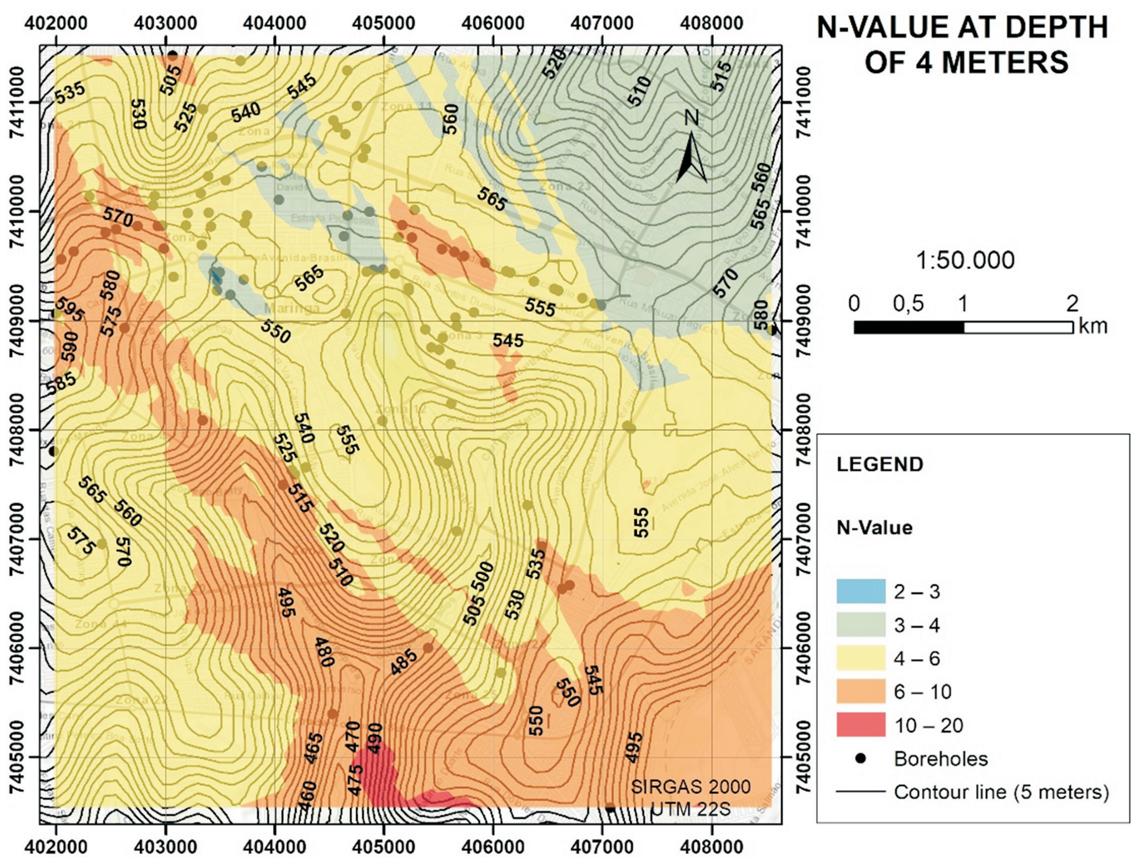

Figure 9. N-value at a depth of 4 m.

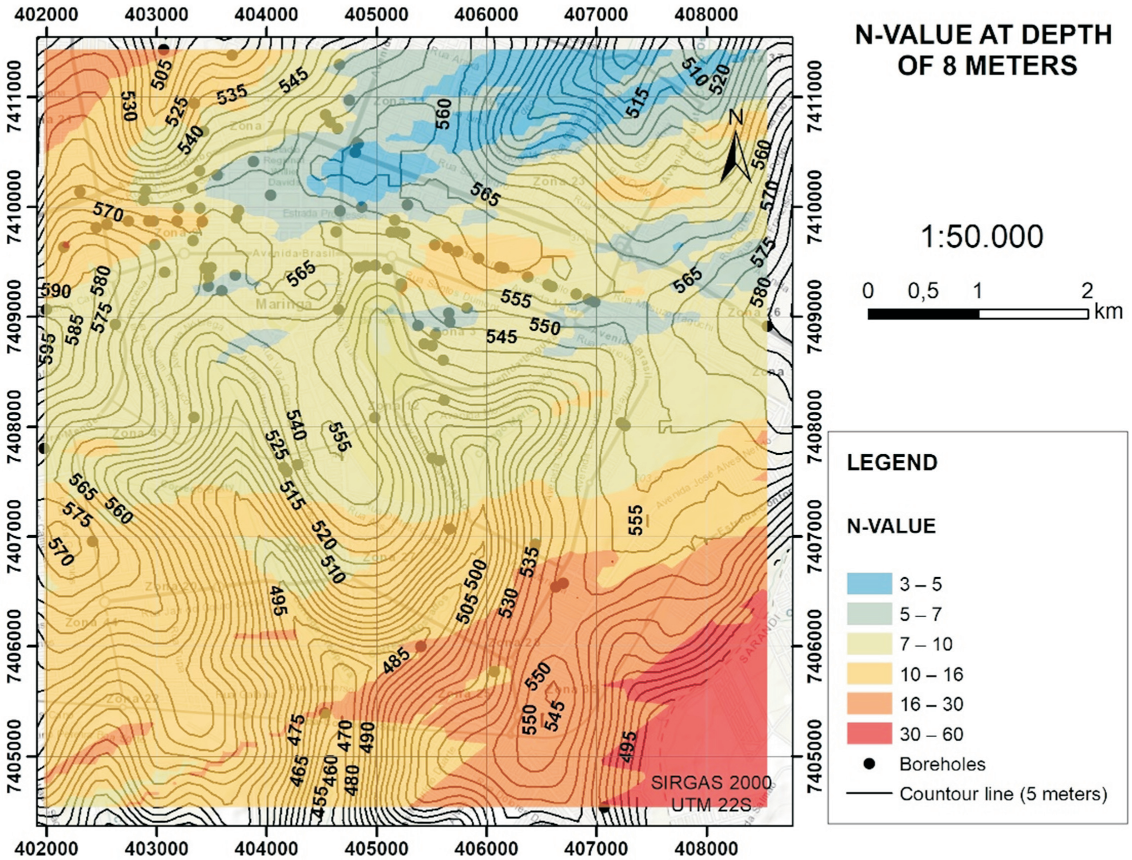

Figure 10. N-value at a depth of 8 m.

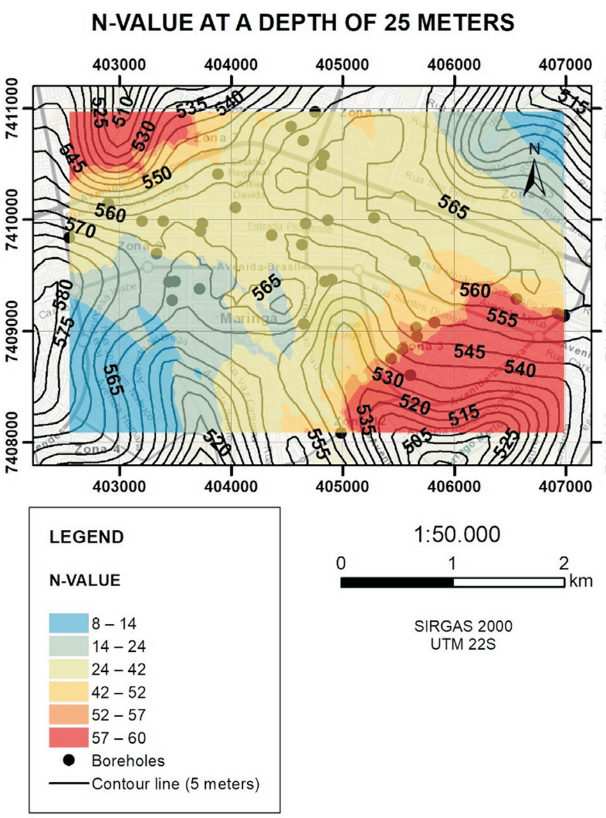

Figure 11. N-value at a depth of 25 m.

presenting soil of intermediate to stiff consistency at more superficial depths.

Due to the presence of little resistant soils on the more superficial layers of the soil, solutions in shallow foundations can be considered unfeasible in most of the central region of the municipality. Solutions in deep foundations are routine in the entire municipality but the possibility of adopting other alternatives due to the better soil resistance at more superficial depths, especially in regions of low to intermediate slopes with steeper declivities, should be verified.

8. Conclusions

The gathering of data from the SPT, in a single database, proves to be extremely positive, since it allows to easily identify some similarities, in addition to allowing several information to be crossed for a better knowledge of the soils. The use of the ordinary kriging technique of geostatistics was satisfactory when considering a general idea of the behavior of soils associated with other variables presenting spatial variability, allowing us to identify possible correlations between its geomorphological properties and characteristics, as was the objective of this study.

This type of study shows how factors such as the shape of the slope and its position are linked to soil behavior, being decisive in the estimation of the impenetrable to the SPT and in the evolution of the N-value, in this particular case. Thus, a series of variables can be studied trying to associate them with the behavior of the soil.

The significant variability of the soils indicates that the results obtained through statistical interpolators must be cautiously analyzed. The higher the density of the sampled points is, the more reliable will be the final products. Thus, insofar as new surveys are conducted, the database can be expanded, reflecting on more accurate estimates and, consequently, more reliable results on the knowledge and applicability of the soils.

Acknowledgments

The authors acknowledge the Coordination for the Improvement of Higher Education (CAPES) and the National Council for Scientific and Technological Development (CNPq) for their support.

References

ABNT NBR 6484 (2001). Soil - Standard Penetration Test - SPT- Soil Sampling and Classification - Test method. *ABNT - Associação Brasileira de Normas Técnicas*, *Rio de Janeiro, RJ* (in Portuguese).

Auvinet, G., Méndez, E., & Juárez, M. (2009). Advances in geotechnical characterization of Mexico City basin subsoil. *Proc. 17th International Conference on Soil Mechanics and Geotechnical Engineering, Alexandria*. IOS Press, 2679-2682. https://doi.org/10.3233/978-1-60750-031-5-2679

Belincanta, A. (1998). *Evaluation of intervenient factors in the penetration resistance of the SPT* [Doctoral thesis, University of São Paulo]. University of São Paulo's repository (in Portuguese). https://www.teses.usp.br/teses/disponiveis/18/18132/tde-12062018-162336/en.php

Besser, M.L., Vasconcellos, E.M.G., & Nardy, A.J.R. (2018) Morphology and stratigraphy of Serra Geral silicic lava flows in the northern segment of the Torres Trough, Maringá Igneous Province. *Brazilian Journal of Geology*, 48(2), 201-219. https://doi.org/10.1590/2317-4889201820180087

Bhering, S.B., Santos, H.G., Manzatto, C.V., Bognola, I., Fasolo, P.J., Carvalho, A.P., Potter, R.O., & Curcio, G.R. (2007). Mapa de solos do estado do Paraná. In *Embrapa Solos. Documentos (INFOTECA-E), Rio de Janeiro*. Embrapa, 1-96 (in Portuguese).

Boezio, M.N.M., Costa, J.F.C.L., & Koppe, J.C. (2013). Kriging with an external drift vs. collocated cokriging for water table mapping. *Applied Earth Science*, 115(3), 103-112. https://doi.org/10.1179/174327506X138896

El May, M.; Dlala, M., & Chenini, I. (2010). Urban geological mapping: geotechnical data analysis for rational development planning. *Engineering Geology*, 116(1-2), 129-138. https://doi.org/10.1016/j.enggeo.2010.08.002

Fletcher, G. (1965). Standard Penetration Test' its uses and abuses. *Journal of the Soil Mechanics Foundation Division*, 91(4), 67-75.

Folle, D. (2009). *Análise e aplicações da geoestatística no contexto geológico-geotécnico urbano* [Doctoral thesis, Federal University of Rio Grande do Sul]. Federal University of Rio Grande do Sul's repository (in Portuguese). http://hdl.handle.net/10183/15707

França Junior, P., Petsch, C., Villa, M.E.C.D., & Manieri, D.D. (2010). Report field on the physical aspects of the Third Plateau Paranaense (Maringá to Paraná River Terraces). *Boletim de Geografia*, 28(2), 185-195 (in Portuguese). https://doi.org/10.4025/bolgeogr.v28i2.10599

Gutierrez, N.H.M., & Belincanta, A. (2004). Características básicas dos solos constituintes do subsolo da Cidade de Maringá: locais de alta e média vertente. *Proc. IV Simpósio de Prática de Engenharia Geotécnica da Região Sul*, *Curitiba*. Vol. 1, ABMS, 39-46 (in Portuguese).

Gutierrez, N.H.M., Luiz, A.M.F., & Nobrega, M.T. (2015). Características e comportamentos geotécnicos de áreas sobre basalto: o caso de Maringá-PR. *Proc. X Simpósio de Prática de Engenharia Geotécnica da Região Sul*, *Maringá*. Vol. 1, ABMS, 17-19 (in Portuguese).

Hvorslev, M.J. (1949). *Subsurface Exploration and Sampling of Soil for Civil Engineering Purposes*. Waterways Experiment Station.

Landim, P.M.B. (2006). About Geostatistics and Maps. *Terrae Didatica*, 2(1), 19-33 (in Portuguese). https://doi.org/10.20396/td.v2i1.8637463

Maroufpoor, S., Fakheri-Fard, A., & Shiri, J. (2017). Study of the spatial distribution of groundwater quality using soft computing and geostatistical models. *Journal of Hydraulic Engineering*, 25(2), 232-238. https://doi.org/10.1080/09715010.2017.1408036

Matheron, G. (1963). Principles of geostatistics. *Economic Geology*, 58(8), 1246-1266. https://doi.org/10.2113/gsecongeo.58.8.1246

Mello, V.F.B. (1971). The Standard Penetration Test. *Proc. 4th Panamerican Conferece on Soil Mechanics anf Foundation Engineering*, *San Juan*. Vol. 1, ASCE, 1-86.

Nakashima, P., & Nóbrega, M.T. (2003). Solos do Terceiro Planalto do Paraná-Brasil. *Proc. I Encontro Geotécnico do Terceiro Planalto Paranaense*, *Maringá*. 66-85 (in Portuguese).

Olea, R.A. (1999). *Geostatistics for Engineers and Earth Scientists*. Springer. https://doi.org/10.1007/978-1-4615-5001-3

Razmyar, A., & Eslami, A. (2018). Evaluating the geotechnical and geophysical characteristics of expanding districts in Tehran using fields experiments. *Civil Engineering Journal*, 4(2), 363-377. https://doi.org/10.28991/cej-030997

Samui, P., & Thallak, S.G. (2010). Spatial variability of SPT data using ordinary and disjunctive kriging. *Georisk: Assessment and Management of Risk for Engineered Systems and Geohazards*, 4(1), 22-31. https://doi.org/10.1080/17499510902792209

Santos, H.G., Jacomine, P.K.T, Anjos, L.H.C., Oliveira, V.A., Lumbreras, J.F., Coelho, & Cunha, T.J.F. (2018). *Sistema Brasileiro de Classificação de Solos*. Embrapa (in Portuguese).

Sharma, B., & Rahman, S.K. (2016). Use of GIS based maps for preliminary assessment of Subsoil of Guwahati City. *Journal of Geoscience and Environment Protection*, 4(5), 106-116. https://doi.org/10.4236/gep.2016.45011

Terzaghi, K., & Peck, R.B. (1948). *Soil Mechanics in Engineering Practice*. John Wiley & Sons.

Thallak, S.G., & Samui, P. (2007). Geostatistical modelling of spatial and depth variability of SPT data for Bangalore. *Geomechanics and Geoengineering*, 2(4), 307-316. https://doi.org/10.1080/17486020701678851

Yunsel, T.Y. (2012). A practical application of geostatistical methods to quality and mineral reserve modelling of cement raw materials. *Journal of the Southern African Institute of Mining and Metallurgy*, 112(3), 239-249.

Zhang, N., Arroyo, M., Ciantia, M., Gens, A., & Butlanska, J. (2019). Standard Penetration Testing in a virtual calibration chamber. *Computers and Geotechnics*, 111(1), 277-289. https://doi.org/10.1016/j.compgeo.2019.03.021

Soils and Rocks
An International Journal of Geotechnical and Geoenvironmental Engineering
www.soilsandrocks.com
ISSN 1980-9743
ISSN-e 2675-5475

Advances on dosages for cement stabilized rammed Guabirotuba silt depending on climate conditions

Jair de Jesús Arrieta Baldovino[1], Ronaldo Luis dos Santos Izzo[1,#], Juliana Lundgren Rose[1]

Article

Keywords
Durability
Porosity/cement index
Several climate conditions
Splitting tensile
Unconfined compression

Abstract

This paper optimizes and compares the behavior of soil-cement compacted blends against several molding and climate conditions under optimum compaction and non-optimum compaction parameters. For this, an intensive laboratory study of silty soil samples treated with different percentages of high early strength Portland cement (PC) was investigated by a series of compaction, unconfined compressive, splitting tensile and durability tests using several climate conditions (i.e. wetting-drying and freeze-thaw cycles). The effects of porosity/cement index (η/C_{iv}) on the unconfined compressive strength (q_u), splitting tensile strength (q_t) and durability by accumulated loss of mass (ALM, in %) of blends for optimum (i.e. maximum dry unit weight and optimum water content) and non-optimum compaction conditions (i.e. the variety of molding dry unit weight and molding moisture content (ω), between 13 and 16 kN/m^3 and 10 % and 34 %, respectively) is the main paper focus. The results show an increase in strength and durability properties of the blends when cement is added, however, the mechanical resistance decreases if the blends are subjected to freeze-thaw (F-T) cycles. The opposite happens when blends are subjected to wet-dry (W-D) cycles where they reach resistances higher than those of curing at 23 °C in a wet chamber. Finally, reasonable dosages employing η/C_{iv} index to stabilize the soil were presented considering the strength and the durability parameters.

1. Introduction

The soils from Guabirotuba geological formation, located in the city of Curitiba, (Brazil), and its metropolitan area are composed predominantly of clayey and silty soils (Baldovino, 2018). Given the low load-bearing capacity and high expansive degree of these soils owing to their physical-mechanical properties, they are not used in construction earthworks, so a technique for the stabilization of soils with cement materials is practical (Baldovino et al., 2020a). Soft soil can be found in numerous places, particularly in coastal areas, which imposes various challenges on geotechnical engineers during the construction process. Low shear strength and bearing capacity are common problems encountered in various geotechnical projects owing to the poor engineering properties of the soil. Therefore, soft soils must be improved before any ground improvement work can commence (Baldovino et al., 2018a). One of the techniques of improvement is to use typical binders such as lime or cement, but the high consumption and emissions of gases during the production of these binders have led researchers to look for new binders based on waste to replace partially the cement or lime.

Despite the negative environmental impacts produced during cement production (CO_2 emissions, mainly) and the use of natural resources such as limestone rock, these aspects have forced the soil stabilization area to look for alternative solutions to improve the engineering properties of soils using binders such as natural pozzolans, fly ash, fibers (natural and synthetic), construction and demolition waste, and new techniques like biocimentation, bioclogging and geopolymerization (Ivanov & Chu, 2008). However, cement continues to be one of the most consumed materials by engineering industry, the fact that demonstrates the great development of the great metropolises in countries around the world. In this way, studies of the soil-cement dosage to find the smallest amounts of cement

[#]Corresponding author. E-mail address: izzo@utfpr.edu.br.
[1]Departamento de Construção Civil, Universidade Federal Tecnológica do Paraná, Curitiba, PR, Brazil.

Submitted on April 7, 2020; Final Acceptance on June 16, 2020; Discussion open until March 31, 2021.
DOI: https://doi.org/10.28927/SR.434631

and compacting effort in the field are necessary to reduce as much as possible the indiscriminate consumption of the binder when it is required to use it in engineering works, either by the economy, workability, access, the durability of the material or its efficiency (Baldovino et al., 2018b; Baldovino & Izzo, 2019).

As a result, several investigations had been conducted on Guabirotuba silts stabilization to calculated reasonable dosages for cement-soil compacted blends. Baldovino et al. (2018a) determined the empirical relationships between the splitting tensile strength (q_t or STS) and q_u of a Guabirotuba silty soil artificially cemented with hydrated lime. To calculate the q_t/q_u ratio, soil-lime specimens were molded by controlling the dry unit weight, lime content (3-9 %), porosity, and water content, followed by curing for 15, 30, 60, 90, and 180 days. The authors calculated a $q_t/q_u = 0.16$ relationship using a reasonable criterion named porosity/lime index (i.e. voids divided by volumetric lime content) independent of curing time and lime content. They suggested a minimum percentage lime of 5 % to stabilize the soil. Baldovino et al. (2018c) evaluated the effects of lime content, curing time, moisture content (ω), and porosity/lime index (η/L_{iv}) on compaction and strength parameters of a Guabirotuba sandy clay. Lime content addition increased the optimum moisture content and decreased the maximum dry density of compacted blends. The study suggests a q_t/q_u between 0.17 and 0.20 dependent of curing time (28-90 days), using the porosity/lime index and the application of the 0.68 exponents on the index [i.e. $(\eta/L_{iv})^{-0.68}$]. The results showed an increasing strength of the soil-lime mixtures. Baldovino & Izzo (2019) calculated the tensile/compressive index (q_t/q_u) as 0.15 for soil-cement compacted blends cured under 7-days. For 7, 14 and 28-days of curing, Baldovino et al. (2020a) suggested the q_t/q_u index for soil-cement compacted blends as 0.15-0.17. Moreira et al. (2019a) investigated the effects of molding dry unit weight, cement content and porosity/cement index on unconfined compressive strength (UCS or q_u) for cement-roof tile waste-silty soil (from Guabirotuba formation) compacted blends. The increase in dry unit weight and cement content increases the UCS for all blends. The UCS was directly affected by η/C_{iv} optimized to 0.28 exponent to improve the coefficient of determinations. In the end, the authors calculated an equation to estimate UCS for any mold condition. Moreira et al. (2019b) evaluated the impact of sustainable granular materials (from construction and demolition) on the behavior sedimentary silt from Guabirotuba formation for road application. The porosity/binder index was employed firstly by Consoli et al. (2009) and extended to study the influence of moisture on strength for soil-cement mixes (Consoli et al., 2016a; 2016b). Baldovino et al. (2019a) calculated the equations that controlling the strength of sedimentary silty soil-cement blends influenced by porosity/cement ratio (η/C_{iv}) and types of cement (pozzolanic PC, high early strength PC, and low hydration heat PC). The results concluded the unconfined compressive strength of the specimens of soil-cement mixtures increased with the addition of cement content and with the increase of the molding dry unit weight. The highest UCS values obtained were with the addition of high early strength PC, followed by pozzolanic PC and finally by low hydration heat PC. To reach 1200 kPa was necessarily added, on average, 6 % cement by weight. Baldovino et al. (2019b) optimizing the evolution of strength for lime-stabilized rammed earth comparing two silty soils employing 28, 90 and 360 days of curing. The study demonstrates the efficiency of porosity/lime index to estimate the unconfined compressive strength of the silt-lime compacted blends for several molding conditions. Finally, Baldovino et al. (2020b) improved the q_u of silty soil-cement mixes using recycled-glass powder in three quantities: 5 %, 15 %, and 30 % by weight.

The literature demonstrates the formulation of reasonable dosage equations for stabilized soils with several binders. Consoli et al. (2019) have already evaluated the effect of three distinct amounts of rice husk ash (RHA), PC and dry unit weights on the ALM, maximum shear modulus at small strains (Go) and q_t of stabilized sands subjected to 12 W-D cycles. The RHA addition improves the q_t values and decreases the ALM. When subjected to W-D cycles, the Go and q_t of the cement-stabilized silty sands with 10-30 % RHA increased up to the sixth cycle and remained practically constant thereafter. Consoli et al. (2016a) determined a unique relationship determining strength of silty/clayey soils (London clay, Paraguayan dispersive clay, Portugal silty sand, Botucatu clayey sand, Nova Santa Rita organic soft clay, and Cachoeirinha red silty clay) improved with PC. Consoli et al. (2011) studied the influence of water content, porosity, and cement content on the strength of artificially cemented silty soil. The authors linked the η/C_{iv} with q_u to establish a general dosage equation considering molding conditions as dry unit weight and curing time. The influence of freeze-thaw on engineering properties of a silty soil was systematically investigated by Qi et al. (2008). The engineering properties of a silty soil were studied under different freezing conditions and with the dry unit weight from 15.3 to 17.3 kN/m^3. It is found that under the same freezing condition, there is a critical dry unit weight, for the change in soil density after freeze-thaw. Arulrajah et al. (2016) combined coffee ground (CG) with Fly ash (FA) as a geopolymer precursor active with Na_2SiO_3-NaOH composts. By replacing 30 % FA into CG at 50/50 Na_2SiO_3-NaOH index, geopolymerization occurred after 7-days cure. Strong geopolymers are obtained at 50 °C and CG-FA stabilized compacted blends are suitable for embankment structural fill material in road embankments. Kua et al. (2016) introducing slag as a geopolymer precursor in CG-FA blends active with Na_2SiO_3 and NaOH. In this research, authors obtained good q_u values of combined raw materials to use them in road construction projects.

Although dosage equations have been found to stabilize soils of the Guabirotuba formation, it has not yet been researched dosage equations for strength and durability when stabilized depending on the climatic conditions (considering wetting-drying and freezing-thawing cycles). Thus, this paper investigates dosage equations for cement stabilized rammed silt using several molding and climate conditions no shown in the literature for the Guabirotuba sedimentary soils.

2. Experimental program

The experimental program was divided into four stages:

(1) the first stage comprised the physical characterization tests of the sedimentary soil and cement: granulometry of the soil according to ASTM D2487 (ASTM, 2017), Atterberg limits of the soil according to ASTM D4318 (ASTM, 2010), the specific gravity of the soil according to ASTM D854 (ASTM, 2014), one-dimensional consolidation properties of soil using the ASTM D2435 (ASTM, 2011a), the direct soil shear parameters of soil (internal angle and cohesion) were obtained according to ASTM D3080 (ASTM, 2011b), the chemical composition of the soil sample using the X-Ray Fluorescence (XRF) technology, and the actual specific gravity of the grains of the cement was calculated according to Brazilian standard ABNT NBR 16605 (ABNT, 2017);

(2) the second stage consisted of molding, curing, and rupture the specimens subjected to unconfined compression tests and splitting tensile tests using curing time between 7 and 28 days.

(3) the third stage comprised molding and curing the specimens subjected to durability test using severe freeze-thaw and wetting-drying cycles; and

(4) The last stage consisted of molding, curing, and rupture the specimens subjected to unconfined compression tests and splitting tensile tests after 3, 6 and 12 freeze-thaw and wetting-dry cycles.

2.1 Materials

The three materials used in the present study were sedimentary Guabirotuba silty soil, early strength (PC), and distilled water.

The soil sample was manually collected in undeformed and deformed state from the southeast zone of the city of Curitiba (Brazil), in the municipality of São José dos Pinhais (metropolitan area of Curitiba), avoiding possible contamination and taken in sufficient quantity to perform all tests. The soil was collected on a road slope and was extracted at a depth of 2~2.5 m. The soil belongs to the second layer of the Guabirotuba Formation (the layer has thicknesses ranging from 1 to 5 m deep). Undeformed samples were collected to perform the unconfined compression, splitting tensile, direct shear and one-dimensional consolidation tests in natural soil state. The undeformed soil was sampled in 15 cm edge blocks, under Brazilian Standard ABNT NBR 9604 (ABNT, 2016). The soil in the natural state had hygroscopic moisture of 40 % and a dry unit weight of 11.60 kN/m^3. The test results of soil sample characterization at deformed state performed conforming to the description in the experimental program, are presented in Table 1. In Table 1, note that the largest soil size corre-

Table 1. Properties of the soil sample.

Properties	Value
Liquid limit, %	50.82
Plastic limit, %	35.96
Plastic index, %	14.86
Specific gravity of soil	2.62
Coarse sand (0.6 mm < diameter < 2 mm), %	5
Medium sand (0.2 mm < diameter < 0.6 mm), %	12
Fine sand (0.06 mm < diameter < 0.2 mm), %	18
Silt (0.002 mm < diameter < 0.06 mm), %	60
Clay (diameter < 0.002 mm), %	5
Effective size (D_{10}), mm	0.003
Mean particle diameter (D_{50}), mm	0.038
Uniformity coefficient (C_u)	8.33
Coefficient of curvature (C_c)	1.33
Classification (USCS)	MH
UCS in natural state, kPa	104.58
STS in natural state, kPa	16.62
STS/UCS ratio in natural state	0.16
Internal friction angle in natural state, degrees	26
Expansion, %	7.5
Cohesion in natural state, kPa	23
Color	Yellow
pH in water	5.5
Preconsolidation pressure (σ'_c), kPa	300
Coefficient of Consolidation (C_v), cm^2/sec	0.02
Optimum moisture content (from Standard effort-SE), %	26.5
Maximum Dry unit weight (from Standard effort-SE), kN/m^3	13.72
Optimum moisture content (from Intermediate effort-IE), %	20.50
Maximum Dry unit weight (from Intermediate effort-IE), kN/m^3	15.43
Optimum moisture content (from Modify effort-ME), %	14.50
Maximum Dry unit weight (from Modify effort)-ME, kN/m^3	16.75

sponds to silt (60 %). The specific gravity was 2.62. The predominant color of the soil is yellow due to the oxidation and important presence of goethite in the subtropical climate in southern Brazil (Baldovino et al., 2020a). The particle diameters corresponding to 10 %, 30 %, 50 %, 60 % and 90 % finer (or passing) were measured as D_{10} = 0.003 mm, D_{30} = 0.01 mm, D_{50} = 0.025 mm, D_{60} = 0.038 mm and D_{90} = 0.3 mm. Besides, the coefficients of uniformity and curvature were measured as C_u = 8.33 and C_c = 1.33, from which soil was characterized as silt of high plasticity with sand (MH) per the Unified Soil Classification System (USCS) criterion.

The total quantitative chemical composition of soil samples was researched through the energy-dispersive X-ray spectroscopy (EDX) using an energy-dispersive X-ray fluorescence spectrometer. Table 2 shows the chemical composition of soil samples, mainly SiO_2, Al_2O_3, and Fe_2O_3, which are usually found in sedimentary soils and participate actively in the process of chemical soil stabilization.

Table 2. Soil sample chemical composition.

Compost	Concentration (%)
SiO_2	48.78
Al_2O_3	44.51
Fe_2O_3	0.61
K_2O	0.84
TiO_2	0.92
SO_3	4.12
CaO	-
Na_2O	-
MgO	
Loss on Ignition	0.22

Table 3. Chemical composition and some physical properties of cement.

Property	Value
Al_2O_3, %	4.30
SiO_2, %	18.96
Fe_2O_3, %	2.95
CaO, %	60.76
MgO, %	3.26
SO_3, %	3.18
Insoluble residue, %	0.77
Strength at 7 days, MPa	44.7
Strength at 28 days, MPa	54.2
Fineness, %	0.04
Specific gravity	3.11

A high early strength Portland cement (Type V in Brazil) (ASTM C150, 2016) is composed principally of calcium oxide (CaO), Silicon dioxide (SiO_2) and aluminum oxide (Al_2O_3) and is produced and sold in the south of Brazil. The test results of the cement characterization performed conforming to the description in the experimental program, are presented in Table 3. The specific gravity of cement was 3.11.

To prevent undesired reactions and limit the number of variables, distilled water at 23 ± 2 °C was used to conduct all the characterization tests of the soil and for molding the test specimens for UCS and durability.

2.2 Unconfined compressive, splitting tensile and durability program

The types of mixes and their respective stabilizations with cement are shown in Tables 4 and 5. Four strategic traces were made with silt and cement. Each trace comprises a type of stabilization with one type of cement, mold moisture, molding dry unit weights, curing times and splitting tensile and compressive strength tests. Each splitting tensile and compression test comprises 15 types of mixtures, which can be seen in detail in Table 6. Some samples also were molded for tensile/compression tests after 3, 6 and 12 wet-dry (W-D) and freeze-thaw (F-T) cycles. This study used high early strength Portland cement (named CP V in Brazil). Its rapid increase of resistance permitted selecting 7 days as the curing period for durability and UCS specimens. In addition, for UCS tests 14 and 28 days of curing periods were chosen. Thus, all compacted silt-cement blends were studying using 7, 14, and 28 days (when convenient as reported in Tables 4-6).

2.3 Preparing specimens

Test specimens having height and diameter of 100 mm and 50 mm, respectively, were molded for the unconfined compression and splitting tensile tests. For the wetting-drying (W-D) and freezing-thawing (F-T) durability tests (to calculate the loss of mass per cycle or accumulated loss of mass), specimens measuring 10 cm in diameter and 12.73 cm in height were molded. However, for measuring UCS and STS after W-D and F-T cycles, specimens measuring 50 mm in diameter and 100 mm in height were used.

The silt soil was dried in an oven at a temperature of 100 ± 5 °C and divided into uniformly distributed portions to be mixed with different cement contents. The percentages of cement chosen for this research were: 3 %, 5 %, 7 % and 9 % about the dry mass of the soil; taking into consideration the current literature and Brazilian experience (Consoli et al., 2016a). Thus, a quantity of dry cement was added to achieve the three different addition contents (3, 5, 7, and 9 %). The mixture of the soil with cement was prepared to be homogenous to the maximum extent. Subsequently, a percentage of water was added, determined about the water

Table 4. Molding points for silt-cement compacted blends.

Silt Type	Molding dry unit weight (γ_d)	Molding moisture (ω)	Type of cement and percentages	Curing time-days	Test
Yellow silt (YS) -mix 1	13, 14.5 and 16 kN/m^3	10, 14.67, 19.33, 24, 28.67 and 33.34 %	Type V: 3, 5, 7 and 9 %	28-d	q_u and q_t - saturated conditions
Yellow silt (YS)-mix 2 (1)	Optimum compaction conditions*	Optimum compaction conditions*	Type V: 3, 5, 7 and 9 %	7, 14 and 28-d	q_u and q_t - saturated conditions
Yellow silt (YS)-mix 3	Optimum compaction conditions*- with wet-dry cycles	Optimum compaction conditions*- with wet-dry cycles	Type V: 3, 5, 7 and 9 %	3, 6 and 12 cycles	q_u and q_t - saturated conditions
Yellow silt (YS)-mix 4	Optimum compaction conditions*- with freeze/thaw cycles	Optimum compaction conditions*- with freeze/thaw cycles	Type V: 3, 5, 7 and 9 %	3, 6 and 12 cycles	q_u and q_t - saturated conditions

*Optimum compaction conditions for yellow silt-cement Type V mixes in details in Table 5.

Table 5. Molding points for yellow silt-cement mixes on optimum molding conditions.

Cement content (%)	MDD-Maximum dry density (kN/m^3)			OMC- Optimum moisture content (%)			Standard
	Standard effort-SE	Intermediate effort-IE	Modified effort-ME	Standard effort-SE	Intermediate effort-IE	Modified effort-ME	
3	13.85	15.65	16.85	26	18	15	Brazilian NBR 7182 (ABNT 2016)
5	13.8	15.55	17.05	26.5	18	15	
7	14	15.55	16.95	26	18.5	14.5	
9	14	15.55	16.95	25.5	18	15	

content of the molding points shown in Table 4 and 5 (when convenient). For the compacted specimens, the required mass of soil plus cement was mixed with the appropriate amount of distilled water to prepare an initial moisture content. The samples for molding the test specimens were statically compacted in three layers (the top of each layer was slightly scarified) with a stainless-steel mold. The molding was done with the help of a manual hydraulic press and the time required for the preparation of each test specimen was approximately 15 min. The specimens were extruded from its molds using a hydraulic device. To ensure the dry unit weight of molding, the mold volume and weight of the wet mixture necessary for each test specimen were calculated, following which the required quantities for each specimen were weighed. The time used to prepare, mix and compact the specimens was always less than 30 min, to avoid the early reactions of soil-cement in water's presence. The test specimens were weighed on a 0.01 g precision scale, and the dimensions were measured using a caliper with a 0.01 mm error. Three wet samples of the mixture were taken to check the mold moisture by oven drying.

The extracted test specimens were wrapped in a transparent plastic film to maintain the moisture content. Finally, the test specimens were stored in a wet chamber for the curing process for 7, 14, and 28 days (when appropriate), at a mean temperature of 24 ± 2 °C and relative humidity above 95 % to prevent significant changes in the moisture until the testing day. After curing, the specimens were submerged in a tank of distilled water for 24 h (1 day) expecting to try to minimize the possibility that the suction would influence the final strength value. This procedure has been used in the current literature to reduce the effect of suction (Moreira et al., 2019a). Additionally, moisture content in the soil-cement mixes was cross-checked by oven drying after the completion of the UCS and STS tests.

The following maximum errors were taken into account when conducting the unconfined compression, splitting tensile and durability for the samples: sample dimensions with a diameter of ± 0.5 mm and height of ± 1 mm, dry unit weight (γ_d) of ± 1 %, and water content (ω) of ± 0.5 % (Baldovino et al., 2018a; Consoli et al., 2009; Moreira et al., 2019a). For each molding point, curing period, cement content, three test specimens were molded. Three replicate samples were tested for each compaction state to check repeatability in UCS and STS results. To perform the unconfined compression and splitting tensile tests, an automatic press was used along with rings calibrated for an axial load with a capacity of 10 kN. The tests were conducted using an automated system at a test speed of 1 mm/min to measure the applied force with a resolution of 2.5 N and deformation with a sensitivity of 0.01 mm. The procedures for the unconfined compression and splitting tensile tests adhered to

Table 6. Optimization for A_q parameter for each mix using the coefficient of determination/MAPE and its corresponding normalization resistance with the parameter $\eta / C_{iv}^{0.50} = 20$.

Mix	Test	Code	A_q ($\times 10^4$) in kPa	R^2	MAPE (%)	q_u and q_t (kPa) at $\eta / C_{iv}^{0.50} = 20$
Yellow Silt+CPV+ mold moisture of 10 % (28-d)	UCS	YS+CPV+[ω = 10 %]+UCS	117.36	0.92	5.9	1291
	STS	YS+CPV+[ω = 10 %]+STS	17.21	0.91	5.5	189
Yellow Silt+CPV+ mold moisture of 14.67 % (28-d)	UCS	YS+CPV+[ω = 14.67 %]+UCS	160.41	0.92	5.4	1765
	STS	YS+CPV+[ω = 14.67 %]+STS	21.46	0.88	9.8	236
Yellow Silt+CPV+ mold moisture of 19.33 % (28-d)	UCS	YS+CPV+[ω = 19.33 %]+UCS	203.55	0.95	4.3	2240
	STS	YS+CPV+[ω = 19.33 %]+STS	27.54	0.90	8.1	303
Yellow Silt+CPV+ mold moisture of 24 % (28-d)	UCS	YS+CPV+[ω = 24 %]+UCS	242.26	0.98	2.8	2666
	STS	YS+CPV+[ω = 24 %]+STS	38.76	0.92	6.3	427
Yellow Silt+CPV+ mold moisture of 28.67 % (28-d)	UCS	YS+CPV+[ω = 28.67 %]+UCS	220.31	0.97	2.3	2424
	STS	YS+CPV+[ω = 28.67 %]+STS	34.68	0.94	5.8	382
Yellow Silt+CPV+ mold moisture of 33.34 % (28-d)	UCS	YS+CPV+[ω = 33.34 %]+UCS	183.57	0.97	4.1	2020
	STS	YS+CPV+[ω = 33.34 %]+STS	25.44	0.92	7.4	280
Yellow silt+CPV+ optimum compaction conditions (7-d)	UCS	YS+OC+7-d+UCS	137.61	0.92	9.5	1514
	STS	YS+OC+7-d+STS	20.45	0.95	6.8	225
Yellow silt+CPV+ optimum compaction conditions (14-d)	UCS	YS+OC+14-d+UCS	167.86	0.90	9.7	1847
	STS	YS+OC+14-d+STS	26.76	0.96	4.2	295
Yellow silt+CPV+ optimum compaction conditions (28-d)	UCS	YS+OC+28-d+UCS	208.83	0.96	5.1	2298
	STS	YS+OC+28-d+STS	35.14	0.96	3.3	387
Yellow silt+CPV+ optimum compaction conditions (3 wet-dry cycles)	UCS	YS+CPV+3W-D+OC+UCS	226.12	0.94	1.8	2488
	STS	YS+CPV+3W-D+OC+STS	30.86	0.96	2.7	340
Yellow silt+CPV+ optimum compaction conditions (6 wet-dry cycles)	UCS	YS+CPV+6W-D+OC+UCS	540.33	0.99	2.4	5946
	STS	YS+CPV+6W-D+OC+STS	64.52	0.99	3.1	710
Yellow silt+CPV+ optimum compaction conditions (12 wet-dry cycles)	UCS	YS+CPV+12W-D+OC+UCS	575.94	0.98	2.9	6338
	STS	YS+CPV+12W-D+OC+STS	83.08	0.97	3.7	914
Yellow silt+CPV+ optimum compaction conditions (3 freeze-thaw cycles)	UCS	YS+CPV+3F-T+OC+UCS	108.93	0.92	8.4	1199
	STS	YS+CPV+3F-T+OC+STS	16.96	0.94	7.2	187
Yellow silt+CPV+ optimum compaction conditions (6 freeze-thaw cycles)	UCS	YS+CPV+6F-T+OC+UCS	94.98	0.96	4.3	1045
	STS	YS+CPV+6F-T+OC+STS	15.09	0.98	1.9	166
Yellow silt+CPV+ optimum compaction conditions (12 freeze-thaw cycles)	UCS	YS+CPV+12F-T+OC+UCS	69.32	0.94	7.5	763
	STS	YS+CPV+12F-T+OC+STS	11.40	0.96	5.9	125

Brazilian ABNT NBR 5739 (ABNT, 2007) and ABNT NBR 7222 (ABNT, 2011), respectively.

The tests followed the recommendations and procedures of the American Standard ASTM D559 (ASTM, 2015) and ASTM D560 (ASTM, 2016) for W-D and F-T cycles, respectively. The specimens were prepared with the different cement content and molding conditions defined in Table 5 (optimum compactions conditions). Additionally, specimens only for W-D cycles, containing 25 % moisture content and dry unit weight of 13, 14 and 15 kN/m^3 were also molded. After hydration of the cement (i.e. 7 days), the W-D and F-T cycles were started. After the W-D and F-T cycles, the samples were subjected to brushing to measure the loss of mass. They were 18 to 19 brushed on the side faces covering them twice, and 4 brushed on the two transverse faces of the test cups applying an average force of 15 N, which was calibrated on a precision scale. To avoid as much as possible operational error variables, all brush tests were performed by the same operator during the 12 cycles. Various specimens employed the standard effort after 12 F-T cycles are presented in Figure 1. The amount of soil-cement mass lost during brushing was measured with the help of an accuracy scale of 0.01 g. Finally, the mass values of the samples before and after brushing in each cycle were recorded. The specimens for UCS and STS tests using W-D and STS cycles (i.e. 3, 6, and 12) were molded under the same conditions as the specimens for mechanical resistance (Figure 1) with normal curing. Consequently, each W-D and STS started after 7-d curing time. Each W-D cycle started with the wet cycle at 23 °C for 5 h in a distilled water tank. After wetting, samples were taken and placed in an oven at 71 ± 2 °C for 42 h. On the other hand, each F-T cycle started with the freeze cycle at -23 °C for 23 h (Figure 1) in a freezer with the capacity to reach a temperature of up to -40 °C. After freezing, samples were taken and placed in a wet chamber for 24 h to thawing. Finally, UCS and STS were conducted after 3, 6 and 12 W-D and STS cycles.

3. Results and discussions

3.1 Effects of initial moisture content and curing time on strength

Figures 2 and 3 shows the effects of initial molding moisture content on unconfined compressive and splitting tensile strength, respectively. Compressive and tensile strength values depending on curing time and porosity/cement index (η/C_{iv}) (named porosity-to-volumetric cement content index, where C_{iv} is a volume of cement divided by the volume of the specimen where it's contained). Good relationships (with R^2 above 0.92 to q_u and 0.88 to q_t) between η/C_{iv}-q_u and η/C_{iv}-q_t are obtained depending on initial moisture content and a curing time of 28 days. Compressive and

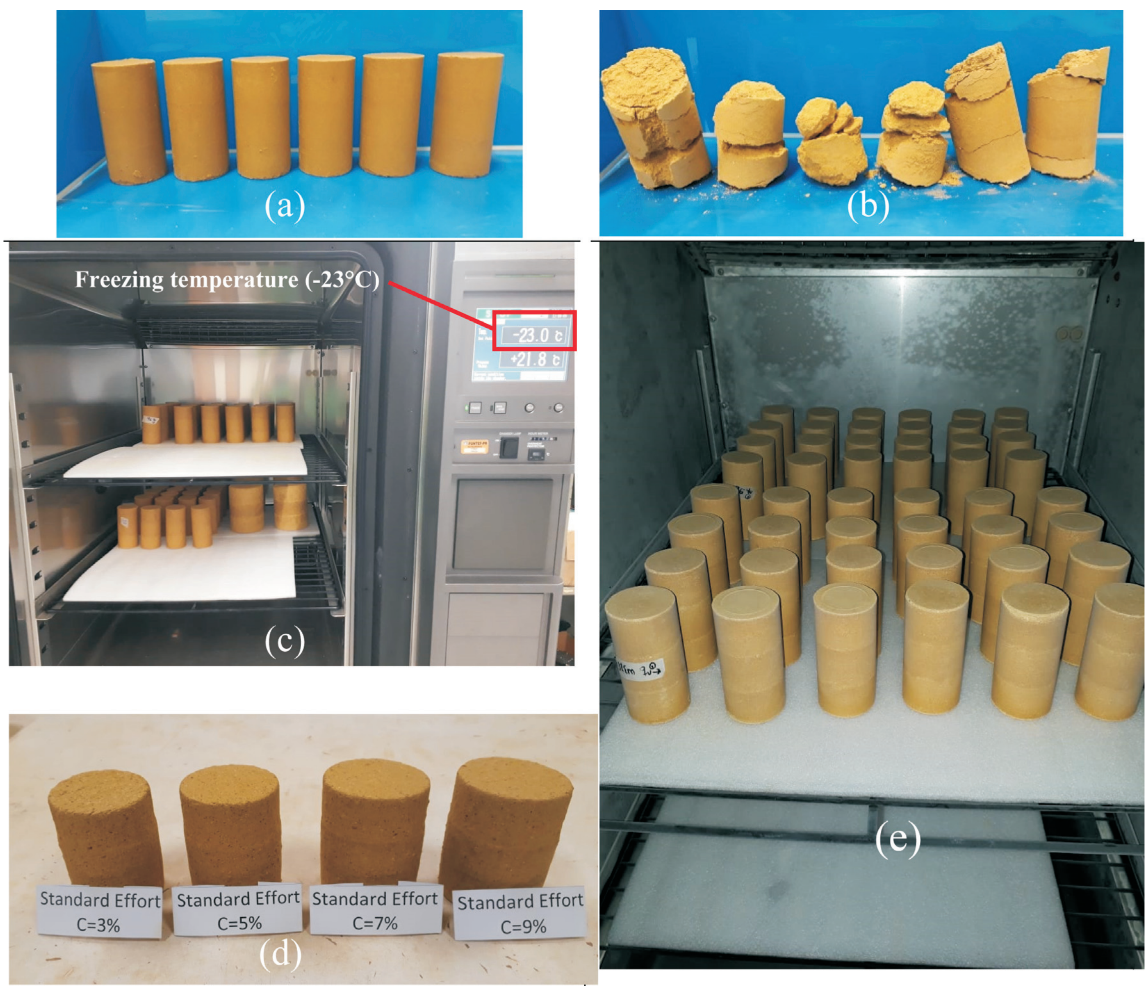

Figure 1. Photos of the specimens**:** (a) compacted specimens with 9 %C employing the standard effort after 12 W-D cycles for UCS and STS tests. (b) UCS and STS compacted specimens with 3 %C using the standard effort after the first W-D cycle. (c) UCS, STS and Durability specimens into a freezer before start freezing cycle for 23 h. (d) Comparing durability specimens compacted at standard effort after 12 F-T cycles. (e) UCS and STS compacted specimens employing standard, intermediate, and modified effort after F-T cycle at -23 °C.

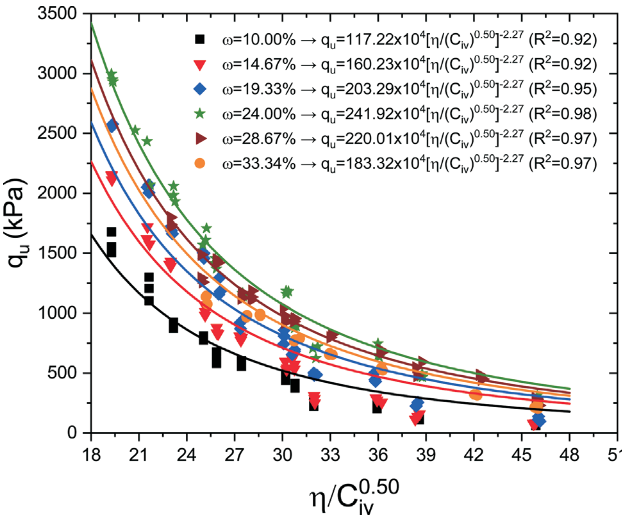

Figure 2. Influence of porosity/cement index ($\eta / C_{iv}^{0.50}$) on unconfined compressive strength considering initial molding moisture of 10, 14.67, 19.33, 24, 28.67, and 33.34 % and considering 28 d- curing time.

splitting tensile values increases when initial moisture content increases between 10 % and 25 %. Above 25 % moisture content, both compressive and tensile strength decreases. To make compatible η and C_{iv}, C_{iv} was raised to exponent b = 0.50 and to make compatible $\mu = \eta/C_{iv}^{0.50}$ and q_t or q_u as a power function, μ factor was raised to exponent c = -2.27. These exponents (b and c) depending on the type of soil and cement properties as related in previous studies (Baldovino et al., 2018a; Consoli et al., 2016b; Moreira et al., 2019a). The variation in the power functions (see Figures 2 and 3) clearly shows that moisture can increase or decrease the mechanical resistance of compacted soil-cement mixtures after 28-days curing. According to molding points presented in Table 5 and Figures 2 and 3, the amount of μ varies from 19 to 46, for compressive and tensile specimens.

One can observe in Figure 4 the influence of porosity/cement index (η/C_{iv}) on unconfined compressive and splitting tensile strength considering optimum compaction conditions (molding points in Table 5) using 7, 14, and 28 days as curing time periods. Figure 4 shows an increase in q_u and q_t when curing time increases. Porosity/cement index controlling q_u and q_t values depending on a power function (with R^2 between 0.90 and 0.96- Figure 4). Optimum compaction conditions are controlling by μ ratio (raised to 0.50 and -2.27 exponents). For specimens compacted on optimum points of compaction curve, the amount of μ varies from 16 to 42 for compression and tensile. Excellent relationships between compression-μ and tensile-μ were reached independently of curing time between 7-28 days. Equations presented in Figures 2 to 4 describe a potential increase (i.e. power function) in tensile strength and unconfined compression for each molding moisture or curing period. Note that growth follows the form: $q_u \vee q_t = A_q\,[\eta / C_{iv}^{\,b}]^{-c}$, where A_q is a constant expressed in kPa. The A_q parameter depends on the type of soil and the type of binder (Baldovino et al., 2019a; MolaAbasi et al., 2019). The physical meaning of this single empirical parameter A_q requires further analysis and additional knowledge of the inherent fabric characteristics of the mixtures tested (Consoli et al., 2019). The existing data clearly show that A_q has a strong correlation, increasing with the curing time, molding moisture and W-D cycles present in the mixtures tested. Diambra et al. (2018), developed a theoretical framework based on the superposition of the individual

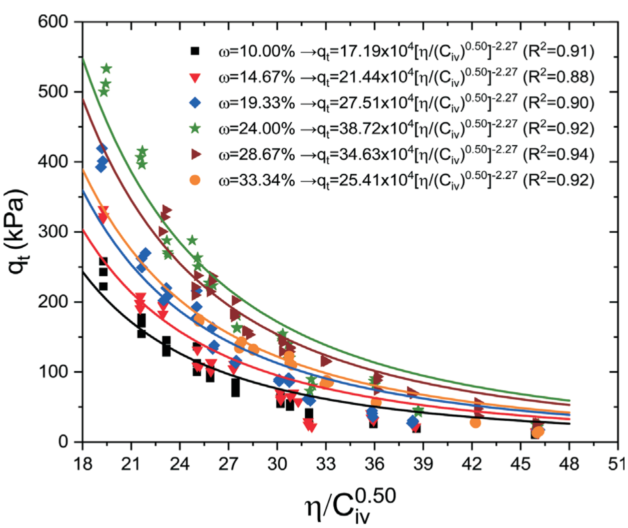

Figure 3. Influence of porosity/cement index ($\eta / C_{iv}^{0.50}$) on splitting tensile strength considering initial molding moisture of 10, 14.67, 19.33, 24, 28.67, and 33.34 % and considering 28 d- curing time.

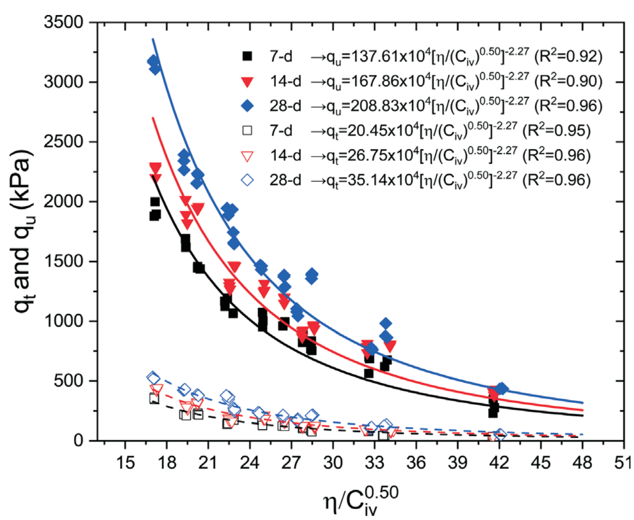

Figure 4. Influence of porosity/cement index ($\eta / C_{iv}^{0.50}$) on unconfined compressive and splitting tensile strength considering optimum compaction conditions (molding points in Table 5) and 7, 14, and 28 days curing time.

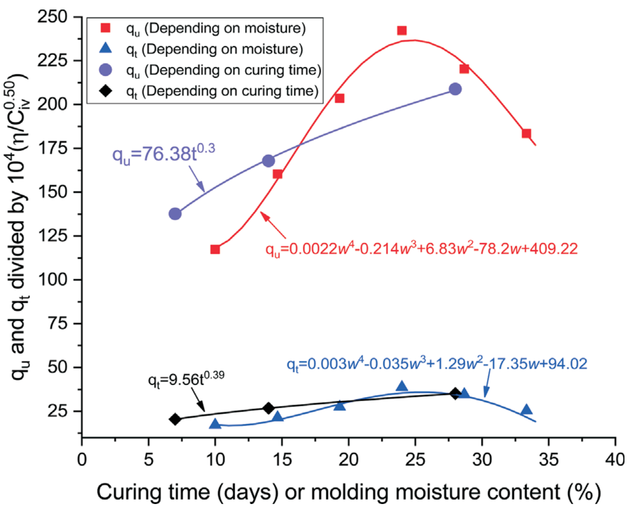

Figure 5. Normalization of UCS and STS depending on curing time periods and molding moisture content.

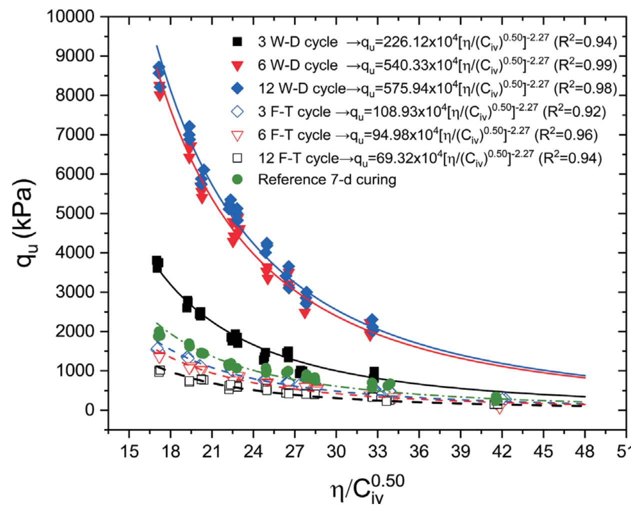

Figure 6. Influence of porosity/cement index ($\eta / C_{iv}^{0.50}$) on unconfined compressive strength against 3, 6, and 12 wet/dry and freeze/thaw cycles, considering optimum compaction conditions (molding points in Table 5) and 7 days as curing period.

failure strength contributions of both constituents to link the empirical coefficients A_q and c governing the unconfined compressive strength (q_u) and split tensile strength (q_t) to both sandy soil and cement properties. The authors concluded that A_q and c depend on the constituents' physical parameters like the critical state soil strength ratio (M), critical state soil porosity (η_{cs}), Poisson's ratio of cement and Poisson's ratio of composite material. However, the measuring of these constituents' physical parameters is outside the scope of the present paper. Diambra et al. (2018) suggested $b = 1/c$ for cemented sands, where theoretically b would be $1/2.27 = 0.44$ but noted in the present study as $1.135/c = 0.50$ for the cemented silt with cement reported on the present study.

When water is mixed with cement, its hydration occurs, which means that cementitious compounds of calcium-silicate-hydrate (C-S-H) and calcium-aluminate-hydrate (C-A-H) are formed, and an excess of calcium hydroxide (CaOH) is released to form extra C-S-H because of the reaction between the soil silica and $Ca(OH)_2$ in cement (MolaAbasi et al., 2019; Puppala, 2016). The formation of C-S-H results in the growth in strength as soon as the cement hydration happens. Meanwhile, Kezdi & Rethati (1988) explain the mechanism by which the stabilizing action of cement is accomplished in fine soils. In fine-grained (silts and clays), the hydrated cement develops strong bonds between the mineral particles, resulting in a ce-

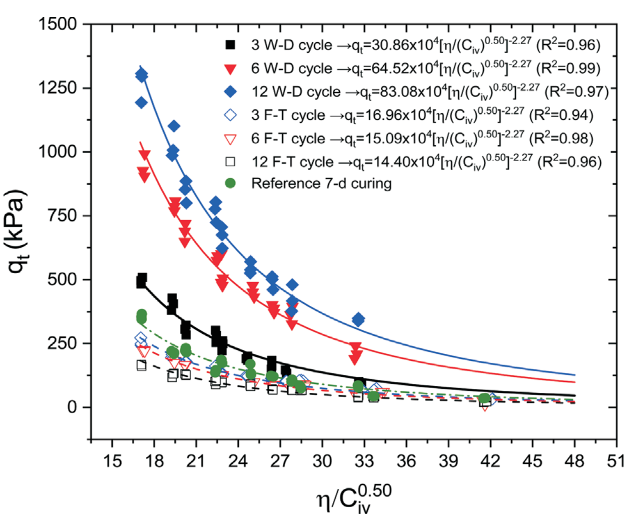

Figure 7. Influence of porosity/cement index ($\eta / C_{iv}^{0.50}$) on splitting tensile strength against 3, 6, and 12 wet/dry and freeze/thaw cycles, considering optimum compaction conditions (molding points in Table 5) and 7 days as curing period.

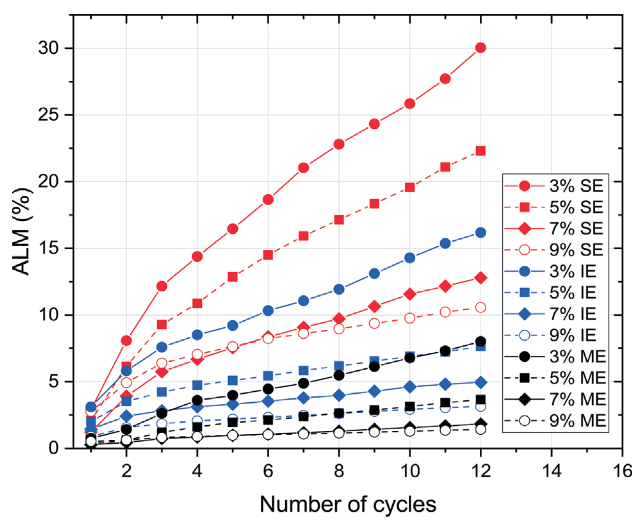

Figure 8. Accumulated Loss of Mass (ALM) vs. freeze/thaw cycles for a silty soil-cement compacted blends considering 3, 5, 7, and 9 % of cement; distinct compaction efforts (dry unit weight of molding) indicated in Table 5 and considering 7 days of curing.

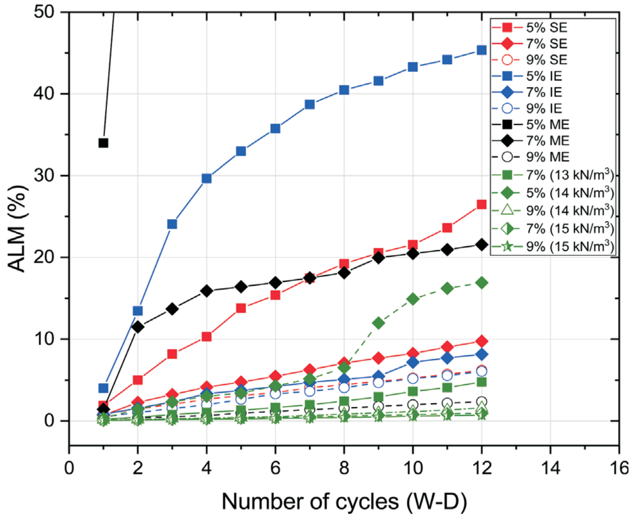

Figure 9. Accumulated Loss of Mass (ALM) vs. wet/dry cycles for a silty soil-cement compacted blends considering 3, 5, 7, and 9 % of cement; distinct compaction efforts (dry unit weight of molding) indicated in Table 5 and specific dry unit weight (13, 14, and 15 kN/m^3) of molding at ω = 25 %, and considering 7 days of curing.

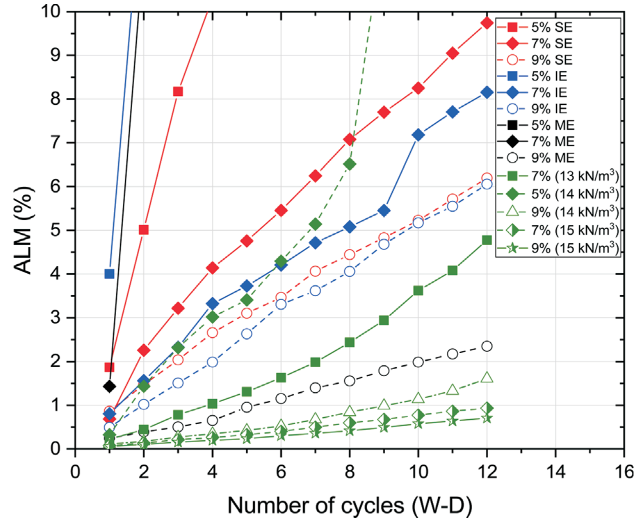

Figure 10. Enlargement of Figure 9 (0-10 % ALM) for different soil-cement compacted blends depending on number of Wet-Dry cycles.

mented matrix, which encases the unbonded soil grains. The honeycomb structure of the matrix is responsible for the strength of the final product. The strength of the clay particles within the matrix is rather low. The bonds prevent the particles from moving towards one another, thereby minimizing the plasticity index and increasing shear resistance. The clay particles are coagulated by the lime liberated during the hydration, reducing their affinity for water and thus the swelling and shrinking properties of the soil.

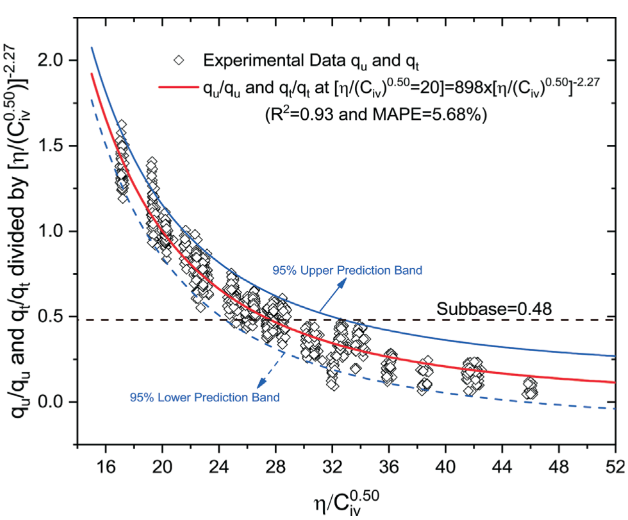

Figure 11. Normalization of q_u and q_t (for the whole range of $\eta / C_{iv}^{0.50}$) by dividing for q_u and q_t at $\eta / C_{iv}^{0.50} = 20$ (Details in Table 6) considering strength of cement- treated silty soil using distinct cement contents, different initial moisture content, dry unit weight, various W-D and F-T durability cycles, and 7, 14, and 28-d of curing time.

Thus, the quantity of water to reach maximum strength must be enough to form the optimum C-S-H and matrix structure. Comparing the effects of molding moisture content (see Figures 2 and 3) and compaction effort (see Figure 4) on strength depending on the $\eta / C_{iv}^{0.50}$ index, the highest values of strength are obtained when compacted in ω = 25 %, these values correspond to 1 % below the average optimum moisture content of soil-cement mixes at standard effort (i.e. ω = 26 %). Consequently, maximum UCS-STS values reported in Figures 2-4 are not dependent on the optimum compaction water content. In that sense, maximum strength values depending on the final honeycomb structure affect by $\eta / C_{iv}^{0.50}$, molding ω, and curing time. On the other hand, independent of moisture content and using three compaction efforts combination with three optimum moisture content, A_q value is higher when blends were compacted at ω between 24 and 28.33 % than the blends compacted on optimum compacted parameters (MDD and OMC), but the effort necessary to reach those dry unit weights requires more energy comparing the employed when MDD and OMC are used.

The equations shown in Figures 2 to 4 can be normalized in terms of $\eta / C_{iv}^{0.50}$, for the same values of molding moisture or curing period. The power functions that describe the growth of q_u and q_t as a function of $\eta / C_{iv}^{0.50}$ can be divided by the same value of $10^4 [\eta / C_{iv}^{0.50}]^{-2.27}$, ensuring, thus, a constant calculated to its corresponding value of molding moisture or curing time, both for q_u and q_t. Therefore, if it is correlated to its respective moisture/curing time with its normalized constant q_u divided by $10^4 [\eta / C_{iv}^{0.50}]^{-2.27}$ or q_t divided by $10^4 [\eta / C_{iv}^{0.50}]^{-2.27}$, a point in the Cartesian plane is found. In this way, the variation of normalized q_u and q_t depends on the moisture content or t (curing time) (see Figure 5). Figure 5 shows that the prime parameter controlling UCS and STS after $\eta / C_{iv}^{0.50}$ is the molding moisture content followed by the curing time. Dosages equations controlling UCS (Equation 1) and STS (Equation 2), according to Figure 5 (depending on molding moisture), are expressed respectively as:

$$q_u = (0.0022\omega^4 - 0.215\omega^3 + 6.83\omega^2 - 78.2\omega + 409.22) \times 10^4 [\eta / C_{iv}^{0.50}]^{-2.27} \quad (R^2 = 0.96) \tag{1}$$

$$q_t = (0.0003\omega^4 - 0.035\omega^3 + 1.29\omega^2 - 17.35\omega + 94.02) \times 10^4 [\eta / C_{iv}^{0.50}]^{-2.27} \quad (R^2 = 0.96) \tag{2}$$

Good relationships (R^2 = 0.96 for UCS and R^2 = 0.95 for STS) were obtained normalizing strength in terms of w. On the other hand, dosage equations controlling UCS (Equation 3) and STS (Equation 4) according to Figure 5 (depending on curing time *t* periods in days) are expressed respectively as:

$$q_u = 79.38t^{0.30} \times 10^4 [\eta / C_{iv}^{0.50}]^{-2.27} \quad (R^2 = 0.97) \tag{3}$$

$$q_t = 9.56t^{0.39} \times 10^4 [\eta / C_{iv}^{0.50}]^{-2.27} \quad (R^2 = 0.96) \tag{4}$$

Excellent relationships (R^2 = 0.97 for UCS and R^2 = 0.96 for STS) were obtained normalizing strength in terms of curing time (*t*). The strength of compacted blends was achieved at humid room considering curing time and molding moisture. These strengths are suitable for engineering earthwork because they reached a minimum value of 1.2 MPa and could be used in subbase construction (see Figures 2-4). But field strength can be modified due to the local climatic conditions (cold or hot). Thus, the effects of freeze/thawing and wet/dry cycles on the resistance and durability of the mixtures are underestimated.

3.2 Effects of wetting-drying and freeze-thawing cycles on strength and durability

Figures 6 and 7 show the impact of η/C_{iv} index on unconfined compressive and splitting tensile strength, respectively; against 3, 6, and 12 wet/dry and freeze/thaw cycles, considering optimum compaction conditions. For these several climates conditions, η/C_{iv} also controlling the strength of silt-cement compacted blends. When specimens were subject W-D cycles the strength increases. On the other hand, when F-T cycles were employed, the strength decreases when the number of cycles was increased to 12 as shown in Figures 6 and 7. It is evident that W-D cycles increases and accelerating the pozzolanic reactions between soil and cement, reaching maximum values of 8500 kPa and 1270 kPa in compression and tensile, respectively. Specimens with C = 3 % could not handle W-D cycles as shown in Figure 1. The specimens partially disintegrated due to the short curing time and the small percentage of cement. The value of A_q decreased with an increasing number of F-T cycles for both q_u and q_t. That is, the strength of the blends was negatively shaved by exposure to extreme freezing temperatures. The creation and formation of cracks due to the cold and deceleration of the pozzolanic reactions and cement hydration promoted the loss of resistance. Thus, UCS = 1.2 MPa is attended when a large amount of cement (above 7 %) was added and compaction energy of 15 kN/m^3 was used.

According to Figure 8, the increase in freeze-thaw cycles means an increase in the mass loss of each mixture due to brushing. These losses are directly related to the amount of cement added and the compaction energy employed since an increase in the density of compaction and cement content caused the mixtures to suffer less mass loss. Thus, Figure 8 also presents the accumulated loss of mass (ALM) of blends subject F-T cycles and considering 7-days curing. The decrease in characteristic loss of mass (i.e. ALM in % per cycle) with increasing, compaction energy was noted. In standard effort, the characteristic loss of mass (CLM) varied, on average, from 2.5 % to 0.88 % of mass loss per cycle. In the intermediate and modified efforts, the CLM value decreased by 1.35 % and 0.67 %, respectively. The loss of mass per cycle is associated with the force applied during brushing (~ 15 N) and the surface strength of the mixtures to abrasion, which increases when adhesion-cementation of the soil-cement particles is increased.

Figure 9 shown the ALM vs. W-D cycles for the blends used. Most of the mixtures did not have mass losses greater than 10 % as presents in detail in Figure 10. Compacted blends using 3 % cement and curing for 7 days did not stand the immersion in water for 5 h (wet cycle). Initial moisture content influences the durability of the blends. Using 5 % cement in different energies, the durability increased when the moisture content increases. Thus, the durability was directly related to the amount of water added to compaction. For this reason, specimens were also compacted with ω = 25 % (optimum moisture content to compact the blends considering the strength- according to Figures 2-3) as shown in Figures 9 and 10. On average, increasing the moisture content of compaction to 25 % improved the durability (W-D) of the mixes by 32 %. In this way, 9 % ME (γ_d = 16.95 kN/m^3 and ω = 15 %) expected to be the most durable blend, but Figure 9 demonstrates the opposite, decreasing γ_d to 15 kN/m^3 and increasing ω to 25 % the ALM decreases from 2.4 % to 1.7 % (improving ALM in 40 %). Besides, other compacted blends with ω = 25 % and 9 % (with γ_d = 14 kN/m^3) or 7 % (with γ_d = 14 kN/m^3) also increase the durability in reference to 9 % ME. However, 3 % of cement compacted blends in ω = 25 % also did not resist the first wet cycle. Consequently, 3 % of cement is not recommendable to stabilization in terms of durability.

The permissible mass loss values for durability tests using F-T/W-D cycles to base construction, for chemically stabilized silt soils, the ALM value should not exceed 7 % or 8 % according to Portland Cement Association (PCA, 2000) and to Corp of Engineer (1994), respectively. All mixtures (using F-T cycles) in the modified and intermediate effort (except C = 3 %) meet this requirement. When W-D cycles are employed to study the durability of compacted blends, 7 % and 9 % above intermediate effort meet the requirement. Nevertheless, to subbase this requirement it may be less strict. Base on ALM = 15 % compacted blends employing average C = 6 % above standard effort fulfill the requirement of durability, and, if ω = 25 % is used to compact the mixes, cement content and effort can be decreased by up to 1 %. However, the requirements of the earthwork will decide the best soil-cement dosage to make it more resistant and more durable taking into account the weather and the curing time.

3.3 Role of porosity/cement index in normalization terms

Table 6 presents the parameters A_q, $\eta / C_{iv}^{0.50}$, R^2, and mean absolute percentage error (MAPE, in %) of all the equations that control the resistance of the mixtures depending on the molding moisture, curing time and climatic conditions. All equations depend on $\eta / C_{iv}^{0.50}$ index (independent of ω, curing time, and W-D/F-T cycles). The value of b = 0.50 means that porosity (η) and voids in the soil-cement mixture exerts a more compelling influence on q_u and q_t than C_{iv}. For this reason, A_q value increases significantly. The exponent b < 1 indicates that the porosity (η) exerts a more significant influence on the splitting tensile and compressive strengths than the volumetric content of binder. A value of b close to 1 means that both parameters (voids and amount of binder) exert the same influence magnitude on q_u and q_t. Therefore, b < 1 value is more frequent when cement and lime are used in fine soils while b closer to 1 is more common for cement-sandy soil mixes considering previously studies (Baldovino et al., 2018a; 2018c; Consoli et al., 2009; 2016a; 2019b; Moreira et al., 2019a).

Considering A_q and $\eta / C_{iv}^{0.50}$ values reported in Table 6, it is possible to determine a normalized equation for all the silt-cement compacted blends as a function of η and C_{iv}. For this, the methodology used by Consoli et al. (2016a; 2016b) and Moreira et al. (2019a) was employed. To normalize (i.e. divide) the equations as a function of $\eta / C_{iv}^{0.50}$, it is necessary to (i) Dividing $q_u \vee q_t = A_q\,[\eta / C_{iv}^{b}]^{-c}$ by an arbitrary specific value of UCS and STS, corresponding to a value of a given adjusted $\mu = \eta / C_{iv}^{b}$. The value of μ in this study is set to be 20, due to the mathematical approximations of Figures 2 to 4 and Figures 6 and 7. (ii) The experimental values of UCS and STS, are divided by the values of constant $\mu = \eta / C_{iv}^{0.50} = 20$ presented in Table 6. The quotients obtained in these mathematical operations form a potential trend with R^2 = 0.93 and MAPE = 5.68 %, described by Equation 5. Thus, Figure 11 presents the normalization of strengths of the test samples and their tendency described as:

$$\frac{q_t}{q_t(\eta / C_{iv}^{0.50} = 20)} \vee \frac{q_u}{q_u(\eta / C_{iv}^{0.50} = 20)} = 898(\eta / C_{iv}^{0.50})^{-2.27} \tag{5}$$

In general, 63 % of soil-cement compacted blends to achieve the minimum requirements for use in subbase and base construction according to American standard TxDOT Tex-120-E (TxDOT, 2013) and Brazilian standard DNIT 143 (DNIT, 2010) as shown in Figure 10 (see dotted lines). The minimum requirement is UCS = 1200 kPa (corresponding in average to $q_u/q_{u(\text{normalized})}$ = 0.48) and UCS = 2100 kPa for subbase and base construction, respectively. The minimum requirement is achieved with approximately 6 % and 9 % cement and sometimes with 5 % cement when compacted in modified effort and molding γ_d above 14.5 kN/m^3. Although 9 % cement is a high content and is not environmentally friendly for stabilization, it is the most efficient content to reach maximum UCS and STS values. In the order to avoid 9 % cement, η/C_{iv} criteria can be employed to achieve 1200 kPa of strength increasing the compaction effort and decreasing the amount of cement up to 5.5 % ~ 6.0 %. There are several technical ways of reaching a q_u (Equations 1 and 3), q_t (Equations 2 and 4) and ALM target value for a given project (different combinations of molding water contents, porosities, and cement contents might be used to get to a chosen q_u, q_t and ALM) and the best solution might change from situation to situation, depending on accessibility to equipment to reach a given porosity, cost of cement and availability of water as suggested by Consoli et al. (2011; 2016a; 2016b) and Moreira et al. (2019a).

4. Conclusions

In this paper, the impact of several climate and molding conditions on strength and durability against wet/dry and freezing/thawing cycles of Guabirotuba silt-cement compacted blends were studied. According to the type of soil, cement, the methodology and the presentation and analyses of results used in this study, the following conclusions can be drawn:

- For all studied soil-cement mixtures, the reduction in initial molding dry unit weight and the increase in the quantity of cement caused an increase in splitting tensile and unconfined compression strength after 7, 14, and 28 days of curing (when appropriate). Meanwhile, in terms of porosity/cement index, the compressive and splitting tensile strength of all soil-cement mixtures increased up to 25 % of molding moisture and decreased down to 33 % of moisture when specimens were cured at humid room for 28 days.
- It was possible to determine the equations that control q_u and q_t as a function of η/C_{iv} (set to a value of 0.50). There exists an equation for each molding and climate condition (see Table 6). Thus, there is a single normalized po-

tential trend (see Equation 5) of q_u and q_t as a function of molding moisture, curing time and the molding dry unit weights used. The single trend can be extended to any molding and climate condition of the silty soil in this study stabilized with high early strength cement. In addition, the scalar b for cemented sands is calculated as $1/c$ ($b = 1/c$), where theoretically b would be $1/2.27 = 0.44$ but in the present study was calculated as $1.135/c = 0.50$ for the cemented silt.

- The cement-silt compacted blends are suitable for subbase construction (UCS > 1.2 MPa and ALM > 15 %) when 5 % of cement is used employing modified effort or when molding moisture of 25 % compacting with a lower effort. Finally, UCS values can be increased when blends are submitted to W-D cycles or decrease when blends are submitted to F-T cycles. Thus, the most convenient thing is to avoid earthworks in winter or in the worst-case increase the amount of cement to 9 % and energy after addressing the 15 kN/m^3.

Acknowledgments

The authors are thankful to the Federal University of Technology-Paraná and to the financial support given by the National Council for Scientific and Technological Development (CNPq, Brazil), Coordination for the Improvement of Higher Education Personnel (CAPES, Brazil)-Finance Code 001, and Fundação Araucária do Paraná in Brazil. Finally, the authors would like to thank the anonymous reviewers for their in-depth comments, suggestions, and corrections, which have greatly improved the manuscript.

References

ABNT NBR 5739. (2007). Mortar and Concrete - Test Method for Compressive Strength of Cylindrical Specimens. *ABNT - Associação Brasileira de Normas Técnicas, Rio de Janeiro, RJ* (in Portuguese).

ABNT NBR 7182. (2016). Soil-Compaction Testing. *ABNT - Associação Brasileira de Normas Técnicas, Rio de Janeiro, RJ* (in Portuguese).

ABNT NBR 7222. (2011). Concrete and Mortar - Determination of the Tension Strength by Diametrical Compression of Cylindrical Test Specimens. *ABNT - Associação Brasileira de Normas Técnicas, Rio de Janeiro, RJ* (in Portuguese).

ABNT NBR 9604. (2016). Well opening and soil profile inspection trench, with removal of disturbed and undisturbed soil samples — Procedure. *ABNT - Associação Brasileira de Normas Técnicas, Rio de Janeiro, RJ* (in Portuguese).

ABNT NBR 16605. (2017). Portland Cement and Other Powdered Materials: Determination of the Specific Mass. *ABNT - Associação Brasileira de Normas Técnicas, Rio de Janeiro, RJ* (in Portuguese).

ASTM D 560-16. (2016). Standard Test Methods for Freezing and Thawing Compacted Soil-Cement Mixtures. *ASTM International, West Conshohocken, PA*. https://doi.org/10.1520/D0560_D0560M-16

ASTM D4318-10. (2010). Standard Test Methods for Liquid Limit, Plastic Limit and Plasticity Index of Soils. *ASTM International, West Conshohocken, PA*. https://doi.org/10.1520/D4318-10

ASTM D2435M-11. (2011a). One-Dimensional Consolidation Properties of Soils Using Incremental Loading. *ASTM International, West Conshohocken, PA*. https://doi.org/10.1520/D2435_D2435M-11

ASTM D3080-11. (2011b). Standard Test Method for Direct Shear Test of Soils Under Consolidated Drained Conditions. *ASTM International, West Conshohocken, PA*. https://doi.org/10.1520/D3080_D3080M-11

ASTM D854-14. (2014). Standard Test Methods for Specific Gravity of Soil Solids by Water Pycnometer. *ASTM International, West Conshohocken, PA*. https://doi.org/10.1520/D0854-14

ASTM D2487-17. (2017). Standard Practice for Classification of Soils for Engineering Purposes (Unified Soil Classification System). *ASTM International, West Conshohocken, PA*. https://doi.org/10.1520/D2487-17

ASTM C150-16. (2016). Standard specification for Portland cement. *ASTM International, West Conshohocken, PA*. https://doi.org/10.1520/C0150_C0150M-16

ASTM D559-15. (2015). Standard Test Methods for Wetting and Drying Compacted Soil-Cement Mixtures. *ASTM International, West Conshohocken, PA*. https://doi.org/10.1520/D0559_D0559M-15

Arulrajah, A., Kua, T.-A., Phetchuay, C., Horpibulsuk, S., Mahghoolpilehrood, F., & Disfani, M.M. (2016). Spent Coffee Grounds-Fly Ash Geopolymer Used as an Embankment Structural Fill Material. *Journal of Materials in Civil Engineering*, 28(5), 4015197. https://doi.org/10.1061/(ASCE)MT.1943-5533.0001496

Baldovino, J.A. (2018). *Comportamento mecânico de um solo siltoso da formação geológica Guabirotuba tratado com cal em diferentes tempos de cura* [Master's thesis, Federal University of Technology-Paraná]. Federal University of Technology-Paraná's repository. http://repositorio.utfpr.edu.br/jspui/handle/1/3408

Baldovino, J.A., Moreira, E.B., Izzo, R.L.S., & Rose, J.L. (2018a). Empirical relationships with unconfined compressive strength and split tensile strength for the long term of a lime-treated silty soil. *Journal of Materials in Civil Engineering*, 30(8), 6018008 1-7. https://doi.org/10.1061/(ASCE)MT.1943-5533.0002378

Baldovino, J.A., Moreira, E.B., & Izzo, R.L.S. (2018b). Discussion of "Control factors for the long term compressive strength of lime treated sandy clay soil". *Transportation Geotechnics*, 15, 1-3. https://doi.org/10.1016/j.trgeo.2017.11.002

Baldovino, J.A., Moreira, E.B., Carazzai, E., Rocha, E., Izzo, R., Mazer, W., & Rose, J.L. (2019a). Equations controlling the strength of sedimentary silty soil-cement blends: influence of voids/cement ratio and types of cement. *International Journal of Geotechnical Engineering*. 1-14. https://doi.org/10.1080/19386362.2019.1612134

Baldovino, J.A., Moreira, E.B., Izzo, R.L.S., & Rose, J.L. (2019b). Optimizing the evolution of strength for lime-stabilized rammed earth. *Journal of Rock Mechanics and Geotechnical Engineering*, 11(4), 882-891. https://doi.org/10.1016/j.jrmge.2018.10.008

Baldovino, J.A., Izzo, R.L.D.S., Pereira, M.D., Rocha, E.V.D.G., Rose, J.L., & Bordignon, V.R. (2020a). Equations controlling tensile and compressive strength ratio of sedimentary soil-cement mixtures under optimal compaction conditions. *Journal of Materials in Civil Engineering*, 32(1), 04019320. https://doi.org/10.1061/(ASCE)MT.1943-5533.0002973

Baldovino, J.A., Izzo, R.L., Silva, É.R., & Rose, J.L. (2020b). Sustainable use of recycled-glass powder in soil stabilization. *Journal of Materials in Civil Engineering*, 32(5), 04020080. https://doi.org/10.1061/(ASCE)MT.1943-5533.0003081

Baldovino, J.A., & Izzo, R.L.S. (2019). Relação porosidade/cimento como parâmetro de controle na estabilização de um solo siltoso. *Colloquium Exactarum*, 11(1), 89-100 (in Portuguese).

Baldovino, J.A., Moreira, E.B., Teixeira, W., Izzo, R.L.S., & Rose, J.L. (2018c). Effects of lime addition on geotechnical properties of sedimentary soil in Curitiba, Brazil. *Journal of Rock Mechanics and Geotechnical Engineering*, 10(1), 188-194. https://doi.org/10.1016/j.jrmge.2017.10.001

Consoli, N.C., Rosa, D.A., Cruz, R.C., & Dalla Rosa, A. (2011). Water content, porosity and cement content as parameters controlling strength of artificially cemented silty soil. *Engineering Geology*, 122(3-4), 328-333. https://doi.org/10.1016/j.enggeo.2011.05.017

Consoli, N.C., Vaz Ferreira, P.M., Tang, C.S., Veloso Marques, S.F., Festugato, L., & Corte, M.B. (2016a). A unique relationship determining strength of silty/clayey soils-Portland cement mixes. *Soils and Foundations*, 56(6), 1082-1088. https://doi.org/10.1016/j.sandf.2016.11.011

Consoli, N.C., Quiñonez, R.A., González, L.E., & López, R.A. (2016b). Influence of molding moisture content and porosity / cement index on stiffness, strength, and failure envelopes of artificially cemented fine-grained soils. *Journal of Materials in Civil Engineering*, 29(5), 1-10. https://doi.org/10.1061/(ASCE)MT.1943-5533.0001819

Consoli, N.C., Silva Lopes, L., & Heineck, K.S. (2009). Key Parameters for the Strength Control of Lime Stabilized Soils. *Journal of Materials in Civil Engineering*, 21(5), 210-216. https://doi.org/10.1061/(ASCE)0899-1561(2009)21:5(210)

Consoli, N.C., Carretta, M.S., Leon, H.B., Schneider, M.E.B., Reginato, N.C., & Carraro, J.A.H. (2019). Behaviour of cement-stabilised silty sands subjected to harsh environmental conditions. *Proceedings of the Institution of Civil Engineers-Geotechnical Engineering*, 173(1), 40-48. https://doi.org/10.1680/jgeen.18.00243

Corp of Engineer. 1994. Soil stabilization for pavement. Washington, DC: *Dept. of the Army,* the Navy, and the Air force.

Diambra, A., Festugato, L., Ibraim, E., Silva, A.P., & Consoli, N.C. (2018). Modelling tensile/compressive strength ratio of artificially cemented clean sand. *Soils and Foundations*, 58(1), 199-211. https://doi.org/10.1016/j.sandf.2017.11.011

DNIT. (2010). Pavimentação - Base de solo-cimento - Especificação de serviço DNIT 143. *DNIT - Departamento Nacional de Infraestrutura de Transportes*, *Rio de Janeiro*, *RJ* (in Portuguese).

Ivanov, V., & Chu, J. (2008). Applications of microorganisms to geotechnical engineering for bioclogging and biocementation of soil in situ. *Reviews in Environmental Science and Biotechnology*, 7(2), 139-153. https://doi.org/10.1007/s11157-007-9126-3

Kezdi, A., & L. Rethati. (1988). Soil mechanics of earthworks, foundations, and highway engineering (volume 3). In *Handbook of Soil Mechanics*. Elsevier.

Kua, T.A., Arulrajah, A., Horpibulsuk, S., Du, Y.J., & Shen, S.L. (2016). *Strength assessment of spent coffee grounds-geopolymer cement utilizing slag and fly ash precursors*. Construction and Building Materials, 115, 565-575. https://doi.org/10.1016/j.conbuildmat.2016.04.021

MolaAbasi, H., Saberian, M., & Li, J. (2019). Prediction of compressive and tensile strengths of zeolite-cemented sand using porosity and composition. *Construction and Building Materials*, 202, 784-795. https://doi.org/10.1016/j.conbuildmat.2019.01.065

Moreira, E.B., Baldovino, J.A., Rose, J.L., & Izzo, R.L.S. (2019a). Effects of porosity, dry unit weight, cement content and void/cement ratio on unconfined compressive strength of roof tile waste-silty soil mixtures. *Journal of Rock Mechanics and Geotechnical Engineering*, 11(2), 369-378. https://doi.org/10.1016/j.jrmge.2018.04.015

Moreira, E.B., Baldovino, J.A., Izzo, R.L.S., & Rose, J.L. (2019b). Impact of sustainable granular materials on the behavior sedimentary silt for road application. *Geotechnical and Geological Engineering*, 38(1), 917-933. https://doi.org/10.1007/s10706-019-01025-6

PCA (1992). *Soil-cement laboratory handbook*. PCA - Portland Cement Association.

Puppala, A.J. (2016). Advances in ground modification with chemical additives: From theory to practice. *Transportation Geotechnics*, 9, 123-138. https://doi.org/10.1016/j.trgeo.2016.08.004

Qi, J., Ma, W., & Song, C. (2008). Influence of freeze-thaw on engineering properties of a silty soil. Cold Regions

Science and Technology, 53(3), 397-404. https://doi.org/10.1016/j.coldregions.2007.05.010

TxDOT Tex-120-E. 2013. Test Procedure for Soil-Cement Testing. *TxDOT - Texas Department of Transportation, Austin*, TX.

List of symbols

D_{50}: the mean particle diameter
D_{10}: the effective size
C_{iv}: the volumetric cement content (expressed in relation to the total specimen volume)
C_c: the coefficient of curvature
C_u: the uniformity coefficient
q_u: the unconfined compressive strength (UCS)
q_t: the splitting tensile strength (STS)
ALM: the accumulated loss of mass
γ_d: the dry unit weight
η: the porosity
ω: the moisture content
μ: the value of a given adjusted porosity/cement
R^2: the coefficient of determination
σ'_c: the preconsolidation pressure of soil
C_v: the coefficient of consolidation of soil
A_q: empirical parameter

Soils and Rocks

An International Journal of Geotechnical and Geoenvironmental Engineering

www.soilsandrocks.com

ISSN 1980-9743
ISSN-e 2675-5475

Constitutive modeling of residual soils based on irreversible strains decomposition

Alessandro Cirone[1,#], Eurípedes Vargas Jr.[1], Tácio de Campos[1]

Article

Keywords
Constitutive relations
Plasticity
Residual soil

Abstract
A constitutive model is proposed for describing the stress-strain behavior of saturated residual soils based on experimental observations from oedometer testing, triaxial and direct shear testing. The model is formulated within the classical theory of plasticity with a non-associated flow rule. In order to reproduce particular features of residual soils, inelastic strains are decomposed in two components, namely the plastic dilation due to the rearrangement of grains and the volumetric collapse resulting from bonds degradation. The yield surface is tear-drop shaped and obeys an isotropic volumetric strain-hardening rule related to collapse strains, along with a shear softening with developing plastic deviatoric strains. Comparison with published experimental data confirms the capability of the model of reproducing observed behavior of tropical residual soils in consolidated drained and undrained triaxial compression.

1. Introduction

The term residual soil is widely used in contrast to *sedimentary (or transported) soil* to designate those soils that do not derive from erosion, transport and deposition of sediments, but result substantially from the in place weathering of the parent rock (Duarte & Rodrigues, 2017). This origin-based definition reflects the importance of lithological characteristics and environmental conditions on the engineering behavior of residual soils, whose description and study cannot be dissociated from the respective weathering history of the parent rock.

Occurring in many regions of Brazil, residual soils may derive from the weathering of granite, gneiss, basalt or sandstone. In southern Brazil residual soils from basalt are dominant (Consoli et al., 1998), whereas weathering profiles of granite-gneiss are commonly encountered around São Paulo and Rio de Janeiro (de Mello, 1972). Martins et al. (2005) have also reported a residual soil originated from the weathering the Aeolian Botucatu sandstone.

The weathering profile reflects the decay of rock towards the residual soil condition. Typical examples from Brazilian literature have been reported by Viana da Fonseca & Coutinho (2008). Ideally, the weathering profile consists of different horizons varying from sound rock, weathered rock to residual soil. If the soil exhibits features from the parent rock, then it is classified as *young residual soil* or *saprolitic soil*. Otherwise, if there is no detectable relic structure, the expression *mature residual soil* is used. On top, one may encounter *lateritic* soils or transported soils (*colluvium*) that may undergo weathering as well. Lateritic soils contains laterite, which is impregnated with, cemented by or partly replaced by hydrated oxides of iron and alluminium (Fookes, 1997). Quite well known by Brazilian engineers, these denominations were further explained by Vargas (1953) and Barata (1969).

Depending on the weathering grade, residual soils may preserve macrostructure inherited from the parent rock (schistosity, fissures, joints, litho-relicts etc.) as well as microstructure (macropores, fabric, bonds between particles). According to Costa Filho et al. (1989), the presence a weakly bonded structure, resulting from predominant chemical weathering, provides to the residual soil:

a) true cohesion in terms of effective stress
b) apparent preconsolidation pressure related to structure and bonds strength
c) higher stiffness at lower stresses and plastic behavior at higher stresses, characterizing a yield surface.

The natural process of weathering influences the composition (clay minerals), grain shape, grain size, void ratio, structure, permeability, strength and deformability of residual soils. Obviously, those features strongly affect the overall engineering behavior of residual soils, as well explained in the general reports provided by Blight (1989)

[#]Corresponding author. E-mail address: acirone@puc-rio.br.
[1]Departamento de Engenharia Civil e Ambiental, Pontifícia Universidade Católica do Rio de Janeiro, Rio de Janeiro, RJ, Brazil.

Submitted on May 15, 2020; Final Acceptance on August 5, 2020; Discussion open until March 31, 2021.
DOI: https://doi.org/10.28927/SR.434647

and Costa Filho et al. (1989). From a mechanical standpoint, weathering is modeled as a softening process (Vaughan & Kwan, 1984).

During the last four decades an extensive laboratory work has been carried out mainly at Rio de Janeiro to study the stress-strain relationships of tropical granite-gneiss residual soils. Testing has been carried out on intact and compacted samples of local lateritic and saprolitic soils, under both saturated and unsaturated conditions. Strong experimental evidences have been produced and some patterns of the geotechnical behavior have been established. The research focused mostly on the geotechnical and geological characterization, analyzing test results according to the conventional principles and methods of soil and rock mechanics. Similar studies have been carried out on residual soils from the São Paulo Metropolitan Area (Futai et al., 2012), North-east of Argentina (Bogado et al., 2019; Francisca & Bogado, 2019), Indonesia and New Zealand (Wesley, 2009) and Hong Kong (Rocchi & Coop, 2015), just to cite a few.

The experimental characterization has been accompanied by the need of developing a modeling framework for predicting the mechanical behavior of residual soils and the response of related geotechnical structures. Various advanced constitutive models have been employed and tested. Some researchers used enhanced versions of Cam Clay, introducing isotropic damage (Puppi et al., 2018), influence of structure (Mendoza et al., 2014) or the subloading surface (Mendoza & Muniz de Farias, 2020). Others (Azevedo et al., 2006) have used the Lade's model (Lade & Kim, 1988; Kim & Lade, 1988) and the discrete element modeling approach (Ibañez, 2008). Unfortunately, most of the aforementioned models were conceived for sedimentary soils and then adjusted to residual soils. In contrast, the authors have developed a constitutive model specifically designed to reproduce the behavior of residual soils starting from experimental observations. The main assumption is the decomposition of irreversible strains into two mechanisms: the particle rearrangement and the bonds degradation. In addition, specific hardening laws have been adopted.

This paper presents the formulation of this new constitutive model within the framework of classical strain hardening plasticity. In doing so, the behavior of saturated residual soils observed from oedometer testing, triaxial and direct shear testing is firstly examined. Then, the constitutive model is formulated and validated in drained and undrained triaxial compression tests.

2. Shear strength and stress-strain behavior of residual soils

For sake of clarity, results of several tests on residual soils are herein summarized to establish patterns of the behaviour observed from oedometer testing, triaxial and direct shear testing.

Figure 1 presents the results of a K_0-test on a partially saturated sample of intact gneissic residual soil carried out by Maccarini (1980, 1987). The sample was obtained from the slope of an excavation at a depth of 8.05 m, measured from the original ground level, where the total vertical in situ stress was estimated to be 130 kPa prior the excavation. The sample was incrementally loaded under stress control allowing drainage from top and bottom against atmospheric pressure.

As shown in Figure 1(a), below a quite pronounced yield stress, σ_{vm}, located around 200-250 kPa, the behavior is stiff and elastic. This first part of the oedometric curve comprises a reloading stage. As the vertical stress is increased, yield occurs, the soil becomes more compressible and the behavior is elastoplastic. This is reflected by the sharp difference of the slopes in the compression curve of Figure 1(a). Figure 1(b) shows that the same trend is clearly followed by the stress path in the (q, p) plane. There is an initial elastic response and stress path draws a straight line up to the yield stress. Further loading deviates the stress path, which gradually approaches the K_0-line of the destructured soil (Leroueil & Vaughan, 1990) as the vertical stress is increased. As shown by Castellanza & Nova (2004), during elastic loading the slope of the stress path is directly linked to Poisson's ratio. Maccarini (1987) measured K_0 as low as 0.1 within the elastic domain, corresponding to a Poisson's ratio of 0.09. At higher stresses, the same author

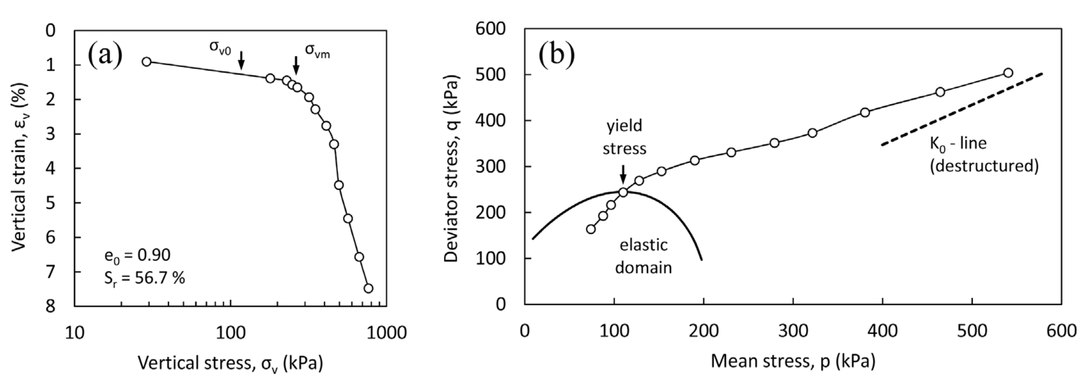

Figure 1. K_0 compression test on gneissic residual soil. Adapted from Maccarini (1980, 1987).

reported values of K_0 6 or 7 times greater, compatible with the destructured soil. It should be noted that Maccarini (1980, 1987) measured K_0 in terms of stress increments, i.e. $K_0 = \Delta\sigma_3/\Delta\sigma_1$, following the definition given by Andrawes and El-Sohby (1973).

Shearing tests on residual soil give plots of the general shape showed in Figure 2, where data from a series of direct shear tests performed by Escalaya (2016) on young granitic residual soil from Duque de Caxias, Rio de Janeiro, are presented. Intact (undisturbed) samples tested in the direct shear apparatus were first sheared in submerged condition to obtain the peak shear strength. Afterwards, the residual strength was determined using the polished cut-plane technique as described by Garga and Seraphim (1975).

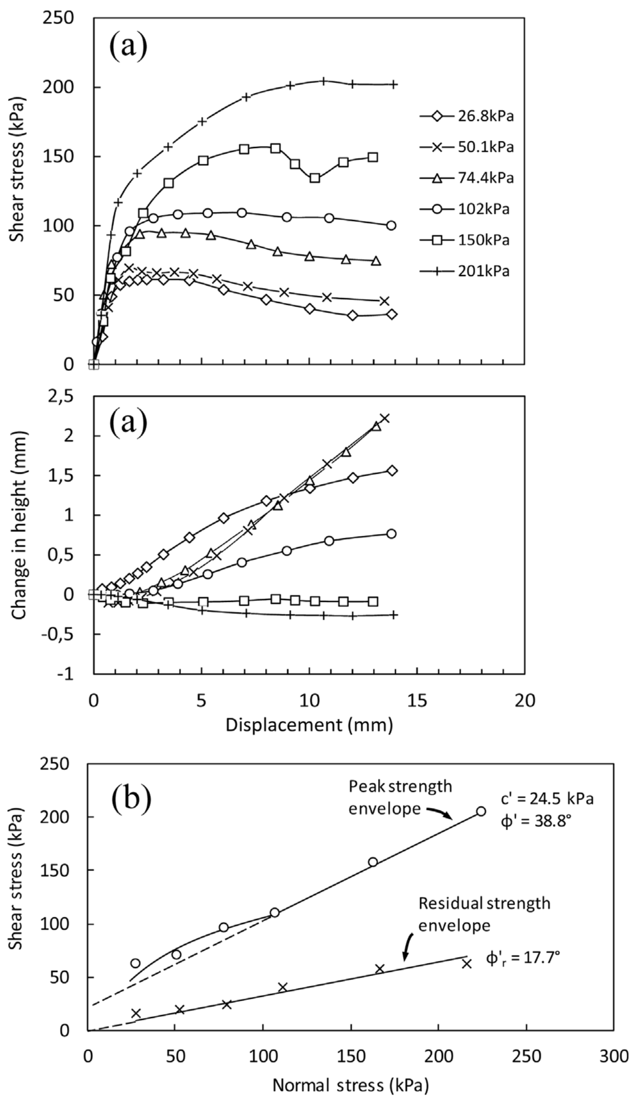

Figure 2. Drained direct shear test on granite saprolitc soil from Duque de Caxias, Rio de Janeiro (after Escalaya, 2016). (a) Stress-displacement curves. (b) Peak and residual strength envelopes.

Results from drained shear tests on residual soil reveal that the shear strength parameters are related to the weathering grade, to the mineralogical content and the macrofabric resulting from weathering of the parent rock (Garga, 1988; Massey et al., 1989; Lacerda, 2010). The behavior is similar to that of a dense sand, yet with less pronounced peak strength at low normal stress. The displacement at failure increases with increasing the applied normal stress and, as shown in Figure 2(a), there is a clear reduction in dilatancy as the normal stress is increased. The gradual loss of strength after peak point is passed may be attributed to a gradual decrease in interlocking and destructuration.

The failure envelopes are shown in Figure 2(b). High mica content in mineralogical composition may explain the significant drop in shear strength between peak and residual condition. The residual shear strength envelope, although passing through the axis origin, is not linear at low vertical stress. At a first approximation, a linear envelope with no cohesion intercept has been assumed in Figure 2(b). The peak strength envelope is markedly curved at lower normal stresses. Adopting a linear strength envelope from tests run at high stresses underestimates the strengths in the low stress range (Brand, 1985). Some authors (Massey et al., 1989; Gan & Fredlund, 1996) attribute this additional strength to dilation and weak bonding derived from weathering. Volume increases which are taking place at failure cause somewhat greater values of shearing strength along the curved portion of the envelope, whereas volume decrease takes place along the straight line portion of the envelope. For the case under consideration, the deviation from a straight line occurs at normal stress of about 100 kPa. This point is often referred as the "critical normal stress" that marks the transition from dilatant to contractant behavior during shear.

Figure 3 shows the result of a set of standard drained triaxial tests performed by De Oliveira (2000) on intact young residual soil derived from biotite-gneiss, collected in Alto Leblon, a neighbourhood in the city of Rio de Janeiro. Specimens were isotropically consolidated to effective stresses of 25, 70 and 150 kPa, and then sheared at constant axial strain rate equal to 8.2×10^{-5} mm/s. It is possible to identify a general trend in the stress-strain behavior under different confining stresses:

a) at low confining pressure, after reaching a well defined peak deviator stress at an axial strain less than 3 %, the specimens exhibits brittle failure associated with dilatant behavior. Softening occurs until a stable deviator stress is reached. Additionally, the lower the confining pressure the more dilatant is the behaviour.

b) at the highest confining pressure, equal to 150 kPa, no peak stress is observed. The stress-strain curve resembles that for an elastic-perfectly plastic material. However, the soil still exhibits the tendency to dilate at failure.

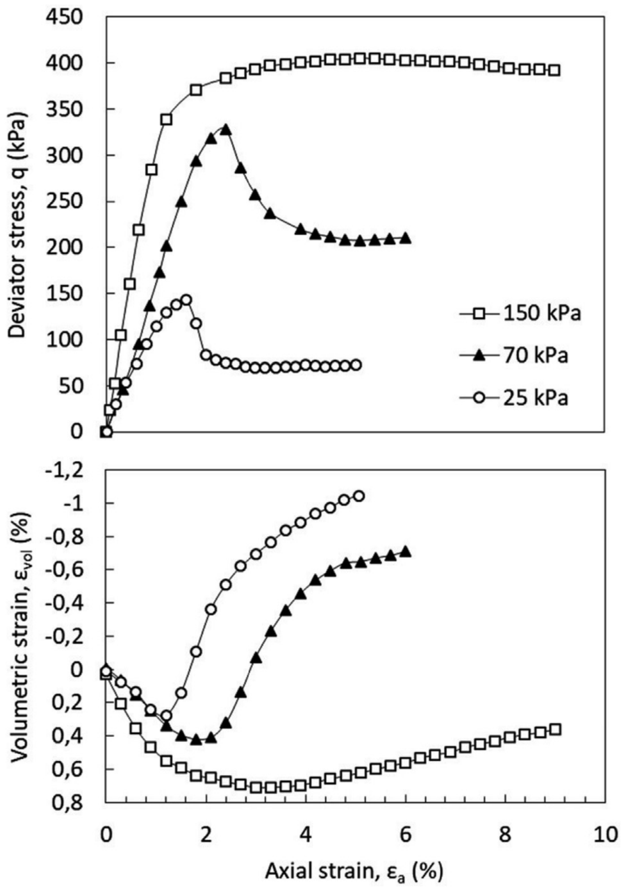

Figure 3. Drained triaxial compression test on intact young residual soil derived from biotite-gneiss. Adapted from De Oliveira (2000).

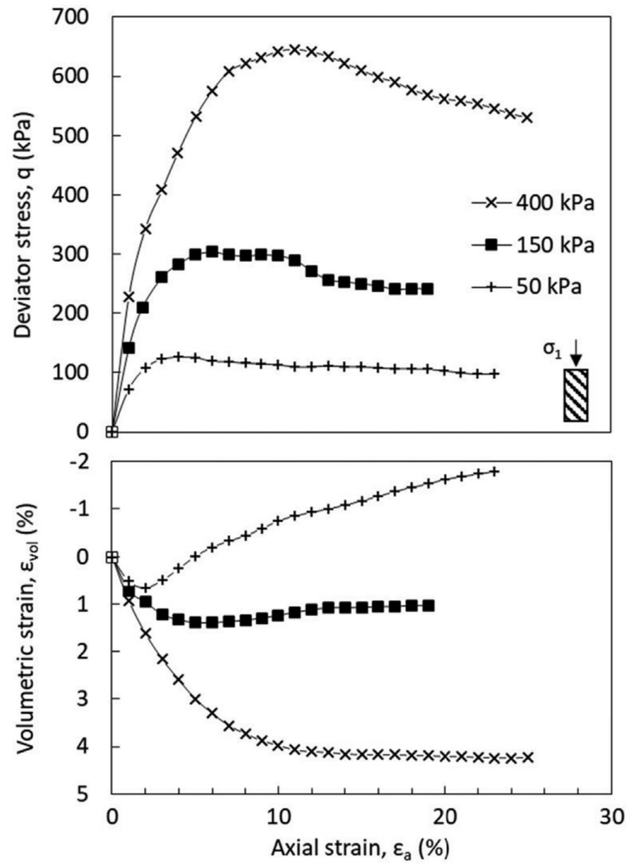

Figure 4. Drained triaxial compression test on young residual soil from gneiss with bands oriented as in the field. Adapted from Reis (2004).

According to De Oliveira (2000), such behavior is typical of soils with bonded structure in the sense described by Leroueil & Vaughan (1990): at low confining stress, peak strength is due to structure, yield is abrupt and the material very brittle; as the confining pressure is increased, the behavior changes from brittle to ductile. De Oliveira (2000) attributed the presence of natural bonding agents between particles to the precipitation of iron oxides between quartz, feldspar and garnet.

Behavior in drained triaxial compression may also follow the trend shown in Figure 4, which is quite different from the one presented in Figure 3. Data are taken from Reis (2004), who tested a gneissic young residual soil from the city of Viçosa, Minas Gerais State, under confining effective stresses ranging from 50 to 400 kPa and obeying the natural banding inclination. The resulting stress-strain curves exhibited less marked peaks and a gradual change from dilatant to contractive behavior with increasing confining stress, which also increased the axial strain at peak. Remarkable was the fact that at the highest confining stress, the soil contracted reaching a peak stress and then it softened at constant volume. This behavior can be explained considering destructuration during the shearing phase, which implies shear strength degradation. Similar results have been presented by Santos et al. (2020), who attributed this kind of behavior to the structure inherited from the parent rock. According to them, the observed peak strength should be attributed to the structural effects, as there is no geological evidence of past overconsolidation in this soil.

Other experimental evidences for the existence of bonded structure in residual soils were given by Consoli et al. (1998). They have shown that prestressing a soil sample produces substantial damage to the bonds, deteriorating its strength and stiffness. According to them, this experimental evidence contrasts with ordinary patterns observed on clay, for which overconsolidation has a positive impact on strength and stiffness.

3. Constitutive model formulation - mathematical treatement of soil behavior

In the proposed model the irreversible strains are decomposed into two parts, namely the strains resulting from the rearrangement of the grains (plastic strains) and those resulting from damage of structure (collapse strains). Therefore, the total strain rate is decomposed into elastic, plastic and collapse components:

$$\dot{\varepsilon}_{ij} = \dot{\varepsilon}_{ij}^{e} + \dot{\varepsilon}_{ij}^{p} + \frac{1}{3}\delta_{ij}\dot{\varepsilon}_{v}^{c} \quad (1)$$

where δ_{ij} is the Kronecker delta. The additive strain decomposition holds under the small strain hypothesis. The elastic strains are, by definition, recoverable and uniquely related to stresses by Hooke's law. Irrecoverable strains are decoupled into those resulting from plastic deformation of the granular matrix, $\dot{\varepsilon}_{ij}^{p}$, and those resulting from volume change due to structure collapse, $\dot{\varepsilon}_{v}^{c}$. Both are calculated according to the classical theory of plasticity by assuming the existence of a yield criterion and a flow rule.

The decomposition of irreversible strains into two parts (plastic collapse strain and plastic expansive strain) is not novel in constitutive modeling. As instance, Lade (1977) used distinct yield surfaces and flow rules to calculate plastic and collapse strains in modeling the behavior of Sacramento River Sand.

Within the framework of modeling the behavior of residual soils, the collapse strains are assumed as the volumetric contraction caused by structure degradation. On the other hand, the plastic strains are associated uniquely to grain rearrangement as described by Chandler (1985).

A suitable stress space to describe the triaxial stress state is (p', q), where $p' = (\sigma'_1 + 2\sigma'_3)/3$ is the effective mean stress and $q = \sigma'_1 - \sigma'_3$ is the deviator stress. The corresponding strain invariants are $\varepsilon_v = \varepsilon_1 + 2\varepsilon_3$, the volumetric strain, and $\varepsilon_d = 2/3*(\varepsilon_1 - \varepsilon_3)$, the deviatoric strain. Furthermore, the ratio between the deviator and effective mean stress, $\eta' = q/p'$, is very useful in calculations and is referred to as the stress ratio. For simplicity, only saturated behavior is considered, being the aim of the model to reproduce the soil response under drained and undrained triaxial compression.

The assumed expression to describe a teardrop shaped yield locus for a residual soil is:

$$f: \left(\frac{p'}{p_0}\right)^2 + \left(\frac{\eta'}{\eta_0}\right)^2 = 1 \quad (2)$$

Figure 5 shows that the model has a single yield function with two portions clearly distinguishable: the compression cap and the shear failure envelope. The transition between the two parts is smooth and occurs at $\eta' = \eta_0/\sqrt{2}$. The parameter p_0 controls the position of the cap, while η_0 is the maximum stress ratio associated to shear failure. They are treated as hardening parameters and both depend on irrecoverable strains.

To develop simple and suitable hardening laws to describe the evolution of the yield surface during loading, the following assumptions are introduced:

1. when soil is loaded under isotropic compression, the irreversible volume strain is only caused by structure collapse. In this sense, the cap hardening depends solely on collapse strains resulting from yielding of soil structure, i.e. $p_0 = p_0(\varepsilon_v^c)$.
2. the shear failure envelope is related to frictional strength and grain rearrangement and, consequently, to plastic strains, i.e. $\eta_0 = \eta_0(\varepsilon_{ij}^p)$.

The dependence on p_0 of the collapse volumetric strain can be derived by assuming convenient expressions for the calculation of total and elastic volumetric strain increments in isotropic loading. The elastic volumetric response associated with changes in mean effective stress may be described by an equation in the form:

$$e = e_k - \kappa \ln p' \quad (3)$$

where e_k is the intercept of the unloading-reloading line at $p = 1$ and κ is its slope in the e - ln p' plot. Equation 3 is a common description of soil elastic behavior and provides the shape of the unloading-reloading lines in the (e, p') plane for stress states within the elastic domain.

For loading beyond the elastic threshold, it is assumed that the reduction in void ratio is directly propor-

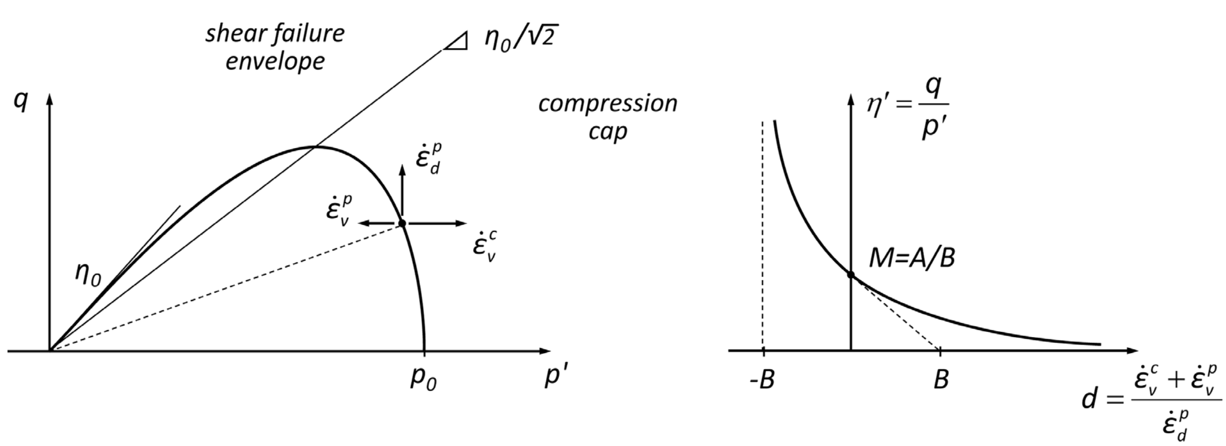

Figure 5. Yield surface, flow vectors and stress-dilatancy relationship.

tional to the void ratio itself and the increase in mean effective stress:

$$de = -\frac{e}{C_b}\,dp' \tag{4}$$

in which a constant of proportionality, C_b, has been introduced. Such constant has the dimension of a stress. It has the role of a stiffness and will be referred herein as the "*compression modulus*". Equation 4 may also be regarded as the constitutive law for hydrostatic compaction. It states that that the compressibility, $\beta = d\varepsilon_v/dp'$, is proportional to the current porosity, $\phi = e/(1 + e)$. Indeed, dividing both sides of Equation 4 by $1 + e$ and recalling that $d\varepsilon_v = -de/(1 + e)$, one obtains:

$$\frac{d\varepsilon_v}{dp'} = \frac{\phi}{C_b} \tag{5}$$

It is worth noting that this result is valid under the hypothesis of incompressible solids ($dV_s = 0$). Equations 4 and 5 are both written in incremental form and are formally identical. Equation 4 can be easily integrated to obtain the equation for the normal compression line:

$$e = e_0 \exp\left(-\frac{p' - p_0}{C_b}\right) \tag{6}$$

that provides a simple description of the shape of the normal compression line, in the (e, p') compression plane, accounting for non-linearity of stress-strain response under applied isotropic compression.

The cap hardening law arises from assumption 1. If plastic volumetric strain are neglected in isotropic compression, then the total volumetric strain resulting from the change in p_0 is just elastic and collapse:

$$d\varepsilon_v = d\varepsilon_v^e + d\varepsilon_v^c \tag{7}$$

recalling Equations 3 and 4, it yields

$$\frac{e}{1+e}\frac{dp_0}{C_b} = \frac{\kappa}{1+e}\frac{dp_0}{p_0} + d\varepsilon_v^c \tag{8}$$

from which the cap hardening law is derived:

$$\frac{dp_0}{d\varepsilon_v^c} = \frac{p_0}{\lambda' - \kappa'} \tag{9}$$

with $\lambda' = \frac{e}{1+e}\frac{dp_0}{C_b}$ and $\kappa' = \frac{\kappa}{1+e}$

where λ' is the slope of the normal compression line and κ' that of the unloading-reloading line in the (ε_v, $\ln p'$) plane. It is worth noting that e, p_0 and, therefore, λ' change as the soil undergoes volumetric deformation.

As introduced in Equation 1, plastic deviatoric strains are assumed to derive from rearrangement of the grains and, thus, are related to grain alignment on a possible slip surface. This latter mechanism is responsible for decreasing the shear strength and will be modeled as an exponential decay of the maximum stress ratio with plastic deviatoric strain:

$$\frac{d\eta_0}{d\varepsilon_d^p} = -B_q(\eta_0 - \eta_r) \tag{10}$$

where B_q is the stress ratio decay rate, η_r is a reference value and η_0 tends asymptotically to it at failure. Equation 10 is the hardening law of the shear failure envelope.

In general, inelastic flow is not normal to the yield surface. This means that the flow rule is non-associated. Plastic strains are derived from a plastic potential, whereas volumetric collapse is derived from a collapse potential. The flow rule is:

$$\begin{aligned}
\dot{\varepsilon}_v^p &= \dot{\lambda}\frac{\partial g}{\partial p'} = -\dot{\lambda}B\eta' \\
\dot{\varepsilon}_d^p &= \dot{\lambda}\frac{\partial g}{\partial q} = \dot{\lambda}\eta' \\
\dot{\varepsilon}_v^c &= \dot{\lambda}\frac{\partial g^c}{\partial p'} = \dot{\lambda}A
\end{aligned} \tag{11}$$

where $\dot{\lambda}$ is the plastic multiplier, η' is the stress ratio, A and B are parameters of the model. Following Chandler (1985), the rate of plastic volumetric change resulting from grains rearrangement is assumed to be proportional to the plastic deviatoric rate by a factor, B, that is a generalization of the angle of dilatancy. In other words, the plastic volumetric strain rate is the expansion necessary for shearing distortion; conversely, the volume collapse is, by definition, the volume contraction due to bonds breakage and mechanical damage. With such a separation, the proposed model has two mechanisms and one criterion (2M1C) according to Chaboche's (2008) classification.

The stress-dilatancy relationship corresponding to Equations 11 is:

$$d = \frac{\dot{\varepsilon}_v^e + \dot{\varepsilon}_v^p}{\dot{\varepsilon}_d^p} = \frac{A - B\eta'}{\eta'} \tag{12}$$

that indicates no irreversible volume change at $\eta' = A/B$, that is the so-called "critical state". Hence, the parameters A and B characterize dilatancy, structure collapse and critical state.

The plastic multiplier, for a given stress increment, is derived according to the consistency condition, $\dot{f} = 0$. From Equation 2, the differential form of the yield function is:

$$\dot{f} = 0 = \frac{\partial f}{\partial p'}\dot{p}' + \frac{\partial f}{\partial q}\dot{q} + \frac{\partial f}{\partial p_0}\dot{p}_0 + \frac{\partial f}{\partial \eta_0}\dot{\eta}_0 \tag{13}$$

which combined with Equations 9, 10 and 11, gives the expression for the plastic multiplier:

$$\dot{\lambda} = \frac{1}{H}\left(\frac{\partial f}{\partial p'}\dot{p}' + \frac{\partial f}{\partial q}\dot{q}\right) \tag{14}$$

where H is the hardening modulus:

$$H = -\left(\frac{\partial f}{\partial p_0}\frac{\partial p_0}{\partial \varepsilon_v^c}\frac{\partial g^c}{\partial p'} + \frac{\partial f}{\partial \eta_0}\frac{\partial \eta_0}{\partial \varepsilon_d^p}\frac{\partial g}{\partial q}\right) \tag{15}$$

The overall value of H depends on two competing terms, each one related to a different mechanism: the first term is linked to volumetric collapse, the second to deviatoric plastic strains.

4. Summary of model parameters - their physical meaning and experimental determination

4.1 Elastic constants

The parameter κ, the so-called "swelling index", coincides with the slope of the unloading-reloading line in the (e, ln p') plot. It can be determined with an isotropic compression test performing unloading-reloading cycles.

The Poisson's ratio relates the bulk modulus, K, with the shear modulus, G, according to the following expression:

$$\frac{G}{K} = \frac{3(1-2\nu)}{2(1+\nu)} \tag{16}$$

The ratio G/K coincides with the gradient of the volume change curve for a conventional drained compression test (Wood, 1990) if the confining pressure is below the in-situ preconsolidation pressure.

4.2 Inelastic flow

The parameters A and B control the inelastic flow. They can be determined using the expression for the stress-dilatancy relationship given in Equation 12. Figure 6 shows the dilatancy ratio ($d\varepsilon_{vol}/d\varepsilon_{dev}$) obtained from drained triaxial compression tests under different confining stresses plotted against the stress ratio (q/p'). Data points were derived from total strain increments. For this reason, the initial branch of the stress-dilatancy curve is strongly affected by elastic strains and is not recommended for calibration. Data points taken from the final branch should be favored because they lies on (or are closer to) the critical state. The intercept with the vertical axis corresponds to $M = A/B$ = 1.32, denoting the critical state. In the present analysis, B was taken equal to M, giving a satisfactory description of the stress-dilatancy relationship. The value of parameter A is the result of the estimation of M and B. Therefore, the selected values are of A = 1.74 and B = 1.32.

The influence of the parameters A and B on the predicted response for a drained triaxial test is shown in Figure 7. The results can be summarized as follows. Increasing B shifts the volume change curve upwards, so greater volume dilation is predicted. Higher and sharper peaks also occur in the stress-strain curve. Conversely, lowering B increases the volume contraction and reduces the peak strength. Since calculations were made with constant M, the ultimate strength is not affected.

4.3 Volumetric hardening

The volumetric hardening law is calibrated by means of an isotropic compression test. Taking logarithms of both sides in Equation 6, a linear relationship is predicted between the mean effective stress and the logarithm of void ratio:

$$p' = p_0 - C_b \ln\left(\frac{e}{e_0}\right) \tag{17}$$

Therefore, the compression modulus, C_b, equals the slope of the straight line obtained from experimental data if ln e is plotted against p', as indicated in Figure 8.

The estimation of the preconsolidation pressure should not follow conventional graphical methods, such as the Casagrande's method. Several authors (Vargas, 1953; Vaughan et al., 1988; Wesley, 1990) questioned the validity of those "conventional" approaches arguing that they were not conceived for residual soils, for which the common definition of "preconsolidation" pressure should not be applied because they do not undergo loading-unloading processes in their formation.

Imposing the continuity of the gradient along the compression curve may be an alternative method to estimate the preconsolidation pressure. If it is assumed that at elastic threshold the unloading-reloading line and the normal compression line have the same slope, one obtains:

$$\frac{\kappa}{p_0} = \frac{e_0}{C_b} \tag{18}$$

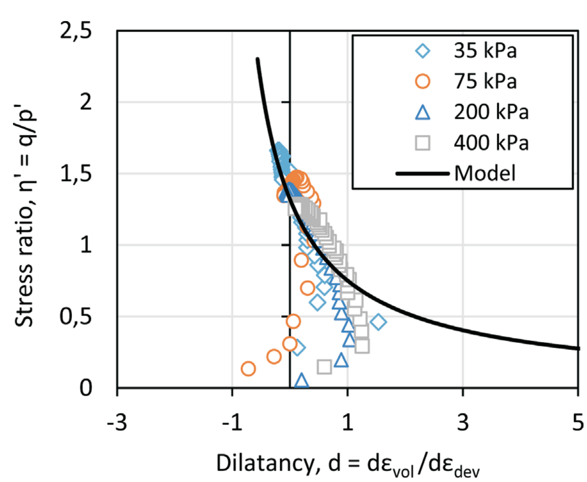

Figure 6. Determination of model parameters A = 1.74 and B = 1.32 from the stress-dilatancy relationship of Ouro Preto residual soil.

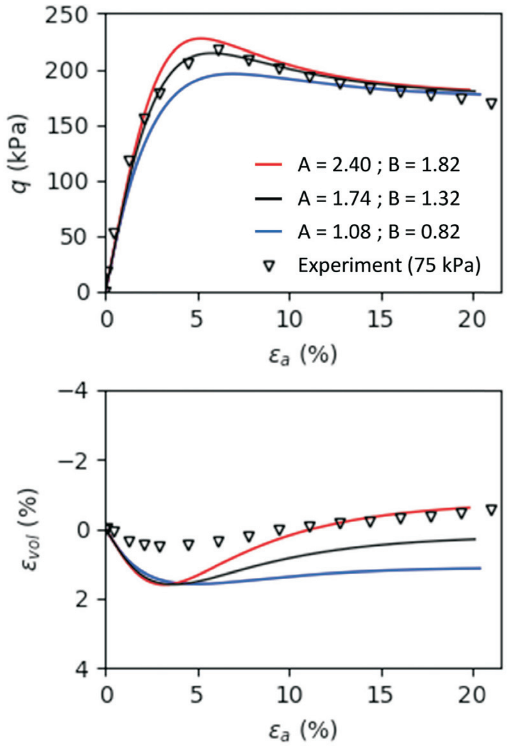

Figure 7. Effect of parametric variation on comparison of model simulations and experimental results for drained triaxial compression under 75 kPa of confining pressure.

from which the in-situ p_0 is easily found, known the swelling index, κ, the in-situ void ratio, e_0, and the compression modulus C_b.

4.4 Deviatoric softening

The softening rule is a function of plastic deviatoric strains and is calibrated along the post-peak portion of the stress-strain curve for a drained triaxial compression test conducted at low confining pressure.

From Equation 10, it is clear that the relationship between ln(η' - M) and ε_d^p is linear, being the parameter B_q equal to the slope of straight line that best fits the experimental data. The diagram of Figure 9 is obtained using data taken from post-peak branch of the stress-strain curves of the drained triaxial compression tests conducted at low confining pressures. Results clearly suggest that B_q depends on the effective confining stress. However, for simplicity, B_q is taken as constant and equal to the average of the slopes.

A general indication of the influence of the value of B_q on the response in the conventional drained triaxial compression test is shown in Figure 10. Increasing B_q increases the rate of deviatoric softening, so the stress-strain relationship shows a lower peak strength and the critical state is quickly reached. On the other hand, when B_q is small, a more ductile behavior is predicted and the model shows higher shear strength. Moreover, the model needs larger deformations to reach the critical state, the volumetric response is strongly affected and the behavior is much more dilative.

5. Model predictions and comparison with experimental results

The model has been employed for predicting the triaxial behavior of Ouro Preto residual soil in drained and undrained conditions. The experimental data have been provided by Futai (2002), who performed isotropic consolidation, consolidated-drained and undrained triaxial compression tests at different cell pressures. Futai et al. (2004) described the testing procedure in detail. The measured stress-strain curves, strain paths and pore pressures responses are presented in the following along with predictions from the present model.

The value of the parameters for Ouro Preto residual soil have been determined from consolidated-drained triaxial compression tests. They are listed in Table 1. A python

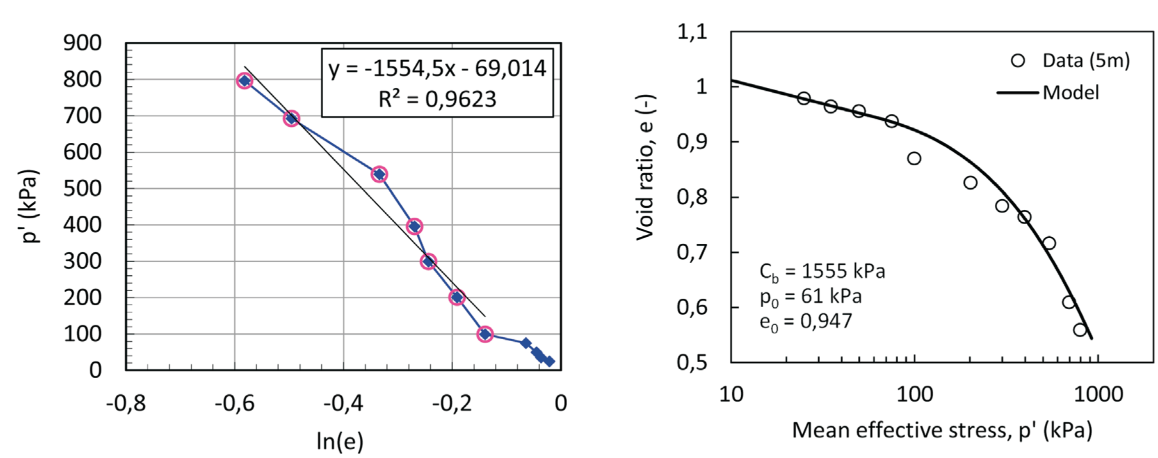

Figure 8. Calibration of compression modulus and comparison with experimental results for Ouro Preto residual soil. Data points are taken from triaxial experiments at the end of isotropic consolidation stage.

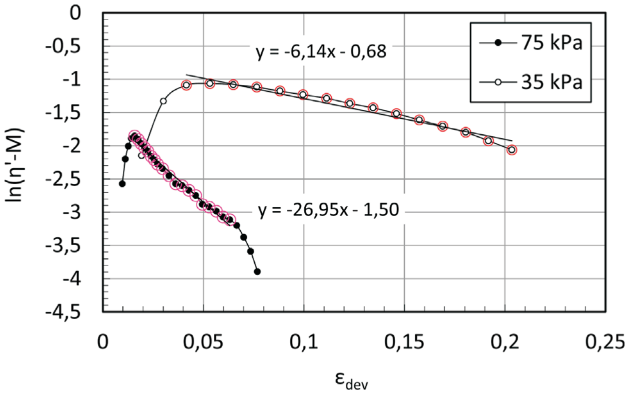

Figure 9. Calibration of softening rule with post-peak reponses from drained triaxial tests conducted at low confining pressures.

Table 1. Summary of parameter values for Ouro Preto residual soil.

Model component	Parameters
Elastic behavior	$\kappa' = 0.018$
	$\nu' = 0.15$
Hardening parameters	$p_0 = 61$ kPa
	$\eta_0 = 1.9$
Inelastic flow	$A = 1.74$
	$B = 1.32$
Hardening/softening law	$C_b = 1555$ kPa
	$e_0 = 0.947$
	$B_q = 16.5$

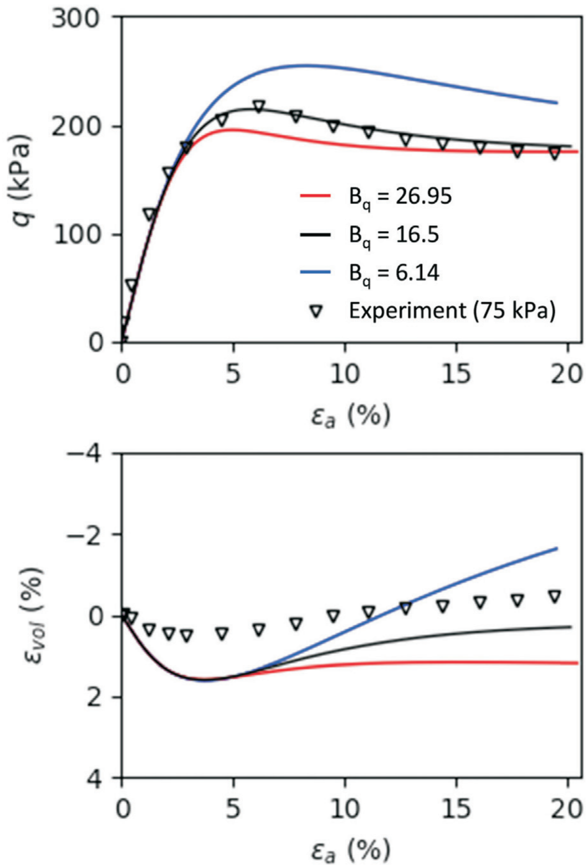

Figure 10. Effect of parametric variation on comparison of model simulations and experimental results for drained triaxial compression under 75 kPa of confining pressure.

code was developed to integrate the constitutive relations using a semi-implicit algorithm.

The results of the drained triaxial tests are shown in Figure 11(a), together with the predictions of the model. Points indicate the measured soil behavior and solid lines are model predictions. The comparison shows a good agreement between the predicted behavior and the experimental observations. The model is able to predict satisfactorily the stress-strain curves, including the gradual change from dilative to contractive behavior, accompanied by a more ductile response, when confining stress is increased. However, the model overpredicts the volume contraction in the beginning of the loading; a drawback attributable to the chosen flow rule, which is very basic.

The results of the consolidated undrained triaxial compression tests are compared with the predictions in Figure 11(b). The predicted response is less accurate, but still good. Although the model parameters were calibrated from the results of the drained triaxial tests, the model reflects the particular trend in the undrained behavior, especially for the stress paths (Figure 12) and the pore-pressure response, which are reasonably predicted. The response switches from initially contractive (increasing pore pressure, decreasing mean effective stress) to dilative (reducing pore pressure, increasing mean effective stress). The rearrangement mechanism is predominant at low confining stress and high stress ratio, so negative pore pressure are consistently predicted for the tests run at 25 kPa and 100 kPa. At higher confining pressures, the dilatancy is suppressed and positive pore pressures are developed. One negative outcome is the stiffer response of the model compared with the test run at 400 kPa of confining pressure.

6. Conclusion

A summary of relevant Brazilian experimental work was presented, involving the main geotechnical laboratory tests, in order to address typical patterns of the mechanical behavior of residual soils. The data were used to develop a constitutive model for residual soils based on the assumption that incremental strains consist of elastic, plastic and collapse components. Decomposition of inelastic strains allowed to distinguish the deformations arising from particle rearrangement from those resulting from bonds degradation and particle breakdown. A non-associated flow rule was assumed by adopting two distinct

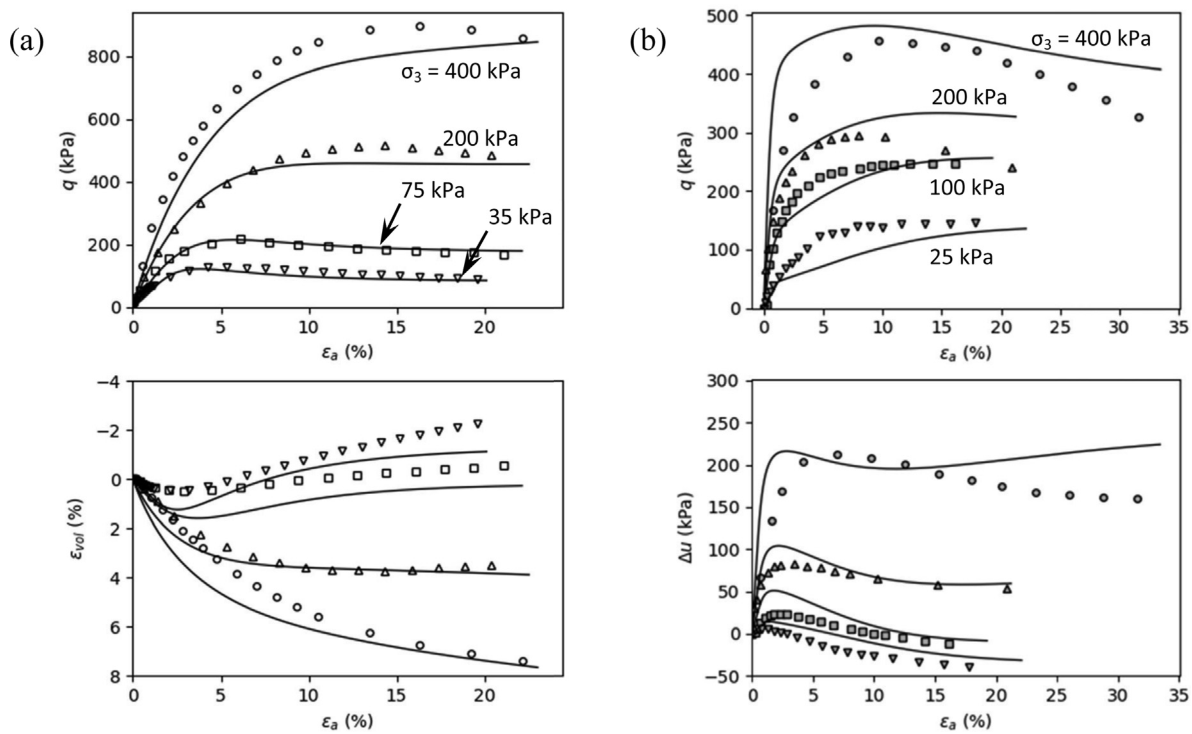

Figure 11. Comparison between experimental data from Futai et al. (2004) and model simulations for Ouro Preto residual soil. (a) Consolidated drained triaxial compression tests. (b) Consolidated undrained triaxial compression tests.

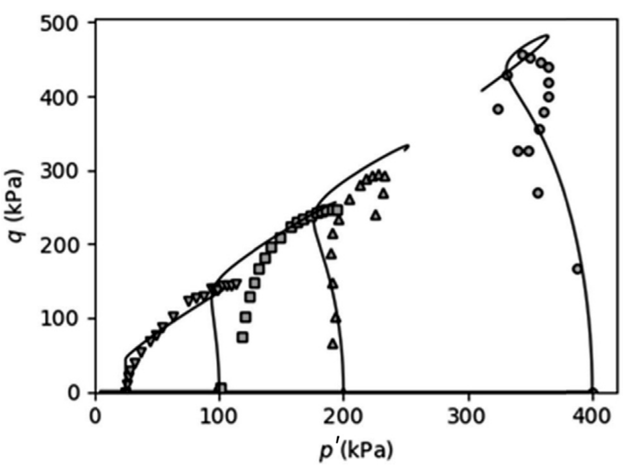

Figure 12. Comparison of measured and predicted effective stress paths for consolidated undrained triaxial compression tests on Ouro Preto residual soil.

potential functions, from which each individual inelastic strain was derived. The yield surface, a single continuous function shaped as a teardrop, was expressed in terms of two stress invariants - the mean effective stress and the stress ratio. The hardening laws were developed in order to reproduce the non-linear volumetric response in the (e, ln p') plane, under purely isotropic compression, and the softening behaviour associated with shearing strains. The model is characterized by nine parameters that can be determined from simple laboratory tests, such as isotropic compression and conventional consolidated drained triaxial compression tests.

The novel feature of the model is the treatment of bond degradation as a strain-inducing process causing primarily volume contraction. Loss of interlocking is modeled as a softening process related to the particle alignment along a slip plane. The description of those two mechanisms is unified under a single yield criterion. Such an approach is pioneer and some generalizations are still under development.

The model may be enhanced to account for some aspects of the engineering behavior of residual soils that were not included in this work. Possible improvements are: extension to partially saturated states, elastic stiffness degradation with mechanical damage, influence of the third stress invariant, addition of a true cohesion and modeling the anisotropic behavior due to structural discontinuities inherited from the parent rock. In addition, the model should also be tested under loading paths that are more complex than conventional CID and CIU triaxial tests.

The comparison made between published experimental behavior and model predictions is overall acceptable and encouraging. The model was validated in conventional triaxial drained and undrained compression tests by comparing the predicted and observed behavior of Ouro Preto residual soil. In particular, trends in stress-strain, dilatancy and pore pressure behavior, as well as the effective stress paths were reasonably captured under a wide range of confining stresses.

Acknowledgments

This study was financed in part by the Coordenação de Aperfeiçoamento de Pessoal de Nível Superior - Brasil (CAPES) - Finance Code 001.

References

Andrawes, K.Z., & El-Sohby, M.A. (1973). Factors affecting coefficient of earth pressure Ko. *Journal of Soil Mechanics and Foundation Engineering Division*, 99 (SM7), 527-539.

Azevedo, R.F., Reis, R.M., & Vilar, O.M. (2006). Elastoplastic modeling of a young gneiss residual soil in saturated and non-saturated conditions. *Proc. 4th Int. Conference Unsaturated Soils*, *Carefree*. ASCE, 1968-1979.

Barata, F.E. (1969). Landslides in the tropical region of Rio de Janeiro. *Proc. 7th Int. Confer. on Soil Mech. and Found. Engng.*, *Mexico City*. ISSMFE, 507-516.

Blight, G.E. (1989) Design assessment of saprolites and laterites. *Proc. 12th Int. Confer. on Soil Mech. and Found. Engng., Rio de Janeiro*. Vol. 4, Pub. Commit. XII ICSMFE, 2477-2484.

Bogado, G.O., Reinert, H.O., & Francisca, F.M. (2019). Geotechnical properties of residual soils from the North-east of Argentina. *International Journal of Geotechnical Engineering*, 13(2), 112-121. https://doi.org/10.1080/19386362.2017.1326682

Brand, E.W. (1985) Predicting the performance of residual soil slopes. *Proc. 11th Int. Confer. on Soil Mech. and Found. Engng.*, *San Francisco*, Vol. 5, Pub. Commit. XI ICSMFE, 2541-2578.

Castellanza, R., & Nova, R. (2004). Oedometric tests on artificially weathered carbonatic soft rocks. *Journal of Geotechnical and Geoenvironmental Engineering*, 130(7), 728-739. https://doi.org/10.1061/(ASCE)1090-0241(2004)130:7(728)

Chaboche, J.L. (2008). A review of some plasticity and viscoplasticity constitutive theories. *International Journal of Plasticity*, 24(10), 1642-1693. https://doi.org/10.1016/j.ijplas.2008.03.009

Chandler, H.W. (1985). A plasticity theory without Drucker's postulate, suitable for granular materials. *Journal of the Mechanics and Physics of Solids*, 33(3), 215-226. https://doi.org/10.1016/0022-5096(85)90012-2

Consoli, N.C., Schnaid, F., & Milititsky, J. (1998). Interpretation of plate load tests on residual soil site. *Journal of Geotechnical and Geoenvironmental Engineering*, 124(9), 857-867. https://doi.org/10.1061/(ASCE)1090-0241(1998)124:9(857)

Costa Filho, L.M., Doebereiner, L., Campos, T.M.P., & Vargas, E. (1989). Fabric and engineering properties of saprolites and laterites. *Proc. 12th Int. Confer. on Soil Mech. and Found. Engng., Rio de Janeiro*. Vol. 4, Pub. Commit. XII ICSMFE, 2463-2476.

Mello, V.F.B. (1972). Thoughts on soil engineering applicable to residual soils. *Proc. 3rd Southeast Asian Conference on Soil Engineering*, *Hong Kong*, Southeast Asian Soc. Soil Engng., 5-34.

Oliveira, C.P. (2000). *Study on the stress-strain-strengh behaviour of a saturated biotite-gnaisse residual soil* [Master's dissertation, Pontifical Catholic University of Rio de Janeiro]. Pontifical Catholic University of Rio de Janeiro's repository (in Portuguese). https://doi.org/10.17771/PUCRio.acad.1788

Duarte I.M.R., & Rodrigues C.M.G. (2017) Residual Soils. In *Encyclopedia of Engineering Geology - Encyclopedia of Earth Sciences Series* (pp. 751-752). Springer.

Escalaya, M.R.A. (2016). *Evaluation of the effect of porepressure increase on the strength characteristics of three tropical soils* [Doctoral thesis, Pontifical Catholic University of Rio de Janeiro]. Pontifical Catholic University of Rio de Janeiro's repository (in Portuguese). https://doi.org/10.17771/PUCRio.acad.30293

Fookes, P.G. (1997). *Tropical Residual Soils: A Geological Society Engineering Group Working Party Revised Report*. Geological Society of London.

Francisca, F.M., & Bogado, G.O. (2019). Weathering effect on the small strains elastic properties of a residual soil. *Geotechnical and Geological Engineering*, 37(5), 4031-4041. https://doi.org/10.1007/s10706-019-00891-4

Futai, M.M. (2002). *Theoretical and experimental study of unsaturated tropical soil behavior: Applied a gully case* [Doctoral thesis, Federal University of Rio de Janeiro]. Federal University of Rio de Janeiro's repository (in Portuguese). http://www.coc.ufrj.br/pt/teses-de-doutorado/146-2002/925-marcos-massao-futai

Futai, M.M, Almeida, M.S.S., & Lacerda, W.A. (2004). Yield, strength and critical state conditions of a tropical saturated soil. *Journal of Geotechnical and Geoenvironmental Engineering*, 130(11), 1169-1179. https://doi.org/10.1061/(ASCE)1090-0241(2004)130:11(1169)

Futai, M.M., Cecilio, M.O., & Abramento, M. (2012). Shear strength and deformability of residual soils from the Sao Paulo metropolitan area. In *Twin Cities - Soils from Sao Paulo and Curitiba Metropolitan Areas* (pp. 155-188), D'Livros.

Gan, J.K., & Fredlund, D.G. (1996). Shear strength characteristics of two saprolitic soils. *Canadian Geotechnical Journal*, 33(4), 595-609. https://doi.org/10.1139/t96-085-307

Garga, V.K. (1988). Effect of sample size on shear strength of basaltic residual soils. *Canadian Geotechnical Journal*, 25(3), 478-487. https://doi.org/10.1139/t88-053

Garga, V.K., & Seraphim, L.A. (1975). A note on some observations on a migmatitic residual soil from Rio de Janeiro. *Soils and Foundations*, 15(4), 1-11. https://doi.org/10.3208/sandf1972.15.4_1

Ibañez, J.P. (2008). *Discrete micro-micromechanical modeling of residual soils* [Doctoral thesis, Pontifical Catholic University of Rio de Janeiro]. Pontifical Catholic University of Rio de Janeiro's repository (in Portuguese). https://doi.org/10.17771/PUCRio.acad.11888

Kim, M.K., & Lade, P.V. (1988). Single hardening constitutive model for frictional materials: I. Plastic potential function. *Computers and Geotechnics*, 5(4), 307-324. https://doi.org/10.1016/0266-352X(88)90009-2

Lacerda, W.A. (2010). Shear strength of soils derived from the weathering of granite and gneiss in Brazil. In *Weathering as a Predisposing Factor to Slope Movements* (pp. 167-182). Geological Society of London. https://doi.org/10.1144/EGSP23

Lade, P.V. (1977). Elasto-plastic stress-strain theory for cohesionless soil with curved yield surfaces. *International Journal of Solids and Structures*, 13(11), 1019-1035. https://doi.org/10.1016/0020-7683(77)90073-7

Lade, P.V., & Kim, M.K. (1988). Single hardening constitutive model for frictional materials II. Yield critirion and plastic work contours. *Computers and Geotechnics*, 6(1), 13-29. https://doi.org/10.1016/0266-352X(88)90053-5

Leroueil, S., & Vaughan, P.R. (1990). The general and congruent effects of structure in natural soils and weak rocks. *Géotechnique*, 40(3), 467-488. https://doi.org/10.1680/geot.1990.40.3.467

Maccarini, M. (1980). *Ensaios triaxiais e cisalhamentos direto de um solo residual jovem, derivado de gneisse* [Master's dissertation]. Pontifical Catholic University of Rio de Janeiro (in Portuguese).

Maccarini, M. (1987). *Laboratory Studies of a weakly bonded artificial soil* [Doctoral thesis, Imperial College London]. Imperial College London's repository. http://hdl.handle.net/10044/1/8129

Martins, F.B., Ferreira, P.M.V., Flores, J.A.A., Bressani, L.A., & Bica, A.V.D. (2005). Interaction between geological and geotechnical investigations of a sandstone residual soil. *Engineering Geology*, 78(1-2), 1-9. https://doi.org/10.1016/j.enggeo.2004.10.003

Massey, J.B., Irfan, T.Y. & Cipullo, A. (1989). The characterization of granitic saprolitic soils. *Proc. 12th International Conference on Soil Mechanics and Foundation Engineering, Rio de Janeiro*. Vol. 6, Publications Committee of XII ICSMFE, 533-542.

Mendoza, C., Farias, M., & Cunha, R.P. (2014). Validación de modelos constitutivos avanzados de comportamiento mecánico para la arcilla estructurada de Brasilia. *Obras y Proyectos*, 15, 52-70. http://dx.doi.org/10.4067/S0718-28132014000100005

Mendoza, C., & Farias, M. (2020). Critical state model for structured soil. *Journal of Rock Mechanics and Geotechnical Engineering*, 12(3), 630-641. https://doi.org/10.1016/j.jrmge.2019.12.006

Puppi, R.F.K., Hecke, M.B., & Romanel, C. (2018). MCC Hyperplastic constitutive model with coupled damage applied to structured soils. *Geotecnia*, 142, 35-61 (in Portuguese). http://dx.doi.org/10.24849/j.geot.2018.142.02

Reis, R.M. (2004) *Stress-strain behavior of two horizons of a residual soil from gneiss* [Doctoral thesis, University of São Paulo]. University of São Paulo's repository (in Portuguese). https://www.teses.usp.br/teses/disponiveis/18/18132/tde-06112006-163715/en.php

Rocchi, I., & Coop, M.R. (2015). The effects of weathering on the physical and mechanical properties of a granitic saprolite. *Géotechnique*, 65(6), 482-493. https://doi.org/10.1680/geot.14.P.177

Santos, O.F., Lacerda, W.A., & Ehrlich, M. (2020). Effects of cyclic variations of pore pressure on the behaviour of a gneiss residual soil. *Geotechnical and Geological Engineering*, 38, 5201-5212. https://doi.org/10.1007/s10706-020-01356-9

Vargas, M. (1953). Some engineering properties of residual clay softs occuring in Southern Brazil, *Proc. 3rd International Conference on Soil Mechanics and Foundation Engineering, Zurich*. Vol. 1, Publications Committee of III ICSMFE, 67-71.

Vaughan, P.R., & Kwan, C.W. (1984). Weathering, structure and in situ stress in residual soils. *Géotechnique*, 34(1), 43-59.

Vaughan, P.R., Maccarini, M., & Mokhtar, S.M. (1988). Indexing the engineering properties of residual soil. *Quarterly Journal of Engineering Geology and Hydrogeology*, 21(1), 69-84.

Viana da Fonseca, A., & Coutnho, R.Q. (2008). Characterization of residual soils. *Proc. 3rd International Conference Site Characterization*, *Taipei*. Vol. 1, Taylor & Francis, 195-248.

Wesley, L.D. (1990). Influence of structure and composition on residual soils. *Journal of Geotechnical Engineering*, 116(4), 589-603. https://doi.org/10.1061/(ASCE)0733-9410(1990)116:4(589)

Wesley, L. (2009). Behaviour and geotechnical properties of residual soils and allophane clays. *Obras y proyectos*, 6, 5-10.

Wood, D.M. (1990). *Soil Behaviour and Critical State Soil Mechanics*. Cambridge University Press.

Technical Notes

Soils and Rocks
An International Journal of Geotechnical and Geoenvironmental Engineering
www.soilsandrocks.com
ISSN 1980-9743
ISSN-e 2675-5475

Determination of liquid limit by the Fall Cone method

C.W. Clemente[1,3,#], V.P. Faro[1], M.P.H. Moncada[2]

Note

Keywords
Atterberg limits
Casagrande
Consistency
Fall Cone

Abstract

The knowledge of soil characterization parameters allows identification and classification of materials. Also, indicates the soil behavior in front of stress and deformation. The aim of this paper was to evaluate the methods available for determining the liquid limit by the Casagrande device and Fall Cone equipment. The classic method of Casagrande was developed by Arthur Casagrande in 1932 and the Swedish Fall Cone was developed by Geotechnical Commission of the Swedish State Railways in 1915. To guarantee the representativeness of the evaluation, 31 Brazilian soil samples from different origins were tested (marine, residual, colluvium and tailings). In order to understand the behavior of the samples and evaluate the applicability of the Swedish Fall Cone method were determined other geotechnical properties as a percentage of fines, specific gravity and plastic limit. The results show that the values obtained with the Casagrande method are slightly lower than with the Fall Cone equipment. It was observed a coherent correlation between the methods for liquid limits values less than 80 % with a corresponding coefficient of determination R^2 of 0,9453. Above this moisture content, it was not possible to verify any correlations between the methods applied.

1. Introduction

For a long time, geotechnical engineering was based on past experiences through a succession of experiments without any real scientific definition. Concerns about soils study and its properties began in the mid-eighteenth century when problems of foundation in older constructions emerged, as is the case of the famous Tower of Pisa in Italy (Das, 2012). The knowledge of soils consistency is relevant, because demonstrate the soil behavior before stress and deformation, influencing on soil penetration resistance and compaction and affecting hydraulic conductivity.

Plasticity is a property of soils that consists of the ability of the soils to be or not molded, under a certain moisture condition, without volume variation. The plastic properties of a soil depend on the water content, the form of the particles and its chemical and mineralogical composition (Lambe & Whitman, 1969).

In 1908, Albert Atterberg published research with the first result about soil plasticity and its several moisture contents and in 1911, explained cohesive soils consistency defining liquid limit, plastic limit and contraction limit. Arthur Casagrande, in 1932, deepened his research on Atterberg's papers and developed the liquid limit device, used until today in laboratories.

The Swedish Fall Cone method was developed between 1914 and 1922 as a fast, simple and accurate method to determine the undrained shear strength, sensitivity of clays and liquid limit, which has encouraged several countries to choose it as a standardized equipment (Karlsson, 1981). The variation of the method between the countries is given by the type of cone applied with different masses and opening angles. The use of the cone to determine liquid limit had the objective of reducing the influence of factors that negatively affected the results obtained with the Casagrande method (Spagnoli, 2012).

Several studies have been made comparing the Fall Cone equipment and the Casagrande apparatus (*e.g.*, Garneau & Le Bihan, 1977; Leroueil & Le Bihan, 1996; Nini, 2014; Spagnoli, 2012; Wood, 1982). However, there is no single standardized test, as there are several methods for estimating a liquid limit with the Fall Cone.

[#]Corresponding author. E-mail address: camilawclemente@yahoo.com.br.
[1]Programa de Pós Graduação em Engenharia Civil, Universidade Federal do Paraná, Curitiba, PR, Brazil.
[2]Departamento de Engenharia de Recursos Hídricos e Meio Ambiente, Universidade Federal Fluminense, Niterói, RJ, Brazil.
[3]Fugro, Pinhais, PR, Brazil.

Submitted on January 19, 2020; Final Acceptance on June 27, 2020; Discussion open until March 31, 2021.
DOI: https://doi.org/10.28927/SR.434661

The aim of this paper is to demonstrate that Swedish Fall Cone can be an alternative method to determine liquid limit, being a practical, fast and with less interferences of the operator in the procedure when compared with the determination by Casagrande apparatus. To evaluate the validity of the liquid limit determination using the Swedish Fall Cone method in this article, the liquid limit of samples was determined using this method and comparing the obtained values and dispersion associated with each determination for Casagrande method. It was intended to indicate the differences between one method and another in order to correlate the methods and it was evaluated if the results obtained with the Swedish Fall Cone are consistent when compared with the Casagrande method.

2. Materials and methods

In order to achieve a greater coverage in the results of the present article, it was select samples from different locations in Brazil (state of Rio de Janeiro, Amapá, Pará and Minas Gerais) and with various geotechnical characteristics (marine, residual, colluvium and tailings), totaling 31 samples.

Soil characterization tests are in general simple tests and relatively fast with international validity and few variations between the methods used in the different countries. These tests have major importance in the study of soils, since they are the beginning in the identification of the material and its later classification, providing important data in the determination of the engineering characteristics of the sample. In the present study were performed the traditional characterization tests (grain size distribution, specific gravity and Atterberg limits) to gain an understanding of the soil properties. All the characterization tests were performed according the Brazilian standards recommendations.

The Casagrande apparatus is composed of a brass shell and a rigid rubber base. This brass shell is struck at the base by a crank. The procedure and apparatus are specified in the Brazilian standard ABNT NBR 6459 (ABNT, 1984). The liquid limit devices specified at the Brazilian, American ASTM D 4318 (ASTM, 2017) and British BS 1377-2 (BSI, 1990) Standards are similar, but there are variations at the details. The American and Brazilian devices have a rubber base, different from the device of the BS proposal (Head, 2006). Therefore, the tests result from the three type of devices may not be well matched. The procedures established by the standards are similar.

The execution of the test begins with the preparation of the sample, in order to obtain a homogeneous paste. Part of the mixture is transferred to the shell of the equipment, molding so that the central region has a thickness of the order of 10 millimeters. With a chisel, a groove opens in its central part, dividing the soil mass into two parts. The consistency of this first paste should close the groove with about 25 blows. The closure occurs at a distance of approximately 12.7 millimeters along the base of the groove. In the graphical representation of the test, the values of moisture content are plotted in the axis of ordinates in arithmetic scale and the number of strokes in the abscissa axis in logarithmic scale. The liquid limit corresponds to the moisture content equivalent to 25 blows.

The equipment of the Swedish Cone consists of a metal cone of a certain mass with a certain angle suspended vertically only with the tip of the cone touching the surface of the sample. When released, the cone falls freely by its own weight on the soil sample, so the final depth of penetration is measured. The equipment is represented in the Figure 1.

In the research presented here, it was worked with the Swedish standard definition SS 027120 (SSC, 1990) and Karlsson's recommendations (Karlsson, 1981) considering that the liquid limit is defined as the moisture content in which a cone with opening angle of 60° and mass of 60 g penetrates 10 mm in the soil. Unlike the Casagrande apparatus, there is no single procedure and equipment for Fall Cone, there are variations in weight and dimensions depending on the standard consulted. For instance, the British Cone standardized by British Standard BS 1377 (BSI, 1990) has a weight of 80 g and an opening angle of 30°, the liquid limit is determined at a 20 mm penetration. The Chinese Cone uses a penetration of 17 mm, it has a weight of 76 g and opening angle of 30°. There is no Brazilian standard available to regulate the liquid limit test using the Cone yet, but some studies have been made by Silveira (2001) and Queiroz de Carvalho (1986).

Figure 1. Fall Cone, 2015.

For the graphical representation, a graph is constructed with the values of moisture content in the axis of the ordinates and the values of the penetration in millimeters in the abscissa axis, both in arithmetic scale, as shown in Figure 2.

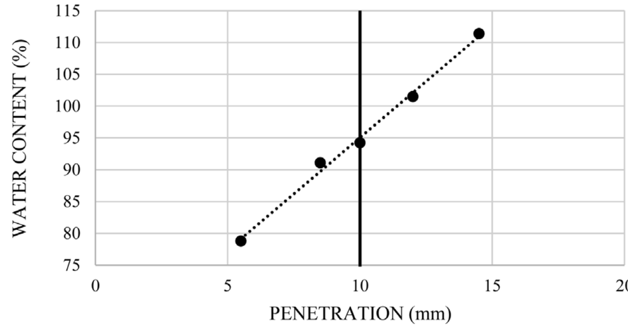

Figure 2. Graphic representation of liquid limit by the Fall Cone method.

3. Results and discussions

The soil samples were numbered from 1 to 31. Three samples did not have enough material to perform specific gravity and distribution size analysis. The Table 1 presents the sample identification with the related origins and the results of characterization tests. The Table 1 also presents the soil samples classification according to Unified Soil Classification System (USCS) as CL (clays of low plasticity), CH (clays of high plasticity), ML (silts of low plasticity), MH (silts of high plasticity) and SC (clayey sands). Three samples (13, 14 and 15) were left unclassified due to lack of material to perform the classification tests.

Table 1. Sample identification and properties of soils tested.

Sample	Origin	Gs – Specific Gravity	Percentage of fines (%)	Liquid limit (%)	Plastic limit (%)	USCS classification	Activity (%)
1	Marine	2.737	93.7	75	39	MH	38.42
2	Marine	2.759	99.0	100	36	CH	64.65
3	Marine	2.708	81.2	64	26	CH	46.80
4	Marine	2.712	88.4	86	36	CH	56.56
5	Marine	2.722	91.5	54	24	CH	32.79
6	Colluvium	2.631	97.0	110	53	MH	58.76
7	Aluminum ore - Tailing	2.698	31.5	18	10	SC	25.40
8	Aluminum ore - Tailing	2.750	88.8	49	25	CL	27.03
9	Marine	2.645	91.5	54	16	CH	41.53
10	Marine	2.635	77.0	63	12	CL	66.23
11	Marine	2.533	71.5	51	9	CL	58.74
12	Marine	2.651	77.7	89	12	CH	99.10
13	Marine	-	-	33	14	-	-
14	Marine	-	-	83	-	-	-
15	Marine	-	-	54	15	-	-
16	Colluvium	2.836	62.9	49	23	CL	41.34
17	Marine	2.485	100.0	94	27	-	67.00
18	Residual	2.837	63.0	34	21	CL	20.63
19	Marine	2.523	100.0	56	28	CH	28.00
20	Residual	2.697	51.0	30	16	CL	27.45
21	Residual	2.660	70.0	41	20	-	30.00
22	Residual	2.689	61.0	52	27	CH	40.98
23	Residual	2.695	68.0	47	20	CH	39.71
24	Residual	2.621	40.0	40	24	SC	40.00
25	Residual	2.776	63.0	51	29	MH	34.92
26	Residual	2.609	65.0	40	22	SC	27.69
27	Residual	2.707	61.0	48	28	ML	32.79

Table 1 (cont.)

Sample	Origin	Gs – Specific Gravity	Percentage of fines (%)	Liquid limit (%)	Plastic limit (%)	USCS classification	Activity (%)
28	Residual	2.644	74.0	43	22	CL	28.38
29	Residual	2.642	80.0	48	24	CL	30.00
30	Residual	2.631	56.0	24	12	CL	21.43
31	Residual	2.830	61.0	32	17	CL	24.59

Table 2 shows the results of liquid limits obtained with the Casagrande and Swedish Fall Cone apparatus, as well as the R^2 values achieved in each test. Due to the amount of material available, not all samples were able to have all the tests performed. But this factor does not influence the evaluation because the fundamental tests - the liquid limit at the two methods - were tested.

The average R^2 values and dispersion values for the Fall Cone method were 0.975 which reveals a good test result and a coherent application for the samples tested. For a better analysis of the liquid limit data and further analysis, a graph was constructed in which in the abscissa axis are the values of liquid limit (LL) using the apparatus of Casagrande and in the axis of the ordinates the values using the Fall Cone. The trendline was fixed at the origin to represent an ideal correlation. The graph is presented at the Figure 3.

The first evaluation that can be done is that the Fall Cone method and Casagrande apparatus generally give different values for the liquid limits, as already proven by some researches (Wood, 1982; Leroueil & Le Bihan, 1996; Crevelin & Bicalho, 2019). And when comparing the values between Casagrande and Fall Cone methods, for most samples, it is noticed that the higher values were obtained with the Fall Cone.

In this graph, the tendency line was considered through the origin (45 degrees), which would imply a perfect correlation between the methods, but it was noticed a dispersion of the points as the moisture increased. Evaluating the data up to a Casagrande liquid limit value of 80 %, the R^2 value is 0.9453, considering the values with LL > 80 %, the R^2 is 0.1485, which shows an increase in the dispersion of the values. This suggests that results can be divided into two groups, with a liquid limit of 80 % as the separation point, however the quantity of tests with LL > 80 % was small (Figure 3, samples 2, 4, 6, 12, 14 and 17). No correlation was observed between the differences between the methods and the properties of the soils tested.

In compliance with previous studies available in the geotechnical literature, there is a certain tendency for Casagrande values to be lower than those obtained by Fall Cone for lower liquid limits and higher than Cone values for higher liquid limits. According to Sridharan & Prakash (1998), this differentiation of the values between the appa-

Table 2. Liquid limit results.

Sample	Liquid limit (%)		R^2 - Casagrande	R^2 - Fall Cone
	Casagrande	Fall Cone		
1	75	80	0.998	0.969
2	100	95	0.985	0.995
3	64	61	0.99	0.978
4	86	76	0.996	0.996
5	54	57	0.997	0.955
6	110	107	0.995	0.998
7	18	23	0.987	0.959
8	49	58	0.989	0.976
9	54	57	0.957	0.986
10	63	63	0.991	0.988
11	51	50	0.952	0.947
12	89	97	0.936	0.999
13	33	34	0.965	0.955
14	83	98	0.966	0.970
15	54	59	0.988	0.990
16	49	58	0.942	0.989
17	94	82	0.986	0.989
18	34	38	0.985	0.970
19	56	63	0.994	0.926
20	30	33	0.944	0.954
21	41	44	0.998	0.962
22	52	57	0.994	0.978
23	47	54	0.964	0.979
24	40	41	0.994	0.973
25	51	60	0.985	0.988
26	40	53	0.990	0.993
27	48	57	0.993	0.979
28	43	52	0.997	0.965
29	48	52	0.973	0.994
30	24	31	0.978	0.967
31	32	36	0.994	0.969

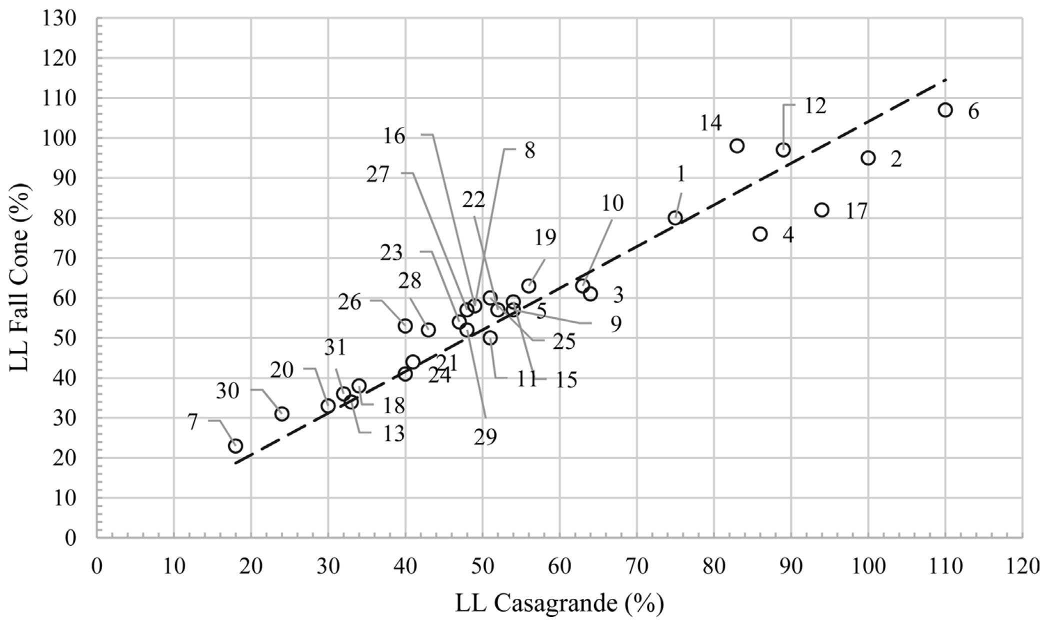

Figure 3. Comparison between Fall Cone method and Casagrande device.

ratus of Casagrande and Swedish Fall Cone is related to the dominant clay mineral and its proportion contained in the clay fraction. Other authors, such as Leroueil & Le Bihan (1996), agree that the clay minerals are an important factor, but should not be the only one to be considered.

In order to explain this difference in behavior, the content of organic matter and the type of clay mineral were determined. Regarding organic matter, the maximum value found was 9,8 %, therefore the samples did not present a significant amount of organic content that could have influenced on the behavior of the test results. Another attempt to identify the existent clay minerals, the points were plotted on a chart - index of plasticity x percentage of the clay fraction - proposed by Lambe & Whitman (1969), as shown at Figure 4. As maximum and minimum values of percentage of clay fraction are, respectively, 100 % and 31.5 % and in the case of plasticity indices, 77 and 12. According to these values and approaching a corresponding area, it is noted that the clay minerals present in the samples are illite and kaolinite. The values of activity of the samples (Table 1) also show inactive clays (A < 0.75) and normal clays (A between 0.75 and 1.25). As described by Sridharan & Prakash (1998), the mechanisms controlling the kaolinitic soils are different than montmorillonite soils and usually, the Cone

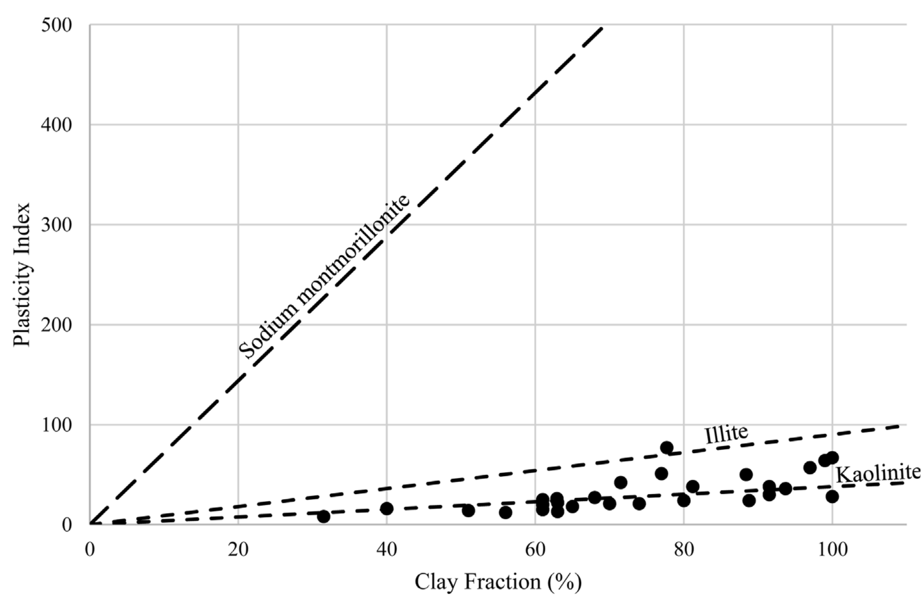

Figure 4. Plasticity index *vs.* clay fraction (Lambe & Whitman, 1969).

method gives a higher liquid limit than the Casagrande device for kaolinitic soils. For these authors, the dominant clay mineral type and its proportion in the clay content are in charge of the variations between the results of the Casagrande and Cone tests. The data obtained do not permit to confirm or discard this assumption, the most part of the materials presents low activity and apparently the same kind of clay minerals.

According to Head (2006), the mechanics of the Fall Cone test depend directly on the static shear strength of the soil, as the Casagrande procedure includes a dynamic component not associated with shear strength in the same way for all soils. By the liquid limit definition, the obtained value is influenced by the point at which the soil begins to gain a detectable shear strength, about 1.7 kN/m^2. For Bicalho et al. (2014), the difference of values between the methods is related to the mechanics of the test and its correlation to estimate the undrained shear strength and the clay content of the samples.

One of the likely explanations for the variation of the values between one method and another can be explained by the differences between behavior to obtain the results. For the execution of a test point in the Casagrande apparatus the groove must close at 12.7 millimeters, in other words, the ground behaves as if in a "dynamic slope stability" test where each stroke generates an acceleration and causes the "slope" to move until the groove closes (Haigh, 2012). In the Swedish Fall Cone, the execution of a test point is done by touching the tip of the cone on the surface of the soil sample and when the cone is released and a quasi-static penetration in millimeters is measured, there is more direct measurement of cone penetration in soil. This behavior may be a more consistent explanation for the justification of differences than the individual assessment of materials.

4. Conclusions and recommendations

This study presented an experimental analysis of the performance of Fall Cone device as an alternative method to determine the liquid limit. The main limitation associated with this method is the lack of an apparatus and methodology internationally adopted. Therefore, the procedure of the test was followed as recommended by Karlsson (1981) and the Swedish Standard, which uses a cone with mass of 60 g and 60° opening angle cone. The current study evaluated 31 soil samples from various regions of Brazil and different geotechnical properties. Besides the execution of liquid limit at Casagrande's method, other tests as the plastic limit, percentage of fines, and specific gravity were determined to expand the database and identify possible deviations.

The Fall Cone test is simpler to perform and factors such as operator influence, trial run time and calculation are smaller than Casagrande. In addition, the Fall Cone method avoid some inconveniences generated by Casagrande device, such as dispersion of the results, small differences in the apparatus, distribution of material in the shell, observation of the slot closure and incorrect homogenization time. Analyzing the individual results, the Fall Cone method obtained acceptable outcome and presents a suitable application for the samples tested. Comparison of the values between Fall Cone and Casagrande shows that the methods present a good correlation in liquid limits of up to 80 % and above this value the differences increase, which relates to the obtained in other studies (Bicalho, 2014; Head, 2006; Leroueil & Le Bihan, 1996). For liquid limit until 80 %, the difference between the method is about 5 %, above 80 % the differences between the values of liquid limit obtained increases to 8 %.

No direct correlation was observed between the soils properties and the differences observed between the methods, however, the quantity the tests with LL > 80 % was reduced. Most of the soils tested present low activity; therefore, it is necessary to investigate further the influence of different clay minerals in the results and correlations between the two methods.

Acknowledgments

We thank Fugro and Universidade Federal do Paraná for their receptivity, technical and administrative support, for encouraging the development of this work.

References

ABNT NBR 6459. (1984) Determinação do Limite de Liquidez. Rio de Janeiro, Associação Brasileira de Normas Técnicas. *ABNT - Associação Brasileira de Normas Técnicas, Rio de Janeiro*, *RJ* (in Portuguese).

ASTM D 4318-17. (2017). Standard Test Methods for Liquid Limit, Plastic Limit, and Plasticity Index of Soils. *ASTM International, West Conshohocken, PA*. https://doi.org/10.1520/D4318-17E01

Bicalho, K.V.; Gramelich, J.C., & Santos, C.L.C. (2014). Comparação entre os valores de limite de liquidez obtidos pelo método de Casagrande e cone para solos argilosos brasileiros. *Comunicações Geológicas*, 101(3), 1097-1099.

BSI BS 1377-2. (1990). Methods of Test for Soils for Civil Engineering Purposes - Part 2. *BSI - British Standards Institution, London*.

Crevelin, L.G., & Bicalho, K.V. (2019). Comparison of the casagrande and fall cone methods for liquid limit determinations in different clay soils. *Revista Brasileira de Ciência do Solo*, 43, e0180105. https://doi.org/10.1590/18069657rbcs20180105

Das, B.M. (2012). *Fundamentos de Engenharia Geotécnica*. Cengage Learning.

Garneau, R., & LeBihan, J.P. (1977). Estimation of some properties of Champlain clays with the Swedish fall cone. *Canadian Geotechnical Journal*, 14(4), 571-581. https:// doi.org/10.1139/t77-058

Haigh, S.K. (2012). Mechanics of the Casagrande liquid limit test. *Canadian Geotechnical Journal*, 49(9),1015-1023. https://doi.org/10.1139/t2012-066

Head, K.H. (2006). *Manual of Soil Laboratory Testing - Volume 1: Soil Classification and Compaction Tests*. Whittles Publishing.

Karlsson, R. (1981). *Consistency Limits*. Swedish Council for Building Research.

Lambe, T.W., & Whitman, R.V. (1969). *Soil Mechanics, SI Version*. John Wiley & Sons.

Leroueil, S., & LeBihan, J.P. (1996). Liquid limits and fall cones. *Canadian Geotechnical Journal*, 33(5), 793-798. https://doi.org/10.1139/t96-104-324

Nini, R. (2014). Effect of the silt and clay fractions on the liquid limit measurements by Atterberg cup and fall cone penetrometer. *Proc. 24th ICTPA Annual Conference & NACGEA International Symposium on Geo-Trans*, Paper No. S3-001.

Oliveira, M.L.; Gedanken, A. & Ruiz, H.A. (2001) Utilização do penetrômetro de cone na determinação do limite de liquidez em latossolos. *Revista Ceres*, 48(275), 95-99.

Queiroz de Carvalho, J.B.Q. (1986) The applicability of the cone penetrometer to determine the liquid limit of lateritic soils. *Géotechnique*, 36(10), 109-111. https://doi.org/10.1680/geot.1986.36.1.109

Silveira, L.C.S. (2001). O cone de penetração como ensaio alternativo na determinação da plasticidade de solos. *Proc. Congresso Brasileiro de Ensino de Engenharia, Porto Alegre*. ABENGE, NTM:16-19 (in Portuguese).

SSC SS027120. (1990). Geotechnical Tests - Cone Liquid Limit. *SSC - Swedish Standards Commission*, *Stockholm*.

Spagnoli, G. (2012) Comparison between Casagrande and drop-cone methods to calculate liquid limit for pure clay. *Canadian Journal of Soil Science*, 92(6), 859-864. https://doi.org/10.4141/cjss2012-011

Sridharan, A., & Prakash, K. (1998). Discussion on “liquid limits and fall cones”. *Canadian Geotechnical Journal*, 35(2), 407-408. https://doi.org/10.1139/t98-004

Wasti, Y. (1987). Liquid and plastic limits as determined from the fall cone and the Casagrande method. *Geotechnical Testing Journal*, 10(1), 26-30. https://doi.org/10.1520/GTJ10135J

Wood, D.M. (1982). Cone penetrometer and liquid limit. *Géotechnique*, 32(2), 152-157. https://doi.org/10.1680/geot.1982.32.2.152

Soils and Rocks

An International Journal of Geotechnical and Geoenvironmental Engineering

www.soilsandrocks.com

ISSN 1980-9743
ISSN-e 2675-5475

The effect of grain size of ground glass particles on the strength of green stabilized sand

Hugo Carlos Scheuermann Filho[1,#], Rafael Luís Sacco[2], Nilo Cesar Consoli[1]

Note

Keywords
Carbide lime
Ground glass
Porosity/binder index
Pozzolanic reactions
Soil stabilization
Sustainable binders
Unconfined compressive strength

Abstract

Regular soil improvement techniques customarily involve the use of ordinary Portland cement (OPC) despite the environmental issues related to the production process of such material. Hence, the establishment of alternative binders through the use of industrial and/or urban waste might be an option to overcome part of those problems. Thus, present research evaluates the strength of a quartz sand stabilized with a binder composed by ground glass powder (having granulometries) and carbide lime. For this, a 2^k factorial design method was employed in order to define the experimental runs in which the effect of the following variables was assessed: dry unit weight, curing period, amount of carbide lime, ground glass content and ground glass milling granulometry. The results have shown the great influence exerted by the dry unit weight, the amount of ground glass powder and the curing period. The effects of ground glass granulometry and carbide lime were, as well, statistically significant. Moreover, the results were correlated to the porosity/binder index (η/B_{iv}) in which great R^2 coefficients were obtained. In general, the proposed binder showed to be effective for soil stabilization purposes, especially if finer ground glass powders are employed.

1. Introduction

Customary soil improvement techniques frequently involve the usage of binders such as Ordinary Portland Cement (OPC) and densification through compaction (Ingles & Metcalf, 1972; Mitchell, 1981). Nevertheless, the production process of Portland cement releases great quantities of CO_2 due to demand for large amounts of energy and natural resources, being notably deleterious to the environment (Habert, 2014; Chen *et al.*, 2010). Thus, the development of binders utilizing alternative materials that posse adequate physical-chemical properties (e.g. urban and/or industrial waste) arises as an alternative in order to partially overcome those issues.

Soda-lime glass corresponds to more than 85 % of the total amount of glass produced in a global scale per year as it is the major constituent of glass containers and as-like objects (Mohajerani *et al.*, 2017, Schmitz *et al.*, 2011). Hence, it is an important source of waste in urban areas, being a problem when not properly recycled. In Brazil, less than 50 % of the glass containers are recycled, while this rate is up to 40 % in USA, 87 % in Germany, and 95 % in Switzerland (CEMPRE, 2015). Ergo, in some countries there still a sizeable amount of glass disposed in landfills. Yet, due to its chemical composition (mainly SiO_2) and amorphous structure, soda-lime waste glass can be grinded and employed in the composition of several binders as a pozzolanic material (Sales, 2015; Rangaraju *et al.*, 2016; Mohajerani *et al.*, 2017). Consequently, in an alkaline and hydrated environment, SiO_2 may combine with calcium hydroxide [$Ca(OH)_2$], yielding binding compounds (Massaza, 2004) such as calcium silicate hydrated (C-S-H) as described in Equation 1.

$$2SiO_2 + Ca(OH)_2 + 5H_2O \rightarrow CaO \cdot 2SiO_2 \cdot 3H_2O \quad (1)$$

Accordingly, notwithstanding of other applications for waste-glass material such as fine and coarse aggregate in concrete (Chen *et al.*, 2006; Park *et al.*, 2004; Malik *et al.*, 2013), incorporation in asphaltic mixtures (Day *et al.*, 1970; Hughes, 1990; Jony *et al.*, 2011) and supplementary filler material (Arulrajah *et al.*, 2017), several studies were conducted aiming to employ fine ground glass waste as a

[#]Corresponding author. E-mail address: 00209266@ufrgs.br.
[1]Programa de Pós Graduação em Engenharia Civil, Universidade Federal do Rio Grande do Sul, Porto Alegre, RS, Brazil.
[2]Universidade Federal do Rio Grande do Sul, Porto Alegre, RS, Brazil.

Submitted on March 10, 2020; Final Acceptance on July 29, 2020; Discussion open until March 31, 2021.
DOI: https://doi.org/10.28927/SR.434669

pozzolan. Pattengil & Shutt (1973) assessed the effect of partial replacement (in mass) of cement in concrete by distinct amounts of ground glass powder (0 %, 15 %, and 30 %). Metwally (2007) conducted a similar study by employing milled non-recyclable waste glass as a partial replacement of cement in concrete. Sales *et al.* (2015) assessed the pozzolanic activity of ground glass obtained of dissimilar colors of soda-lime glasses and did not find differences between the examined glass types. Consoli *et al.* (2019) evaluated the strength and stiffness of a cement composed by finely ground glass and carbide lime molded at distinct degrees of compaction. Baldovino *et al.* (2020) appraised the mechanical response of a sedimentary silty soil stabilized with ground waste glass and Portland cement using three curing times (7, 28 and 90 days). Consoli *et al.* (2018a) studied the performance of a quartz sand stabilized with distinct amounts of a finely ground glass (10 %, 20 %, and 30 %) and carbide lime (3 %, 5 %, and 7 %) through strength, stiffness and durability tests, whereas Consoli et. al (2020a) conducted a similar study but using three different silica sands.

It is known that the pozzolanic activity of a material is influenced, among other factors, by the specific surface area (SSA) of the pozzolan (Massaza, 2004). Yet, in spite of the several works conducted aiming to evaluate the performance of ground glass as a pozzolanic material, none of them assessed the influence of the grain size of the glass obtained after a milling process which is directly linked to the SSA. Thus, present research intends to assesses the impact of three distinct ground glass granulometries on the strength and stiffness of compacted sand - ground glass - carbide lime blends. For this, a 2^k factorial design was employed in which the content of carbide lime (CL), the dry unit weight, the amount of ground glass and the curing period were varied at two levels. This design approach (2^k factorial design) was separately conducted using each one of the obtained ground glass granulometries. Besides, the results were correlated to the porosity/binder content index (Consoli *et al.*, 2018a, 2018b).

2. Experimental program

The experimental program was conducted in three parts. Initially, the soil, the carbide lime and the ground glass powders were characterized. Thereafter, unconfined compressive strength tests were carried out based on a 2^k factorial design approach (Montgomery, 2008). Finally, the strength results were statistically analyzed in order to assess the influence of the studied controllable factors (i.e. variables) which are depicted in Table 1.

2.1 Materials

The physical properties of the materials employed herein are summarized in Table 2 and the grain size distribution of each one is depicted in Figure 1. The grain size distribution results were obtained by means of laser diffraction analysis. According to ASTM D2487 (ASTM 2017), the soil is a poorly graded quartz sand with silt (SP-SM) which was obtained nearby Porto Alegre (south of Brazil). This sand is known as Osorio sand. Carbide lime [$Ca(OH)_2$] was used as an alkaline activator. Such lime is a by-product

Table 1. Controllable factors.

Controllable factor	Levels
Granulometry of ground glass powder	a b and c
Amount of ground glass (%)	10 and 30
Amount of carbide lime (%)	4 and 7
Dry unit weight (kN/m^3)	15.5 and 17.5
Curing period (days)	7 and 28

Table 2. Physical properties of the materials.

Physical properties	Ground glass powder			Carbide lime	Osorio sand
	Type A	Type B	Type C		
Plasticity index	Non-plastic				
Specific gravity	2.47	2.47	2.47	2.19	2.65
Specific surface area* (m^2/g)	2.48	2.21	1.50	22.60	-
Coarse sand (2.00 mm < d < 4.75 mm) (%)	-	-	-	-	-
Medium sand (0.425 mm < d < 2.00 mm) (%)	-	-	-	-	10
Fine sand (0.075 mm < d < 0.425 mm) (%)	-	20	50	-	87
Amount of silt (0.002 < d < 0.075 mm) (%)	99	79	50	97	3
Amount of clay (d < 0.002 mm) (%)	1	1	-	3	-
Coefficient of uniformity	2	8.33	10	10	2.5
Coefficient of curvature	0.55	1.33	2.5	0.9	0.9

*Obtained via BET analysis.

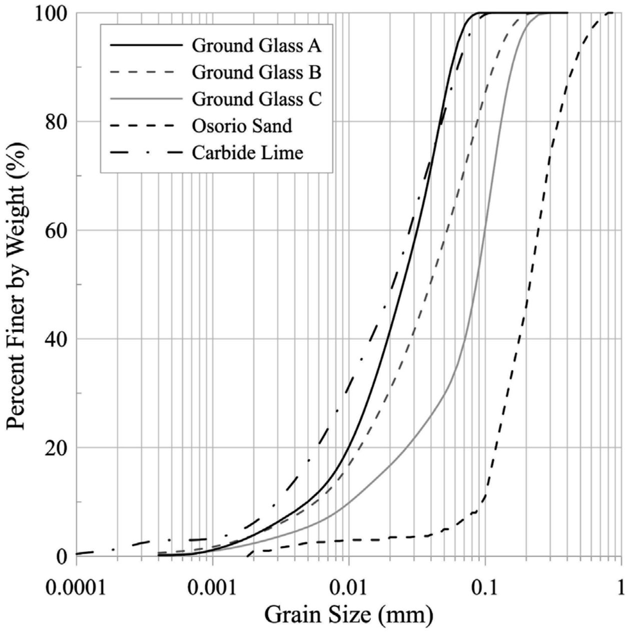

Figure 1. Grain size distribution of the employed materials.

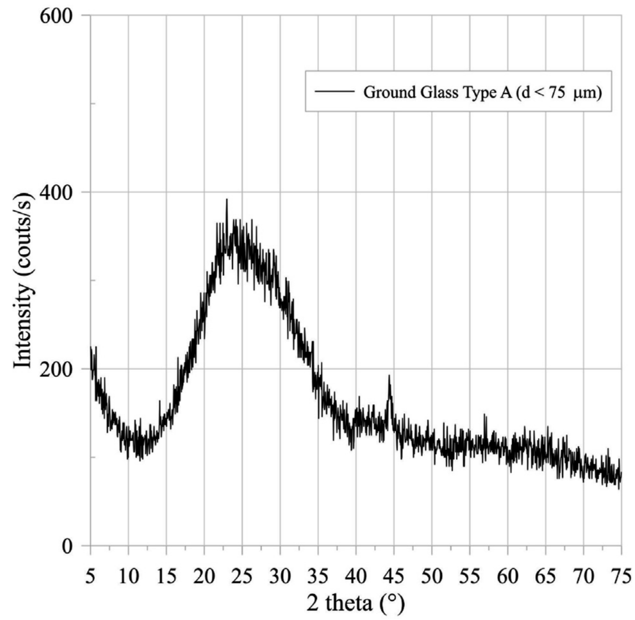

Figure 2. X-ray diffraction test of ground glass.

of the production of acetylene-gas and was obtained in an industry located in the region of Porto Alegre. Further information regarding the physical, chemical and mineralogical characterization of the carbide lime can be found on Saldanha *et al.* (2018). The ground glass powder was obtained via milling transparent waste glass in a ball mill following a regular procedure. This encompassed a fixed time (5 h), a defined amount of glass (1.5 kg) and specific quantity of milling balls. After the milling process was accomplished, the powder was separated in three distinct fractions (corresponding to different granulometries) via screening using sieves. The first fraction (A) corresponded to the particles smaller than 75 μm, the second fraction (B) corresponded to the portion greater than 75 μm and smaller than 149 μm and the third amount (C) was composed by particles greater than 149 μm. The chemical composition of the glass was obtained via X-Ray Fluorescence (XRF) and revealed that it is mainly composed by SiO_2 (75 %), CaO (17 %), Al_2O_3 (3 %) and Na_2O (2 %). The X-ray Diffraction pattern (Figure 2) was obtained in the fraction (A) and is typical of an amorphous material (Music *et al.*, 2011).

2.2 Methods

The studied variables (and their levels) were defined based on the previous work of Consoli *et al.* (2018a), which was performed using the same sand, carbide lime and type of soda-lime glass (transparent). Therefore, the following variables were assessed: dry unit weight (γ_d), amount of carbide lime (CL) and ground glass powder quantity (GG). The amounts of ground glass (GG) and of carbide lime content (CL) are both based upon the total dry mass of the specimen. The molding moisture content (*w*) was set as 10 %. Table 3 exhibits the experimental runs (dosages) and duplicates were molded within each experimental design (treatment).

2.3 Specimens molding and curing

Cylindrical specimens (50 mm in diameter and 100 mm in height) were molded for the unconfined compressive strength tests according to the undercompaction method (Ladd, 1978). Each specimen was individually molded following a randomized order aiming to guarantee the statistical independence of the error. The molding process started by the weighing of the dry materials (sand, ground glass powder and carbide lime). Right after they were mixed until a uniform consistency was acquired. Next, distilled water was added and the materials were thoroughly mixed until a homogeneous mass was created. After this mixing, three small portions of this mass were taken in order to verify the molding moisture content. Following, each specimen was statically compacted in three layers inside a split mold to the specified dry unit weight. Then, the specimen was removed from the mold, weighed, measured (precisions of nearly 0.01 g and 0.1 mm) and sealed in a plastic bag to be cured in a humid room with controlled environment (at 23 ± 2 °C with relative moisture of about 95 %). Each specimen was considered suitable for testing if they met the following limits: dry unit weight within ±1 % of the target value, molding moisture content within ±0.5 % of the target value and dimensions within ±1 % of the target values.

In order to compute each specimen porosity (η), the Equation 2 can be employed. In this, γ_d refers to the dry unit weight, S to the sand quantity, GG to the amount of ground glass powder and CL to the carbide lime content. Besides, each substance posses its own specific grains weight as fol-

Table 3. Experimental runs.

Experimental run	γ_d (kN/m^3)	CL (%)	GG (%)	GG Type	η/B_{iv}
1	15.5	4	10	A	4.46
2	15.5	4	10	B	4.46
3	15.5	4	10	C	4.46
4	15.5	4	30	A	1.83
5	15.5	4	30	B	1.83
6	15.5	4	30	C	1.83
7	17.5	4	10	A	3.20
8	17.5	4	10	B	3.20
9	17.5	4	10	C	3.20
10	17.5	4	30	A	1.31
11	17.5	4	30	B	1.31
12	17.5	4	30	C	1.31
13	15.5	7	10	A	3.58
14	15.5	7	10	B	3.58
15	15.5	7	10	C	3.58
16	15.5	7	30	A	1.66
17	15.5	7	30	B	1.66
18	15.5	7	30	C	1.66
19	17.5	7	10	A	2.56
20	17.5	7	10	B	2.56
21	17.5	7	10	C	2.56
22	17.5	7	30	A	1.18
23	17.5	7	30	B	1.18
24	17.5	7	30	C	1.18

lowing: soil (γ_s), carbide lime (γ_{CL}) and ground glass powder (γ_{GG}).

$$\eta = 100 - 100\left[\left(\frac{\gamma_d}{\frac{S}{100}+\frac{GG}{100}+\frac{CL}{100}}\right)\left(\frac{\frac{S}{100}}{\gamma_s}+\frac{\frac{GG}{100}}{\gamma_{GG}}+\frac{\frac{CL}{100}}{\gamma_{CL}}\right)\right] \quad (2)$$

2.4 Unconfined compressive strength tests

One day before the curing period was accomplished (6 or 27 days) the specimens were submerged in a water tank (23 ± 2 °C) along 24 h in order to minimize possible suction effects (Consoli *et al.*, 2011). Following, the strength tests were conducted based on the ASTM C39/C39M (ASTM, 2020) using an automatic loading press with maximum capacity of 50 kN. A displacement rate equal to 1.14 mm/min was adopted and the maximum load was recorded for each tested specimen with a resolution equal to 0.005 kN.

3. Results and discussion

3.1 Unconfined compressive strength

Figure 3a presents the unconfined compressive strength (q_u) results for the specimens cured along 7 days, while Figure 3b exhibits the results for a curing period equal to 28 days. For both curing periods, the q_u results are correlated to the porosity/volumetric binder content index (η/B_{iv}) as previously proposed by Consoli *et al.* (2018b). The volumetric binder content (B_{iv}) is designated as the sum between the volumetric contents of carbide lime (V_{CL}) and pozzolan (V_{GG}), both divided by the total volume of the specimen (V) as presented in Equation 3.

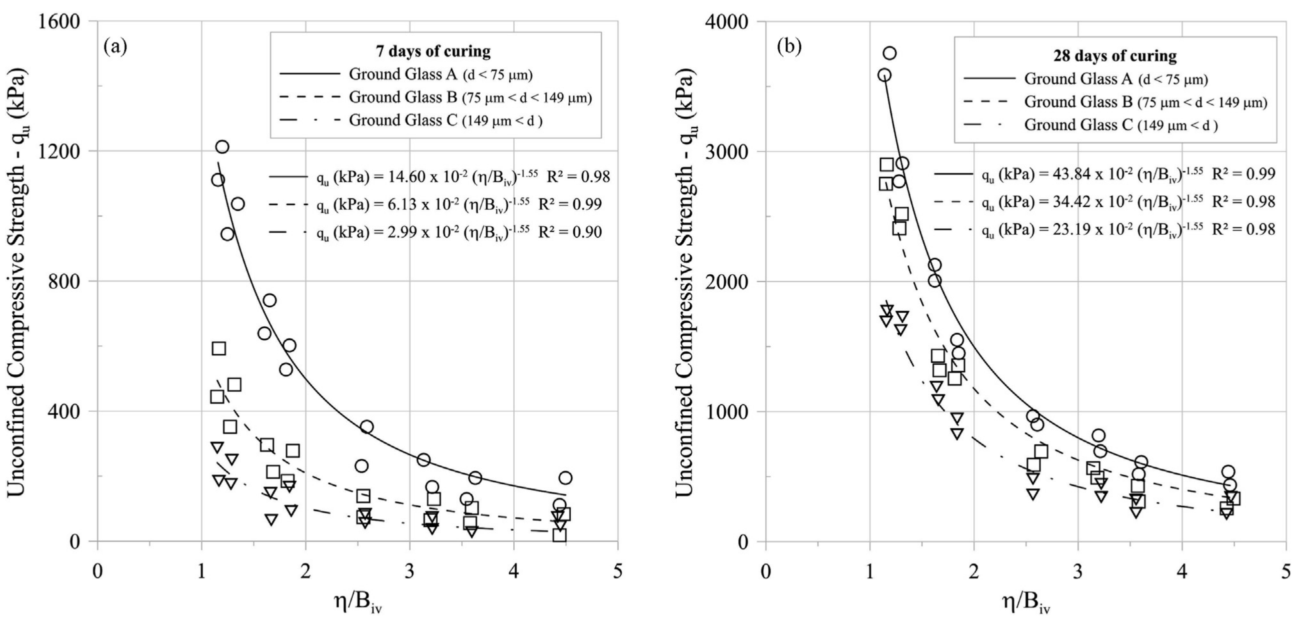

Figure 3. Unconfined compressive strength results (a) 7 days of curing (b) 28 days of curing.

$$B_{iv} = \frac{V_{GG} + V_{CL}}{V} \tag{3}$$

The η/B_{iv} index inputs into a single parameter the influence of porosity and the amount of binder on the mechanical behavior of the compacted mixtures. The relative importance between the compactness and the binder quantity may be adjusted, if necessary, through an exponent applied to the B_{iv}. As formerly attained in other studies (Henzinger *et al.*, 2018, Consoli *et al.*, 2018a, 2018b, 2019, Ekinci *et al.*, 2019), a power equation was obtained between the unconfined compressive strength and the η/B_{iv} parameter considering each type of employed ground glass and each curing period. Hence, an equation of the following type was obtained, in which the scalar "*A*" and the coefficient of determination (R^2), considering each curing period and each ground glass type, are presented in Table 4.

$$q_u\ (\text{kPa}) = A \times 10^2 \left(\frac{\eta}{B_{iv}}\right)^{-1.55} \tag{4}$$

Regardless the ground glass type, the only difference between the attained power equations relies on the scalar "*A*". This must account for the differences related to the curing period and, as well, to the type of ground glass powder. Such trend is in accordance to what was formerly demonstrated by Diambra *et al.* (2017). Hence, within the same ground glass type, higher strength values were observed for the highest curing period. Otherwise, considering the same curing period, greater strengths were attained when the finer ground glass powder was used. The causes and implications of such outcomes are discussed in the next section.

Moreover, in order to validate the results obtained herein, a normalization procedure was carried out following the procedure previously adopted by Consoli *et al.* (2017, 2020b). Thus, all the q_u values obtained in the present research were normalized by a respective q_u value related to a η/B_{iv} equal to 3. The index value equal to 3 was chosen because it lies within the η/B_{iv} boundaries that vary from 1.0 to 4.5. The results obtained herein, in conjunction with the ones attained by Consoli *et al.* (2018a), are plotted in Figure 4 in the normalized form. The single equation ($R^2 = 0.95$) was obtained through the employment of such approach:

Table 4. Summary of parameters for Equation 4.

Ground glass type	Curing period (days)	A (kPa)	R^2
A	7	14.60	0.98
B	7	6.13	0.99
C	7	2.99	0.90
A	28	43.84	0.99
B	28	34.42	0.98
C	28	23.19	0.98

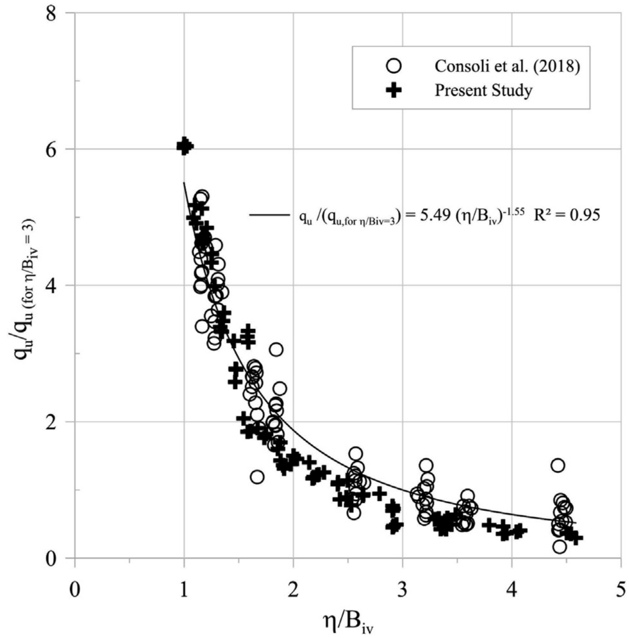

Figure 4. Normalized strength results.

$$\frac{q_u}{q_{u\left(\frac{\eta}{B_{iv}}=3\right)}} = 5.49\left(\frac{\eta}{B_{iv}}\right)^{-1.55} \tag{5}$$

3.2 Statistical analysis

In order to statistically assess the significance of the controllable factors (and their interactions), an analysis of variance (ANOVA) was conducted at a significance level (α) of 5 %. In addition, the Pareto chart of the standardized effects was employed (Figure 5) aiming to graphically demonstrate the magnitude of the standardized effects of the studied variables and the second order interactions. In this graph, a reference line delimits the significant factors at the adopted α. Such line is the quantile in the Students t-distribution and depends upon α.

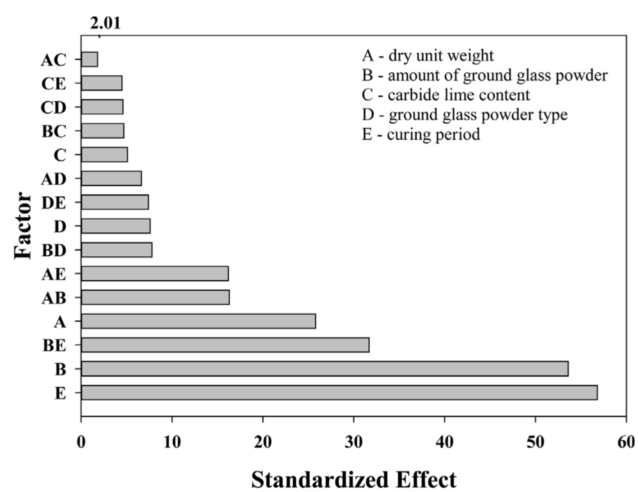

Figure 5. Pareto chart of the standardized effects.

Through the analysis of the results depicted in Figure 5, it is clear that all the factors influence the strength of the studied blends at the adopted α. However, the curing period (*E*), the amount of ground glass powder (*B*), their interaction (*BE*) and the dry unit weight (*A*) are the most relevant factors in controlling the unconfined compressive strength of the amended soil. In addition, although statistically significant, the effects exerted by the ground glass type (*D*) and by the amount of carbide lime (*C*) are sensibly smaller compared to those exerted by the other variables.

The kinetics of the pozzolanic reactions explains the great influence of the curing period on the strength of the tested specimens. Namely, higher curing periods enable the fixation of greater quantities of carbide lime, yielding the formation of cementitious binding compounds that contribute to enhance the strength of the blends, regardless the ground glass powder type (Saldanha & Consoli, 2015; Saldanha *et al.*, 2016; Bilondi *et al.*, 2018). In this sense, neglecting the change in fabrics due to distinct amounts of glass powder, the availability of greater quantities of reactive material (i.e. pozzolan) facilitates the yielding of cementitious materials along the curing period. This explains the appreciable effect of the amount of ground glass powder and its interaction with curing period in altering the strength of the tested blends.

The substantial influence of the dry unit weight is related to the compactness of the specimens. That is, lower porosity values imply in greater degrees of interlocking between the particles and, therefore, in broader strength values. Besides, the proximity between the particles that compose the mixture influences the kinetics of the pozzolanic reactions, facilitating it. This explains the interactions of the dry unit weight with curing period (*AE*) and with the ground glass powder quantity (*AB*). As well, the amount of carbide lime (*C*) had little influence in altering the q_u, probably because the minimum amount of 4 % might be sufficient for the pozzolanic reactions development considering the curing periods employed herein. Similar trend was observed by Consoli *et al.* (2018a, 2018b, 2019, 2020). Nonetheless, for distinct curing conditions (i.e. higher curing period and/or temperature) this might not be true.

Although not so impacting, the type of ground glass showed to be statistically significant. This is mostly explained by the higher specific surface area observed in the finer powder which is intimately linked to the reactivity of the material and, consequently, to the kinetics of the pozzolanic reactions (Massaza, 2004; Cordeiro *et al.*, 2011; Walker & Pavia, 2011). Besides, through the uniformity coefficients (C_U) of the distinct ground glass powders (Table 2), it is possible to infer that the increment in the strength is not related to change of gradation existing between the three tested ground glass granulometries. Usually, higher strengths are attained for well-graded or gap-graded soils (Igwe *et al.*, 2006; Krim *et al.*, 2017). This was not the case herein if the gradations of the ground glass powders are individually considered. Namely, the best performance was observed amongst the finest powder ($C_U = 2$), whereas the coarser ground glass powders exhibited higher C_U values and worse strength values. That is, no relationship could be observed between unconfined compressive strength and gradation of the pozzolan.

4. Conclusions

The present research was carried out aiming to assess the influence, among other variables, of the granulometry of the ground glass powder used in conjunction with carbide lime to stabilize a quartz sand. Hence, from the results presented herein, the following conclusions can be drawn considering the experimental limits:

Good correlations were obtained between the unconfined compressive strength and the η/B_{iv} index as the coefficients of correlation were, in general, greater than 97 %. Moreover, the results could be normalized and followed a unique curve.

The curing period was the most influent factor in altering the strength response of the studied specimens. This is clearly related to the kinetics of the pozzolanic reactions that occur between the carbide lime and the ground glass powder. Therefore, up to a certain limit, greater amounts of binding compounds will precipitate for higher curing periods, contributing to enhance the mechanical strength of the sand - binder blends.

Although not so impacting in comparison with the other experimental variables, the type of ground glass powder (i.e. the granulometry) was statistically significant in altering the strength of the studied blends. This is related to the higher surface area obtained for the finer grain size distribution which enhances the pozzolan' reactivity. Such trend was easily demonstrated when the unconfined compressive strength results were correlated to the η/B_{iv} index, being the adjustment scalar "A" higher for the finer granulometries.

Possible effects of different gradation existing between each ground glass granulometry type can be neglected as no apparent relationship between uniformity coefficients (C_U) and strength was obtained. Therefore, the specific surface area appears as the main factor of influence regarding the performance when different grain sizes distributions of glass were employed.

In general, either an increase in the amount of ground glass powder and a decrease in the porosity has led to higher unconfined compressive strength values. Statistically, the amount of ground glass showed to be more influent regarding the strength of the studied mixtures, which is explained by the availability of reactant material to induce the formation of cementing binding compounds. Nonetheless, the Pareto graph has also shown the great effect exerted by the dry unit weight and, as well, by the interaction between amount of pozzolan and dry unit weight. Thereafter, a less porous environment is favorable to the development of pozzolanic reactions.

The ground glass powder showed to be an effective pozzolanic material to be used for sandy soil stabilization purposes. This is especially valid if finer portions of it are used.

Acknowledgments

The authors wish to express their gratitude to the Brazilian Research Council CNPq (INCT, Produtividade em Pesquisa, Universal), to FAPERGS-CNPq (PRONEX) and MEC-CAPES (PROEX) for their financial support of the research group.

References

ASTM D2487-06. (2006). Standard Practice for Classification of Soils for Engineering Purposes (Unified Soil Classification System). *ASTM International, West Conshohocken, PA*. https://doi.org/10.1520/D2487-06

ASTM C39M-20. (2020). Standard Test Method for Compressive Strength of Cylindrical Concrete Specimens. *ASTM International*, *West Conshohocken*, *PA*. https://doi.org/10.1520/C0039_C0039M-20

Arulrajah, A., Kua, T.A., Horpibulsuk, S., Mirzababaei, M., & Chinkulkijniwat, A. (2017). Recycled glass as a supplementary filler material in spent coffee grounds geopolymers. *Construction and Building Materials*, 151(1), 18-27. https://doi.org/10.1016/j.conbuildmat.2017.06.050

Baldovino, J.J.A., Izzo, R.L.S., Silva, É.R., & Rose, J.L. (2020). Sustainable use of recycled-glass powder in soil stabilization. *Journal of Materials in Civil Engineering*, 32(5), 4020080. https://doi.org/10.1061/(ASCE)MT.1943-5533.0003081

Bilondi, M.P., Toufigh, M.M., & Toufigh, V. (2018). Using calcium carbide residue as an alkaline activator for glass powder-clay geopolymer. *Construction and Building Materials*, 183(20), 417-428. https://doi.org/10.1016/j.conbuildmat.2018.06.190

CEMPRE. (2015). CEMPRE review 2015. *CEMPRE - Compromisso Empresarial para Reciclagem, São Paulo, SP* (in Portuguese).

Chen, C.H., Huang, R., & Yang, C.C. (2006). Waste E-glass particles used cementitious mixtures. *Cement and Concrete Research*, 36(3), 449-456. https://doi.org/10.1016/j.cemconres.2005.12.010

Chen, C., Habert, G., Bouzidi, Y., & Jullien, A. (2010). Environmental impact of cement production: Detail of the different processes and cement plant variability evaluation. *Journal of Cleaner Production*, 18(5), 478-485. https://doi.org/10.1016/j.jclepro.2009.12.014

Consoli, N.C., Dalla Rosa, A., & Saldanha, R.B. (2011). Variables governing strength of compacted soil-fly ash-lime mixtures. *Journal of Materials in Civil Engineering*, 23(4), 432-440. https://doi.org/10.1061/(ASCE)MT.1943-5533.0000186

Consoli, N.C., Marques, S.F.V., Floss, M.F., & Festugato, L. (2017). Broad-spectrum empirical correlation determining tensile and compressive strength of cement-bonded clean granular soils. *Journal of Materials in Civil Engineering*, 29(6), 06017004. https://doi.org/10.1061/(ASCE)MT.1943-5533.0001858

Consoli, N.C., Winter, D., Leon, H.B., & Scheuermann Filho, H.C. (2018a). Durability, strength, and stiffness of green stabilized sand. *Journal of Geotechnical Geoenvironmental Engineering*, 144(9), 04018057. https://doi.org/10.1061/(ASCE)GT.1943-5606.0001928

Consoli, N.C., Marin, E.J.B. Samaniego, R.A.Q., Heineck, K.S., & Johann, A.D.R. (2018b). Use of sustainable binders in soil stabilization. *Journal of Materials in Civil Engineering*, 31(2), 06018023. https://doi.org/10.1061/(ASCE)MT.1943-5533.0002571

Consoli, N.C., Carreta, M.S., Leon, H.B., Scheuermann Filho, H.C., & Tomasi, L.F. (2019). Strength and stiffness of ground waste glass-carbide lime blends. *Journal of Materials in Civil Engineering*, 31(10), 06019010. https://doi.org/10.1061/(ASCE)MT.1943-5533.0002862

Consoli, N.C., Festugato, L., Scheuermann, H.C., Miguel, G.D., Neto, A.T., & Andreghetto, D. (2020a). Durability assessment of soil-pozzolan-lime blends through ultrasonic pulse velocity test. *Journal of Materials in Civil Engineering*, 32(8), 04020223. https://doi.org/10.1061/(ASCE)MT.1943-5533.0003298

Consoli, N.C., Carretta, M.S., Festugato, L., Leon, H.B., Tomasi, L.F., & Heineck, K.S. (2020b). Ground waste glass-carbide lime as sustainable binder stabilizing three different silica sands. *Géotechnique*, 1-14. Advance online publication. https://doi.org/10.1680/jgeot.18.P.099

Cordeiro, C.G., Toledo Filho, R.D., Tavares, L.M., Fairbairn, E.N.R. & Hempel, A. (2011). Influence of particle size and specific surface area on the pozzolanic activity of residual rice husk ash. *Cement and Concrete Composites*, 33(5), 529-534. https://doi.org/10.1016/j.cemconcomp.2011.02.005

Day, D.E., Malish, W.R., & Wixsom, B.G. (1970). Improved bonding of waste glass aggregate with bituminous binders. *American Ceramic Society Bulletin*, 49(12), 1038-1041.

Diambra, A., Ibraim, E., Peccin, A., Consoli, N.C., & Festugato, L. (2017). Theoretical derivation of artificially cemented granular soil strength. *Journal of Geotechnical and Geoenvironmental Engineering*, 143(5), 04017003. https://doi.org/10.1061/(ASCE)GT.1943-5606.0001646

Ekinci, A., Scheuermann Filho, H.C., & Consoli, N.C. (2019). Copper slag-hydrated lime-Portland cement stabilized marine deposited clay. *Proceedings of the*

Institution of Civil Engineers - Ground Improvement, 1-30. https://doi.org/10.1680/jgrim.18.00123

Habert, G. (2014). *Assessing the Environmental Impact of Conventional and 'Green' Cement Production*. Woodhead Publishing Limited.

Henzinger, C., Schuhmacher, S.A., & Festugato, L. (2018). Applicability of the porosity/binder index to nonhomogeneous mixtures of fine-grained soil with lignite fly ash. *Journal of Materials in Civil Engineering*, 30(9), 06018013. https://doi.org/10.1061/(ASCE)MT.1943-5533.0002447

Hughes, C.S. (1990). Feasibility using recycled glass in asphalt - report VTRC90-R3. *Virginia Transportation Research Council, Charlottesville, VA.*

Igwe, O., Sassa, K., & Wang, F. (2006). The influence of grading on the shear strength of loose sands in stress-controlled ring shear tests. *Landslides*, 4(1), 43-51. https://doi.org/10.1007/s10346-006-0051-2

Ingles, O.G., & Metcalf, J.B. (1972). *Soil Stabilization: Principles and Practice*. Butterworths.

Jony, H.G., Al-Rubaie, M.F., & Jahad, I.Y. (2010). The effect of using glass powder filler on hot asphalt concrete mixture properties. *Engineering and Technology Journal*, 29(1), 44-57.

Krim, A., Arab, A., Chemam, M., Brahim, A., Sadek, M., & Shahrour, I. (2017). Experimental study on the liquefaction resistance of sand-clay mixtures: Effect of clay content and grading characteristics. *Marine Georesources & Geotechnology*, 37(2), 129-141. https://doi.org/10.1080/1064119X.2017.1407974

Ladd, R.S. (1978). Preparing test specimens using under-compaction. *Geotechnical Testing Journal*, 1(1), 16-23. https://doi.org/10.1520/GTJ10364J

Massaza, F. (2004). Pozzolana and pozzolanic cements. In *Leas Chemistry of Cement and Concrete* (pp. 471-631). Hewlett.

Malik, M.I., Bashir, M., Amad, S., Tariq, T., & Chowhary, U. (2013). Study of concrete involving use of waste glass as partial replacement of fine aggregates. *IOSR Journal of Engineering*, 3(7), 8-13.

Metwally, I.M. (2007). Investigations on the performance of concrete made with blended finely milled waste glass. *Advances in Structural Engineering*, 10(1), 47-53. https://doi.org/10.1260 %2F136943307780150823

Mitchell, J.K. (1981). Soil improvement: State-of-the-art report. *Proc. 10th International Conference on Soil Mechanics and Foundation Engineering*, *Stockholm*. Publications Committee of X ICSMFE, 509-565.

Montgomery, D.C. (2009). *Design and Analysis of Experiments*. John Wiley & Sons.

Mohajerani, A., Vajna, J., Cheun, T.H.H., Kurmus, H., Arulrajah, A., & Horpibulsuk, S. (2017). Practical recycling applications of crushed waste glass in construction materials: a review. *Construction and Building Materials*, 156(15), 443-447. https://doi.org/10.1016/j.conbuildmat.2017.09.005

Music, S., Filipovic-Vincekovic, N., & Sekovanic, L. (2011). Precipitation of amorphous SiO2 particles and their properties. *Brazilian Journal of Chemical Engineering*, 28(1), 89-94.

Park, S., & Lee, B. (2004). Studies on expansion properties in mortar containing waste glass and fibers. *Cement and Concrete Research*, 34(7), 1140-1152. https://doi.org/10.1590/S0104-66322011000100011

Pattengil, M., & Shutt, T. (1973). Use of ground glass as pozzolan. *Proc. Symposium on Utilization of Waste Glass in Secondary Products*, *Albuquerque*. Univ. of New Mexico.

Rangaraju, P.R., Rashidian-Dezfouli, H., Nameni, G., Amekuedi, G.Q. (2016). Properties and performance of ground glass fiber as a pozzolan in Portland cement concrete. *Proc. 11th International Concrete Sustainability Conference*, *Washington*. National Ready Mixed Concrete Association, 1-12.

Saldanha, R.B., & Consoli, N.C. (2015). Accelerated mix design of lime stabilized materials. *Journal of Materials in Civil Engineering*, 28 (3), 06015012. https://doi.org/10.1061/(ASCE)MT.1943-5533.0001437

Saldanha, R.B., Mallmann, J.E.C., & Consoli, N.C. (2016). Salts accelerating strength increase of coal fly ash-carbide lime compacted blends. *Géotechnique Letters*, 6, 23-27. https://doi.org/10.1680/jgele.15.00111

Saldanha, R.B., Scheuermann Filho, H.C., Mallmann, J.E.C., Consoli, N.C., & Reddy, K.R. (2018). Physical-mineralogical-chemical characterization of carbide lime: An environment-friendly chemical additive for soil stabilization. *Journal of Materials in Civil Engineering*, 30 (6), 06018004. https://doi.org/10.1061/(ASCE)MT.1943-5533.0002283

Sales, R.B.C., Sales, F.A., Correa, E.C.S., Patricio, P.S.O., Mohallem, N.D.S., & Aguilar, M.T.P. (2015). Study of the influence of chemical composition on the pozzolanicity of soda-lime glass microparticles. *Materials Research*, 18(2), 43-47. http://dx.doi.org/10.1590/1516-1439.343914

Walker, R., & Pavía, S. (2011). Physical properties and reactivity of pozzolans, and their influence on the properties of lime-pozzolan pastes. *Materials and Structures*, 44, 1139-1150. https://doi.org/10.1617/s11527-010-9689-2

List of symbols

S: soil content

CL: carbide lime content

C_U: uniformity coefficient

C_c: curvature coefficient

GG: ground glass powder content

q_u: unconfined compressive strength

R^2: coefficient of determination

V: total volume of specimen

V_{GG}: volume of ground glass powder
V_{CL}: volume of carbide lime
η: porosity
B_{iv}: volumetric binder content (expressed in relation to the total specimen volume) which means the volumetric content of ground glass plus carbide lime
η/B_{iv}: porosity/binder index
γ_d: dry unit weight
γ_S: unit weight of soil grains
γ_{CL}: unit weight of carbide lime grains
γ_{GG}: unit weight of ground glass powder

Soils and Rocks
An International Journal of Geotechnical and Geoenvironmental Engineering
www.soilsandrocks.com
ISSN 1980-9743
ISSN-e 2675-5475

Mechanical and environmental performance of polymer stabilized iron ore tailings

Andressa de Araujo Carneiro[1,2,#], Michéle Dal Toé Casagrande[1]

Note

Keywords
Iron mine tailings
Polymer
Stabilization
Strength parameters

Abstract
The huge amounts of residues generated by the mining industry have caused a number of environmental problems, not only in Brazil but worldwide. During the extraction of iron ore, the process of beneficiation produces a considerable volume of tailings, making the disposal of these materials a challenge for the environmental and geotechnical engineering. In this context, numerous researchers have been looking for alternative solutions for the disposal and use of these materials, focusing on stabilization, improvement or reinforcement in geotechnical works. Polymers are currently being increasingly used as a stabilizer for sandy soils, due to their stable chemical property and shorter curing time, compared to traditional stabilizers, such as cement, lime, fly ash and bituminous materials. This research presents the study of improvement techniques of iron ore tailings by insertion of a polymer. The mechanical and environmental properties of the composite are analyzed, aiming at the application in geotechnical structures, such as landfills and slopes. The results show that the use of this composite is interesting from the technical, economic, structural and environmental safety point of view.

1. Introduction

Huge amounts of residues generated by the mining industry have caused a number of environmental problems, not only in Brazil but worldwide. During extraction of iron ore, process of beneficiation produces a considerable volume of tailings, making the disposal of these materials a challenge for the environmental and geotechnical engineering. However, the characteristics of mine tailings limit direct use in structures, due to structural and environmental restrictions. In recent years, the implementation of alternative materials associated with tailings has guided several geotechnical works, for stabilization, improvement or reinforcement, making it a topic of great interest.

Festugato et al. (2015), Consoli et al. (2017), Sotomayor (2018) among others studied efficient methods of reinforcing ore tailings by creating a composite that meets engineering requirements. These authors found that the insertion of fibers in the tailings brings benefits to the strength parameters of the matrix.

On the other hand, the use of polymers in the formation of composites with tailings is an interesting stabilization alternative. The references show that, when correctly applied and using an adequate dosage, the polymer becomes a stabilizing agent in non-paved roads, landfills, protection and stability of slopes, erosion in paving layers, due the agglutination of grains and improving the stability of the soil matrix.

Mirzababaei et al. (2017) analyzed the effect of polymers using a non-confined compressive strength test in a sample of clay soil. Xing et al. (2018) and Liu et al. (2018, 2019) investigated the behavior of sand soil adding polymer in wet and dry conditions. Barreto et al. (2018) analyzed the improvement of sand soil with use of butadiene and modified styrene copolymer (XSBR). Okonta (2019) analyzed application of acrylic polymeric solution at different curing times, percentages and temperatures for a soil characteristic of the South African region. Lee et al. (2019) investigated the feasibility of applying biopolymer (xanthan gun), to stabilize local soil, for construction of the road in Sri Lanka, through the unconfined compression test. Silva (2020) conducted experimental studies a sand soil improved with polymeric solution as a stabilizing agent. Li et al. (2020) investigated the shear behavior of the polymer-bentonite interface.

The above and recent research results show that polymeric solutions can effectively improve the strength, de-

[#]Corresponding author. E-mail address: andressa.deac@gmail.com.
[1]Departamento de Engenharia Civil e Ambiental, Universidade de Brasília, Brasília, DF, Brazil.
[2]Departamento de Recursos Hídricos, Geotecnia e Saneamento Ambiental, Universidade Federal do Piauí, Teresina, PI, Brazil.

Submitted on April 21, 2020; Final Acceptance on June 17, 2020; Discussion open until March 31, 2021.
DOI: https://doi.org/10.28927/SR.434679

spite physical property of composite is rarely studied. As the polymer is a chemical material, it can cause changes in the matrix. That is why studying the mechanical behavior of the composite, through laboratory tests, is so important to understand and apply these new geotechnical materials in structures.

In this context, this research presents the study of improvement techniques of iron ore tailings by insertion of a polymer. The mechanical properties of the composite are analyzed, aiming at the application in geotechnical structures, such as landfills and slopes. The results show that the use of this composite is interesting from the technical, economic, structural, and environmental safety point of view.

2. Material and methods

The iron ore tailings analyzed are sourced in the raising dikes, compacted by the passage of equipment over a dam. Samples deformed, presenting moisture of 14 %, were collected in different positions, 50 m away from the central axis.

The polymer used is an acrylic copolymer of organic styrene, obtained by random polymerization reactions through an anionic aqueous emulsion presenting density of 0.98-1.04 g/cm^3 and pH of 8.0-9.0.

2.1 Geotechnical characterization

Physical characterization tests were performed by Sotomayor (2018) to obtain index properties such as natural specific weight and grain density. The maximum dry weight and optimal moisture were obtained through the compaction test with Proctor Normal energy in samples with and without polymer to verify the influence of the additive.

In all tests, the mixing of the polymer with the tailings was done in the same way. A homogeneous solution containing 25 % of polymer and 75 % of water (using the proportion 1:3 in volume) was mixed with the tailing and molded into samples. The abbreviation T and TP was used to refer, respectively, to tailing and tailing -polymer.

After obtaining the maximum dry weight and optimal moisture, the specimens used to perform the shear test were molded in a metal mold square of transversal section, with sides of 60 mm and height of approximately 25 mm. The quantity of material was calculated according to the physical parameters and volume of the mold.

It must be noted that by the moment when occurs the mixture of tailing and polymeric solution a pasty consistency is verified. Then, the composite stiffens in contact with air and over the days of curing. The curing of the samples occurred in room temperature, approximately 26 °C, which was done to analyze the mechanical behavior of the tailings and the influence of the additive over time, considering the same conditions.

After conventional direct shearing test, a sheared plane with polished surface test was performed. Last one was carried out by a "polishing" using a thin line of resistant nylon through the sheared surface, between both boxes, in the direction of the shearing plane. After separating the boxes the polishing of the surfaces was done, always in the direction of the shearing plane. The complete test was performed again, since the stage of densification until shearing. The samples were densified during the necessary period for the occurrence of 100 % of the primary densification, being applied containment stresses of 50 kPa, 100 kPa, 200 kPa and 400 kPa for the construction of the Mohr-Coulomb shear strength envelope. The maximum horizontal displacement tested was 8 mm, in function of the equipment characteristics.

The curing periods analyzed were of 0, 7, 14 and 28 days for both tests, conventional direct shearing and sheared plane with polished surface. The analysis of the material resistance was performed using also the conventional direct shearing and sheared plane with polished surface.

2.2 Complementary tests

For a better understanding of the composite behavior, complementary tests were performed, such as hydraulic, chemical-environmental and mineralogical tests.

Test of permeability was performed using the constant and variable permeameter for the pure tailing and composite, respectively. The water absorption test, according the Brazilian Standard ABNT NBR 13555 (ABNT, 2012), was also performed to verify the reduction of voids in the tailing after the insertion of the polymer.

The total suction was determined by the use of a psychrometer (WP4C), according to ASTM D6836-16 (ASTM, 2016). The test was performed with two daily readings, at 9 a.m. and another reading at 6 p.m. The readings occurred with the composite and pure tailing, both with 10 % of moisture content. The objective of the test was not the obtainment of the material characteristic curve, but understanding, over time, the increase of suction as the curing of the composite advances.

To verify if the polymer had leaching potential, it was performed leaching test according to the Brazilian Standard ABNT NBR 10005 (ABNT, 2004). X-ray Diffraction Analyses (XRD) were performed with the Rigaku Ultima IV equipment. Energy dispersive spectroscopy (EDS) and scanning electron microscopy (SEM) were performed using the JEOL JSM 7100F Scanning Electron Microscope with acceleration voltage of 30 KV, 3 nm resolution, up to 300,000 X with EDS X-ray microanalysis system. Before being tested, the samples were submitted to the metallization process by high vacuum evaporation. This procedure consists of depositing an ultrafine coating of electrically conductive material on the samples, in which case gold was used. The tests were performed for the microstructural characterization of the tailing-polymer composite with 28 days of curing and pure tailing.

3. Results

3.1 Geotechnical characterization

The specific mass of mine tailings is generally greater than most natural soils, since in the tailings it is found a concentration of oxides whose specific mass is greater than that of the dominant minerals in natural soils, as the quartz and kaolinite. The particles of iron present density of solids of approximately 5.25 g/cm^3, while quartz grains are characterized by presenting a density of solids of about 2.65 g/cm^3.

Figure 1 presents the particle-size distribution of the iron ore tailings used in the research. The tailing of iron ore studied has density of grains of 2.89 g/cm^3 and it is classified as silt sand according to Unified Soil Classification System (USCS).

Figure 2 presents the compaction curves of the studied materials. After polymer addition, the unit weight increases and the moisture content decreases. Therefore, the polymer works as a particle binder, reducing the space of voids.

Figure 3 presents the curves of shear stress by horizontal displacement of pure tailing and composites studied. The applied stresses were of 50 kPa, 100 kPa, 200 kPa and 400 kPa to tailing, T, and tailing -polymer, TP, in respectively separated with curing periods of 0, 7, 14 and 28 days.

After the polymer insertion, a gain of shearing strength of the iron ore tailing was observed for all mixtures and stresses tested. For the samples with 0 days of curing, there was no significant decrease in the post-peak, tending to a curve stabilization indicating the strength after shear. Considering the samples submitted to different curing periods, it was verified an increase of resistance to shearing for all composites, observing a more significant peak for the samples with longer period of curing and for high stresses.

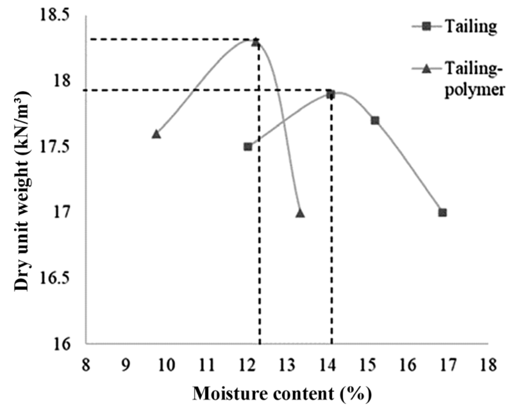

Figure 2. Compaction curves.

Tests performed on shearing plan with polished surface were performed after the conventional test. The results for each period of curing of 0, 7, 14 and 28 days are presented in Figure 4.

Considering the tests with shearing plan polished surface, there was not a peak on the curves, since the samples were already sheared. A greater resistance for the composites submitted to greater normal stress was noticed; however, there was not a significant change in strength over the curing time. In other words, after the shearing, there is no strength reduction and the change in the composite only occurred during the initial rupture, indicating the inexistence of a greater instability in the samples tested with polished surface.

Figure 5 shows the curves of vertical displacement vs. horizontal displacement for composites tailing-polymer (TP) with 0 and 28 days of curing at the conventional shear test and at shearing plan polished surface test.

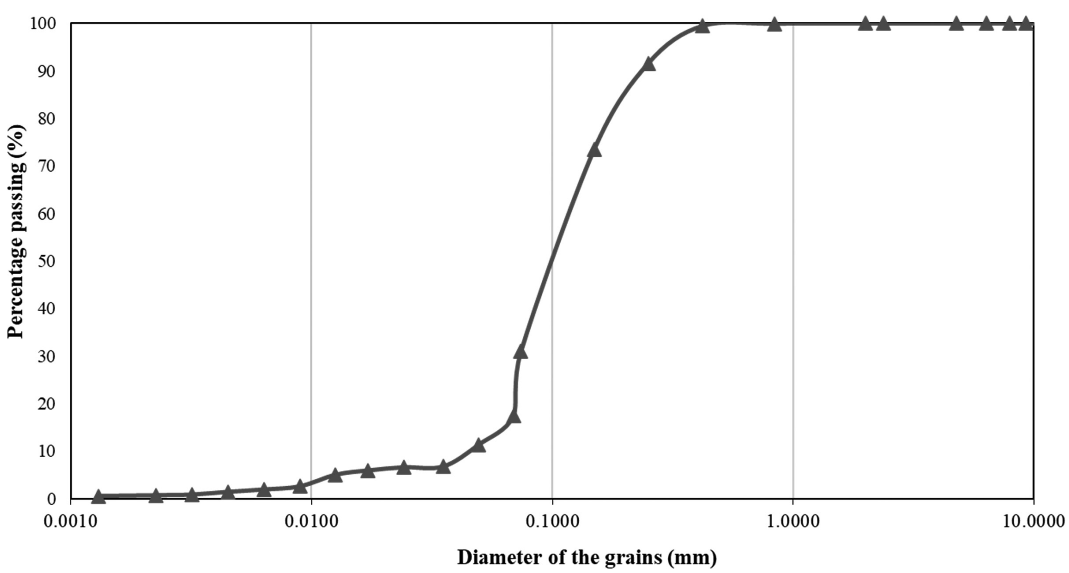

Figure 1. Granulometric distribution of the iron ore tailings.

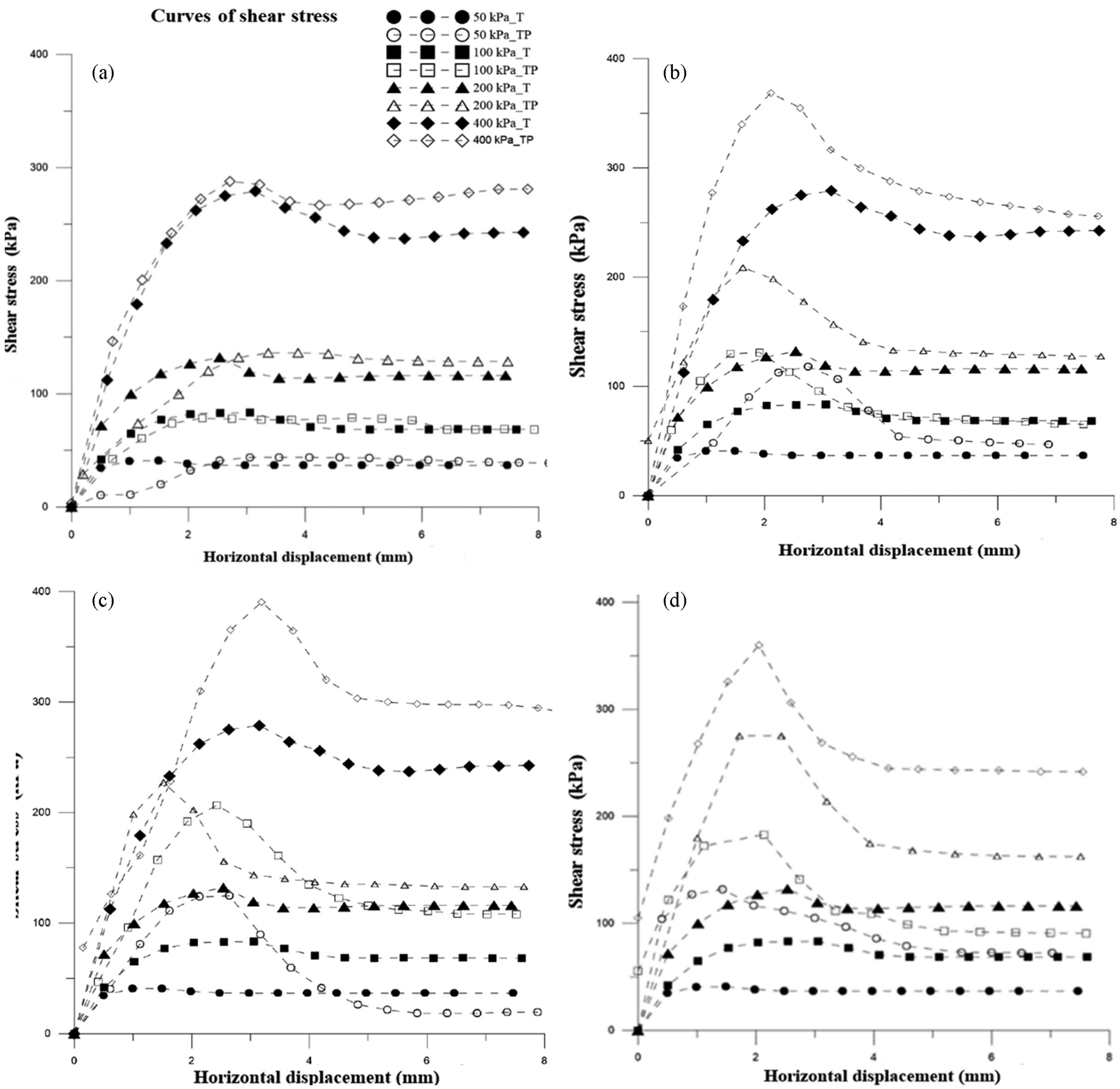

Figure 3. Shear stress-horizontal displacement responses: (a) 0 days; (b) 7 days; (c) 14 days and (d) 28 days.

Figure 5a indicates that the behavior of the composite with no curing showed an expansion, mainly, for higher normal stress. When cured, the composites tended to be compressed, but the tendency is suppressed by 4 mm. Afterwards, there is a stabilization until the end of the test for all normal vertical stresses. The curves in Figure 5b show a similar trend for all normal vertical stresses showing some homogeneity in the behavior of the composite with a polished surface.

Figure 6 presents the shear strength envelopes obtained at peak and residual stresses during the direct shearing test of the tailing -polymer, TP. The residual stresses refer to the horizontal displacement of 7 mm.

An increase in the shear strength parameters for the composites was observed according to the curing period. Considering the composite without period of curing, no significant change was not found. This was expected given that by adding the polymer the sample had a higher moisture content, therefore reducing its resistance.

For the peak strength, it is observed an increase on the values of the effective angle of friction and apparent cohesion, mainly for the greatest curing periods. The apparent cohesion increased considerably over the curing period, which was expected when the polymer was added.

The friction angle and cohesive intercept obtained by Silva (2020) using soil-polymer composite with the same

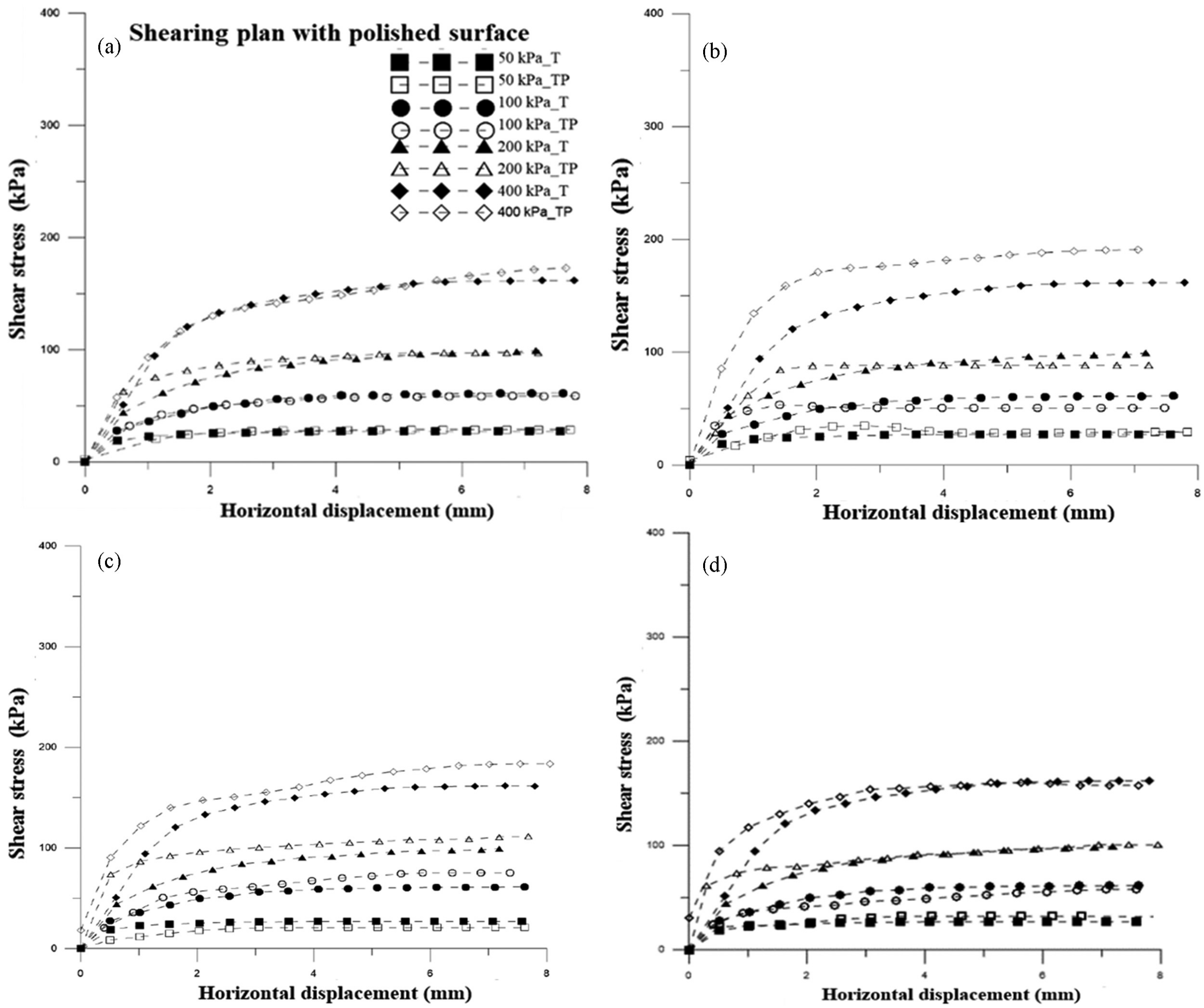

Figure 4. Shear stress-horizontal displacement responses for shearing plan with polished surface: (a) 0 days; (b) 7 days; (c) 14 days e (d) 28 days.

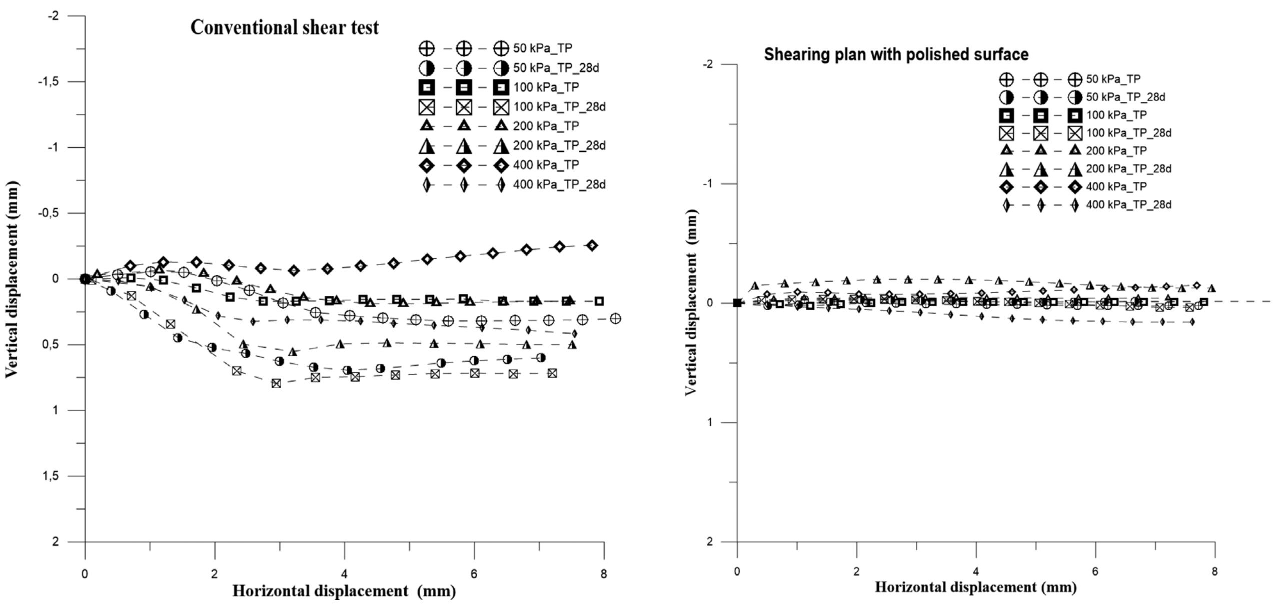

Figure 5. Curves vertical displacement vs. horizontal displacement: (a) conventional test and (b) polished surface.

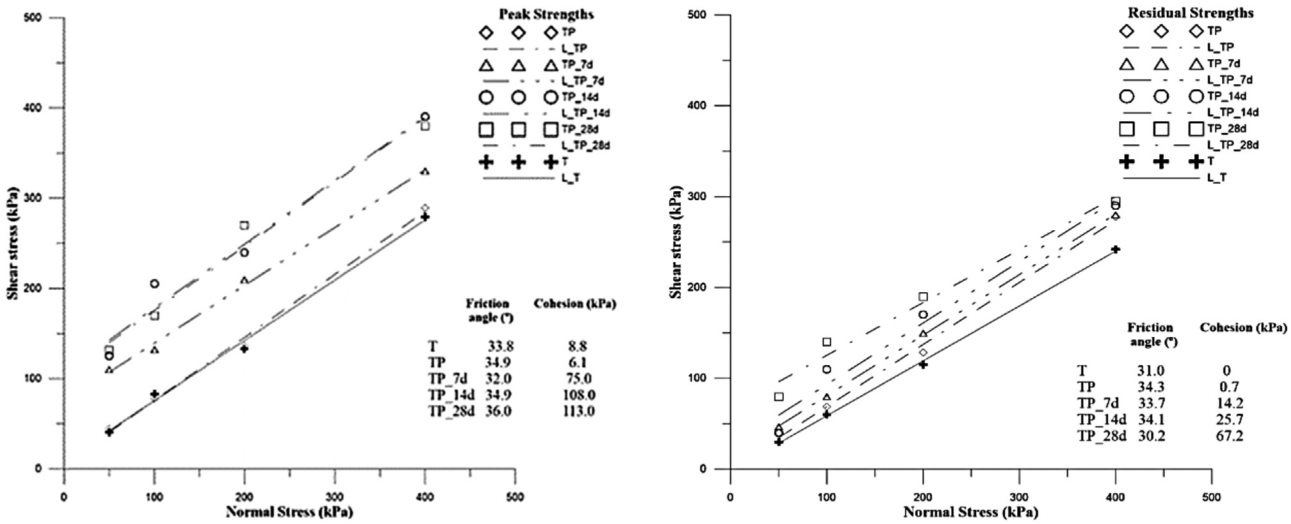

Figure 6. The Mohr failure line (a) peak strength and (b) residual strength.

proportion of the present research increased, respectively, from 31.9° to 32.9° and from 4.05 kPa up to 169.67 kPa, with 30 days of curing. The values are similar to those found in the current study, which indicates similar performance of the polymer when added to the soil or iron ore tailings.

Considering the residual strength, there was an increase on the friction angle and apparent cohesion, showing that the polymer insertion was positive for the samples submitted to the conventional shearing test.

The shear strength envelopes obtained with the direct shearing tests on tailing -polymer samples, TP, with polished surface are presented in Figure 7. As reported previously, the samples were already sheared, thus there was not discrepancy in the values of the parameters of resistance for the peak and residual strength.

Regarding the samples with polished surface, there was a reduction on the effective angle of friction, since the samples were already sheared, however, the apparent cohesion increases. Thus, even with previous shearing, the grains remained with a certain adherence, hence it is observed an improvement of one shear strength parameter.

3.2 Complementary tests

The permeability coefficient is a necessary parameter to be analyzed, mainly regarding the improvement and stabilization of tailing. The values of the permeability coefficient of the tailing with 0 days and of the tailing-polymer composite with 28 days of curing were 2.96×10^{-5} and 6.08×10^{-7} m/s, respectively. The polymer significantly reduced the iron ore tailing permeability. Therefore, the action of the polymer application in the tailing permeability.

Due the significant reduction of permeability, it was verified the absorption rate of water of the composite with 28 days of curing. The temperature of the test was main-

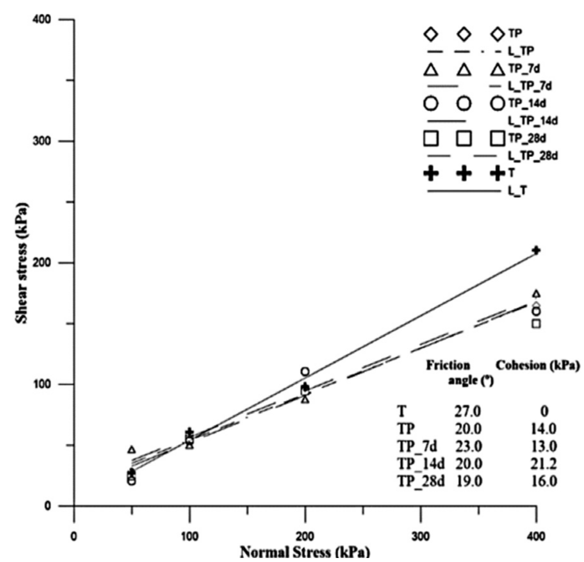

Figure 7. The Mohr failure line in polished.

tained at 25 °C and an absorption rate of 18.37 % in the composite was observed, which occurs because the polymer stiffen the material, reducing the water percolation.

The psychrometer test (WP4C) was conducted to check the hypothesis that the gain of shear strength is only associated to the increase of suction over the curing period. In day 0, with no curing of the tailing-polymer composite, the suction was of 95.37 MPa. The day 0 for the tailing added with water resulted in a value of 67.84 MPa. There was observed a stabilization of the values of total suction, what is seen on day 28 when the tailing-polymer composite resulted in a value of 98.53 MPa. The final measurement for the pure tailing occurred on day 4 of curing, until near total evaporation of water and the last possible reading obtained a value of 92.5 MPa. The composite with short period of curing already presented stabilization of the values of suction, while the tailing with water had greater humidity and thus lower value of suction.

It is possible to affirm that the curing outdoor would cause the shear strength to increase, since the moisture content is decreases and, thus, the suction increases. However, it was proved that the addition of polymer acted more intensely on the increase of shear strength, given that there was no significant change of the composite tailing-polymer suction with increase of the curing period.

Any contamination that may occurs will be through process of infiltration. The water when initially touches the composite infiltrates it and may cause contamination. Such process may be called leaching. The water of the tailing-polymer composite with 28 days of curing was collected and chemically analyzed. Table1 lists the chemical elements in the samples analyzed.

Evaluating the data of leachate, through the resolution CONAMA 420 (CONAMA, 2009), which regulates the maximum values allowed and advisors for soil and groundwater, the maximum values allowed (MVA) for dissolved copper in groundwater is of 2 mg/L and for tailing-polymer composite is less than 0.1 mg/L.

Another element described in the norm is aluminum, its MVA being 3.5 mg/L, the value of the composite is inferior than 1 (0.0018 mg/L), according to the resolution.

The last element cited in the resolution is manganese, whose MVA is 0.4 mg/L, thus there is no coherence between that and the value found for the composite, since it was found in larger amounts. However, the manganese MVA may pose risk to human health when consumed, not to direct contamination of natural elements.

Considering the leachate as an effluent of a polluting source, the Section II Article 16 of the resolution determines the conditions and procedures for the directly discharge of effluents from any polluting source at the receptor body. Thus, according to the resolution, all elements from both leachates are possible to be directly discharged to the hydric body. The MVA of all analyzed elements were within the values specified by the regulation.

Considering the application of polymer for the tailing stabilization, even when the polymer is applied to an area of environmental preservation, there would not be contamination of water bodies.

Table 1. Values of leaching of the composite tailing-polymer.

Element	Values
pH	8.94
Total nitrogen (mg/L)	1.98
Iron (mg/L)	0.1554
Copper (mg/L)	< 0.1000
Manganese (mg/L)	0.7505
Aluminum (mg/L)	< 0.0018

X-ray Diffraction (XRD) analysis was conducted to evaluate the possibility any geological alteration of the soil caused by the polymer addition. Figure 8 presents the diffractogram referring to the XRD test of the pure tailing and tailing-polymer composite with 28 days of curing. Figure 9 presents the microscopic images of pure tailing and tailing-polymer composite.

With the use of phase analysis via XRD one can note that the iron ore tailing studied is basically composed by minerals of quartz (SiO_2), goethite ($FeO(OH)$), hematite (Fe_2O_3), kaolinite ($Al_2Si_2O_5(OH)_4$)), and other minerals in smaller quantities, independently of the addition of polymer (Figure 10).

An increase of the hematite proportion is observed in the diffractogram of the composite. It is worth mentioning that hematite is known by its thin texture and as a cementing agent for the formation of aggregate. It is considered that the increase of hematite occurs due the presence of the polymer in the matrix, in nodular format and also as a cementing agent for the grains, which presents properties similar to hematite.

Using the optical microscopy, it is verified that the grains of iron ore tailing are looser and it is identified the light and dark grains, probably minerals of quartz and hematite, as indicated in the test XRD. In Figure 9 is possible

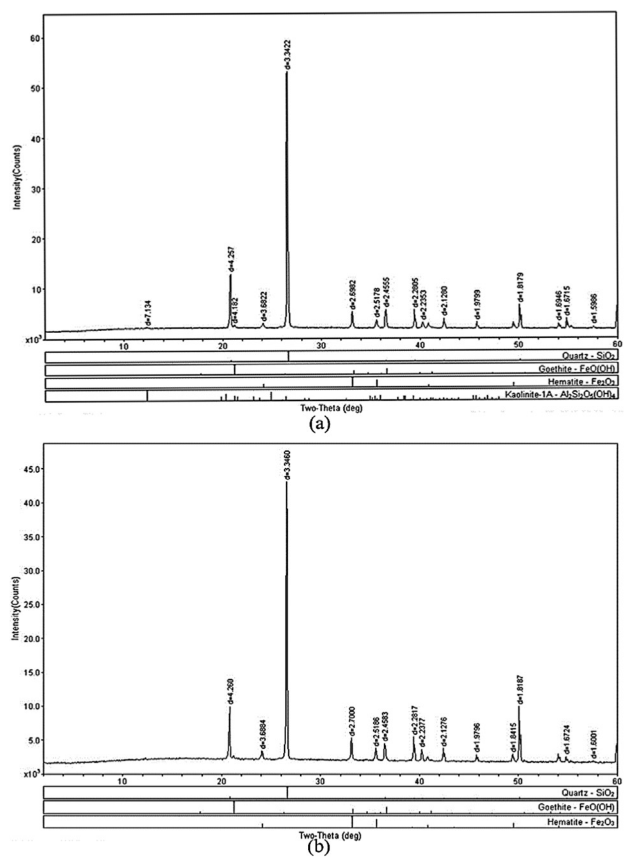

Figure 8. Test of XRD (a) pure tailing and (b) tailing-polymer composite.

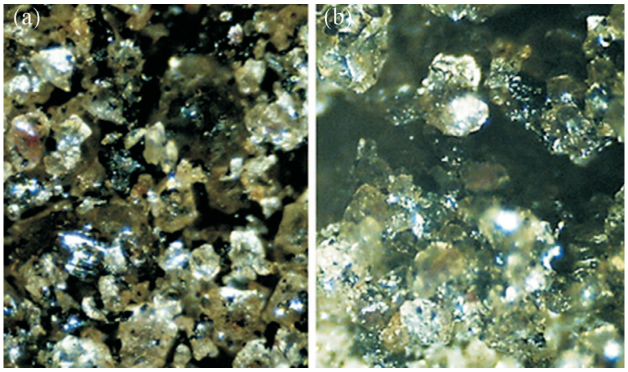

Figure 9. Images obtained by the microscopy increase 40 x: (a) pure tailing and (b) tailing-polymer composite.

to respectively verify the pure tailing and tailing-polymer composite with 28 days of curing.

Considering the images obtained by the microscopy, it is possible to note the bond of the tailing grains when the polymer is added, a brighter appearance may also be noted on the grains, similar to a glue or pellicle that envelopes the grains.

Figure 10 shows the main chemical elements found in the pure tailing and in the tailing-polymer composite with 28 days of curing, using the EDS test.

The tests of EDS were performed to confirm what was found by the XRD test. The considerable difference is that the XRD performed show chemical elements as minerals, to geologically classify them, while the EDS scans constitutive

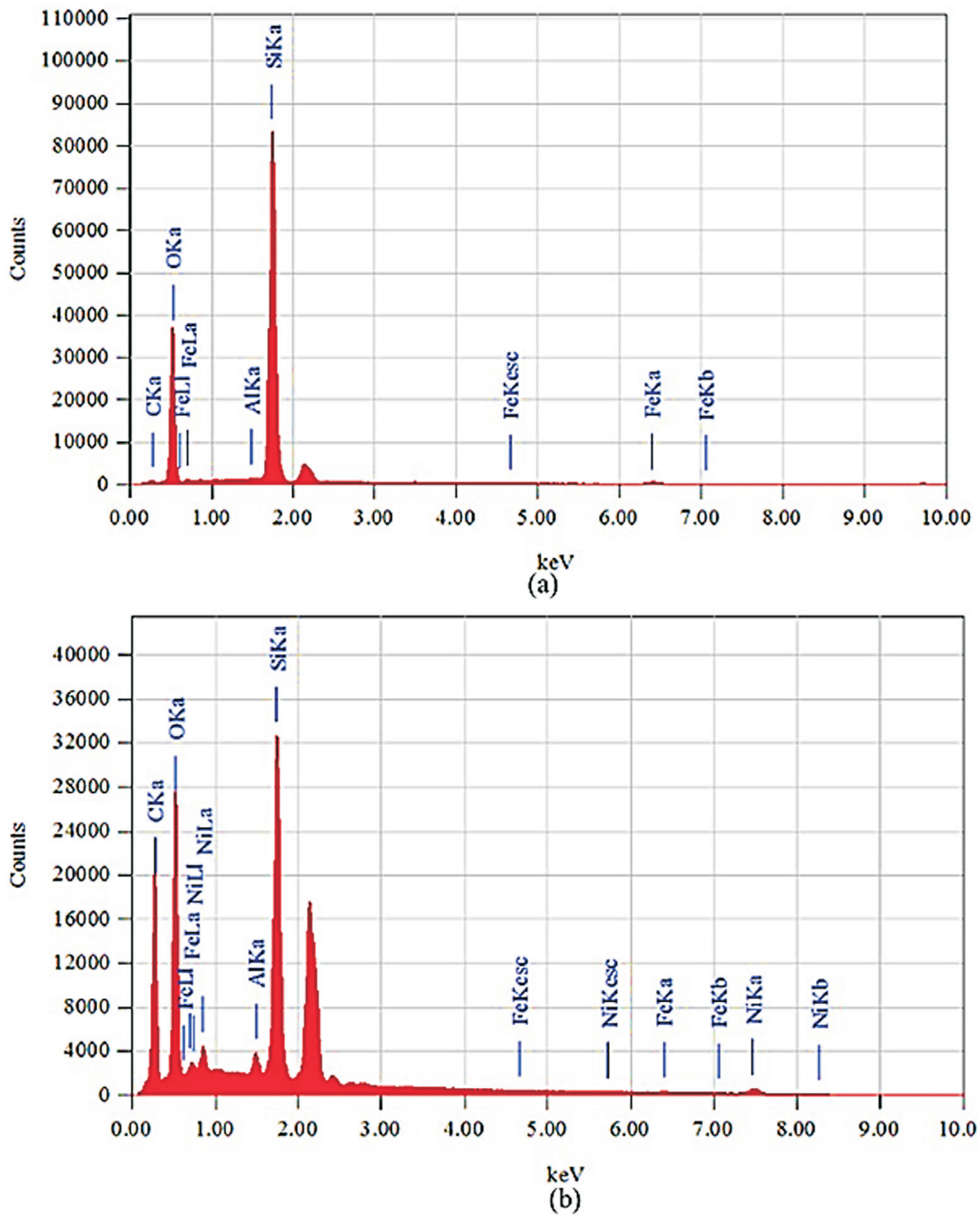

Figure 10. EDS (a) pure tailing and (b) tailing-polymer composite.

chemical elements. The tests of EDS detected chemical elements of silicon (Si), Iron (Fe), Carbon (C) and Oxygen (O). With the addition of polymer, an even greater increase in these chemical elements and a reduction in silicon was observed. The letter K is not related to the chemical element, but with the manner that these chemical elements were identified by the method. Thus, although the data interpretation, both samples exhibit similar chemical elements.

Obtained with the use of using scanning electron microscopy (SEM) for the microscopical characterization, Figure 11 exhibits the distribution of voids in the iron ore tailing studied in its pure form.

It is observed in Figure 11a that the grains are loosen and with a number of sizes. It is not observed an element that bonds the grains, the smaller grains are close to the bigger ones, as if they occupy the void spaces (Figure 11a). The existing voids and the grain surface are well seen in Figure 11b.

In Figure 12, using the analysis from the scanning electron microscopy for the microscopical characterization, it is possible to observe in the iron ore tailing studied the voids distribution after the insertion of the polymer solution and 28 days of curing.

Based on Figure 12, it is possible to verify that, after the addition of polymeric solution insertion, a greater bond occurred between the grains. Figure 12b shows that, in certain grains, their boundaries cannot be seen due to the bond between the particles. It is considered that these bonds and meniscus arise from the increment of polymer, and over the curing period it externs the grains bonding them and causing the cementation of the particles.

4. Conclusions

This paper emphasized the main results obtained through tests of direct shearing using polymer stabilized iron ore tailings for application in geotechnical works such as landfills and slopes. For the mechanic tests, a mix of the tailing a solution containing 25 % of polymer and 75 % of water was evaluated. Chemical and mineralogical tests

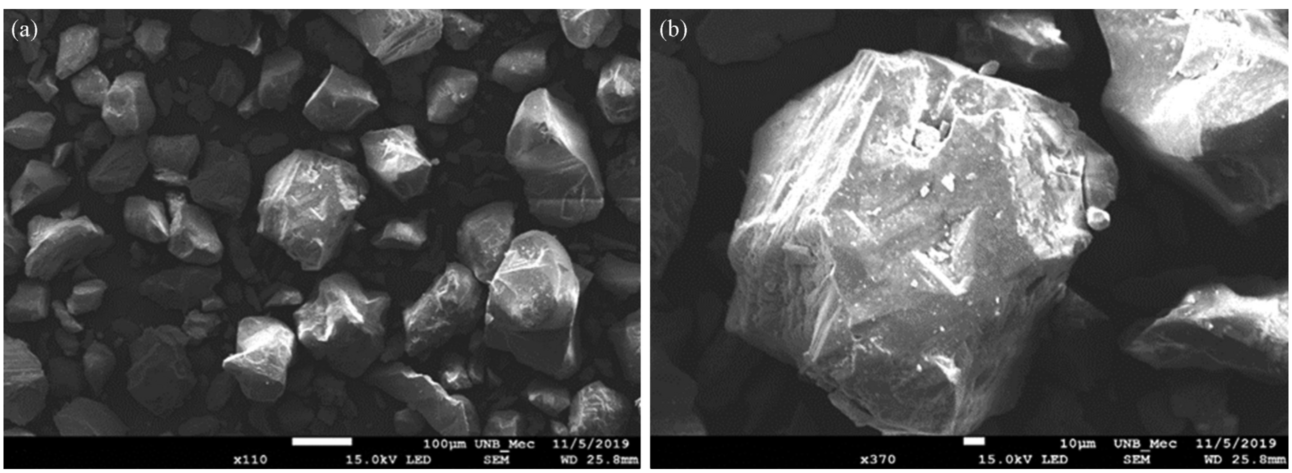

Figure 11. SEM (a) pure tailing grains increase 110 x e (b) increased grain surface 370 x.

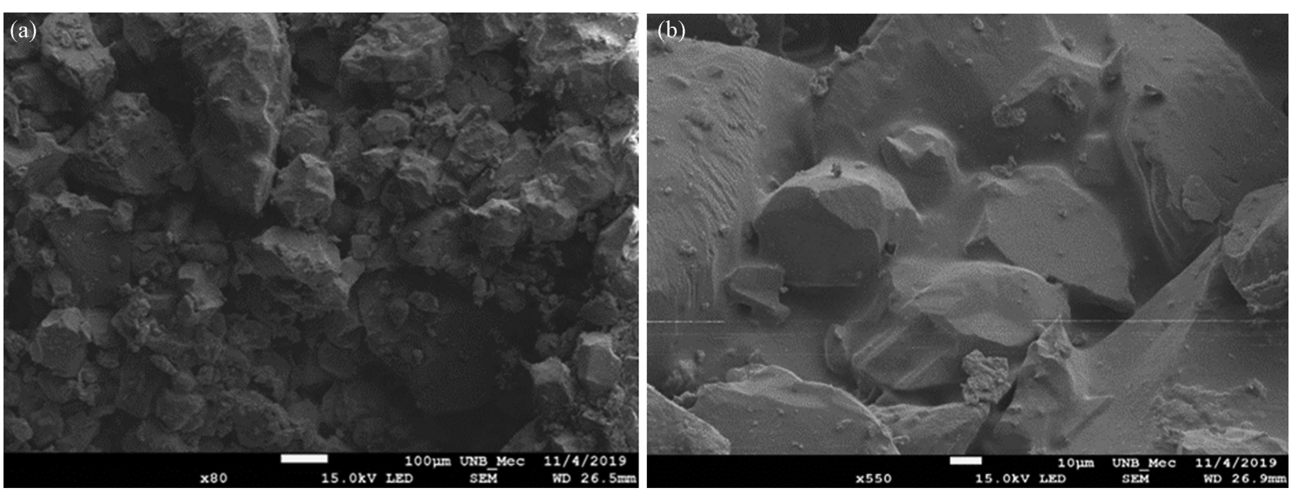

Figure 12. SEM (a) tailing-polymer composite grains increase e 80 x (b) tailing-polymer composite grains increase 550 x.

were performed to better understand the behavior of the studied material.

The analysis allowed a better understanding of the mechanical behavior of the tailings and the influence of the additive over time. However, more research is necessary for a further comprehension of the behavior of this composite.

According to the research performed, regarding the mechanical and environmental behavior of the iron ore tailing composite with polymer insertion, it can be concluded that:

- The addition of polymer to the iron ore tailing is viable given the improvement of the shear strength as the curing period of the composites increase. The composite microstructure shows that there was cementation between the grains, by polymer addition, forming a film on the grains and bonding them;
- A reduction of permeability was verified for the tailing-polymer composite when compared to the pure tailing due the fact that the polymeric solution fills the voids between the grains;
- The resistance gain of the composite due only to the suction increase is discarded for longer curing days, since suction was maintained nearly constant during 30 days, and the values of suction were close to the tailing without additive;
- The analysis of the leachate material from the tailing-polymer composite did not present exceeding values of chemical elements that could cause contamination to the environment;
- There is technical feasibility for the application of the tailing-polymer composite in geotechnical works, as landfills and slopes, thus presenting considerable technical, economical, security, maintenance reduction and environmental viability, which grants a more proper end to this material.

Acknowledgments

The authors thanks Waterflows Bioquímica do Brasil for supplying the Polymer studied.

References

ABNT NBR 10005. (2004). Procedure for Obtention Leaching Extract of Solid Wastes. *ABNT - Associação Brasileira de Normas Técnicas*, *Rio de Janeiro*, *RJ* (in Portuguese).

ABNT NBR 13555 (2012). Soil-Cement - Determination of Water Absorption - Test Method. *ABNT - Associação Brasileira de Normas Técnicas*, *Rio de Janeiro*, *RJ* (in Portuguese).

ASTM D6836-16. (2016). Standard Test Methods for Determination of the Soil Water Characteristic Curve for Desorption Using Hanging Column, Pressure Extractor, Chilled Mirror Hygrometer, or Centrifuge. *ASTM International*, *West Conshohocken*, *PA*. https://doi.org/10.1520/D6836-16

Barreto, T.M.; Repsold, L.L., & Casagrande, M.D.T. (2018). Melhoramento de solos arenosos com polímeros. *Proc. 19 °Congresso Brasileiro de Mecânica dos Solos e Engenharia Geotécnica*, *Salvador*. Vol. 2, ABMS, CBMR, ISRM & SPG, 1-11 (in Portuguese).

CONAMA. (2009). Resolução n° 420, de 28 de dezembro de 2009. *DOU n° 249, Brazilian Ministry of Environment, Brasília*.

Consoli, N.C., Nierwinski, H.P., Silva, A.P.E., & Sosnoski J. (2017). Durability and strength of fiber-reinforced compacted gold tailings-cement blends. *Geotextiles and Geomembranes*, 45(2), 98-102. https://doi.org/10.1016/j.geotexmem.2017.01.001

Festugato, L., Consoli, N.C., & Fourie, A. (2015). Cyclic shear behaviour of fibre reinforced mine tailings. *Geosynthetics International*, 22(2), 196-206. https://doi.org/10.1680/gein.15.00005

Lee, S., Chung, M., Park, H.M., Song, K., & Chang, I. (2019). Xanthan gum biopolymer as soil-stabilization binder for road construction using local soil in Sri Lanka. *Journal of Materials in Civil Engineering*, 31(11), 1-9. https://doi.org/10.1061/(ASCE)MT.1943-5533.0002909

Li, M., Fang, H., Du, M., Zhang, C., Su, Z., & Wang, F. (2020). The behavior of polymer-bentonite interface under shear stress. *Construction and Building Materials*, 248, 1-10. https://doi.org/10.1016/j.conbuildmat.2020.118680

Liu, J., Chen, Z., Song, Z., Bai, Y., Qian, W., Wei, J., & Kanungo, D.P. (2018). Tensile behavior of polyurethane organic polymer and polypropylene fiber-reinforced sand. *Polymers*, 10(5), 499-513. https://doi.org/10.3390/polym10050499

Liu, J., Wang, Y., Kanungo, D.P., Wei, J., Bai, Y., Li, D., Song, Z., & Lu, Y. (2019). Study on the brittleness characteristics of sand reinforced with polypropylene fiber and polyurethane organic polymer. *Fibers and Polymers*, 20(3), 620-632. https://doi.org/10.1007/s12221-019-8779-1

Mirzababaei, M., Arulrajah, A., & Ouston, M. (2017). Polymers for stabilization of soft clay soils. *Procedia Engineering*, 189, 25-32. https://doi.org/10.1016/j.proeng.2017.05.005

Okonta, F. (2019). Pavement geotechnical properties of polymer modified weathered semiarid shale subgrade. *International Journal of Pavement Research and Technology*, 12(1), 54-63. https://doi.org/10.1007/s42947-019-0007-2

Silva, N.A.B.S. (2020). *Performance of a soil-polymer composite for applicability in geotechnical and paving works* [Master's dissertation, University of Brasilia], University of Brasilia's repository (in Portuguese). https://repositorio.unb.br/handle/10482/38789

Sotomayor, J.M.G. (2018). *Evaluation of drained and non-drained mechanical behavior of iron and gold mine tailings reinforced with polypropylene fibers* [Doctoral thesis, Pontifical Catholic University of Rio de Janeiro]. Pontifical Catholic University of Rio de Janeiro's repository (in Portuguese). https://doi.org/10.17771/PUCRio.acad.36102

Xing, C, Liu, X., & Anupam, K. (2018). Response of sandy soil stabilized by polymer additives. *Open Access Journal of Environmental and Soil Sciences*, 1(3), 64-71. https://doi.org/10.32474/OAJESS.2018.01.000112

List of symbols

T: tailing

TP: tailing -polymer

L: linear adjustment

7d, *14d*, *28d*: 7,14 and 28 days respectively

DRX: X-ray diffractometry

EDS: energy dispersive spectroscopy

SEM: scanning electron microscopy

d: diffractometric pattern (calculated by the focal point of the diffractometer optics)

Si: silicon

Fe: Iron

C: Carbon

O: Oxygen

Al: Aluminum

Ni: Nickel

Kev: Critical Ionization Energy

K, *L*: layer where ionization occurred

a, *esc*, *b*, *l*: layer from which the electron came out

Case Study

www.soilsandrocks.com

Soils and Rocks

An International Journal of Geotechnical and Geoenvironmental Engineering

ISSN 1980-9743
ISSN-e 2675-5475

Compression and shear strengths of sandy limestone and the role of the porosity: a case study

Yousr Koobaa[1,#], Houda Guiras[1], Mehrez Jamei[1,2]

Case Study

Keywords
Compression strength
Fissured rock
Porosity
Sandy limestone rock
Shear strength

Abstract

This paper focuses on the study of the mechanical behavior of sandy limestone rocks. These rocks are provided from the historical caves of El Haouaria, which are located on of the North Eastern seacoast of Tunisia, and were created during the Punic era. Nowadays, these caves suffer from cracks, randomly distributed with a variable opening size. While, it appears that damage risk monitoring of the El Haouaria caves is a priority, linked questions concerning the mechanical behavior of the cave's rocks still remain, mainly because of its variable porosity and evolution with time. Understating its behavior will be a main tool to build a monitoring program, leading to an optimum reinforcement solution. Aside from uniaxial tests performed on several undistributed samples of a porosity ranged between 30 % and 50 %, triaxial tests were also conducted on undistributed specimens with a porosity of 30 % and 50 %. All the results showed a significant effect of the porosity on the mechanical properties. The nonlinear Hoek-Brown criterion was used to model the shear failure, introducing few changes in order to consider the porosity influence. It was found that this criterion provides a satisfactory estimation of shear strength and its dependency on the porosity. Intact rock parameters and their porosity dependency were determined from compression and bending tests of undistributed samples. However, in situ rocks were considered as micro-fissured, principally for U3 layer, and the Geological Strength Index (*GSI*) was determined for the fissured rock.

1. Introduction

The caves of El Haouaria are carved inside sedimentary rock mass dating from the Punic era. They are a historical monument located in the seacoast of the Cap Bon region in the North East of Tunisia (Figure 1). The caves have undergone the impact of climate change, such as humidity cycles characterized by a high variation of the relative humidity across the day. Evidently, the caves have been exposed to a range of seasonal temperature variation, atmospheric evaporation and humidity cycles. The caves are composed of 5 types of rocks, successively noted U1, U2, U3, U4, U5, respectively from base up to ground surface (Figure 2). The rocks composing the caves are biogenic sedimentary rocks, which are induced by cementation and compaction during sediment digenesis. Porosity varies from 25 % to 55 %. Currently, the caves contain a crack network that compromises their stability. Due to potential risk of collapse of cave parts, three caves among the set were completely closed off tourist visitors (Figure 2). In order to preserve these caves and predict the risks of failure, the Tunisian National Agency for the Protection of National Monuments, has proposed a research study, starting by the investigation of the behavior of the rocks.

All the reasons cited above highlight the importance of the investigations on the origins of the cracks. The authors proposed a two-phase study. The first was to understand and define the caves of El Haouaria rock's mechanical behavior. Then, the last stage of the study, which is not included in this paper, will be the reinforcement of the three caves based mainly on the conclusions and the failure model retained in this paper.

Laboratory tests have been performed on undistributed samples provided from blocks placed near the caves, since sampling from the caves was not permitted. This paper focuses particularly on compressive and shear behavior of these rocks in their current state. The dependency of compression strength and shear strength was quantified.

[#]Corresponding author. E-mail address: y.koobaa@gmail.com.
[1]University of Tunis EL Manar, National Engineering School of Tunis, Civil Engineering Laboratory, Le Belvédère, Tunis, Tunisia.
[2]Northern Borders University, Engineering College, King Saudi Arabia.

Submitted on July 26, 2019; Final Acceptance on June 17, 2020; Discussion open until March 31, 2021.
DOI: https://doi.org/10.28927/SR.434693

Regarding research literature, many studies have focused on the sustainability of rocks involved in restoration of monuments (Yu & Oguchi, 2010; Al-Omari et al., 2015, Aldoasri et al., 2017, Rahmouni et al., 2017). Several previous studies have described mechanical compaction in various porous rocks (Baud et al., 2004) and carbonate rocks (Evans et al., 1990, Nicolas et al., 2016). Some researchers at universities and at industries were carried out specifically on soft rocks. Kanji (2014), for example, discuss the critical issues in soft rocks. In fact, the author discussed the currently widespread classification systems of weak and soft rocks. As a conclusion of the cited paper, it was established that besides uniaxial compression strength (*UCS*), often admitted as criterion to classify soft rocks (for example the upper limit of 25 MPa was practically retained), porosity of rocks was also considered as a parameter. Thus, Bosio & Kanji (1998) proposed a correlation between porosity, absorption (%) and *UCS*. Other researchers have investigated the mechanical behavior of soft rocks with high porosity and low mechanical strength (Guilloux, 2005; Asef & Farrokhrouz, 2010). Whereas some researchers, such Elliott & Brown (1985), considered that high porosity determines rock's belonging to soft rock class. Relying on these results, many authors have significantly contributed to a general understanding of strength and elastic deformation of soft rocks (e.g. Price & Farmer, 1979; Daoud et al., 2017; Baud et al., 2014).

In the current study, the authors tested rocks exhibiting a variable mineralogy and a wide range of porosity. The authors also focused on the shear behavior of such sandy limestone rock and the effect of porosity on the maximum deviatoric stress and then on shear strength. Water content during shear tests was considered constant since suction was controlled. Triaxial tests show that stress-strain response changes from fragile behavior to ductile behavior.

On the other hand, the generalized Hoek-Brown model was applied to predict compressive and shear strength. The role of porosity was indirectly taken into-account when main parameter m_i was introduced as function of both compression and tensile strengths (Hoek & Brown, 2019).

The discussion in this paper focuses on the efficiency and relevance of generalized Hoek-Brown criterion for U3 rock modeling of El Haouaria caves. The model was used to predict the behaviour of the samples with variable porosity and then the behavior of soft intact rocks constituting the cave's structure in which the fissures are randomly distributed, with variable length and opening; for which the authors used *GSI* system as it was recently discussed in the paper of Hoek & Brown (2019).

2. Materials and methods

The caves are carved inside the consolidated dunes (aeolianites), formed during the Late Quaternary period (Tyrrhenian stage). These dunes are composed of a stratification of five geological layers (Paskoff & Sanlaville, 1983). The base layer U1 is composed of limestone debris and quartz and have oblique stratifications. The second layer U2 is composed of limestone debris and quartz without stratification. The third layer U3 is very thick. It is made of limestone debris from fossils (algae, echinoderms, mollusks), rare foraminifera, quartz grains (scattered, or in clusters and have a small size). The fourth layer U4 is composed of limestone debris and quartz without color with variable thickness (from 30 cm to 1 m) and has frequent foraminifera and pellets (totally micritic grains). The upper layer is thin and topped with a crust composed of limestone debris from fossils algae, echinoderms, mollusks and quartz grains. These caves provided the rock material that was once used for building Carthage, as shown in Figure 1.

The caves are large semi-dark caves made of latomies, carved in the shape of a pyramid with a narrow upper opening. There is also some narrow opening that communicate between caves. Due to bombing raids during the Second World War, followed by natural collapses, wider lateral openings were created. Visits to the site became possible (Harrazi, 1995).

The authors focused on the study of mechanical properties, in particular U3 (the third layer) rock properties, since it is the thickest and contains a series of developed cracks that compromise cave stability (Figure 2b). Therefore, unconfined compression tests and triaxial tests were performed on samples extracted from this same layer, but with various initial porosities. Micro-structural characteristics and mineralogical composition of U3 rocks were examined by light microscope, scanning electron microscope (SEM), XRD analysis and chemical analysis (for more details, see Koubaa et al., 2018). Chemical analysis and diffraction technique (XRD) showed that the minerals of U3 rocks are composed mainly of calcite ($CaCO3$, $SiO2$) and some other minerals such as Aragonite, halite (Koubaa et al., 2018) The. U3 rocks were examined by light microscope and scanning electron microscope (*SEM*). It has been shown that the rocks are grainstone, well graded and very porous. They were composed of algae debris (*Al*), lamellibranches, gastropods echinoderms (*Ech*) and Quartz grains (*Qz*). For this mineralogical composition, experiments show that rocks had various porosity and different particle size distribution trends. Rock porosity varied from 25 % to 55 %. Besides, the cement connecting the grain is very thin which reinforce its classification as a soft rock. Previously, it has been shown that environmental cycles cause increase of porosity by dissolving some minerals in the rock (Koubaa et al., 2018). The *SEM* analysis showed that the cement is thin, opaque (thickness close to 35 µm) and covers the majority of grains (Figure 3). Pores between grains are interconnected. The digenesis of the cement is precocious; except when salt dissolves under the effect of water, then deposits of salt and minerals between grains are created.

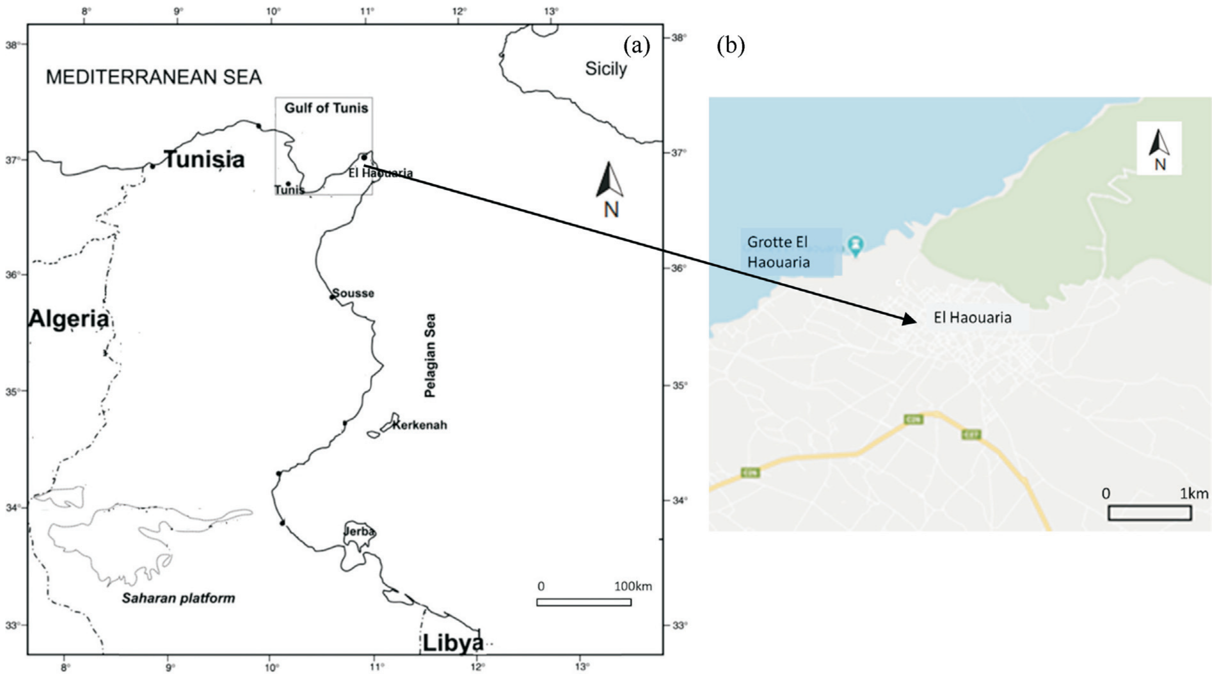

Figure 1. (a) El Haouaria location in Tunisia (b) El Haouaria caves location.

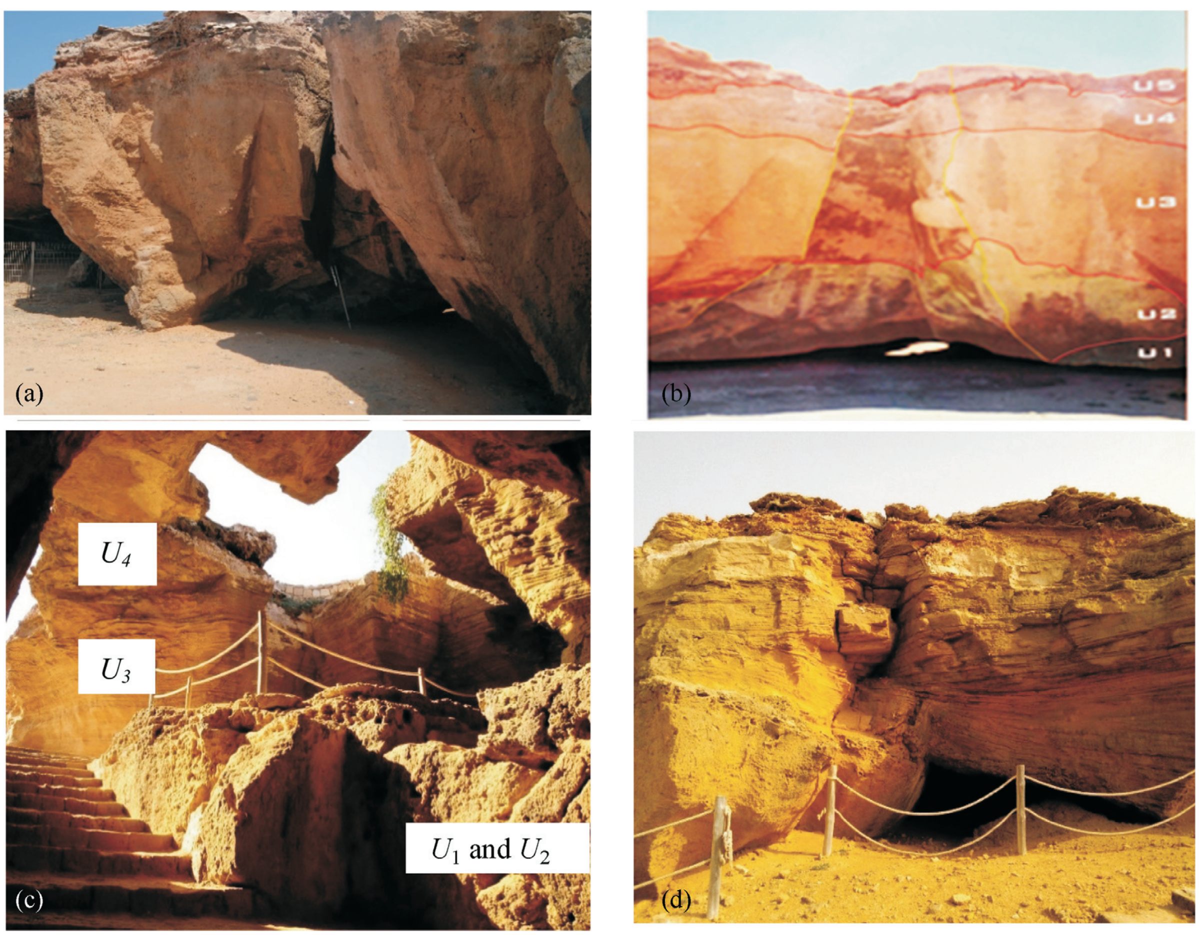

Figure 2. Photographs of caves: a) front of caves, b) Stratified layers called U1 to U5 that constitute the caves, c) the surface of well- distributed caves, d) layers of fractured caves.

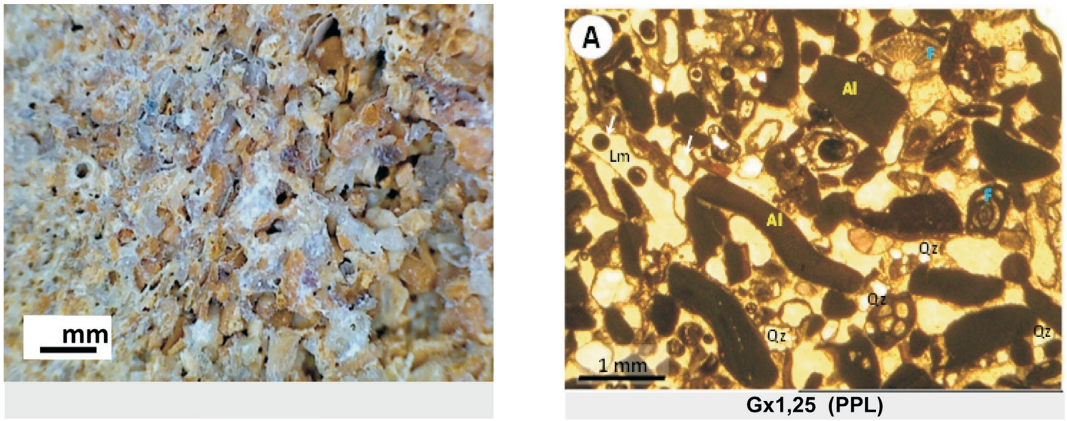

Figure 3. Thin sections (1 mm and 200 µm) of specimens from U3 layers in plane polarized light U3 (*AL*: algae, *QZ*: quartz, *Ech*: echinoderms, *F*: Foraminifera, *Lm*: Lamellibranch).

This leads to replacement of pore connectivity (Figures 4-a, 4-b).

First porosity was measured for each tested sample. Tests were repeated minimum three times. An average value was retained. Porosity was determined according the ISO 5017 Standard (ISO, 2013), which defines porosity as the ratio of total pore volume in a porous body to its apparent volume (total volume). So, porosity (*n*) was computed as following:

$$n = 100\frac{V_{void}}{V_{total}} = 100\frac{V_{total} - V_{solid}}{V_{total}} = 100\left(1 - \frac{\rho_a}{\rho_s}\right) \quad (1)$$

where V_{void} is the volume of voids, V_{solid} is the volume of solid and V_{total} is the total volume.

The authors have used a simplified method to determine apparent density by measuring the dimensions of specimens to obtain the total volume, and the mass of solid. Apparent density is computed as:

$$\rho_a = \frac{M_s}{V_{total}} \quad (2)$$

and specific density is computed as:

$$\rho_s = \frac{M_s}{V_s} \quad (3)$$

where specific density ρ_s was determined according to the standard NF P94-054 (AFNOR, 1991), using a Pycnometer with a volume of 50 cm^3, which resulted in 2.72 g/cm^3. Three values of mass were determined as following:

- The mass of the Pycnometer filled with water to obtain the mass M_w,
- The mass of the dry mass of the sample of crushed rock (very fine) to obtain: M_1
- The mass of the Pycnometer filled with dry rock, very fine, and filled with water: M_2

The density of solids was thus determined as follows:

$$\rho_s = \frac{m_s}{m_e} = \frac{M_1}{M_w + M_1 - M_2} \quad (4)$$

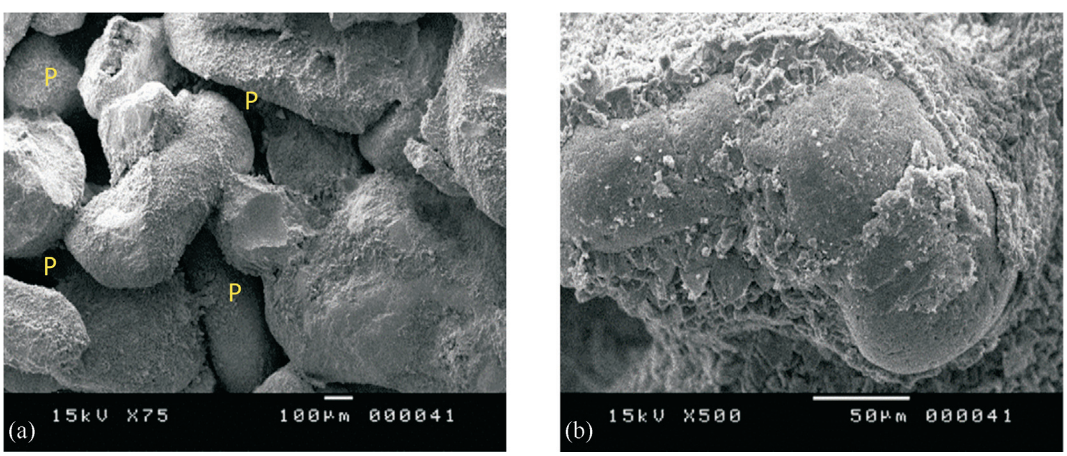

Figure 4. *SEM* micrographs of rock from El Haouaria caves U3: a) grains and bonding material and inter-granular porosity, b) lodges of a foraminifer partially covered by a fine cement 10 to 20 µm thick.

Two types of compression tests were performed on U3 specimens. In fact, separately compression force -controlled (using Instron 4485 press) and displacement-controlled rates were performed on rectangular prism specimens (of square section with edges of 4 cm, and a height of 8 cm). Due to low strength and randomly distributed porosity, specimen preparation for testing were problematic. Diamond discs using water were specifically used to obtain specimens from blocks from the caves field. Uniaxial compression device has a maximum load capacity of 300 kN. Force was controlled with a 1/100 of standard deviation value. A number of 23 dry specimens of uniaxial compression tests were tested. The porosity of each sample was computed using sample's solid density, mass and volume values. Sample's porosity varied from 25 % to 55 %.

In the other hand, series of uniaxial compression tests, under controlled displacement rate (4 mm/min), were added. However, for these series, specimens were cylindrical of a 10 cm diameter and a 20 cm height (Standards AFNOR P94-420, 2000, and ASTM D 7012-04, 2004). The force-controlled tests were performed on sets of 5 pieces of U3 and samples with porosity ranging between 30 % and 50 %.

From stress-strain curves, mechanical characteristics, such as uniaxial compressive strength σ_c, Young's modulus E and Poisson's ratio ν were identified. Meanwhile, some specific tests as ultrasonic tests were performed in order to measure the dynamic elastic modulus and its dependency on porosity. Wave's velocity (V_p) was recorded according to AFNOR P94-411 (AFNOR, 2002) Standard, on cylindrical specimens of 40 mm diameter and 80 mm height. The specimen was placed between a transmitter of ultrasonic wave (with frequency of 54 kHz) and a receptor.

The ratio of the distance separating the transmitter from the receptor to the time taken by a wave (P) to cross it gives the velocity V_p. The time was measured using PUNDIT ultrasound machine.

Adding two series of uniaxial compression tests, some indirect tensile tests were performed using bending beam tests. These tests aim was to obtain tensile strength.

In addition to the demonstrate the role of the porosity in the uniaxial compression tests, the authors have to emphasize that our original contribution is the report of results of triaxial tests, which have been performed on specimens with conventional dimensions (a diameter of 38 mm, and a 76 mm high) with porosity variation.

It is also important to mention here that triaxial tests were carried out only on sets of specimens with average porosity of 30 % and 50 %. The limiting factor was the difficulty in sampling from the same blocks due to the constraint of keeping the same physical properties of specimens. The triaxial device had automatically controlled stresses. Axial (ε_1) and radial (ε_3) strains were obtained using axial and lateral transducers. For samples with 50 % porosity, the confining pressures were respectively, 500 kPa, 800 kPa and 1200 kPa. However, due to limitation of load frame (allowable axial force), confining pressures for specimens of 30 % porosity were 100 kPa and 500 kPa.

The radial deformation ε_3 response was monitored with an electro-optical laser system mounted on two diametrically-opposite sides. Vertical displacements were measured by the means of an external *LVDT* (including corrections due to cell deformability). The triaxial setup comprised two electro-pneumatic pressure regulators (*QB*1 Proportion Air) for chamber and axial piston pressure.

Two stepper motors using air pressure regulators were used to continuously control both deviator and confining stresses. Stepper motors and measurements of 14 sensors were managed by automatic data acquisition and control system that allow to apply a generated stress and to perform strain-controlled tests (for more details see Romero, 1999).

3. Experimental results

3.1 Physical properties

The physical properties of the rock samples are given in Table 1. Low dry unit weight for high porosity were obtained. Therefore, a large dry density variation corresponds to the porosity range.

3.2 Elastic properties

Figures 5a and 5b respectively show the dynamic elastic modulus (from Ultrasonic tests and using Equation 5) and the static elastic modulus (defined as the initial secant tangent between unconfined compression stress and corresponding strain). The two elastic moduli were obtained from several tested specimens with different porosities. Both curves indicate the same trend of dynamic and static moduli with porosity. Indeed, when porosity increases, elastic modulus decreases significantly.

However, it has to be emphasized that due to the difficulty to reproduce the same porosity for prepared undistributed specimens (remember that such specimens were extracted and prepared from a given large block), it was very problematic to prepare specimens with a longed for porosity for both unconfined compression tests and ultrasonic tests. For this reason, curves presented in the following, for Ultrasonic tests and static compression, tests corresponded to different ranges of porosity.

Dynamic elastic modulus was computed as given in Equation 5:

Table 1. Physical properties of tested rocks.

Physical characteristics	Rock U3
Dry density (g/cm^3)	from 1.5 to 2.5
Bulk density (g/cm^3)	2.72
Porosity	from 25 % to 55 %

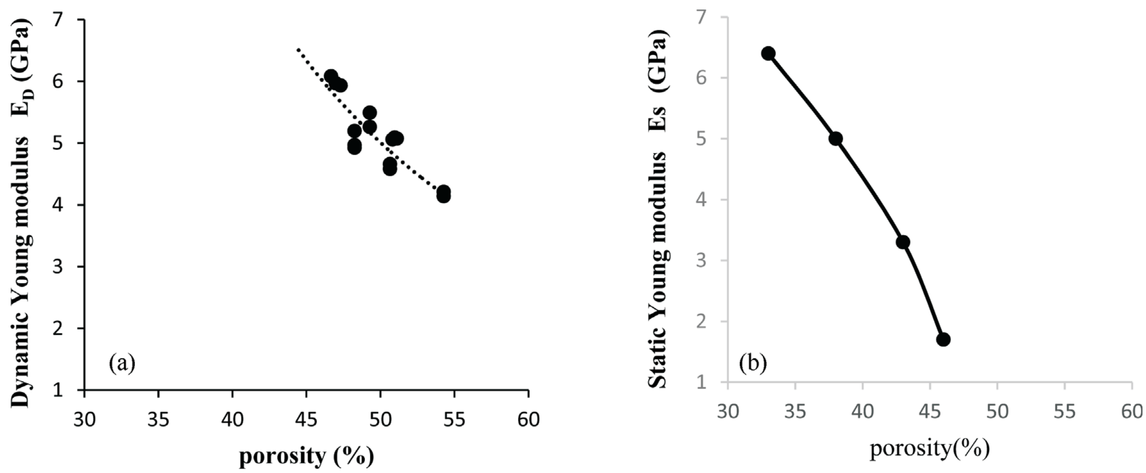

Figure 5. Elastic moduli vs. rock porosity: a) dynamic moduli, b) static moduli.

$$E_D = \rho (V_p)^2 \frac{(1+\nu)(1-2\nu)}{(1-\nu)} \quad (5)$$

where ρ is the rock density by Equation 2, ν is the Poisson's ratio which is supposed equal to 0.33, *Vp* is the velocity of the primary (compression) wave (in m/s).

3.3 Effect of porosity on uniaxial compressive strength (*UCS*)

Because U3 layer is fissured, all experiences were prepared using blocks provided from this layer. It was found that *UCS* decreases from 14 MPa to 1.2 MPa since the porosity increases from 30 % to 50 % (Figure 6). These low *UCS* values correspond to soft rock characteristics. The *UCS* was controlled by porosity (see for instance Koubaa et al., 2018). To reach compressive failure, stress-strain curves exhibited two important features. The first is that axial strain at failure increases with porosity (it varies from 2 % to 4 %, when porosity varies from 33 % to 46 %). The second fact is that post-failure behavior has a significant negative hardening.

In addition to the experiments performed specially to provide a database for the modeling, the authors performed bending tests. The results of indirect tensile strength (*ITS* = *Rt*) indicated that the *ITS* varies from 0.3*UCS* to *UCS*. The *ITS* is approximately equals to the *UCS* for the high porosity of 50 %.

3.4 Triaxial compression results

Deviatory stress-strain-curves were obtained at different confining stresses increasing from 0.5 MPa up to 1.2 MPa. Deviatory stress q is defined as $q = \sigma_1 - \sigma_3$. Stresses σ_1 and σ_3 represent respectively axial and lateral stresses. In this paper, the authors assume that compressive stresses and contraction strains are positive.

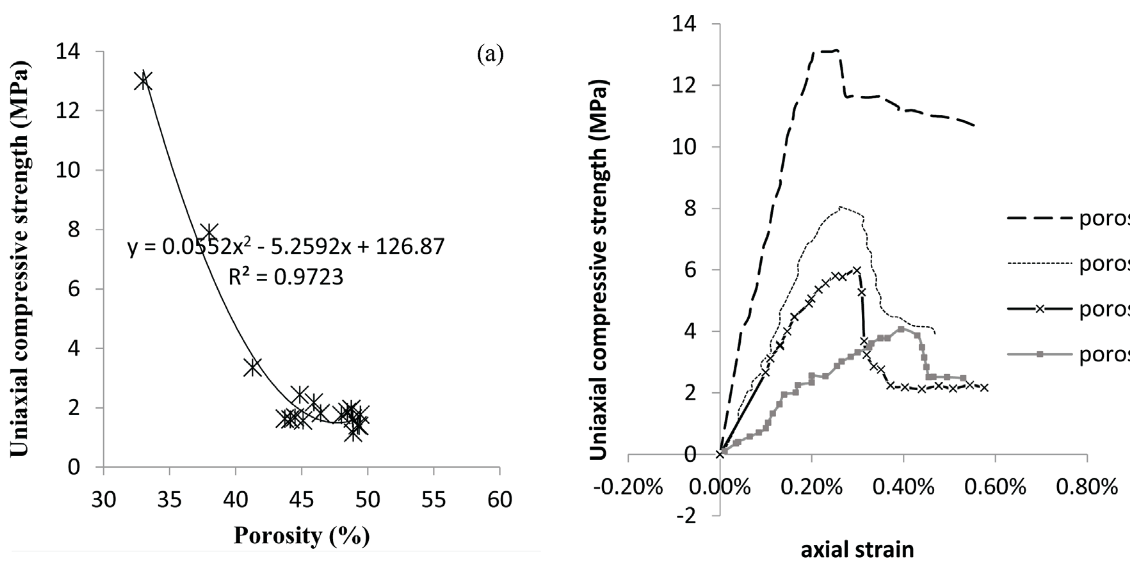

Figure 6. Uniaxial compressive strength vs. : a) porosity, b) axial strain.

Test results are illustrated in Figures 7 and 8 in terms of deviatory stress ($q = \sigma_1 - \sigma_3$) vs. strain (two kinds of strain were measured: axial strain ε_1, and radial strain ε_3). Volumetric strain $\varepsilon_v = \varepsilon_1 + 2\varepsilon_3$ was then deduced. Each curve in Figures 7 and 8 was identified by its corresponding strain.

As it will be discussed below, two series of specimens were tested with different average porosity ranging of 30 % to 50 %. In addition, for a confining stress of 0.8 MPa, two kinds of rock specimens were tested (provided from two blocks from U3). Figures 7a to 7d provide results associated to a porosity of 50 %. Figures 8a to 8b provide results corresponding to porosity of 30 %.

Two main conclusions can be drawn from the trends indicated in Figures 7 and 8:

(1) In Figures 7a and 7b, the curves are characterized by a linear elastic deformation of axial strain of 2 % and 4 %, respectively. Maximum deviatory stress was observed around 2.5 MPa and 3.5 MPa, respectively associated to 2 % and 4 % axial strain for σ_3 = 800 kPa and σ_3 = 500 kPa, respectively. Moreover, as shown in Figure 7, the deviatory strain tendency displays an asymptotic behavior (two phases: elastic and perfectly plastic for relatively lower confinement stresses), and a hardening behavior for higher confining stress.

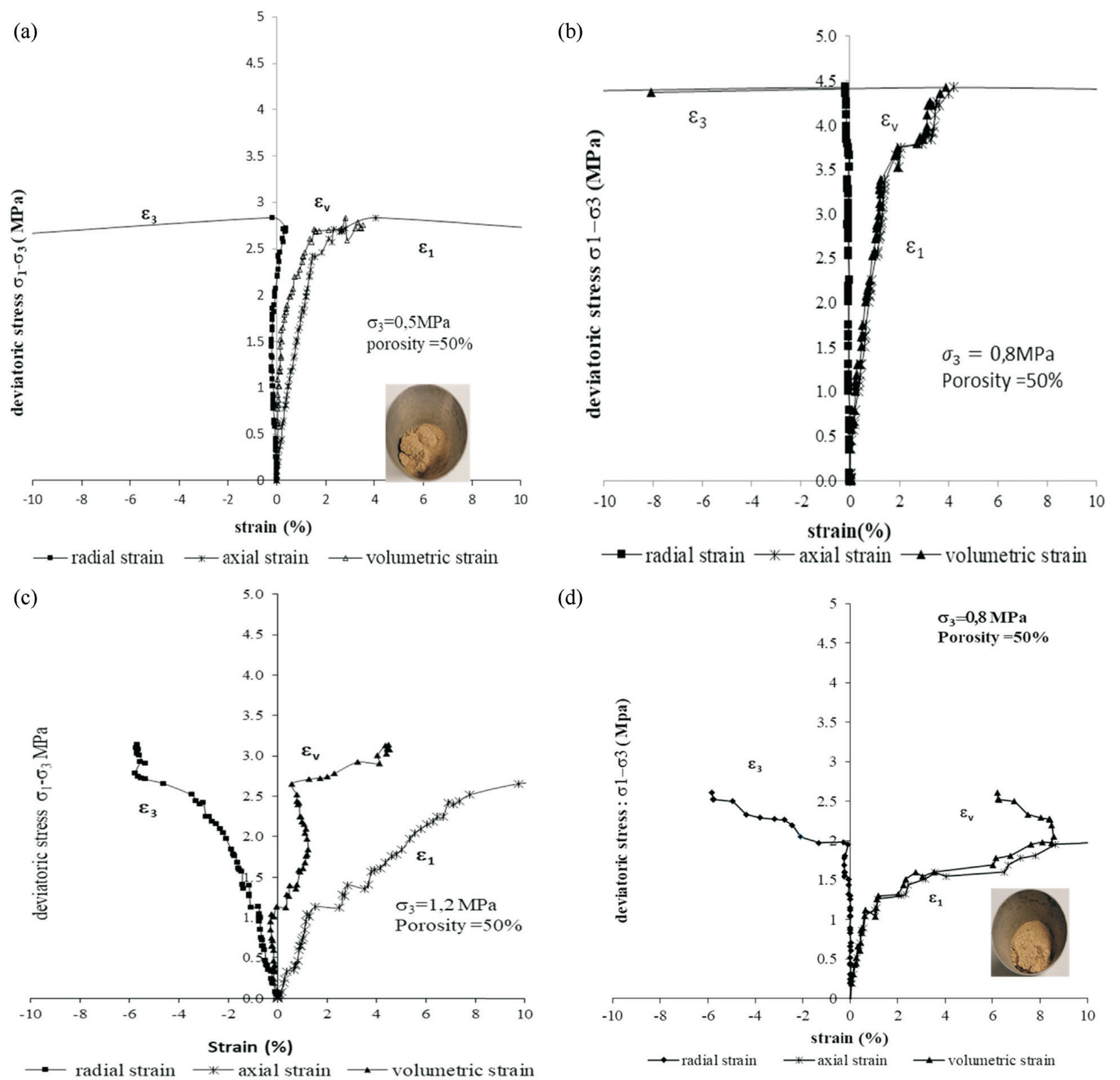

Figure 7. Deviatory stress vs. strains (axial, volumetric and deviatoric strains) under confining stress for values of a) 0.5 MPa, b) 0.8 MPa, c) 1.2 MPa, d) 0.8 MPa.

(2) In Figures 7c and 7d, respectively, the curves exhibit a typical behavior of compact cataclysmic flow regime, where both samples display similar differential stress--axial strain curves. Indeed, both samples display strain hardening, large strains and no stress drop. Beyond these stress levels, deviatory stress provided a significant contribution to the compact strain, and no shearing is observed.

According to visual observations on the tested specimens, no shearing localization was observed. As the number of cracks created in samples progressively rose during deformation, tendency of brutal crushing of samples under triaxial stresses was frequently observed for low confining stress.

All these features are commonly attributed to cataclysmic (or ductile) flow regime. As confining stress increases, inner structure of sandy limestone becomes more compact and hence and fracturing becomes inhibited. Deformation changes progressively from ductile to hardening behavior (see Figures 7a and 7b and then Figures 7c and 7d). Since high confining stress suppresses initiation, growth and propagation of cracks, compaction phase before onset of dilatation lasts longer while fracture percolation occurs later on at high lateral stresses. From a volumetric strain evolution, dilatation appears after some contractive volume values. Dilatation appears much later (for higher axial strain) with an increasing lateral confining stress.

On the other hand, results corresponding to 30 % porosity clearly showed an elastic response followed by some hardening (Figure 8a and 8b). A completely dilatory response was observed even for a relatively low confining stress. Naturally, compact rock exhibits a similar behavior as it was usually observed in the geotechnical field for dense sands. Initial high density did not allow a contractive movement of grains. Because of limited loading by the triaxial device, only two confining high pressures were selected, for which high values of deviator stress were reached.

4. Modeling of the experimental results

First, for intact rock mass, Hoek-Brown criterion was written as following:

$$\sigma_1 = \sigma_3 + \sigma_{ci}\sqrt{m_{br}\frac{\sigma_3}{\sigma_{ci}} + 1} \tag{6a}$$

Zuo et al. (2008, 2015) replaced m_{br} par the term; $\frac{\mu}{k}\frac{\sigma_{Ci}}{|\sigma_t|}$, where, $\mu = \tan\phi$ (ϕ is the crack surface friction) and $k = \sqrt{\frac{2}{3}}$. For $\phi = 45°$, $\mu = \tan\phi = 1$. The Equation 6a is then written as:

$$\sigma_1 = \sigma_3 + \sigma_{ci}\sqrt{\left(\frac{\mu}{k}\frac{\sigma_{ci}}{|\sigma_t|}\right)\frac{\sigma_3}{\sigma_{ci}} + 1} \tag{6b}$$

where σ_1 is the major principal stress and σ_3 is the minor principal stress, σ_{ci} is the compressive strength of intact rocks. In this equation, σ_t is the direct tensile strength. Table 2 summarizes the values for these parameters.

It is to be noted that, since tested specimens were considered undistributed, the authors admitted, the Hoek-

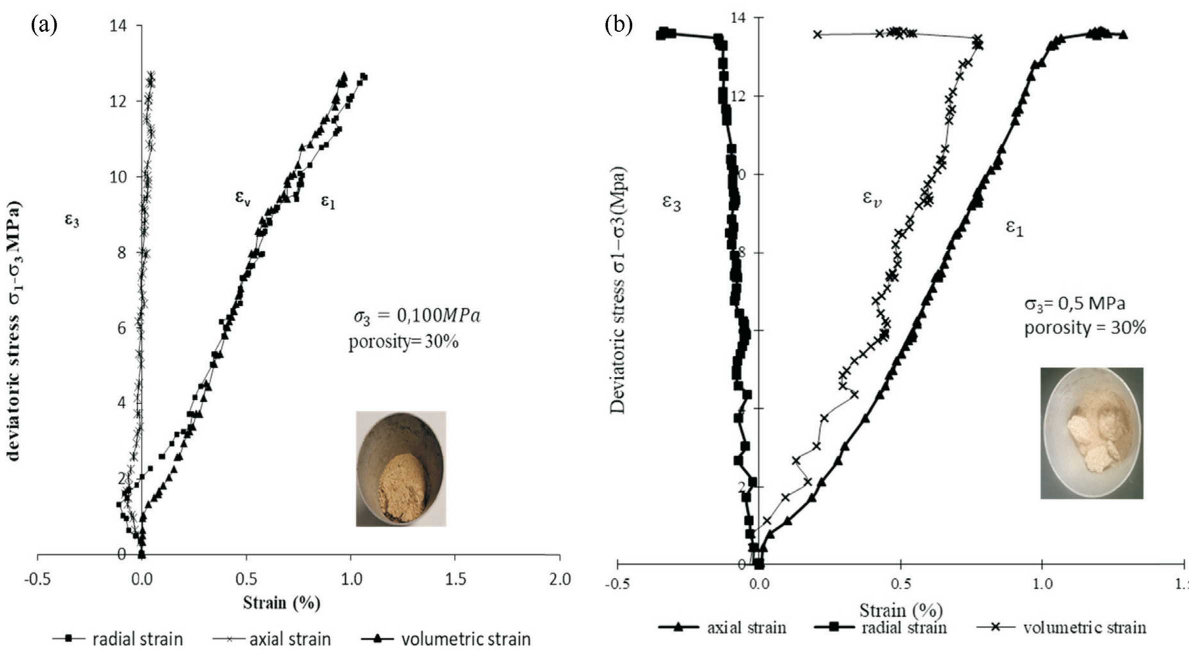

Figure 8. Deviatory stress vs. strains (axial, volumetric and deviatoric strains) for dry rocks under confining stress a) 0.1 MPa, b) 0.5 MPa. Rock samples were dried with a porosity of 30 %.

Table 2. Parameters of Hoek-Brown criterion, obtained by adjusting the experimental data.

Porosity	*k*	$\mu = \tan\phi$	Tensile strength *ITS* (MPa)	Correction to obtain an approximation value of direct tensile strength $\sigma_t = 0.7$ *ITS* (MPa)	σ_{ci} (MPa)	$m_{br} = \mu^*\sigma_{ci}/(k^*\sigma_t)$
30 %	0.82	1	2	1.4	10	10
50 %	0.82	1	0.6	0.7	1.7	5

Brown criterion given by Equation 6. Figure 9 shows the results of predicted compression and shear strengths. The tension cutoff was also included by the value of direct tensile strength obtained by a given correction of the indirect tensile strength ITS. The authors introduced a correction coefficient of 0.7 on the ITS measured by the three bending tests to obtain an estimation of direct tensile strength σ_t.

As it can be observed in Figure 9, experimental results were fitted based on Equation 6 and using the set of experimental results.

In the other hand, for fissured rocks mainly in U3 layer (see Figure 10), the authors propose here an extension of Hoek-Brown criterion (Generalized Hoek-Brown criterion, see Hoek and Brown, 2018). This is aiming to provide a failure criterion adjusted to U3 rock (typically a sandy limestone), which will be used for monitoring and eventually for a reinforcement solution proposal of U3 layer. Note that the degradation observed in U3 was taken into account via the parameters *s*, m_b and *a* in Equation 7 (Hoek & Brown, 2019).

The parameters m_b, *s* and *a* are defined as following:

$$\sigma_1 = \sigma_3 + \sigma_{ci}\left(m_b \frac{\sigma_3}{\sigma_{ci}} + s\right)^a \tag{7}$$

$$m_b = m_i \exp\left(\frac{GSI - 100}{20 - 14D_m}\right) \tag{8}$$

$$s = \exp\left(\frac{GSI - 100}{9 - 3D_m}\right) \tag{9}$$

$$a = \frac{1}{2} + \frac{1}{6}\left(e^{-\frac{GSI}{15}} - e^{-\frac{20}{3}}\right) \tag{10}$$

The requested model parameters of the rock requested to obtain the shear criterion envelope are compressive strength of intact rocks σ_{ci}, intact rock parameter m_{br}, geological strength index *GSI*, and perturbation factor D_m.

Now, for the other remaining parameters, the authors considered *Dm* as a perturbation parameter ranging from 0 to 1, depending on the perturbation level of rock mass, and m_b as the constant for fractured mass.

The *GSI index* was determined using an empirical table proposed by Hoek (2007). *GSI* depended on the presence or not of cracks. U3 rock, which contains cracks, were

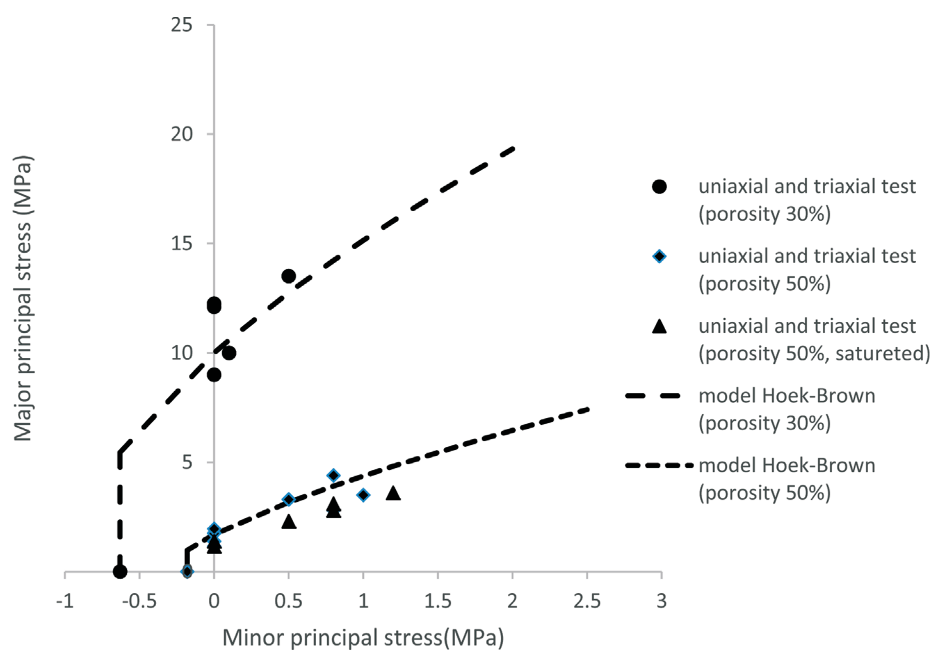

Figure 9. Hoek-Brown criterion fitted on *UCS* and triaxial tests for two different porosity (Undistributed specimens).

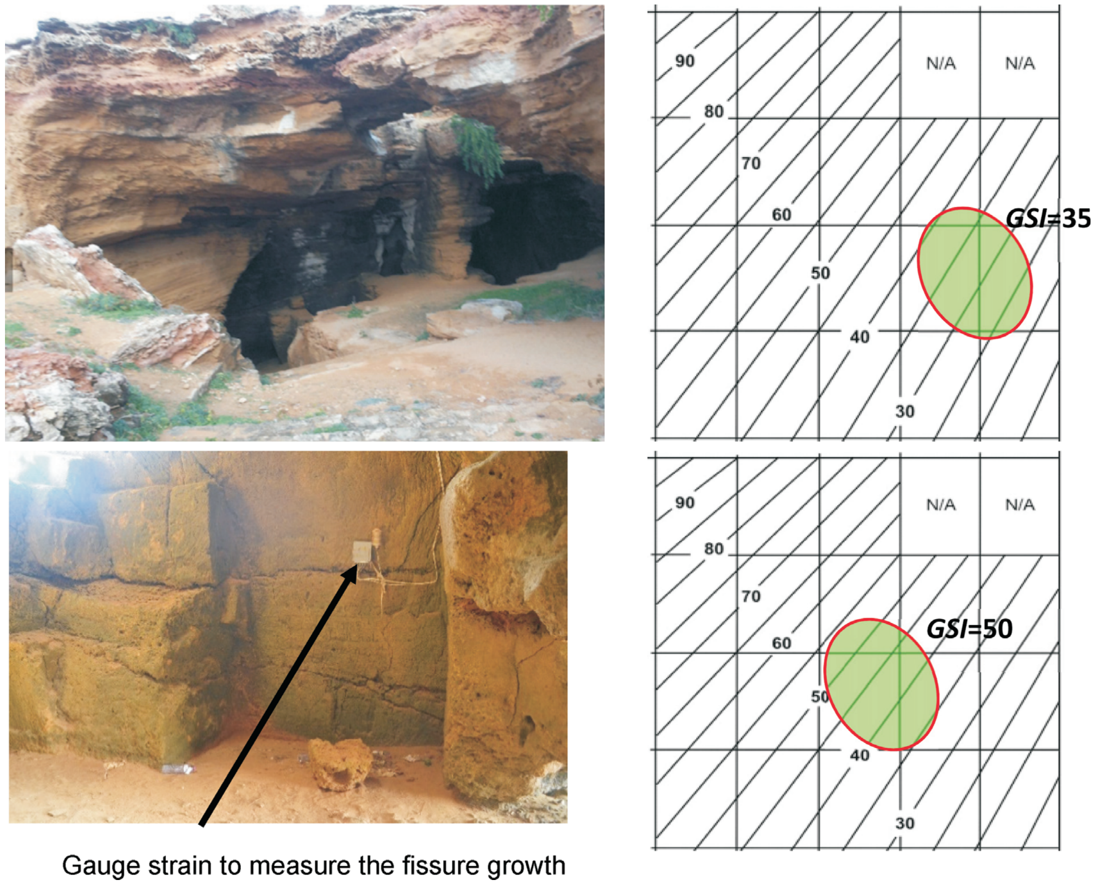

Figure 10. Horizontal and oblique fissures in U3 layer and gauge strain monitoring.

assumed to be fractured rocks. Besides, the rock mass was disturbed and its surface was strongly altered (see the photos in Figure 10). Thus, considering cracks, two *GSI* values were determined for a porosity of 50 % and of 30 %. The *Dm* value depended on the level of perturbation incurred by the mass through explosive excavation and stress relaxation. The authors used the Hoek-Brown guide to determine this disturbance factor (Hoek et al., 2002). Considering that there is no recent excavation in cave location, D_m value was set to zero. Table 3 summarizes the triaxial data and Table 4 summarizes the Hoek-Brown criterion parameters used to obtain a shear criterion for U3 rock at its fractured state in situ (see Figure 11). In addition, to estimate the shear strength for the caves structure, rock mass deformation modulus was required. Then, using the empirical relation (Equation 9) to estimate the rock mass modulus proposed by Hoek & Diederichs (2006), U3 rock modulus was estimated considering its fractured aspect. The results are presented in Figure 12.

$$E_{rm} = E_i \left[0.02 + \frac{1 - \frac{D_m}{2}}{1 + \exp\left(\frac{60 + 15D_m - GSI}{11} \right)} \right] \quad (11)$$

Table 3. Experimental data of s_1, s_3 from triaxial test.

Porosity (%)	σ_1 (MPa)	σ_3 (MPa)
50 %	3.3	0.5
	4.4	0.8
	2.8	0.8
	3.7	1.2
35 %	13.2	0.1
	13.5	0.5

Table 4. Parameters of the generalized Hoek-Brown criterion *GSI*, m_b, *s*, *a*.

Porosity	*GSI*	m_b	*s*	*a*
30 %	35	1.08	0.001	0.52
50 %	35	0.294	0.001	0.52
30 %	50	1.84	0.004	0.51
50 %	50	0.53	0.004	0.51

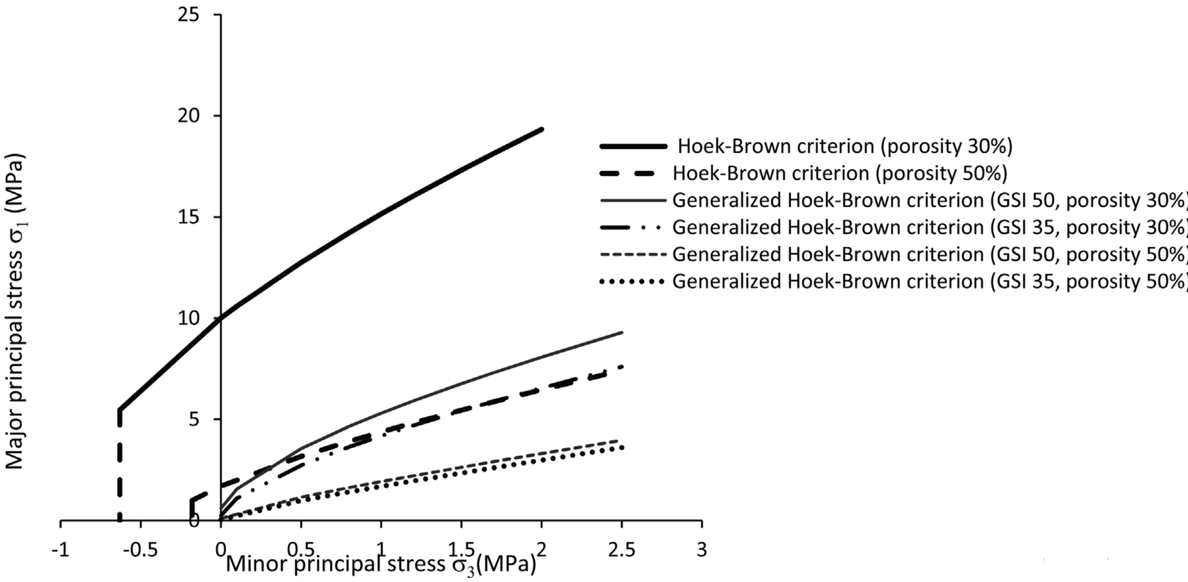

Figure 11. Generalized Hoek-Brown criterion associated to U3 rock for two porosity values.

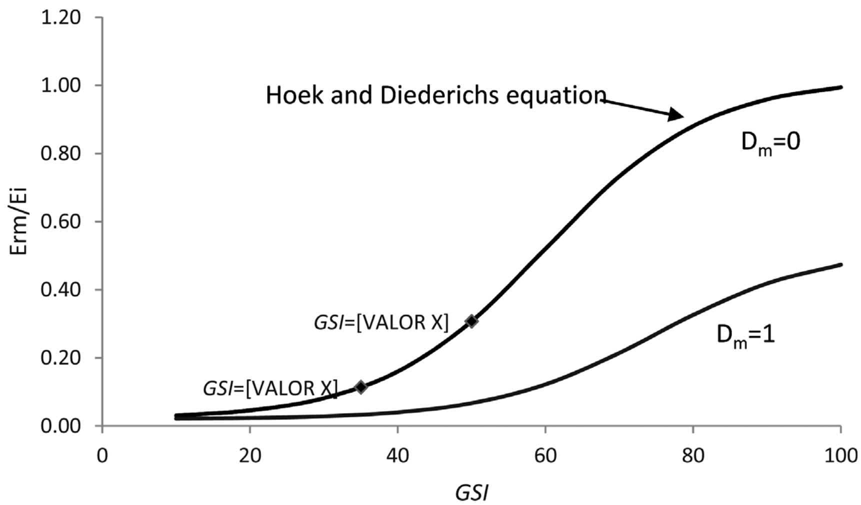

Figure 12. In-situ U3 rock mass deformation modulus for two porosity (35 % and 50 %) for two levels of perturbation (D_m = 0 without recent excavation, D_m = 1 taking into account a certain significant recent human action on the caves).

5. Conclusion

The study aimed to characterize physical and mechanical properties, compression and shear Strength, of rocks of the monument of Elhaouria caves. Therefore, physical and mineralogical characteristics along with compression and triaxial tests were conducted on sandy limestone rock samples obtained from blocks from outside of the caves structure (without any deterioration of the caves). The samples of sandy limestone rock were mainly considered as undistributed. Experimental results showed the important influence of porosity on both compression and shear strengths. Compression strength varied from 13 MPa for 33 % porosity to 1.5 MPa for 50 % porosity. Therefore, both elastic static modulus and dynamic elastic modulus, were determined from Ultrasonic tests, depending on porosity. Their values significantly decreased with the increase of porosity. Concerning the volumetric behavior computed using measured principal strains, role of porosity was well highlighted. For example, a contractive behavior was well noted for a porosity of 50 %, for different confining stresses. Obtained results confirmed the soft rock character of U3 layer. Therefore, shear strength criterion obtained by the Generalized Hoek-Brown approach, showed low values of the compression and shear Strengths, especially for high porosity (50 % in this case). The rock mass modulus was dressed, giving a response similar to results published in Hoek & Diederichs (2006). Even though the authors tested few specimens with a larger range of porosity variation, shear Strength was clearly affected by porosity. Low values of confining stress applied in triaxial experiences can be considered in the range of in-situ confining stresses (of the cave's structures), since the caves are embedded in deposit soil with a depth between 50 cm to 120 cm.

At this stage of modeling, Hoek-Brown model provided an appropriate prediction of soft rock shear criterion for sandy limestone undistributed samples, porosity variation taken into account. However, for in situ fractured rocks belonging to the caves structure, generalized Hoek-Brown model was proposed, integrating the data recently summarized in "The Hoek-Brown failure criterion and *GSI*- 2018 edition". This compression and shear criterion could be used now for any monitoring technique design. Furthermore, the associated elastoplastic model could be considered as a tool to follow the displacement field of the caves structure. Such monitoring could also help to provide efficient improvement techniques that would enhance the safety of this historic monument.

References

AFNOR NF P94-054. (1991). Roches - Détermination de la Résistance à la Compression Uniaxiale. *AFNOR - Association Française de Normalisation, Paris* (in French).

AFNOR NF P94-411. (2002). Roches - Détermination de la Vitesse de Propagation des Ondes Ultrasonores en Laboratoire - Méthode par Transparence. *AFNOR - Association Française de Normalisation, Paris* (in French).

AFNOR NF P94-420. (2000). Sols: Reconnaissance et Essais - Détermination de la Masse Volumique des Particules Solides des Sols - Méthode du Pycnomètre à Eau. *AFNOR - Association Française de Normalisation, Paris* (in French).

ASTM D7012-04. (2004). Standard Test Method for Compressive Strength and Elastic Moduli of Intact Rock Core Specimens under Varying States of Stress and Temperatures. *ASTM International, West Conshohocken, PA*. https://doi.org/10.1520/D7012-04

Al-Omari, A., Beck, K., Brunetaud, X., Török, Á., & Al-Mukhtar, M. (2015). Critical degree of saturation: A control factor of freeze-thaw damage of porous limestones at Castle of Chambord, France. *Engineering Geology*, 185, 71-80.

http://dx.doi.org/10.1016/j.enggeo.2014.11.018

Aldoasri M.A., Darwish S.S., Adam M.A., Elmarzugi N.A., & Ahmed, S.M. (2017). Enhancing the durability of calcareous stone monuments of ancient Egypt using $CaCO_3$ nanoparticles. *Sustainability*, 9(8), 1392. https://doi.org/10.3390/su9081392

Asef, M.R., & Farrokhrouz, M. (2010). Governing parameters for approximation of carbonates. *Electronic Journal of Geotechnical Engineering*, 15, 1581-1592.

Baud, P., lle Kleina, E., & Wongb, T.F. (2004). Compaction localization in porous sandstones: Spatial evolution of damage and acoustic emission activity. *Journal of Structural Geology*, 26(4), 603-624. http://dx.doi.org/10.1016/j.jsg.2003.09.002

Baud, P., Wong, T.F., & Zhu, W. (2014). Effects of porosity and crack density on the compressive strength of rocks. *International Journal of Rock Mechanics and Mining Sciences*, 67, (April 2014), 202-211. http://dxdoiorg /101016/jijrmms201308031

Bosio, J.J., & Kanji, M.A. (1998). Soft rocks of the Rio de la Plata Basin. *Proc. 2nd International Symposium on Indurated Soils and Soft Rocks, Naples*. Balkema, 65-71.

Daoud, H.S., Rashed, K.A., & Alshkane, Y.M. (2017). Correlations of uniaxial compressive strength and modulus of elasticity with point load strength index, pulse velocity and dry density of limestone and sandstone rocks in Sulaimani Governorate, Kurdistan Region, Iraq. *Journal Zankoy Sulaimani Part A (Pure Appl. Sci.)*, 19(3-4), 57-72. https://doi.org/10.1002/2017JB014627

Elliot, G.M., & Brown, E.T. (1985). Yield of a soft, high porosity rock. *Géotechnique*, 35(4), 413-423. https://doi.org/10.1680/geot.1985.35.4.413

Evans, B., Fredrich, J.T., & Wong, T-F. (1990). The brittle-ductile transition in rocks: Recent theoretical and experimental progress. *Geophysical Monograph Series*, 56, 1-20, https://doi.org/10.1029/GM056p0001

Guilloux, A. (2005). Note sur la définition des "sols indurés roches tendres" (SIRT). *Revue Française de Géotechnique*, 111, 59-66 (in French). https://doi.org/10.1051/geotech/2005111059

ISO 5017:2013. (2013). Dense Shaped Refractory Products - Determination of Bulk Density, Apparent Porosity and True Porosity. *ISO - International Organization for Standardization, Geneva*. https://www.iso.org/standard/56179.html

Kanji, M.A. (2014). Critical issues in soft rocks. *Journal of Rock Mechanics and Geotechnical Engineering*, 6(3), 186-195. https://doi.org/10.1016/j.jrmge.2014.04.002

Koubaa, Y., Jamei M., & Guiras H. (2018). Hydro-mechanical properties of highly porous limestone rock used for historic monuments in North-East Tunisia. *Journal of Civil and Environmental Engineering*, 8(3), 1000310. https://doi.org/10.4172/2165-784X.1000310

Harrazi, N. (1995). *Les Carrières Antiques d'el Haouaria: The Ancient Quarries of el Haouaria*. Agence nationale du Patrimoine, Tunis.

Hoek, E., Carranza-Torres, C., & Corkum, B. (2002). Hoek-Brown criterion - 2002 edition. *Proc. 5th North American Rock Mechanics Symposium & 17th Tunnelling Association of Canada Conference, Toronto*. Vol. 1, University of Toronto, 267-273.

Hoek, E., & Diederichs, M.S. (2006). Empirical estimation of rock mass modulus. *International Journal of Rock Mechanics and Mining Sciences*, 43(2), 203-215. http://doi.org/10.1016 /j.ijrmms.2005.06.005

Hoek, E. (2007). *Practical Rock Engineering. E-book version.* Rocscience Editors.

Hoek, E., & Brown, E.T. (2019). The Hoek-Brown failure criterion and GSI-2018 edition. *Journal of Rock Mechanics ang Geotechnical Engineering*, 11(3), 445-463. https://doi.org/10.1016/j.jrmge.2018.08.001

Nicolas, A., Fortin, J., Regnet, J.B., Dimanov, A., & Gueguen, Y. (2016). Brittle and semibrittle behaviours of a carbonate rock: influence of water and temperature. *Geophysical Journal International*, 206(1), 438-456. https://doi.org/10.1093/gji/ggw154

Price, A.M., & Farmer, I.W. (1979). Application of yield models to rock. *International Journal of Rock Mechanics and Mining Sciences & Geomechanics Abstracts*, 16(2), 157-159. https://doi.org/10.1016/0148-9062(79)91454-2

Rahmouni, A., Boulanouar, A., Samaouali, A., Boukalouch, M., Géraud, Y., & Sebbani, J. (2017). Prediction of elastic and acoustic behaviors of calcarenite used for construction of historical monuments of Rabat, Morocco. *Journal of Rock Mechanics and Geotechnical Engineering*, 9(1), 74-83. https://doi.org/10.1016/j.jrmge.2016.11.005

Paskoff, R., & Sanlaville, P. (1983). *Les Côtes de la Tunisie. Variations du Niveau Marin Depuis le Tyrrhénien*. Collection de la Maison de l'Orient et de la Méditerranée Jean Pouilloux, 14(1). ERA 345 du CNRS (in French).

Romero, E. (1999). *Characterization and thermo-hydromechanical behavior of unsaturated boom clay* [Doctoral thesis, Polytechnic University of Catalonia]. Polytechnic University of Catalonia's repository. http://hdl.handle.net/2117/93536

Yu, S., & Oguchi, C.T. (2010). Role of pore size distribution in salt uptake, damage, and predicting salt susceptibility of eight types of Japanese building stones. *Engineering Geology*, 3(115), 226-236. http://dx.doi.org/10.1016/j.enggeo.2009.05.007

Zuo, J.P., Li, H.T., Xie, H.P., Ju, Y., & Peng, S.P. (2008). A nonlinear strength criterion for rock like materials based on fracture mechanics. *International Journal of Rock Mechanics and Mining Sciences*, 45(4), 594-599. https://doi.org/10.1016/j.ijrmms.2007.05.010

Zuo, J.P., Liu, H., & Li, H. (2015). A theoretical derivation of the Hoek-Brown failure criterion for rock materials. *Journal of Rock Mechanics and Geotechnical Engineering*, 7(4), 361-366. https://doi.org/10.1016/j.jrmge.2015.03.008

SOILS and ROCKS
An International Journal of Geotechnical and Geoenvironmental Engineering
Publication of
ABMS - Brazilian Association for Soil Mechanics and Geotechnical Engineering
SPG - Portuguese Geotechnical Society
Volume 43, N. 4, October-December 2020

Author index

Abbaszadeh, Javad 521
Abreu, A.V. 287
Almeida, M.C.F. 219
Almeida, M.S.S. 287, 535
Andrade, H.M.C. 535
Arêdes, A.C.N.B. 85
Assis, A.P. 171, 311, 591
Assis, L.E. 57
Augusto Filho, O. 71
Baldovino, Jair de Jesús Arrieta 631
Bicalho, K.V. 103
Bilfinger, Werner 397
Bobet, A. 123
Bonan, V.H.F. 11
Borges, J.L. 199
Borges, R.G. 219
Boscov, Maria Eugenia Gimenez 461
Boufarh, R. 247
Bragagnolo, L. 159, 279
Braun, A.B. 97
Bressani, L.A. 31
Campos, Tácio de 647
Carneiro, Andressa de Araujo 679
Carvalho, L.O. 607
Carvalho, T.R.R. 297
Casagrande, Michéle Dal Toé 679
Celestino, T.B. 123
Cirone, Alessandro 647
Clemente, C.W. 661
Consoli, Nilo Cesar 159, 339, 669
Craig, A.M.L. 71
Cui, Y.X. 43
da Silva, J. Lins 231
Dantas Neto, Silvrano Adonias 575
de Freitas, A.C. 3, 141
Debbab, O.Y. 181
Dias Neto, S.L.S. 271
Domiciano, M.L. 231
Donato, M. 151
Dong, J.G. 21
dos Santos, L. F. 3, 141
Dzialoszynski, B.S. 369
Ehrlich, M. 419
Faro, V.P. 661
Favretto, J. 151
Ferrazzo, S.T. 279
Ferreira, S.R.M. 191
Festugato, Lucas 339
Flores, J.A. 31
Floss, M.F. 151
Fontoura, T.B. 263
Freitas Neto, O. 263
Fucale, S. 191
García, Julián Buriticá 591
Ghassem, Ali 521
Guiras, Houda 693
Gusmão, Alexandre Duarte 441
Gutierrez, Nelcí Helena Maia 619
Hachich, W.C. 497
Heidemann, M. 31
Hemsi, Paulo Scarano 461
Hisatugu, W.H. 103
Hou, T.S. 43
Izzo, Ronaldo Luis dos Santos 631
Jamei, Mehrez 693
Koobaa, Yousr 693
Korf, E.P. 159, 279
Kuang, Du-min 567
Laouar, M.S. 247
Leão, M.F. 297
Leite, Ana Raquel Sena 575
Lima, C.A. 57
Lima, D.C. 271
Lira, Bruna Silveira 549
Liu, J.L. 43
Long, Zhi-lin 567
Lopes, Ma.B. 171
Luiz, Augusto Montor de Freitas 619
Luo, Y.S. 43
Machado, S.L. 535
Marques, E.A.G. 57, 85, 297
Melchior Filho, J. 11
Mello, L.G.F.S. 369
Mello, Luiz Guilherme de 397
Menezes, S.J.M.C. 57
Messad, A. 181
Miguel, G.D. 151, 339
Mirmoradi, S.H. 419
Moncada, M.P.H. 661
Moreira, Eclesielter Batista 339
Moura, A.S. 11
Moussai, B. 181
Nascimento, G. 419
Nóbrega, Edilza Rakel 549
Oliveira Filho, A.G. 103
Oliveira, A.H.C. 85
Pak, Ali 521
Palmeira, Ennio M. 351
Pitanga, H.N. 271
Prestes, E. 279
Prietto, P.D.M. 159, 279
Ribeiro, D.B. 607
Roque, L.A. 57
Rose, Juliana Lundgren 631
Saadi, D. 247
Sacco, Rafael Luís 669
Sales, Maurício Martines 441
Santos Junior, Olavo Francisco dos 263, 549
Santos, E.C.G. 231
Santos, Gustavo Clementino 549
Santos, R.M. 199
Saraiva, A. 141
Scheuermann Filho, Hugo Carlos 669
Schnaid, F. 369
Silva, A.C. 191, 441
Silva, T.O. 271
Silva, W.G. 271
Silvani, Carina 549
Silveira, A.A. 159
Soares de Almeida, M.S. 219
Sousa, Maria Natália de Melo 549
Souza Junior, L.O. 219
Souza Junior, P.L. 263
Thomé, A. 97
Tímbola, R.S. 279
Totola, L.B. 103
Trentin, A.W.S. 97
Trindade, T.P. 271
Ulsen, C. 159
Vardé, Oscar A. 503
Vargas Jr., Eurípedes 647
Vargas, G.D.L.P. 279
Villacreses, Juan P. 591
Visentin, C. 97
Vitali, O.P.M. 123
Wang, Jie 567
Wei, G.F. 21
Wolle, Claudio Michael 397
Yu, Piao-yi 567
Zhou, Xu-tong 567

Conheça mais:
www.geobrugg.com/pt/taludes

GEOBRUGG®
BRUGG
Safety is our nature

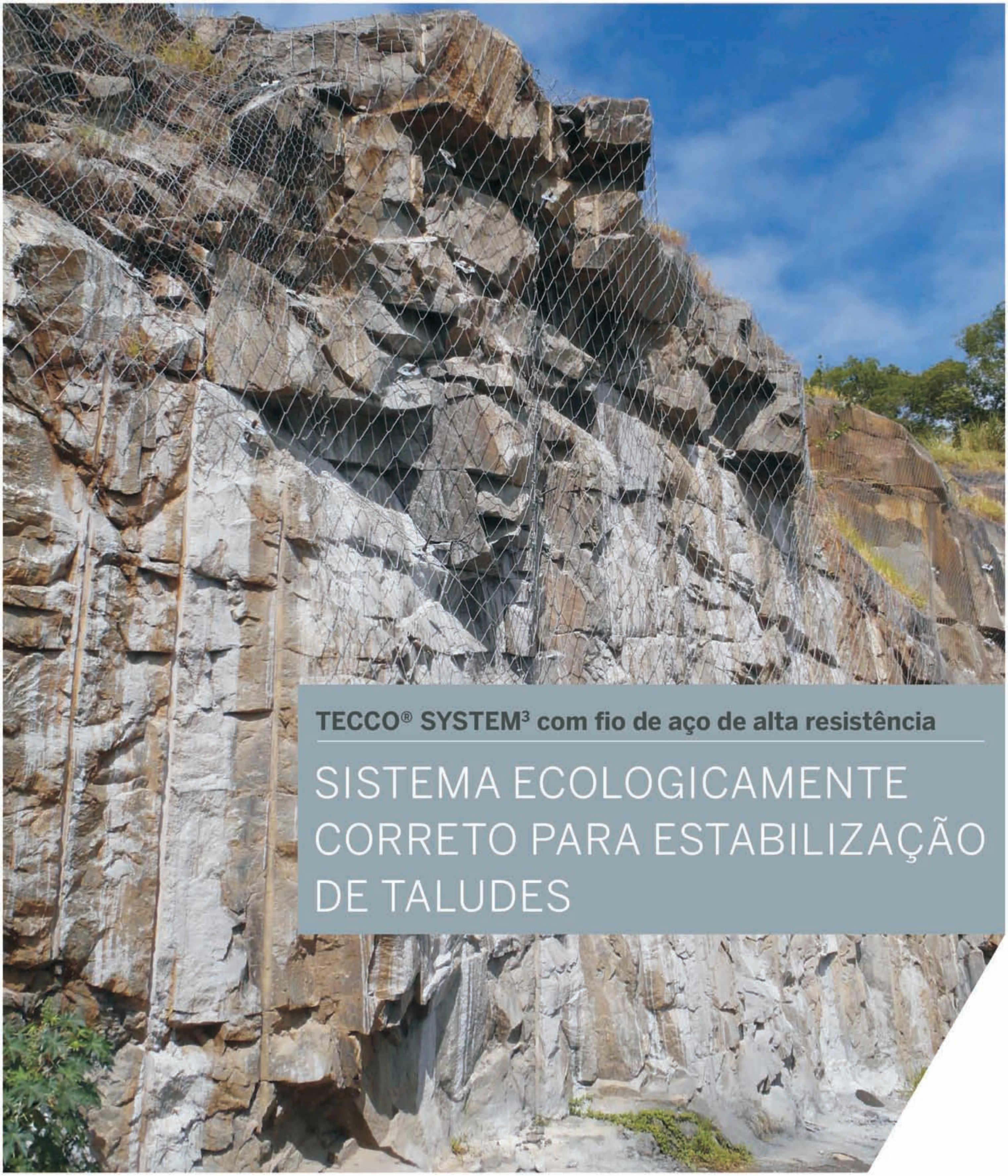

Geobrugg AG | Rua Visconde de Pirajá, 82 sl.606 | 22410-003 - Rio de Janeiro, Brasil | Phone + 55 21 3624 1449 | www.geobrugg.com | info@geobrugg.com

Instructions for Submission of Manuscripts

Category of the Papers

Soils and Rocks is the international scientific journal edited by the Brazilian Association for Soil Mechanics and Geotechnical Engineering (ABMS) and the Portuguese Geotechnical Society (SPG). The aim of the journal is to publish (in English) original research and technical works on all geotechnical branches.

According to its content the accepted paper is classified in one of the following categories: Article paper, Technical Note, Case Study or Discussion. An article paper is an extensive and conclusive dissertation about a geotechnical topic. A paper is considered as a technical note if it gives a short description of ongoing studies, comprising partial results and/or particular aspects of the investigation. A case study is a report of unusual problems found during the design, construction or the performance of geotechnical projects. A case study is also considered as the report of an unusual solution given to an ordinary problem. The discussions about published papers, case studies and technical notes are made in the Discussions Section.

When submitting a manuscript for review, the authors should indicate the category of the manuscript, and is also understood that they:

a) assume full responsibility for the contents and accuracy of the information in the paper;

b) assure that the paper has not been previously published, and is not being submitted to any other periodical for publication.

Manuscript Instructions

Manuscripts must be written in English. The text is to be typed in a word processor (preferably MS Word), **single column**, using ISO A4 page size, left, right, top, and bottom margins of 25 mm, Times New Roman 12 font, and line spacing of 1.5. All lines and pages should be numbered. The text should be written in the third person.

The first page of the manuscript must include the title of the paper followed by the names of the authors with the abbreviation of the most relevant academic title. The affiliation, address and e-mail must appear below each author´s name. An abstract of 200 words follows after the author´s names. A list with up to six keywords at the end of the abstract is required.

Although variations on the sequence and title of each section are possible, it is suggested that the text contains the following sections: Introduction, Material and Methods, Results, Discussions, Conclusions, Acknowledgements, References and List of Symbols. A brief description of each section is given next.

Introduction: This section should indicate the state of the art of the problem under evaluation, a description of the problem and the methods undertaken. The objective of the work should be clearly presented at the end of the section.

Materials and Methods: This section should include all information needed to the reproduction of the presented work by other researchers.

Results: In this section the data of the investigation should be presented in a clear and concise way. Figures and tables should not repeat the same information.

Discussion: The analyses of the results should be described in this section.

Conclusions: The content of this section should be based on the data and on the discussions presented.

Acknowledgenments: If necessary, concise acknowledgements should be presented in this section.

References: References to other published sources must be made in the text by the last name(s) of the author(s), followed by the year of publication, similarly to one of the two possibilities below:

...while Silva & Pereira (1987) observed that resistance depended on soil density... or *It was observed that resistance depended on soil density (Silva & Pereira, 1987).*

In the case of three or more authors, the reduced format must be used, *e.g.*: Silva *et al.* (1982) or (Silva *et al.*, 1982). Two or more citations belonging to the same author(s) and published in the same year are to be distinguished with small letters, *e.g.*: (Silva, 1975a, b, c.). Standards must be cited in the text by the initials of the entity and the year of publication, *e.g.*: ABNT (1996), ASTM (2003).

Full references shall be listed alphabetically at the end of the text by the first author´s last name. Several references belonging to the same author shall be cited chronologically. Some examples are listed next:

Papers: Bishop, A.W. & Blight, G.E. (1963). Some aspects of effective stress in saturated and unsaturated soils. Geotechnique, 13(2):177-197.

Books: Lambe, T.W. & Whitman, R.V. (1979). Soil Mechanics, SI Version. John Wiley & Sons, New York, 553 p.

Book with editors: Sharma, H.D.; Dukes, M.T. & Olsen, D.M. (1990). Field measurements of dynamic moduli and Poisson's ratios of refuse and underlying soils at a landfill site. Landva, A. & Knowles, G.D. (eds), Geotechnics of Waste Fills - Theory and Practice, American Society for Testing and Materials - STP 1070, Philadelphia, pp. 57-70.

Proceedings (printed matter or CD-ROM): Jamiolkowski, M.; Ladd, C.C.; Germaine, J.T. & Lancellotta, R. (1985). New developments in field and laboratory testing of soils. Proc. 11th Int. Conf. on Soil Mech. and Found. Engn., ISSMFE, San Francisco, v. 1, pp. 57-153. (specify if CD ROM).

Thesis and dissertations: Lee, K.L. (1965). Triaxial Compressive Strength of Saturated Sands Under Seismic Loading Conditions. PhD Dissertation, Department of Civil Engineering, University of California, Berkeley, 521 p.

Standards: ASTM (2003). Standard Test Method for Particle Size Analysis of Soils - D 422-63. ASTM International, West Conshohocken, Pennsylvania, USA, 8 p.

Internet references: Soils and Rocks available at http://www.abms.com.br and downloaded on August 6th 2003.

On line first publications must also bring the digital object identifier (DOI) at the end.

Figures shall be either computer generated or drawn with India ink on tracing paper. Computer generated figures must be accompanied by the corresponding digital file (.tif, .jpg, .pcx, etc.). All figures (graphs, line drawings, photographs, etc.) shall be numbered consecutively and have a caption consisting of the figure number and a brief title or description of the figure. This number should be used when referring to the figure in text. Photographs should be black and white, sharp, high contrasted and printed on glossy paper.

Tables shall be numbered consecutively in Arabic and have a caption consisting of the table number and a brief title. This number should be used when referring to the table in the text. Units should be indicated in the first line of the table, below the title of each column. Acronyms should be avoided. When applicable, the units should come right below the corresponding column heading. Additional comments can be placed as footnotes.

Equations shall appear isolated in a single line of the text. Numbers identifying equations must be flushed with the right margin. International System (SI) units must be used. The definitions of the symbols used in the equations must appear in the List of Symbols. It is recommended that the symbols used are in accordance with Lexicon in 8 Languages, ISSMFE (1981) and the ISRM List of Symbols.

The text of the submitted manuscript (including figures, tables and references) intended to be published as an article paper or a case history should not contain more than 30 pages, formatted according to the instructions mentioned above. Technical notes and discussions should have no more than 15 and 8 pages, respectively. Longer manuscripts may be exceptionally accepted if the authors provide proper explanation for the need of the required extra space in a cover letter.

Discussion

Discussions must be written in English. The first page of a discussion should contain:

The title of the paper under discussion;

Name of the author(s) of the discussion, followed by their position, affiliation, address and e-mail. The author(s) of the discussion should refer to himself (herself/themselves) as the reader(s) and to the author(s) of the paper as the author(s).

Figures, tables and equations should be numbered following the same sequence of the original paper. All instructions previously mentioned for the preparation of article papers, case studies and technical notes also apply to the preparation of discussions.

Editorial Review

Each paper will be evaluated by reviewers selected by the editors according to the subject of the paper. The authors will be informed about the results of the review process. If the paper is accepted, the authors will be required to submit a version of the revised manuscript with the suggested modifications. If the manuscript is rejected for publication, the authors will be informed about the reasons for rejection. In any situation comprising modification of the original text, classification of the manuscript in a category different from that proposed by the authors, or rejection, the authors can reply presenting their reasons for disagreeing with the reviewer comments.

Submission

The author(s) must upload a digital file of the manuscript to the Soils and Rocks website.

Follow Up

The online management system will provide a password to the corresponding author, which will enable him/her to follow the reviewing process of the submitted manuscript at the Soils and Rocks website.

SOILS and ROCKS
An International Journal of Geotechnical and Geoenvironmental Engineering

Volume 43, N. 4, October-December 2020

LECTURE

Lessons learned from dam construction in Patagonia Argentina 503
Oscar A. Vardé

ARTICLES

Evaluation of the accuracy of the cubic law for flow through fractures using Lattice Boltzmann method 521
Ali Ghassem, Javad Abbaszadeh, Ali Pak

The influence of the fluid dielectric constant on the shear strength of a unsaturated soil 535
M.S.S. Almeida, S.L. Machado, H.M.C. Andrade

Mass movements in the Northeast region of Brazil: a systematic review 549
Bruna Silveira Lira, Maria Natália de Melo Sousa, Olavo Francisco dos Santos Junior, Carina Silvani, Edilza Rakel Nóbrega, Gustavo Clementino Santos

Experimental study on particle size effect on mechanical behaviour of dense calcareous sand 567
Du-min Kuang, Zhi-lin Long, Jie Wang, Xu-tong Zhou, Piao-yi Yu

A predictive model for the peak shear strength of infilled soft rock joints developed with a multilayer perceptron 575
Ana Raquel Sena Leite, Silvrano Adonias Dantas Neto

Behavioral evaluation of earth dams built with materials above optimum moisture contentin high rainfall areas 591
Julián Buriticá García, André Pacheco de Assis, Juan P. Villacreses

Application of kernel k-means and kernel x-means clustering to obtain soil classes from cone penetration test data 607
L.O. Carvalho, D.B. Ribeiro

Geostatistical data analysis of the Standard Penetration Test (SPT) conducted in Maringá-Brazil and correlations with geomorphology 619
Augusto Montor de Freitas Luiz, Nelcí Helena Maia Gutierrez

Advances on dosages for cement stabilized rammed Guabirotuba silt depending on climate conditions 631
Jair de Jesús Arrieta Baldovino, Ronaldo Luis dos Santos Izzo, Juliana Lundgren Rose

Constitutive modeling of residual soils based on irreversible strains decomposition 647
Alessandro Cirone, Eurípedes Vargas Jr., Tácio de Campos

TECHNICAL NOTES

Determination of liquid limit by the Fall Cone method 661
C.W. Clemente, V.P. Faro, M.P.H. Moncada

The effect of grain size of ground glass particles on the strength of green stabilized sand 669
Hugo Carlos Scheuermann Filho, Rafael Luís Sacco, Nilo Cesar Consoli

Mechanical and environmental performance of polymer stabilized iron ore tailings 679
Andressa de Araujo Carneiro, Michéle Dal Toé Casagrande

CASE STUDY

Compression and shear strengths of sandy limestone and the role of the porosity: a case study 693
Yousr Koobaa, Houda Guiras, Mehrez Jamei